

**ISTANBUL TECHNICAL UNIVERSITY★FACULTY OF MINES**

**GRADUATION DESIGN PROJECT**

**Berat Tuğberk Günel 050210724**

**Enis Kırca 050190407**

**Defne Acar 050180458**

**Abdulkadir Sarıoğlu 050180454**

**Yusuf Sinan Şahin 050190429**

**Department of Petroleum and Natural Gas Engineering**

**June 24**



**LORD OF THE RIGS PETROLEUM COMPANY**

Berat Tuğberk Günel 050210724, Enis Kırca 050190407, Defne Acar 050180458, Abdulkadir Sarıoğlu 050180454, Yusuf Sinan Şahin 050190429 Undergraduate students of Istanbul Technical University Faculty of Mines Petroleum and Natural Gas Engineering Department successfully presented the graduation design project entitled “FIELD DEVELOPMENT, A CASE STUDY”, which he/she/they prepared after fulfilling the requirements specified in the associated legislations, before the jury whose signatures are below.

**Head of Department:**      **Prof. Dr. Ömer İnanç TÜREYEN**

**Jury Members:**            **Prof. Dr. Ömer İnanç TÜREYEN**

**Prof. Dr. Gürsat ALTUN**

**Assoc. Prof. Dr. Hasan Özgür YILDIZ**

**Assist. Prof. Dr. E. Didem Korkmaz BAŞEL**

**Assist. Prof. Dr. İ. Metin MIHÇAKAN**

**Assist. Prof. Dr. İ. Burak KULGA**

**Assist. Prof. Dr. Şenol YAMANLAR**

**Assist. Prof. Dr. Yıldırıay PALABIYIK**

**Date of Submission : 13 June 2024**

**Date of Presentation : 10 June 2024**

## **FOREWORD**

At the very beginning of our study, we encountered various inconveniences owing to missing data in the log and production records of the 25 wells located in the Mount Doom Oil Field between the years of 1988 and 2013. However, thanks to being goal oriented and having the same vision, we carried out the studies meticulously. Throughout the process, we understood the importance of teamwork and collective effort.

As Lords of the Rigs Company, we would like to thank each person of the ITU Petroleum and Natural Gas Department for their encouragement and inspiration along this journey.

We would also like to thank [omnicalculator.com](http://omnicalculator.com) for providing ease with geothermal gradient calculations, Python programming language, and RUBIS simulation software developed by KAPPA Engineering for helping to read and illustrate the well log graphs, constructing and running various simulations, and Surfer for the reservoir's three-dimensional representations. We hope that our research will serve as an inspiration to the petroleum and natural gas industries, as well as future generations.

Best Regards,

June 2024

Lord of the Rigs Company

## TABLE OF CONTENTS

	<u>Page</u>
<b>FOREWORD.....</b>	ii
<b>TABLE OF CONTENTS.....</b>	iv
<b>LIST OF TABLES .....</b>	xiii
<b>LIST OF FIGURES .....</b>	xix
<b>ABBREVIATIONS .....</b>	xxix
<b>SYMBOLS .....</b>	xxxiv
<b>ABSTRACT.....</b>	1
<b>ÖZET.....</b>	li
<b>1. INTRODUCTION.....</b>	1
<b>2. FORMATION EVALUATION .....</b>	4
2.1. Wireline Logs .....	4
2.1.1. Calliper logs .....	4
2.1.2. Gamma ray logs .....	6
2.1.2.1. volume of shale estimation .....	7
2.1.3. Spontaneous potential logs.....	8
2.2. Resistivity Logs.....	10
2.2.1. Use of resistivity logs.....	11
2.2.2. Potential hydrocarbon zones .....	11
2.2.3. Invaded zone .....	11
2.2.4. Potential water zones.....	12
2.2.5. Shale zones.....	12
2.3. Porosity Logs.....	13
2.3.1. Density log .....	13
2.3.2. Neutron log .....	14

2.3.3.	Sonic log .....	15
2.3.4.	Interpreting the combination of porosity logs .....	16
<b>3.</b>	<b>METHODOLOGY.....</b>	<b>17</b>
3.1.	Reservoir Identification .....	18
3.1.1.	Hydrocarbon reservoir .....	20
3.1.2.	Water reservoir.....	20
3.2.	Volume of Shale Estimation.....	20
3.3.	Lithology Identification.....	21
3.4.	Porosity Estimation .....	21
3.5.	Estimation of Saturation Levels .....	21
3.5.1.	Temperature variation with elevation .....	22
3.5.2.	Estimation of water saturation .....	22
3.5.3.	Estimation of invaded zone saturation .....	25
3.5.4.	Estimation of oil saturation .....	26
3.6.	Estimation of Permeability .....	27
3.7.	Determination of Cut-Off Values .....	28
3.8.	Estimation of Hydrocarbon Mobility Index .....	29
3.9.	Estimation of Net to Gross Ratio .....	30
<b>4.</b>	<b>WELL LOG ANALYSIS.....</b>	<b>31</b>
4.1.	Analysis of Well-14.....	32
4.1.1.	Reservoir identification .....	32
4.1.2.	Volume of shale estimation.....	33
4.1.3.	Lithology identification.....	35
4.1.4.	Porosity estimation.....	35
4.1.5.	Estimation of saturation levels .....	36
4.1.6.	Determination of cut-off values .....	37

4.1.7.	Estimation of net to gross ratio .....	39
4.1.8.	Estimation of hydrocarbon mobility index .....	39
4.1.9.	Estimation of recovery factor.....	39
4.2.	Analysis of Well-01.....	41
4.2.1.	Reservoir identification.....	41
4.2.2.	Volume of shale estimation.....	42
4.2.3.	Lithology identification.....	43
4.2.4.	Porosity estimation.....	43
4.2.5.	Estimation of saturation levels .....	43
4.2.6.	Determination of cut-off values .....	44
4.2.7.	Estimation of net to gross ratio .....	44
4.2.8.	Estimation of hydrocarbon mobility index .....	44
4.2.9.	Estimation of recovery factor.....	44
4.3.	Analysis of Well-18.....	46
4.3.1.	Reservoir identification.....	46
4.3.2.	Volume of shale estimation.....	46
4.3.3.	Lithology identification.....	48
4.3.4.	Porosity estimation.....	48
4.3.5.	Estimation of saturation levels .....	51
4.3.6.	Determination of cut-off values .....	51
4.3.7.	Estimation of net to gross ratio .....	52
4.3.8.	Estimation of hydrocarbon mobility index .....	52
4.3.9.	Estimation of recovery factor.....	52
<b>5.</b>	<b>MODEL OF THE RESERVOIR.....</b>	<b>54</b>
<b>6.</b>	<b>RESERVES ESTIMATION.....</b>	<b>55</b>
<b>7.</b>	<b>MECHANICAL EARTH MODEL .....</b>	<b>61</b>

7.1.	Target.....	61
7.2.	Preparation for the Modelling .....	62
7.3.	Dynamic Shear Modulus .....	66
7.4.	Dynamic Bulk Modulus .....	67
7.5.	Dynamic Young's Modulus .....	67
7.6.	Dynamic Poisson's Ratio .....	67
7.7.	Internal Friction Angle .....	68
7.8.	Overburden Stress .....	68
7.9.	Pore Pressure .....	69
7.10.	Formation Fracture Pressure.....	70
7.10.1.	Eaton's fracture pressure estimation .....	71
7.10.2.	Modified Kelly and Matthew's fracture pressure estimation.....	72
7.11.	Results And Discussion .....	73
<b>8.</b>	<b>CASING DESIGN.....</b>	<b>80</b>
8.1.	Casing And Bit Sizes.....	81
8.2.	Surface Casing.....	82
8.2.1.	Burst design.....	83
8.2.2.	Collapse design .....	84
8.3.	Production Casing .....	87
8.3.1.	Burst design.....	87
8.3.2.	Collapse design .....	89
8.4.	Casing Selection, Tension Design and Collapse Correction .....	90
8.5.	Casing Landing.....	100
<b>9.</b>	<b>CEMENT DESIGN.....</b>	<b>105</b>
9.1.	Conductor Stage .....	108
9.2.	Surface Stage .....	109

9.3. Production Stage.....	<b>110</b>
<b>10. DRILL STRING DESIGN .....</b>	<b>113</b>
10.1. Bottom Hole Assembly (BHA) Design .....	<b>114</b>
10.2. Tension.....	<b>120</b>
10.2.1. Drill string design where only axial stress is taken into account .....	<b>120</b>
10.2.2. Drill string design that takes pressure-related stress into account ....	<b>122</b>
10.3. Buckling.....	<b>125</b>
10.3.1. Drill string design that takes buckling into account.....	<b>125</b>
10.3.2. Make-up torque .....	<b>126</b>
10.4. Bending.....	<b>128</b>
10.4.1. String design, existance of bending with dog-leg scenarios .....	<b>128</b>
10.5. Neutral Point .....	<b>130</b>
10.6. Shock Loading .....	<b>132</b>
10.7. Amount of Elongation of The Suspended Drill String .....	<b>133</b>
10.8. Stabilizer Design.....	<b>133</b>
10.9. Drilling Jar Selection .....	<b>135</b>
<b>11. DRILLING FLUID DESIGN.....</b>	<b>136</b>
11.1. Rheological Models .....	<b>138</b>
11.1.1. Bingham Plastic model .....	<b>138</b>
11.1.2. Herschel-Bulkley model.....	<b>140</b>
11.1.3. Selection of the rheology model .....	<b>143</b>
11.2. Cutting Transport.....	<b>144</b>
<b>12. DRILLING HYDRAULICS OPTIMIZATION.....</b>	<b>152</b>
12.1. Surface Stage .....	<b>156</b>
12.2. Production Stage .....	<b>158</b>
<b>13. FIELD DESIGN .....</b>	<b>163</b>

13.1.	Rig Selection.....	<b>163</b>
13.2.	Drawworks Selection.....	<b>165</b>
13.3.	Mud Pit Selection.....	<b>166</b>
13.4.	Wellhead Construction .....	<b>168</b>
13.4.1.	Blowout preventer .....	<b>168</b>
13.4.2.	Christmas tree.....	<b>169</b>
<b>14.</b>	<b>DRILING COST ANALYSIS .....</b>	<b>171</b>
14.1.	General Expenses.....	<b>172</b>
14.2.	Rate of Penetration Estimation .....	<b>173</b>
14.3.	Construction of Scenarios.....	<b>177</b>
14.3.1.	Worst-case scenario .....	<b>177</b>
14.3.2.	Middle-case scenario.....	<b>179</b>
14.3.3.	Best-case scenario .....	<b>181</b>
14.4.	Statistical Model .....	<b>184</b>
14.5.	Results.....	<b>187</b>
<b>15.</b>	<b>RESERVOIR ENGINEERING .....</b>	<b>189</b>
15.1.	Required Parameters for the Havlena and Odeh Straight Line Approach 189	
15.2.	Havlena and Odeh Straight Line Approach.....	<b>196</b>
15.3.	Reservoir Simulation Input Parameters .....	<b>200</b>
15.4.	Reservoir Model and History Matching .....	<b>206</b>
15.5.	Results and Discussion .....	<b>211</b>
15.6.	Conclusion .....	<b>213</b>
<b>16.</b>	<b>ESTIMATION OF GAS PROPERTIES .....</b>	<b>214</b>
16.1.	Dranchuk and Abou-Kassem (DAK) Z-Factor Correlation .....	<b>214</b>
16.2.	Lee, Gonzalez, and Eakin (LGS) Gas Viscosity Correlation .....	<b>217</b>

16.3.	Matching the Specific Gravity of the Associated Gas .....	<b>217</b>
<b>17.</b>	<b>SIMULATION FORECASTS AND FIELD DEVELOPMENT PLANS</b>	
	<b>219</b>	
17.1.	Base Scenario.....	<b>221</b>
17.2.	Project: Watcher In the Water .....	<b>225</b>
17.3.	Project: Deflate The Smaug.....	<b>233</b>
17.4.	Project: One Rig to Drill Them All .....	<b>237</b>
17.5.	Final Decision on the Development.....	<b>242</b>
<b>18.</b>	<b>PRODUCTION ENGINEERING: SEPARATORS</b>	<b>245</b>
18.1.	Separator Types .....	<b>245</b>
18.1.1.	Vertical separators.....	<b>246</b>
18.1.2.	Horizontal separators .....	<b>246</b>
18.1.3.	Spherical separators .....	<b>248</b>
18.2.	Two-Phase Separator Design Theory .....	<b>249</b>
18.2.1.	The common separator parts .....	<b>251</b>
18.2.1.1.	inlet divertor section .....	<b>251</b>
18.2.1.2.	liquid collection section .....	<b>251</b>
18.2.1.3.	Gravity settling section .....	<b>252</b>
18.2.1.4.	Mist extractor section.....	<b>252</b>
18.2.2.	Settling velocity .....	<b>253</b>
18.2.3.	Droplet size .....	<b>254</b>
18.2.4.	Gas capacity .....	<b>255</b>
18.2.5.	Liquid capacity .....	<b>255</b>
18.2.6.	Seam-to-seam length.....	<b>256</b>
18.3.	Two-Phase Separator Design Result.....	<b>257</b>
18.4.	Three-Phase Separator Design Theory .....	<b>260</b>

18.4.1.	Oil-water settling.....	260
18.4.2.	Retention time .....	261
18.4.3.	Gas capacity .....	262
18.4.4.	Settling water droplets from oil-phase .....	262
18.4.5.	Separating oil droplets from water-phase .....	263
18.4.6.	Seam-to-seam length.....	264
18.4.7.	Slenderness ratio .....	265
18.5.	Three-Phase Separator Design Results .....	265
18.5.1.	Separator for the base scenario .....	266
18.5.2.	Separator for the best-case scenario .....	268
<b>19.</b>	<b>ENVIRONMENTAL AND SOCIAL SUSTAINABILITY .....</b>	<b>272</b>
19.1.	Evaluation of Environmental Impact of Development Scenarios .....	272
19.2.	Evaluation of Social Impact of Development Scenarios .....	278
19.3.	Sustainable Solutions for Future Development .....	280
<b>20.</b>	<b>HSE REGULATIONS .....</b>	<b>282</b>
20.1.	Health and Safety .....	282
20.2.	Environment.....	283
<b>21.</b>	<b>CONCLUSION.....</b>	<b>285</b>
<b>REFERENCES.....</b>		<b>289</b>
<b>APPENDICES .....</b>		<b>297</b>
A.	<b>APPENDIX: Well Log Charts .....</b>	<b>297</b>
B.	<b>APPENDIX: Estimated Petrophysical Properties Summary .....</b>	<b>320</b>
C.	<b>APPENDIX: Estimated Petrophysical Properties and Visualizations.....</b>	<b>327</b>
D.	<b>APPENDIX: Reserves Estimation .....</b>	<b>353</b>
E.	<b>APPENDIX : Mechanical Earth Model .....</b>	<b>375</b>
F.	<b>APPENDIX: Drill String Design .....</b>	<b>378</b>

<b>G. APPENDIX: Drilling Fluid Design.....</b>	<b>388</b>
<b>H. APPENDIX: Drilling Cost Analysis .....</b>	<b>391</b>
<b>I. APPENDIX: Reservoir Engineering .....</b>	<b>395</b>
<b>J. APPENDIX: Simulation Forecasts and Field Development Plans .....</b>	<b>402</b>

## LIST OF TABLES

	<u>Page</u>
<b>Table 2.1:</b> Matrix densities of common reservoir rocks (Bassiouni, 1994) .....	<b>14</b>
<b>Table 2.2:</b> Commonly used drilling muds mud filtrate densities (Bassiouni, 1994). ....	<b>14</b>
<b>Table 4.1:</b> Available well log types for each well. Cross marks represent unavailable well logs while the empty cells indicate available ones.....	<b>31</b>
<b>Table 6.1:</b> Total volume of each reservoir layer based on the modelling. ....	<b>56</b>
<b>Table 6.2:</b> OOIP results for each reservoir layer.....	<b>60</b>
<b>Table 6.3:</b> ROIP results for each reservoir layer.....	<b>60</b>
<b>Table 7.1:</b> Target information regarding to Bane-01. ....	<b>61</b>
<b>Table 7.2:</b> Information about casing setting depths, and mud weights that will be used during the drilling operation. ....	<b>78</b>
<b>Table 8.1:</b> Resulted parameters regarding to casings and bit sizes. ....	<b>81</b>
<b>Table 8.2:</b> Commonly used bit sizes for running API casing (Bourgoyn Jr, Millheim, Chenevert , & Young Jr, 1991) .....	<b>82</b>
<b>Table 8.3:</b> Burst pressure load and design lines for the surface casing.....	<b>84</b>
<b>Table 8.4:</b> Collapse pressure load and design lines for the surface casing. ....	<b>86</b>
<b>Table 8.5:</b> Burst pressure load and design lines for the production casing.....	<b>88</b>
<b>Table 8.6:</b> Collapse pressure load and design lines for the production casing.....	<b>90</b>
<b>Table 8.7:</b> Selected casing grades and their properties. ....	<b>91</b>
<b>Table 8.8:</b> Axial tension results for both surface and production casing. ....	<b>91</b>
<b>Table 8.9:</b> Estimated empirical coefficients used for collapse mode determination for each casing. ....	<b>95</b>
<b>Table 8.10:</b> Estimated collapse mode boundaries for each casing grade. ....	<b>96</b>
<b>Table 8.11:</b> Estimated properties for each casing. ....	<b>96</b>
<b>Table 8.12:</b> Final estimated correct collapse, burst pressures, and axial tensions for the surface and production casings. ....	<b>97</b>
<b>Table 8.13:</b> Final casing design properties.....	<b>97</b>
<b>Table 8.14:</b> Calculated axial tension design factors for casings, and couplings. ....	<b>99</b>
<b>Table 8.15:</b> Parameters for the first scenario.....	<b>103</b>
<b>Table 8.16:</b> Parameters for the second scenario.....	<b>103</b>
<b>Table 8.17:</b> The comparison of scenarios.....	<b>104</b>

<b>Table 9.1:</b> MKP-750 model pump motor information.....	<b>108</b>
<b>Table 9.2:</b> Necessary data for the cement operation of the conductor casing.....	<b>109</b>
<b>Table 9.3:</b> The cement operation results of the conductor casing.....	<b>109</b>
<b>Table 9.4:</b> Necessary data for the cement operation of the surface casing.....	<b>110</b>
<b>Table 9.5:</b> The cement operation results of the surface casing.....	<b>111</b>
<b>Table 9.6:</b> Necessary data for the cement operation of the production casing.....	<b>111</b>
<b>Table 9.7:</b> Cementing results of production casing.....	<b>112</b>
<b>Table 10.1:</b> Unit weight on bit and RPM values according to formation type (Özbayoğlu & Altun, 2010). .....	<b>114</b>
<b>Table 10.2:</b> WOB parameters according to each section.....	<b>114</b>
<b>Table 10.3:</b> Drill collar weight data according to drill collar outer diameter and inner diameter (Özbayoğlu & Altun, 2010). .....	<b>115</b>
<b>Table 10.4:</b> Related parameters for the calculation of the drill collar and their results for both sections.....	<b>117</b>
<b>Table 10.5:</b> Drill pipe dimensional data (Özbayoğlu & Altun, 2010). .....	<b>117</b>
<b>Table 10.6:</b> Bending stress ratio results according to inner and outer diameters of drill string design. .....	<b>119</b>
<b>Table 10.7:</b> BHA weight and length results for both sections. ....	<b>120</b>
<b>Table 10.8:</b> Related parameters for the calculation of drill string design where only axial stress is taken into account and their results for both sections.....	<b>122</b>
<b>Table 10.9:</b> Collapse mode and $d_n/t$ results for both sections. ....	<b>124</b>
<b>Table 10.10:</b> Related parameters for the calculation of drill string design that takes pressure-related stress into account and their results for both sections. ....	<b>124</b>
<b>Table 10.11:</b> Related parameters for the calculation of drill string design that takes buckling into account and their results for both sections.....	<b>126</b>
<b>Table 10.12:</b> Parameters according to connection type (Özbayoğlu & Altun, 2010). .....	<b>127</b>
<b>Table 10.13:</b> Tension values occurring in the relevant drill string element cross section according to connection type. ....	<b>127</b>
<b>Table 10.14:</b> Related parameters for the calculation of make-up torque and their results for both sections.....	<b>128</b>

<b>Table 10.15:</b> Related parameters for the calculation of drill string design that takes bending into account applying dog-leg scenarios and their results for both sections.	131
<b>Table 10.16:</b> Related parameters for the calculation of neutral point and their results for both sections .....	132
<b>Table 10.17:</b> Related parameters for the calculation of shock loading and their results for both sections.....	133
<b>Table 10.18:</b> Related parameters for the calculation of the stabilizer design and their results for both sections.....	134
<b>Table 11.1:</b> Rheological properties of the 9.5 ppg KCl/Polymer mud.....	137
<b>Table 11.2:</b> Rheological properties of the 11 pgg KCl/Polymer mud.....	137
<b>Table 11.3:</b> Cutting transport model results for the conductor stage. ....	148
<b>Table 11.4:</b> Cutting transport model results for the surface stage.....	149
<b>Table 11.5:</b> Cutting transport model results for the production stage.....	150
<b>Table 12.1:</b> The set intervals summary for each stage. ....	153
<b>Table 12.2:</b> Frictional pressure losses per foot based on the Bingham Plastic model. .....	156
<b>Table 12.3:</b> Frictional pressure losses per foot based on the Herschel-Bulkley model. .....	156
<b>Table 12.4:</b> Pressure losses of the surface stage for each interval based on the Bingham Plastic model. ....	157
<b>Table 12.5:</b> Pressure losses of the surface stage for each interval based on the Herschel-Bulkley model.....	157
<b>Table 12.6:</b> Optimum operating conditions of the surface stage for each interval based on the Bingham Plastic model. ....	157
<b>Table 12.7:</b> Optimum operating conditions of the surface stage for each interval based on the Herschel-Bulkley model.....	157
<b>Table 12.8:</b> Pressure losses of the production stage for each interval based on the Bingham Plastic model. ....	159
<b>Table 12.9:</b> Pressure losses for the production stage for each interval based on the Herschel-Bulkley model.....	159

<b>Table 12.10:</b> Optimum operating conditions of the production stage for each interval based on the Bingham Plastic model.....	<b>161</b>
<b>Table 12.11:</b> Optimum operating conditions of the production stage for each interval based on the Herschel-Bulkley model.....	<b>162</b>
<b>Table 13.1:</b> Properties of F-200 drilling rig.....	<b>164</b>
<b>Table 13.2:</b> Properties of TESCO 250 EMI 400 Top Drive (250 EMI 400 Top Drive - TESCO Corporation, 2011).....	<b>165</b>
<b>Table 13.3:</b> Properties of TF-25 Drawworks (upet.com, 1991). ....	<b>166</b>
<b>Table 13.4:</b> Specifications and Dimensions of NOV Ideal Mud Pit System (BRANDT™ Ideal Mud Tank System). .....	<b>167</b>
<b>Table 14.1:</b> Cost of power provided for three distinct engines used in the drilling rigs (Marchiano, Meola, Lopez, & Ajayi, 2019).....	<b>172</b>
<b>Table 14.2:</b> Authorization for expenditure table. ....	<b>174</b>
<b>Table 14.3:</b> Assumed parameters for the construction of the worst-case scenario. ....	<b>178</b>
<b>Table 14.4:</b> The estimated trip scheme for the worst-case scenario.....	<b>178</b>
<b>Table 14.5:</b> Assumed parameters for the construction of the middle-case scenario. ....	<b>180</b>
<b>Table 14.6:</b> The estimated trip scheme for the middle-case scenario. ....	<b>181</b>
<b>Table 14.7:</b> The estimated trip scheme for the best-case scenario.....	<b>182</b>
<b>Table 14.8:</b> Assumed parameters for the construction of the best-case scenario....	<b>183</b>
<b>Table 14.9:</b> Assumed parameters, and their corresponding results for each scenario based on the statistical drilling cost prediction. ....	<b>187</b>
<b>Table 14.10:</b> Estimated overall cost for the drilling operation for each scenario. ..	<b>188</b>
<b>Table 15.1:</b> The given properties of the reservoir fluid, and the formation. ....	<b>199</b>
<b>Table 16.1:</b> Regression coefficient for (Eq. 16-1) (Dranchuk & Abou-Kassem, 1975). ....	<b>216</b>
<b>Table 17.1:</b> Economical properties used for the various field development scenarios. ....	<b>219</b>
<b>Table 18.1:</b> Features of impingement type of mist extractors (Arnold & Stewart, 2008). ....	<b>253</b>
<b>Table 18.2:</b> Retention time for two-phase separators (Arnold & Stewart, 2008)...	<b>255</b>

<b>Table 18.3:</b> Calculated parameters for the two-phase separator for the 25-years of production .....	<b>258</b>
<b>Table 18.4:</b> Calculated different design dimensions of two-phase separators for the 25-years of production. ....	<b>259</b>
<b>Table 18.5:</b> The suggest oil retention times based on the field experience (Arnold & Stewart, 2008). .....	<b>262</b>
<b>Table 18.6:</b> Calculated different design dimensions of three-phase separators for the base scenario. ....	<b>267</b>
<b>Table 18.7:</b> Calculated parameters for the three-phase separator for the base scenario. ....	<b>268</b>
<b>Table 18.8:</b> Calculated parameters for the three-phase separator for Project One Rig to Drill Them All.....	<b>270</b>
<b>Table 18.9:</b> Calculated different design dimensions of three-phase separators for Project One Rig to Drill Them All.....	<b>271</b>
<b>Table 19.1:</b> Non-technical and other Causes in field development (Laking & McNicoll, 2013). ....	<b>279</b>
<b>Table B.1:</b> Summary table about lithology. ....	<b>321</b>
<b>Table B.2:</b> Average values of the estimated petrophysical properties. ....	<b>323</b>
<b>Table B.3:</b> Standard deviation values of the estimated petrophysical properties....	<b>325</b>
<b>Table E.1:</b> Mechanical earth model results.....	<b>376</b>
<b>Table E.2:</b> Pressure gradient results from Eaton's and modified Matthew and Kelly's methods. ....	<b>377</b>
<b>Table F.1:</b> Tensile and buckling capacities for a new drill pipe (Özbayoğlu & Altun, 2010). ....	<b>379</b>
<b>Table F.2:</b> Collapse and burst pressure capacities for a new drill pipe (Özbayoğlu & Altun, 2010). ....	<b>380</b>
<b>Table F.3:</b> Related BHA design parameters and their results for both section.....	<b>381</b>
<b>Table F.4:</b> Related parameters for design the drill string and calculations made for both section. ....	<b>382</b>
<b>Table F.5:</b> Drill pipe and related connection type physical properties. ....	<b>384</b>
<b>Table G.1:</b> The cutting transport ratio modelling parameters for the conductor stage. ....	<b>389</b>

<b>Table G.2:</b> The cutting transport ratio modelling parameters for the surface stage.	<b>389</b>
<b>Table G.3:</b> The cutting transport ratio modelling parameters for the production stage.	<b>390</b>
<b>Table H.1:</b> Authorization of Expenditure of the worst-case scenario.....	<b>392</b>
<b>Table H.2:</b> Authorization for Expenditure of the middle-case scenario. ....	<b>393</b>
<b>Table H.3:</b> Authorization for Expenditure of best-case scenario.....	<b>394</b>
<b>Table J.1:</b> Cash flow table for the base scenario.....	<b>403</b>
<b>Table J.2:</b> Cash flow table for Project Watcher in the Water. ....	<b>404</b>
<b>Table J.3:</b> Cash flow table for Project Deflate the Smaug.....	<b>405</b>
<b>Table J.4:</b> Cash flow table for Project One Rig to Drill Them All. ....	<b>406</b>

## LIST OF FIGURES

	<u>Page</u>
<b>Figure 1.1:</b> Map of wells.....	3
<b>Figure 2.1:</b> Borehole environment representation in the presence of mud cake, consolidated, and unconsolidated formations (Serra, 1984). .....	6
<b>Figure 3.1:</b> Cross-plot of neutron porosity for lithologies (Bassiouni, 1994). ....	17
<b>Figure 4.1:</b> Well log display of Well-14. ....	34
<b>Figure 4.2:</b> Lithology determination from NPHI and RHOB. ....	35
<b>Figure 4.3:</b> Resistivity of adjacent shales for Well-14.....	37
<b>Figure 4.4:</b> Determination of cut-off permeability and cut-off effective porosity....	38
<b>Figure 4.5:</b> Cut-off water saturation determination from permeability and water saturation.....	38
<b>Figure 4.6:</b> Well log display of Well-14 along with designated formations.....	40
<b>Figure 4.7:</b> Well log display of Well-01. ....	42
<b>Figure 4.8:</b> Well log display of Well-01 along with designated formations.....	45
<b>Figure 4.9:</b> Well log display of Well-18. ....	47
<b>Figure 4.10:</b> Lithology determination from NPHI and RHOB for Oil-Zone.....	49
<b>Figure 4.11:</b> Lithology determination from NPHI and DT for Oil-Zone.....	49
<b>Figure 4.12:</b> Lithology determination from NPHI and DT for Water-Zone.....	50
<b>Figure 4.13:</b> Lithology determination from NPHI and RHOB for Water-Zone.....	50
<b>Figure 4.14:</b> $R_{sh}$ determination from $V_{sh}$ and deep resistivity. ....	51
<b>Figure 4.15:</b> Well log display of Well-18 along with designated formations.....	53
<b>Figure 6.1:</b> Thickness isopach map of the Precious-1 reservoir layer. ....	57
<b>Figure 6.2:</b> In place reserves per acre isopach for the Precious-1 reservoir layer. ...	57
<b>Figure 6.3:</b> OOIP estimation result for the Precious-1 reservoir layer. ....	59
<b>Figure 6.4:</b> ROIP estimation result for the Precious-1 reservoir layer.....	60
<b>Figure 7.1:</b> 3D model of the Precious-1 reservoir layer.....	62
<b>Figure 7.2:</b> Porosity decline curve for Bane-01. ....	64
<b>Figure 7.3:</b> Bulk density extrapolation result of Miller's method for Bane-01. ....	65
<b>Figure 7.4:</b> Poisson's ratio as a function of depth for various formations, and the acceptable range of the Poisson's ratio (Bourgoyne Jr, Millheim, Chenevert , & Young Jr, 1991).....	75

<b>Figure 7.5:</b> Mechanical earth model and estimated pressure gradients from Eaton's correlation .....	<b>76</b>
<b>Figure 7.6:</b> Mechanical earth model and estimated pressure gradients from modified Matthew and Kelly's correlation.....	<b>77</b>
<b>Figure 7.7:</b> The resulted mud window of the Eaton's method.....	<b>78</b>
<b>Figure 7.8:</b> The resulted mud window of the modified Matthew and Kelly's method.	<b>79</b>
<b>Figure 7.9:</b> The resulted casing, and mud weight program from the Eaton's method.	<b>79</b>
<b>Figure 8.1:</b> Burst pressure criteria for the surface casing. ....	<b>86</b>
<b>Figure 8.2:</b> Burst pressure criteria for the production casing.....	<b>88</b>
<b>Figure 8.3:</b> Collapse pressure criteria for the surface casing. ....	<b>89</b>
<b>Figure 8.4:</b> Collapse pressure criteria for the production casing. ....	<b>94</b>
<b>Figure 8.5:</b> Resulted tension design for the surface and production casings. ....	<b>95</b>
<b>Figure 8.6:</b> Final resulted tension design for the surface and production casings....	<b>98</b>
<b>Figure 8.7:</b> Illustration of the casing design. Constructed by using Halliburton eRed Book (2010). .....	<b>99</b>
<b>Figure 10.1:</b> Geometric representation for BSR calculation (Özbayoğlu & Altun, 2010). .....	<b>118</b>
<b>Figure 11.1:</b> Shear stress and shear rate relationship of Bingham Plastic model (Bourgoyn Jr, Millheim, Chenevert , & Young Jr, 1991). .....	<b>139</b>
<b>Figure 11.2:</b> Shear stress and shear rate relationship of rheological models (Swaco, 1998). .....	<b>141</b>
<b>Figure 11.3:</b> Shear stress vs shear rate curve of 9.5 ppg KCl polymer mud with the 95% confidence interval.....	<b>144</b>
<b>Figure 11.4:</b> The particle slip velocity with respect to the yield point (Darley & Gray, 1983). .....	<b>146</b>
<b>Figure 11.5:</b> The cutting transport efficiencies of different mud types (Darley & Gray, 1983). .....	<b>146</b>
<b>Figure 11.6:</b> The cutting transport ratio modelling for the conductor stage. ....	<b>149</b>
<b>Figure 11.7:</b> The cutting transport ratio modelling for the surface stage.....	<b>150</b>
<b>Figure 11.8:</b> The cutting transport ratio modelling for the production stage. ....	<b>151</b>

<b>Figure 12.1:</b> P-q test result obtained from the Bingham Plastic model for the surface stage.....	<b>158</b>
<b>Figure 12.2:</b> P-q test results obtained from the Herschel-Bulkley model for the surface stage.....	<b>160</b>
<b>Figure 12.3:</b> P-q test result obtained from the Bingham Plastic model for the production stage.....	<b>161</b>
<b>Figure 12.4:</b> P-q test result obtained from the Herschel-Bulkley model for the production stage.....	<b>162</b>
<b>Figure 13.1:</b> BOP and wellhead equipments (Weatherford, 2006).....	<b>170</b>
<b>Figure 14.1:</b> Predicted ROP values as function of depth with its linear regression. Blue shaded parts represent the 95% confidence interval.....	<b>175</b>
<b>Figure 14.2:</b> Estimated cumulative trip times as a function of depth for the worst-case scenario.....	<b>179</b>
<b>Figure 14.3:</b> The predicted ROP values versus predicted cumulative drilling time for the worst-case scenario.....	<b>180</b>
<b>Figure 14.4:</b> The predicted ROP values versus predicted cumulative drilling time for the middle-case scenario.....	<b>182</b>
<b>Figure 14.5:</b> Estimated cumulative trip times as a function of depth for the middle-case scenario.....	<b>183</b>
<b>Figure 14.6:</b> Estimated cumulative trip times as a function of depth for the best-case scenario.....	<b>185</b>
<b>Figure 14.7:</b> The predicted ROP values versus predicted cumulative drilling time for the best-case scenario.....	<b>186</b>
<b>Figure 14.8:</b> Cost per depth relation for each scenario.....	<b>188</b>
<b>Figure 15.1:</b> The formation volume factor of oil behavior with respect to pressure.....	<b>190</b>
<b>Figure 15.2:</b> The solution gas-oil ratio behavior with respect to pressure.....	<b>191</b>
<b>Figure 15.3:</b> The formation volume factor of gas behavior with respect to pressure.....	<b>192</b>
<b>Figure 15.4:</b> Cumulative oil production volume with respect to elapsed month. ...	<b>194</b>
<b>Figure 15.5:</b> Average reservoir pressure reduction along the cumulative oil production.....	<b>194</b>

<b>Figure 15.6:</b> Regression line for the values above the bubble point pressure on the formation volume factor of oil with the 95% confidence interval .....	<b>195</b>
<b>Figure 15.7:</b> Regression line for the values above the bubble point pressure on the formation volume factor of gas with the 95% confidence interval .....	<b>195</b>
<b>Figure 15.8:</b> The cumulative produced gas-oil ratio with respect to the elapsed time. ....	<b>197</b>
<b>Figure 15.9:</b> The Havlena and Odeh straight-line approach reserves estimation for the Precious-1 reservoir layer.....	<b>200</b>
<b>Figure 15.10:</b> The viscosity of oil behaviour with respect to the pressure. ....	<b>201</b>
<b>Figure 15.11:</b> The formation volume factor of gas behavior with respect to the pressure. ....	<b>202</b>
<b>Figure 15.12:</b> The viscosity of gas behaviors with respect to the pressure.....	<b>203</b>
<b>Figure 15.13:</b> The relative permeability curves for oil, and water phases. ....	<b>204</b>
<b>Figure 15.14:</b> The relative permeability curves for oil, and gas phases.....	<b>204</b>
<b>Figure 15.15:</b> The capillary pressure curve for the oil-water system.....	<b>205</b>
<b>Figure 15.16:</b> The capillary pressure curve for the oil-gas system. ....	<b>206</b>
<b>Figure 15.17:</b> The model of the reservoir. ....	<b>208</b>
<b>Figure 15.18:</b> Average reservoir pressure comparison of original and simulation data. ....	<b>209</b>
<b>Figure 15.19:</b> Cumulative oil production comparison of original and simulation data. ....	<b>210</b>
<b>Figure 15.20:</b> Cumulative oil and water production. ....	<b>210</b>
<b>Figure 15.21:</b> The comparison of oil rates for Well-01. ....	<b>212</b>
<b>Figure 15.22:</b> The oil recovery factor along the production. ....	<b>212</b>
<b>Figure 16.1:</b> The gas viscosity matching based on the LGS correlation to estimate the specific gravity of the associated gas. ....	<b>218</b>
<b>Figure 17.1:</b> The cumulative discounted net cash flow in million dollars showing the project's breakthrough time .....	<b>221</b>
<b>Figure 17.2:</b> Oil production versus water production for the base scenario. ....	<b>222</b>
<b>Figure 17.3:</b> Average reservoir pressure profile along with the cumulative oil production throughout the forecast. ....	<b>223</b>

<b>Figure 17.4:</b> The cumulative oil produced along with water for Bane-01 during 10 years of production forecast.....	<b>224</b>
<b>Figure 17.5:</b> The relationship between number of wells, and the net present value.	<b>225</b>
<b>Figure 17.6:</b> The map of the Project Watcher in the Water .....	<b>228</b>
<b>Figure 17.7:</b> Fractional flow curve for each water saturation values.....	<b>229</b>
<b>Figure 17.8:</b> Tangent points above the average water saturation at the breakthrough.	<b>229</b>
<b>Figure 17.9:</b> Average water saturation values after breakthrough with their corresponding fractional flow values.....	<b>231</b>
<b>Figure 17.10:</b> Calculated cumulative water injection rates and oil production amounts versus average water saturation after the breakthrough. ....	<b>231</b>
<b>Figure 17.11:</b> Oil production versus water production for the Project Watcher in the Water.....	<b>232</b>
<b>Figure 17.12:</b> Average reservoir pressure profile along with the cumulative oil production throughout the Project Watcher in the Water. ....	<b>232</b>
<b>Figure 17.13:</b> The cumulative discounted net cash flow in million dollars showing the project's breakthrough time for the Project Watcher in the Water. ....	<b>233</b>
<b>Figure 17.14:</b> The map of Project Deflate the Smaug.....	<b>234</b>
<b>Figure 17.15:</b> Oil production versus water production for the Project Deflate the Smaug.....	<b>235</b>
<b>Figure 17.16:</b> The cumulative discounted net cash flow in million dollars showing the project's breakthrough time for the Project Deflate the Smaug.....	<b>236</b>
<b>Figure 17.17:</b> Average reservoir pressure profile along with the cumulative oil production throughout the Project Deflate the Smaug.....	<b>237</b>
<b>Figure 17.18:</b> The map of Project One Rig to Drill Them All.....	<b>238</b>
<b>Figure 17.19:</b> Oil production versus water production for the Project One Rig to Drill Them All.....	<b>239</b>
<b>Figure 17.20:</b> Average reservoir pressure profile along with the cumulative oil production throughout the One Rig to Drill Them All. ....	<b>240</b>
<b>Figure 17.21:</b> The cumulative discounted net cash flow in million dollars showing the project's breakthrough time for Project One Rig to Drill Them All. ....	<b>241</b>

<b>Figure 17.22:</b> Sensitivity analysis on Project One Rig to Drill Them All .....	<b>242</b>
<b>Figure 17.23:</b> Recovery factor of oil comparison. ....	<b>243</b>
<b>Figure 18.1:</b> Vertical separator (Ikoku, 1992).....	<b>247</b>
<b>Figure 18.2:</b> Horizontal separator (Arnold & Stewart, 2008).....	<b>248</b>
<b>Figure 18.3:</b> Spherical separator (Arnold & Stewart, 2008).....	<b>249</b>
<b>Figure 18.4:</b> Horizontal separator, and its parts (Arnold & Stewart, 2008).....	<b>250</b>
<b>Figure 18.5:</b> The representation of the seam-to-seam length, effective length for a horizontal separator (Arnold & Stewart, 2008).....	<b>257</b>
<b>Figure 18.6:</b> Anticipated daily production regimes for each phase during 25-years of production. ....	<b>259</b>
<b>Figure 18.7:</b> Coefficient $\beta$ for a horizontal half-full liquid (Arnold & Stewart, 2008). .....	<b>264</b>
<b>Figure 18.8:</b> Daily production rates for each phase during 10 years of production in the base scenario. ....	<b>266</b>
<b>Figure 18.9:</b> Daily production rates for each phase during 10 years of production in One Rig to Drill Them All. ....	<b>269</b>
<b>Figure 19.1:</b> GHG emission distributions for Base Scenario (Brandt & Masnadi, 2022) .....	<b>274</b>
<b>Figure 19.2:</b> Energy consumption distribution for Base Scenario (Brandt & Masnadi, 2022) .....	<b>274</b>
<b>Figure 19.3:</b> GHG emission distributions for Project Watcher in the Water (Brandt & Masnadi, 2022).....	<b>275</b>
<b>Figure 19.4:</b> Energy consumption distribution for Watcher in the Water (Brandt & Masnadi, 2022).....	<b>275</b>
<b>Figure 19.5:</b> GHG emission distribution for Project Deflate the Smaug (Brandt & Masnadi, 2022).....	<b>276</b>
<b>Figure 19.6:</b> Energy consumption distribution for Project Deflate the Smaug (Brandt & Masnadi, 2022) .....	<b>276</b>
<b>Figure 19.7:</b> GHG emission distribution for One Rig to Drill Them All (Brandt & Masnadi, 2022).....	<b>277</b>
<b>Figure 19.8:</b> Energy consumption distribution for One Rig to Drill Them All (Brandt & Masnadi, 2022). .....	<b>277</b>

<b>Figure 19.9:</b> Stakeholders mapping diagram. ....	<b>279</b>
<b>Figure A.1:</b> Well log display of Well-02 along with designated formations. ....	<b>298</b>
<b>Figure A.2:</b> Well log display of Well-03 along with designated formations. ....	<b>299</b>
<b>Figure A.3:</b> Well log display of Well-04 along with designated formations. ....	<b>300</b>
<b>Figure A.4:</b> Well log display of Well-05 along with designated formations. ....	<b>301</b>
<b>Figure A.5:</b> Well log display of Well-06 along with designated formations. ....	<b>302</b>
<b>Figure A.6:</b> Well log display of Well-07 along with designated formations. ....	<b>303</b>
<b>Figure A.7:</b> Well log display of Well-08 along with designated formations. ....	<b>304</b>
<b>Figure A.8:</b> Well log display of Well-09 along with designated formations. ....	<b>305</b>
<b>Figure A.9:</b> Well log display of Well-10 along with designated formations. ....	<b>306</b>
<b>Figure A.10:</b> Well log display of Well-11 along with designated formations. ....	<b>307</b>
<b>Figure A.11:</b> Well log display of Well-12 along with designated formations. ....	<b>308</b>
<b>Figure A.12:</b> Well log display of Well-13 along with designated formations. ....	<b>309</b>
<b>Figure A.13:</b> Well log display of Well-15 along with designated formations. ....	<b>310</b>
<b>Figure A.14:</b> Well log display of Well-16 along with designated formations. ....	<b>311</b>
<b>Figure A.15:</b> Well log display of Well-17 along with designated formations. ....	<b>312</b>
<b>Figure A.16:</b> Well log display of Well-19 along with designated formations. ....	<b>313</b>
<b>Figure A.17:</b> Well log display of Well-20 along with designated formations. ....	<b>314</b>
<b>Figure A.18:</b> Well log display of Well-21 along with designated formations. ....	<b>315</b>
<b>Figure A.19:</b> Well log display of Well-22 along with designated formations. ....	<b>316</b>
<b>Figure A.20:</b> Well log display of Well-23 along with designated formations. ....	<b>317</b>
<b>Figure A.21:</b> Well log display of Well-24 along with designated formations. ....	<b>318</b>
<b>Figure A.22:</b> Well log display of Well-25 along with designated formations. ....	<b>319</b>
<b>Figure C.1:</b> Porosity map of Precious-1.....	<b>328</b>
<b>Figure C.2:</b> Porosity map of Gollum-1.....	<b>329</b>
<b>Figure C.3:</b> Porosity map of Thorin-1. ....	<b>330</b>
<b>Figure C.4:</b> Initial water saturation map of Precious-1.....	<b>331</b>
<b>Figure C.5:</b> Initial water saturation map of Gollum-1. ....	<b>332</b>
<b>Figure C.6:</b> Initial water saturation map of Thorin-1.....	<b>333</b>
<b>Figure C.7:</b> Initial oil saturation map of Precious-1. ....	<b>334</b>
<b>Figure C.8:</b> Initial oil saturation map of Gollum-1.....	<b>335</b>
<b>Figure C.9:</b> Initial oil saturation map of Thorin-1 .....	<b>336</b>

<b>Figure C.10:</b> Net pay thickness map of Precious-1 .....	<b>337</b>
<b>Figure C.11:</b> Net pay thickness map of Gollum-1.....	<b>338</b>
<b>Figure C.12:</b> Net pay thickness map of Thorin-1 .....	<b>339</b>
<b>Figure C.13:</b> The permeability map of Precious-1 reservoir layer .....	<b>340</b>
<b>Figure C.14:</b> The permeability map of Gollum-1 reservoir layer.....	<b>341</b>
<b>Figure C.15:</b> The permeability map of Thorin-1 reservoir layer.....	<b>342</b>
<b>Figure C.16:</b> Various cross sections of the Mount Doom Oil Field. ....	<b>343</b>
<b>Figure C.17:</b> 3D representation of the Mount Doom Oil Field. ....	<b>344</b>
<b>Figure C.18:</b> Bird-eye view of the Mount Doom Oil Field. ....	<b>345</b>
<b>Figure C.19:</b> Initial oil saturation and movable oil saturation as a function of depth for Well-01 Precious-1 layer.....	<b>346</b>
<b>Figure C.20:</b> Initial oil saturation and movable oil saturation as a function of depth for Well-01 Gollum-1 layer. ....	<b>347</b>
<b>Figure C.21:</b> Initial oil saturation and movable oil saturation as a function of depth for Well-01 Thorin-1 layer.....	<b>348</b>
<b>Figure C.22:</b> Initial oil saturation and movable oil saturation as a function of depth for Well-14 Precious-1 layer.....	<b>349</b>
<b>Figure C.23:</b> Initial oil saturation and movable oil saturation as a function of depth for Well-14 Gollum-1 layer. ....	<b>350</b>
<b>Figure C.24:</b> Initial oil saturation and movable oil saturation as a function of depth for Well-14 Thorin-1 layer.....	<b>351</b>
<b>Figure C.25:</b> Initial oil saturation and movable oil saturation as a function of depth for Well-18 Precious-1 layer.....	<b>352</b>
<b>Figure D.1:</b> Total porosity distribution obtained from all wells for Precious-1 reservoir layer.....	<b>354</b>
<b>Figure D.2:</b> Effective porosity distribution obtained from all wells for Precious-1 reservoir layer.....	<b>355</b>
<b>Figure D.3:</b> Initial water saturation distribution obtained from all wells for Precious- 1 reservoir layer.....	<b>356</b>
<b>Figure D.4:</b> Total porosity distribution obtained from all wells for Gollum-1 reservoir layer.....	<b>357</b>

<b>Figure D.5:</b> Effective porosity distribution obtained from all wells for Gollum-1 reservoir layer.....	<b>358</b>
<b>Figure D.6:</b> Initial water saturation distribution obtained from all wells for Gollum-1 reservoir layer.....	<b>359</b>
<b>Figure D.7:</b> Total porosity distribution obtained from all wells for Thorin-1 reservoir layer.....	<b>360</b>
<b>Figure D.8:</b> Effective porosity distribution obtained from all wells for Thorin-1 reservoir layer.....	<b>361</b>
<b>Figure D.9:</b> Initial water saturation distribution obtained from all wells for Thorin-1 reservoir layer.....	<b>362</b>
<b>Figure D.10:</b> Random 10000 samples of total porosity for Precious-1 reservoir layer.	
.....	<b>363</b>
<b>Figure D.11:</b> Random 10000 samples of effective porosity for Precious-1 reservoir layer.....	<b>363</b>
<b>Figure D.12:</b> Random 10000 samples of initial water saturation for Precious-1 reservoir layer.....	<b>364</b>
<b>Figure D.13:</b> Random 10000 samples of volume for Precious-1 reservoir layer ..	<b>364</b>
<b>Figure D.14:</b> Random 10000 samples of total porosity for Gollum-1 reservoir layer.	
.....	<b>365</b>
<b>Figure D.15:</b> Random 10000 samples of effective porosity for Gollum-1 reservoir layer.....	<b>365</b>
<b>Figure D.16:</b> Random 10000 samples of initial water saturation for Gollum-1 reservoir layer.....	<b>366</b>
<b>Figure D.17:</b> Random 10000 samples of volume for Gollum-1 reservoir layer....	<b>366</b>
<b>Figure D.18:</b> Random 10000 samples of total porosity for Thorin-1 reservoir layer.	
.....	<b>367</b>
<b>Figure D.19:</b> Random 10000 samples of effective porosity for Thorin-1 reservoir layer.....	<b>367</b>
<b>Figure D.20:</b> Random 10000 samples of initial water saturation for Thorin-1 reservoir layer.....	<b>368</b>
<b>Figure D.21:</b> Random 10000 samples of volume for Thorin-1 reservoir layer. ....	<b>368</b>
<b>Figure D.22:</b> Recovery factor uniform distribution based on the literature.....	<b>369</b>

<b>Figure D.23:</b> Thickness isopach map of the Gollum-1 reservoir layer.....	<b>369</b>
<b>Figure D.24:</b> Thickness isopach map of the Thorin-1 reservoir layer. ....	<b>370</b>
<b>Figure D.25:</b> OOIP estimation result for the Gollum-1 reservoir layer. ....	<b>371</b>
<b>Figure D.26:</b> ROIP estimation result for the Gollum-1 reservoir layer. ....	<b>372</b>
<b>Figure D.27:</b> OOIP estimation result for the Thorin-1 reservoir layer. ....	<b>373</b>
<b>Figure D.28:</b> ROIP estimation result for the Thorin-1 reservoir layer. ....	<b>374</b>
<b>Figure F.1:</b> Drill string tally for the surface stage.....	<b>386</b>
<b>Figure F.2:</b> Drill string tally for the production stage.....	<b>387</b>
<b>Figure I.1:</b> The Distribution map of reservoir tops.....	<b>396</b>
<b>Figure I.2:</b> The distribution map of the pay thicknesses.....	<b>396</b>
<b>Figure I.3:</b> The distribution map of the net to gross ratios. ....	<b>397</b>
<b>Figure I.4:</b> The distribution map of the initial water saturation.....	<b>397</b>
<b>Figure I.5:</b> The distribution map of permeabilities in absolute.....	<b>398</b>
<b>Figure I.6:</b> The distribution map of effective porosities. ....	<b>398</b>
<b>Figure I.7:</b> The depth of the reservoir in 3-D given with its grid blocks. ....	<b>399</b>
<b>Figure I.8:</b> The porosity values of the reservoir in 3-D given with its grid blocks. <b>400</b>	
<b>Figure I.9:</b> The permeability values of the reservoir in 3-D given with its grid blocks. ....	<b>401</b>

## **ABBREVIATIONS**

<b>AFE</b>	: Authorization for expenditure
<b>AR</b>	: Aspect ratio
<b>B</b>	: Connection type parameter
<b>BF</b>	: Bouncy factor
<b>BHA</b>	: Bottom hole assembly
<b>BS</b>	: Bit size
<b>BSR</b>	: Bending stress ratio
<b>CAL</b>	: Calliper log
<b>CAPEX</b>	: Capital expenses
<b>CCP</b>	: Corrected compaction factor
<b>cm</b>	: Centimetre
<b>CNL*</b>	: Compensated neutron log
<b>cp</b>	: Centipoise
<b>DC</b>	: Drill collar
<b>DHC</b>	: Drill hole cost
<b>DHD</b>	: Drill hole days
<b>DI</b>	: Drilling interval
<b>DP</b>	: Drill pipe
<b>DPI</b>	: Discounted profitability index
<b>DRHO</b>	: Density-porosity correction
<b>DT</b>	: Delta time, sonic
<b>EOR</b>	: Enhanced oil recovery

<b>ft</b>	: Foot/feet
<b>FWL</b>	: Free water level
<b>gal</b>	: Gallon
<b>GOC</b>	: Gas oil contact
<b>GR</b>	: Gamma ray
<b>GWC</b>	: Gas water contact
<b>h</b>	: Hour
<b>HB</b>	: Herschel-Bulkley model
<b>HCI</b>	: Hole cleaning index
<b>HCMI</b>	: Hydrocarbon mobility index
<b>HD</b>	: Horizontal displacement
<b>HP</b>	: Horsepower
<b>HWDP</b>	: Heavy weight drill pipe
<b>ID</b>	: Inner diameter of a pipe
<b>IDL</b>	: Deep induction log
<b>IRR</b>	: Internal rate of return
<b>in</b>	: Inch
<b>JAS</b>	: Joint association survey
<b>JS</b>	: Joint strength
<b>KB</b>	: Kelly bushing
<b>kWh</b>	: Kilo watt hour
<b>lbf</b>	: Pound force
<b>lb</b>	: Pound mass

<b>LL8</b>	: Laterelog8
<b>LWD</b>	: Logging while drilling
<b>M</b>	: Connection type parameter
<b>m</b>	: Meter
<b>min</b>	: Minute
<b>MLL</b>	: Micro-laterolog
<b>MMSCF</b>	: One million cubic feet
<b>MMSTB</b>	: One million stock tank barrel
<b>MOP</b>	: Maximum overpull
<b>MRI</b>	: Mechanical risk index
<b>MSCF</b>	: One thousand cubic feet
<b>MSL</b>	: Mean sea level
<b>MSTB</b>	: One thousand stock tank barrel
<b>MWD</b>	: Measurement while drilling
<b>NO<sub>t</sub></b>	: Number of trips
<b>NPHI</b>	: Neutron-porosity
<b>NPV</b>	: Net present value
<b>NS</b>	: Number of strings
<b>NTG</b>	: Net to gross ratio
<b>NWTC</b>	: Nominal weight threads and couplings
<b>OD</b>	: Outer diameter of a pipe, inch
<b>OGIP</b>	: Original gas in place
<b>OOIP</b>	: Original oil in place

<b>OPEX</b>	: Operational expenses
<b>OWC</b>	: Oil water contact
<b>ppg</b>	: Pounds per gallon
<b>psi</b>	: Pounds per square inch
<b>psia</b>	: Pounds per square inch in absolute condition
<b>psig</b>	: Pounds per square inch in gauge condition
<b>PV</b>	: Pore volume
<b>PVT</b>	: Pressure-volume-temperature
<b>Q</b>	: Connection type parameter
<b>RB</b>	: Reservoir barrel
<b>RF<sub>o</sub></b>	: Recovery factor of oil, %
<b>RF<sub>g</sub></b>	: Recovery factor of gas, %
<b>RHOB</b>	: Density-porosity
<b>ROIP</b>	: Recoverable oil in place
<b>ROP</b>	: Rate of penetration
<b>ROR</b>	: Rate of return
<b>RPM</b>	: Revolutions per minute
<b>RTL</b>	: Round thread long coupling
<b>RTS</b>	: Round thread short coupling
<b>SCF</b>	: Standard cubic foot
<b>SF</b>	: Safety factor
<b>SG</b>	: Specific gravity of a fluid
<b>SN</b>	: Short normal log

<b>SP</b>	: Spontaneous potential
<b>SR</b>	: Slenderness ratio
<b>STB</b>	: Stock tank barrel
<b>TVD</b>	: True vertical depth
<b>TWD</b>	: Total well cost
<b>USD</b>	: United States dollar
<b>WD</b>	: Water depth
<b>W<sub>e</sub></b>	: Cumulative water influx
<b>WOB</b>	: Weight on bit
<b>W<sub>p</sub></b>	: Cumulative water production
<b>WT</b>	: Well type
<b>X</b>	: Connection type parameter
<b>°F</b>	: Fahrenheit degree
<b>°R</b>	: Rankine
<b>μs</b>	: Microsecond

## SYMBOLS

<b>A</b>	: Area, ft <sup>2</sup>
<b>A<sub>box</sub></b>	: Cross-sectional area of box, in <sup>2</sup>
<b>A<sub>d</sub></b>	: Cross sectional area of the droplet, ft <sup>2</sup>
<b>A<sub>w</sub></b>	: Area occupied by water, ft <sup>2</sup>
<b>A<sub>sep</sub></b>	: Area of separator, ft <sup>2</sup>
<b>A<sub>pin</sub></b>	: Cross-sectional area of pin, in <sup>2</sup>
<b>AR</b>	: Aspect ratio, unitless
<b>A<sub>s</sub></b>	: Surface area, in <sup>2</sup>
<b>(A<sub>t</sub>)<sub>opt</sub></b>	: Optimum total nozzle area, in <sup>2</sup>
<b>A<sub>w</sub></b>	: Pipe body section area, in <sup>2</sup>
<b>a<sub>2</sub></b>	: ROP constant, unitless
<b>B<sub>g</sub></b>	: Formation volume factor of gas, RB/SCF
<b>B<sub>o</sub></b>	: Formation volume factor of oil, RB/STB
<b>B<sub>oi</sub></b>	: Initial formation volume factor of oil, RB/STB
<b>B<sub>t</sub></b>	: Total formation volume factor, RB/STB
<b>B<sub>ti</sub></b>	: Initial total formation volume factor, RB/STB
<b>B<sub>2</sub></b>	: Contribution of the cemented casing weight to buckling, lbf
<b>B<sub>3</sub></b>	: Contribution of the cemented portion to buckling, lbf
<b>B<sub>4</sub></b>	: Contribution of the mud inside the casing to buckling, lbf
<b>c</b>	: Well inclination, rad/in
<b>C<sub>a</sub></b>	: Annular coefficient, unitless
<b>C<sub>a<sub>p</sub></sub></b>	: Capacity of a pipe, bbl/ft

<b>C<sub>a<sub>shoe</sub></sub></b>	: Capacity of a casing shoe, bbl/ft
<b>C<sub>c</sub></b>	: Inner pipe coefficient, unitless
<b>C<sub>D</sub></b>	: Drag coefficient, dimensionless
<b>C<sub>d</sub></b>	: Empirical discharge coefficient, unitless
<b>c<sub>f</sub></b>	: Formation compressibility, $\text{psi}^{-1}$
<b>c<sub>p</sub></b>	: Drill pipe inclination, rad/in
<b>c<sub>w</sub></b>	: Water compressibility factor, $\text{psi}^{-1}$
<b>d</b>	: Borehole diameter, inch
<b>D</b>	: Depth, ft
<b><math>\bar{D}</math></b>	: Average depth, ft
<b>D<sub>b</sub></b>	: Drill bit size, in
<b>d<sub>CAL</sub></b>	: Borehole calliper reading, inch
<b>D<sub>cycle</sub></b>	: Depth of the log cycle, ft
<b>DHC</b>	: Dry-hole cost, million \$
<b>DHD</b>	: Dry-hole day, day
<b>d<sub>hole</sub></b>	: Diameter of open hole, inch
<b>DI</b>	: Drilling interval, 100 m
<b>D<sub>in</sub></b>	: Tripping depth in, ft
<b>d<sub>i</sub></b>	: Invasion diameter, inch
<b>D<sub>lc</sub></b>	: Loss circulation depth, ft
<b>DLS<sub>max</sub></b>	: Maximum dog-leg inclination, °/100 ft
<b>D<sub>m</sub></b>	: Depth of mud level fall, ft
<b>d<sub>m</sub></b>	: Liquid droplet to be separated, micron

<b>D<sub>n</sub></b>	: Distance of n <sup>th</sup> well to the reference point, m
<b>d<sub>n/t</sub></b>	: Collapse mode ratio, unitless
<b>D<sub>out</sub></b>	: Tripping depth out, ft
<b><math>\frac{dp_f}{dL_{annulus}}</math></b>	: Frictional pressure loss inside the annulus, psi/ft
<b><math>\frac{dp_f}{dL_{pipe}}</math></b>	: Frictional pressure loss inside the pipe, psi/ft
<b>dp<sub>dc/dl</sub></b>	: Frictional pressure loss gradient in drill collar, psi/ft
<b>dp<sub>dca/dl</sub></b>	: Frictional pressure loss gradient in drill collar annulus, psi/ft
<b>dp<sub>dp-ca/dl</sub></b>	: Frictional pressure loss gradient in drill pipe casing annulus, psi/ft
<b>dp<sub>dp/dl</sub></b>	: Frictional pressure loss gradient in drill pipe, psi/ft
<b>dp<sub>dpa/dl</sub></b>	: Frictional pressure loss gradient in drill pipe annulus, psi/ft
<b>D<sub>s</sub></b>	: Depth of sediment, ft
<b>D<sub>seat</sub></b>	: Casing seat depth, ft
<b>d<sub>sep</sub></b>	: Diameter of the separator, in
<b>(d<sub>sep</sub>)<sub>max</sub></b>	: Maximum separator diameter, in
<b>D<sub>shoe</sub></b>	: Casing shoe depth, ft
<b>D<sub>target</sub></b>	: Target depth, ft
<b>D<sub>TVD @</sub></b>	: True vertical depth at a specific point, ft
<b>E</b>	: Elastic modulus of steel, psi
<b>E<sub>p</sub></b>	: Efficiency of the mud pump, %
<b>e</b>	: Elongation, in
<b>ECD</b>	: Equivalent circulating density, ppg
<b>E<sub>dyn</sub></b>	: Dynamic Young's modulus, Mpsi

<b>E<sub>n</sub></b>	: Elevation of n <sup>th</sup> well, ft
<b>F</b>	: Formation factor, unitless
<b>F<sub>D</sub></b>	: Drag force, lbf
<b>f</b>	: Fanning frictional factor, unitless
<b>f<sub>w</sub></b>	: Fractional flow of water, fraction
<b>f<sub>w'</sub></b>	: Fractional flow of water after breakthrough, fraction
<b>F<sub>a</sub></b>	: Axial force, lbf
<b>F<sub>ASF</sub></b>	: Safety factor applied force
<b>F<sub>cr</sub></b>	: Bending force according to Lubinski's equation, lbf
<b>F<sub>ext</sub></b>	: Any external force acting on the drill pipe, lbf
<b>F<sub>seat</sub></b>	: Force at casing seat, lbf
<b>F<sub>seatSF</sub></b>	: Safety factor applied force at casing seat, psi
<b>F<sub>T</sub></b>	: Cutting transport ratio, unitless
<b>F<sub>1</sub></b>	: Empirical collapse coefficient, unitless
<b>F<sub>2</sub></b>	: Empirical collapse coefficient, unitless
<b>F<sub>3</sub></b>	: Empirical collapse coefficient, unitless
<b>F<sub>4</sub></b>	: Empirical collapse coefficient, unitless
<b>F<sub>5</sub></b>	: Empirical collapse coefficient, unitless
<b>g</b>	: Gravitational acceleration, ft/s <sup>2</sup>
<b>G<sub>dyn</sub></b>	: Dynamic shear modulus, Mpsi
<b>h</b>	: Thickness of a reservoir, ft
<b>h<sub>c</sub></b>	: Length of the cemented portion, ft
<b>HD</b>	: Horizontal displacement, 100m

<b><math>h_{gross}</math></b>	: Gross thickness of a zone, ft
<b><math>h_{mc}</math></b>	: Mud cake thickness, inch
<b><math>HP_{max}</math></b>	: Maximum horse power, hp
<b><math>h_{net}</math></b>	: Net thickness of a zone, ft
<b><math>h_{gross}</math></b>	: Gross thickness of a zone, ft
<b><math>h_o</math></b>	: Maximum oil pad thickness, in
<b><math>h_{sh}</math></b>	: Shale layer thickness of a zone, ft
<b><math>(h_w)_{max}</math></b>	: Maximum water pad thickness, in
<b><math>I</math></b>	: Moment of inertia, ft <sup>4</sup>
<b><math>i^*</math></b>	: Interest rate, %
<b><math>ID_{dc}</math></b>	: Drill collar inner diameter, in
<b><math>ID_p</math></b>	: Drill pipe inner diameter, in
<b><math>I_{GR}</math></b>	: Gamma ray index, fraction
<b><math>J</math></b>	: The polar moment of inertia, in <sup>4</sup>
<b><math>K</math></b>	: Surface penetration rate, ft/h
<b><math>k</math></b>	: Permeability, md
<b><math>k_{HB}</math></b>	: Fluid consistency index, unitless
<b><math>K_{decline}</math></b>	: Porosity decline constant
<b><math>K_{dyn}</math></b>	: Dynamic bulk modulus, Mpsi
<b><math>K_{rg}</math></b>	: Relative permeability of gas to oil, fraction
<b><math>K_{rog}</math></b>	: Relative permeability of oil to gas, fraction
<b><math>K_{row}</math></b>	: Relative permeability of oil to water, fraction
<b><math>K_{rw}</math></b>	: Relative permeability of water to oil, fraction

<b>k<sub>1</sub></b>	: Matrix stress coefficient, unitless
<b>L</b>	: Measured length, ft
<b>L<sub>BHA</sub></b>	: Length of bottom hole assembly, ft
<b>L<sub>casing</sub></b>	: Length of casing, ft
<b>L<sub>dc</sub></b>	: Drill collar length, ft
<b>L<sub>dp</sub></b>	: Drill pipe length, ft
<b>L<sub>eff</sub></b>	: Effective length of the separator, ft
<b>L<sub>ss</sub></b>	: Seam to seam length of the separator, ft
<b>L<sub>h</sub></b>	: Half length of the drill pipe, in
<b>L<sub>hwdp</sub></b>	: Length of heavy weight drill pipe, ft
<b>L<sub>open</sub></b>	: Length of the uncemented portion, ft
<b>L<sub>rat-hole</sub></b>	: Length of the rat hole, ft
<b><math>\bar{L}_s</math></b>	: Average length of one stand pipe, ft
<b>L<sub>shoe</sub></b>	: Length of a casing shoe, ft
<b>L<sub>st</sub></b>	: Stabilizer location, ft
<b>L<sub>1</sub></b>	: Stabilizer placed right above the bit, ft
<b>M<sub>g</sub></b>	: Molecular mass of gas, atomic unit
<b>M<sub>w</sub></b>	: Molecular rate of gas, lb/lb.mole
<b>m</b>	: Slope of hydraulic line, unitless
<b>n</b>	: Saturation exponent, unitless
<b>n<sub>HB</sub></b>	: flow behavior index, unitless
<b>N<sub>b</sub></b>	: Number of bits, unitless
<b>N<sub>p</sub></b>	: Cumulative oil production, MM STB

<b>N<sub>precovery</sub></b>	: Cumulative recoverable oil production, STB
<b>NS</b>	: Number of strings, unitless
<b>OD</b>	: Outer diameter of a pipe, in
<b>OD<sub>dc</sub></b>	: Drill collar outer diameter, in
<b>OD<sub>p</sub></b>	: Drill pipe outer diameter, in
<b>P</b>	: Maximum tensile yield strength, lbf
<b>P<sub>a</sub></b>	: Maximum axial force to which the drill pipe may be subjected, psi
<b>P<sub>atm</sub></b>	: Atmospheric pressure, psi
<b>P<sub>b</sub></b>	: Bubble point pressure, psi
<b>P<sub>br</sub></b>	: Burst pressure of a pipe, psi
<b>P<sub>c</sub></b>	: Collapse pressure of a pipe, psi
<b>P<sub>cp</sub></b>	: Capillary pressure, psi
<b>P<sub>cr</sub></b>	: Corrected collapse pressure of a pipe, psi
<b>P<sub>cog</sub></b>	: Capillary pressure of oil to gas, fraction
<b>P<sub>cow</sub></b>	: Capillary pressure of oil to water, fraction
<b>P<sub>fg</sub></b>	: Fracture pressure gradient, ppg
<b>P<sub>h</sub></b>	: Hydrostatic pressure exerted by drilling mud, psi
<b>P<sub>i</sub></b>	: Internal pressure, psi
<b>P<sub>i,res</sub></b>	: Initial reservoir pressure, psi
<b>P<sub>i@</sub></b>	: Initial pressure at a specific depth, ft
<b>P<sub>inj</sub></b>	: Injection pressure, psi
<b>P<sub>i<sub>seat</sub></sub></b>	: Injection pressure at casing seat, psi
<b>P<sub>max</sub></b>	: Maximum pump pressure, psi

<b>P<sub>op</sub></b>	: Operating pressure, psi
<b>P<sub>pg</sub></b>	: Pore pressure gradient, ppg
<b>P<sub>pc</sub></b>	: Pseudo critical pressure, psia
<b>P<sub>pr</sub></b>	: Pseudo reduced pressure, fraction
<b>P<sub>reservoir</sub></b>	: Reservoir pressure, psia
<b>P<sub>s</sub></b>	: Stress from slip crushing, psi
<b>P<sub>seat</sub></b>	: Pressure at casing seat, psi
<b>P<sub>tb</sub></b>	: Tensile force on the drill pipe that causes bending, lbf
<b>Q</b>	: Flow rate for HB model, m <sup>3</sup> /s
<b>q</b>	: Flow rate, gal/min
<b>Q<sub>crit</sub></b>	: Critical flow rate for the cutting transport, gal/min
<b>q<sub>opt</sub></b>	: Optimum flow rate, gal/min
<b>R</b>	: Inside drill pipe radius, m
<b>R<sub>a</sub></b>	: Apparent resistivity, Ω.m
<b>Re</b>	: Reynold's number, unitless
<b>Re<sub>eq</sub></b>	: Equivalent Reynold's number, unitless
<b>Re<sub>eq,cr</sub></b>	: Critical equivalent Reynold's number, unitless
<b>R<sub>m</sub></b>	: Drilling mud resistivity, Ω.m
<b>R<sub>mc</sub></b>	: Mud cake resistivity, Ω.m
<b>R<sub>mf</sub></b>	: Mud filtration resistivity, Ω.m
<b>R<sub>o</sub></b>	: Fully saturated formation resistivity, Ω.m
<b>R<sub>p</sub></b>	: Cumulative produced gas-oil ratio, SCF/STB
<b>R<sub>s</sub></b>	: Adjacent bed resistivity, Ω.m

$R_{so}$	: Solution gas-oil ratio
$R_{soi}$	: Initial solution gas-oil ratio
$R_t$	: True formation resistivity, $\Omega.m$
$R_w$	: Formation water resistivity, $\Omega.m$
$R_{wa}$	: Apparent water resistivity, $\Omega.m$
$R_{xo}$	: Invaded zone resistivity, $\Omega.m$
$R_1$	: Hole radius, m
$R_2$	: Outer radius of a pipe, m
$S$	: The tension occurring in the relevant string element cross section, psi
$S_g$	: Gas saturation, fraction
$S_{gc}$	: Critical gas saturation, fraction
$S_{mo}$	: Movable oil saturation, fraction
$S_{oi}$	: Initial oil saturation, fraction
$S_o$	: Oil saturation, fraction
$S_{ro}$	: Residual oil saturation, fraction
$SVC$	: Slip velocity correction, unitless
$S_w$	: Water saturation, fraction
$S_{wa}$	: Average water saturation after breakthrough, fraction
$S_{wb}$	: Saturation of bound water shale, fraction
$S_{wi}$	: Initial water saturation, fraction
$S_{wirr}$	: Irreducible water saturation, fraction
$S_{wAr}$	: Water saturation found by Archie Equation, %
$S_{wcorr}$	: Corrected water saturation, fraction

<b>S<sub>xo</sub></b>	: Invaded zone saturation, fraction
<b>T</b>	: Temperature, °F
<b>T<sub>reservoir</sub></b>	: Reservoir temperature, °R
<b>t</b>	: Wall thickness, in
<b>t<sub>i*</sub></b>	: Time exposed to interest, years
<b>TWC</b>	: Total well cost, million \$
<b>t<sub>b</sub></b>	: Average bit life, h
<b>̄t<sub>d</sub></b>	: Average drilling time, h
<b>t<sub>displacement</sub></b>	: Displacement time of the cement, h
<b>t<sub>mixing</sub></b>	: Mixing time the cement, h
<b>t<sub>r</sub></b>	: Desired retention time for the liquid, min
<b>(t<sub>r</sub>)<sub>o</sub></b>	: Retention time for oil, min
<b>(t<sub>r</sub>)<sub>w</sub></b>	: Retention time for water, min
<b>̄t<sub>s</sub></b>	: Average required time to make connection, min
<b>̄t<sub>t</sub></b>	: Average trip time, h
<b>T<sub>op</sub></b>	: Operating temperature, °F
<b>T<sub>pc</sub></b>	: Pseudo critical temperature, °R
<b>T<sub>pr</sub></b>	: Pseudo recued temperature, dimensionless
<b>T<sub>q</sub></b>	: Torque, lbf-ft
<b>V</b>	: Velocity of compressional/shear waves, ft/μs
<b>v<sub>a</sub></b>	: Annular velocity, ft/min
<b>V<sub>additive</sub></b>	: Volume of cement additives, bbl
<b>v<sub>annulus</sub></b>	: Fluid velocity in annulus, ft/s

$V_{ca}$	: Volume of casing annulus, bbl
$V_{cased-hole}$	: Cased hole annulus volume, bbl
$V_{ds}$	: Volume of drill string, bbl
$V_{dis}$	: Displacement volume, bbl
$V_{dyn}$	: Dynamic Poisson's ratio, unitless
$V_{open-hole}$	: Open hole casing annulus volume, bbl
$v_{min}$	: Minimum annular velocity, ft/min
$V_{oh}$	: Volume of open hole annulus, bbl
$v_p$	: Fluid velocity in pipe for HB model, m/s
$V_{p0}$	: Velocity of compressional waves in horizontal direction, ft/ $\mu$ s
$v_{pipe}$	: Fluid velocity in pipe, ft/s
$V_{rat-hole}$	: Rat hole volume, bbl
$V_{s0}$	: Velocity of shear waves in horizontal direction, ft/ $\mu$ s
$v_{sc}$	: Corrected slip velocity, ft/min
$V_{sh}$	: Shale volume, %
$V_{shoe}$	: Volume of a casing shoe, bbl
$v_{slip}$	: Slip velocity, ft/min
$V_{slurry}$	: Cement slurry volume, bbl
$V_t$	: Settling velocity, ft/s
$v_T$	: Transport velocity, ft/min
$Q_g$	: Gas rate, MMSCF/D
$Q_o$	: Oil rate, STB/D
$Q_w$	: Water rate, STB/D

<b>WD</b>	: Water depth, 100 m
<b>WT</b>	: Well type, unitless
<b>w''</b>	: Average weight of casing, lb/ft
<b>W<sub>BHA</sub></b>	: Weight of bottom hole assembly, lbf
<b>W<sub>casing</sub></b>	: Unit weight of casing, lb/ft
<b>W<sub>cement</sub></b>	: Wellhead load when the cement hardens, lbf
<b>W<sub>dc</sub></b>	: Drill collar weight, lb/ft
<b>W<sub>dp</sub></b>	: Drill pipe weight, lb
<b>W<sub>engines(total)</sub></b>	: Total power of the drilling system, kWh
<b>W<sub>hwdp</sub></b>	: Weight of heavy weight drill pipe, lb
<b>W<sub>i</sub></b>	: Cumulative water injection, STB
<b>W<sub>n</sub></b>	: Nominal weight, lb/ft
<b>W<sub>3</sub></b>	: Air weight of the casing, lbf
<b>W<sub>4</sub></b>	: Weight of the cement, lbf
<b>W<sub>5</sub></b>	: Weight of the cement in the annulus, lbf
<b>W<sub>6</sub></b>	: Weight of the mud inside the casing, lbf
<b>y</b>	: Herschel-Bulkley flow behavior coefficient, unitless
<b>Y<sub>m</sub></b>	: Minimum yield strength, psi
<b>Y<sub>pa</sub></b>	: Equivalent axial stress, psi
<b>z</b>	: Gas deviation factor, unitless
<b>z<sub>HB</sub></b>	: Herschel-Bulkley flow behavior coefficient, unitless
<b>ΔP<sub>a</sub></b>	: Sum of pressure losses in the annulus, psi
<b>ΔP<sub>b</sub></b>	: Pressure loss at the bit, psi

$\Delta P_d$	: Parasitic pressure loss, psi
$\Delta P_{dc}$	: Pressure loss in drill collar, psi
$\Delta P_{dca}$	: Pressure loss in drill collar annulus, psi
$\Delta P_{dp}$	: Pressure loss in drill pipe, psi
$\Delta P_{dpa}$	: Pressure loss in drill pipe annulus, psi
$\Delta P_{dp-ca}$	: Pressure loss in drill pipe casing annulus, psi
$\Delta P_s$	: Pressure loss in surface equipment, psi
$\frac{\Delta p}{\Delta L}$	: Frictional pressure loss gradient, Pa/m
$\Delta S$	: Buckling force, lbf
$\Delta t$	: Interval transit time, $\mu\text{s}/\text{ft}$
$\Delta t$	: Transit time, $\mu\text{s}/\text{ft}$
$\Delta t_{comp}$	: Transit time of compressional waves, $\mu\text{s}/\text{ft}$
$\Delta t_f$	: Interval transit time of a fluid, $\mu\text{s}/\text{ft}$
$\Delta t_m$	: Interval transit time of a matrix, $\mu\text{s}/\text{ft}$
$\Delta t_{shear}$	: Transit time of shear waves, $\mu\text{s}/\text{ft}$
$\sum \bar{t}_d$	: Cumulative drilling time, h
$\sum \bar{t}_t$	: Cumulative trip time, h
$\emptyset$	: Porosity, fraction
$\emptyset_a$	: Apparent porosity, fraction
$\emptyset_{corr}$	: Corrected porosity, fraction
$\emptyset_D$	: Density porosity, fraction
$\emptyset_e$	: Effective porosity, fraction
$\emptyset_N$	: Neutron porosity, fraction

$\phi_o$	: Surface porosity, %
$\phi_s$	: Sonic porosity, fraction
$\phi_t$	: Total or true porosity, fraction
$\phi_{target}$	: Target porosity, %
$\bar{x}$	: Weighted average elevation, ft
$\rho$	: Density, g/cm <sup>3</sup>
$\rho_b$	: Bulk density, g/cm <sup>3</sup>
$\rho_c$	: Density of a cement, ppg
$\rho_{continues}$	: Density of the continues face, lb/ft <sup>3</sup>
$\rho_f$	: Fluid density, g/cm <sup>3</sup>
$\rho_{fp}$	: Fracture pressure mud equivalent, ppg
$\rho_g$	: Density of gas, g/cc
$\rho_h$	: Hydrocarbon density in the invaded zone, g/cm <sup>3</sup>
$\rho_i$	: Density of the completion fluid inside a casing, ppg
$\rho_l$	: Liquid density, lb/ft <sup>3</sup>
$\rho_{ma}$	: Matrix density, g/cm <sup>3</sup>
$\rho_{mf}$	: Mud filtrate density, g/cm <sup>3</sup>
$\rho_{m_{next}}$	: Density of next section's mud, ppg
$\rho_o$	: Oil density, lb/ft <sup>3</sup>
$\rho_r$	: Reduced density, lb/ft <sup>3</sup>
$\rho_s$	: Surface density, g/cc
$\rho_w$	: Density of water, g/cc
$\sigma_{PBYS}$	: Pipe body yield strength, lbf

$\sigma_{ob}$	: Overburden stress, psi
$\sigma_{yield}$	: Yield strength of a pipe, lbf
$(\sigma_{yield})_e$	: Effective yield strength of a pipe, lbf
$\sigma_z$	: Axial stress, lbf
$\mu$	: Poisson ratio
$\gamma$	: Shear rate, 1/s
$\gamma_g$	: Specific gravity of gas, fraction
$\gamma_{GR}$	: Gamma ray reading, GAPI
$\gamma_{max}$	: Maximum gamma ray reading, GAPI
$\gamma_{min}$	: Minimum gamma ray reading, GAPI
$\theta_{300}$	: Dial reading of rotational viscometer at 300 RPM
$\theta_{600}$	: Dial reading of rotational viscometer at 600 RPM
$\mu_p$	: Plastic viscosity, cp
$\mu_g$	: Gas viscosity, cp
$\mu_o$	: Oil viscosity, cp
$\sigma_a$	: Axial stress, psi
$\sigma_b$	: Bending stress, psi
$\sigma_{b-max}$	: Maximum bending stress, psi
$\sigma_e$	: Effective stress, psi
$\sigma_r$	: Radial stress, psi
$\sigma_t$	: Tangential stress, psi
$\tau$	: Shear stress, lbf/ft <sup>2</sup>
$\tau_b$	: Buckling stress, psi

$\tau_y$  : Yield point, lbf/100ft<sup>2</sup>

$\beta$  : Coefficient for half full horizontal separator, dimensionless

$\phi$  : Internal friction angle,

## **ABSTRACT**

This study aims to cover the entire operations for the prospective well, Bane-01, in the Mount Doom Oil Field. Comprehensive assessments of well log and production data from 25 previously gathered wells in the area were used to develop a three-dimensional model of the field based on petrophysical characteristics. Following this comprehensive technique, which allows for better viewing of the subsurface formation, Bane-01 was assigned the ideal coordinates of 791288.6 latitude and 407557.6 longitude. A "mechanical earth model" was then developed to collect data on the formation's mechanical properties, which allowed casing, cementing, drill string, mud, and field designs to be neatly calculated. Cost assessments were performed, which played a significant role in the decision-making procedure. Original oil in place (OOIP) values of the newly drilled well Bane-01 in the Mount Doom Oil Field is calculated, and a field simulation that is compatible with the production data of 25 previously drilled wells using the historical matching approach was provided. The simulation program was created using the RUBIS simulation software developed by KAPPA Engineering. The simulation employed the wells' topography map, petrophysical characteristics obtained from well log investigations, and the field's historical production data to construct reservoir boundaries by trial-and-error methods. The most appropriate model for the reservoir was developed, and the field's behavior was investigated. The purpose was to predict Bane-01's future production behavior; and trying to developed a best-case scenario in terms of production, economy, and sustainability. Lastly, it was found to be important to mention that all of the engineering designs during this project was based on API standards.

## ÖZET

Bu çalışma, Mount Doom Oil Field'daki yeni açılacak olan Bane-01 isimli kuyunun bütün prosedürünü içermeyi amaçlamaktadır. Sahada bulunan ve daha önce elde edilmiş olan 25 kuyunun kuyu günlükleri ve üretim verilerinin kapsamlı analizleri sonucu petrofiziksel özelliklerin ışığı altında, sahanın üç boyutlu modellenmesi çıkartılmıştır. Yer altındaki formasyonun hayal edilmesini biraz daha kolaylaştıran bu detaylı süreçten sonra Bane-01 için optimum lokasyon 791288.6 enleminde, 407557.6 boylamında olacak şekilde seçilmiştir. Daha sonra, “mekanik dünya modeli” çıkartılarak formasyonun mekanik özellikleri hakkında bilgi sahibi olunmuştur ve böylelikle, kuyunun muhafaza borusu, üretim borusu, çimentolama, çamur ve saha tasarımları özenle belirlenmiştir. Karar oluşturma sürecindeki önemli rolü açısından maaliyet analizleri yapılmıştır. Bane-01'den alınan üretim sonucunda elde edilen miktarın, bu kuyunun araştırılmasında, tasarımlarında, sondajında, taşınmasında ve personellerin ihtiyaçlarının karşılanmasındaki masraflardan daha karlı olması planlanmıştır. Mount Doom Oil Field'da yeni açılan Bane-01 kuyusunun orijinal yerinde petrol (OOIP) değerleri hesaplanmış ve tarihsel çakıştırma yaklaşımı kullanılarak daha önce açılan 25 kuyunun üretim verileriyle uyumlu bir saha simülasyonu sağlanmıştır. Simülasyon programı olarak KAPPA Engineering'in RUBIS yazılımından yararlanılmıştır. Kuyuların bulunduğu topografya haritası, kuyu logları analizlerinden elde edilen petro-fiziksel özellikler ve sahanın eski üretim verileri simülasyona işlenerek, deneme-yanılma yöntemi ile rezervuarın sınırları belirlenmiştir. Rezervuarı yansitan en uygun model tasarlanıp sahanın davranışını gözlemlenmiştir. Bane-01 kuyusunun gelecekteki üretim davranışının tahmini ve sahanın genel anlamda en üretken, en ekonomik ve çevresel koşullara uygun senaryosu saptanmaya çalışılmıştır. Son olarak, bu proje kapsamında yapılan bütün mühendislik tasarımlarının API standartlarına uygun olarak yapıldığını belirtmekte fayda olduğu görülmüştür.

## **1. INTRODUCTION**

The investigation for an oil and gas reservoir consists of meticulous steps such as analyzing huge data sets. The primary objective of this study is to find a location of the new well on Figure 1.1 to be drilled and design the whole process considering the API standards with following safety regulations. After carefully examining the well log data of 25 previously drilled wells, an economic and valuable location for Bane-01 was chosen to be in a place where the porosity, permeability, saturation, and thickness values assigned. Then, construction of the Bane-01 was performed by designing the casings, cement, drill string, drilling fluid and field in accordance with the pressure values. The cost analysis was done in order to understand the importance of the probable reserves; Precious-1, Gollum-1 and Thorin-1. Later on, OOIP calculations were implemented by using Havlena and Odeh method. Using the RUBIS as a simulation program, history matching was applied. After the model of the field was created, 3 different production scenarios were developed in addition to the base scenario. Separator designs were made as two-phase and three-phase to extent the engineering approach.

The initial stage in reservoir characterization is to do well log analysis, which provides macroscopic-level data. The Mount Doom Oil Field's lithology and three-dimensional images were created utilizing well log data from 25 previously drilled wells in tracks 1, 2, and 3. This research aims to calculate the initial oil in place, OOIP, value. As a consequence, three hydrocarbon zones were discovered, and the location of the future well, Bane-01, was predicted using the gathered data. After determining the optimal location based on petrophysical factors such as saturation, porosity, and permeability, the well designs for Bane-01, which included the three previously stated hydrocarbon zones, were programmed.

A mechanical earth model was used to better comprehend the formation process and stress-strain relationships. These designs included casing, tubing, cement, and mud while accounting for the mud window and formation pressure. Casings protect the region from formation to the surface and can be either surface or production casing. Drilling assembly that are compatible with the calculated weight on bit (WOB) values

based on formation parameters are used, and casing diameters must match. Cement is designed to secure casings and sustain pressure values. Furthermore, a drilling fluid, usually called as mud, is designed to regulate the amount of hydrostatic pressure and formation pressure, resulting in a drilling fluid that does not harm the formation while efficiently carrying cuttings to the surface. Finally, wellhead designs suited for the projected well performance are used. The analysis of Bane-01 should result in a considerable profit between the costs of equipment, operations, transportation, and personnel services and the output from this well. This significant profit is crucial for guaranteeing that the investment yields a reasonable return. As a result, a comprehensive cost analysis was conducted, including everything from the smallest to the greatest components of the project scope and taking into account the contribution of each component. As a result, it is one of the most important variables to consider while making project selections.

Understanding the flow of gas, water and oil in the subsurface, particularly in relation to hydrocarbon recovery, are the main focuses on reservoir engineering. In this project, simulation, modelling and reserve estimation, which are sub-headings of reservoir engineering, were utilized. In order to perform reserve estimation in a field, various petrophysical parameters such as net pay thickness, area, effective porosity, water saturation and formation volume factor must be known. Due to the uncertainties in resource estimation, a combination of both statistical and analytical approaches should be performed. The material balance equation is conducted to evaluate production data, estimate reserves and predict the flow performance can be considered under the category of the analytical approach, while the Monte Carlo simulation, which uses random variables to predict future behavior by examining production data and reservoir properties, is an example of a statistical approach. These methods were used in this project for reserve estimation and OOIP calculations. As a result of processing PVT, reservoir, and production data into RUBIS, an optimum simulation scenario was designed that was compatible with previously provided production data in the Mount Doom Oil Field. The generated simulation aimed to forecast the production behavior of Bane-01. It also sought to develop a best-case scenario in terms of production, economy, and sustainability.

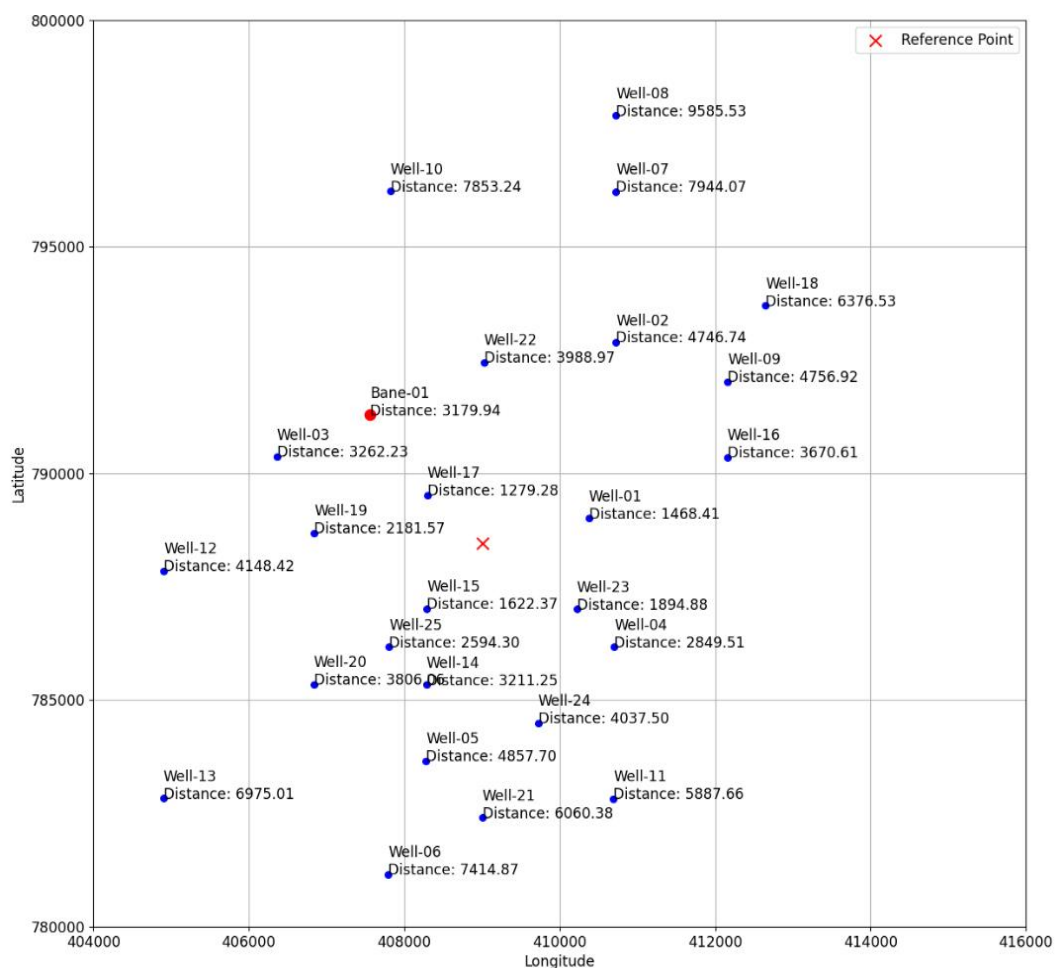


**Figure 1.1:** Map of wells.

## **2. FORMATION EVALUATION**

Under this section, there are three main subsections of Wireline Logs, Resistivity Logs, and Porosity Logs. Since every well-logging type and device has its own unique benefits to estimate critical petrophysical or formation properties, the types of well-logs that have been used will be covered, along with their usages, advantages, disadvantages, and limitations.

### **2.1. Wireline Logs**

In the oil and gas sector, wireline logging is a method used to gather data regarding subsurface formations. Using a wireline cable, a tool string is lowered into the wellbore to measure different physical characteristics of the rocks and fluids. Among the most widely used wireline logs are GR, CAL, and SP.

#### **2.1.1. Calliper logs**

The measurement of the diameter of the borehole is made using two arms, symmetrically placed on each side of a logging tool. The arms are linked to the cursor of potentiometer. Variations in hole diameter cause the arms to close or open, and the movement is reflected in resistance changes in the potentiometer. A simple calibration allows the changes in resistance to be scaled to variations in diameter. As the CAL arms are spring loaded the tool preferentially opens to the maximum hole diameter, in an ellipse along the major axis. It may, therefore, be useful to use a tool that has four arms, in order to get a more precise idea of the hole shape and of the hole volume. The CAL is a tool for measuring the diameter and shape of a borehole. The CAL log is show in Track-1 of the log display together with the bit size for reference. The scale is generally given in inches, which is standard for measuring bit sizes.

Borehole diameters can be enlarged or narrowed apart from borehole size. The diameter of the borehole depends mainly on the lithology, texture, and structure of the rock. Certain rocks may be soluble in the drilling mud. It disintegrates and cave in (i.e., sands, gravel, shale) which bore hole caves will appear. The lithology must be consolidated, in that case, the hole will be gauge (Serra, 1984). Drilling safety usually requires that the hydrostatic head of the mud column be kept above formation pressure. This pressure difference causes the mud to flow into permeable formations. The solid particles that exceed the pore size are retained at the formation face. Their build-up forms a plaster-like thin layer of very low permeability called a mud cake (Bassiouni, 1994). Therefore, the CAL log measures a smaller borehole diameter value than expected. The CAL log measurements are used for the followings:

- The detection of porous and permeable zones (presence of mud cake), and the estimation of mud cake thickness as given in (Eq. 2-1). Further, this borehole contraction was displayed in Figure 2.1 to display delineation.

$$h_{mc} = \frac{d - d_{CAL}}{2} \quad (\text{Eq. 2-1})$$

- The detection of consolidated, and in gauge sections for the scaling of packers for well testing, workover, and production.
- The correction of several log types for the effect of the borehole, and of mud cake in order to obtain a more precise interpretation.
- A guide lithology.

### 2.1.2. Gamma ray logs

The GR log is a continuous record of the intensity of natural gamma radiations emitted from formation with which the borehole interacts, measured in comparison with depth (Bassiouni, 1994). Considering that all geological formations have some radioactivity, and although many radioactive isotopes are known, the most abundant in nature is the uranium series, thorium series, and potassium-40 isotope. Because these isotopes are generally concentrated in shales and clays, they reflect the amount of shale in sedimentary rocks.

Limestones, sandstones, and dolomites have very low radioactive content compared to shaly zones. As the shale content increases in the formation, the GR log measurement increases due to the concentration of radioactive material in the shale. However, clean sandstone produces a high GR response if the sandstone contains water rich in potassium feldspar, mica, glauconite or uranium (Asquith, 1982). GR log is often measured in conjunction with porosity-type logs such as RHOB, NPHI, and DT.

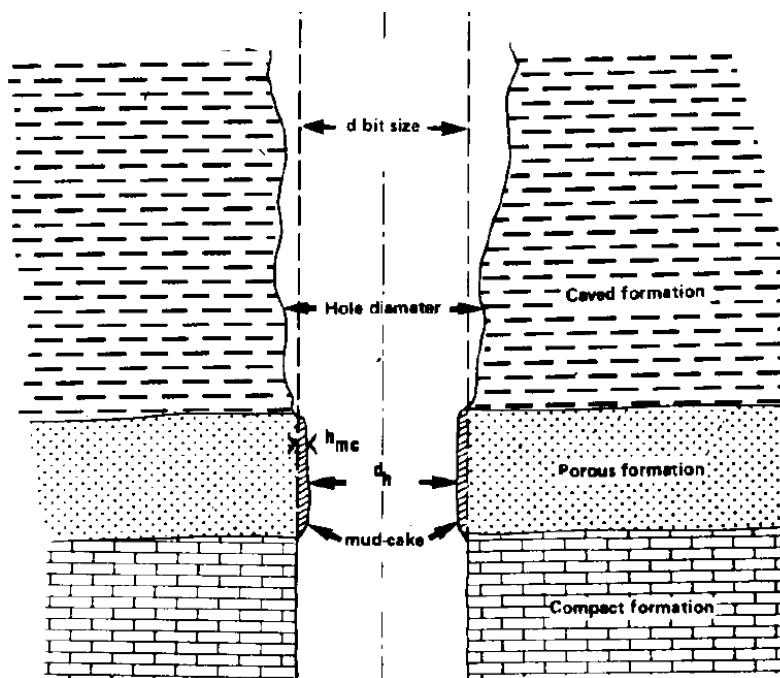


**Figure 2.1:** Borehole environment representation in the presence of mud cake, consolidated, and unconsolidated formations (Serra, 1984).

The line drawn vertically from the point where the GR reading is highest called the shale base line, and likewise sandstone line is drawn where the reading is the lowest. Thus, another vertical is drawn to locate the trade-off point between shale and sandstone formations called cut-off line. Overall, formation type can be estimated according to the distribution of the curves; shale, sandstone or shaly sand.

Shale volume estimation can be made based on the GR log readings, and also by evaluating the water saturation in shale-bearing formations with some shaly-sand techniques. Since GR responds to the radioactive properties of the formations and not their electrical properties, they do not get affected by formation's water resistivity,  $R_w$ , how SP logs do. Consequently, it can be used in cased holes and open holes containing non-conducting drilling fluids such as oil-based muds. The GR log is usually displayed in the Track-1 of a standard log display, commonly with a CAL and SP curves. Track-2, and Track-3 are often seen to include resistivity or porosity logs.

#### **2.1.2.1. volume of shale estimation**

In light of the drawn shale base line, sandstone line, and cut-off line, once can estimate shale content of the designated zone of interest if potassium is assumed to be only or the major contributor of the shale radioactivity (Eq. 2-2). This shale content is called GR index,  $I_{GR}$ , thus, it can be converted into shale volume.

$$I_{GR} = \frac{\gamma_{GR} - \gamma_{min}}{\gamma_{max} - \gamma_{min}} \quad (\text{Eq. 2-2})$$

In order to convert GR index to the volume of shale for the zone of interest, once can perform equality, which is GR index equals to the volume of shale. However, this assumption overestimates the zone of interest's shale volume. To overcome this overestimation, and interpret reasonable shale volumes, there are lots of correlations within the literature. The strictly used ones are Larionov's tertiary rocks (Eq. 2-3), Larionov's older rocks (Eq. 2-4), Clavier (Eq. 2-5), and Stieber (Eq. 2-6) equations.

Thus, one can look for DT log to understand the compaction of the zone of interest to choose appropriate equation. For instance, if the interval transit time of the zone of interest is lower than 100  $\mu\text{s}/\text{ft}$ , it indicates the formation is fairly consolidated; in contrast, the values above 100  $\mu\text{s}/\text{ft}$  dictates unconsolidated formation. If the formation is fairly consolidated Larionov's older rocks correlation can be used; otherwise, if the formation is unconsolidated, it is better to use Larionov's tertiary rocks correlation.

$$V_{sh} = 0.083(2^{3.7I_{GR}} - 1) \quad (\text{Eq. 2-3})$$

$$V_{sh} = 0.33(2^{2I_{GR}} - 1) \quad (\text{Eq. 2-4})$$

$$V_{sh} = 1.7 - \sqrt{[3.38 - (I_{GR} + 0.7)^2]} \quad (\text{Eq. 2-5})$$

$$V_{sh} = \frac{I_{GR}}{3 - 2I_{GR}} \quad (\text{Eq. 2-6})$$

### 2.1.3. Spontaneous potential logs

The SP log is one of the oldest measurements used in the petroleum industry, and it continues to play a significant role for interpreting the well logs. The SP log's capacity to differentiate between permeable and impermeable zones is utilized to determine the overall lithology, or potential reservoirs (Bassiouni, 1994).

The SP log is a record of direct current voltage that develops spontaneously between a moveable electrode in the wellbore and a fixed electrode located at the surface. Its unit is millivolt, mV. The electrochemical reactions occurring in the borehole and surrounding rock are primarily responsible for the electric voltages recorded, which in turn contribute to the SP log response. These electrochemical variables result from differences in salinity between the formation water in permeable beds and the mud filtrate. When the drilling mud is fresher than the formation water  $R_{mf} > R_w$ , there is a negative SP deflection due to the salinity differential. The SP readings have a very little change if the salinities of the formation water and the mud are similar  $R_{mf} = R_w$  since the logarithm of their ratio is zero. On the other hand, a positive SP deflection occurs if the formation water is fresher than the mud (Bassiouni, 1994). Lastly, the SP log cannot be used in non-conductive drilling muds or in air filled holes, because a conductive fluid is needed in the borehole in order to generate voltage.

When SP and GR logs in a wellbore exhibit similar behavior and are read together, it suggests that both logs are responding to the same lithological properties or characteristics in the subsurface formations. Similar behavior in SP and GR logs generally indicates that both logs are sensitive to shale-rich intervals. Shale formations typically have a higher clay content, which affects both logs. Therefore, when SP and GR logs exhibit similar responses, it is a strong indicator of the presence of shale in the formations. In case where SP and GR both exhibit low values, it suggests the presence of clean intervals. However, when SP and GR logs exhibit similar behavior, they may not always be interchangeable, as they measure different physical properties. SP log is sensitive to electrical potential differences due to clay content, while GR log is sensitive to natural gamma radiation. Their responses can differ in cases where non-shale formations contain radioactive, minerals or where there are variations in environmental conditions.

## **2.2. Resistivity Logs**

For petroleum engineers, a critical component of reservoir characterization is formation evaluation, which offers important information about a reservoir's subsurface characteristics. Of all the logging methods used to assess a formation, resistivity logging is one of the most important and useful. Fluid saturation levels and permeability are two critical criteria for reservoir study that may be estimated with the use of resistivity logs, such as  $R_t$  (Deep Induction),  $R_s$  (Short Normal), and  $R_{xo}$  (Laterolog8, or Micro-Laterolog). These logs are crucial for comprehending the petrophysical characteristics of formations.

Measuring the electrical resistivity of subsurface formations is the main purpose of resistivity logs. Because the kind of fluids in the reservoir rock have a significant impact on this electrical property, resistivity logs are a crucial tool for figuring out the fluid content and distinguishing between various fluid phases. Plotting the resistivity logs on Track-2 using a logarithmic scale allows for a more thorough representation of the electrical properties of the formation.

Based on the information that was given well logging data with their abbreviations, during the resistivity measurements of formations, Deep Induction, Short Normal, and Laterolog8 type resistivity logging devices were used (Bateman, 2020). Further, logs of Deep Induction resistivity ( $R_t$ ) offer a more comprehensive view of the features of the reservoir by revealing information on the resistivity of the formation at deeper depths. Conversely, Short Normal resistivity ( $R_s$ ) logs highlight shallower depths and offer a high-resolution picture of the area close to the wellbore. By including eight distinct readings, Laterolog8/Micro-Laterolog resistivity ( $R_{xo}$ ) logs improve the evaluation process and provide a more thorough examination of formation resistivity.

The ability of resistivity logs to estimate important reservoir properties, like fluid saturation levels and permeability, is one of its main advantages. Engineers are able to fairly analyse the economic potential of the reservoir by distinguishing between hydrocarbons and water by understanding the resistivity values. Resistivity logs also help with the computation of water saturation, which is an important metric to comprehend the amount of the reserves, and producibility of the reservoir.

Resistivity logs can be used to indirectly estimate another crucial parameter: permeability. Once the water saturation above the transition zone, and porosity is determined, the permeability of that designated zone can be estimated by using charts provided by service companies (Schlumberger, Log Interpolation Charts, 1997).

### **2.2.1. Use of resistivity logs**

With different behavior in different geological zones, resistivity logs provide a more nuanced understanding of subsurface formations. For the purpose of detecting the existence of shale, characterizing water-bearing formations, telling invaded zones apart, and identifying prospective hydrocarbon zones, resistivity data interpretation is key. For the purpose of evaluating the formation as a whole, each geological zone exhibits distinct resistivity signatures.

### **2.2.2. Potential hydrocarbon zones**

High resistivity values are indicative of potential hydrocarbon zones' resistivity behavior. Because hydrocarbons are poor electrical conductors, the resistivity of the formation increases. These zones frequently show a distinct separation between the surrounding formations and the intervals bearing hydrocarbons in the resistivity log responses. Determining the location of these zones and accurately characterizing them are essential for determining the amount of reserves and maximizing production tactics.

### **2.2.3. Invaded zone**

Resistivity logs show a clear response in the invaded zone, where drilling mud filtrate enters the formation. The invaded zone usually has lower resistivity values because of the drilling mud filtrate that is conductive when salt-water-based muds are being used during drilling. To assess the degree of invasion and comprehend the surroundings around the wellbore, it is crucial to compare the zones that have been invaded and

those that have not. Developing efficient reservoir stimulation and well completion strategies is facilitated by the accurate interpretation of these logs.

#### **2.2.4. Potential water zones**

Low resistivity values are a characteristic of formations that contain water. Resistivity decreases as a result of formation water's high conductivity. The ability to distinguish between hydrocarbon and water zones using resistivity logs is essential for precise water saturation level calculation. Engineers can evaluate the reservoir's producibility and create the best production schedules with the aid of this information, which is essential for reservoir engineering.

#### **2.2.5. Shale zones**

Because of their high bound water saturation and high clay content, shale zones usually have low resistivity values. In contrast, hydrocarbon zones have low water saturation and high resistivity values. Thus, the shale and hydrocarbon zones can be found by examining the resistivity logs.

Nevertheless, there are a number of difficulties with this approach. Resistivity can be suppressed by conductive minerals, giving the appearance of wet zones in pay zones. It can be challenging to distinguish hydrocarbons from fresh water. Additionally, problematic are thinly laminated pay zones, for which resistivity and gamma ray logs may not adequately account for the thin reservoir layers. Last but not least, certain clays and well completion methods may harm the formation, which may result in the dismissal of promising pay zones as non-prospective.

## 2.3. Porosity Logs

In the complex field of petroleum engineering, the use of well logging tools is a vital technique for imagining the structure underneath the surface. With these logging devices, engineers can interpret the subsurface structure, which is crucial for making well-informed decision related to hydrocarbon exploration. Of these methods, log display Track-3, consists of density (RHOB), neutron (NPHI), sonic (DT), and density correction (DRHO) logs which helps to interpret the lithology of the zone of interest; thus, estimate the porosity.

### 2.3.1. Density log

RHOB log is found by measuring the electron density values of the rock and comparing it with its bulk density, that is, the sum of the minerals that make up the rock and the type of liquid contained in the pores, and is also directly proportional to the electron density. Therefore, porosity can be expressed as is (Eq. 2-7). Matrix densities of typical porous reservoir rocks are given in Table 2.1 (Bassiouni, 1994). The density logging tool interacts with the electrons of formation's constituent elements by emitting gamma rays from a chemical source. The device counts the gamma rays that return using detectors. The electron density of the elements in the formation is related to these gamma rays that are returning.

$$\phi_D = \frac{\rho_{ma} - \rho_b}{\rho_{ma} - \rho_f} \quad (\text{Eq. 2-7})$$

Since the density tools explore the invaded zone due to their shallow depth of investigation,  $\rho_f$  is expressed as in (Eq. 2-8). In addition to that,  $\rho_f$  and  $\rho_{mf}$  are identical to one another since  $S_{xo}$  is equal to one in water-bearing zones. Based on the given values of different type of drilling muds given in Table 2.2,  $\rho_{mf}$  can be approximated (Bassiouni, 1994).

**Table 2.1:** Matrix densities of common reservoir rocks (Bassiouni, 1994).

<b>Rock Type</b>	<b>Matrix Density (g/cm<sup>3</sup>)</b>
Sand or sandstone	2.65
Limestone	2.71
Dolomite	2.87
Anhydrite	2.98

**Table 2.2:** Commonly used drilling muds mud filtrate densities (Bassiouni, 1994).

<b>Mud Base</b>	<b>Mud Filtrate Density (g/cm<sup>3</sup>)</b>
Oil	0.9
Fresh water	1.0
Saturated salt water	1.1

Most of the gamma rays that reach the detectors pass through the formation because both the source and the detector are in touch with the borehole wall. Gamma rays in permeable formations also pass through a mudcake, that affects the detector count rate and produces a bulk density value between the densities of the formation and mudcake. However, within this study, invaded zone fluid density will be assumed to be equal to the fluid density.

$$\rho_f = S_{xo}\rho_{mf} + (1 - S_{xo})\rho_h \quad (\text{Eq. 2-8})$$

### 2.3.2. Neutron log

The NPHI log measures the amount of hydrogen in the formation. Since the amount of hydrogen per unit volume is roughly the same for water and oil, the NPHI log calculates the liquid filled porosity (gas filled porosity is not included).

Elastic scattering, in which neutrons lose kinetic energy upon collision with nuclei in the formation, primarily hydrogen-influenced nuclei, is the basis for the NPHI log. Because hydrogen's mass is similar to that of the incident neutron, it has a substantial

effect on the neutron's slowing down. Therefore, formations rich in hydrogen have lower neutron concentrations and absorb gamma rays. Porosity and hydrogen concentration are inversely related because hydrogen is mostly found in pore space fluids (Bassiouni, 1994).

The porosity curve is recorded on the panel using a scale that matches the predominate formation matrix. Dolomite, sandstone, or limestone are chosen as the matrix. Typically, the formation density is used in conjunction with the corrected neutron tool. Plotting of the density and neutron tools is done on the same scale (Bassiouni, 1994).

### 2.3.3. Sonic log

The reciprocal of the compressional wave's velocity is measured by conventional sonic instruments. This metric, which is measured in microseconds per foot, is known as interval transit time,  $\Delta t$ , or slowness. By using Wyllie' equation (Eq. 2-9), the porosity of consolidated formations is related to  $\Delta t$  (Bassiouni, 1994). The DT logs give the primary porosity while the total porosity is obtained from the NPHI and RHOB logs. Further, if the zone of interest is found to be unconsolidated, which can be estimated by looking at where  $\Delta t > 100 \mu\text{s}/\text{ft}$ , the correction factor indicated in (Eq. 2-10) should be computed. Then, the estimated porosity from the DT log should be divided to the correction factor.

$$\phi_s = \frac{\Delta t - \Delta t_{ma}}{\Delta t_f - \Delta t_{ma}} \quad (\text{Eq. 2-9})$$

$$CCP = \frac{\Delta t_{sh}}{100} \quad (\text{Eq. 2-10})$$

While correcting the apparent sonic porosity values, for shale,  $\Delta t_{ma}$  and  $\Delta t_f$  were taken as 62.5, 189  $\mu\text{s}/\text{ft}$  respectively, assuming for a water salinity of 20% of NaCl based on Carmichael, since the formation water has a low resistivity due to dissolved salts as a general knowledge (Handbook of Physical Properties of Rocks Volume II , 1982).

### 2.3.4. Interpreting the combination of porosity logs

The lithology is limestone, pores filled 100% by water and both logs are presenting the true porosity where  $\phi_N$  and  $\phi_D$  are almost equal to each other. Shale is typically associated with a negative separation, where  $\phi_N > \phi_D$ . A Positive separation characterizes sandstones when  $\phi_N < \phi_D$ . In this scenario,  $\phi_N$  and  $\phi_D$  are both apparent porosities. Using the appropriate density/neutron and litho/porosity crossplots, a true porosity can be ascertained from  $\phi_N$  and  $\phi_D$ . Using Figure 3.1 and  $\phi_N$  alone, the true porosity can be ascertained. It can also be estimated from  $\phi_D$  alone by back calculating the bulk density reading, then entering the calculated value into (Eq. 2-13) along with the sandstone matrix density (Bassiouni, 1994).

Shales adjacent to the formation of interest are thought to be comparable to the shale present beside it for pragmatic reasons. Therefore, (Eq. 2-11), (Eq. 2-12), (Eq. 2-13) can be written for both sonic, neutron, and density logs; thus, using (Eq. 2-14), one can estimate the true porosity of an oil-bearing formation. Thus, in order to overcome the shale content within the formation, once can use the following equation, (Eq. 2-15), to estimate effective porosity of the formation of interest if volume of shale assumed to be equal to the saturation of the bound water,  $S_{wb}$  (Bassiouni, 1994).

$$\phi_N = \phi + V_{sh}(\phi_N)_{sh} \quad (\text{Eq. 2-11})$$

$$\phi_s = \phi + V_{sh}(\phi_s)_{sh} \quad (\text{Eq. 2-12})$$

$$\phi_D = \phi + V_{sh}(\phi_D)_{sh} \quad (\text{Eq. 2-13})$$

$$\phi_t = \frac{\phi_D + \phi_N}{2} \quad (\text{Eq. 2-14})$$

$$\phi_e = \phi_t(1 - S_{wb}) \quad (\text{Eq. 2-15})$$

### 3. METHODOLOGY

In order to identify possible permeable zones and execute correlation with depth, wireline logs like GR, SP, and CAL logs were used. Furthermore, clean and shale formations were estimated by the help of GR, and SP logs. Once the possible oil or water reservoir was determined, porosity values for each depth point were estimated by utilizing porosity logs such as NPHI, RHOB, DT, and DRHO. Finally, thanks to resistivity logs, saturation levels within possible reservoirs were estimated for each depth point. However, as some of the wells do not contain crucial log measurements to determine lithology, and porosity, a proximity approach was utilized to estimate desired parameters.

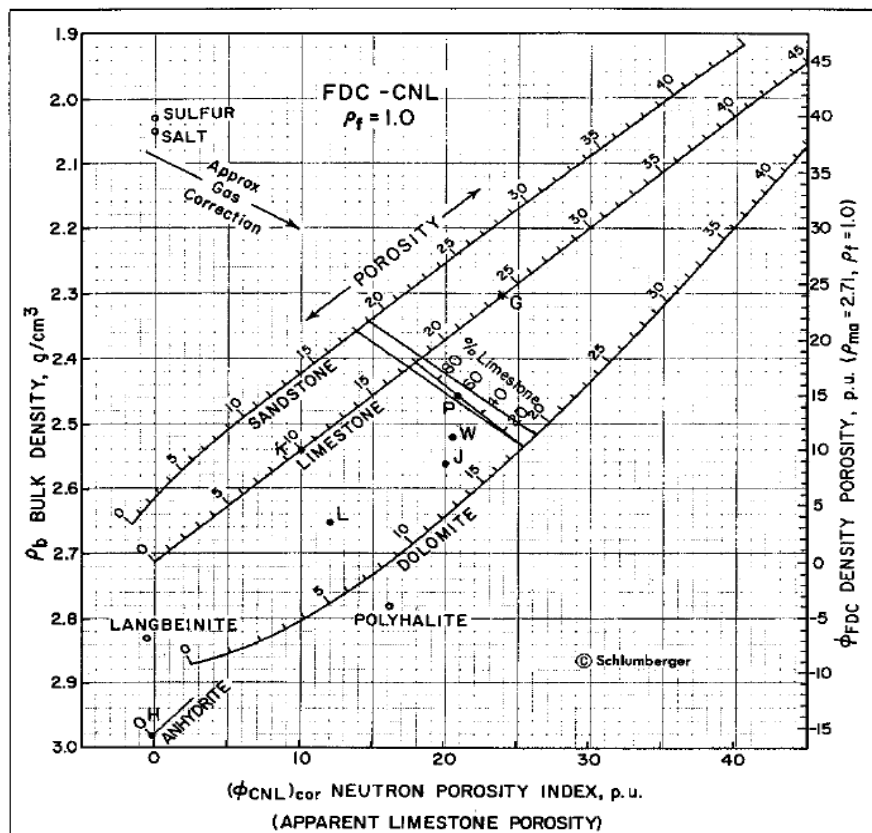


**Figure 3.1:** Cross-plot of neutron porosity for lithologies (Bassiouni, 1994).

On the other hand, formation evaluation analysis was carried out on all of the given wells; however, the representation will be on the designated wells in the Introduction section. Moreover, to compare and analyze the continuity of the possible reservoir formations, wells will be compared. Thus, in order to compare designated depths of wells that lie within the same reference line, all of the wells should be shifted onto same elevation point. To accomplish, and avoid having lots of negative depth measurements caused by offset depth, weighted average method was utilized to carry out calculation of the reference point (Eq. 3-1). According to the result obtained from (Eq. 3-1), the reference elevation point was found to be 7300.11 ft.

### **3.1. Reservoir Identification**

The only region of economic significance that has the capacity to hold fluids—water or hydrocarbons—is the reservoir zone. The presence of hydrocarbons, high porosity, and permeability are the characteristics of an ideal reservoir rock. The interpretation of the available log data was necessary for this investigation's identification of reservoir rock. Due to the low concentration of radioactive elements in sandstone reservoirs, radioactivity is generally low, so the gamma ray log was crucial in this identification. Furthermore, resistivity logs were used because reservoir zones typically exhibit higher resistivity values than non-reservoir zones. Also, the beneficial effect of NPHI-RHOB crossover was used to mark the presence of gas.

$$\bar{x} = \frac{\sum_{i=1}^n E_i D_i}{\sum_{i=1}^n D_i} \quad (\text{Eq. 3-1})$$

For the purpose of identifying hydrocarbon pay zones and calculating water saturation and formation water resistivity in subsurface formations, the  $R_{wa}$  approach is a useful reconnaissance, quick-look, technique. The process is computing  $R_{wa}$  using the (Eq. 3-2) in which  $F$  is the formation resistivity factor observed from a porosity log, such

as the sonic or density log, and  $R_t$  is the true formation resistivity determined from a deep resistivity log (Bassiouni, 1994).

$$R_{wa} = \frac{R_t}{F} \quad (\text{Eq. 3-2})$$

Since the  $R_t$  value will go closer to the  $R_o$  value in clean water zones,  $R_{wa}$  becomes equal to  $R_w$  because of the relationship given in Eq. 3-3. On the other hand, since  $R_t$  is greater than  $R_o$ ,  $R_{wa}$  would be higher than  $R_w$  in a hydrocarbon zone (Bassiouni, 1994).

$$R_o = F \times R_w \quad (\text{Eq. 3-3})$$

The  $R_{wa}$  approach can still be used even in cases where water resistivity ( $R_w$ ) is unknown. However, a water zone must present in the section being evaluated and there should be no sudden changes in salinity. In these situations,  $R_w$  can be defined using the computed  $R_{wa}$  value that is consistently lowest in water-bearing and clean zones (Bassiouni, 1994).

The  $R_{wa}$  method is either calculated over a certain interval or evaluated by plotting and comparing with lithology logs, mostly with SP, as it is affected from the salinity of the formation water. The possibility of hydrocarbons is very high where  $R_{wa} > R_w$ , however it may not always be the case. An analyst should be in caution due to the tendency of  $R_{wa}$  to rise in areas like high-resistivity shale and coal seams. In addition to that, because the neutron reading drops in gas bearing formations, it is likely to miss possible hydrocarbon zones when interpreting  $R_{wa}$  with neutron and density logs.

### **3.1.1. Hydrocarbon reservoir**

The neutron log in the presence of oil within the zone of interest will be impacted by the hydrogen content of the oil, thereby increasing the formation's apparent porosity. Oil will also have an impact on the density log because it will lower the formation's bulk density. Oil will have less of an impact on the sonic log, but it can still have an impact because of changes in the formation's mechanical characteristics.

### **3.1.2. Water reservoir**

When there is water in the zone of interest, the hydrogen content of the water will have an impact on the neutron log, reducing the formation's apparent porosity. Water will also have an impact on the density log because it will raise the formation's bulk density. Water will not have as much of an impact on the sonic log, but it can still have an impact because of changes in the formation's mechanical characteristics.

## **3.2. Volume of Shale Estimation**

Shale volume calculation is important because it aids in determining the formation porosity, fluid content, and overall quality of the rock. (Eq. 2-1), (Eq. 2-2), and (Eq. 2-3) were used in this study's GR logs method to estimate the volume of shale. Thus, the corrections will be performed based on the previously mentioned equations. The selection of the corrections will be based on whether the rock is consolidated or unconsolidated. To do that, BS data and CAL readings as well as DT readings will be compared when they are available. If BS data is fairly equal to CAL readings indicate well in gauge, thus consolidated rock. On the other hand, the interval transit time lower than  $100 \mu\text{s}/\text{ft}$  represents consolidated rock. Further, these consolidated rocks will be assumed to be older rock which will enable the usage of Larionov's older rock equation. Lastly, the vice versa is true for unconsolidated cases. And this enables the usage of Larionov's tertiary rock equation.

### **3.3. Lithology Identification**

Since lithology identification directly affects petrophysical parameters like porosity and permeability, it is essential to the characterization of reservoirs. Furthermore, the determination of fluid saturations is strongly related to particular types of lithology. GR logs were used in this study's context to identify the lithology in wells located within the Mount Doom Oil Field

Different kinds of logs were used in cross-plots to define petrophysical and lithology parameters. To infer lithology and formation porosity, specifically, the NPHI–RHOB–GR and NPHI–RHOB–DT cross-plots were used, with the M-N plot being used when pertinent data were available. During the usage of the mentioned charts, Log Interpretation Charts by Schlumberger was used as it was assumed that all of the formation evaluation has done by Schlumberger (1997).

### **3.4. Porosity Estimation**

Porosity plays a crucial role in the reserve estimations as it indicates the amount of void space that hydrocarbons can be stored. Within this study, total and effective porosities were estimated by using (Eq. 2-15). Effective porosity stands for the shale affect free porosity. Lastly, if there is a scarcity on available porosity logs, the available one or ones will be used.

### **3.5. Estimation of Saturation Levels**

To calculate original oil in place (OOIP), accurate estimation of saturation levels including water, invaded zone, hydrocarbon, and movable oil saturation is essential. Resistivity logs were utilized in this investigation to derive representative values for these saturation levels. By improving saturation estimation accuracy and advancing our knowledge of reservoir dynamics, these logs help us make better decisions for more effective hydrocarbon extraction and decision-making.

### **3.5.1. Temperature variation with elevation**

It is necessary to comprehend the average surface temperature and the GTG unique to the geological area in order to render the resistivity of formation water at different depths within a wellbore with accuracy. However, surface temperature and GTG data were not included in this study. An estimate was used to make up for the loss: an average GTG of  $1.5^{\circ}\text{F}/100 \text{ ft}$  was assumed, and the average temperature at MSL was taken to be  $59^{\circ}\text{F}$ . The lack of an active geothermal field, faulting, and generally mild weather in the area served as the foundation for these hypotheses.

A linear temperature decrease was assumed up to the end of the troposphere, with a decrement of roughly  $0.04^{\circ}\text{F}$  per 100 feet based on the U.S. Standard Atmosphere of 1976, because the wells in question are both elevated differently and located within the troposphere. Given that the wells are not exactly at MSL and are located within the tropospheric range, this assumption functions as a generalized approximation (1976).

### **3.5.2. Estimation of water saturation**

A popular empirical formula that links the formation's porosity ( $\phi$ ), formation factor ( $F$ ), true formation resistivity ( $R_t$ ), and water saturation ( $S_w$ ) is called the Archie equation. This empirical relation is shown in (Eq. 3-4). Thus, the resulted water saturation will be assumed to be equal to the initial water saturation.

$$S_{w\text{Ar}} = \left( \frac{FR_w}{R_t} \right)^{1/n} \quad (\text{Eq. 3-4})$$

Saturation exponent,  $n$ , ranges between 1 and 2.5; and, it was observed by the laboratory experiments that saturation exponent increases in oil-wet formations. Thus, in order to use (Eq. 3-4), the following assumptions should be accepted:

- The formation is homogeneous and isotropic.
- The formation is fully saturated with water.
- The formation is electrically conductive.
- The formation is at reservoir conditions.
- The formation is not invaded by drilling mud or other fluids.
- The formation is fairly consolidated.

The fully saturated formation resistivity,  $R_o$ , is regarded as being equal to the formation resistivity factor ( $R_t$ ) in the water zone. The formula in (Eq. 3-5), can be used to estimate the formation water resistivity ( $R_w$ ) as a result of this correlation. Utilizing the equality of  $R_o$  and  $R_t$  in the water zone, this streamlined relationship offers a simple way to calculate  $R_w$ .

$$R_w = \frac{R_o}{F} \quad (\text{Eq. 3-5})$$

The formula that is used to find the formation water resistivity ( $R_w$ ) in the oil zone is stated in the (Eq. 3-6) where  $R_{w1}$  stands for the average resistivity values in the water zone,  $T_1$  for the average water zone temperature, and  $T_2$  for the oil zone temperature (Schlumberger, Log Interpolation Charts, 1997).

$$R_{w2} = R_{w1} \frac{6.77 + T_1}{6.77 + T_2} \quad (\text{Eq. 3-6})$$

Furthermore, as can be seen from (Eq. 3-6), estimation of water saturation requires the knowledge of the formation resistivity of the zone of interest. In the literature, lots of different correlation have been published by the authorities and scientists. The most

accepted and widely used ones Humble (Eq. 3-7), Chevron (Eq. 3-8), Chalky rocks (Eq. 3-9). One can pay attention while using Chevron Equation that it requires a porosity range in between 15% and 30%. Lastly, (Eq. 3-7), and (Eq. 3-8) stands for sandstones reservoirs while (Eq. 3-9) stands for carbonate reservoirs.

$$F = \frac{0.81}{\phi^2} \quad (\text{Eq. 3-7})$$

$$F = \frac{1.13}{\phi^{1.73}} \quad (\text{Eq. 3-8})$$

$$F = \frac{1}{\phi^2} \quad (\text{Eq. 3-9})$$

Moreover, (Eq. 3-4) is valid for the formations that do not contain shale content, indicating completely clean sandstone. However, in reality, there is no such formation. To overcome this occasion, Simandoux proposed (Eq. 3-10) to correct the water saturation in the shaly formations (Bassiouni, 1994). During this study, this corrected water saturation values will be used.

$$S_{w\text{corr}} = \frac{0.4R_w}{\phi_e^2} \times \left\{ -\frac{V_{sh}}{R_{sh}} + \sqrt{\left[ \left( \frac{V_{sh}}{R_{sh}} \right)^2 + \frac{5\phi_e^2}{R_w R_t} \right]} \right\} \quad (\text{Eq. 3-10})$$

Irreducible water saturation ( $S_{w\text{irr}}$ ) will be estimated using Crain's formula as shown in (Eq. 3-11), which will then be used to calculate permeability since permeability computation requires knowledge of the irreducible water saturation (Crain, 2011). It is important to remember that even though  $S_{w\text{irr}}$  and  $S_{wi}$  values might be equal to each other, they do not refer to the same meaning.  $S_{wi}$  is the water saturation at which the

reservoir is initially saturated, while  $S_{\text{wirr}}$  indicates the irreducible portion, which is, the water saturation that persists even with the best extraction techniques.

$$S_{\text{wirr}} = \frac{\phi_t \times S_{\text{wi}}}{\phi_e} \quad (\text{Eq. 3-11})$$

### 3.5.3. Estimation of invaded zone saturation

The water saturation of the formation that has changed due to the invasion of the drilling fluid filtrate is known as the invaded zone saturation ( $S_{\text{xo}}$ ). It is a crucial metric for assessing the movable oil saturation ( $S_{\text{mo}}$ ) and oil saturation ( $S_o$ ) in the uninvaded zone. The invaded zone resistivity ( $R_{\text{xo}}$ ), formation factor ( $F$ ), formation water resistivity ( $R_w$ ), and saturation exponent ( $n$ ) must all be known in order to estimate  $S_{\text{xo}}$ .

Depending on the kind and extent of the tools' investigation, the extent and geometry of the invasion, and the availability of additional logs like resistivity images or SP, there are a number of ways to estimate from the resistivity logs.

Considering the available well-logs, Micro-Laterolog can be used to estimate the. It is assumed by the method that the invasion is uniform and that the depth of investigation of the micro-resistivity tools is smaller than the diameter of the invasion. Applications of the method include formations with low to moderate resistivity contrast and shallow invasion. When the mentioned assumptions are made, (Eq. 3-12), and (Eq. 3-13) come into use but, note that the correction might need to be applied to certain scenarios. All in all, one can estimate invaded zone saturation from (Eq. 3-14) after the implantation of designated assumptions.

$$R_t = R_{\text{ILD}} \quad (\text{Eq. 3-12})$$

$$R_{\text{xo}} = R_{\text{MLL}} \quad (\text{Eq. 3-13})$$

$$S_{xo} = \left( \frac{FR_w}{R_{xo}} \right)^{\frac{1}{n}} \quad (\text{Eq. 3-14})$$

Furthermore, since some of the wells do not have measurement recordings on MLL, a rule of thumb could be applied in order to make rough estimation about invaded zone resistivity. Following relationship, (Eq. 3-15), can be applied to moderate invasion and typical residual oil saturation; however, it is merely empirical and may differ significantly from the real situation.

$$S_{xo} = \sqrt[5]{S_{w\text{corr}}} \quad (\text{Eq. 3-15})$$

### 3.5.4. Estimation of oil saturation

The percentage of the formation's pore space that is filled with oil is known as the oil saturation ( $S_o$ ). It is a crucial metric for assessing the reservoir's recovery factor and hydrocarbon potential. Understanding the gas saturation ( $S_g$ ) and water saturation ( $S_w$ ) in the uninvaded zone is necessary for estimating  $S_o$ .

Depending on the kind and extent of the tools' investigation, the depth and shape of the invasion, and the availability of additional logs like SP, density, neutron, or sonic, there are a number of ways to estimate  $S_o$  from the resistivity logs. Several of the typical techniques are:

- The Archie method
- The Simandoux method
- The Waxman-Smits method
- The Indonesia method

The Simandoux method was already introduced in the previous subsections; thus, for simplicity, the Simandoux method will be used during the study. Furthermore, the process operates under the assumption that the formation is fairly consolidated, homogeneous, isotropic, fully saturated, electrically conductive, at reservoir conditions, and not invaded. Additionally, the method assumes that along the formation of interest, the saturation exponent and the formation factor remain constant. Clean sandstone reservoirs with a low to moderate shale content can use this method. However, note that the correction term will be applied as discussed in (Eq. 3-10). Thus, if it was assumed that there are only two-phase fluids within the pore volume, (Eq. 3-16) can be applied to estimate initial oil saturation. Moreover, one can estimate the residual oil saturation after estimating the invaded zone saturation by using (Eq. 3-17). Finally, with residual oil saturation and initial oil saturation, moveable oil saturation was estimated using equation (Eq. 3-18).

$$S_{oi} = 1 - S_{w_{corr}} \quad (\text{Eq. 3-16})$$

$$S_{or} = 1 - S_{xo} \quad (\text{Eq. 3-17})$$

$$S_{mo} = S_{oi} - S_{or} \quad (\text{Eq. 3-18})$$

### **3.6. Estimation of Permeability**

The ability of subsurface rocks to transfer fluids largely dependent on permeability, a basic feature in reservoir characterisation. It is a measure of how easily liquids pass through porous materials. Since permeability directly affects fluid flow rates and the effectiveness of extraction operations, assessing permeability is essential to understanding the reservoir's production potential.

Sandstone core samples of 155 from three distinct North American oil fields were used for laboratory measurements of permeability ( $k$ ), porosity ( $\phi$ ), and residual water

saturation ( $S_{wir}$ ) in order to test a number of hypotheses on the link between the two. The empirical equation is given in (Eq. 3-19) (Timur, 1968).

$$k = 0.136 \times \frac{\phi_e^{4.4}}{S_{wir}^2} \quad (\text{Eq. 3-19})$$

### 3.7. Determination of Cut-Off Values

The lowest values of petrophysical parameters that specify a reservoir's net pay zone are known as the cut-off properties. The cut-off shale volume, cut-off water saturation, and cut-off porosity are examples of the cut-off characteristics. The characteristics of the reservoir, the fluid properties, and the economic factors all influence the cut-off properties. The hydrocarbon pore volume, the net-to-gross ratio, and the reservoir recovery factor are all determined using the cut-off properties. (Baker, Jensen, & Yarranton, 2015) So, the questions are:

- Considering the economic feasibility, is the permeability of the formation sufficient enough to produce hydrocarbons?
- Existence of the movable hydrocarbon volumes. Are they sufficient enough to be produced in the given economic scenario?

Lastly, estimation of cut-off values for porosity, permeability and water saturation will be performed on Well-14 as it has the largest amount of available data; then, it will be assumed that these estimated properties are characteristic throughout the reservoir.

The term cut-off porosity refers to the lowest effective porosity value that indicates the rock's hydrocarbon-holding capacity. Permeability is a property of rocks that indicates how easily a fluid can pass through them; hence, it is commonly used to calculate the cut-off porosity (Baker, Jensen, & Yarranton, 2015). Plotting effective porosity values against permeability values that were estimated using the rough correlation given in (Eq. 3-19). Considering permeability as a function of effective porosity -as the

effective porosity implies the interconnected pore space within a rock texture-, this conventional plotting technique is particularly handy as it incorporates estimated effective porosity values along with estimated permeability values to capture the rock's ability to store and transmit the desired fluid at the lowest possible conditions.

The highest water saturation value that denotes the presence of hydrocarbons in the rock is known as the cut-off water saturation (Bassiouni, 1994). Thus, this property will also be estimated by plotting permeability values versus initial water saturation values on a semi-log scale. Thus, a linear line will be fitted to represent the inverse relation between permeability and water saturation. Then, the line will be drawn from the obtained cut-off permeability value to estimate cut-off water saturation.

The highest value of shale volume that represents the non-clay content of the rock is known as the cut-off shale volume. The impact of shale on the rock's porosity, permeability, and resistivity typically determines the cut-off shale volume. Thus, the cut-off shale volume will be determined for each well's GR readings; but, in general, 40% of shale volume was taken as cut-off shale volume. Further, the aim will be trying to increase the effectively producible hydrocarbon volumes.

### **3.8. Estimation of Hydrocarbon Mobility Index**

An indicator of how well hydrocarbons can move through reservoir rock is the hydrocarbon mobility index. A hydrocarbon condition that is moveable is indicated by a  $S_w / S_{xo}$  value less than 0.7, whereas a value equal to or greater than 1.0 indicates that the hydrocarbon is not moveable. According to the following equation, the hydrocarbon movability index is the ratio of the uninvaded zone water saturation to the invaded zone saturation as described in (Eq. 3-20) (Islam, Habib, Islam, & Mita, 2013).

$$HCMI = \frac{S_w}{S_{xo}} \quad (Eq. 3-20)$$

### **3.9. Estimation of Net to Gross Ratio**

Determining the net pay thickness is crucial for calculating the original oil in place present. The ratio of the sand-containing economically producible hydrocarbon thickness to the total thickness of the sand formation is known as the net-to-gross ratio (NTG). This phenomenon is highly correlated with cut-designated off values as cut-off values dictate the minimum requirements to produce at a projected economic rate.

### **3.10. Estimation of Recovery Factor**

The recovery factor (RF) indicates how effective the extraction operation was. Greater extraction efficiency is indicated by higher recovery factors, whilst lower values imply difficulties in recovering a substantial amount of the hydrocarbons (Eq. 3-21) was used for calculating the recovery factor for all 25 wells in the reservoir.

$$RF = \frac{S_{mo}}{S_{oi}} \quad (\text{Eq. 3-21})$$

#### 4. WELL LOG ANALYSIS

During this section of the study, the calculations and estimations on representative wells will be shown as discussed in the previous sections. The formation evaluation will be executed from the available well-log data that was demonstrated in Table 4.1. These selected wells are Well-01, Well-14, and Well-18 due to their representation of highest production, highest amount of data, and being located at the edge of the reservoir respectively.

**Table 4.1:** Available well log types for each well. Cross marks represent unavailable well logs while the empty cells indicate available ones.

	BS	CAL	GR	RS	RT	RXO	SP	NPHI	RHOB	DRHO	DT
<b>Well-01</b>								x	x	x	
<b>Well-02</b>								x	x		
<b>Well-03</b>								x	x		
<b>Well-04</b>								x	x		
<b>Well-05</b>		x						x	x		
<b>Well-06</b>								x	x		
<b>Well-07</b>											
<b>Well-08</b>								x	x	x	
<b>Well-09</b>								x	x	x	
<b>Well-10</b>								x	x	x	
<b>Well-11</b>								x	x	x	
<b>Well-12</b>								x	x	x	
<b>Well-13</b>				x				x	x	x	
<b>Well-14</b>											x
<b>Well-15</b>					x		x				x
<b>Well-16</b>					x		x				x
<b>Well-17</b>					x		x		x	x	
<b>Well-18</b>											x
<b>Well-19</b>	x	x				x				x	
<b>Well-20</b>					x		x				x
<b>Well-21</b>					x		x		x	x	
<b>Well-22</b>					x		x				x
<b>Well-23</b>					x		x				x
<b>Well-24</b>					x		x		x	x	
<b>Well-25</b>					x		x				x

## **4.1. Analysis of Well-14**

As was already mentioned, the large amount of consistent data in this particular well makes it stand out. It contains RHOB and NPHI logs, which are essential for evaluating possible lithologies in the designated zone Table 4.1. The well log for Well-14 can be seen in Figure 4.1. The first track includes an estimated apparent water resistivity curve, CAL, GR, API measurements, and BS data. IDL, SN, and MLL readings are recorded on the second track. The third track additionally shows porosity logs like NPHI and RHOB.

The first track's shaded GR area is designed to show the intensity of GR readings. An increase in shale content is indicated by a shift in shade towards reddish hues. Although there should be a relationship between GR and SP readings, this specific case disproved the theory.

### **4.1.1. Reservoir identification**

Based on the clearness of the formation on GR readings, possible mudcake build-up section observed from CAL and BS readings, the interval between 7419 feet and 7600 feet, 8127 feet and 8150.5 feet, and 8198.5 feet and 8217.5 feet were chosen as a possible hydrocarbon bearing formations. Moreover, this estimation was found to be supported by apparent water resistivity increment within the selected zones. All the selected intervals were determined to be a possible hydrocarbon-bearing formation based on the clarity of the formation in GR readings and observations of possible mudcake build-up from CAL and BS readings. Additionally, this evaluation finds evidence in the apparent rise in water resistivity in this particular zone. Furthermore, there is compelling evidence supporting these zones of interest from the resistivity readings in the second track. It was found that  $R_{xo} < R_t$  in this zone, indicating invasion and, as a result, a porous and permeable zone. Lastly,  $R_{xo} > R_s > R_t$  was noted as a step-profile resistivity.

Finding a possible water zone became essential to the calculations in order to estimate formation water resistivity, which is a critical component in figuring out saturation

levels. After further examination, a water zone that is probably present was found to be between 8250 and 8340 feet deep. This conclusion was based on two things; first, the GR readings indicated that the formation was free of shale, and second, the apparent water resistivity curve showed that the rock resistivity was fully saturated. Resistivity readings further confirmed the zone's suitability as a representative water zone. The second track data showed a decreasing trend in the deep induction readings, which further supported the possibility that this is a water zone, and a pattern where  $R_{xo} > R_s > R_t$ , signalling invasion with step-profile resistivity. Lastly, these indicated possible hydrocarbons zones were demonstrated in Figure 4.6.

The values of  $R_{wa}$  were determined by using (Eq. 3-2), which was a crucial step in identifying the hydrocarbon zones in the reservoir.

#### **4.1.2. Volume of shale estimation**

The volume of shale in a reservoir must be estimated for complete reservoir characterisation. To calculate shale volume, Larinov's older rock equation (Eq. 2-4) was used for  $I_{GR}$  values, a well-established approach in petrophysics. Based on the given GR readings of Well-14, maximum and minimum GR readings were found to be 117 GAPI, and 7 GAPI respectively. Furthermore,  $I_{GR}$  values were evaluated to be used in calculating the volume of shale as referred in (Eq. 2-2).

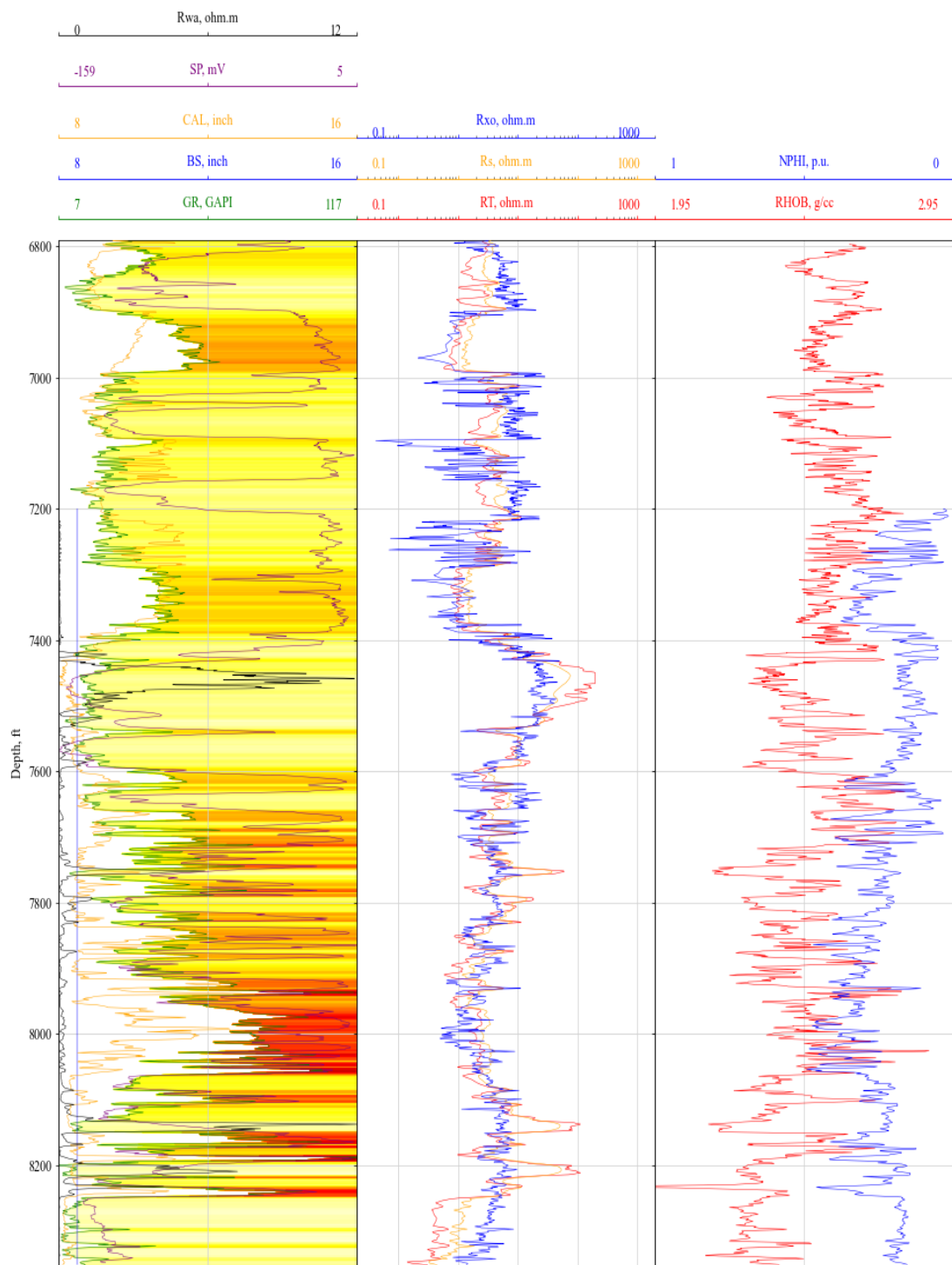


**Figure 4.1:** Well log display of Well-14.

#### 4.1.3. Lithology identification

After applying corrections to the NPHI and RHOB values obtained from the log readings, a lithology graph was prepared by plugging NPHI percentage values on the x-axis and RHOB values in g/cm<sup>3</sup> on the y-axis as seen in Figure 4.2. The lithology of the first reservoir is determined by whichever lithology line the resulting distribution gets closest to. In conclusion, the first reservoir is estimated to be 71% sandstone, 27% limestone, and 2% of dolomite, the second and third reservoirs are found to be 99% sandstone, 1% limestone.

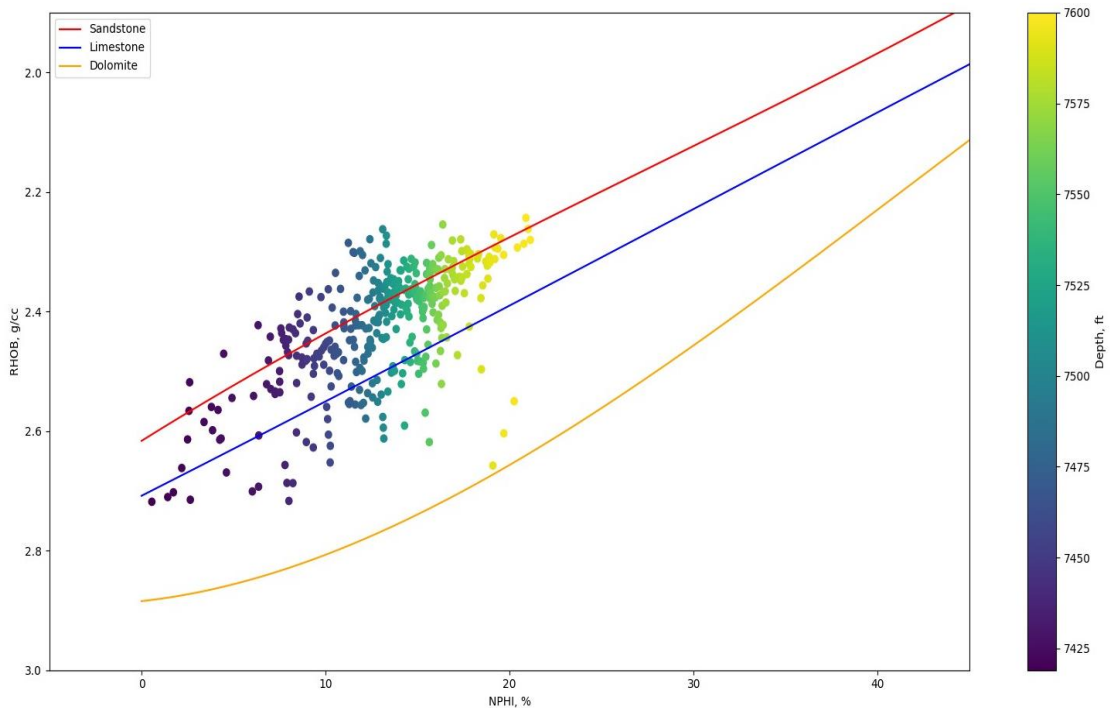


**Figure 4.2:** Lithology determination from NPHI and RHOB.

#### 4.1.4. Porosity estimation

Density porosity was calculated using (Eq. 2-7) with the help of RHOB log readings, and necessary corrections were made. Likewise, after correction was applied to the NPHI values, the average of these correction values was taken to find the total porosity,

which were found to be 0.15, 0.24, 0.22 for all the zones in order, since it is an oil zone. To find the effective porosity of 0.14, 0.23, 0.21 for all the zones respectively, (Eq. 2-15) was used.

#### **4.1.5. Estimation of saturation levels**

Simandoux equation (Eq. 3-10) was used for a more reliable estimate after finding nonlogical  $S_{wi}$  results from Archie's equation (Eq. 3-4) during our reservoir investigation. The reason for choosing the Simandoux equation in this research was because of the presence of nearby shale strata surrounding the reservoir. Log observations visualized from using the Python code revealed shale obstacles above, below, or both near the reservoir, effecting the computations. To handle these difficulties and improve the accuracy of judgments, Simandoux equation was adopted. Resistivity of shale ( $R_{sh}$ ) in the equation was determined as 1.4 ohm.m using the programming language Python. The developed Python code is intended to compute  $I_{GR}$  and then calculate  $V_{shale}$ . It selectively filters segments with more than 40%  $V_{shale}$  value and displays them on a scatter plot by plugging the  $V_{sh}$  values on the x-axis and  $R_t$  values on the y-axis. Following that, a horizontal line is formed from the lowest point of the graph, setting that number as  $R_{sh}$  as shown in the Figure 4.3.

Important factors including invaded zone saturation ( $S_{xo}$ ), initial oil saturation ( $S_{oi}$ ), residual oil saturation ( $S_{or}$ ), and movable oil saturation ( $S_{mo}$ ) were computed using the  $S_{wi}$  values as a basis with the help of (Eq. 3-15), (Eq. 3-16), (Eq. 3-17), and (Eq. 3-18) respectively. The mentioned calculations provide enhanced comprehension of the composition and fluid distribution of the reservoir, hence enabling well-informed decision-making concerning the exploration and extraction of hydrocarbon resources.

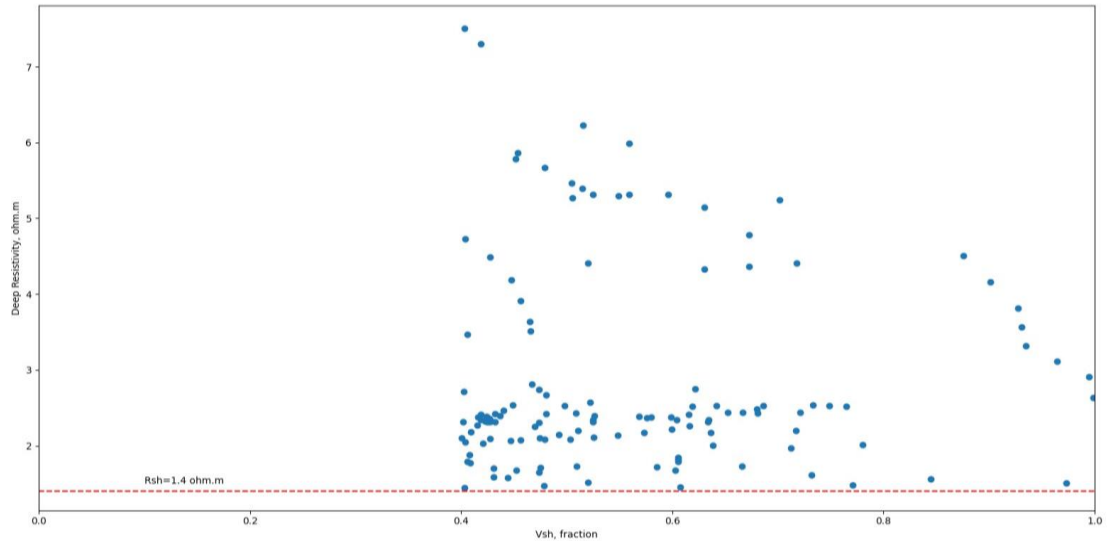


**Figure 4.3:** Resistivity of adjacent shales for Well-14.

#### 4.1.6. Determination of cut-off values

Based on the explanation given in the Methodology section, effective porosity values along with roughly estimated permeability values were plotted on the semi-log scale with a linear regression line. From the lowest value that can be seen on the plot, a line was drawn to intersect the regression line. The corresponding y-axis value and the x-axis value were determined as cut-off permeability, and cut-off porosity value respectively. This graph is demonstrated in Figure 4.4. Based on this approach, the cut-off porosity, and cut-off permeability values were estimated to be 3.38% and 0.08 md respectively.

On the other hand, since the cut-off permeability value was estimated, the cut-off water saturation can be estimated by utilizing a permeability versus initial water saturation plot on a semi-log scale. To achieve the cut-off water saturation value, the estimated cut-off permeability was plugged onto the y-axis, and then, a horizontal line was drawn until the fitted linear regression line. Finally, the cut-off water saturation was estimated as 77% as demonstrated in Figure 4.5.

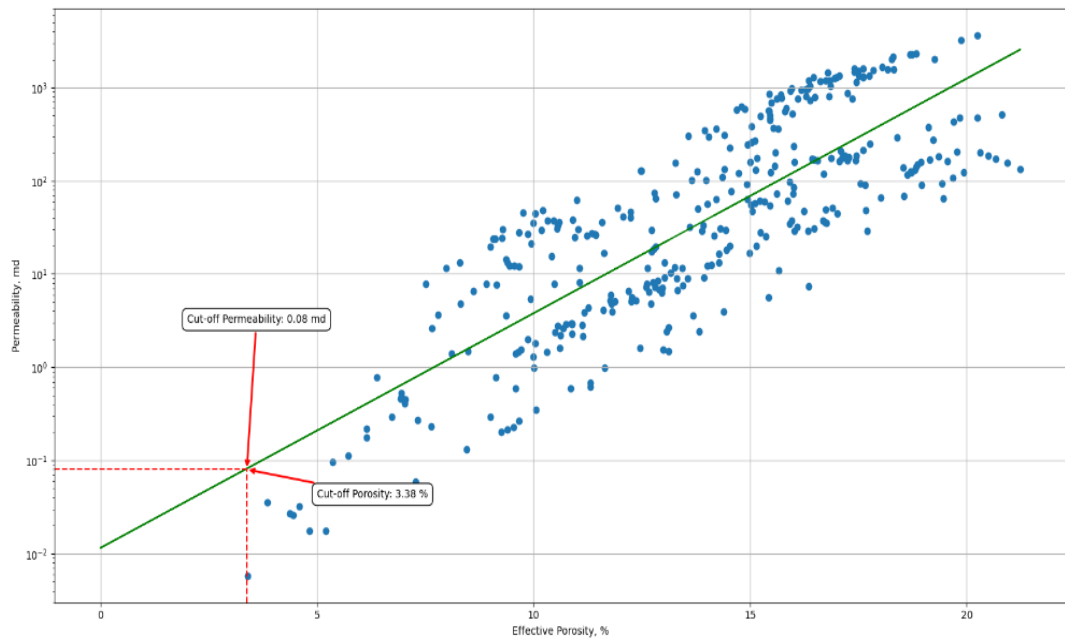


**Figure 4.4:** Determination of cut-off permeability and cut-off effective porosity.

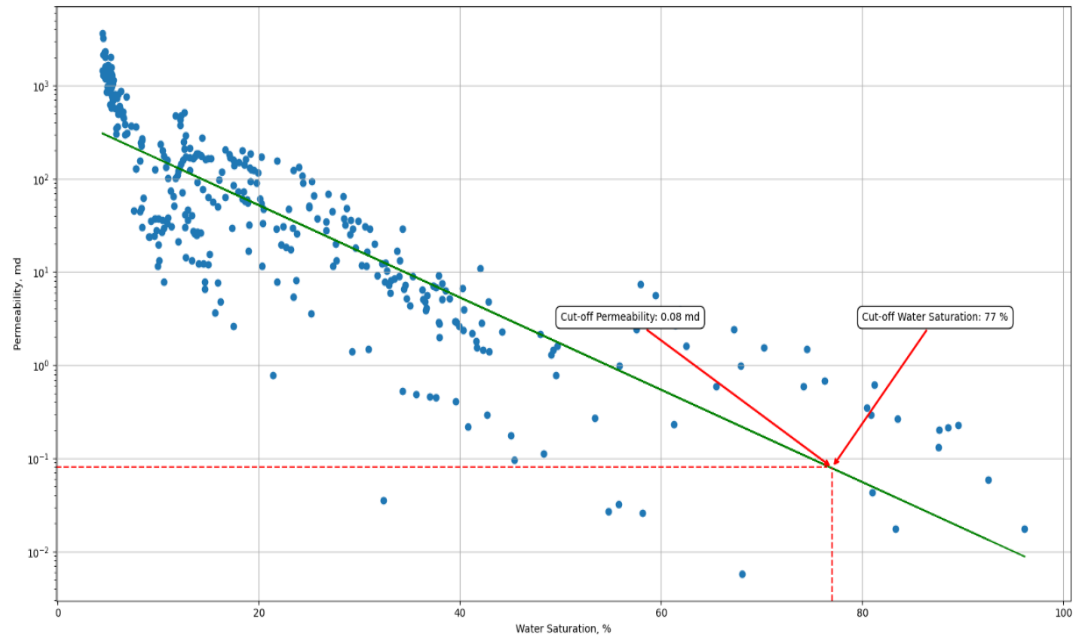


**Figure 4.5:** Cut-off water saturation determination from permeability and water saturation.

Further, net pay thicknesses will be determined based on the results where the following conditions are satisfied at the same time:

- $\phi_e < \phi_c = 0.0338$
- $S_{wi} < S_{wc} = 0.77$
- $k > k_c = 0.08 \text{ md}$

#### **4.1.7. Estimation of net to gross ratio**

When the reservoir zone from 7419 to 7600 feet is subjected to the inequalities described in the Estimation of Cut-off Values section, a non-productive zone with a depth of 19 feet is found. The net pay thickness is obtained by subtracting this amount from the gross thickness. The result of dividing the net pay thickness by the gross thickness is the net-to-gross ratio, which has a value of 0.9.

#### **4.1.8. Estimation of hydrocarbon mobility index**

Hydrocarbon index was found by dividing the initial water saturation ( $S_{wi}$ ) value to the invaded zone saturation ( $S_{xo}$ ) value as shown in the (Eq. 3-20). For productive zones Precious-1, Gollum-1 and Thorin-1, the hydrocarbon mobility indexes were found to be 0.27, 0.15 and 0.14 respectively. Given that all values are less than 0.7, the results are regarded credible and consistent within the predicted range.

#### **4.1.9. Estimation of recovery factor**

Recovery factor was obtained as 0.63, 0.57 and 0.57 for Precious-1, Gollum-1 and Thorin-1 productive zones by using the (Eq. 3-21). These fractions reveals that the more than half of the in place reserves are producible.

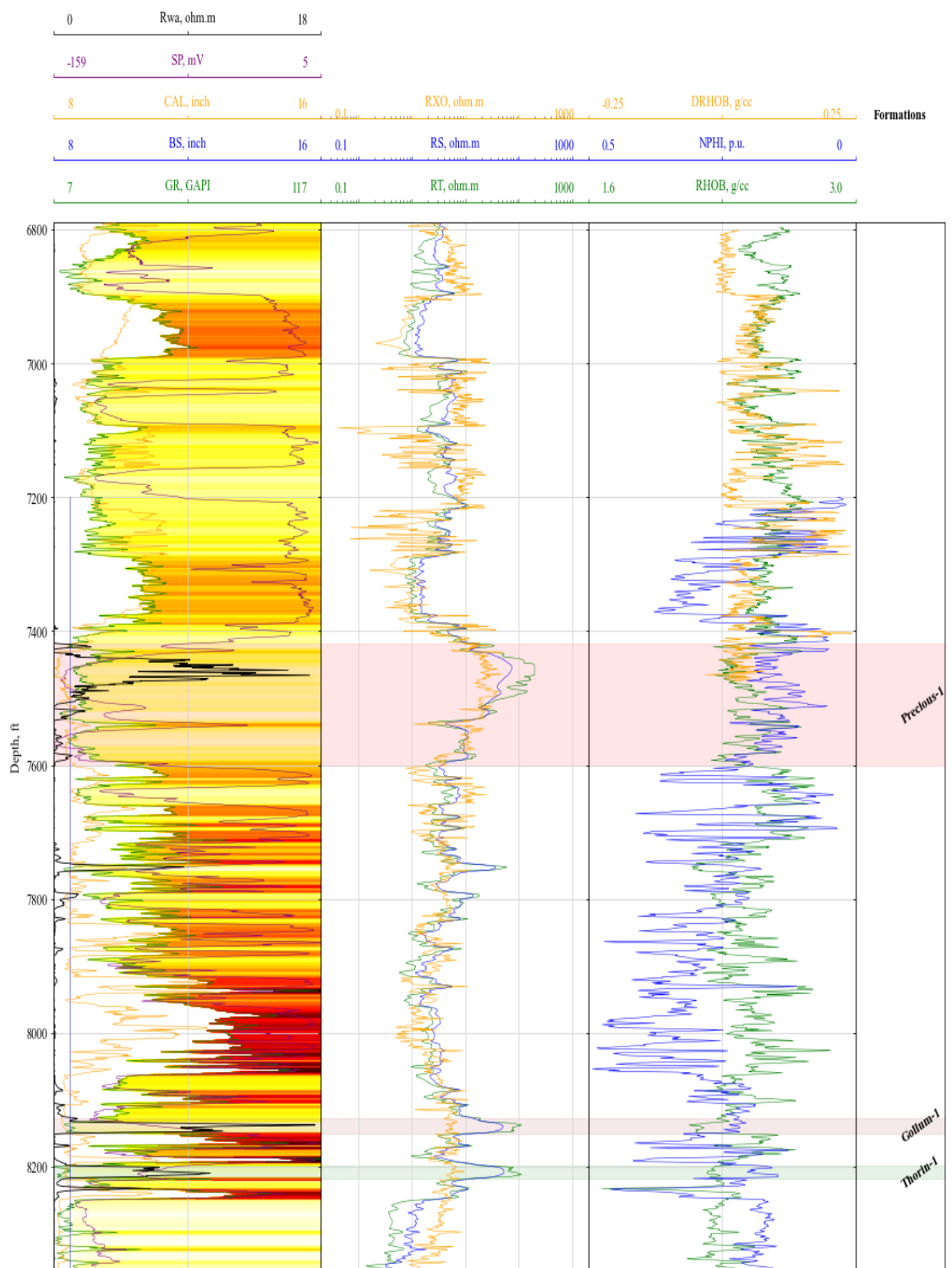


**Figure 4.6:** Well log display of Well-14 along with designated formations.

## **4.2. Analysis of Well-01**

The analysis of Well-01 is vital for the geological and petrophysical aspects of the reservoir since it is one of the most productive wells, it is drilled to a considerable amount of depth, and it plays a crucial role as the first well drilled during the exploratory phase. The logging tracks supplement the well's overall evaluation. The well log for Well-01 can be seen in Figure 4.7. Track 1 consist of SP, CAL, and GR logs, while track 2 has resistivity logs of  $R_t$ ,  $R_{xo}$  and  $R_s$ . Finally, track 3 only uses the Neutron Porosity (NPHI) log to provide insightful information on porosity. Lastly, these indicated possible hydrocarbons zones were demonstrated in Figure 4.8.

### **4.2.1. Reservoir identification**

Gamma Ray (GR) and Spontaneous Potential (SP) logs were used to draw boundaries for clean zones. By utilizing the maximum and minimum values of the GR log reading, the shale volume was computed first by obtaining the gamma ray index via using the (Eq. 2-2), yielding important details regarding the composition of shale in the formations. Thus, evaluating  $R_{wa}$  values showed in (Eq. 3-2) helped to find the hydrocarbon zones in the reservoir. This information further made it easier to estimate the water and three possible hydrocarbon zones. The water zone was located between 8320 and 8400 feet. The first hydrocarbon zone was found between 7275 and 7400 feet, the second hydrocarbon zone was observed between 8195 to 8246.5 feet, and finally the third hydrocarbon zone was estimated between 8568 to 8620 feet in depth. This methodical approach, which incorporates a range of well logging instruments and analytical methodologies, enhances our comprehension of the underlying geology and facilitates the identification of hydrocarbon and water-bearing formations.

#### 4.2.2. Volume of shale estimation

The maximum and the minimum GR values were determined to be 765 GAPI and 2 GAPI, respectively, based on the Well-01 GR readings that were provided.  $I_{GR}$  values were assessed using (Eq. 2-2) in order to be employed in the computation of the shale volume mentioned in (Eq. 2-4).

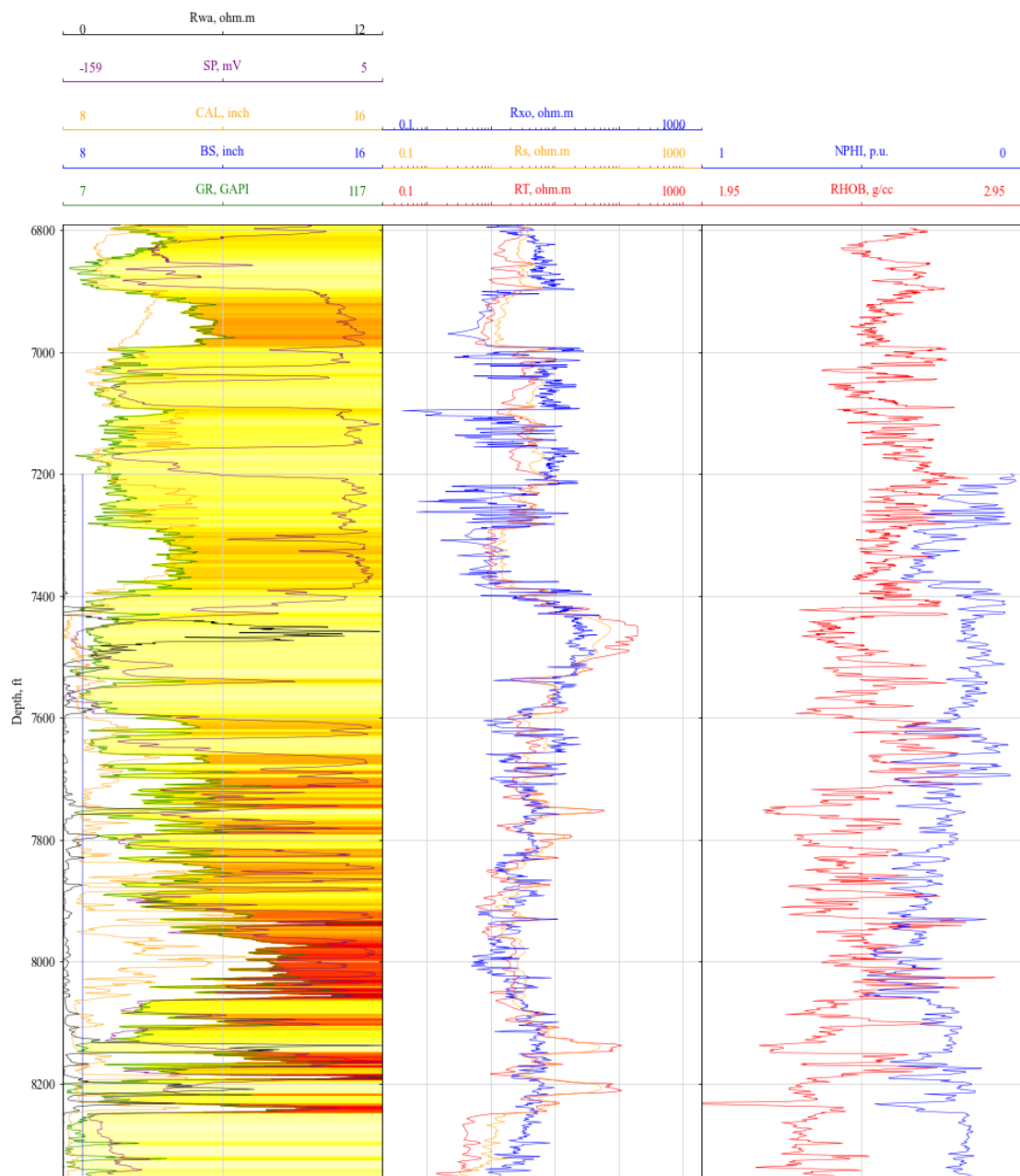


**Figure 4.7:** Well log display of Well-01.

#### **4.2.3. Lithology identification**

As a result of Well-01's lack of porosity logs, which is necessary for a precise lithological study, it was decided to use the lithology of the physically closest well as a cross-well approach. For the both hydrocarbon zones, Well-02 was depended on by comparing the off-set depths of Well-01 and Well-02. The lithology was assumed to be 76% sandstone, 21% limestone, and 3% dolomite for Precious- 1, 100% sandstone for both Gollum-1 and Thorin-1 zones.

#### **4.2.4. Porosity estimation**

Since Well-01 has only NPHI porosity log, the corrected values were taken as the same as log reading values. Thus, the effective porosity was also taken as the same. Based on the calculations, for both total and effective porosity values were taken as 0.13, 0.17, and 0.1 for zones Precious-1, Gollum-1 and Thorin-1.

#### **4.2.5. Estimation of saturation levels**

(Eq. 3-10) was utilized for a more reliable estimate in our reservoir investigation (see section 4.1.5). Despite adjacent shale resistivity estimation in Well-14,  $R_{sh}$  value was adopted from the nearest well, Well-02, due to the absence of representative existing shale beds. This is because, after filtering shale volumes exceeding 40%, no observations were made in deep induction resistivity measurements. In conclusion,  $R_{sh}$  value was estimated as 1.28 ohm.m. Key factors, including invaded zone saturation ( $S_{xo}$ ), initial oil saturation ( $S_{oi}$ ), residual oil saturation ( $S_{or}$ ), and movable oil saturation ( $S_{mo}$ ), were computed using  $S_{wi}$  values as a basis with equations (Eq. 3-15), (Eq. 3-16), (Eq. 3-17), and (Eq. 3-18), resulting in final values of 0.73, 0.78, 0.27, and 0.51, respectively.

#### **4.2.6. Determination of cut-off values**

All of the cut-off values that were identified from the analysis of Well- 14 will be used; cut-off porosity of 3.33%, cut-off permeability of 0.08 md and 77% for cut-off water saturation.

#### **4.2.7. Estimation of net to gross ratio**

A non-productive zone with a depth of 2.5 feet is discovered when the first reservoir zone between 7275 and 7400, the second hydrocarbon zone between 8195 and 8246.5, and the third productive zone between 8568 and 8620 feet is subjected to the inequalities mentioned in the Estimation of Cut-off Values section. This amount is subtracted from the gross thickness to determine the net pay thickness which were found as 112.5, 51.5, 26.5 respectively. The net-to-gross ratio is the outcome of dividing the net pay thickness by the gross thickness which ranges from 0 to 1. In conclusion, net to gross values were calculated as 0.98, 1 and 0.51 for all three productive zones in order.

#### **4.2.8. Estimation of hydrocarbon mobility index**

Hydrocarbon index was found by dividing the initial water saturation ( $S_{wi}$ ) value to the invaded zone saturation ( $S_{xo}$ ) value as shown in the (Eq. 3-20). For productive zones Precious-1, Gollum-1 and Thorin-1, the hydrocarbon mobility indexes were found to be 0.3, 0.22 and 0.42 respectively. Given that all values are less than 0.7, the results are regarded credible and consistent within the predicted range.

#### **4.2.9. Estimation of recovery factor**

Recovery factor was computed as 0.66, 0.63 and 0.7 for Precious-1, Gollum-1 and Thorin-1 productive zones by using the (Eq. 3-21).

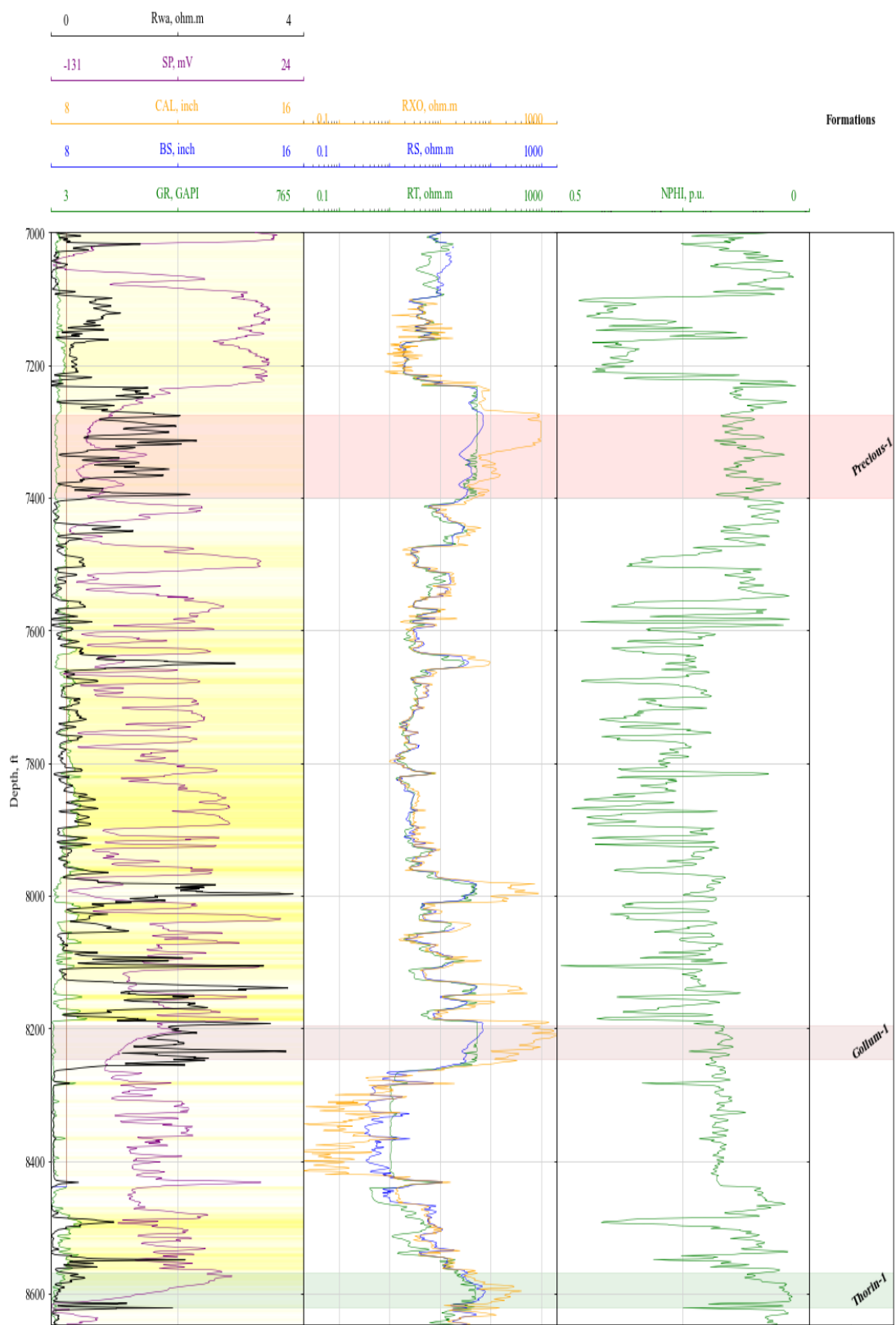


**Figure 4.8:** Well log display of Well-01 along with designated formations.

### **4.3. Analysis of Well-18**

An extensive collection of logging tools was used to analyze the well logging data for Well-18 in order to describe the underlying formations. The well log for Well-18 can be seen in Figure 4.9. On track one, GR, SP and CAL, on track two,  $R_s$ ,  $R_t$  and  $R_{xo}$  tools were used while NPHI, RHOB and DT were used on track 3 for porosity and further lithology estimations. Lastly, these indicated possible hydrocarbons zones were demonstrated in Figure 4.15.

#### **4.3.1. Reservoir identification**

Gamma Ray (GR) and Spontaneous Potential (SP) logs were used to draw boundaries for clean zones. By utilizing the maximum and minimum values of the GR log reading, the shale volume was computed first by obtaining the gamma ray index via using the (Eq. 2-2), yielding important details regarding the composition of shale in the formations. Thus, evaluating  $R_{wa}$  values showed in (Eq. 3-2) helped to find the hydrocarbon zones in the reservoir. This information further made it easier to estimate the water and two possible hydrocarbon zones. The water zone was located between 7700 and 7730 feet, while the hydrocarbon zone was found between 7460 and 7660 feet in depth. This methodical approach, which incorporates a range of well logging instruments and analytical methodologies, enhances our comprehension of the underlying geology and facilitates the identification of hydrocarbon and water-bearing formations.

#### **4.3.2. Volume of shale estimation**

Well-18's GR data were used to determine the maximum and minimum GR values, which were determined to be 88 GAPI and 2 GAPI, respectively.  $I_{GR}$  values were assessed to be used in figuring out the volume of shale mentioned in (Eq. 2-4) using (Eq. 2-2).

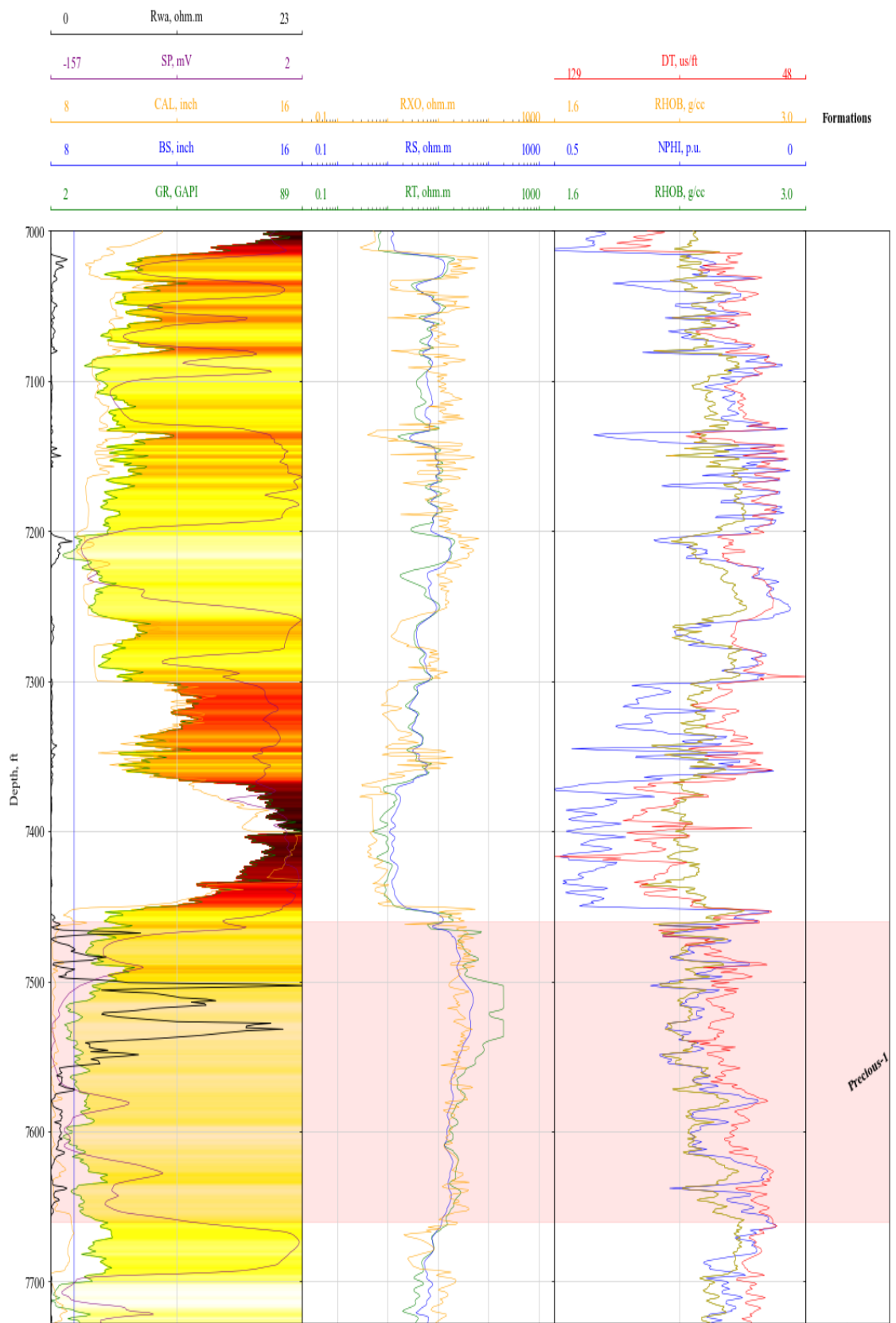


**Figure 4.9:** Well log display of Well-18.

#### **4.3.3. Lithology identification**

After applying corrections to the NPHI, RHOB and DT values obtained from the log readings, two graphs were prepared for the lithology. As seen in Figure 4.10, when NPHI percentage values are entered on the x-axis and RHOB values in g/cm<sup>3</sup> are entered on the y-axis, the lithology of the reservoir is determined by whichever lithology line the resulting distribution gets closest to. In Figure 4.11, NPHI percentage values are plugged on the x-axis and DT values plugged on the y-axis. As can be seen from these two graphs, the reservoir is estimated to be 44% sandstone and 56% limestone. In addition to that, the lithology of the water zone was found as 6% of sandstone and 94% of limestone. Figure 4.12 and Figure 4.13 shows the distribution of NPHI-RHOB and NPHI-DT lithology plots respectively.

#### **4.3.4. Porosity estimation**

Density porosity was calculated using (Eq. 2-7) with the help of RHOB log readings, and necessary corrections were made. Likewise, after correction was applied to the NPHI values, the average of these correction values was taken to find the total porosity, which was found to be 0.18, since it is an oil zone. To find the effective porosity of 0.16, (Eq. 2-15) was used.

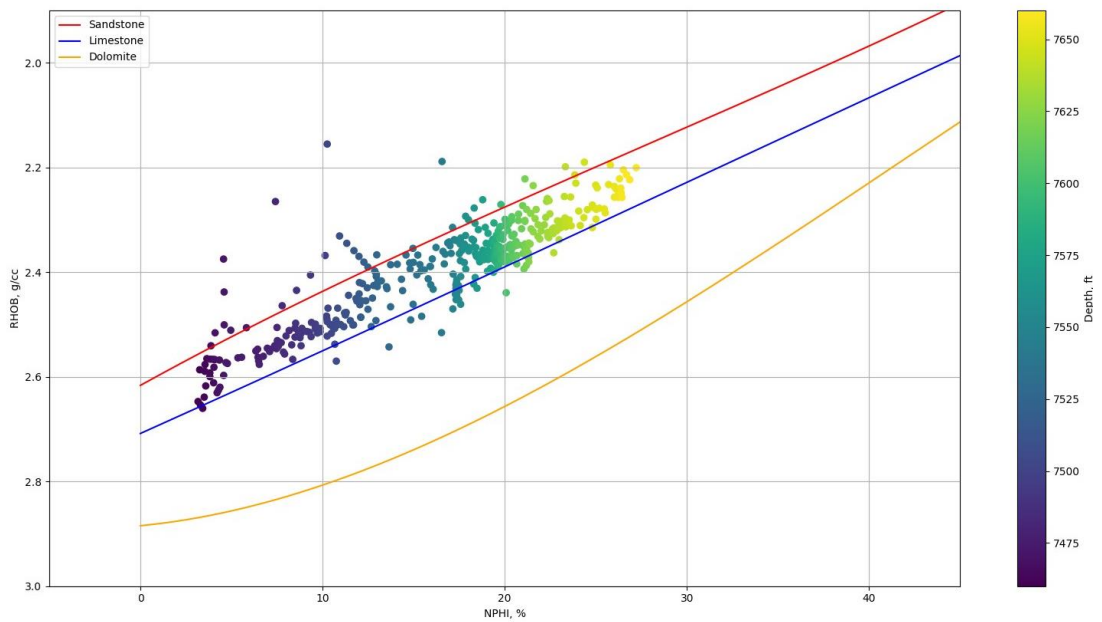


**Figure 4.10:** Lithology determination from NPHI and RHOB for Oil-Zone.

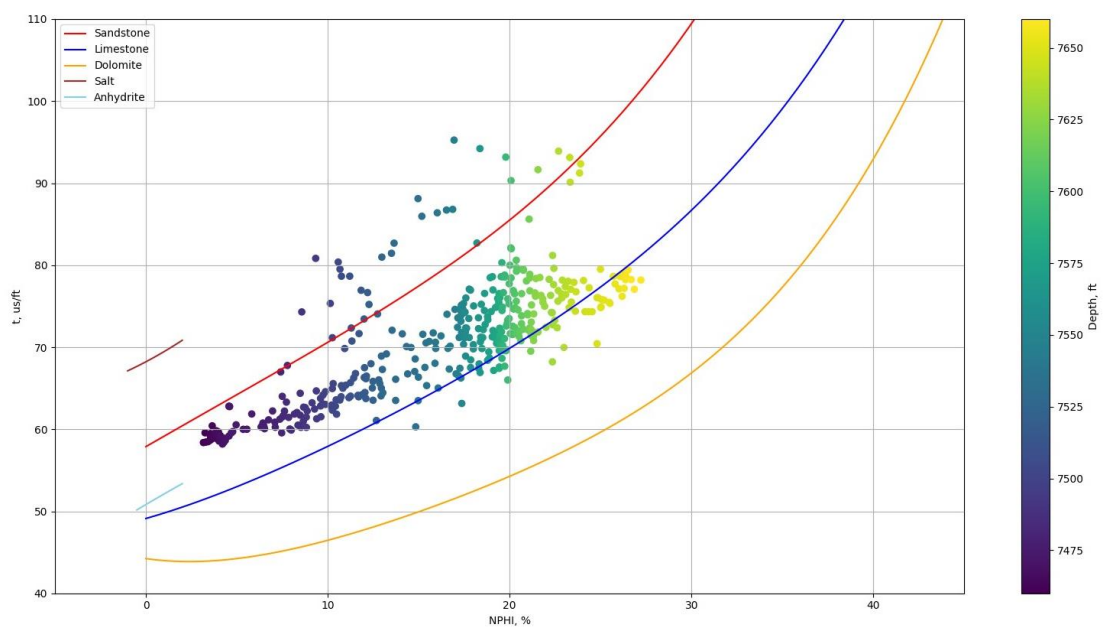


**Figure 4.11:** Lithology determination from NPHI and DT for Oil-Zone.

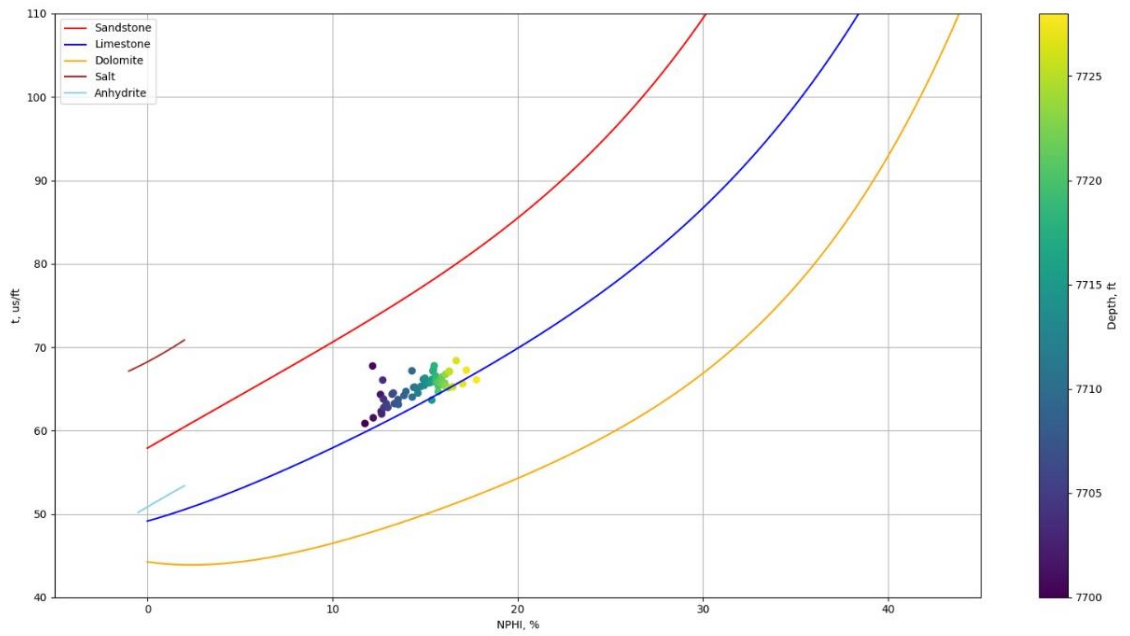


**Figure 4.12:** Lithology determination from NPHI and DT for Water-Zone.

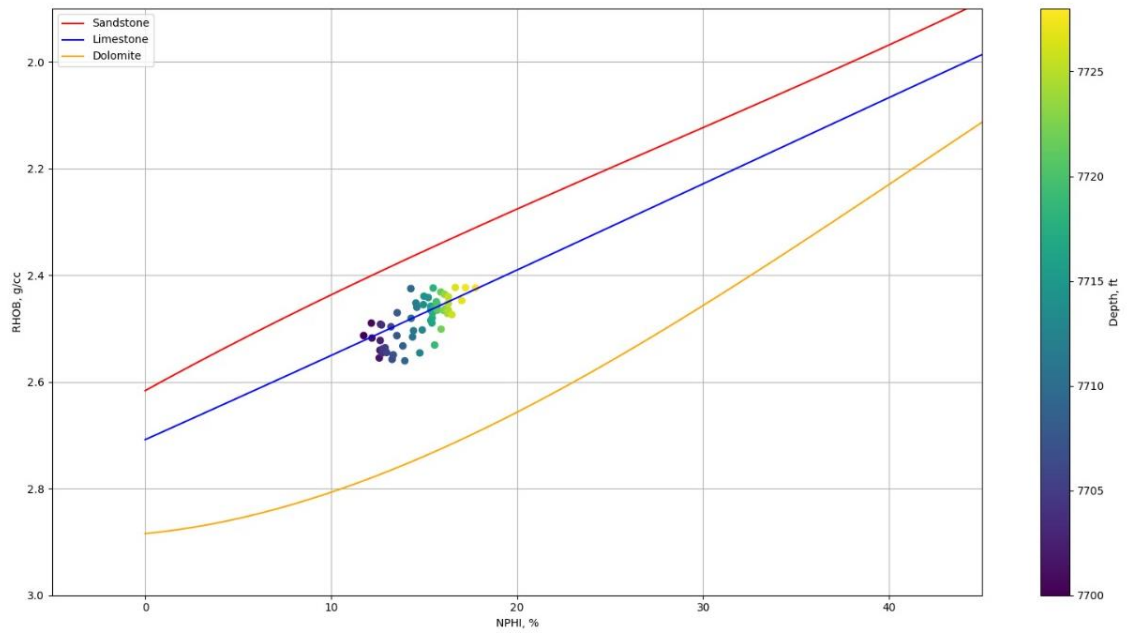


**Figure 4.13:** Lithology determination from NPHI and RHOB for Water-Zone.

#### 4.3.5. Estimation of saturation levels

Section 4.1.5. explains why (Eq. 3-10) was employed for a more credible estimate throughout the reservoir investigation. Finally, the  $R_{sh}$  value was determined to be 0.49 ohm.m, as illustrated in Figure 4.14

Important factors including invaded zone saturation ( $S_{xo}$ ), initial oil saturation ( $S_{oi}$ ), residual oil saturation ( $S_{or}$ ), and movable oil saturation ( $S_{mo}$ ) were computed using the  $S_{wi}$  values as a basis with the help of (Eq. 3-15), (Eq. 3-16), (Eq. 3-17), and (Eq. 3-18) respectively. The final values were 0.67, 0.84, 0.33 and 0.51 in order.

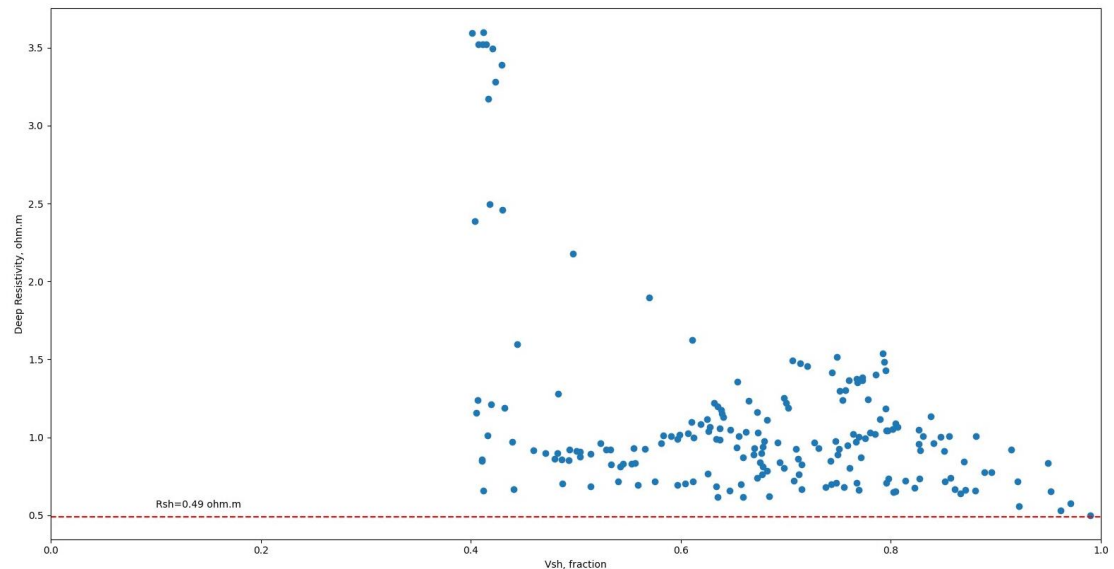


**Figure 4.14:**  $R_{sh}$  determination from  $V_{sh}$  and deep resistivity.

#### 4.3.6. Determination of cut-off values

All of the cut-off values that were identified from the analysis of Well- 14 will be used; cut-off porosity of 3.33%, cut-off permeability of 0.08 md and 77% for cut-off water saturation.

#### **4.3.7. Estimation of net to gross ratio**

Applying the inequalities mentioned in the Estimation of Cut-off Values section to the reservoir zone spanning from 7460 and 7660 feet, a non-productive zone measuring 11.5 feet is discovered. Thus, this amount is deducted from the gross thickness to get the net pay thickness which was 188.5. One can calculate the net-to-gross ratio, which was found to be 0.94, by dividing the net pay thickness by the gross thickness.

#### **4.3.8. Estimation of hydrocarbon mobility index**

Hydrocarbon index was found by dividing the initial water saturation ( $S_{wi}$ ) value to the invaded zone saturation ( $S_{xo}$ ) value as shown in the (Eq. 3-20). For productive zone Precious-1, the hydrocarbon mobility index was found to be 0.23. Given that the value is less than 0.7, the result is regarded credible and consistent within the predicted range.

#### **4.3.9. Estimation of recovery factor**

Recovery factor was computed as 0.61 for Precious-1 by using the (Eq. 3-21), which reveals that more than half of the in place reserves are producible.

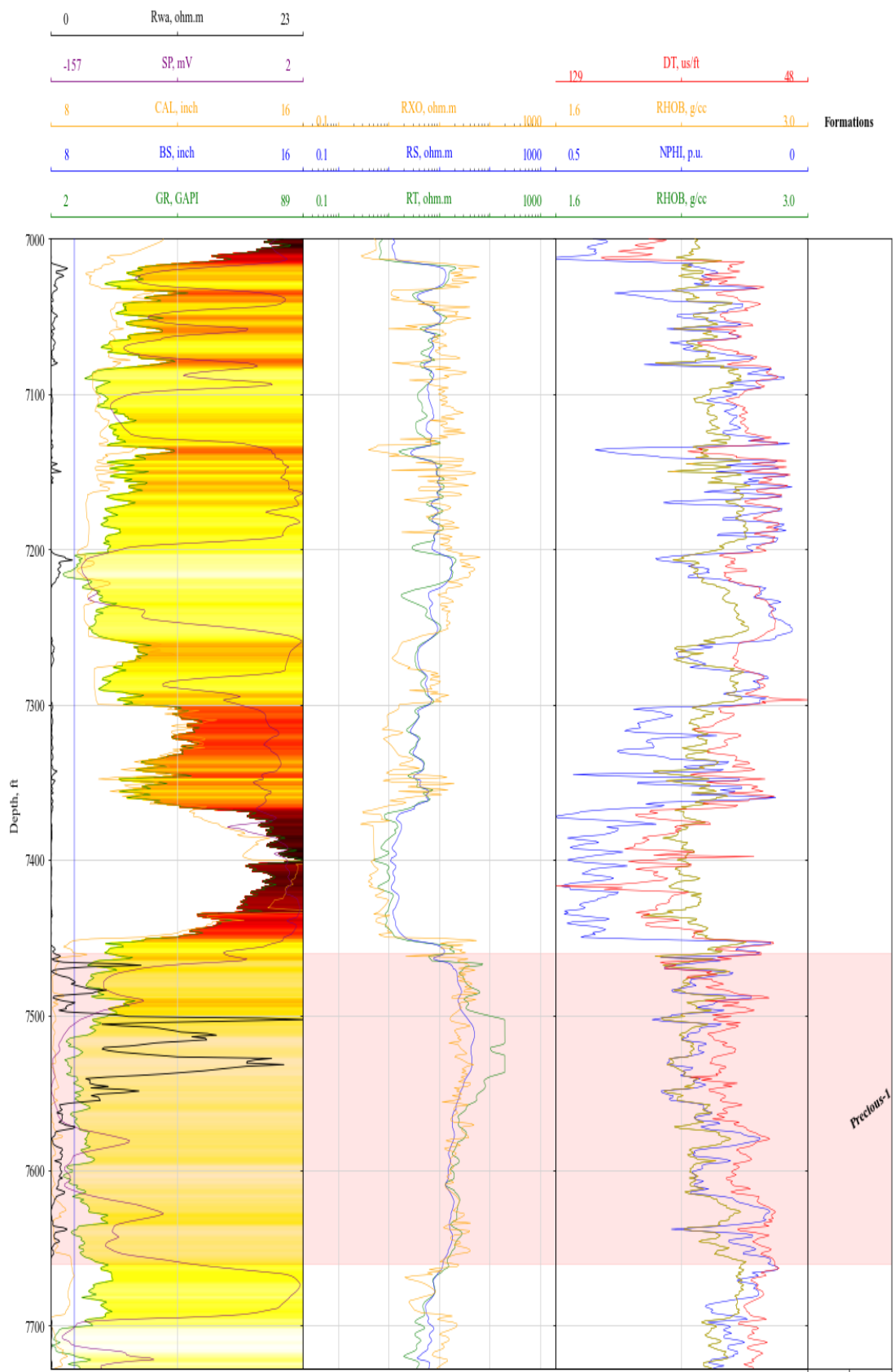


**Figure 4.15:** Well log display of Well-18 along with designated formations.

## **5. MODEL OF THE RESERVOIR**

As seen in Figure C.16., four side sections of the reservoir were obtained. These cross-sections facilitate the identification of reservoir top layers, shale and water zones based on GR and SP log data. Reservoir sections were determined as northwest to southeast (NW-SE), west to east (W-E), north to south (N-S) and southwest to northeast (SW-NE). In the (N-S) section in Figure C.16, the oil zone appears to pass through the water zone. The reason for this visualize is that the oil zone is behind the water zone from the perspective of the section taken which is north to south section and the water rises. The reservoir location was established using the offset depth, layer top and bottom depth from the GR and SP logs. After identifying the reservoir location, as seen in the below Figure C.17 a three-dimensional model was constructed by using the reservoir top and bottom depths in all wells and zooming in on the data in the Surfer software using the 'inverse distance' technique. A three-dimensional model, provides a major occasion to see the structure of the reservoir and the separation of layers. Subsequently, as seen in Figure C.18, which is a bird's eye view of the reservoir, contributed to a clearer view of the distance between the wells. As a result, these cross-sections and a three-dimensional model are demonstrate changes over the reservoir layer and a beneficial indicate for locating the site of new well.

Three-dimensional modeling can better represent how the reservoir will look in reality and allow problems to be noticed quicker in the design process. three-dimensional models enable for more accurate study of fluid flow, pressure distribution, and leak notices inside the reservoir. This might help in the optimization of the design. However, modeling reservoirs in three-dimensional may have significant drawbacks. It may take time to create a thorough model, especially for large and complicated reservoirs; also, two-dimensional modeling may be chosen for simplicity and understandability.

## 6. RESERVES ESTIMATION

In this study, petrophysical properties were successfully estimated in the previous chapters. Thus, based on these various properties, distribution maps were constructed to analyze the potential of the reservoir. For this section, in light of the estimated properties, the original oil in place and recoverable oil in place will be estimated by using the volumetric approach along with Monte-Carlo simulation. Monte-Carlo simulation was used since the petrophysical properties have lots of uncertainties. Further, by looking at the dataset given, there is no information about the well test, which creates a huge uncertainty on the drainage area, and the reservoir's total area. By utilizing the Monte-Carlo simulation, our company hopes to overcome uncertainties by constructing possibilities on reserve estimations rather than supplying a certain volumetric value.

In the context of the volumetric estimation, (Eq. 6-1) can be used to estimate the original oil in place (OOIP). Further, by modifying (Eq. 6-1) a little, (Eq. 6-2) can be used to estimate recoverable oil in place (ROIP). By comparing these two equations, one can observe that there are two main differences between them; which are recovery factor (RF), and effective porosity (Craft, Hawkins, & Terry, 1991).

$$OOIP = \frac{Ah\phi_t(1 - S_{wi})}{5.615B_{oi}} \quad (\text{Eq. 6-1})$$

$$ROIP = \frac{Ah\phi_e(1 - S_{wi})}{5.615B_{oi}} \times RF \quad (\text{Eq. 6-2})$$

Considering the properties in (Eq. 6-1), and (Eq. 6-2), one can conclude that assumptions should be made on area terms to estimate OOIP and ROIP. In this context, based on our company's experience, the total area and volume of the oilfield can be approximated by constructing thickness isopach maps. A Python program was coded to model such thickness isopach maps for each reservoir layer; hence, this program generates mesh-grides based on the supplied data. Thus, it extrapolates the gaps between points lying within the reservoir layer by utilizing cubic spline extrapolation as it maintains best approximation (Towler, 2002). Furthermore, based on the literature, isopach map approaches were found to be giving better estimations in the estimation of reserves; thus, the total volume of each reservoir layer was estimated by using Simpson's 1/3 method as it gives the better results (Towler, 2002). At the end of the modelling, the minimum and maximum volume of each reservoir layer was estimated, and the isopach map of Precious-1 layer was demonstrated in Figure 6.1. In addition, the minimum and maximum volume of each reservoir layer was summarized in Table 6.1.

In addition to the construction of thickness isopach maps, oil in place per feet square isopach map was constructed to evaluate which part of the field contains more in place reserves per area. To do that, (Eq. 6-3) was used, and the results were given as inputs to the Python program. As a result, Figure 6.2 was obtained. By examining this figure, one can conclude that the highest in place reserves per area could be found around Well-05, Well-17, and Well-07 respectively.

$$\frac{\text{OOIP}}{\text{ft}^2} = \frac{\emptyset_t h(1 - S_{wi})}{5.615 B_{oi}} \quad (\text{Eq. 6-3})$$

**Table 6.1:** Total volume of each reservoir layer based on the modelling.

Reservoir Layer	Min. Volume, ft <sup>3</sup>	Max. Volume, ft <sup>3</sup>
Precious-1	342403508129	362175245315
Gollum-1	24101268667	295645386399
Thorin-1	4411585142	4493893372

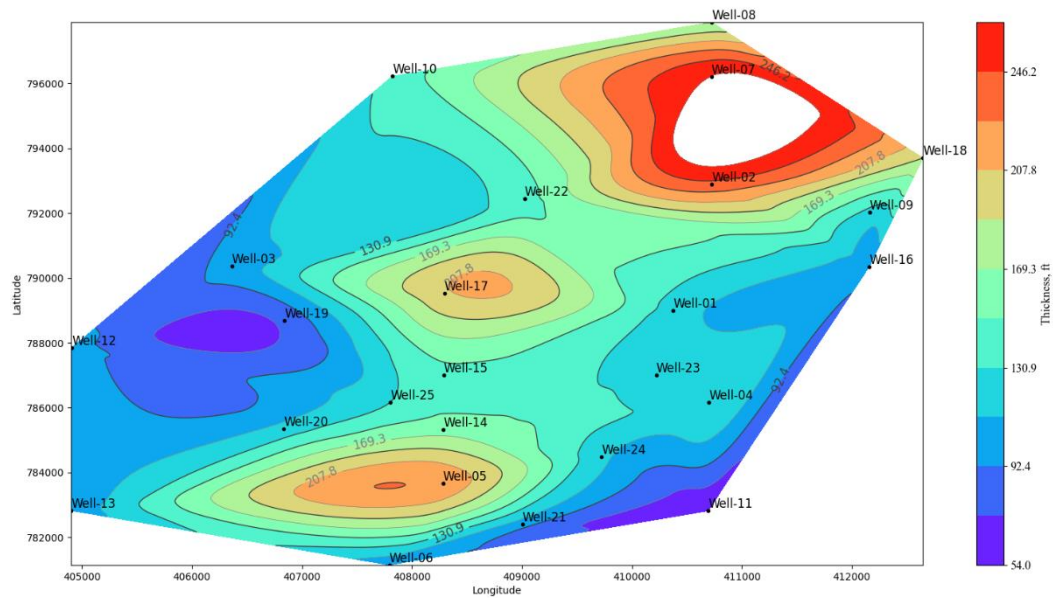


**Figure 6.1:** Thickness isopach map of the Precious-1 reservoir layer.

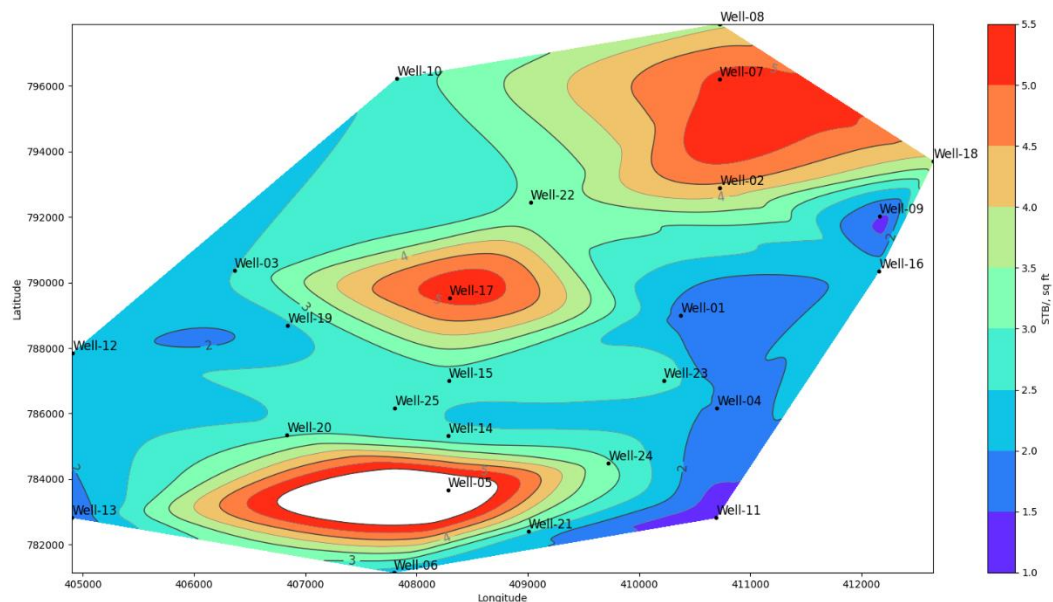


**Figure 6.2:** In place reserves per acre isopach for the Precious-1 reservoir layer.

Furthermore, to be able to construct a Monte-Carlo simulation on the volumetric reserves' estimation, distributions of petrophysical properties must be obtained. To achieve this, each reservoir layer's distributions of petrophysical properties were obtained. By looking at plots in Appendix D, the following observations regarding to distributions were concluded:

- Total porosity and effective porosity were found to be following the normal distribution.
- Initial water saturation was found to be following the lognormal distribution.
- Other properties were assumed to be uniform since their behavior can not be identified. Those are the volume, and recovery factor.

The above observations were done on the reservoir layer Precious-1. Thus, these distribution behaviours were assumed to be followed by other reservoir layers, Gollum-1, and Thorin-1. After these estimations and assumptions, 10000 samples were generated based on the distribution types of each petrophysical property; thus, the initial oil formation volume factor was taken from PVT analysis as 1.19 RB/STB at initial reservoir pressure. These generated sample pools of petrophysical properties can be found in Appendix D.

On the other hand, based on the petrophysical estimations in the previous chapter, the recovery factor had been found in between 50% to 75%. However, such estimations on the recovery factor using well logging data were found to be controversial. Hence, by searching through the literature, one can observe that the recovery factor of black oil reservoirs varies between 2.5% to 30% (Glover, 2001). That's why, it was found to be safer to rely on the literate and field observations. Based on these lower and upper limits of the recovery factor, a uniform distribution was constructed for the recovery factor to use in the ROIP estimations.

Finally, by iterating through all of the generated sample pools the original oil in place, and recoverable oil in place were estimated. Based on the simulation that was written in Python, Figure 6.3, Figure 6.4 were obtained. Further, these figures showcase the results of the Monte-Carlo simulation on OOIP and ROIP estimations for the Precious-

1 reservoir layer. The results of the Monte-Carlo simulation on other reservoir layers, - Gollum-1, and Thorin-1- can be found in Appendix D. Finally, the overall results for OOIP, and ROIP were demonstrated in Table 6.2, and Table 6.3 respectively. As a result, the estimated ROIP values were found to be promising; thus, it was extraordinarily logical to develop this field.

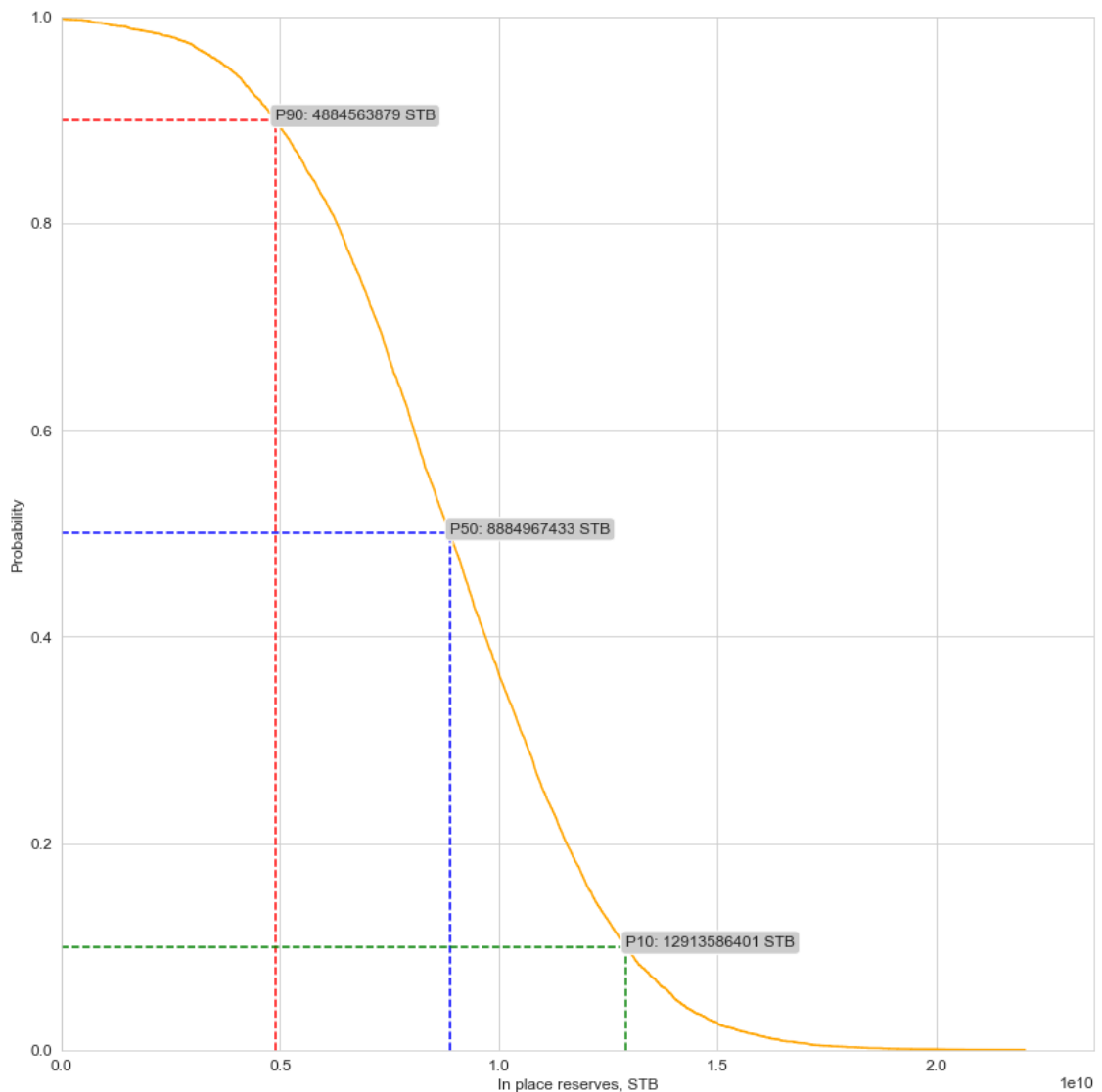


**Figure 6.3:** OOIP estimation result for the Precious-1 reservoir layer.

**Table 6.2:** OOIP results for each reservoir layer.

Reservoir Layer	P90 - OOIP, STB	P50 - OOIP, STB	P10 – OOIP, STB
Precious-1	4884563879	8884967433	12913586401
Gollum-1	604396345	854965634	1124186733
Thorin-1	74274580	143455009	213089191

**Table 6.3:** ROIP results for each reservoir layer.

Reservoir Layer	P90 - ROIP, STB	P50 - ROIP, STB	P10 – ROIP, STB
Precious-1	343745159	1194331146	2541419750
Gollum-1	39499583	124426725	237214041
Thorin-1	5765159	20228717	43554742

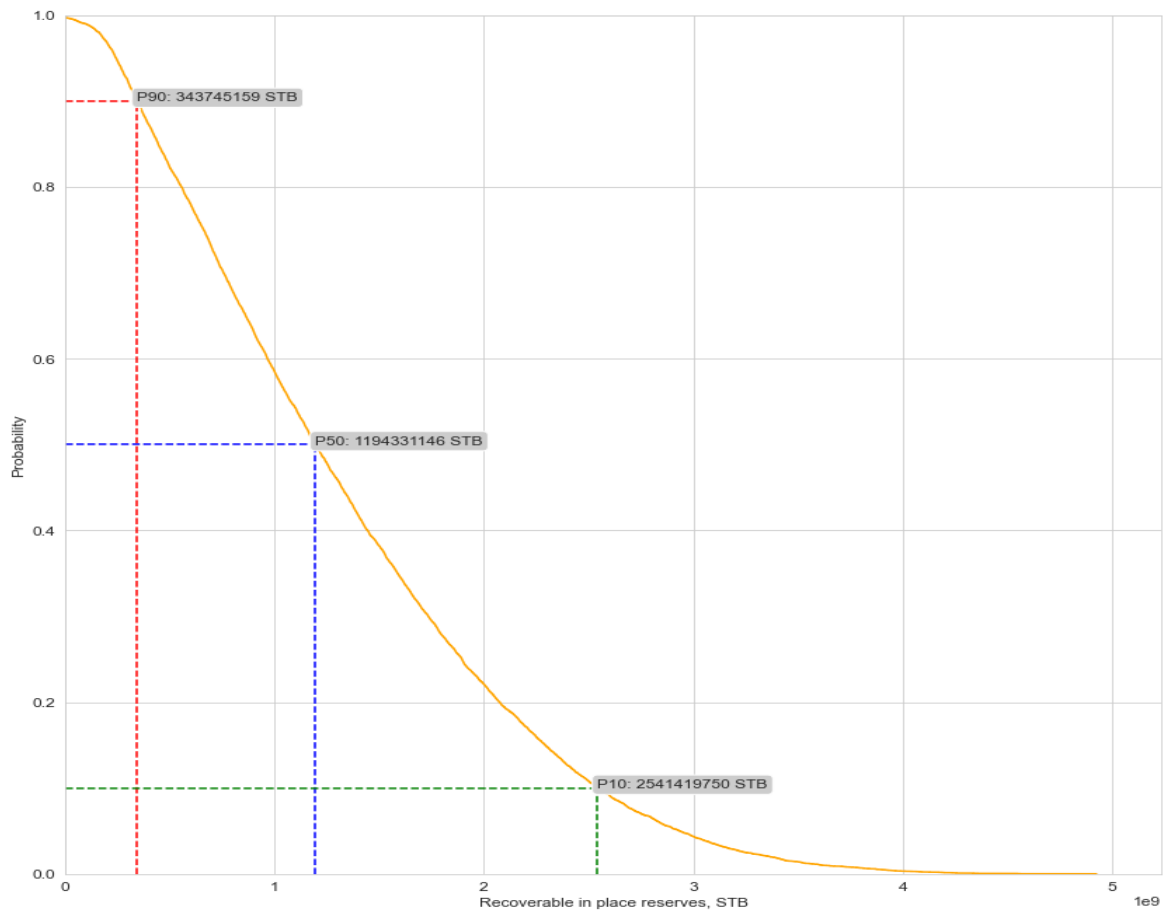


**Figure 6.4:** ROIP estimation result for the Precious-1 reservoir layer.

## 7. MECHANICAL EARTH MODEL

The elastic properties of rocks give information about how to evaluate the strength of the rocks and their reflection under in-situ stresses. Young's modulus, Poisson ratio, shear modulus, and bulk modulus are elastic characteristics which depend on the sonic slowness and density log. The dynamic elastic moduli are calculated by assuming elastic isotropy and the compressional and shear slowness associated with the bulk density logs (Schlumberger, Techlog Geomechanics Workflow/Solutions Training Version 2016, 2017). However, those properties may fluctuate due to different temperature and pressure values in addition to the geophysical structures under the surface. Lastly, during the estimation of MEM, the bulk formation will be assumed as shale sediments through the depth of interest; hence, the estimated properties can be found in Appendix E.

### 7.1. Target

First of all, a Python program has been coded to model the Mount Doom Oil Field's Precious-1 reservoir layer. In this modelling, coordinate and top of reservoir information was utilized along with the mesh gridding technique to demonstrate the shape of the reservoir. Consequently, the prospective well, Bane-01, and its coordinates were given as inputs to locate the prospective well's the top of the reservoir, the bottom of the reservoir, and the elevation from MSL. The result of this modelling simulation is shown in Figure 7.1. Thus, the information obtained from the modelling simulation is displayed in Table 7.1.

**Table 7.1:** Target information regarding to Bane-01.

Well Name	Longitude	Latitude	Top of Reservoir, ft	Bottom of Reservoir, ft	Elevation, ft
Bane-01	407557.6	791288.6	7407	7523	7249

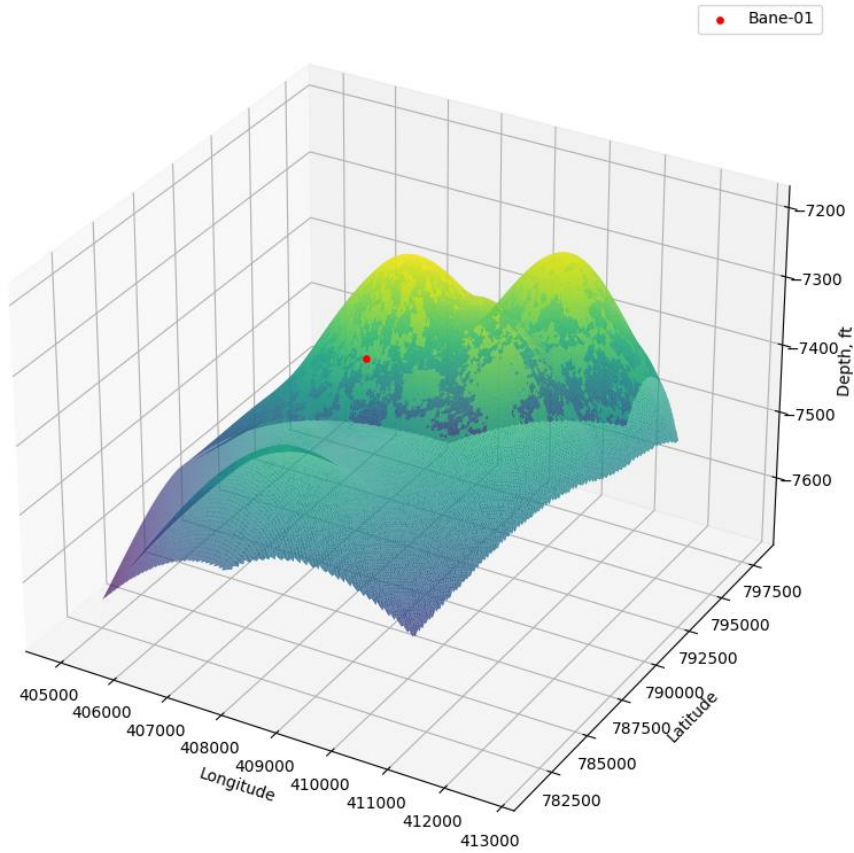


**Figure 7.1:** 3D model of the Precious-1 reservoir layer.

## 7.2. Preparation for the Modelling

To proceed with the construction of MEM, it is highly important to have properties like density, porosity, compressional, and shear wave velocities (Najibi, Ghafoori, Lashkaripour, & Asef, 2017). Thus, Well-19 has been selected as a reference well for the construction of the MEM due to its proximity; and, it was assumed that geomechanical properties display fairly same behavior. In addition, it was found to be substantial to indicate that, these estimated parameters such as shear modulus, bulk modulus, Young's modulus, and Poisson's ratio were designated as dynamic since the estimations are based on the well logging. On the other hand, often, the static versions of these properties are used by engineers to evaluate the stability of the wellbore; thus, these static properties are estimated by applying the calibrated from laboratory experiments. Since the Mount Doom Oil Field does not have laboratory measurements

regarding geomechanics, specific correlations between static and dynamic properties cannot be used as these conversions can lead to huge errors. Hence, the overall wellbore stability will be determined from estimated dynamic properties.

By examining the data available in Well-19, one can conclude that there is no available data before 6700 feet in the bulk density. That's why, by utilizing the existing bulk density data, and setting the surface porosity as 44.2%, the bulk density curve was extrapolated through the surface, same as in the literature (Bourgoyn Jr, Millheim, Chenevert , & Young Jr, 1991). The surface porosity,  $\phi_o$ , was estimated by using sediment grain density as  $2.68 \text{ g/cm}^3$  for shales, the density of the pore water as  $1.03 \text{ g/cm}^3$ , and the surface sediment's bulk density as  $1.95 \text{ g/cm}^3$  (Zhang J. , 2013). Thus, in order to construct the porosity decline curve with depth, the decline constant,  $K_{\text{decline}}$ , was estimated by utilizing (Eq. 7-1).

$$K_{\text{decline}} = \frac{\ln \frac{\phi_o}{\phi_{\text{target}}}}{D_{\text{target}}} \quad (\text{Eq. 7-1})$$

By locating the target depth as 7600 ft, the porosity at this specific point was estimated to be  $0.00012 \text{ ft}^{-1}$ . Then, a typical porosity-depth relation on a semi log graph was obtained; and it was illustrated in Figure 7.2. Thus, at 7101 ft, an undercompaction has been observed thanks to Figure 7.1.

Since the porosity decline curve has been constructed successfully, the extrapolation of bulk densities can be done. To achieve this, Miller has proposed a method to estimate the shallow or mudline densities. In this method, the average density of the sediments was taken as  $2.68 \text{ g/cm}^3$  for shales, and the density of pore water was taken as  $1.03 \text{ g/cm}^3$ . Thus, this correlation was highlighted in (Eq. 7-2)

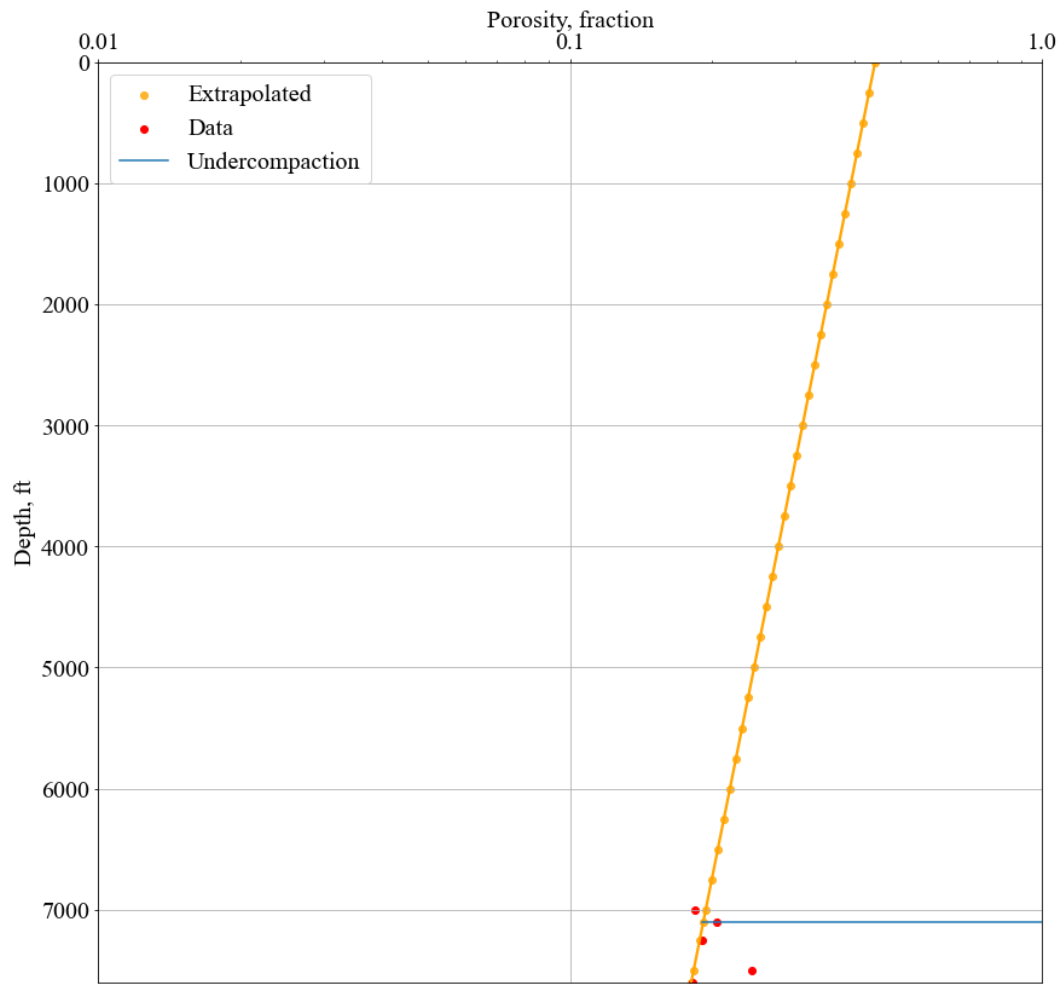


**Figure 7.2:** Porosity decline curve for Bane-01.

In the end, the extrapolated bulk density values were demonstrated in Figure 7.3. Note that this correlation was modified; and, the modification was done on the porosity term. Since the porosity values were constructed in Figure 7.2 already, these values will be used for the porosity term.

$$\rho_s = \rho_{ma}(1 - \emptyset) + \rho_w \emptyset \quad (\text{Eq. 7-2})$$

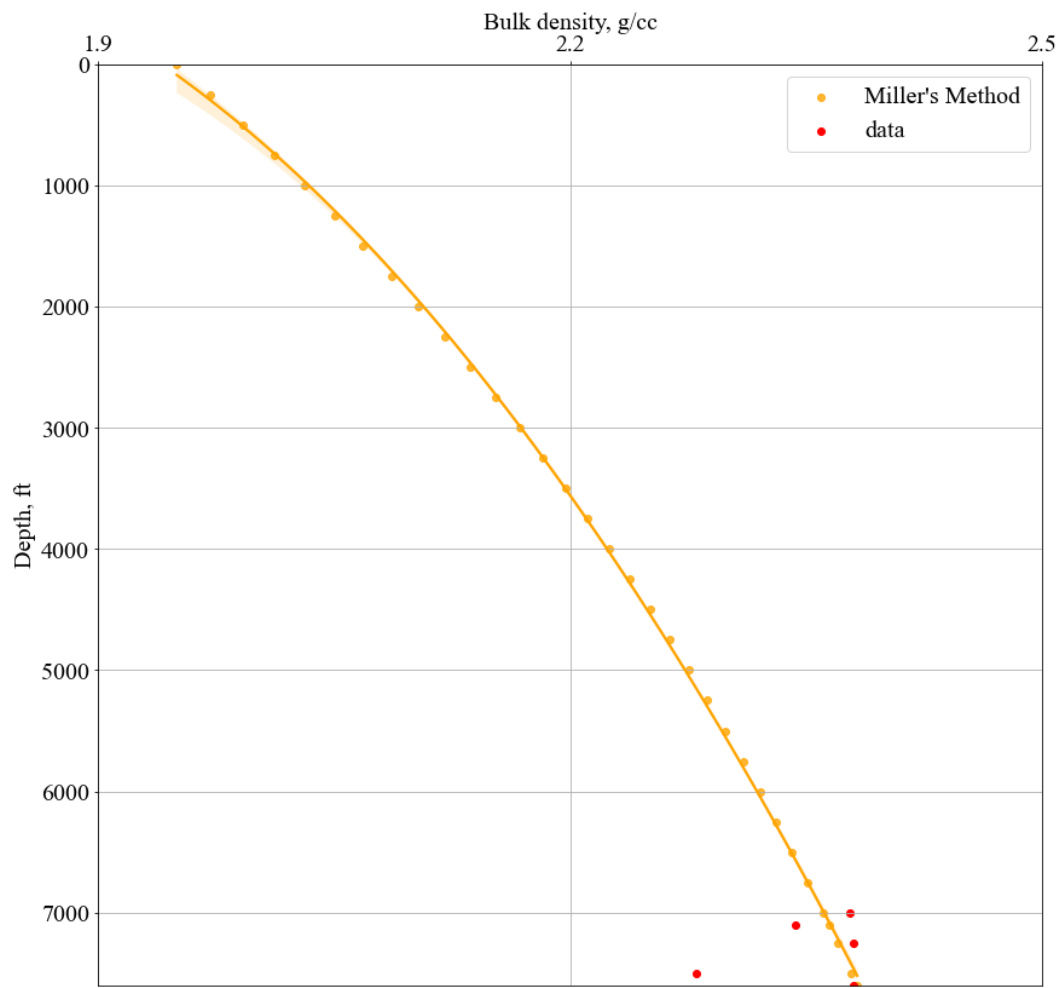


**Figure 7.3:** Bulk density extrapolation result of Miller's method for Bane-01.

On the other hand, since there is no information regarding to shear slowness of the bulk formation which is an essential property for the sake of the MEM, a correlation between shear and compressional velocities of the bulk formations will be used. This correlation was constructed on the laboratory experiments. In these specific experiments, scientists have studied the relation between S and P waves in shale sediments along with the contributions of mineralogy, anisotropy, and fluid saturations. Thus, they concluded that the correlation may result in errors other than reservoir sections due to variations in fluid saturation and content. This empirical correlation was given in (Eq. 7-3) along with a r-squared value of 0.9, and it assumes the waves propagate in the horizontal direction (Qin, et al., 2022).

$$V_{s0} = 0.5070V_{p0} + 0.3809 \quad (\text{Eq. 7-3})$$

In the literature, it has been found that geophysicists were using the reciprocal of the velocity of the bulk formation as slowness for representation purposes. To convert the compressional slowness of the bulk formation into the compressional velocity of the bulk formation, (Eq. 7-4) can be utilized (Glover, 2001). Thus, since the compressional of the shale sediments varies between in the range of 61 to 91  $\mu\text{s}/\text{ft}$ , the average slowness of the shale sediments was estimated from Well-19's well log measurements due to its proximity to the Bane-01; and, it will be assumed to be constant through the depth (Alford, et al., 2012). Finally, the estimated average compressional slowness of the shale sediment was found to be 89.5  $\mu\text{s}/\text{ft}$ , which aligns with the literature range. Consequently, with the estimation of the average compressional slowness of the shale sediments, the average shear slowness of the shale sediments was found to be 176.5  $\mu\text{s}/\text{ft}$ . It is important to highlight that these correlated properties will be used during the study.

$$\Delta t = \frac{10^6}{V} \quad (\text{Eq. 7-4})$$

### 7.3. Dynamic Shear Modulus

The modulus of rigidity, commonly known as the shear modulus, is a measure of a material's resistance to shearing stress, and it is designated as letter G. Its unit is Mpsi. The formula is given in (Eq. 7-5), where  $\Delta t_{\text{shear}}$  is referred as shear slowness of the bulk formation in  $\mu\text{s}/\text{ft}$  (Schlumberger, Techlog Geomechanics Workflow/Solutions Training Version 2016, 2017)

$$G_{\text{dyn}} = (13474.45) \frac{\rho_b}{\Delta t_{\text{shear}}^2} \quad (\text{Eq. 7-5})$$

#### **7.4. Dynamic Bulk Modulus**

Dynamic bulk modulus, as shown in (Eq. 7-6), is called as the relative volume change caused by a unit compressive or tensile stress or hydrostatic pressure applied uniformly over a body's surface. It can also be referred as the module of incompressibility.  $\Delta t_{comp}$  indicates compressional slowness of the bulk formation in  $\mu s/ft$ . Thus, it's unit is Mpsi (Schlumberger, Techlog Geomechanics Workflow/Solutions Training Version 2016, 2017).

$$K_{dyn} = (13474.45)\rho_b \frac{1}{\Delta t_{comp}^2} - \frac{4}{3} G_{dyn} \quad (\text{Eq. 7-6})$$

#### **7.5. Dynamic Young's Modulus**

The modulus of elasticity, E, reflects the rigidity of earth materials. It is the ratio of the stress to strain values. The greater the tension required to produce the deformation should be implied if a rock needs to be lengthened or shorter without breaking it. (Eq. 7-7) shows the formula below; thus, it's unit is Mpsi (Schlumberger, Techlog Geomechanics Workflow/Solutions Training Version 2016, 2017).

$$E_{dyn} = \frac{9G_{dyn} \times K_{dyn}}{G_{dyn} + 3K_{dyn}} \quad (\text{Eq. 7-7})$$

#### **7.6. Dynamic Poisson's Ratio**

Poisson's ratio is a material elastic parameter that is the ratio of the absolute values of lateral strain and axial strain when the substance is subjected to uniaxial tension or compression. (Eq. 7-8) shows how to calculate the Poisson's ratio; thus, it's unitless (Schlumberger, Techlog Geomechanics Workflow/Solutions Training Version 2016, 2017).

$$V_{\text{dyn}} = \frac{3K_{\text{dyn}} - 2G_{\text{dyn}}}{6K_{\text{dyn}} + 2G_{\text{dyn}}} \quad (\text{Eq. 7-8})$$

## 7.7. Internal Friction Angle

The Mohr-Coulomb failure principle is the source of the rock's friction angle, a crucial metric for determining its shear strength under normal stress. This principle uses two characteristics of rocks, cohesion and friction angle, to link shear and normal stresses on a failure plane. This angle can be determined using techniques such as tilt testing, triaxial compression testing, and direct shear testing; or from correlations.

When it comes to the horizontal axis of the stress plane, the friction angle essentially indicates the slope of the shear resistance line. On the failure plane, it measures a rock's resistance to sliding. Whereas a lower angle suggests weaker resistance and a higher chance of sliding, a higher angle suggests stronger resistance to shearing and a decreased propensity to slide (Ruiz & C., 2014). The mineralogy of the rock, the joint's water pressure, size, weathering, and surface roughness all affect this angle's value (Lukić, 2018). Furthermore, even within the same rock type, different friction angles can result from differences in surface conditions and testing techniques (Ruiz & C., 2014). Moreover, the empirical correlation that relates the porosity and the volume of shale with the internal friction angle was given in (Eq. 7-9) (Najibi, Ghafoori, Lashkaripour, & Asef, 2017). Lastly, note that the porosity term was utilized from the obtained porosity decline curve.

$$\varphi = 26.5 - 37.4(1 - \phi - V_{\text{sh}}) + 62.1(1 - \phi - V_{\text{sh}})^2 \quad (\text{Eq. 7-9})$$

## 7.8. Overburden Stress

The weight of the material layers covering the rock at a particular depth below the earth's surface exerts pressure on it, causing overburden stress in the rock. Some names for it include vertical stress and lithostatic pressure.

The maximum force per unit area that the rock can bear without collapsing or fracturing is known as the overburden stress. Under various loading scenarios, it shows the rock's strength and stability. More stability and strength are indicated by a higher overburden stress. The rock is less stable and weaker when the overburden stress is lower.

Since the bulk density and porosity values were already extrapolated through the surface, the overburden stress gradient can be estimated by using (Eq. 7-10) Note that, from this equation, the effect of the sea water has been extracted since the Mount Doom Oil Field is an onshore oil field (Bourgoyne Jr, Millheim, Chenevert , & Young Jr, 1991).

$$\sigma_{ob} = \rho_g g D_s - \frac{(\rho_g - \rho_f) g \phi_o}{K_{decline}} (1 - e^{-K_{decline} D_s}) \quad (\text{Eq. 7-10})$$

## 7.9. Pore Pressure

The pressure that the fluids in the rock pores exert is known as formation pore pressure. It is affected by the formation's fluid flow, fluid density, and the weight of the rock layers above it.<sup>12</sup> Formation pore pressure matters for a number of reasons, including:

- It has an impact on the borehole's stability and the density of drilling fluid needed to stop fluid inflow or loss.
- It suggests the possibility of subsurface hydrocarbon migration and accumulation.
- It modifies the effective stress and rock properties, which in turn affects the productivity and quality of the reservoir.

For these reasons, during exploration and production operations, it is crucial to estimate and track the formation pore pressure.

When the literature was examined, several distinct pore pressure estimations can be

found such as the pore pressure estimation from the porosity decline, pore pressure estimation from resistivity logs, etc. However, since the Mount Doom Oil Field does not have quite good amount of data, a few assumptions will be done in order to estimate the pore pressure behavior.

After the investigation of the dataset, it was found that the initial reservoir pressure is given as 3777.1 psi at 7300 ft. However, there is no information about from which well this measurement was conducted. That's why, it was assumed that the measurement of the initial reservoir pressure was conducted from Well-01 as this well is the first well ever drilled within the Mount Doom Oil Field. Since the elevation point in the location of Well-01 is 7050 ft whereas the elevation points in the location of Bane-01 is 7249 ft, 199 ft elevation difference was observed. Due to this elevation difference, the datum which the initial reservoir pressure was taken corresponds to 7101 ft on Bane-01's location. In fact, by looking in Figure 7.2, once can observe the start of the undercompaction on that specific depth. Lastly, by using (Eq. 7-11), the pore pressure gradient below 7101 ft was estimated as 0.532 psi/ft.

$$P_{pg} = \frac{P_i @ 7101 \text{ ft}}{D_{TVD} @ 7101 \text{ ft}} \quad (\text{Eq. 7-11})$$

Since the formation water density was taken as 1.03 g/cm<sup>3</sup>, the hydrostatic pressure gradient becomes 0.446 psi/ft. Hence, the hydrostatic pressure gradient was assumed to be constant until 3000 ft thanks to our company experience. Lastly, the interval between 3000 ft and 7101 ft was interpolated for the sake of the pore pressure increment.

## 7.10. Formation Fracture Pressure

The pressure at which fluid injection will cause a rock formation to hydraulically fracture is known as the formation fracture pressure. The in-situ stress, the fluid characteristics, and the fracture gradient all have an impact. There are several reasons

why formation fracture pressure matters, including (Ya-nan, et al., 2021):

- It establishes the highest pressure that may be put on the formation without damaging or unintentionally breaking it.
- It has an impact on the planning and execution of hydraulic fracturing treatments, which are frequently employed to raise the output of gas and oil wells.
- It affects the stability of the wellbore and the likelihood of producing sand, both of which are vital for the effectiveness and safety of drilling and completion activities.

### 7.10.1. Eaton's fracture pressure estimation

A technique for calculating the fracture gradient—the pressure at which a formation will fracture as a result of high pore pressures—is the Eaton's fracture pressure correlation. It is based on the idea of the minimal injection pressure put out by Hubbert and Willis, and it computes the fracture gradient from the overburden stress and the pore pressure using the formation's Poisson's ratio; thus, the correlation was given in (Eq. 7-12) (Eaton, 1975).

$$P_{fg} = \frac{v}{1-v} (\sigma_{ob} - P_{pg}) + P_{pg} \quad (\text{Eq. 7-12})$$

Eaton's fracture pressure correlation method has the following advantages (Zhang & Yin, 2017):

- With just three parameters—Poisson's ratio, overburden stress, and pore pressure—it is straightforward and simple to use.
- It can be used on a variety of formation types, including carbonate, sandstone, and shale.
- To increase accuracy, leak-off test data can be used to calibrate it.

On the other hand, Eaton's method has the following disadvantages (Zhang & Yin, 2017):

- For certain formations, the assumption of a linear connection between the pore pressure and the fracture gradient may not hold true.
- It does not take into consideration how the fracture gradient is impacted by in-situ stress, fluid characteristics, and rock characteristics.
- Depending on the magnitude of Poisson's ratio, it may exaggerate or underestimate the fracture gradient.

### **7.10.2. Modified Kelly and Matthew's fracture pressure estimation**

A formula for calculating a formation's fracture gradient—that is, the highest pressure that can be applied without forcing the formation to fracture—is provided by Matthews and Kelly's fracture pressure technique. The empirical parameter known as the matrix stress coefficient, or  $k_1$ , is reliant on the features of the formation and the depth. It may be computed using Poisson's ratio or taken from a chart. Thus, the Matthew and Kelly's method was given in (Eq. 7-13).

$$P_{fg} = k_1(\sigma_{ob} - P_{pg}) + P_{pg} \quad (\text{Eq. 7-13})$$

Based on an analysis of global leak-off test (LOT) data from offshore drilling, Zhang and Yin present an enhanced version of Matthews and Kelly's fracture pressure estimation approach (Zhang & Yin, 2017). They have calibrated the Matthew and Kelly's method based on the six different offshore field's leak-off tests. Thanks to this calibration and the mathematical fitting, they have introduced (Eq. 7-14) to estimate depth dependent effective stress coefficient.

$$k_1 = k + \frac{a}{e^{D_s/b}} \quad (\text{Eq. 7-14})$$

Furthermore, they have introduced 3 different scenarios for the coefficients in (Eq. 7-14). as follows (Zhang & Yin, 2017):

- For the lower case:  $k = 0.5$ ,  $a = 0.1$ , and  $b = 5100$
- For the most likely case:  $k = 0.75$ ,  $a = 0.15$ , and  $b = 7200$
- For the highest case:  $k = 0.9$ ,  $a = 0.4$ , and  $b = 12500$

In this study, the most likely case has been selected to be used. Hence, the equation to estimate formation fracture pressure gradient of Matthew and Kelly's becomes as in (Eq. 7-15).

$$P_{fg} = \frac{v}{1-v} (\sigma_{ob} - P_{pg}) + P_{pg} \quad (\text{Eq. 7-15})$$

## 7.11. Results And Discussion

Figure 7.5 and Figure 7.6, respectively, show the mechanical earth model and the calculated pressure gradient for Eaton's correlation and Matthew and Kelly's modified correlation. Based on the model obtained, the Poisson's ratio stays constant at 0.33 throughout all depths, which is typical for many rock types but it requires further investigation. But this indicates that the rock is isotropic and has uniform elastic capabilities in all directions. This makes it easier to analyze and simulate the behavior of rocks. On the other hand, this number is also extremely near to the Poisson's ratio upper bound of 0.5, indicating that the rock has a low bulk modulus and is exceedingly incompressible. This has to be confirmed with additional data sources since it can have an impact on the rock's pore pressure and fluid flow characteristics. On the other hand, from Figure 7.4, it seems the interested formation within the acceptable and producing formations range (Bourgoyne Jr, Millheim, Chenevert, & Young Jr, 1991).

Good consolidation of the formations with increasing depth is shown by the steady increase in Young's modulus. However, to have a thorough grasp of formation consolidation, it would be helpful to connect these mechanical characteristics with additional data, such as core analysis.

The friction angle likewise rises with depth, suggesting that the rock's shear strength and resistance to failure have increased. The rising Young's modulus values are consistent with this. At 1750 and 3500 feet below the surface, the friction angle value does, however, decrease. This might point to problematic shaly formations with a reduced ability to withstand shear forces. Thus, during the drilling process, these zones will be thoroughly drilled. As such, the drilling mud's properties and the hydrostatic pressure exerted should be appropriately adjusted when drilling through these formations. Additionally, starting from at 7101 feet, dynamic properties along with friction angle deviates too much and starts to decrease. This is not surprising as this depth was already found to be the starting depth of the undercompaction. Compared to the troublesome shale formations above, probably, the reservoir section will not be exposing such troubles. However, a care should be taken as the properties deviate.

In addition to mechanical earth model, mud windows were constructed by applying  $\pm 0.5$  pound per gallon safety factor for both Eaton's method (see Figure 7.7), and modified Matthew and Kelly's method (see Figure 7.8) as a company policy.

Furthermore, by comparing Figure 7.7 and Figure 7.8, it can be seen that modified Matthew and Kelly's method has resulted in wider mud window. Possibly, it was occurred since the modified Matthew and Kelly's method was based on the offshore fields. Thus, it includes the sea water column above the mudline. That's why, the Eaton's method has been selected to be used for the casing and drilling design.

Followingly, based on Figure 7.7, it was found that it could be enough to have two casings to handle the overall operation. Hence, Figure 7.9 was constructed to display the surface and production casing setting depths with the respective mud weights for the drilling operation. As a result of this figure, Table 7.2 was created to display summary information about intervals, mud weights, casing setting depths.

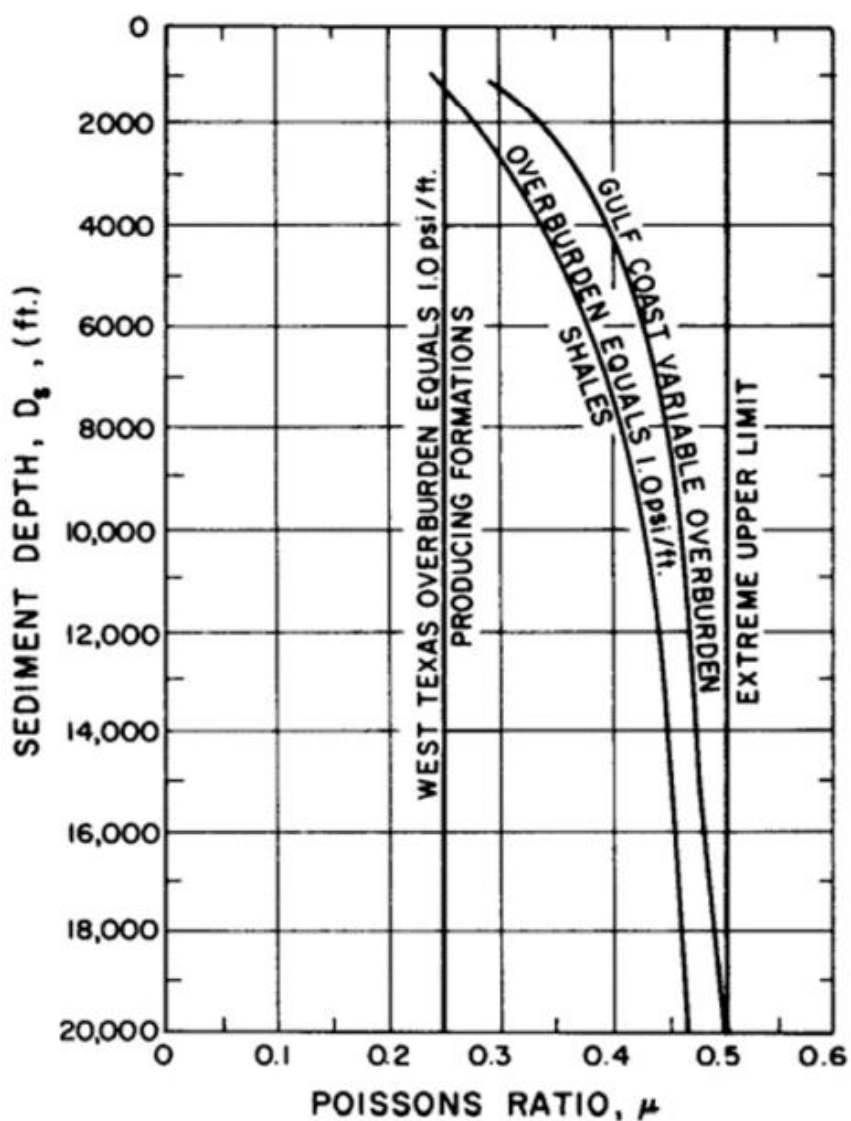


**Figure 7.4:** Poisson's ratio as a function of depth for various formations, and the acceptable range of the Poisson's ratio (Bourgoyn Jr, Millheim, Chenevert , & Young Jr, 1991).

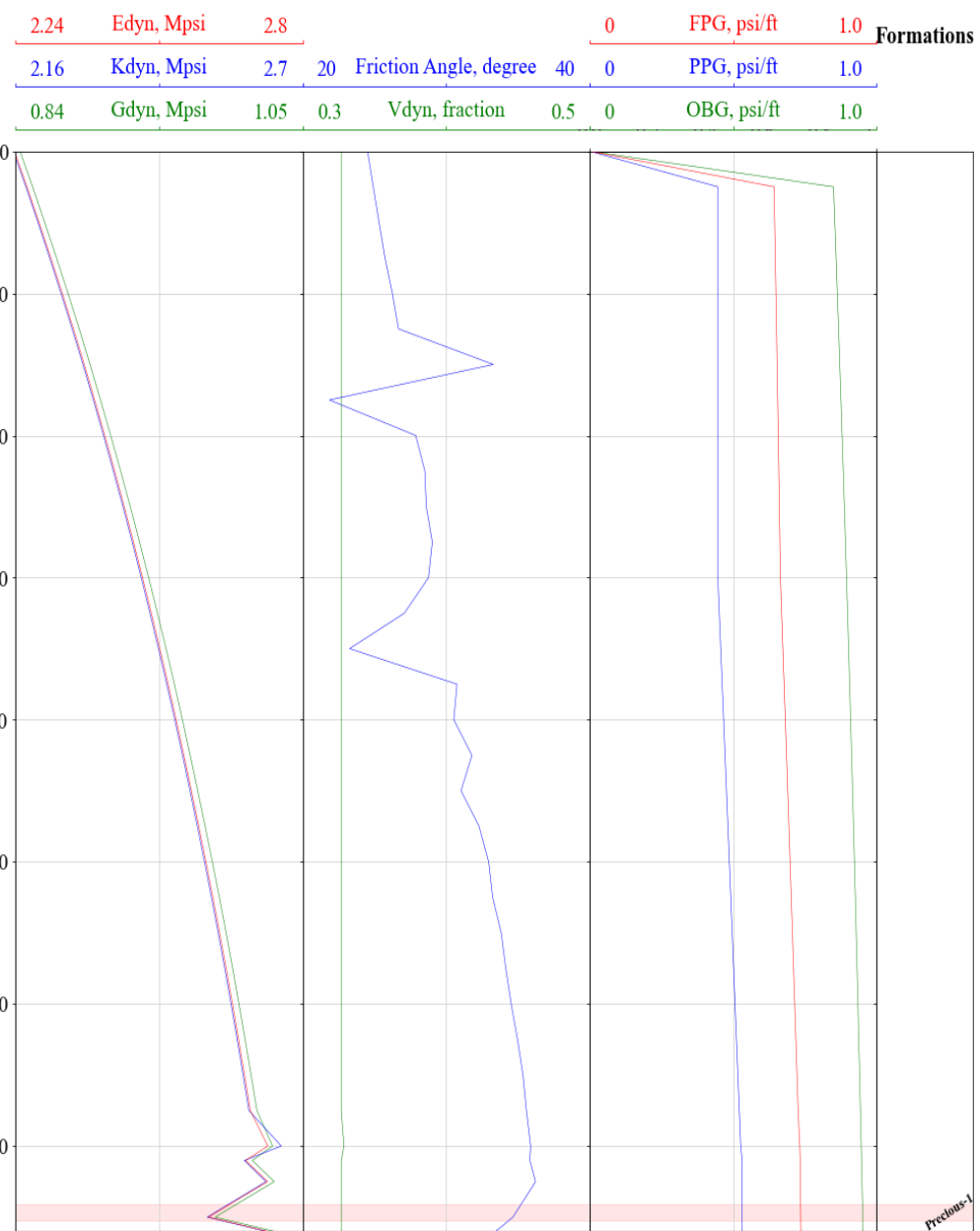


**Figure 7.5:** Mechanical earth model and estimated pressure gradients from Eaton's correlation.

2.24	Edyn, Mpsi	2.8		0	FPG, psi/ft	1.0	Formations	
2.16	Kdyn, Mpsi	2.7	20	Friction Angle, degree	40	0	PPG, psi/ft	1.0
0.84	Gdyn, Mpsi	1.05	0.3	Vdyn, fraction	0.5	0	OBG, psi/ft	1.0

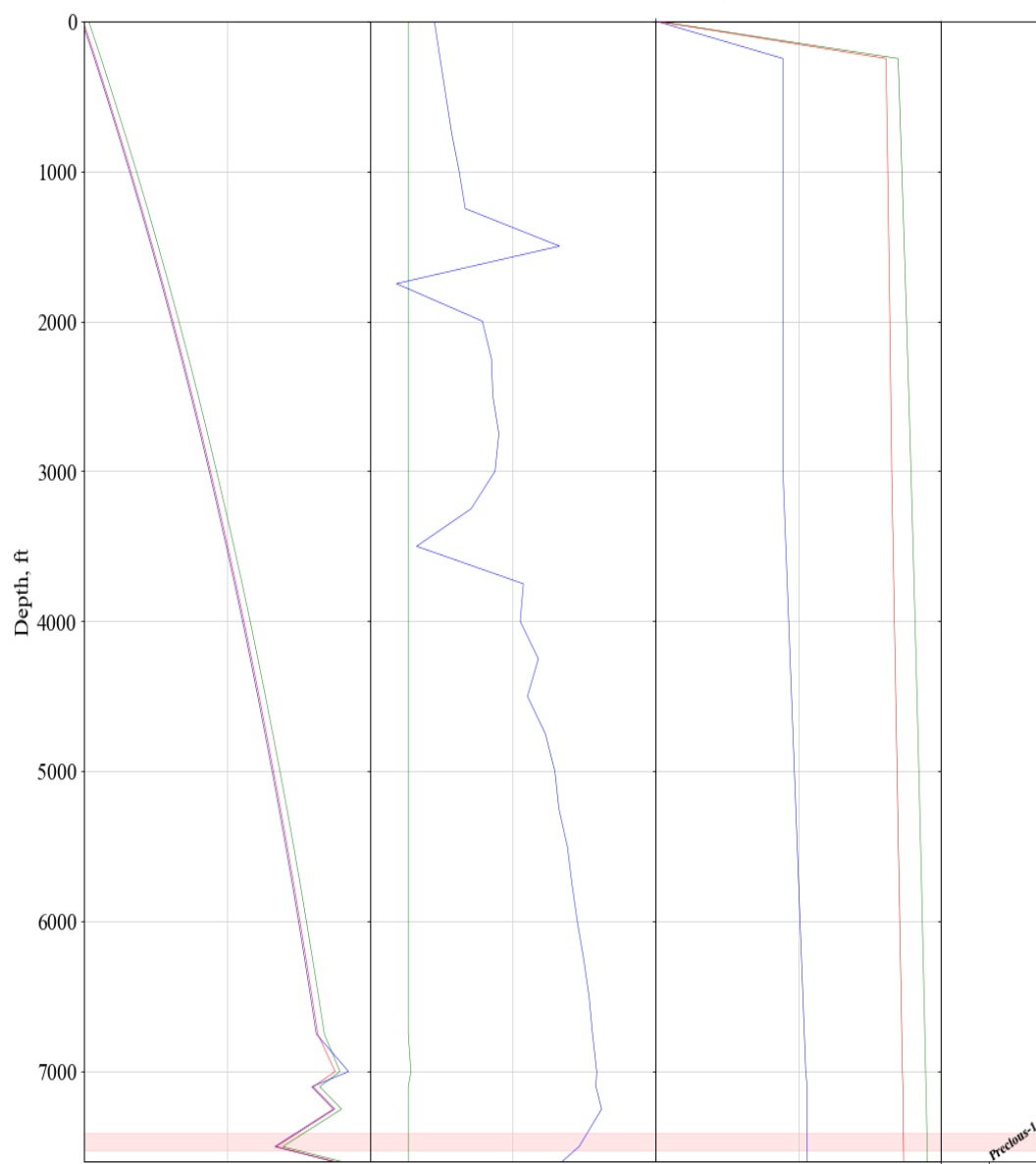


**Figure 7.6:** Mechanical earth model and estimated pressure gradients from modified Matthew and Kelly's correlation.

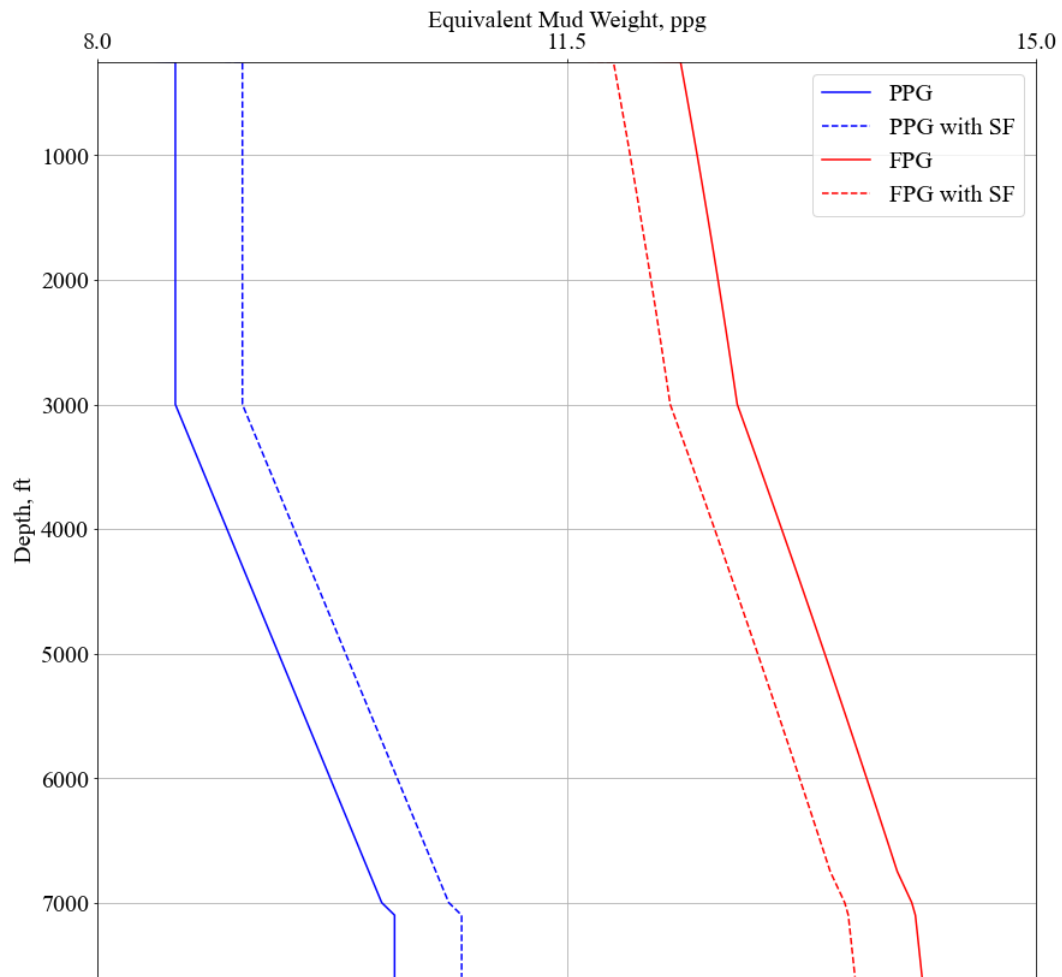


**Figure 7.7:** The resulted mud window of the Eaton's method.

**Table 7.2:** Information about casing setting depths, and mud weights that will be used during the drilling operation.

Section	Casing Type	Interval, ft	Length, ft	Mud Weight, ppg
1	Surface Casing	0 – 3000	3000	9.5
2	Production Casing	0 - 7600	7600	11

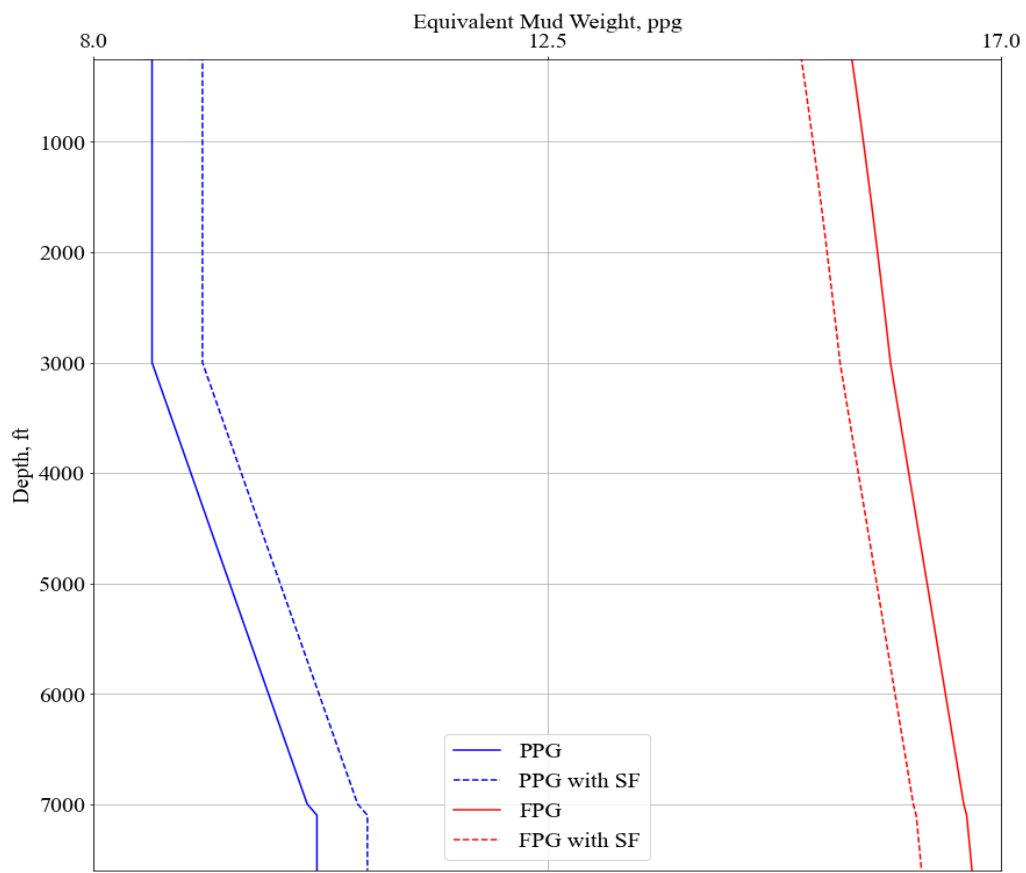


**Figure 7.8:** The resulted mud window of the modified Matthew and Kelly's method.

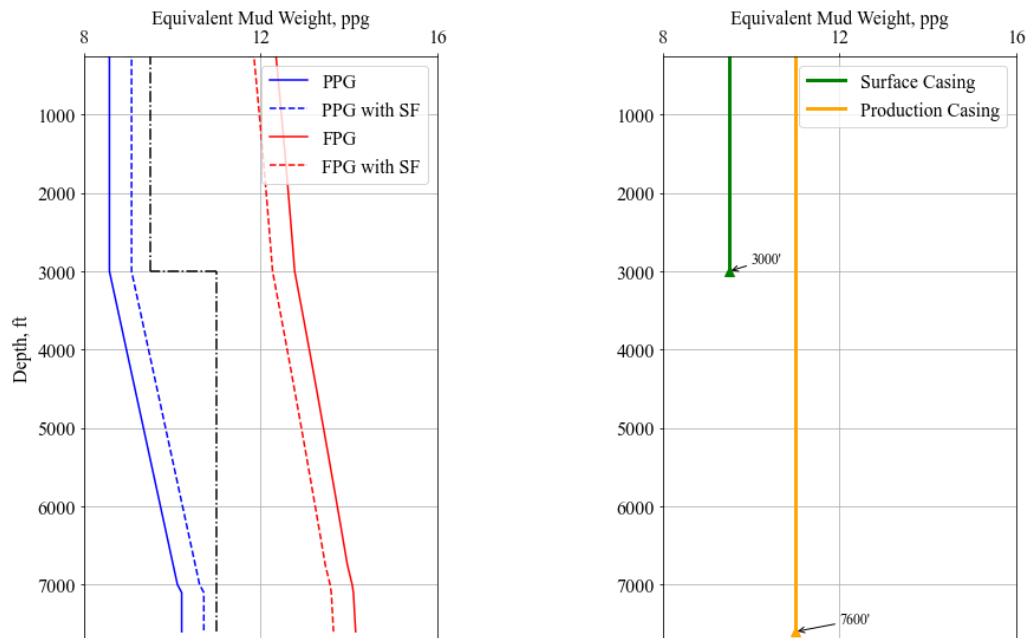


**Figure 7.9:** The resulted casing, and mud weight program from the Eaton's method.

## **8. CASING DESIGN**

When designing an oil and gas well, casing design is a crucial responsibility. It permits the movement of hydrocarbons from the reservoir to the surface, lowers well expenses, and guarantees the mechanical integrity of the well.

Although the exact well circumstances and goals determine the design parameters, production and surface casings typically contain the following:

- Production casing:
  - The casing must be able to endure the pressure loads that the well may experience during its lifetime, including axial, bending, and thermal pressures.
  - For the casing to not fail or leak, it must have enough tensile strength, collapse resistance, and burst resistance.
  - The atmosphere and reservoir fluids must be compatible with the casing's metallurgical and corrosion characteristics.
  - For the casing to provide dependable and leak-proof joints, the right connection types and ratings must be present.
  - For drilling instruments, logging tools, completion equipment, and production fluids to pass through, the casing has to have the right hole and pipe diameters.
  - For the well's performance and costs to be balanced, the shoe depths and number of strings in the casing must be ideal.
- Surface casing:
  - The wellbore must be shielded by the casing from superficial dangers such as gas and water sands, lost circulation zones, and unconsolidated formations.
  - The freshwater aquifers must be kept separate from the reservoir and drilling fluids by the casing.
  - The wellhead equipment and the blowout preventer (BOP) need a sturdy foundation, which the casing must supply.
  - For the production tubing and the succeeding casing strings to be supported, the casing needs to be strong and durable enough.
  - In order to guarantee zonal isolation and well integrity, the casing has to have enough cement covering and of high quality.

## 8.1. Casing And Bit Sizes

In order to determine the size of surface and production casing, the database of wells which are close to Bane-01's location was reviewed. When looking at Well-03, which is one of the closest well to the prospective well, it can be seen that  $8^{1/2}$ " bit was used before running the production casing. According to API standards (Table 8.2), the  $8^{1/2}$ " bit is commonly used to run  $6^{5/8}$ " casing (Bourgoyne Jr, Millheim, Chenevert , & Young Jr, 1991). Considering this, it was found to be appropriate to choose  $6^{5/8}$ " as the production casing's outer diameter. Hence, the bit size for this section to be drilled was selected as  $8^{1/2}$ ".

According to the commonly used API casing size,  $8^{1/2}$ " bit size is commonly used to pass through  $9^{5/8}$ " casing (Bourgoyne Jr, Millheim, Chenevert , & Young Jr, 1991). Therefore, it was found to be appropriate to choose  $9^{5/8}$ " for surface casing size. Thus, by examining Table 8.2, the appropriate bit size for this section to be drilled can be chosen as  $12^{1/4}$ ".

On the other hand, the conductor casing setting depth was selected as 150 ft; hence, based on the commonly used API casing sizes that correspond to the specific bit size, the outer diameter of the conductor casing was selected as  $13^{3/8}$ ". Consequently, the selection of the conductor casing size, the bit size for this section to be drilled was chosen as  $17^{1/2}$ " based on Table 8.2. Lastly, all of these parameters were summarized in Table 8.1.

**Table 8.1:** Resulted parameters regarding to casings and bit sizes.

Section	Casing Type	OD, inch	Bit Size, inch	Seat Depth, ft	$\rho_m$ , ppg	$P_{PG}$ , ppg	$P_{FG}$ , ppg
1	Conductor	$13^{3/8}$	$17^{1/2}$	150	9.5	9.08	11.8
2	Surface	$9^{5/8}$	$12^{1/4}$	3000	9.5	9.08	12.27
3	Production	$6^{5/8}$	$8^{1/2}$	7600	11	10.71	13.65

## 8.2. Surface Casing

Surface casing is the first section of casing that is erected in an oil well, and it is crucial to safety and integrity. Located at a level beneath the shallowest aquifer, this casing fulfills several vital purposes. Its main function is to protect the water table from possible hydrocarbon and drilling fluid contamination. Moreover, it prevents collapse in upper formations by stabilizing the wellbore. It also serves as a shield against high-pressure areas inside the well, reducing the possibility of blowouts and maintaining drilling safety.

As the cornerstone of casing design, surface casing is essential for preserving the well's structural integrity and operational security. It serves as the basis for other components.

In the previous section, the elevation of the prospective well was found to be 7249 ft. By utilizing the relation that was constructed in the Methodology section, the surface temperature was estimated to be 33.15 °F at 7249 ft. Hence, the geothermal gradient along the wellbore was taken as 1.5 °F/100ft. Moreover, for simplicity, the gas behaviour was assumed to be ideal pure methane. Followingly, these assumptions will be creating the worst-case scenario.

**Table 8.2:** Commonly used bit sizes for running API casing (Bourgoyne Jr, Millheim, Chenevert , & Young Jr, 1991)

Casing Size (OD in.)	Coupling Size (OD in.)	Common Bit Sizes Used (in.)
4½	5.0	6, 6⅛, 6¼
5	5.563	6½, 6¾
5½	6.050	7⅓, 8⅓
6	6.625	7⅓, 8⅓, 8½
6⅔	7.390	8½, 8⅔, 8¾
7	7.656	8⅔, 8¾, 9½
7⅔	8.500	9⅓, 10⅓, 11
8⅔	9.625	11, 12¼
9⅔	10.625	12¼, 14¾
10¾	11.750	15
13⅔	14.375	17½
16.0	17.0	20
20.0	21.0	24, 26

### 8.2.1. Burst design

In order to analyze the determined pressure as a burst threshold, surface casing burst design entails determining the greatest internal pressure the casing can withstand without failing. A cartesian graph is used in this procedure to plot load and design lines against depth for a thorough study. Because surface casing failure can have disastrous consequences for the well and the surrounding area, it is crucial to have a robust burst design. Hence, the design criteria were to creating the worst-case scenario.:

- Estimating the injection pressure at setting depth
- Estimating the internal pressure at the surface
- Evaluating external pressure
- Establishing burst pressure
- Constructing load and design lines

In order to determine the injection pressure,  $P_{inj}$ , at the setting depth, (Eq. 8-1) can be used. The decimal term, 0.3, in the equation indicates that the injection pressure is greater than the fracture pressure.

$$P_{inj} = 0.052(\rho_{fp} + 0.3)D_{seat} \quad (\text{Eq. 8-1})$$

It is essential to compute the gas gradient in order to determine the pressure at the surface. This entails measuring the methane gas-induced pressure differential between the surface and the setting depth. In particular, the gas gradient depends on applying the methane-specific real gas equation to obtain this crucial value as indicated in (Eq. 8-2) (Bourgoyn Jr, Millheim, Chenevert , & Young Jr, 1991). Afterwards, the pressure at the surface can be estimated from (Eq. 8-3).

$$0.052\rho_g = \frac{(P_{inj} + P_{atm})M_g}{80.3zT} \quad (\text{Eq. 8-2})$$

$$P_s = P_{inj} - 0.052\rho_m D_{shoe} \quad (\text{Eq. 8-3})$$

When it comes to the estimation of the external pressure at the surface, it can be assumed that the pressure is 0 psi since there is no hydrostatic pressure. However, at the setting depth, the external pressure can be calculated from the hydrostatic pressure from the formation. That's why the pore pressure at the setting depth, which is 9.08 ppg, should be used.

Utilizing all of these calculations, as a result, Table 8.3 was obtained. Following to the table construction, Figure 8.1 was obtained. According to Wu, the safety factor of 1.1 permits a reasonable safety margin since the burst pressure rating calculations of API standards based on Barlow's equation (2021). That's why, the safety factor was taken as 1.1 in the construction of the burst design.

**Table 8.3:** Burst pressure load and design lines for the surface casing.

Depth, ft	Load Line, psig	Design Line, psig
0	1847	2031
3000	545	600

### 8.2.2. Collapse design

Surface casing collapse design is crucial for maintaining the mechanical integrity of the well and avoiding casing failure. When the pressure inside the shell is greater than the pressure outside, collapse happens. The pressure from drilling fluids or pore pressure may be the cause of this. Environmental risks, trapped pipes, and a loss of well control may result from the casing collapsing.

When designing the casing for collapse, the engineer has to take into account the worst-case situation, which is when there is no fluid in the casing and the maximum mud weight acting as the external force throughout the casing's run. In addition, the engineer has to choose the right casing size, material, and connection type. Based on the pipe geometry and yield strength, the engineer must also use the proper formula to determine the collapse pressure. To take into consideration ambiguities and variances in the loading circumstances and formation characteristics, the engineer must also calculate a safety factor. According to the API 5C3 standards, based on the experimental results, only a small portion of casings collapse below the specified collapse resistances; hence, based on these experimental results, and statistical analysis, it was found that the safety factor during the construction of the collapse design can be taken as 1.15 (Wu, 2021).

- Identifying the depth at which mud falls
- Estimation of internal pressure at each surface casing segment
- Estimation of the external pressure at each surface casing segment
- Constructing load and design lines

Since the scenario is based on the worst-case, the fluid loss will be assumed in the next section of the casing, which is 7600 ft. Hence, the depth of the mud level fall can be estimated by using (Eq. 8-4); and, the internal pressure at the casing seat can be estimated by utilizing (Eq. 8-5). On the other hand, the external pressure at the surface, again, will be assumed as 0 psig since there is no hydrostatic column. In contrast, to estimate the external pressure at the casing seat, and mud level fall can be estimated by using the hydrostatic pressure exerted by the drilling mud (Bourgoyn Jr, Millheim, Chenevert , & Young Jr, 1991).

$$D_m = \frac{\rho_{m_{next}} - \rho_{pore}}{\rho_{m_{next}}} D_{lc} \quad (\text{Eq. 8-4})$$

$$P_{i\text{seat}} = 0.052D_m\rho_m \quad (\text{Eq. 8-5})$$

As a result of these assumptions, and estimation, Table 8.4 was constructed. Following to the construction of the table, Figure 8.3 was demonstrated to display them as a function of depth.

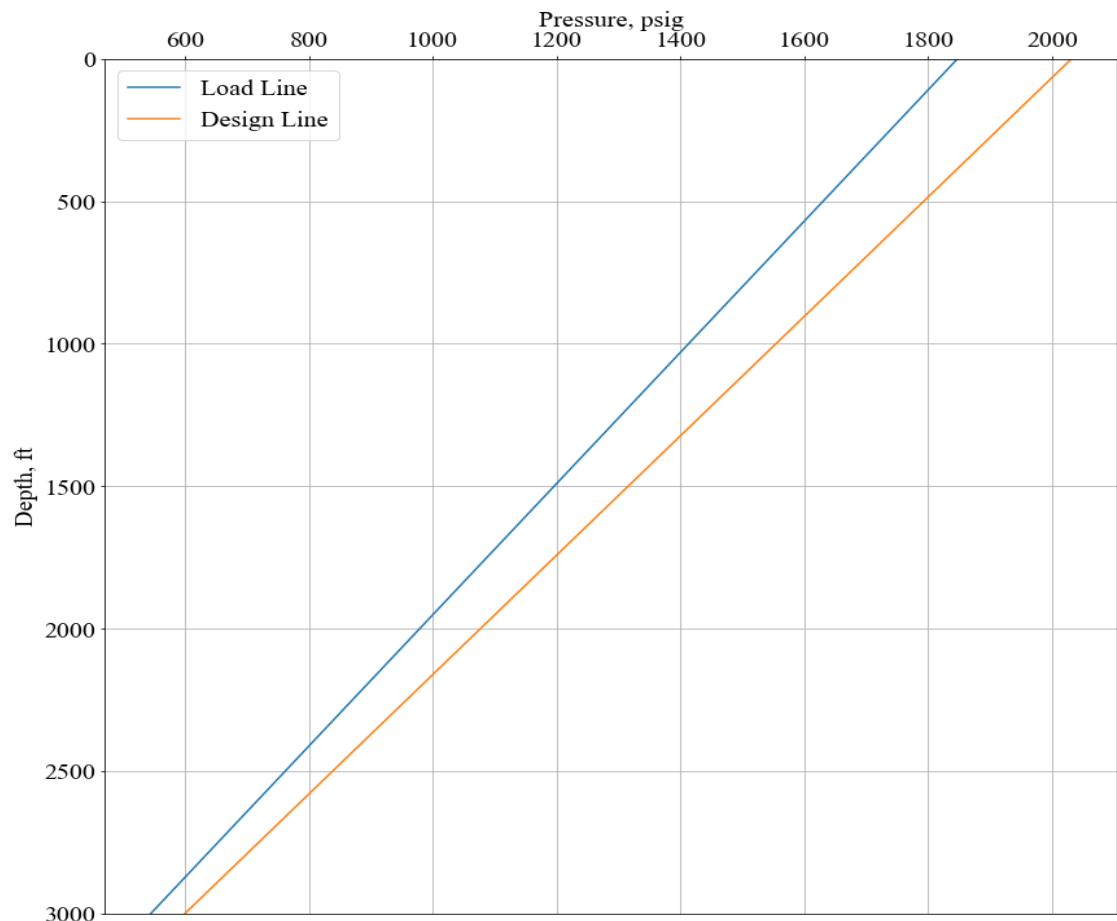


**Figure 8.1:** Burst pressure criteria for the surface casing.

**Table 8.4:** Collapse pressure load and design lines for the surface casing.

Depth, ft	Load Line, psig	Design Line, psig
0	0	0
1673.5	827	952
3000	723	832

### **8.3. Production Casing**

The last casing string in a well, known as production casing, serves to separate the production zone from the remainder of the wellbore. It matters for a number of reasons, including:

- It keeps cement, drilling fluids, and other fluids from contaminating the reservoir.
- It acts as a channel to carry hydrocarbons from the reservoir to the surface.
- It makes it possible to install packers, production tubes, and other finishing equipment.
- It permits the use of increased recuperation techniques, artificial lift, or stimulation.
- It makes well integrity and reservoir performance easier to monitor and manage.

#### **8.3.1. Burst design**

For the purpose of the burst design criteria, a gas kick will be assumed at the production casing seat; thus, the pressure exerted by the gas kick will be assumed as the pressure exerted by the formation. This pressure can be estimated from the pore pressure given in Table 8.1. When the necessary calculations were done, the pressure at the production casing seat was found to be 4233 psig. On the other hand, inside and outside the casing, there will be two fluids; namely the drilling fluid, and the completion fluid. For simplicity, and having more secure design conditions, the density of these two fluids was assumed to be equal to each other. Based on this assumption, the burst design criteria become the gas kick at the bottom and its effect on the surface. In order to estimate the reduction in the pressure due to the gas kick, the pressure gradient of the gas was estimated by using (Eq. 8-2). Based on this estimation, the gas pressure gradient was estimated to be 0.0944 psi/ft.

By using these pieces of information, and the accepted safety factor, the estimated pressure levels for the burst design were summarized in Table 8.5. Moreover, the representation of the burst design is provided in Figure 8.2.

**Table 8.5:** Burst pressure load and design lines for the production casing.

Depth, ft	Load line, psig	Design Line, psig
0	3515	3867
7600	4233	4656

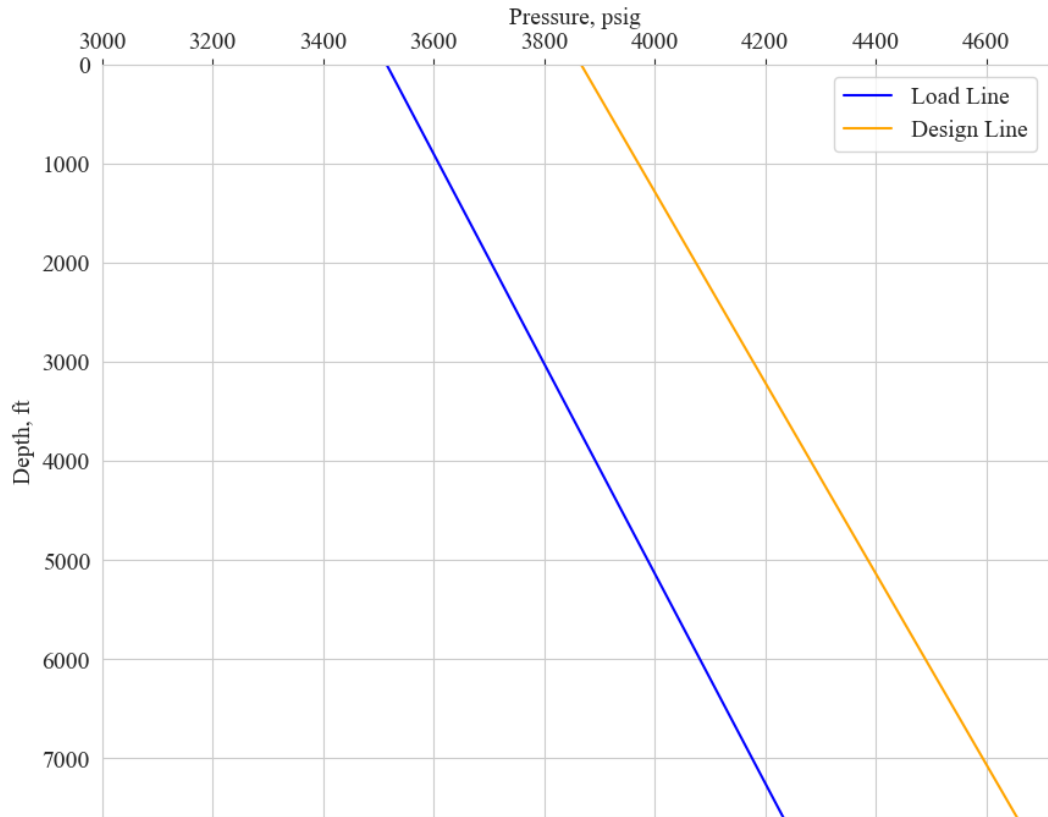


**Figure 8.2:** Burst pressure criteria for the production casing.

### 8.3.2. Collapse design

For the purpose of the collapse design criteria, the same approach will be implemented as it has been done in the design of surface casing's collapse conditions; except a complete loss of drilling mud will be assumed. To recall the approach, the internal pressure within the casing was assumed to be 0 psig to acquire the highest external pressure. Hence, the external pressure at the setting depth will be estimated by using hydrostatic pressure exerted by the drilling mud, which can be found in Table 1; whereas the external pressure at the surface was kept as 0 psig. As a result of these procedures, Table 8.6 along with Figure 8.4 were constructed.

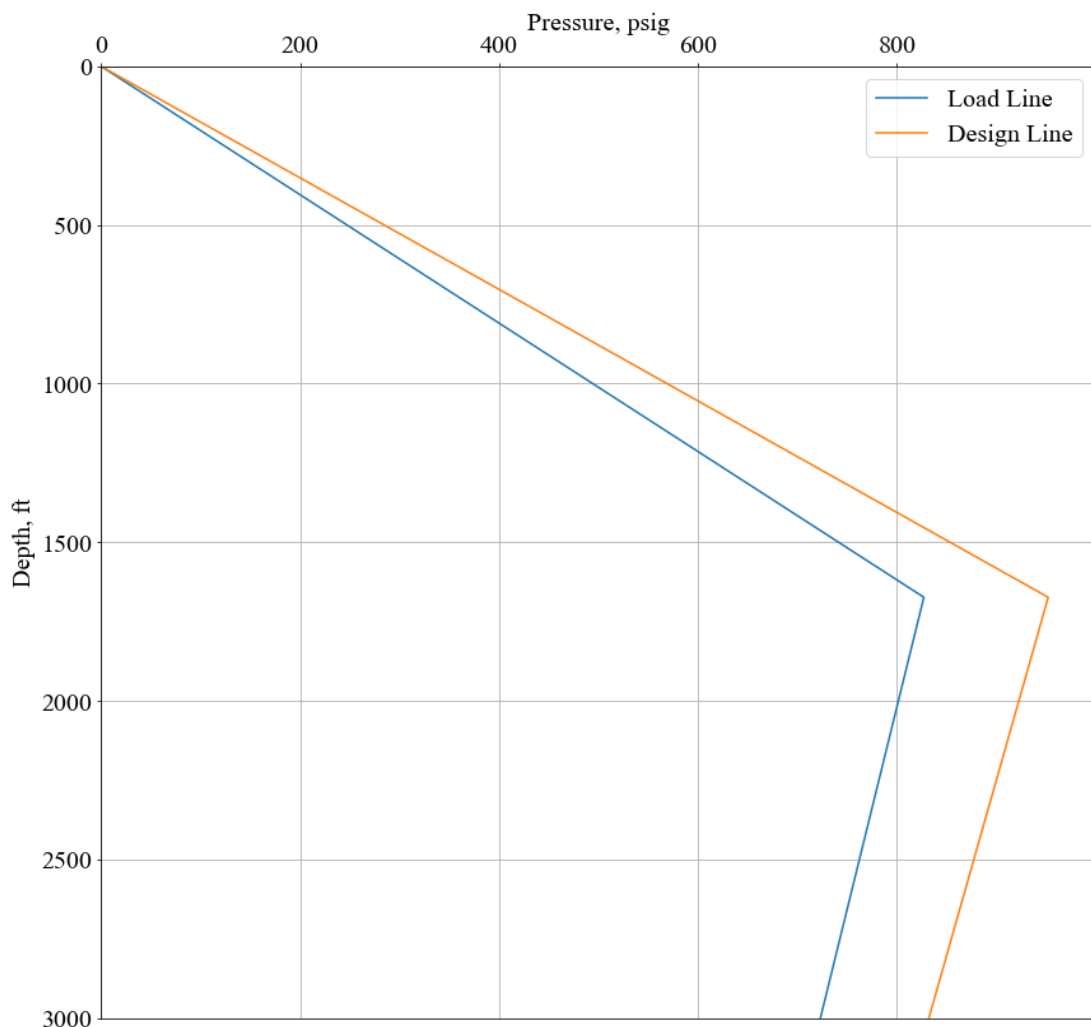


**Figure 8.3:** Collapse pressure criteria for the surface casing.

**Table 8.6:** Collapse pressure load and design lines for the production casing.

Depth, ft	Load Line, psig	Design Line, psig
0	0	0
7600	4347	5000

#### 8.4. Casing Selection, Tension Design and Collapse Correction

According to the obtained results, it was tried to determine the proper casing grades for both surface and production casings. To achieve this, the range which is satisfied for both burst and collapse designs were considered. Hence, the appropriate casing grades were determined by the help of API casing table as shown in Table 8.7 (Bourgoyne Jr, Millheim, Chenevert , & Young Jr, 1991).

Following to the selection of the casing grades, the tension design will be performed by utilizing a force diagram. The determination of the tension criteria is particularly important as it influences the collapse pressure rating of a casing. That's why, once the tension profile as a function of depth is acquired, the collapse ratings for casings in Table 8.7 will be corrected. Since the axial loading on the casing design creates huge uncertainties due to the threads, the safety factor for this study was taken as 1.6 (Wu, 2021).

In order to construct a tension design for each casing, the properties will be utilized from Table 8.7. In addition to these properties, other properties such as the calculated ones, can be found in Table 8.8. Hence, the surface area for each casing was calculated by using (Eq. 8-6) (Bourgoyne Jr, Millheim, Chenevert , & Young Jr, 1991). These calculated surfaces areas were used to estimate the upward forces below each casing seat; thus, these forces were indicated as negative values since the upward forces were taken as compression. The upward force at the bottom of the casing seat was estimated by multiplying the hydrostatic pressure exerted by the drilling mud with the surface area (Eq. 8-7). Lastly, the overall axial tension at the surface was estimated by using (Eq. 8-8), and the results were visualized in Figure 8.5. Note that the selected casing grades should always satisfy both burst and collapse design conditions at the same time. That's why a single-grade casing was chosen for each setting interval. Because there is no lower-grade casing that satisfies the design criteria of the surface casing.

On the other hand, for the production casing, it can be seen that the selected one is the only casing grade which satisfies the burst and collapse conditions at the same time. Already tried by our engineers to design multiple casing grades, especially in the section of production, but the results were found to be failing as the burst criteria require more durable casing grades at the surface sections. Thus, in either way, there will be at least 1000 feet section around surface which requires at least C-75 grade casing. That's why, it is better to proceed with one single grade for each casing sections.

**Table 8.7:** Selected casing grades and their properties.

Section	Depth, ft	Casing Grade	NWTC, lbm/ft	OD, inch	ID, inch	Wall Thickness, inch	P <sub>br</sub> , psi	P <sub>c</sub> , psi	σ <sub>PBYS</sub> , lbf
1	0-3000	H-40	32.3	9 <sup>5/8</sup>	9.001	0.312	2270	1370	365000
2	0-7600	C-75	24	6 <sup>5/8</sup>	5.921	0.352	6970	5550	520000

$$A_s = \frac{OD^2 - ID^2}{4} \pi \quad (\text{Eq. 8-6})$$

$$F_{\text{seat}} = P_{\text{seat}} A_s \quad (\text{Eq. 8-7})$$

$$F_a = W_{\text{casing}} L_{\text{casing}} - F_{\text{seat}} \quad (\text{Eq. 8-8})$$

**Table 8.8:** Axial tension results for both surface and production casing.

Section	Length, ft	Casing Grade	Surface Area, ft <sup>2</sup>	P <sub>seat</sub> , psig	F <sub>seat</sub> , lbf	F <sub>a</sub> , lbf	F <sub>seatSF</sub> , lbf	F <sub>asSF</sub> , lbf
1	3000	H-40	9.128	1482	-13529	83372	-21645	133395
2	7600	C-75	6.937	4347	-30157	152244	-48250	243590

As a result of Table 8.8, it can be seen that the selected casing grades withstand the estimated axial tensions (see Table 8.7). From the now on, it was found to be essential to consider the corrected collapse pressures under the operating conditions. To achieve this, the empirical coefficients for the collapse mode determination were estimated by using (Eq. 8-9), (Eq. 8-10), (Eq. 8-11), (Eq. 8-12), and (Eq. 8-13) (Özbayoğlu & Altun, 2010). Thus, once these coefficients were estimated for each casing, one can estimate the boundary limits for yield strength collapse, plastic collapse, transition collapse, and elastic collapse. The empirical estimations for these boundaries were given in (Eq. 8-14), (Eq. 8-15), (Eq. 8-16) (Bourgoyne Jr, Millheim, Chenevert , & Young Jr, 1991). As can be seen from (Eq. 8-14), (Eq. 8-15), (Eq. 8-16), the boundary estimation for the collapse modes requires the knowledge of the effective yield strength value for the specific casing. This adjective, effective, stands for the yield strength of the material under the operating conditions. Hence, since the collapse resistance of the material is affected by the tensile loads, the effective yield strength value can be estimated using (Eq. 8-17) (Bourgoyne Jr, Millheim, Chenevert , & Young Jr, 1991). In addition, as can be examined from (Eq. 8-17), there is a term called internal pressure,  $P_i$ , in the estimation of the effective yield stress. This term stands for the internal pressure encountered during the operations; hence, this term was taken to be equal to the hydrostatic pressure exerted by the density difference between cement and drilling mud. By looking at the Halliburton's Red Book, it can be seen that the average cement density is around 15.7 ppg (Halliburton, 2010).

$$F_1 = 2.8762 + 0.10679 \times 10^{-5} \sigma_{yield} + 0.21301 \times 10^{-10} \sigma_{yield}^2 - 0.53132 \times 10^{-16} \sigma_{yield}^3 \quad (\text{Eq. 8-9})$$

$$F_2 = 0.026233 + 0.50609 \times 10^{-6} \sigma_{yield} \quad (\text{Eq. 8-10})$$

$$F_3 = -465.93 + 0.030867 \sigma_{yield} - 0.10483 \times 10^{-7} \sigma_{yield}^2 + 0.36989 \times 10^{-13} \sigma_{yield}^3 \quad (\text{Eq. 8-11})$$

$$F_4 = \frac{46.95 \times 10^6 \left[ \frac{\frac{3F_2}{F_1}}{2 + \frac{F_2}{F_1}} \right]^3}{\sigma_{yield} \left[ \frac{\frac{3F_2}{F_1}}{2 + \frac{F_2}{F_1}} - \frac{F_2}{F_1} \right] \left[ 1 - \frac{\frac{3F_2}{F_1}}{2 + \frac{F_2}{F_1}} \right]^2} \quad (\text{Eq. 8-12})$$

$$F_5 = \frac{F_4 F_2}{F_1} \quad (\text{Eq. 8-13})$$

$$\left(\frac{d_n}{t}\right) \text{yield}_{\max} = \frac{\sqrt{(F_1 - 2)^2 + 8 \left[ F_2 + \frac{F_3}{(\sigma_{yield})_e} \right] + (F_1 - 2)}}{2 \left[ F_2 + \frac{F_3}{(\sigma_{yield})_e} \right]} \quad (\text{Eq. 8-14})$$

$$\left(\frac{d_n}{t}\right) \text{plastic}_{\max} = \frac{(\sigma_{yield})_e (F_1 - F_4)}{F_3 + (\sigma_{yield})_e (F_2 - F_5)} \quad (\text{Eq. 8-15})$$

$$\left(\frac{d_n}{t}\right) \text{elastic}_{\text{lower}} = \frac{2 + \frac{F_2}{F_1}}{\frac{3F_2}{F_1}} \quad (\text{Eq. 8-16})$$

For this study and the selected casing grades, the empirical coefficients along with the boundary limits for various collapse modes were estimated with the given above equations. The empirical coefficient results for each casing grade were demonstrated in Table 8.9; hence, the boundary limits of the collapse modes were constructed in Table 8.10. Since the  $d_n/t$  is 30.85 for the H-40 grade type casing, and 18.82 for the C-75 type casing, the collapse modes were found to be transition based on Table 8.10 for both of them.

$$\frac{(\sigma_{yield})_e}{\sigma_{yield}} = \sqrt{1 - \frac{3}{4} \left( \frac{\sigma_z + P_i}{\sigma_{yield}} \right)} - \frac{1}{2} \left( \frac{\sigma_z + P_i}{\sigma_{yield}} \right) \quad (\text{Eq. 8-17})$$

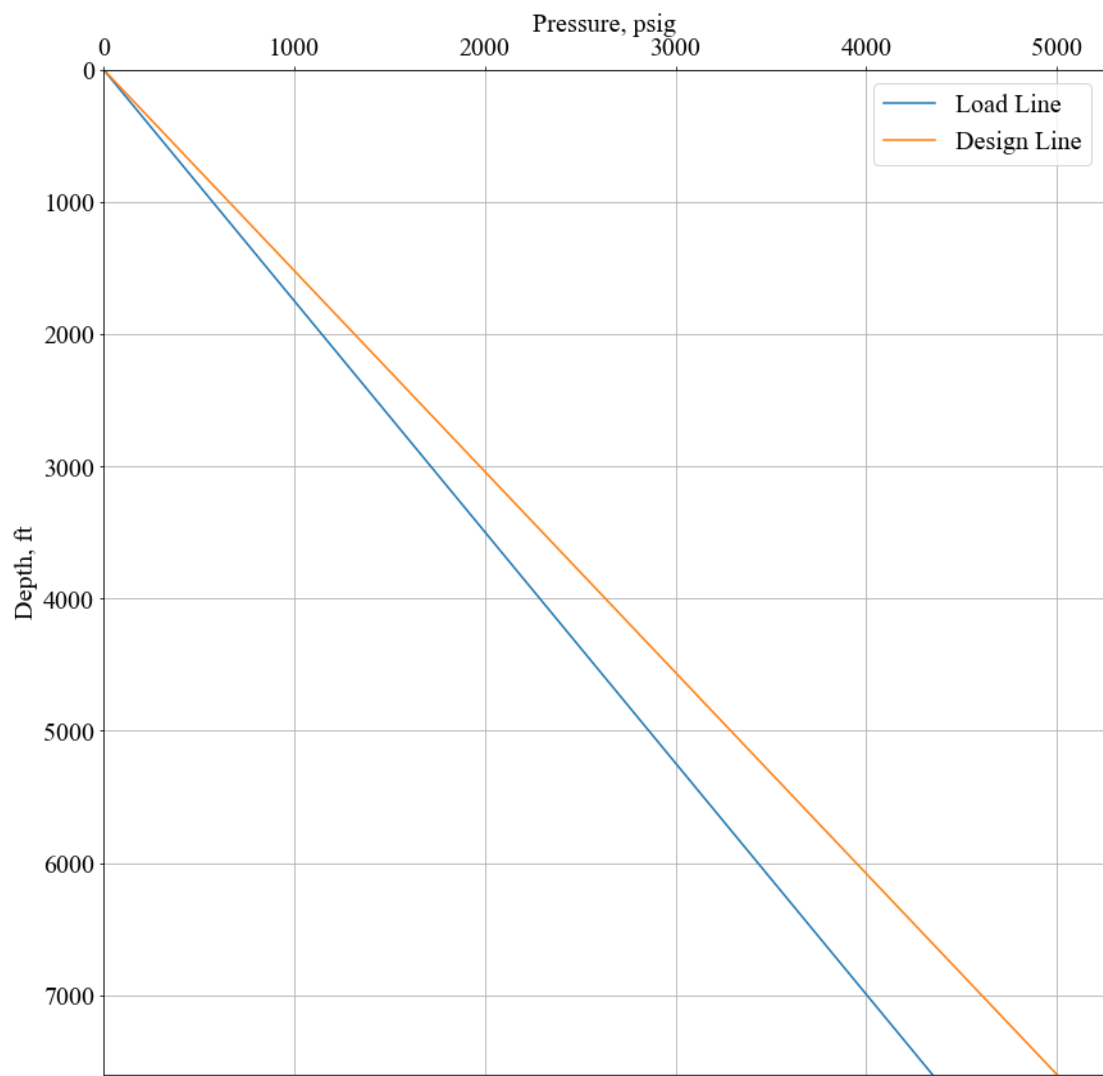


**Figure 8.4:** Collapse pressure criteria for the production casing.

**Table 8.9:** Estimated empirical coefficients used for collapse mode determination for each casing.

Grade	F <sub>1</sub>	F <sub>2</sub>	F <sub>3</sub>	F <sub>4</sub>	F <sub>5</sub>
<b>H-40</b>	2.9496	0.04648	754.344	2.06308	0.03251
<b>C-75</b>	3.03537	0.06419	1805.73	1.98993	0.04183

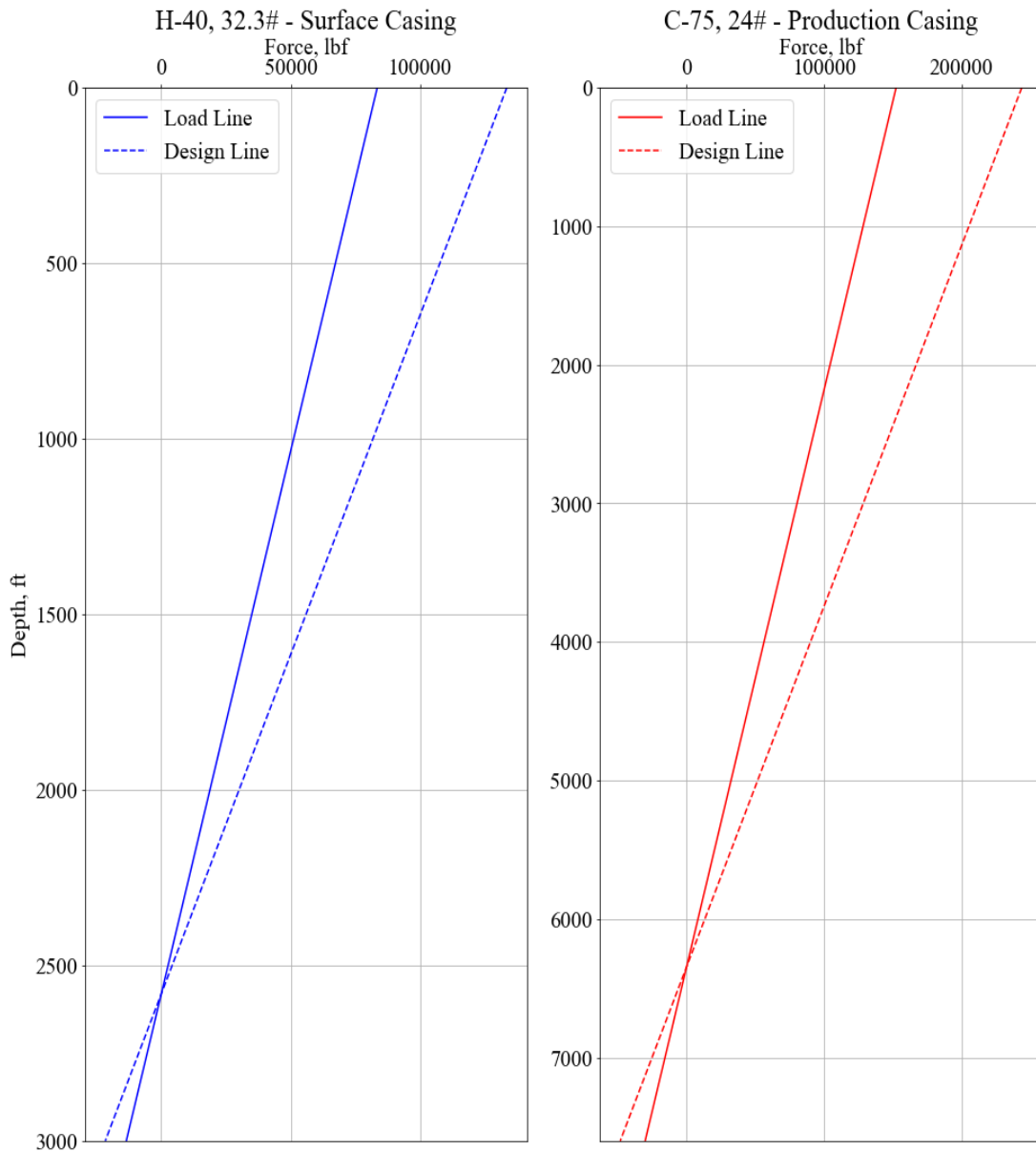


**Figure 8.5:** Resulted tension design for the surface and production casings.

Based on the found collapse modes, the transition collapse (see (Eq. 8-17) corrections were employed on H-40, and C-75 casings respectively (see Table 8.11). As a result, the corrected collapse pressure rating for H-40 was found to be 1026 psi, which still satisfies the collapse design criteria. However, the corrected collapse pressure rating for C-75 was found to be 3151 psi, which fails under the operating conditions. That's why, it is highly prominent to select a higher-grade casing.

**Table 8.10:** Estimated collapse mode boundaries for each casing grade.

Grade	Collapse Mode						
	Yield Strength	$d_n/t$	Plastic	$d_n/t$	Transition	$d_n/t$	Elastic
<b>H-40</b>		14.78		21.68		42.64	
<b>C-75</b>		12.24		18.48		32.05	

**Table 8.11:** Estimated properties for each casing.

Section	Length, ft	Casing Grade	$\frac{d_n}{t}$	$P_i$ , psi	$\frac{\sigma_{yield}}{(\sigma_{yield})_e}$	$(\sigma_{yield})_e$ , lbf	$P_{cr}$ , psi
<b>1</b>	3000	H-40	30.85	982	0.746	29853	1026
<b>2</b>	7600	C-75	18.82	1872	0.658	49322	3151

When the necessary iterations were applied to the production casing section, it was found that the C-75 casing with 32 lbm/ft NWTC satisfies the constructed burst and collapse design criteria (see Table 8.12). On the other hand, since the casing grades are same, the empirical coefficients were not changed; hence, since the collapse mode boundaries are functions of the empirical coefficients, they were also not changed. However, according to Table 8.12, it can be seen that  $d_n/t$  ratio has become 13.95; which was resulted in plastic collapse mode of failure. In order to estimate the corrected collapse pressure rating under the plastic collapse mode of failure, (Eq. 8-18) can be used (Bourgoyn Jr, Millheim, Chenevert , & Young Jr, 1991). Further, again, it was found to be unnecessary to determine different casing grades in the design of the production casing. It could have been chosen C-75 casing grade with 24 lbm/ft NWTC for the shallow depths; however, since the grades are the same, this scenario

will not be creating a huge economic benefit.

$$P_{cr} = (\sigma_{yield})_e \left( \frac{F_4}{d_n/t} - F_5 \right) \quad (\text{Eq. 8-18})$$

Furthermore, the new axial tension design was constructed to evaluate the durability of the newly selected casing grades (see Figure 8.6). Based on Figure 8.6, it was found that the both casings satisfy the estimated axial tension design criteria. Hence, the available coupling types were also found to be satisfying under the operating conditions; and, the overall casing design was illustrated in Figure 8.7. Lastly, the properties of the overall design were given in Table 8.13

$$P_{cr} = (\sigma_{yield})_e \left( \frac{F_1}{d_n/t} - F_2 \right) - F_3 \quad (\text{Eq. 8-19})$$

**Table 8.12:** Final estimated correct collapse, burst pressures, and axial tensions for the surface and production casings.

Length, ft	Casing Grade	NWTC, lbm/ft	$\frac{d_n}{t}$	$\frac{\sigma_{yield}}{(\sigma_{yield})_e}$	$(\sigma_{yield})_e$ , lbf	P <sub>cr</sub> , psi	P <sub>br</sub> , psi	F <sub>seat</sub> , lbf	F <sub>a</sub> , lbf
3000	H-40	32.3	30.85	0.746	29853	1026	2270	-13529	83372
7600	C-75	32	13.95	0.654	49022	5781	9410	-39896	203304

**Table 8.13:** Final casing design properties.

Interval, ft	Casing Type	Grade	NWTC, lbm/ft	OD, inch	ID, inch	RTS	RT L	P <sub>br,coupling</sub> , psi		JS, 1000 lbf
								RTS	RTL	
0 – 150	Conductor	H-40	48	13 <sup>3/8</sup>	12.715	173 0	-	814	-	541
0 – 3000	Surface	H-40	32.3	9 <sup>5/8</sup>	9.001	227 0	-	254	-	365
0 – 7600	Production	C-75	32	6 <sup>5/8</sup>	5.675	-	9410	-	638	688

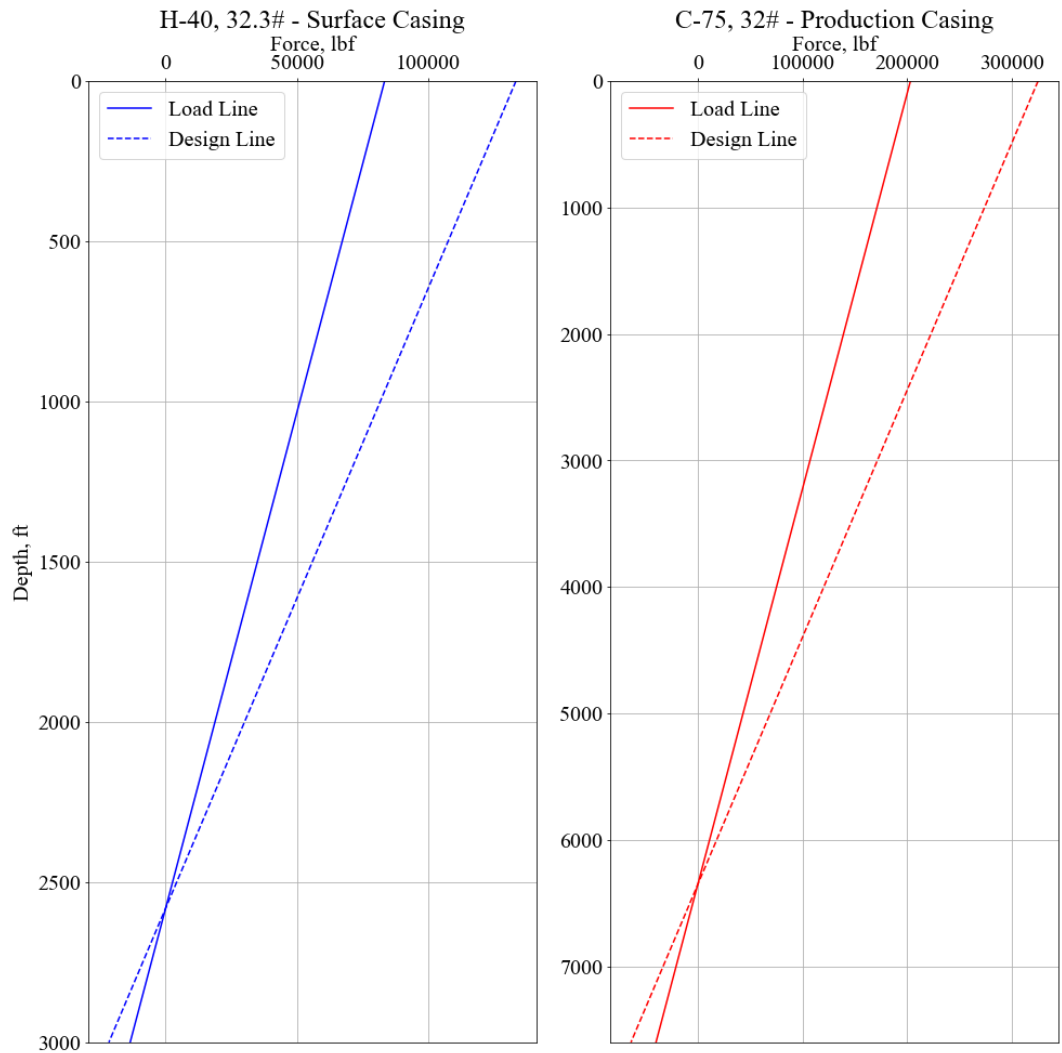


**Figure 8.6:** Final resulted tension design for the surface and production casings.

Since the axial tension criteria were estimated, and determined for both the surface and production casings, the axial tension design factors must be calculated to dictate that the selected casing grades can withstand the constructed scenarios. To achieve this, a simple equation, (Eq. 18-16) can be used. For the denominator, the maximum estimated axial tension values were used along with their applied safety margins. As a result, the calculated axial tension design factors were summarized in Table 8.14; furthermore, since all of the values are greater than 1, both casings and couplings can withstand the constructed scenarios.

$$DF_t = \frac{\text{Yield Strength of casing or coupling}}{\text{Axial Tension}} \quad (\text{Eq. 8-20})$$

**Table 8.14:** Calculated axial tension design factors for casings, and couplings.

Casings and Couplings	Design Factor, ratio
H-40   RTS	2.74   1.90
C-75   RTL	2.12   1.96

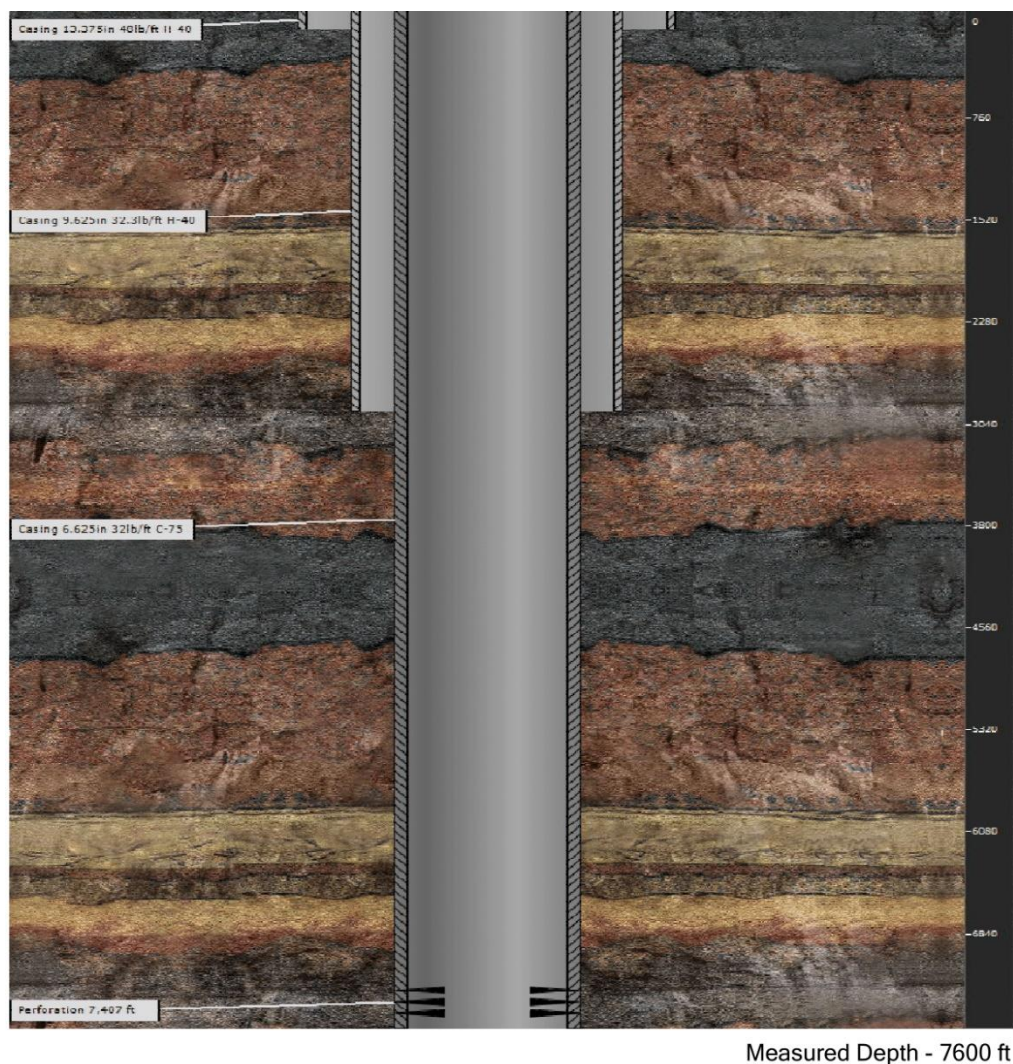


**Figure 8.7:** Illustration of the casing design. Constructed by using Halliburton eRed Book (2010).

## **8.5. Casing Landing**

In order to proceed into the design stage of the cementing operation, it was found to be important to denote the portions that will be cemented. The hole portions within conductor casing and the surface casing will be fully cemented due the environmental concerns. To provide some instances regarding to such issues, the followings can be listed (Devereux, 1998):

- Preventing the possible pollution of fresh water zones.
- Sustaining a strong foundation, and constructing a precise alignment for the well.
- Isolating zones.
- Supplying an adequate support to overall wellhead and casing structure.
- Preventing possible wellhead subsidence.

On the contrary, the production casing part can be partially cemented; hence, this design will yield lower expenses compared to cementing the hole section. Because when the portion that will be cemented is shorten, the amount of time and the amount of volume required will be decreased. However, a care must be taken as the buckling may occur when the cement hardens, especially in the partially cemented casing parts. In the literature, lots of methods have been published by scientist for the estimation of buckling forces. The most common ones are Goins and Lubinski methods. They have different advantages and disadvantages; furthermore, the Goins methods is used when the mud weight is lower than 12.5 ppg (Bourgoyne Jr, Millheim, Chenevert , & Young Jr, 1991). On the contrary, the Lubinski method is used. However, it was stated that the Lubinski method can also be used for full range of mud weights. In this study, the Lubinski method was selected to be used in the estimation of buckling forces when the cement hardens. Hence, the Lubinski method assumes that the well is vertical, and a helical buckling may occur (Mitchel, 1988). Rather stating the hole complex formula, the following assumptions were done to simplify the estimation:

- There will be no temperature change while cement hardens.
- There will be no change in the densities within the annulus.
- There will be no change in the densities within the casing.
- There will be no change in pressure within the annulus.
- There will be no change in pressure within the casing.
- There will be no fluid level fall within the annulus.
- There will be no fluid level fall within the casing.

When the above assumptions were applied, only the following parameters become pivotal:

- The weight of the casing that is cemented (Eq. 8-21).
- The weight of the cemented portion (Eq. 8-22).
- The weight of the mud inside the casing (Eq. 8-23).

$$B_2 = -h_c w \quad (\text{Eq. 8-21})$$

$$B_3 = (0.0408)OD^2 h_c \rho_c \quad (\text{Eq. 8-22})$$

$$B_4 = -(0.0408)ID^2 h_c \rho_i \quad (\text{Eq. 8-23})$$

Furthermore, the buckling forces can be found by using (Eq. 8-24). Based on the obtained value from (Eq. 8-24), one can conclude whether the buckling will occur or not. This is achieved by examining the sign of the resulted value. If the value is negative, the buckling will not occur at any point; thus, the reverse is true for the occurrence of the buckling.

$$\Delta S = B_2 + B_3 + B_4 \quad (\text{Eq. 8-24})$$

If the above assumptions are accepted for the estimation of the wellhead loads when the cement hardens, the estimation of the wellhead loads are also simplified. In these assumed conditions, the following parameters are the ones that affect the wellhead loads when the cement hardens:

- Air weight of the casing (Eq. 8-25).
- The weight of the cement (Eq. 8-26)
- The weight of the cement within annulus (Eq. 8-27).
- The weight of the mud inside the casing (Eq. 8-28).

$$W_3 = w''(h_c + L_{open}) \quad (\text{Eq. 8-25})$$

$$W_4 = -(0.0408)(OD^2)h_c\rho_c \quad (\text{Eq. 8-26})$$

$$W_5 = -(0.0408)(OD^2)L_{open}\rho_e \quad (\text{Eq. 8-27})$$

$$W_6 = -(0.0408)(ID^2)(h_c + L_{open})\rho_i \quad (\text{Eq. 8-28})$$

Moreover, the resultant wellhead load can be estimated using (Eq. 8-29). Hence, the resultant wellhead loads are expecting to be reduced when the cement hardens. Because, when the cement hardens, the casing will not be suspended in the air; the cemented portion will be supported by cement. Lastly, the parameters that were used throughout the estimations of the buckling and wellhead loads were given in Table 8.15 and Table 8.16. Thus, one can understand from these tables, the different scenarios were tested: cementing 2000 ft and 3000 ft.

$$W_{\text{cement}} = W_3 + W_4 + W_5 + W_6 \quad (\text{Eq. 8-29})$$

**Table 8.15:** Parameters for the first scenario.

<b><math>\rho_i</math>, ppg</b>	11.5
<b><math>\rho_e</math>, ppg</b>	11.5
<b><math>\rho_c</math>, ppg</b>	16
<b><math>h_c</math>, ft</b>	2000
<b><math>L_{\text{open}}</math>, ft</b>	5600
<b><math>w''</math>, lbm/ft</b>	32
<b>OD, inch</b>	6.625
<b>ID, inch</b>	5.675

Based on the estimation results, Table 8.17 was obtained. Based on Table 8.17, one can conclude that the buckling will not occur in both scenarios since the resultant forces are negative. On the other hand, when the resultant wellhead loads are compared, it can be seen that the resultant wellhead loads are smaller in Scenario 2. This was found to be meaningful since the cemented portion is 3000 ft in Scenario 2. Additionally, in both scenarios, the resulted wellhead loads are smaller compared to loads obtained in the axial tension design of the production casing. Again, this was found to be meaningful as the cemented portion supports the casing.

**Table 8.16:** Parameters for the second scenario.

<b><math>\rho_i</math>, ppg</b>	11.5
<b><math>\rho_e</math>, ppg</b>	11.5
<b><math>\rho_c</math>, ppg</b>	16
<b><math>h_c</math>, ft</b>	3000
<b><math>L_{\text{open}}</math>, ft</b>	4600
<b><math>w''</math>, lbm/ft</b>	32
<b>OD, inch</b>	6.625
<b>ID, inch</b>	5.675

**Table 8.17:** The comparison of scenarios.

Scenarios			
Scenario 1		Scenario 2	
$\Delta S, \text{ lbf}$	$W_{\text{cement}}, \text{ lbf}$	$\Delta S, \text{ lbf}$	$W_{\text{cement}}, \text{ lbf}$
-36918	185416	-55377	177357

In conclusion, both scenarios were tested and both of them were found to be satisfying the designed conditions. However, one of them should be selected in order to proceed with the cement design. Considering the economics, and the time that will be required to complete the cement operation, Scenario 1 was chosen as the required cement volume is smaller than Scenario 2.

## **9. CEMENT DESIGN**

Cementing is the process of filling the well wall-casing and casing-casing gaps after casing operations in drilling operations with cement of different contents depending on the petrophysical structure of the well. Cementing has vital importance in drilling such as:

- Sustaining the zonal isolation.
- Preventing underground blowouts.
- Providing support for overall well structure.
- Enhancing the wellbore stability.
- Preventing unexpected environmental hazards.

Since the surface casing cementing depth is 3000 ft according to the API cement classes table, it is appropriate to use Class A cement, which is suitable for use in the range of 0-6000 ft. Considering that the production casing depth is 7600 ft, it is appropriate to use Class G cement suitable for this depth (Bourgoyne Jr, Millheim, Chenevert , & Young Jr, 1991).

Calculations were made to determine the volume of cement to be used to perform the cementing process. Necessary laboratory tests were performed to determine the cement mixture. After the surface coating process, Class A cement with 8% bentonite will be used in Lead cementing between 0-2000ft, and Class A cement without additives will be used in Tail cementing between 2000-3000ft. After the production casing operation, Class G cement with 8% bentonite addition will be used in Lead cementing between 5600-6600ft, and Class G cement with 10% pure additive will be used in Tail Cementing between 6600-7600ft. In the preparation of these cement mixtures, API Class A Bentonite Cement, API Class G Bentonite Cement and Class G Cement Salt tables were used and slurry density and slurry efficiency values were taken from these tables. (Halliburton, 2010). MKP-750 model pump belonging to the PT Mudking Asia Pacific Raya brand was chosen to carry out the cementing operations. For the specifications regarding to the selected pump model, Table A was

constructed provide related properties of MKP-750 pump. Lastly, the single-acting triplex pump was chosen since it has the following benefits (Kolesnikov, Kolesnikov, Bocharkov, Kozinskaya, & Denisova, 2023)

- It is more efficient than the duplex pumps.
- It can provide more output per stroke.
- It provides smoother flow.
- It has less vibration and wear compared to the duplex pump. Moreover, these benefits result in low maintenance cost and increment in the overall pump life.

In order to design a proper cementing operation, there are several parameters that should be estimated. First of all, the necessary volumes should be estimated. To achieve this, (Eq. 9-1) was utilized to estimate the open-hole casing annulus volume while (Eq. 9-2) was used to estimate cased-hole annulus volume.

$$V_{\text{open-hole}} = \frac{\pi}{4} (d_{\text{hole}}^2 - OD^2)(D_{\text{shoe}} - D) \quad (\text{Eq. 9-1})$$

$$V_{\text{cased-hole}} = \frac{\pi}{4} (OD^2 - ID^2) \quad (\text{Eq. 9-2})$$

In addition to the such volume estimation, one can use (Eq. 9-3) to estimate the displacement volume. On the other hand, the volume of the casing shoe joint was estimated using (Eq. 9-4). Those capacity factors dictated in (Eq. 9-3) and (Eq. 9-4) was gathered from API casing tables.

$$V_{\text{dis}} = Ca_p D \quad (\text{Eq. 9-3})$$

$$V_{\text{shoe}} = Ca_{\text{shoe}} L_{\text{shoe}} \quad (\text{Eq. 9-4})$$

Since the target depth is 7600 ft and the bottom of the reservoir is 7523 ft, there will be 77 ft long empty hole below the bottom of the reservoir. This empty hole was called as rat-hole in the literature; hence, the volume of the rat hole can be estimated using (Eq. 9-5). Lastly, the required amount of sack can be estimated from (Eq. 9-6).

$$V_{\text{rat-hole}} = \frac{\pi}{4} d_{\text{hole}} L_{\text{rat-hole}} \quad (\text{Eq. 9-5})$$

$$\text{Sack of cement} = \frac{V_{\text{slurry}}}{\text{Slurry yield}} \quad (\text{Eq. 9-6})$$

In the oil and gas industry, during the cement operation design, an excess factor is strictly used to overcome the possible loss circulation problems. In this study, the excess factor was determined from Well-22's well logging data since it is one of the closest wells and contains caliper readings. First of all, the average wash-out was read from the caliper readings as 10.8 in. Afterward, utilizing (Eq. 9-7), the excess factor was determined as 20%. This means that the estimated overall volume to be cemented will be multiplied by a factor of 1.2.

$$\text{Excess Factor} = \frac{|d_{\text{hole}} - d_{\text{CAL}}|}{d_{\text{hole}}} \times 100 \quad (\text{Eq. 9-7})$$

Mixing time is the time taken during the mixing of cement and additives to be used in the cementing operation. The mixing process takes place in the mixing truck in the company's inventory and the mixing capacity of the truck is 20 ft<sup>3</sup>/min. The mixing time can be estimated using (Eq. 9-8). Displacement time is the time it takes to displace the slurry pumped into the well towards the outer surface of the casings by pumping another liquid behind it. To estimate the displacement time (Eq. 9-9) can use. As a company policy after the mixing and displacement processes in cementing operations, 8-hour thickening period is added to the mixing displacement periods to thickening the cement.

$$t_{\text{mixing}} = \frac{\text{Sack of cement} + V_{\text{additive}}}{\text{Mixing capacity}} \quad (\text{Eq. 9-8})$$

$$t_{\text{displacement}} = \frac{V_{\text{slurry}} + V_{\text{dis}}}{\text{Pump output} \times 60 \times E_p} \quad (\text{Eq. 9-9})$$

**Table 9.1:** MKP-750 model pump motor information.

<b>Rated Horse power</b>	750								hp
<b>Rated Pump Speed</b>	150								spm
<b>Maximum Liner Size</b>	7								in
<b>Stroke Length</b>	8								in
<b>Weight (Pump)</b>	19500								lbs
<b>Min. Speed</b>	-								RPM
<b>Max. Speed</b>	145								RPM
<b>Flowrate</b>	Up to 580								gal/min
<b>Max. Working Pressure</b>	5000	4830	3912	3233	2717	2504	2315	1996	psi
<b>Liner Size</b>	4	4-1/2	5	5-1/2	6	6-1/4	6-1/2	7	in
<b>Displacement</b>	189	240	296	358	426	462	500	580	gpm

## 9.1. Conductor Stage

In conductor casing cement calculation To calculate the volume between the well wall and conductor casing (Eq. 9-1) was used (Bourgoyne Jr, Millheim, Chenevert , & Young Jr, 1991). Necessary data for cementing calculation of conductor casing are shown in Table 9.2 and after these calculations, cementing results of conductor casing are shown in Table 9.3.

**Table 9.2:** Necessary data for the cement operation of the conductor casing.

<b>Hole Diameter</b>	17.5	inch
<b>Casing Depth</b>	150	ft
<b>Casing OD</b>	13.375	inch
<b>Casing ID</b>	12.72	inch
<b>Pump Model</b>	MKP-750	
<b>Pump Stroke</b>	11.9	bbl/min
<b>Pump Efficiency</b>	90%	

**Table 9.3:** The cement operation results of the conductor casing.

<b>Slurry Density</b>	13	ppg
<b>Sack of Cement</b>	50	sacks
<b>Required Water</b>	12.88	bbl
<b>Open Hole Annulus</b>	18.56	bbl
<b>Total Annulus Vol</b>	18.56	bbl
<b>Total Slurry Volume with Excess 20%</b>	22.27	bbl
<b>Displacement Volume</b>	23.56	bbl
<b>Pump Stroke</b>	11.9	bbl/min
<b>Displacement Time</b>	0.08	hour
<b>Mixing Time</b>	0.1	hour
<b>Total Time</b>	8.18	hours

## 9.2. Surface Stage

In surface casing cement calculation, to calculate the volume between conductor casing and surface casing, (Eq. 9-2) , to calculate the volume between the well wall and surface casing, (Eq. 9-1) and to calculate the displacement volume (Eq. 9-3) were used (Bourgoyne Jr, Millheim, Chenevert , & Young Jr, 1991). To calculate the volume of cement in the shoe joint, (Eq. 9-4) was used (Halliburton, 2010). Necessary data for cementing calculation of surface casing are shown in Table 9.4 and after these calculations, cementing results of surface casing are shown in Table 9.5.

### **9.3. Production Stage**

In production casing cementing calculation, to calculate the volume between the well wall and surface casing, (Eq. 9-1) and to calculate the displacement volume, (Eq. 9-3) were used (Bourgoyne Jr, Millheim, Chenevert , & Young Jr, 1991). To calculate the volume of cement in the shoe joint, (Eq. 9-4), to calculate the sack of cement (Eq. 9-6) was used (Halliburton, 2010). To calculate the rat hole volume (Eq. 9-5) was used. Necessary data for cementing calculation of surface casing are shown at Table 9.6 and after these calculations, cementing results of surface casing are shown at Table 9.7.

**Table 9.4:** Necessary data for the cement operation of the surface casing.

<b>Hole Diameter</b>	12.25	inch
<b>Casing Depth</b>	3000	ft
<b>OD</b>	9.625	inch
<b>ID</b>	9.001	inch
<b>Pump Model</b>	MKP-750	
<b>Pump Stroke</b>	11.9	bbl/min
<b>Pump Efficiency</b>	90%	

**Table 9.5:** The cement operation results of the surface casing.

<b>LEAD CEMENT</b>	<b>Slurry Density</b>	13	lbm/gal
	<b>Slurry Yield</b>	1.92	ft <sup>3</sup> /sack
	<b>Sack of Cement</b>	785.32	sack
	<b>Required Water</b>	194.46	bbl
	<b>Shoe Track Volume</b>	13.41	bbl
	<b>Lead Cement Volume with Excess 20%</b>	255.14	bbl
	<b>Total Slurry Volume with Excess 20%</b>	268.55	bbl
	<b>Displacement Volume (Total)</b>	444.42	bbl
	<b>Pump Stroke</b>	11.9	bbl/min
	<b>Displacement Time (Total)</b>	0.69	hour
<b>TAIL CEMENT</b>	<b>Mixing Time</b>	0.31	hour
	<b>Total Time</b>	1	hour
	<b>Slurry Density</b>	15.6	lbm/gal
	<b>Slurry Yield</b>	1.18	ft <sup>3</sup> /sack
	<b>Sack of Cement</b>	726.85	sack
	<b>Required Water</b>	89.99	bbl
	<b>Shoe Track Volume</b>	11.01	bbl
	<b>Lead Cement Volume with Excess 20%</b>	141.75	bbl
	<b>Total Slurry Volume with Excess 20%</b>	152.76	bbl
	<b>Displacement Volume (Total)</b>	444.42	bbl
	<b>Pump Stroke</b>	11.9	bbl/min
	<b>Displacement Time (Total)</b>	0.69	hour
	<b>Mixing Time</b>	0.21	hour
	<b>Total Time</b>	9.21	hour

**Table 9.6:** Necessary data for the cement operation of the production casing.

<b>Hole Diameter</b>	8.5	inch
<b>Casing Depth</b>	7600	ft
<b>Casing OD</b>	6.625	inch
<b>Casing ID</b>	5.675	inch
<b>Pump Model</b>	MKP-750	
<b>Pump Stroke</b>	11.9	bbl/min
<b>Pump Efficiency</b>	90%	

**Table 9.7:** Cementing results of production casing

<b>LEAD CEMENT</b>	<b>Slurry Density</b>	13.2	lbm/gal
	<b>Slurry Yield</b>	1.89	ft <sup>3</sup> /sack
	<b>Sack of Cement</b>	251.94	sack
	<b>Required Water</b>	61.18	bbl
	<b>Lead Cement Volume with Excess 20%</b>	32.7	bbl
	<b>Total Slurry Volume with Excess 20%</b>	84.81	bbl
	<b>Displacement Volume (Total)</b>	245.01	bbl
	<b>Pump Stroke</b>	11.9	bbl/min
	<b>Displacement Time (Total)</b>	0.38127	hour
	<b>Mixing Time</b>	0.09699	hour
	<b>Total Time</b>	0.47826	hour
<b>TAIL CEMENT</b>	<b>Slurry Density</b>	15.6	lbm/gal
	<b>Slurry Yield</b>	1.65	ft <sup>3</sup> /sack
	<b>Sack of Cement</b>	114.87	sack
	<b>Required Water</b>	18.6	bbl
	<b>Shoe Joint Volume</b>	3.67	bbl
	<b>Tail Cement Volume with Excess 20%</b>	30.08	bbl
	<b>Total Slurry Volume with Excess 20%</b>	33.76	bbl
	<b>Displacement Volume (Total)</b>	245.01	bbl
	<b>Pump Stroke</b>	11.9	bbl/min
	<b>Displacement Time (Total)</b>	0.38127	hour
	<b>Mixing Time</b>	0.04013	hour
	<b>Total Time</b>	8.51839	hour

## **10. DRILL STRING DESIGN**

In this study, drill string design was carried out using the Huber – Von Mises Law. The process of establishing and choosing the necessary components and requirements for a drill string, which is the column of pipe utilized for drilling a well, is known as drill string design. Drill pipe, heavy-weight drill pipe, drill collars, and drill bits are all components of the drill string. The drill string design is critical for a successful well design. The main objectives of this design are to ensure sufficient strength to sustain tension and to consider the weight of the drill bit. Different calculations are conducted at each level, and while the drill string is made up of several components, it should be seen as a whole. Drill string design begins at the hole's bottom with the Bottom Hole Assembly (BHA). A BHA can be found in the drill string above and below the drill bit. The primary objectives of developing the BHA design were to protect the drill pipe in the drill string from severe bending and torsional loads, to allow drilling straight holes to provide vertical well optimization, to reduce the severity of doglegs, and to improve drill bit performance. The drill collar is the most important part of the BHA. The drill bit is not technically a part of the BHA. It does, however, create and transmit axial and torsional loads to the BHA, and its job is to cut rock at the bottom of the hole (Lake, 2006)

The bit size was determined due to casing design considerations. The weight on bit (WOB) is calculated after bit selection. The correct WOB will ensure that the drill bit cuts and drills the rock efficiently while also restricting damage to the drill string and wellbore. Lithology and predicted well size are taken into account while determining WOB. The weight to be given to the recommended drill during drilling and the rotation speed to which the string will be rotated can be determined from Table 10.1 below, considering the formation characteristics (Özbayoğlu & Altun, 2010). Since it was seen from the well log data that the hardness of the rock increases as the depth increases in the well to be drilled, it was decided to use a soft drill type for the surface and conductor and a medium drill type for production. In this case, the unit weight on bit was taken into account as an average of 4000 lb/in for surface and conductor, and 6000 lb/in for production. WOB values were calculated for each section with the multiplying unit weight on bit-by-bit size and the result is shown in the Table 10.2.

**Table 10.1:** Unit weight on bit and RPM values according to formation type (Özbayoğlu & Altun, 2010).

Formation type	WOB (1000 lbf/in)	RPM
<b>Soft</b>	2.27-6.75	100-250
<b>Medium</b>	4.50-9.00	40-100
<b>Hard (casting bit)</b>	5.60-11.25	35-70
<b>Hard (insert bit)</b>	2.25-9.00	35-70
<b>Hard (friction bit)</b>	4.50-6.75	35-70

**Table 10.2:** WOB parameters according to each section.

Bit Size (in)	WOB (1000 lb/in)	WOB (lbf)	RPM
<b>Conductor</b>	17.5	4000	70000
<b>Surface</b>	12.25	4000	49000
<b>Production</b>	8.5	6000	51000

### 10.1. Bottom Hole Assembly (BHA) Design

The weight given to the bit in a drill string is generally carried out using drill collars. Particularly vertical and in low angle wells, the full weight given to the bit is given by the drill collar and no weight support is expected from the drill pipe. Due to the weight given to the bit, the bottom part of the string is subjected to compression; However, since the wall thickness of the drill collar is much higher than the drill pipe, it is not possible for the drill collar to be affected by this compression as much as the drill pipe. The reason for this is that due to the high wall thickness of the drill collar, bending is felt to a minimum and fatigue does not occur (Özbayoğlu & Altun, 2010).

The outer diameter of the drill collar can be found approximately by the equation (u) below using Drill bit size value ( $D_b$ ). Drill collar outer diameters ( $OD_{dc}$ ) for surface and production were calculated using the (Eq. 10-1), and it was not deemed necessary to place a drill collar for the conductor part. After  $OD_{dc}$  determination, drill collar inner

diameters ( $ID_{dc}$ ) and drill collar weights ( $W_{dc}$ ) were determined according to Table 10.3.

$$OD_{dc} = 0.75D_b \quad (\text{Eq. 10-1})$$

**Table 10.3:** Drill collar weight data according to drill collar outer diameter and inner diameter (Özbayoğlu & Altun, 2010).

(1)	(2)	(3)	(4)	(5)	(6)	(7)	(8)	(9)	(10)	(11)	(12)	(13)	(14)
Drill Collar OD, inches	Drill Collar ID, inches												
	1	1 $\frac{1}{4}$	1 $\frac{1}{2}$	1 $\frac{3}{4}$	2	2 $\frac{1}{4}$	2 $\frac{1}{2}$	2 $\frac{13}{16}$	3	3 $\frac{1}{4}$	3 $\frac{1}{2}$	3 $\frac{3}{4}$	4
2 $\frac{7}{8}$	19	18	16										
3	21	20	18										
3 $\frac{1}{8}$	22	22	20										
3 $\frac{1}{4}$	26	24	22										
3 $\frac{1}{2}$	30	29	27										
3 $\frac{3}{4}$	35	33	32										
4	40	39	37	35	32	29							
4 $\frac{1}{8}$	43	41	39	37	35	32							
4 $\frac{1}{4}$	46	44	42	40	38	35							
4 $\frac{1}{2}$	51	50	48	46	43	41							
4 $\frac{3}{4}$			54	52	50	47	44						
5		61	59	56	53	50							
5 $\frac{1}{4}$		68	65	63	60	57							
5 $\frac{1}{2}$		75	73	70	67	64	60						
5 $\frac{3}{4}$		82	80	78	75	72	67	64	60				
6		90	88	85	83	79	75	72	68				
6 $\frac{1}{4}$		98	96	94	91	88	83	80	76	72			
6 $\frac{1}{2}$		107	105	102	99	96	91	89	85	80			
6 $\frac{3}{4}$		116	114	111	108	105	100	98	93	89			
7		125	123	120	117	114	110	107	103	98	93	84	
7 $\frac{1}{4}$		134	132	130	127	124	119	116	112	108	103	93	
7 $\frac{1}{2}$		144	142	139	137	133	129	126	122	117	113	102	
7 $\frac{3}{4}$		154	152	150	147	144	139	136	132	128	123	112	
8		165	163	160	157	154	150	147	143	138	133	122	
8 $\frac{1}{4}$		176	174	171	168	165	160	158	154	149	144	133	
8 $\frac{1}{2}$		187	185	182	179	176	172	169	165	160	155	150	
9		210	208	206	203	200	195	192	188	184	179	174	
9 $\frac{1}{2}$		234	232	230	227	224	220	216	212	209	206	198	
9 $\frac{3}{4}$		248	245	243	240	237	232	229	225	221	216	211	
10		261	259	257	254	251	246	243	239	235	230	225	
11		317	315	313	310	307	302	299	295	291	286	281	
12		379	377	374	371	368	364	361	357	352	347	342	

Notes:

1. See API Specification 7, Table 13 for API standard drill collar dimensions.
2. For special configurations of drill collars, consult manufacturer for reduction in weight.

To calculate the length of the drill collar, (Eq. 10-2) will be used to find the weight of the drill collar ( $W_{dc}$ ). The Buoyancy factor (BF) and the length of the drill collar required for the drill string design is calculated using (Eq. 10-3) and (Eq. 10-4). When calculating the length of the drill collar, the steel density was taken as 65.5 ppg and mud density was determined is 11 ppg for production whereas 9.5 ppg for surface. The drill collar safety factor (SF) was taken as 1.15. Since there is no inclination, a value is taken as 0 and  $\cos(a)$  value is found as 1.

$$W_{dc} = 2.6722(OD_{dc}^2 - ID_{dc}^2) \quad (\text{Eq. 10-2})$$

$$L_{dc} = \frac{(SF)(WOB)}{(W_{dc})(BF)\cos(a)} \quad (\text{Eq. 10-3})$$

$$BF = 1 - \frac{\rho_m}{\rho_{steel}} \quad (\text{Eq. 10-4})$$

Following the establishment of the drill collar length, an estimation of the required number of drill collars can be determined. Given the correspondence of one pipe to approximately 30 feet, the length of the drill collar (DC) was divided by 30 to ascertain the count of drill collars necessary (API R. 7.-1., 1998). Considering that each pipe equates to 30 feet, the calculated value for  $L_{dc}$  was rounded to the closest multiple of 30. Similarly, owing to the prerequisite for the number of drill collars to be an integer, it was determined as the closest feasible value. A comprehensive presentation of all calculated values at the conclusion of this section is outlined in Table 10.4.

Opting for a widely utilized dimension in the oil and gas sector, the Range-2 pipe (27-30 ft) was selected, and the 'new' drill pipe type was chosen based on wear class compatibility, referencing accessible information from a pertinent table in Appendix F. In accordance with production data from the Mount Doom Oil Field, the selected E-75 drill pipe for the conductor and surface segments features outer diameter of 6.625 inches and a weight of 25.2 lb/ft. Additionally, the E-75 drill pipe chosen for the

production section has outer diameter of 4.5 inches and a weight of 20 lb/ft. Specific characteristics conforming to API standards for these drill pipes are detailed in Table 10.5 (API R. 7.-1., 1998).

**Table 10.4:** Related parameters for the calculation of the drill collar and their results for both sections.

Drill Collar Parameters	Surface	Production
<b>OD<sub>dc</sub>, in</b>	9	6.5
<b>ID<sub>dc</sub>, in</b>	3	2
<b>W<sub>dc</sub>, lb/ft</b>	192.40	102.21
<b>L<sub>dc</sub>, ft</b>	360	690
<b>BF, unitless</b>	0.855	0.832
<b>The number of drill collar</b>	12	23

**Table 10.5:** Drill pipe dimensional data (Özbayoğlu & Altun, 2010).

(1) Size OD in. <i>D</i>	(2) Nominal Weight Threads and Couplings, lb/ft	(3) Plain End Weight <sup>1</sup> lb/ft	(4) Wall Thickness in.	(5) ID in. <i>d</i>	(6) Section Area Body of Pipe <sup>2</sup> sq. in. <i>A</i>	(7) Polar Sectional Modulus <sup>3</sup> cu. in. <i>Z</i>
2 <sup>3</sup> / <sub>8</sub>	4.85	4.43	.190	1.995	1.3042	1.321
	6.65	6.26	.280	1.815	1.8429	1.733
2 <sup>7</sup> / <sub>8</sub>	6.85	6.16	.217	2.441	1.8120	2.241
	10.40	9.72	.362	2.151	2.8579	3.204
3 <sup>1</sup> / <sub>2</sub>	9.50	8.81	.254	2.992	2.5902	3.923
	13.30	12.31	.368	2.764	3.6209	5.144
	15.50	14.63	.449	2.602	4.3037	5.847
4	11.85	10.46	.262	3.476	3.0767	5.400
	14.00	12.93	.330	3.340	3.8048	6.458
	15.70	14.69	.380	3.240	4.3216	7.157
4 <sup>1</sup> / <sub>2</sub>	13.75	12.24	.271	3.958	3.6004	7.184
	16.60	14.98	.337	3.826	4.4074	8.543
	20.00	18.69	.430	3.640	5.4981	10.232
	22.82	21.36	.500	3.500	6.2832	11.345
5	16.25	14.87	.296	4.408	4.3743	9.718
	19.50	17.93	.362	4.276	5.2746	11.415
	25.60	24.03	.500	4.000	7.0686	14.491
5 <sup>1</sup> / <sub>2</sub>	19.20	16.87	.304	4.892	4.9624	12.221
	21.90	19.81	.361	4.778	5.8282	14.062
	24.70	22.54	.415	4.670	6.6296	15.688
6 <sup>5</sup> / <sub>8</sub>	25.20	22.19	.330	5.965	6.5262	19.572
	27.70	24.22	.362	5.901	7.1227	21.156

Regarding the connection of drill collars to drill string there is one thing to consider; bending stress ratio (BSR). In order to determine whether the drill collars can be used by connecting them directly to the drill pipes, it is necessary to look at the bending stress ratio. This ratio must be calculated when connecting pipes of different diameters to each other and ensure that it does not exceed 5.5. For drilling operations, the recommended ratio for transitions from drill collar to heavy weight drill pipe or drill pipe is 2.5 – 3.0. The bending resistance ratio can be calculated as following (Eq. 10-5) and it can be understood better by looking at Figure 10.1 (Özbayoğlu & Altun, 2010).

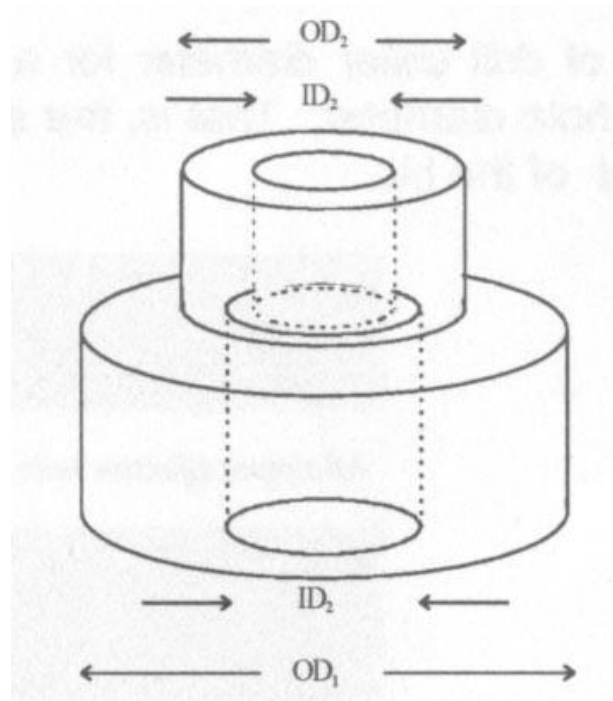


**Figure 10.1:** Geometric representation for BSR calculation (Özbayoğlu & Altun, 2010).

$$BSR = \frac{(OD_1^4 - ID_1^4)OD_2}{(OD_2^4 - ID_2^4)OD_1} \quad (\text{Eq. 10-5})$$

Due to the BSR (Bending Stress Ratio) exceeding 5 for both surface and production considerations in the computation, it was deemed necessary to introduce a transitional element between the drill pipe and drill collar. Consequently, two sections of HWDP (Heavy Weight Drill Pipe) were strategically inserted between them. Subsequent to rigorous calculations, HWDP with specific attributes—30 ft in length, 6.625 in outer diameter, 4 in inner diameter, and a weight of 70 lb/ft—was designated for the surface section. Similarly, for the production section, HWDP measuring 30 ft in length, 5 in outer diameter, an inner diameter of 3 in, and a weight of 50 lb/ft was chosen.

In this context, the BSR values were recalculated for the interfaces between HWDP to DC and HWDP to DP. The selection of HWDP was deemed acceptable, as the ratios fell within the range of 2.5 to 3, indicating the absence of any practical issues. Thus, an acceptable BHA-drill pipe transition was achieved. All BSR calculations between the pipes used are given in Table 10.6.

**Table 10.6:** Bending stress ratio results according to inner and outer diameters of drill string design.

	DC-DP		DC-HWDP		HWDP-DP	
Bending Stress Ratio	Surface	Production	Surface	Production	Surface	Production
<b>OD<sub>1</sub> (in)</b>	9	6.5	9	6.5	6.625	5
<b>ID<sub>1</sub> (in)</b>	3	2	3	2	4	3
<b>OD<sub>2</sub> (in)</b>	6.625	4.5	6.625	5	6.625	4.5
<b>ID<sub>2</sub> (in)</b>	5.965	3.64	4	3	5.965	3.64
<b>BSR</b>	7.22	5.22	2.86	2.50	2.53	2.09

After that, the weight and length of BHA for surface and BHA for production were calculated using the (Eq. 10-6) and (Eq. 10-7) and the results are shown in the Table 10.7.

$$W_{BHA} = (BF)(L_{dc}W_{dc} + L_{hwdp}W_{hwdp}) \quad (\text{Eq. 10-6})$$

$$L_{BHA} = L_{dc} + L_{hwdp} \quad (\text{Eq. 10-7})$$

**Table 10.7:** BHA weight and length results for both sections.

	Surface	Production
<b>W<sub>BHA</sub>, lbf</b>	64604	62426
<b>L<sub>BHA</sub>, ft</b>	450	780

## 10.2. Tension

One of the most significant forces acting on the string during drilling is stress. Stress can be expressed as the total loads acting perpendicular to the drill pipe body cross-sectional area. Due to the load given to the drill, part of the string is under stress and the other part is under compression.

### 10.2.1. Drill string design where only axial stress is taken into account

Huber – Von Mises law states that axial stress and effective stress are considered equal if only axial stress is taken into account. The string's own weight and the axial direction of the drilling fluid perpendicular to different surface areas on the drill string is the stress caused by the total forces. At the same time load given to the drill, string pulling force, string and well factors such as friction forces between axial they have a share in the tension (Özbayoglu & Altun, 2010). This stress is calculated by the following (Eq. 10-8). By applying this equation, the maximum usable length for the drill pipe was calculated then compared to net drill pipe length. The net drill pipe length was determined by subtracting the BHA length from the total length.

At this stage, additional slip crushing calculations need to be made. The drilling string remains suspended on the slips placed in the kelly bushing for a while, both during the

maneuver and during the addition of the drill string. Meanwhile, due to reasons arising from the structure of the slip, there is a deformation at the point where the knee contacts the slip. The stress occurring due to this effect is called "slip crushing" stress and is calculated as following (Eq. 10-9) (Özbayoğlu & Altun, 2010). The K value was accepted as 4 and the  $L_s$  value was accepted as 16 due to these values are generally used average values. The stress that occurs as a result of determining the slip crushing stress is found with the help of the (Eq. 10-10) below. Since the total net string lengths (Net  $L_{dp}$ ) for surface and production were much smaller than the drill string length ( $L_s$ ) calculated in the equation, it was determined that there was no need to put a heavier pipe on the E-75 drill pipes used, and for this reason, E-75 was used for the entire surface and production string. All results are shown in Table 10.8.

$$\sigma_a = \frac{\sum(W_{dc}L_{dc} + W_{dp}L_{dp})\cos(a)(BF) + \sum F_{ext}}{A_w} \quad (\text{Eq. 10-8})$$

$$\frac{\sigma_s}{\sigma_a} = \sqrt{1 + \frac{OD_pK}{2L_s} + \left(\frac{OD_pK}{2L_s}\right)^2} \quad (\text{Eq. 10-9})$$

$$P_s = P_a \left( \frac{\sigma_s}{\sigma_a} \right) \quad (\text{Eq. 10-10})$$

**Table 10.8:** Related parameters for the calculation of drill string design where only axial stress is taken into account and their results for both sections.

	<b>Surface</b>	<b>Production</b>
<b>L<sub>dp</sub>, ft</b>	13907.7	13586.5
<b>Net L<sub>dp</sub>, ft</b>	2550	6820
<b>P<sub>a</sub>, psi</b>	124122	187779.4
<b>Slip crushing</b>	1.59	1.37
<b>P<sub>s</sub>, psi</b>	196799.6	257395.2

### 10.2.2. Drill string design that takes pressure-related stress into account

The Huber – Von Mises law is analyzed as following the (Eq. 10-11), if pressure-related stresses are taken into account along with axial stresses. P<sub>h</sub> value can be determined with the (Eq. 10-12) given below (Özbayoğlu & Altun, 2010). Since the L<sub>dp</sub> calculated is again higher than the Net L<sub>dp</sub>, the tensions caused by slip crushing are equal in first case as well. The permanent damage that may occur when the pressure on the outer part of the knee is greater than the pressure on the inner part of the knee is called "collapse". The place where the collapse situation is most critical is the region of the string at the bottom of the well. Collapse is generally at its most dangerous during the "drill stem test" because the inside of the string is considered completely empty and the pressure on the outside of the string is assumed to be equal to the formation pressure. In this case, the external-internal pressure difference occurs at the highest level. While the pressure differential between the interior and exterior of the drill string is anticipated to be minimal during the drilling process, it is postulated that the drill string could potentially serve the purpose of "drill stem testing." Under the most challenging hypothetical scenario, wherein the pressure within the drill string is considered to be "0," and the pressure outside aligns with the hydrostatic pressure of the mud, the collapse pressure capacity of the E-75 drill pipe at the juncture with heavy weight drill pipes is computed as (Eq. 10-13) (Özbayoğlu & Altun, 2010).

The equivalent axial stress value ( $Y_{pa}$ ) acting on the drill string due to the weight below the relevant point was calculated by calculating the  $F$  values separately and the collapse pressure was calculated.

The disparity between the external pressure exerted on the outer wall of the drill string and the pressure within the drill string induces tension within the assembly. When the external pressure on the drill pipes outer surface surpasses the internal pressure, a force is generated towards the central axis of the drill string. Should this force exceed a critical threshold, collapse ensues in the drill string. The calculation of the collapse pressure for the drill pipe was conducted using the collapse pressure calculation method applicable to the casing design section.

The calculation of the collapse pressure for the drill pipe was conducted using the collapse pressure calculation method applicable to the casing section. Upon completion of the calculations, the surface collapse pressure was determined to exhibit plastic collapse characteristics, while the production collapse was identified as yield strength collapse and the results are shown in the Table 10.9. In addition, the outcomes obtained through the prescribed equations are detailed in Table 10.10 below.

$$\sigma_e = \sigma_a + P_h \quad (\text{Eq. 10-11})$$

$$P_h = 0.052(\rho_m)(L_{dp} - L_{BHA}) \quad (\text{Eq. 10-12})$$

$$Y_{pa} = \left[ \sqrt{1 - 0.75 \left( \frac{\sigma_a}{Y_m} \right)^2} - 0.5 \left( \frac{\sigma_a}{Y_m} \right) \right] (Y_m) \quad (\text{Eq. 10-13})$$

**Table 10.9:** Collapse mode and  $d_n/t$  results for both sections.

Section	Collapse Mode			
	Yield Strength	$\frac{d_n}{t}$	Plastic	$\frac{d_n}{t}$
Surface		14.06		23.97
Production		14.10		24.04

**Table 10.10:** Related parameters for the calculation of drill string design that takes pressure-related stress into account and their results for both sections.

	Surface	Production
$L_{dp}$ , ft	13556	12420
Net $L_{dp}$ , ft	2550	6820
$\rho_m$ , ppg	9.5	11
$P_h$ , psi	1260	3901
$P_a$ , psi	124122	187779
Slip crushing	1.59	1.37
$P_s$ , psi	196799	257395
$\sigma_a$ , psi	9904	11360
$Y_{pa}$ , psi	69556	68672
$F_1$	3.05	3.05
$F_2$	0.06	0.06
$F_3$	1643	1616
$F_4$	1.96	1.96
$F_5$	0.04	0.04
$P_{cr}$ , psi	4664	11870

### **10.3. Buckling**

Since the drill is constantly in contact with the formation during the drilling operation, the lowest point of the drill string acts as a fixed end. Therefore, the drill string is subjected to a significant buckling stress at the moment of rotation. At the same time, it is possible to talk about an increase in the buckling stress under the influence of the drill string due to the contacts of the drill string with the well (Özbayoğlu & Altun, 2010).

#### **10.3.1. Drill string design that takes buckling into account**

Taking into account the stress generated by rotation of the drill string, the Huber–Von Mises law should be used with the following (Eq. 10-14).

$$\sigma_e = \frac{1}{\sqrt{2}} \sqrt{2((\sigma_a + P_h)^2 + 6\tau_b^2)} \quad (\text{Eq. 10-14})$$

In the scenario where the mechanical horsepower required to rotate the drill string is assumed to be 120 HP for surface whereas 55 HP for production, the torque is calculated first with (Eq. 10-15) and the polar moment of inertia ( $J$ ) values calculated with (Eq. 10-17), after the buckling calculation is determined with the following (Eq. 10-16). The calculated buckling value was compared with the table values which are shown in Appendix F of the maximum yield resistance of the selected drill pipes based on buckling, and it was observed that the drill pipes were resistant to this buckling amount. The results of the buckling calculations are shown in Table 10.11.

$$T_q = \frac{5250(\text{HP})}{\text{RPM}} \quad (\text{Eq. 10-15})$$

$$\tau_b = \frac{6T_q(OD_p)}{J} \quad (\text{Eq. 10-16})$$

$$J = \frac{\pi}{32} (OD_p^4 - ID_p^4) \quad (\text{Eq. 10-17})$$

**Table 10.11:** Related parameters for the calculation of drill string design that takes buckling into account and their results for both sections.

	Surface	Production
<b>HP</b>	120	55
<b>RPM</b>	150	75
<b>T<sub>q</sub>, lbf/ft</b>	4200	3850
<b>J, in<sup>4</sup></b>	64.80	23.01
<b>OD<sub>p</sub>, in</b>	6.625	4.5
<b>τ<sub>b</sub>, psi</b>	2577	4517

### 10.3.2. Make-up torque

Part of the resistance of the drilling string comes from the fasteners that connect the drill pipe to each other. When the fastener is not tightened with sufficient torque, premature failure due to bending occurs in the male and female elements. Additionally, if the drill pipe shoulders are not seated properly during the connection, successful fluid insulation cannot be achieved and the fluid will corrode the metal. In addition, applying too much torque may cause the shoulders to open outwards and the connection points to break or tear. The calculation of the weakest cross-sectional areas can be calculated with the equations given in (Eq. 10-18) and (Eq. 10-19) for the beginning and end parts. According to the research, 6 5/8 REG with an outer diameter of 8 in and an inner diameter of 5 in was selected for the surface pipe connection types, while NC50 with an outer diameter of 6.625 and an inner diameter of 3.625 was chosen for production section. Constants for pipe connection types are given in Table 10.12 and Table 10.13. The tightening torque recommended by the API that should be

applied when connecting the pipes can be determined as followin (Eq. 10-20). In the end, all calculations for make-up torque are shown in Table 10.14 (Özbayoğlu & Altun, 2010).

$$A_{\text{pin}} = \frac{\pi}{4} (M - ID_t^2) \quad (\text{Eq. 10-18})$$

$$A_{\text{box}} = \frac{\pi}{4} (OD_t^2 - B) \quad (\text{Eq. 10-19})$$

$$T_q = \frac{SA}{12} [X + 0.02(OD_t + Q)] \quad (\text{Eq. 10-20})$$

**Table 10.12:** Parameters according to connection type (Özbayoğlu & Altun, 2010).

Type of Connection	X	M	B	Q
NC 31 (2 7/8 IF)	0.1753	9.133	11.496	3.4531
NC 38 (3 1/2 IF)	0.2022	13.30	16.124	4.0780
NC 46 (4 IF)	0.2381	19.94	23.460	4.9060
NC 50 (4 1/2 IF)	0.2573	23.82	27.560	5.3125
6 5/8 Regular	0.2885	31.04	36.000	6.0625
7 5/8 Regular	0.3228	42.48	49.000	7.0940
8 5/8 Regular	0.3660	55.80	63.250	8.0470

**Table 10.13:** Tension values occurring in the relevant drill string element cross section according to connection type.

	Make up Torque Calculation	Maximum allowable Torque Calculation
Tool joint of drill pipes	S= 72,000 psi	S = 120,000 psi (2)
Drill collar (OD < 7")	62,500 (1)	110,000 (2)
Drill collar (OD> 7")	62,500 (1)	100,000 (2)

(1) API recommendation (RP7G)

(2) Minimum yield strength of material, specified by API (Spec. 7)

**Table 10.14:** Related parameters for the calculation of make-up torque and their results for both sections.

	Surface	Production
$A_{pin}$ , in <sup>2</sup>	4.74	8.39
$A_{box}$ , in <sup>2</sup>	21.98	12.82
$T_q$ , lbf-ft	16209	24951

## 10.4. Bending

One of the effects that a drill string is subjected to is bending. Bending of the string may occur in relation to the path followed by the well in a directional drilling, or it may occur as a result of the compressive force acting on the string. In addition, it is known that factors such as the structure and geological characteristics of the formations being drilled have an important role on bending.

### 10.4.1. String design, existance of bending with dog-leg scenarios

One of the prevailing causes of drill string rupture is attributed to fatigue wear, a form of abrasion commonly occurring in dog-leg areas. In these regions, the drilling string is subjected to cyclic tension. Analyzing the cross-section of a bent drill string, tension is experienced in one section while compression occurs in the corresponding section. The stressed segment of the drill string undergoes a rapid transition from tensile stress to compressive stress upon rotating half a turn. Similarly, the region previously under compressive stress now encounters tension. In the context of fatigue-induced damage, the occurrence of rupture becomes a critical concern when the dog-leg angle exceeds a specified threshold (Özbayoğlu & Altun, 2010). The anticipated depths for the occurrence of dog-leg formations were established based on shale zone intervals ( $D_{sh}$ ), set at 1750 ft for the surface and 3500 ft for production. Subsequently, the weight of the drill string beneath the dog-leg zone ( $P$ ) was determined using (Eq. 10-21). Following this, the moment of inertia ( $I$ ) was calculated through (Eq. 10-22) to derive the  $K$  value, with the elastic modulus ( $E$ ) held constant at 30000000 psi, as previously

specified. The value for  $\sigma_{b\text{-max}}$  was obtained by substituting the  $\sigma_t$  value, determined using (Eq. 10-23), into (Eq. 10-24).

In the subsequent calculation, the average value for range-2, representing half the length of the drill string ( $L$ ), was set at 180 inches, and the determination of the maximum acceptable dog-leg angle in degrees per 100 feet can be computed using the first (Eq. 10-25) then (Eq. 10-26). A comprehensive summary of all calculations performed is presented in Table 10.15.

$$P = W_{BHA} + (W_{dp})(BF)(Net L_{dp} - D_{sh}) \quad (\text{Eq. 10-21})$$

$$I = \frac{\pi}{64} (OD_p^4 - ID_p^4) \quad (\text{Eq. 10-22})$$

$$\sigma_t = \frac{P}{A_w} \quad (\text{Eq. 10-23})$$

$$\sigma_{b\text{-max}} = 19500 - \frac{10}{67} \sigma_t - \frac{0.6}{670^2} (\sigma_t - 33500)^2 \quad (\text{Eq. 10-24})$$

$$K = \sqrt{\frac{P}{EI}} \quad (\text{Eq. 10-25})$$

$$DLS_{max} = \left( \frac{432000}{\pi} \right) \left( \frac{\sigma_{b\text{-max}}}{E(OD_p)} \right) \left( \frac{\tanh(KL_h)}{KL_h} \right) \quad (\text{Eq. 10-26})$$

Using the determined dog-leg angles, the well curvature was found with (Eq. 10-27). Then the ( $r$ ) value for the connection types on the drill pipe was obtained from (Eq. 10-28). In order to find the drill pipe slope, (Eq. 10-29) must be examined. If the

equality is true,  $c_p$  value can be determined from (Eq. 10-30). (Eq. 10-31) was used to calculate the bending stress, and since the value found was small compared to the max value in the table, it was seen that the work was done at a level below the "endurance" limit, and it was understood that there was no fatigue due to bending.

$$c = \frac{DLS_{\max}}{68755} \quad (\text{Eq. 10-27})$$

$$r = \frac{1}{2}(OD_{ct} - ID_{ct}) \quad (\text{Eq. 10-28})$$

$$c < \frac{\left(\frac{r}{180^2}\right)}{\frac{1}{2} - \frac{\cosh(KL_h) - 1}{(KL_h) \sinh(KL_h)}} \quad (\text{Eq. 10-29})$$

$$c_p = c \frac{KL_h}{\tanh(KL_h)} \quad (\text{Eq. 10-30})$$

$$\sigma_b = \frac{E(OD_p)(c_p)}{2} \quad (\text{Eq. 10-31})$$

## 10.5. Neutral Point

Due to the applied load on the drill, different segments of the string experience either tensile or compressive forces. Within the string, there exists a specific point where no tension is present, known as the neutral point. In academic terms, the neutral point is defined as the point where the axial stress equals the average of the tangential and radial stresses. When the neutral point coincides with the drill pipe, susceptibility to bending increases, leading to excessive fatigue in the drill pipe subjected to compression stress during string rotation. This significantly elevates the risk of the

string breaking away from these drill pipe. Conversely, drill collar requires a substantial force to bend, resulting in comparatively lower fatigue levels. Therefore, the likelihood of the string breaking is considerably reduced. If the neutral point is on drill collar, the location of the neutral point can be found with (Eq. 10-32). If the neutral point is on drill pipe, the location of the neutral point can be found with (Eq. 10-33). The computations based on the equations reveal that the neutral point is situated above the drill pipes. This determination is substantiated by a negative value for the drill pipe and a positive value for the DC. The specific position of the neutral point, expressed in ft, is provided in Table 10.16.

**Table 10.15:** Related parameters for the calculation of drill string design that takes bending into account applying dog-leg scenarios and their results for both sections.

	Surface	Production
<b>P, lbf</b>	83276	123448
<b>I, in<sup>4</sup></b>	32.4	11.5
<b>K, in<sup>-1</sup></b>	0.009	0.019
<b>KL<sub>b</sub>,</b>	1.67	3.40
<b>A, in<sup>2</sup></b>	6.52	5.49
<b>σ<sub>t</sub>, psi</b>	12767	22464
<b>σ<sub>b-max</sub>, psi</b>	17020	15984
<b>DLS<sub>max</sub>, °/100ft</b>	6.58	4.77
<b>E, psi</b>	30x10 <sup>6</sup>	30x10 <sup>6</sup>
<b>c, rad/in</b>	0.0000958	0.0000694
<b>r, in</b>	1.5	1.5
<b>c<sub>p</sub>,</b>	0.0001714	0.000236925
<b>σ<sub>b</sub>,</b>	15332	12936

$$L_{np} = \frac{WOB}{W_{dc}(BF)\cos(a)} \quad (\text{Eq. 10-32})$$

$$L_{np} = \frac{WOB - W_{dc}L_{dc}(BF)\cos(a)}{W_{hwdp}(BF)\cos(a)} \quad (\text{Eq. 10-33})$$

**Table 10.16:** Related parameters for the calculation of neutral point and their results for both sections.

	Surface	Production
<b>L<sub>np</sub>, ft (on DC)</b>	298.5	600.9
<b>L<sub>np</sub>, ft (on DP)</b>	-170.72	-184.64
<b>Net interval, ft</b>	2701	6999

## 10.6. Shock Loading

During a drilling operation, when the drilling string gets stuck for some reason, the string is tried to be freed by pulling it upwards with a certain force. This suspension can be achieved with a force that has a certain upper limit, otherwise the knee may break. The maximum amount of suspension that could be applied to the drill string was calculated first by using (Eq. 10-34), which gives the load on the hook ( $F_H$ ), and then by entering the values determined in (Eq. 10-35) and result are given in Table 10.17.

$$F_H = [(W_{dp}L_{dp}) + (W_{dc}L_{dc})](BF) \quad (\text{Eq. 10-34})$$

$$MOP = 0.9Y_m A_w - F_H \quad (\text{Eq. 10-35})$$

**Table 10.17:** Related parameters for the calculation of shock loading and their results for both sections.

	Surface	Production
<b>F<sub>H</sub></b>	123354	194960
<b>A<sub>w</sub></b>	6.52	5.49
<b>Y<sub>m</sub></b>	75000	75000
<b>MOP</b>	316939	175973

### 10.7. Amount of Elongation of The Suspended Drill String

A drill string suspended freely in a well may extend due to its own weight. The amount of elongation made by a tool suspended freely in the well due to its own weight can be calculated as following the (Eq. 10-36). Given that the raw material for the drill pipe is identified as steel, the weight density of steel, denoted as  $\rho_{\text{steel}}$  in the welded equation, is established as 65.5 ppg (pounds per gallon). Simultaneously, the Poisson's ratio constant ( $\mu$ ) is ascertained as 0.28, accounting for the material properties of steel. Additionally, the elastic modulus constant ( $E$ ), representing the steel's inherent stiffness, is determined as  $30 \times 10^6$  psi.

$$e = \frac{L_{dp}^2}{3.208E} [\rho_{\text{steel}} - 2\rho_m(1 - \mu)] \quad (\text{Eq. 10-36})$$

Based on the outcomes derived from the equation, amount of elongation of the suspended drill string measurement for the surface section was computed as 4.84 inches, whereas the elongation for the production section registered a value of 29.80 inches.

### 10.8. Stabilizer Design

Due to the weight applied to the bit by the drill string A force of the same strength but in the opposite direction acts on the BHA. This force causes a certain part of the BHA on the drill to come under the compression effect. This compression causes the BHA

to bend in certain modes. This bending also causes a change on the surface where the drill contacts the formation and a deviation occurs in the direction of the well. In order to prevent such deviations, a "stabilizer" is added to the section of the BHA under compression stress and the well direction is controlled. Predicting where stabilizers should be placed for this purpose, Euler's critical bending force (Eq. 10-37) and Lubinski's first order bending equation (Eq. 10-38) for a steep well are used. If WOB value greater than  $F_{cr}$ , stabilizer use is required. The location of the second stabilizer to be used after the stabilizer placed right above the bit is found by solving the following equation (Eq. 10-39) for  $L_{st1}$  (Özbayoğlu & Altun, 2010). As a result of the calculations, it was found that the use of 2 stabilizers was appropriate and given in the Table 10.18.

$$P_{tb} = \frac{\pi^2 EI}{L_{st}^2} \quad (\text{Eq. 10-37})$$

$$F_{cr} = 1.94(W_{dc})(BF) \left( \sqrt[3]{\frac{EI}{W_{dc}(BF)}} \right) \quad (\text{Eq. 10-38})$$

$$WOB - \frac{L_{st1}(W_{dc})(BF)}{2} = \frac{\pi^2 EI}{L_{st1}^2} \quad (\text{Eq. 10-39})$$

**Table 10.18:** Related parameters for the calculation of the stabilizer design and their results for both sections.

	Surface	Production
<b>WOB, lbf</b>	49000	51000
<b>E, lbf/ft<sup>2</sup></b>	$432 \times 10^7$	$432 \times 10^7$
<b>I, ft<sup>4</sup></b>	0.0153	0.00418
<b>W<sub>dc</sub>, lbf/ft</b>	192.40	102.21
<b>BF</b>	0.855	0.832
<b>F<sub>cr</sub>, lbf</b>	23565	9847
<b>L<sub>1</sub>, ft</b>	130.7	60.7

According to calculations, the second stabilizer will be placed 130 ft above the first stabilizer for surface section. In other words, there will be four drill collars between the first stabilizer and the second stabilizer. For the production section, this value is calculated as 60 and accordingly, there will be two drill collars between the first stabilizer and the second stabilizer.

### **10.9. Drilling Jar Selection**

In drilling design section, a jar is the first method used to save the stuck drill string in tool jams. In all jar types, the striking force required to free the jammed string is created by the sudden release of the string elements (DC, HWDP and DP) tensioned by the pulling force. Jars are mechanisms that allow drill string elements to be stretched and then released instantly. Since the probability of jamming of drill string elements is highest in equipment with large diameters, placing the jar in the area closest to the stabilizer (at least two DCs above) will ensure that the jar makes the highest contribution to saving the string in case of string jamming caused by the stabilizers (Tekin, 2013). Accordingly, it was decided to place a jar of the same diameter as the drill collar 60 ft above the stabilizer for surface section. This value is 30 ft for production section.

## **11. DRILLING FLUID DESIGN**

In many ways, KCl/Polymer mud is regarded as one of the most powerful fluid systems capable of tackling a wide range of difficulties in tough drilling settings. As the first-generation high-performance water-based mud, they have been effectively employed to drill water-sensitive shale formations from the beginning of 1970s. By using this system, hydration and dispersion of the shale zones are reduced, in addition to that, good wellbore stability, lubrication, torque and drag reduction, and little formation damage can be supplied (Gucuyener, 2023). The KCl component acts as an inhibitor, reducing the swelling of clays within shales. This aids in the prevention of wellbore collapse and increases overall wellbore stability. Polymer additives, such as polyacrylamides or xanthan gum, aid in the encapsulation of shale particles, providing a protective barrier that improves shale dispersion inhibition.

Troublesome shaly zones have been discovered at depths of 1750 and 3500 feet below the surface during the investigation of the Bane-01 well. Given the well's design, which includes a surface casing at 0-3000 feet and a production casing at 3000-7600 feet as can be seen from Table B, it is critical that these problematic intervals be addressed during drilling operations. To address the issues provided by the shaly formations, it was decided to use potassium chloride (KCl) polymer drilling fluids.

In difficult situations, non-aqueous drilling fluids, in particular, oil-based muds (OBM), are frequently preferred. A wealth of evidence supports their exceptional drilling performance, including optimum shale inhibition, chemical wellbore stability, notable rate of penetration (ROP), efficient lubrication, and a lower probability of experiencing stuck pipe problems. However, there is rising concern over the use of oil-based drilling fluids, mostly because of environmental regulations in offshore regions and the significant disposal costs involved (Peng, 2009). In the instance of Bane-01, however, environmental concerns drove the use of a KCl polymer mud instead. This decision demonstrates a dedication to environmentally friendly drilling techniques.

The first stage is to ascertain the rheological characteristics of two different weights of mud (9.5 and 11 ppg) in the absence of specific mud data. The purpose of this exploratory study is to optimize the mud program's formulation and set a baseline. The

criteria for choosing an effective mud program include important elements including hole cleaning effectiveness, mud weight optimization, and shale inhibition. To limit the dangers associated with shaly deposits and prevent wellbore instability, shale inhibition and analysis are essential. Mud weight optimization has an important role for preventing problems such as lost circulation and formation damage by carefully adjusting the density of the drilling fluid to balance wellbore. Furthermore, effective hole cleaning is essential for eliminating drilled cuttings, which improves drilling performance all around.

Table 11.1 shows the rheological properties that were accepted to be used in the surface casing interval, from 0 to 3000 feet (Stawaisz, 2002).

**Table 11.1:** Rheological properties of the 9.5 ppg KCl/Polymer mud.

<b>Mud Weight, ppg</b>	9.5
<b>Temperature, F</b>	120
<b>Plastic Viscosity, cp</b>	23
<b>Yield Point, lb<sub>s</sub>/100 ft<sup>2</sup></b>	30
<b>Gel Strength-10 seconds, lb/100 ft<sup>2</sup></b>	6
<b>Gel Strength-10 minutes, lb/100 ft<sup>2</sup></b>	8
<b>pH</b>	9.1

The rheological characteristics of the KCl/Polymer drilling fluid were evaluated, as per AlBajalan and Haias's investigation, to ascertain its appropriateness for the current drilling conditions as shown in Table 11.2 (2021).

**Table 11.2:** Rheological properties of the 11 ppg KCl/Polymer mud.

<b>Mud Weight, ppg</b>	11
<b>Temperature, F</b>	-
<b>Plastic Viscosity, cp</b>	24
<b>Yield Point, lb<sub>s</sub>/100 ft<sup>2</sup></b>	25
<b>Gel Strength-10 seconds, lb/100 ft<sup>2</sup></b>	6
<b>Gel Strength-10 minutes, lb/100 ft<sup>2</sup></b>	11
<b>pH</b>	9.1

## **11.1.Rheological Models**

Rheological models explain the behaviour of the fluid in a mathematical concept which considers the rheological properties of the fluid such as plastic viscosity and yield point, under stress and strain. To be able to imagine the behaviour of the non-Newtonian fluids in the pipe and in the annulus more accurately, defining a rheology model is important. There are several different models for defining laminar or turbulent flow regimes however, Bingham plastic and Herschel-Bulkley models are focused on in this study.

### **11.1.1. Bingham Plastic model**

The Bingham plastic model is expressed as in the (Eq. 11-1) where  $\tau_y$  is the yield point,  $\mu_p$  is plastic viscosity and,  $\gamma$  is shear rate. Yield point is referred to the value which the fluid starts to flow after an applied shear stress, while plastic viscosity is the slope of the line where the relationship between shear stress and shear rate become proportional (Bourgoyn Jr, Millheim, Chenevert , & Young Jr, 1991). In Figure 11.1, Bingham plastic model is illustrated graphically.

Whether the flow regime is laminar or turbulent in pipe and pipe annulus, by using (Eq. 11-2) and (Eq. 11-3) calculations of velocity is done. For laminar flow, (Eq. 11-4) and (Eq. 11-5) are used while (Eq. 11-6) and (Eq. 11-7) are for turbulent flow. The flow types are determined based on the comparison between the estimated pressure drop values; the greater value is taken into account. In this quick method, considerable amount of time was saved by eliminating the prediction of the Reynold's number. The same processes were also followed for drill collar and drill collar annulus.

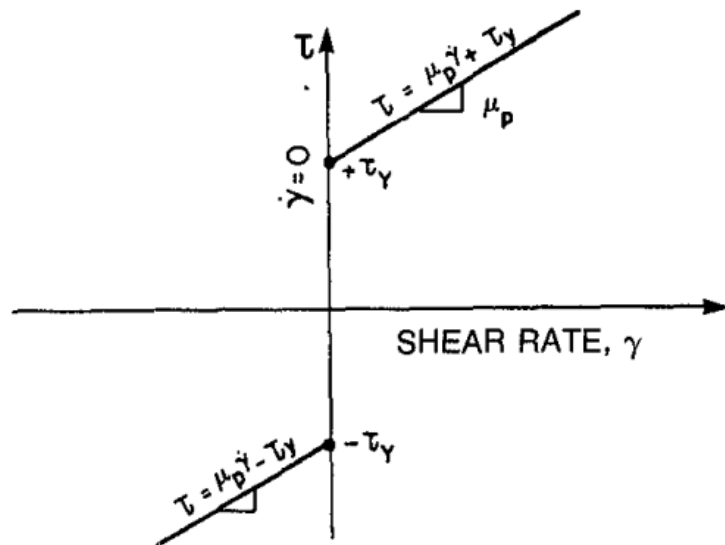


**Figure 11.1:** Shear stress and shear rate relationship of Bingham Plastic model (Bourgoyn Jr, Millheim, Chenevert , & Young Jr, 1991).

$$\tau = \tau_y + \mu_p \gamma \quad (\text{Eq. 11-1})$$

$$v_{\text{pipe}} = \frac{q}{2.448ID^2} \quad (\text{Eq. 11-2})$$

$$v_{\text{annulus}} = \frac{q}{2.448(d_{\text{hole}}^2 - OD^2)} \quad (\text{Eq. 11-3})$$

$$\frac{dp_f}{dL_{\text{pipe}}} = \frac{\mu_p v}{1500ID^2} + \frac{\tau_y}{225ID} \quad (\text{Eq. 11-4})$$

$$\frac{dp_f}{dL_{\text{annulus}}} = \frac{\mu_p v}{1000(d_{\text{hole}}^2 - OD^2)} + \frac{\tau_y}{200(d_{\text{hole}} - OD)} \quad (\text{Eq. 11-5})$$

$$\frac{dp_f}{dL_{\text{pipe}}} = \frac{\rho^{0.75} v^{1.75} \mu_p^{0.25}}{1800 ID^{1.25}} \quad (\text{Eq. 11-6})$$

$$\frac{dp_f}{dL_{\text{annulus}}} = \frac{\rho^{0.75} v^{1.75} \mu_p^{0.25}}{1396(d_{\text{hole}} - OD)^{1.25}} \quad (\text{Eq. 11-7})$$

### 11.1.2. Herschel-Bulkley model

Herschel-Bulkley, or modified power law, rheology model (H-B) can be indicated by using (Eq. 11-8), similar to Bingham plastic. The flow behavior index is symbolized as  $n$ . In order to find the flow regime, two parameters should be calculated in H-B model;  $Re_{\text{eq}}$  and  $Re_{\text{eq,cr}}$ . For laminar flow, the relationship is  $Re_{\text{eq}} < Re_{\text{eq,cr}}$  and when  $Re_{\text{eq}} > Re_{\text{eq,cr}}$  the flow is considered as turbulent (Merlo, 1995). The comparison of rheological models in a graphical example is shown in Figure 11.2.

$$\tau = \tau_y + \mu_p \gamma^{n_{HB}} \quad (\text{Eq. 11-8})$$

For pipe, equations (Eq. 11-9) to (Eq. 11-15) below are used for the purpose of calculating the pressure drop values based on the estimated flow regime. (Eq. 11-16) and (Eq. 11-17) are used for laminar flow while for turbulent flow, (Eq. 11-18) and (Eq. 11-19) are utilized (Merlo, 1995).

$$Re_{\text{eq}} = Cc \times Re \quad (\text{Eq. 11-9})$$

$$Cc = 1 - \frac{1}{2n_{HB} + 1} \left[ \frac{\tau_y}{\tau_y + k_{HB} \left[ \frac{(3n_{HB} + 1)q}{n_{HB}\pi R^3} \right]^{n_{HB}}} \right] \quad (\text{Eq. 11-10})$$

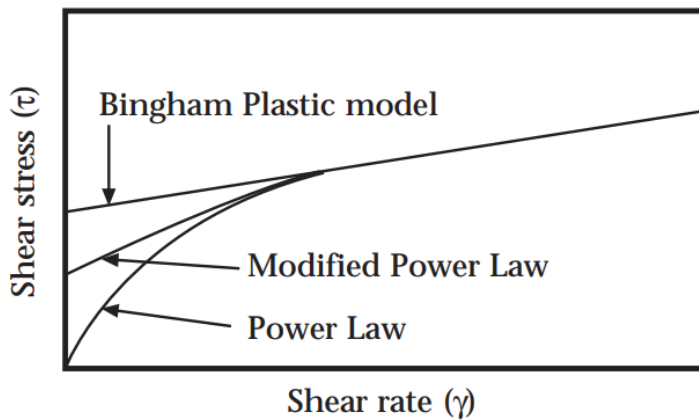


**Figure 11.2:** Shear stress and shear rate relationship of rheological models (Swaco, 1998).

$$Re = \frac{2\rho Q}{\mu \pi R} \quad (\text{Eq. 11-11})$$

$$Re_{eq} = \left(2 \frac{3n_{HB} + 1}{n_{HB}}\right) \left[ \frac{\rho v_p^{(2-n_{HB})} R^{n_{HB}}}{\tau_y \left(\frac{R}{v_p}\right)^{n_{HB}} + k_{HB} \left(\frac{3n_{HB} + 1}{n_{HB} C_c}\right)^{n_{HB}}} \right] \quad (\text{Eq. 11-12})$$

$$Re_{eq,cr} = \left[ \frac{4(3n_{HB} + 1)}{n_{HB} y} \right]^{\left(\frac{1}{1-z_{HB}}\right)} \quad (\text{Eq. 11-13})$$

$$y = \frac{\log(n_{HB}) + 3.93}{50} \quad (\text{Eq. 11-14})$$

$$z_{HB} = \frac{1.75 - \log(n_{HB})}{7} \quad (\text{Eq. 11-15})$$

$$\frac{\Delta p}{\Delta L}, \text{laminar pipe} = f_p \frac{Q^2}{\pi^2 R^5} \quad (\text{Eq. 11-16})$$

$$f = \frac{4}{Re_{eq}} \left( \frac{3n_{HB} + 1}{n_{HB}} \right) \quad (\text{Eq. 11-17})$$

$$\frac{\Delta p}{\Delta L}, \text{turbulent pipe} = f_D \frac{Q^2}{\pi^2 R^5} \quad (\text{Eq. 11-18})$$

$$f = y(Cc \times Re)^{-z_{HB}} \quad (\text{Eq. 11-19})$$

The modified steps that were taken for determining the flow type in the pipe are also used for the pipe annulus. (Eq. 11-25) and (Eq. 11-26) are used for laminar flow while (Eq. 11-27), and (Eq. 11-28) are utilized for turbulent flow. (Eq. 11-14), and (Eq. 11-15) for estimating the  $y$  and  $z$  values are exactly used to obtain  $Re_{eq,cr}$  value (Merlo, 1995).

$$Re_{eq} = Ca \times Re \quad (\text{Eq. 11-20})$$

$$Ca = 1 - \frac{1}{n_{HB} + 1} \left[ \frac{\tau_y}{\tau_y + k_{HB} \left[ \left( \frac{2(2n_{HB} + 1)}{n_{HB}(R_2 - R_1)} \right) \left( \frac{Q}{\pi(R_2^2 - R_1^2)} \right) \right]^{n_{HB}}} \right] \quad (\text{Eq. 11-21})$$

$$Re = \frac{2\rho Q}{\mu \pi (R_1 + R_2)} \quad (\text{Eq. 11-22})$$

$$Re_{eq} = \left( 4 \frac{2n_{HB} + 1}{n_{HB}} \right) \left[ \frac{\rho v_p^{(2-n_{HB})} (R_2 - R_1)^{n_{HB}}}{\tau_y \left( \frac{R_2 - R_1}{v_a} \right)^{n_{HB}} + k_{HB} \left( 2 \frac{2n_{HB} + 1}{n_{HB} Ca} \right)^{n_{HB}}} \right] \quad (\text{Eq. 11-23})$$

$$Re_{eq,cr} = \left[ \frac{8(2n_{HB} + 1)}{n_{HB} y} \right]^{\left( \frac{1}{1-z_{HB}} \right)} \quad (\text{Eq. 11-24})$$

$$\frac{\Delta p}{\Delta L}, \text{laminar annulus} = f_0 \frac{Q^2}{\pi^2 (R_2 - R_1)(R_2^2 - R_1^2)^2} \quad (\text{Eq. 11-25})$$

$$f = \frac{8}{Re_{eq}} \left( \frac{2n_{HB} + 1}{n_{HB}} \right) \quad (\text{Eq. 11-26})$$

$$\frac{\Delta p}{\Delta L}, \text{turbulent annulus} = f_0 \frac{Q^2}{\pi^2 (R_2 - R_1)(R_2^2 - R_1^2)^2} \quad (\text{Eq. 11-27})$$

$$f = y(Ca \times Re)^{-z_{HB}} \quad (\text{Eq. 11-28})$$

The parameters of fluid flow index,  $n$  and, fluid consistency index,  $k$ , are found by using (Eq. 11-29) and (Eq. 11-30) (Rheology and Hydraulics of Oil-well Drilling Fluids, 2006).

$$n_{HB} = 3.32 \log \left( \frac{\theta_{600} - \tau_y}{\theta_{300} - \tau_y} \right) \quad (\text{Eq. 11-29})$$

$$k_{HB} = \frac{\theta_{300} - \tau_y}{511^{n_{HB}}} \quad (\text{Eq. 11-30})$$

### 11.1.3. Selection of the rheology model

The determination of the convenient rheological model for KCl polymer mud samples with mud weight values of 9.5 and 11 ppg was Herschel-Bulkley model due to its better fitting characteristics with the chosen collected measurements. Figure 11.3 highlights the similarity of the plotted curve with the modified power law curve showed in Figure 11.2. This selection also considered the fact that the Herschel-Bulkley model provides a wider range of calculations, yielding accuracy on the results.

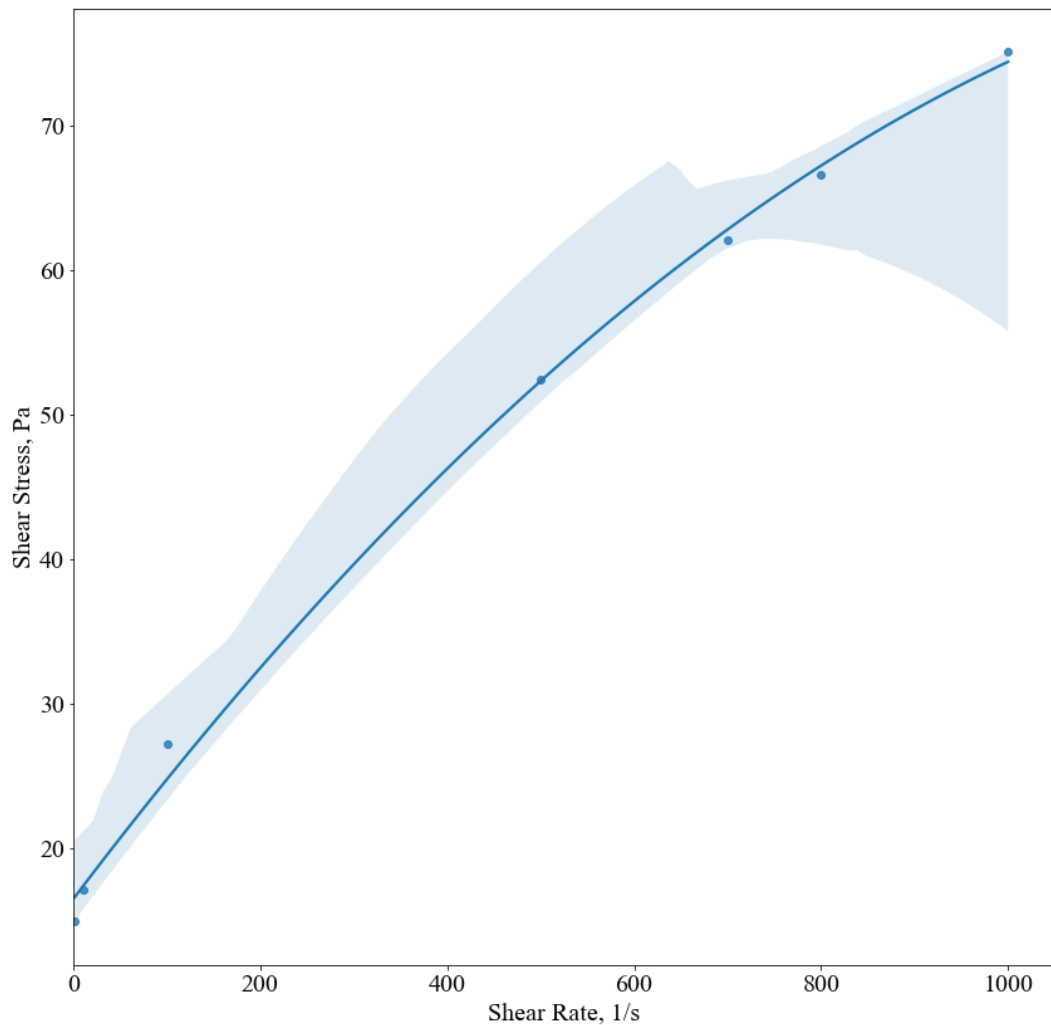


**Figure 11.3:** Shear stress vs shear rate curve of 9.5 ppg KCl polymer mud with the 95% confidence interval.

## 11.2.Cutting Transport

In the previous subsections, the drilling mud and its properties were selected for each hole section. Considering the benefits of using the drilling mud, the cutting transport efficiency of the drilling mud is the most important one. To execute a safe and efficient drilling operation, the cutting transport efficiency of the drilling mud should be estimated to determine the minimum flow rate at which cuttings can be transported.

Cutting transport is affected by various parameters, such as drilling fluid parameters, cutting parameters, wellbore configuration, and operational parameters (Jiimaa, 2014). That's why all of these parameters should be maintained in an optimum condition. In the literature, to estimate the optimum condition in which the drilling mud can transport cuttings, various models have been published so far. In general, the main objective is encircled around the annular velocity for efficient cutting transport as the annular velocity is the most determinative one due to its low velocity (Jiimaa, 2014).

The velocity at which the cutting particle can settle within the flowing fluid is defined as the particle slip velocity; moreover, this property is affected by its geometry, and drilling fluid's rheological properties (Jiimaa, 2014). In general, the model proposed by researchers in the literature tries to simulate the flow behavior of the cutting particle. However, this requires strictly controversial parameters such as the diameter, and the density of the cutting particle. To overcome this issue, Hopkins has observed that the rheological properties of the mud have an advantageous effect on the cutting transport; moreover, he has observed that the yield point of the drilling mud is the most influential property (Darley & Gray, 1983). The experimental results that he has obtained was demonstrated in Figure 11.4. On the other hand, Hopkins' theory has been cross-proved by other scientists; as such, it was observed that the thick muds have better cutting transport efficiency compared to other drilling muds (see Figure 11.5) (Darley & Gray, 1983).

Considering these facts, and circumstances, for each section, the thick drilling mud has been chosen. Following to this selection, the minimum flow rate at which cutting can be transported will be examined. Hopkins has proposed a series of steps to estimate the minimum flow rate. The first step is to determining the particle slip velocity for a given drilling mud from Figure 11.4. Then, he has established a correction term for the particle slip velocity considering the drilling mud's weight as shown in (Eq. 11-31) (Jiimaa, 2014). Once the slip velocity is corrected for the existed mud weight, one can estimate the minimum cutting transport velocity from (Eq. 11-33) (Jiimaa, 2014).

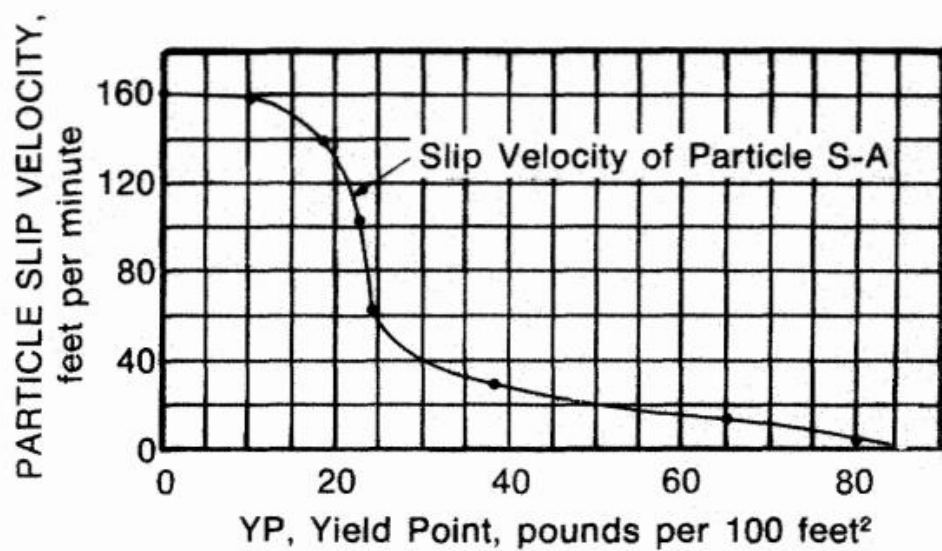


**Figure 11.4:** The particle slip velocity with respect to the yield point (Darley & Gray, 1983).

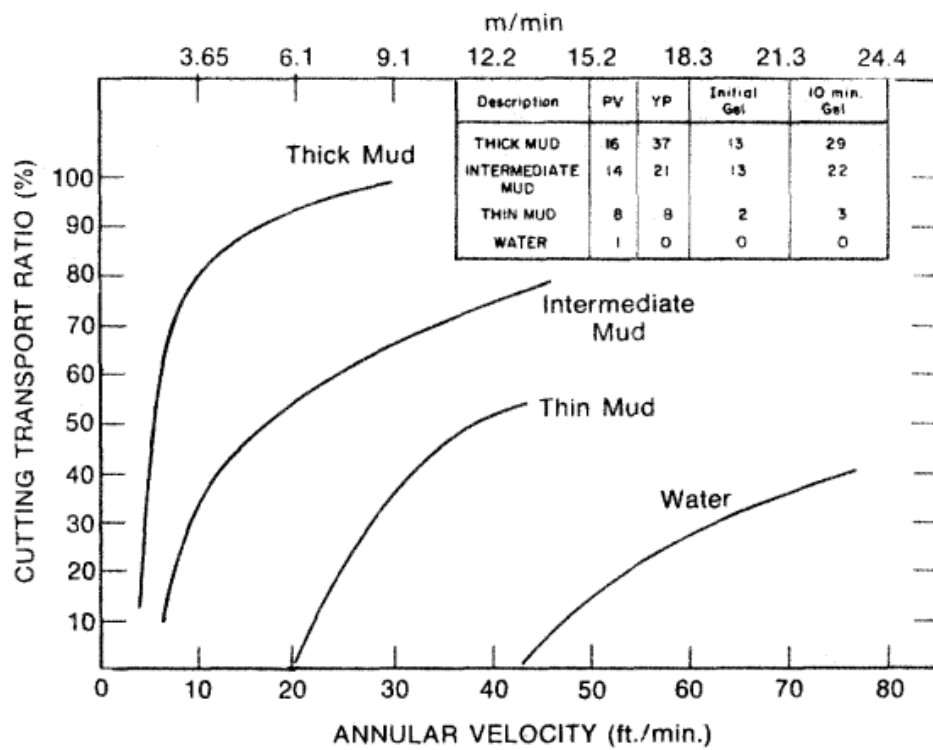


**Figure 11.5:** The cutting transport efficiencies of different mud types (Darley & Gray, 1983).

$$SVC = 2.117 - 0.1648\rho_m + 0.003681\rho_m^2 \quad (\text{Eq. 11-31})$$

$$v_{sc} = (SVC)v_{slip} \quad (\text{Eq. 11-32})$$

$$v_{min} = v_{sc} \cos \theta + v_2 \sin \theta \quad (\text{Eq. 11-33})$$

Since the theta term in (Eq. 11-33) represents the degree of inclination and the prospective well was designed to be a vertical well, the minimum cutting transport velocity will be simplified into (Eq. 11-34). Lastly, the critical flow rate at which cutting can be transported can be estimated from (Eq. 11-35) (Jiimaa, 2014).

$$v_{min} = v_{sc} \cos \theta \quad (\text{Eq. 11-34})$$

$$Q_{crit} = 0.04079(d_{hole}^2 - OD^2)v_{min} \quad (\text{Eq. 11-35})$$

The transport velocity is defined as the difference between the annulus velocity and the slip velocity (Eq. 11-36). Moreover, a simple ratio which quantifies the efficiency of the cutting transport is defined as the transport ratio; hence, the relation was given in (Eq. 11-37) (Jiimaa, 2014).

$$v_T = v_a - v_{sc} \quad (\text{Eq. 11-36})$$

$$F_T = \frac{v_T}{v_a} \quad (\text{Eq. 11-37})$$

By using the above methodology, the results were obtained for each section. Thus, these results were demonstrated in Table 11.3, Table 11.4, and Table 11.5 for the conductor, surface, and production stages respectively. On the other hand, to model the cutting transport ratio, different flow rates were selected up to 500 gal/min to estimate the cutting transport ratio at the specific flow rate.

**Table 11.3:** Cutting transport model results for the conductor stage.

<b><math>\rho_m</math></b>	9.5	ppg
<b><math>\tau_y</math></b>	30	lbf/100sq ft
<b><math>d_{hole}</math></b>	17.5	in
<b>OD</b>	6.625	in
<b><math>v_{slip}</math></b>	40	ft/min
<b>SVC</b>	0.88	
<b><math>v_{sc}</math></b>	35	ft/min
<b><math>v_{min}</math></b>	35	ft/min
<b><math>Q_{crit}</math></b>	375	gal/min

The flow rate was increased up to 500 gal/min as it is the maximum flow rate that the MKP-750 pump can supply. As a result of this basic modelling, Appendix G tables were maintained for the conductor, surface, and production stages respectively.

Aside from tabulating the modelling results, the annular velocities versus the corresponding cutting transport ratios were demonstrated in Figure 11.6, Figure 11.7, and Figure 11.8 for the conductor, surface, and production stages respectively. By examining those figures, one can observe that the obtained behavior is very similar to the those in the literature. Moreover, the flow rate seems to be losing its effect on the cutting transport ratio after a specific point for each stage.

In conclusion, the overall modelling for the cutting transport was found to be reasonable. The critical flow rates were found as 375 gal/min, 152 gal/min, and 59 gal/min for the conductor, surface, and production stages respectively. Those values indicate that flow rates below these will not be transporting cuttings from the bottom to the surface. Lastly, negative cutting transport ratios dictate that there is no cutting transport; on the contrary, positive values indicate that the cutting transport performs.

**Table 11.4:** Cutting transport model results for the surface stage.

$\rho_m$	9.5	ppg
$\tau_y$	30	lbf/100sq ft
$d_{hole}$	12.25	in
<b>OD</b>	6.625	in
$v_{slip}$	40	ft/min
<b>SVC</b>	0.88	
$v_{sc}$	35	ft/min
$v_{min}$	35	ft/min
$Q_{crit}$	152	gal/min

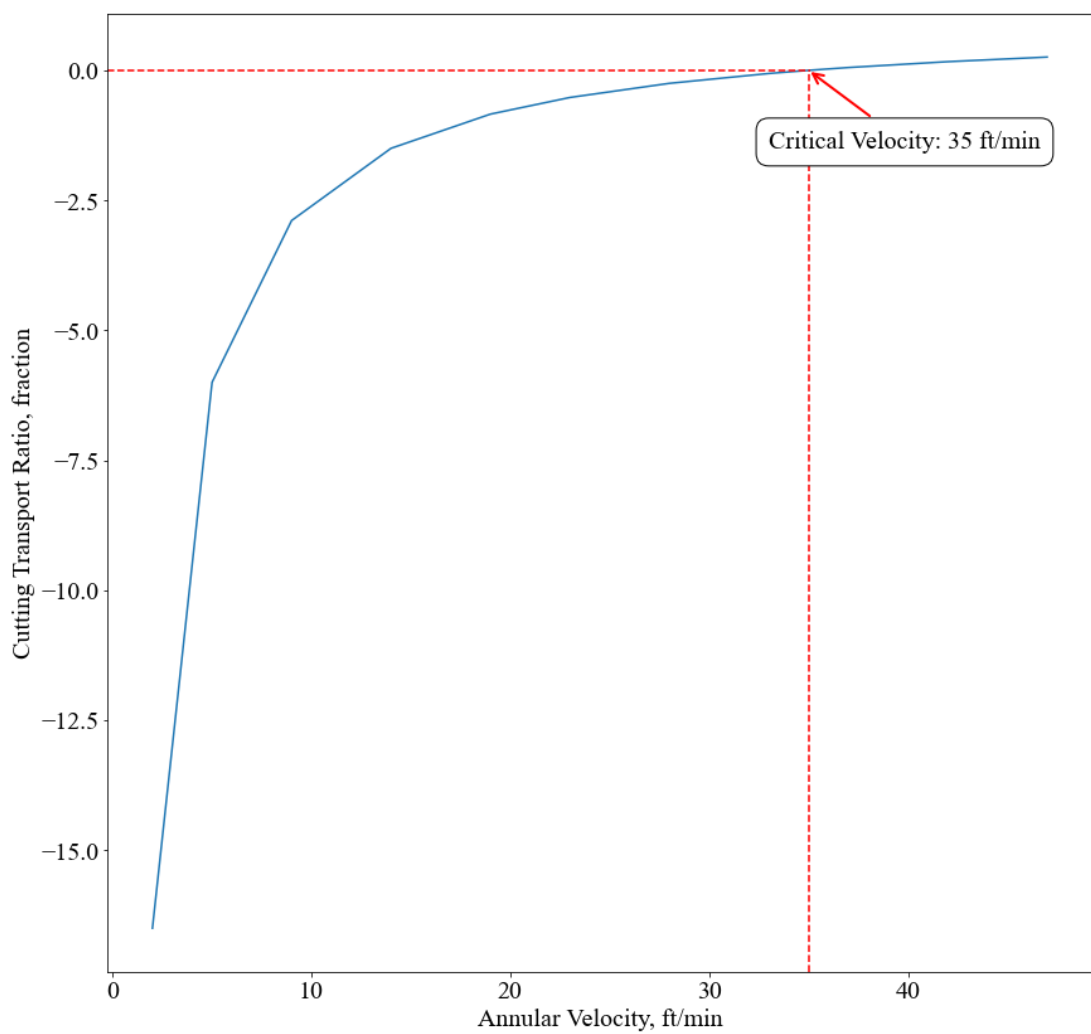


**Figure 11.6:** The cutting transport ratio modelling for the conductor stage.

**Table 11.5:** Cutting transport model results for the production stage.

$\rho_m$	11	ppg
$\tau_y$	25	lbf/100sq ft
$d_{hole}$	8.5	in
$OD$	4.5	in
$v_{slip}$	60	ft/min
$SVC$	0.75	
$v_{sc}$	45	ft/min
$v_{min}$	45	ft/min
$Q_{crit}$	95	gal/min

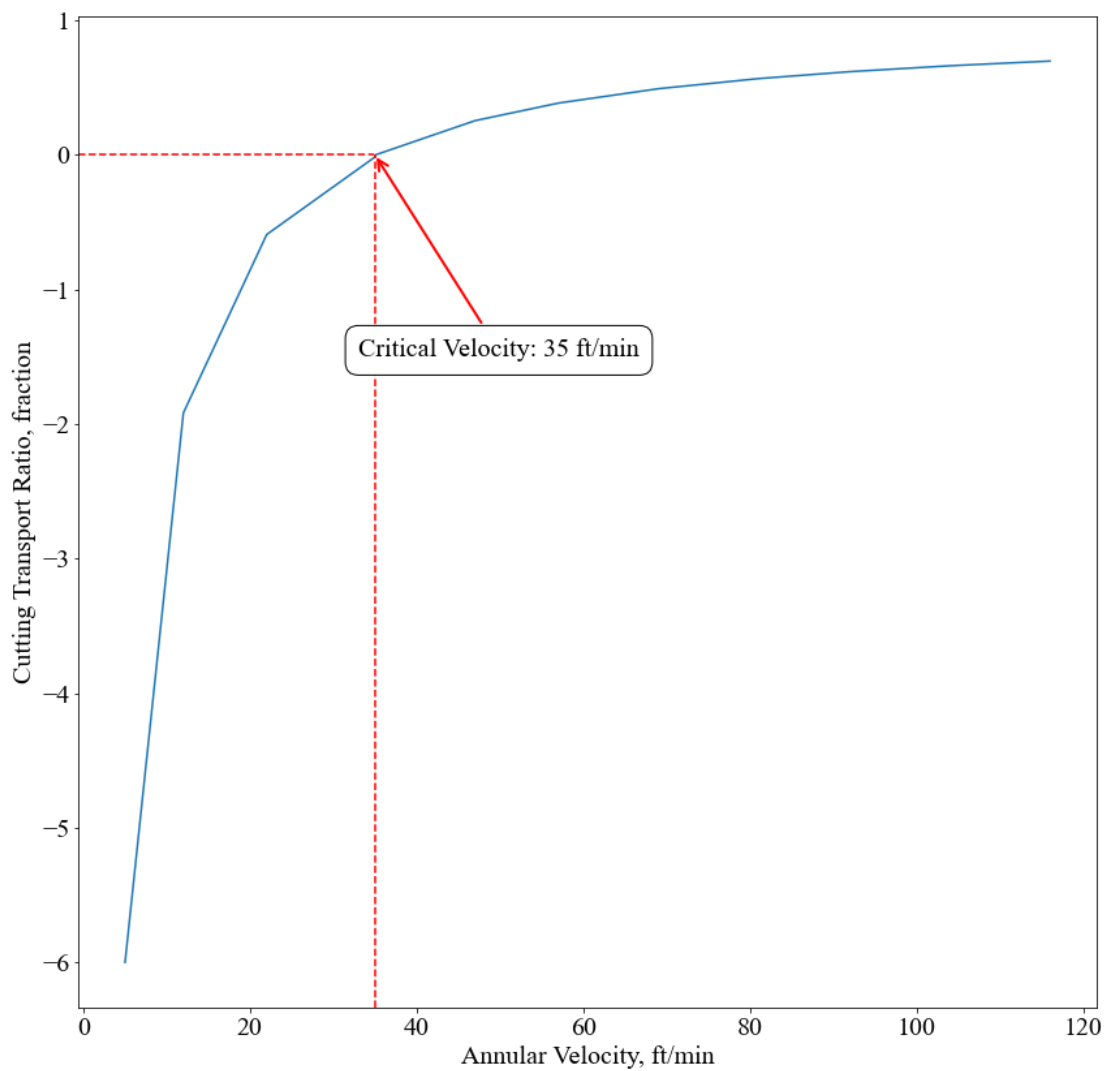


**Figure 11.7:** The cutting transport ratio modelling for the surface stage.

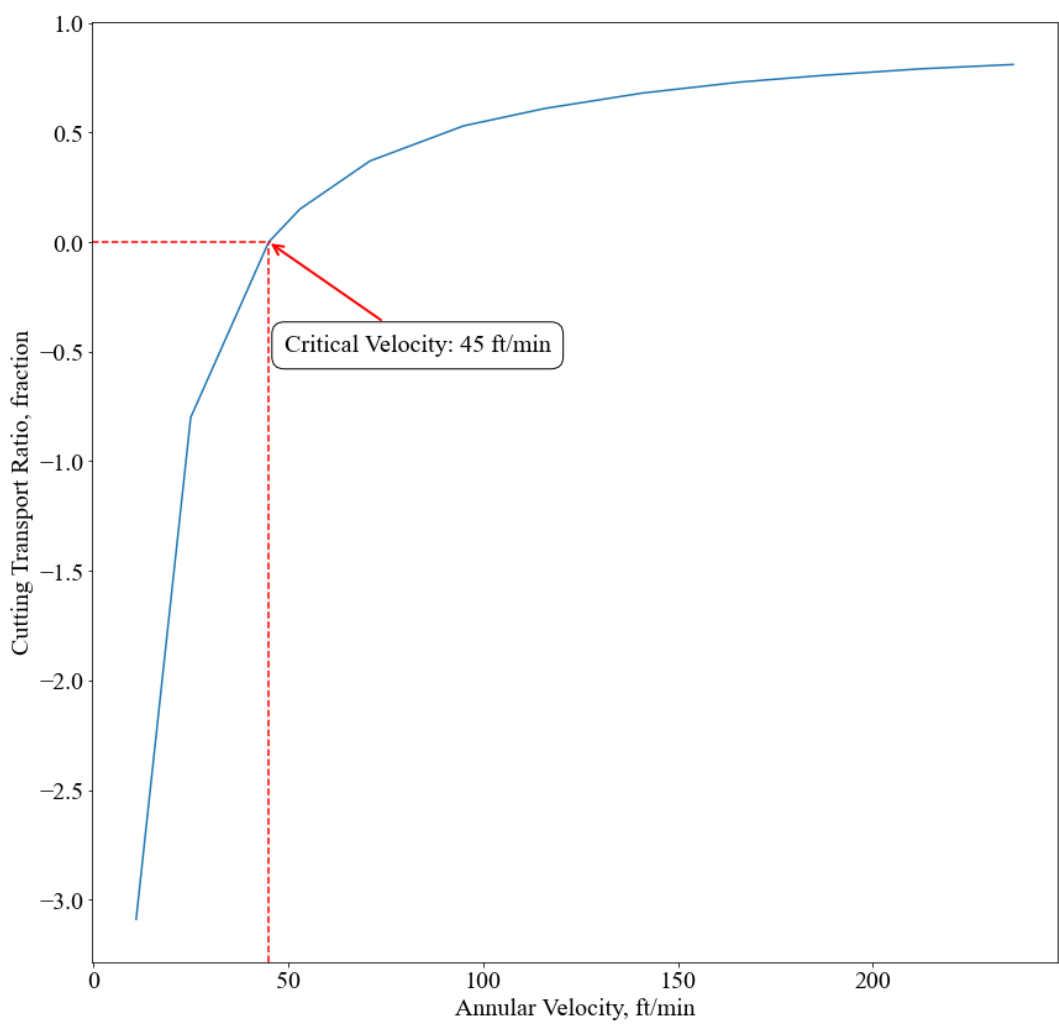


**Figure 11.8:** The cutting transport ratio modelling for the production stage.

## 12. DRILLING HYDRAULICS OPTIMIZATION

Drilling hydraulics optimization aims to understand the fluid flow behavior and the corresponding pressure drop within the system. This system encircles the surface facilities, drill string, annuluses, and bit nozzles. Up to now, various models have been proposed by researches to estimate the entire pressure drop in a drilling operation. In this study, a graphical optimization approach will be used (Bourgoyn Jr, Millheim, Chenevert , & Young Jr, 1991). The indicated graphical solution requires a slope coefficient called m; and, this coefficient can be found by fitting a linear slope on the observed data. However, since there is no prior data about the flow rate versus its corresponding pressure, an empirical value of 1.75 will be taken as the slope (Bourgoyn Jr, Millheim, Chenevert , & Young Jr, 1991).

Furthermore, in order to solve the optimization problem, this method requires three distinct intervals to set boundaries. The first interval specifies the maximum flow rate during the operation. Since the selected mud pump's maximum executable flow rate is 500 gal/min, the first interval was set as 500 gal/min. On the other hand, the second interval dictates the parasitic pressure loss -the sum of the pressure losses except the bit- at the highest allowable surface pressure. Hence, as the maximum allowable pressure for the selected mud pump model is 2315 psi, the parasitic pressure loss at the maximum pressure can be estimated using (Eq. 12-1). By using (Eq. 12-1) via plugging the necessary inputs, the parasitic pressure loss at the maximum operating pressure was found to be 842 psi.

$$\Delta P_d = \left( \frac{1}{m + 1} \right) P_{max} \quad (\text{Eq. 12-1})$$

For the specification of the third interval, the literature uses the minimum flow rate at which cuttings can be transported. A rule of thumb minimum annular velocity can be used to achieve this. However, since the critical flow rates were found for each stage, those estimated critical flow rates will be used during the optimization. Hence, those values are 152 gal/min, and 95 gal/min for the surface, and production stages

respectively. Lastly, these specified intervals for each stage were summarized in Table 12.1.

**Table 12.1:** The set intervals summary for each stage.

Stage	Interval 1, gal/min	Interval 2, psi	Interval 3, gal/min
Surface	500	842	152
Production	500	842	95

To execute the drilling hydraulic optimization, the solution was separated into two stages surface, and production. Hence, the drilling hydraulics optimization was investigated for each 1000 ft increments for other stages. Moreover, within each 1000 ft increment, parasitic pressure losses, equivalent circulating densities, optimum flow rates, optimum pressure losses on the bit, and nozzle areas were estimated. To estimate parasitic pressure losses for each section, the Bingham Plastic, and the Herschel-Buckley models were utilized. Their corresponding equations were already mentioned in the Drilling Fluids Design section. That's why, equations will not be specified within this section.

On the other hand, to estimate the equivalent circulating density for each section drilled, (Eq. 12-2) was utilized. In this equation, the pressure loss in the annulus section was taken as the pressure loss in the drill collar open-hole annulus. In addition to this, (Eq. 12-3) was derived to estimate the corresponding optimum flow rates more accurately. This equation is easy to use yet gives more accurate results rather than reading the corresponding flow rates. The coefficient  $a$  in (Eq. 12-3) can be estimated by plugging the corresponding parasitic pressure loss for the section drilled, and the maximum flow rate, which is 500 gal/min.

$$ECD = \rho_m + \frac{\Delta P_a}{0.052TVD} \quad (\text{Eq. 12-2})$$

$$\log \Delta P_d = \log 1.75q + a \quad (\text{Eq. 12-3})$$

Further, the optimum pressure loss on the bit for the section drilled can be estimated using (Eq. 12-4), if the constructed linear line for the section drilled crosses with the  $HP_{max}$  line within the minimum and maximum flow rate lines. If this is not the case, the minimum flow rate was chosen as the optimum flow rate with its corresponding pressure loss on the bit when the linear line for the section drilled crosses the  $HP_{max}$  line outside of the designated boundary conditions. Finally, once the optimum conditions are set for the section drilled, one can estimate the total optimum bit nozzle area using (Eq. 12-5). Note that, there is an empirical term called discharge coefficient,  $C_d$ , in the equation. For the practical purposes, the discharge coefficient was taken as 0.95.

$$\Delta P_b = P_{max} - \Delta P_d \quad (\text{Eq. 12-4})$$

$$(A_t)_{opt} = \sqrt{\frac{8.311 \times 10^{-5} ECD q_{opt}}{C_d^2 (\Delta P_b)_{opt}}} \quad (\text{Eq. 12-5})$$

Since the parasitic pressure loss includes the pressure losses that occur within the surface equipment, it is necessary to estimate the pressure losses that can occur within the surface equipment during the drilling operation. However, since there is no experiment available to estimate the pressure loss that occurs within the surface facility, an assumption has to be applied. For this study, the pressure drop across the surface facility was assumed to be equal to the potential pressure drop within a 470 ft long drill pipe (Bourgoyne Jr, Millheim, Chenevert, & Young Jr, 1991).

Furthermore, the optimization aims to maximize the pressure loss that might occur around the drilling bit for the surface stage. In contrast, the maximum jet impact force

was aimed at the optimization of the production stage. These two methods were chosen since the frictional pressure losses during drilling the surface stage will be small compared to the production stage.

Before getting started to the drilling hydraulics optimization, it is found to be important to display the results obtained from both the Bingham Plastic, and Herschel-Bulkley models. Table 12.2 demonstrates the frictional pressure losses per foot obtained from the Bingham Plastic model whereas Table 12.3 showcases the frictional pressure losses sustained from the Herschel-Buckley model. Based on the tables given, one can conclude that the frictional pressure loss gradient inside the drill pipe estimated from the Herschel-Buckley model is greater than the Bingham-Plastic model for both stages. Thus, for the surface stage, the estimated frictional pressure loss gradient inside the drill collar is also greater in the Herschel-Bulkley model. Considering the other frictional pressure loss gradients, the Bingham Plastic was resulted in higher values.

Lastly, when the optimum operating conditions were found for each interval, the hole cleaning indicator (HCI) for those specific conditions was calculated. HCI is a fractional term that takes into account of drilling fluid properties, and the annular velocity expected during drilling (Al-Rubaii, Al-Shehri, Mahmoud, Al-Harbi, & Al-Qahtani, 2021). Hence, it was stated by the several authors that if the HCI is greater than, the hole cleaning is said to be good. In contrast, if the HCI is smaller than 1, it indicates bad hole cleaning (Al-Rubaii, Al-Shehri, Mahmoud, Al-Harbi, & Al-Qahtani, 2021). In summary, to compute the HCI, (Eq. 12-6) was utilized (Al-Rubaii, Al-Shehri, Mahmoud, Al-Harbi, & Al-Qahtani, 2021).

$$HCI = \frac{510 \left( (\mu_p + \tau_y) - (2R_3 - R_6) \right) - \left[ 3.322 \log \frac{(2\mu_p + \tau_y) - (2R_3 - R_6)}{(\mu_p + \tau_y) - (2R_3 - R_6)} \right]}{5867} \quad (Eq. 12-6)$$

**Table 12.2:** Frictional pressure losses per foot based on the Bingham Plastic model.

	$dp_{dp}/dl$ , psi/ft	$dp_{dc}/dl$ , psi/ft	$dp_{dpa}/dl$ , psi/ft	$dp_{dca}/dl$ , psi/ft	$dp_{dp-ca}/dl$ , psi/ft
<b>Surface</b>	0.025	0.327	0.028	0.052	0.026
<b>Production</b>	0.095	1.632	0.035	0.091	0.031

**Table 12.3:** Frictional pressure losses per foot based on the Herschel-Bulkley model.

	$dp_{dp}/dl$ , psi/ft	$dp_{dc}/dl$ , psi/ft	$dp_{dpa}/dl$ , psi/ft	$dp_{dca}/dl$ , psi/ft	$dp_{dp-ca}/dl$ , psi/ft
<b>Surface</b>	0.034	0.355	0.016	0.029	0.014
<b>Production</b>	0.118	1.612	0.020	0.060	0.018

## 12.1.Surface Stage

To apply the optimization on the surface stage, the mud pump was operated at 450 gal/min. By leveraging the flow rate, the parasitic pressure losses for each interval were estimated and tabulated in Table 12.4 and Table 12.5. The results obtained from the Bingham Plastic model were demonstrated in Table 12.4; whereas the results from the Herschel-Bulkley in Table 12.5. Likewise, the tabulated pressure losses and the optimum operating conditions were tabulated; thus, Table 12.6 summarizes the optimum conditions maintained from the Bingham Plastic model. The same summary was done on the Herschel-Bulkley model in Table 12.7. These tables were constructed by analyzing Figure 12.1, and Figure 12.2.

As it was stated before this subsection, the optimum conditions were based on the maximum bit pressure loss. This approach was applied because the pressure losses in the surface stage are quite low. Thus, the maximum jet impact force cannot be achieved as can be seen in Figure 12.1, and Figure 12.2.

To summarize the results, both models were found to be very close to each other by comparing the tabulated results. However, since the Herschel-Bulkley model can capture the thixotropic behavior of the drilling fluid, the optimized conditions maintained from the Herschel-Bulkley model were selected. In addition, based on both model's results, one can observe that the HCI values for each section are greater than

1; which dictates good cleaning operation for each section. This also validates the optimization results.

**Table 12.4:** Pressure losses of the surface stage for each interval based on the Bingham Plastic model.

Section	Depth, ft	$\rho_m$ , ppg	$\Delta P_{dp}$ , psi	$\Delta P_{dc}$ , psi	$\Delta P_{dpa}$ , psi	$\Delta P_{dca}$ , psi	$\Delta P_{dp-ca}$ , psi	$\Delta P_s$ , psi	$\Delta P_d$ , psi
1	1000	9.5	16	118	14	19	4	12	183
2	2000	9.5	40	118	42	19	4	12	235
3	3000	9.5	65	118	70	19	4	12	288

**Table 12.5:** Pressure losses of the surface stage for each interval based on the Herschel-Bulkley model.

Section	Depth, ft	$\rho_m$ , ppg	$\Delta P_{dp}$ , psi	$\Delta P_{dc}$ , psi	$\Delta P_{dpa}$ , psi	$\Delta P_{dca}$ , psi	$\Delta P_{dp-ca}$ , psi	$\Delta P_s$ , psi	$\Delta P_d$ , psi
1	1000	9.5	22	128	8	11	2	16	187
2	2000	9.5	56	128	23	11	2	16	236
3	3000	9.5	89	128	39	11	2	16	285

**Table 12.6:** Optimum operating conditions of the surface stage for each interval based on the Bingham Plastic model.

Section	$\Delta P_d$ , psi	ECD, ppg	$q_{opt}$ , gal/min	$(\Delta P_b)_{opt}$ , psi	$(A_t)_{opt}$ , in <sup>2</sup>	HCI
1	203	10.21	500	2112	0.334	4.15
2	261	10.13	500	2054	0.337	4.15
3	320	10.10	500	1995	0.341	4.15

**Table 12.7:** Optimum operating conditions of the surface stage for each interval based on the Herschel-Bulkley model.

Section	$\Delta P_d$ , psi	ECD, ppg	$q_{opt}$ , gal/min	$(\Delta P_b)_{opt}$ , psi	$(A_t)_{opt}$ , in <sup>2</sup>	HCI
1	208	9.90	500	2107	0.329	4.15
2	262	9.85	500	2053	0.332	4.15
3	317	9.83	500	1998	0.337	4.15

## 12.2.Production Stage

To apply the optimization on the production stage, the mud pump was operated at 350 gal/min. By leveraging the flow rate, the parasitic pressure losses for each interval were estimated and tabulated in Table 12.8 and Table 12.9. The results obtained from the Bingham Plastic model were demonstrated in Table 12.8; whereas the results from the Herschel-Bulkley in Table 12.9.

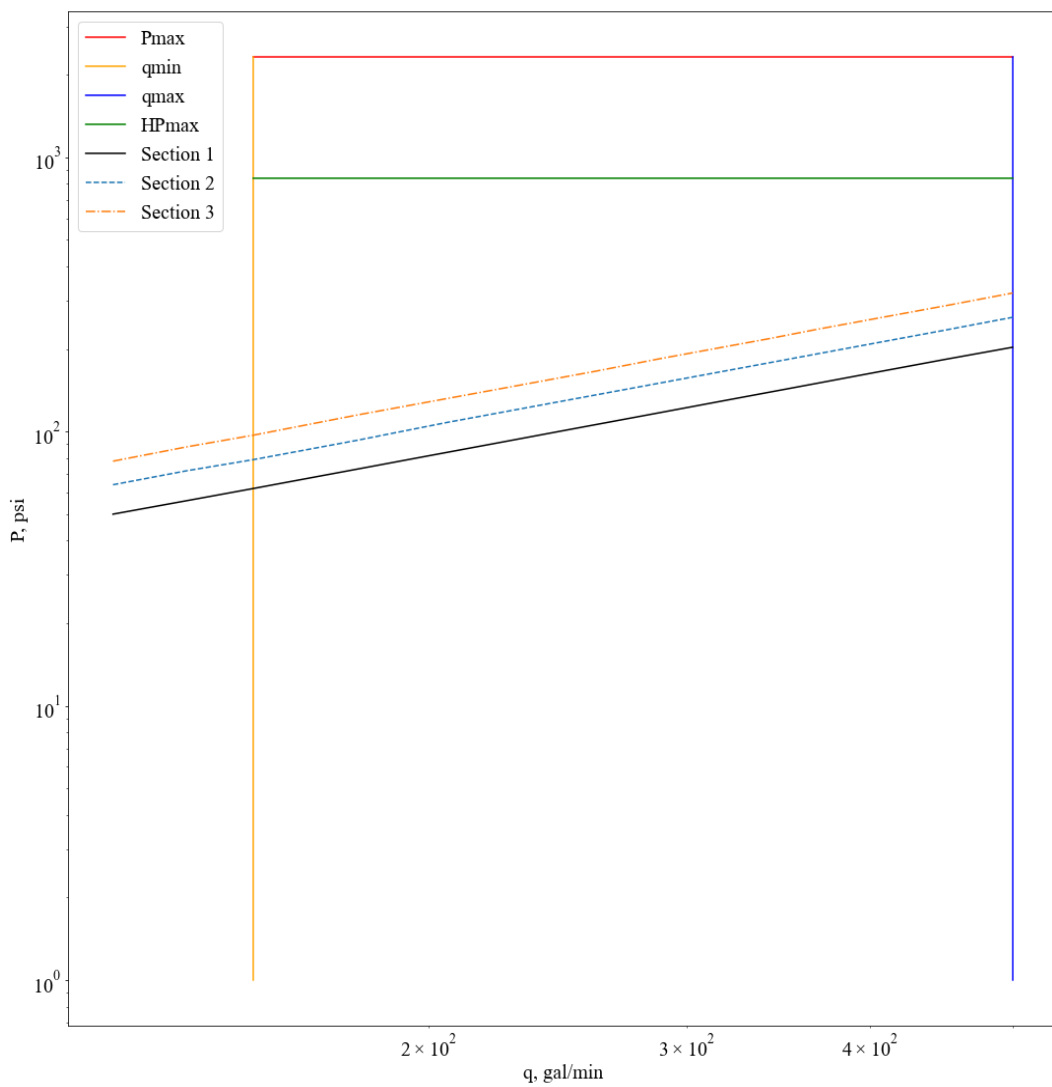


**Figure 12.1:** P-q test result obtained from the Bingham Plastic model for the surface stage.

Likewise, the tabulated pressure losses and the optimum operating conditions were tabulated; thus, Table 12.10 summarizes the optimum conditions maintained from the Bingham Plastic model. The same summary was done on the Herschel-Bulkley model in Table 12.11. These tables were constructed analyzing Figure 12.3, and Figure 12.4.

**Table 12.8:** Pressure losses of the production stage for each interval based on the Bingham Plastic model.

Section	Depth, ft	$\rho_m$ , ppg	$\Delta P_{dp}$ , psi	$\Delta P_{dc}$ , psi	$\Delta P_{dpa}$ , psi	$\Delta P_{dca}$ , psi	$\Delta P_{dp-ca}$ , psi	$\Delta P_s$ , psi	$\Delta P_d$ , psi
1	4000	11	488	1748	11	68	94	69	2478
2	5000	11	635	1748	48	68	94	69	2662
3	6000	11	782	1748	84	68	94	69	2845
4	7000	11	930	1748	121	68	94	69	3030
5	7600	11	1018	1748	143	68	94	69	3410

**Table 12.9:** Pressure losses for the production stage for each interval based on the Herschel-Bulkley model.

Section	Depth, ft	$\rho_m$ , ppg	$\Delta P_{dp}$ , psi	$\Delta P_{dc}$ , psi	$\Delta P_{dpa}$ , psi	$\Delta P_{dca}$ , psi	$\Delta P_{dp-ca}$ , psi	$\Delta P_s$ , psi	$\Delta P_d$ , psi
1	4000	11	582	1676	6	62	54	83	2463
2	5000	11	758	1676	27	62	54	83	2660
3	6000	11	934	1676	47	62	54	83	2856
4	7000	11	1110	1676	68	62	54	83	3053
5	7600	11	1215	1676	80	62	54	83	3170

As it was stated before this subsection, the optimum conditions were based on maximizing the jet impact force on the bit. This approach was applied since if the system were operated at the maximum flow rate, the pressure losses would exceed the maximum allowable surface pressure; which would lead to the fizzling of the hole structure. Thus, as can be seen in Figure 12.3, and Figure 12.4, the pressure losses exceed the maximum allowable surface pressure. However, each section intersects with the maximum horsepower line within the designated intervals. Tabulated summaries were based on the intersection point of the section lines with the maximum horsepower line.

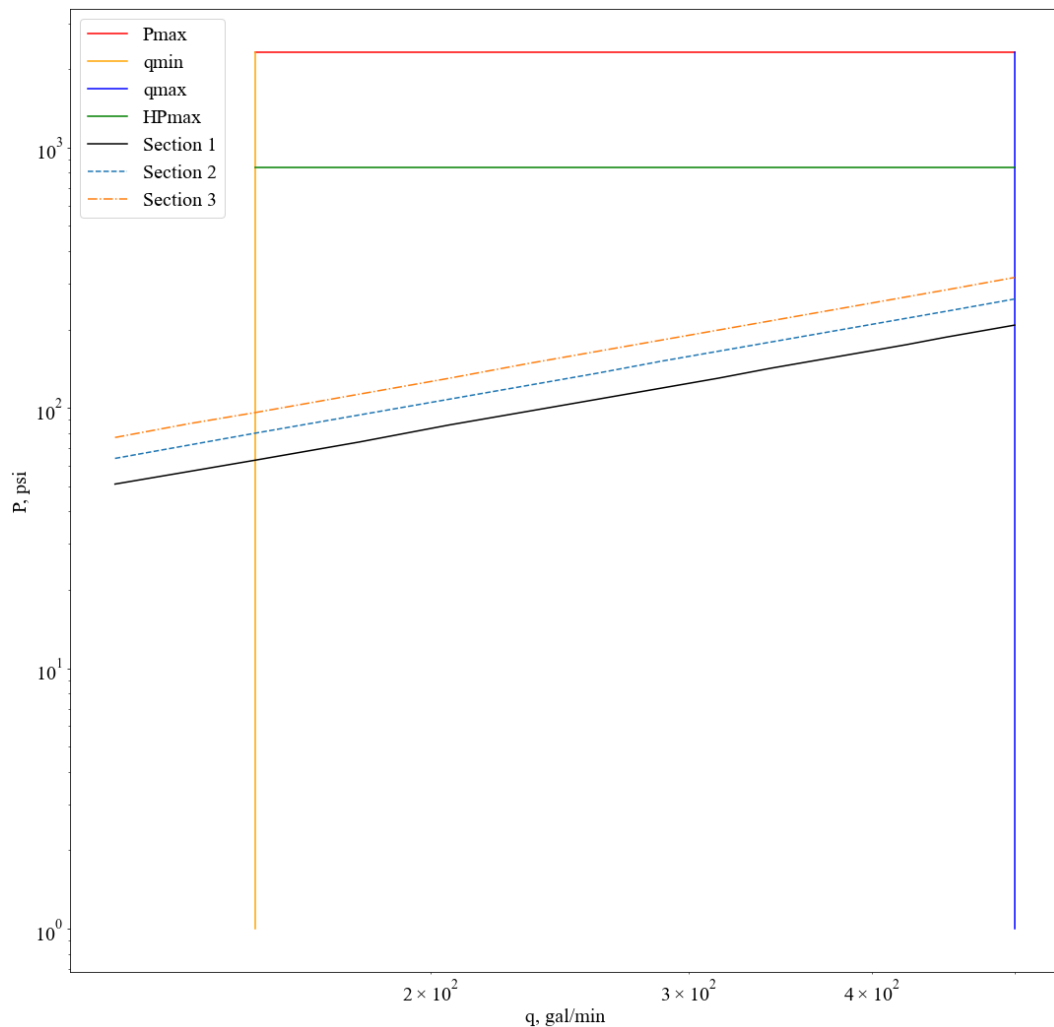


**Figure 12.2:** P-q test results obtained from the Herschel-Bulkley model for the surface stage.

To summarize the results, both models were found to be very close to each other by comparing the tabulated results. However, since the Herschel-Bulkley model can capture the thixotropic behavior of the drilling fluid, the optimized conditions maintained from the Herschel-Bulkley model were selected. In addition, based on both model's results, one can observe that the HCI values for each section are greater than 1; which dictates good cleaning operation for each section. This also validates the optimization results.

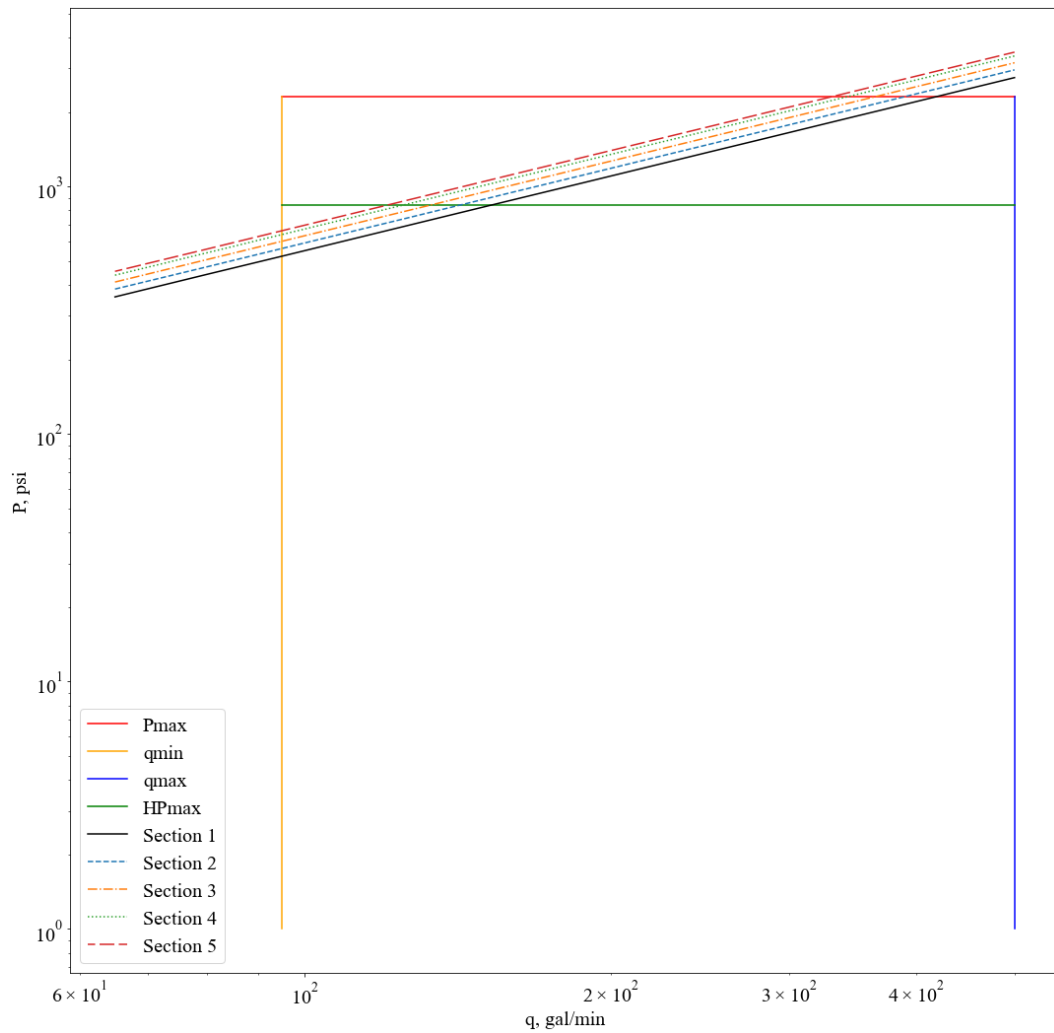


**Figure 12.3:** P-q test result obtained from the Bingham Plastic model for the production stage.

**Table 12.10:** Optimum operating conditions of the production stage for each interval based on the Bingham Plastic model.

Section	$\Delta P_d$ , psi	ECD, ppg	$q_{opt}$ , gal/min	$(\Delta P_b)_{opt}$ , psi	$(A_t)_{opt}$ , in <sup>2</sup>	HCI
1	842	11.83	153	1473	0.135	3.83
2	842	11.81	142	1473	0.132	3.83
3	842	11.79	133	1473	0.124	3.84
4	842	11.78	125	1473	0.117	3.84
5	842	11.77	121	1473	0.110	3.85

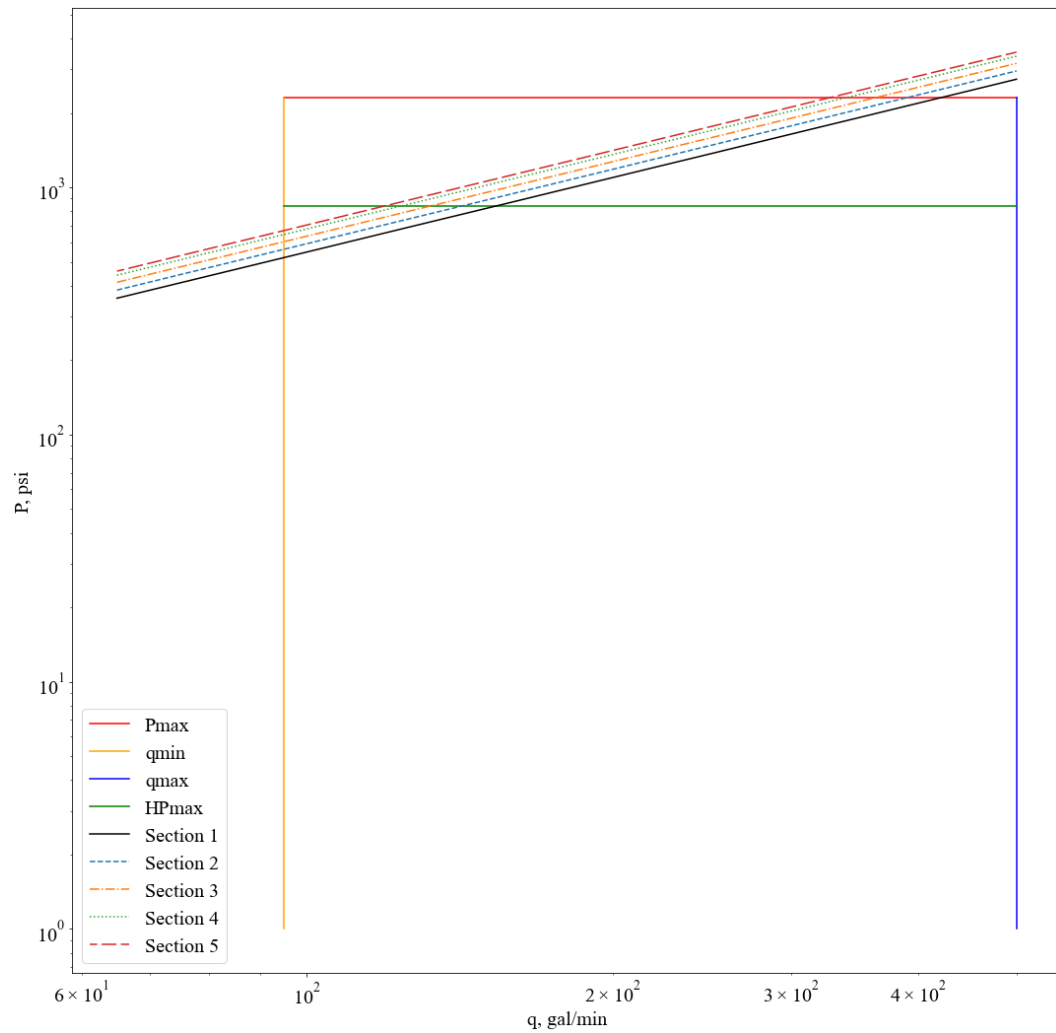


**Figure 12.4:** P-q test result obtained from the Herschel-Bulkley model for the production stage.

**Table 12.11:** Optimum operating conditions of the production stage for each interval based on the Herschel-Bulkley model.

Section	$\Delta P_d$ , psi	ECD, ppg	$q_{opt}$ , gal/min	$(\Delta P_b)_{opt}$ , psi	$(A_t)_{opt}$ , in <sup>2</sup>	HCI
1	842	11.59	154	1473	0.131	3.83
2	842	11.55	142	1473	0.126	3.83
3	842	11.52	133	1473	0.118	3.84
4	842	11.51	125	1473	0.113	3.84
5	842	11.50	120	1473	0.108	3.85

## **13. FIELD DESIGN**

Drilling field design is vital to the start and progress of the drilling operation. All equipment to be used for the drilling operation must be ready for use, complete and backed up to be used when necessary. Before the operation begins, all equipment must be inspected before and during assembly. Before drilling can begin, the field must be examined and approved by spud teams. The rigs, drawworks, lines, manifolds, tanks, pumps, pits, engines, generators, mixers, offices, containers, warehouses, laboratories and security equipment to be used in the field should all be placed in harmony with each other. Positioning equipment that will work together close to each other will make things easier. In this project, all these criteria were taken into consideration when designing the drilling field and placing the equipment in the field.

### **13.1.Rig Selection**

Drilling rigs are structures used to perform drilling operations to reach the fluid in the reservoir. In addition to the main mast of these structures, drawworks, rotary table or top drive, mud tanks, mud pumps, the drillstring, the power generation equipment, and other auxiliary equipment are used as auxiliary components. There are many different brands and models of drilling rigs. The points to be considered when choosing the appropriate rig for the catheterization process are as follows:

- power
- hoisting
- derrick and substructure
- rotary system
- circulating system
- pressure control

Since it can bear the weight of the casing during the casing operation and the weight of the drill string during the drilling operation; The F-200 model rig of the Upetrom brand was chosen due to its affordable price and high performance. The features of the F-200 drilling rig are shown in Table 13.1. The part of the rig that holds the drilling string and applies rotational force to rotate it is the top drive. When choosing a top drive, attention should be paid to the rotating power and rotation speed of the machine. To excavate the formation, the string must rotate at 150 RPM. The 250 EMI 400 model top drive of the TESCO brand meets all requirements with 400 HP power and 200 RPM rotation speed. In addition, it works in harmony with F-200 rigs and this combination is widely used. The specifications of the 250 EMI 400 model top drive are given in Table 13.2 (250 EMI 400 Top Drive - TESCO Corporation, 2011).

**Table 13.1:** Properties of F-200 drilling rig.

<b>Substructure</b>	Upetrom
<b>Mast</b>	MA-200
<b>Type</b>	A- Frame Cantilever
<b>Crown Block</b>	Upetrom 240 ton
<b>Travelling Block</b>	Upetrom 5-32-MC 200
<b>Hook Block</b>	Upetrom 200 Ton
<b>Height (ft)</b>	137
<b>Net Gross Capacity, lbf</b>	715000
<b>Hook Load, lbf</b>	440000
<b>Type</b>	Pin Type
<b>Table Height, ft</b>	16,4
<b>Casing Load, lbf</b>	440000
<b>Setback Load, lbf</b>	275000
<b>Horsepower Rating, HP</b>	1350
<b>Max. Line Pull, lbf</b>	62400
<b>Drilling Capacity, ft</b>	10000
<b>Drilling Line Ø, inch</b>	1 1/4
<b>Auxillary Brake</b>	FE-1400 ES EX
<b>Top Drive</b>	TESCO 250 EMI 400
<b>Rotary Table</b>	Upetrom MRL- 275
<b>Mud Pump</b>	MKP-750
<b>Shale Shakers</b>	Swaco ALS shakers
<b>Drawworks</b>	TF-25

### **13.2.Drawworks Selection**

Drawworks are the most important equipment in the drilling rig's maneuvering system. It is used for transporting the drilling string or casings and breaking the up and down movements. The basic functions of drawworks are:

- Lifting and lowering of drilling strings and casings by means of maneuvering and braking system.
- It enables drilling pipes and casings to be removed from the band with the help of an elevator during drilling and casing operations.

**Table 13.2:** Properties of TESCO 250 EMI 400 Top Drive (250 EMI 400 Top Drive - TESCO Corporation, 2011).

<b>Specifications</b>		
<b>250 TON EMI 400 HP (with a 250 ton integrated swivel)</b>	<b>Imperial</b>	<b>Metric</b>
Rated Capacity	250ton	227tonne
Rated Power	400HP	298kW
Hook Weight	13,684lbs.	6 220kg
Operating Length (including 9 ft. links & elevators)	253in.	6 426mm
Width	44.5in.	1 730mm
Max. Continuous Drill Torque	21,000ft-lb.	2 847daN-m
Make-up / Breakout Torque	32,000ft-lb.	4 336daN-m
Max Speed	200RPM	200RPM
Quill ID	2.5in.	63.5mm
Quill Connection	NC50	

The TF-25 model of the Upetrom brand was preferred to use during the drilling operation. This model is very compatible with the F-200 drilling rig in terms of power, transportation, maneuverability, wire-line diameter and braking. TF-25 model drawworks are very compatible with F-200 model drilling rig and are widely used. The features of the TF-25 model are shown in Table 13.3.

**Table 13.3:** Properties of TF-25 Drawworks (upet.com, 1991).

Maximum input power	700 HP
Number of drums	1
<b>MAIN DRUM</b>	
Maximum main wire line pull	25 tf
Diameter of the main wire line	28,6 mm (1 1/8 in)
Dimensions of the wire line drum over the groove	Ø 558 mm x 1053 mm
Main drum clutch type	AVB 900 x 300
Brake sheaves dimensions	1120 x 265 mm
Cooling of the brake sheaves	with coolant
The specification on which it was designed	API 7 K

### 13.3.Mud Pit Selection

Mud pit system is one of the most critical parts of drilling operations. It enables important events such as preparation and storage of drilling mud, ensuring circulation during drilling, separating the mud in circulation from the cuttings and transferring it back to the tanks. This system consists of tanks with different purposes and features, mud hoppers and mixers used in the preparation of mud, shale shakers, desanders and desilters that separate the mud in circulation from cuttings, lines that provide circulation and pumps with different functions. Mud pit system should be designed to completely contain the volume of mud in circulation. Therefore, the required mud pit volume needs to be calculated. The volume of the mud pit system to be used in this

project was calculated with (Eq. 13-1). As a result of the calculations, the required mud pit volume was found to be 1262 bbl.

$$V_{\text{pit}} = V_{\text{oh}} + V_{\text{ca}} + V_{\text{ds}} \quad (\text{Eq. 13-1})$$

The capacity of the mud pit system to be used must be more than 1262 bbl. NOV Ideal Mud Pit System was preferred because it fulfilled the requirements and high quality. This system allows the preparation, storage, circulation and separation of drilling mud from cuttings to be carried out quickly and safely. The specifications and dimensions of the NOV Ideal Mud Pit System are shown in Table 13.4 (BRANDT™ Ideal Mud Tank System).

**Table 13.4:** Specifications and Dimensions of NOV Ideal Mud Pit System (BRANDT™ Ideal Mud Tank System).

<b>GENERAL</b>		
Equipment type	Two-tank, Ideal Mud Tank System	
Total active capacity (Trip tank volume not included)	1318 bbl (at 12 in below mud rim)	
Pill (slug) tank volume	109 bbl	
Batch mix tank volume	125.5 bbl	
Sand trap volume	115.2 bbl	
Maximum mud weight	18 lb/gal	
Process capacity (nominal)	1500 gal/min	
Degasser capacity (nominal)	1000 gal/min	
Flowline	12-in manifold with cement and active bypass	
<b>ELECTRICAL</b>		
	<b>60 Hz</b>	<b>50 Hz</b>
Total required horsepower	615	615
Voltage	230/460 VAC	190/380 VAC
Phase	3	3
Ambient temperature	40°C (104°F)	
<b>DIMENSIONS AND WEIGHTS</b>		
	<b>L x W x H</b>	<b>WEIGHT</b>
Shaker Tank	55 ft x 12 ft x 8 ft 6 in	
Suction Tank	55 ft x 12 ft x 8 ft 6 in	
Shaker Assembly Skid 1	20 ft x 11 ft 10 in x 1 ft	
Shaker Assembly Skid 2	20 ft x 9 ft 7 in x 1 ft	
Equipment Skid	27 ft 6 in x 8 ft x 2 ft	
	70000 lb	
	70000 lb	
	13000 lb	
	10000 lb	
	14000 lb	

## **13.4. Wellhead Construction**

Wellhead is a system consisting of safety parts, valves and various adapters that provide pressure control during the drilling operation and production process of the well. It is the most important safety system against dangers that may come from the well to the surface. It is used by welding it to casings on the well surfaces, with different types of boplers and fittings selected according to the pressure and temperature values of the well.

### **13.4.1. Blowout preventer**

BOP is the equipment used to secure the well against a possible kick that may come from the well during the drilling operation. It works with a hydraulic system and when there is a kick from the well, the rubber inside fills with hydraulic oil and closes the hole leaving no gap. When selecting the equipment to be used in wellhead design, the safety factor is accepted as 2.5 in accordance with company policy. Since the highest pressure in the well is 4035 psi, the equipment to be used has a resistance of 10000 psi. Wellhead equipment was supplied from SENRTY WELLHEAD SYSTEMS company (Sentry Wellhead, 2017). After surface casing and cementing operations are completed, installation of wellhead equipment begins. The 13-5/8" casing head is welded onto the 13-3/8" conductor casing. In order to extend the wellhead, two 11" casing hangers are placed on top of each other by connecting them with spool studs and salmon. A drilling spool is placed on top of the hanger spools. Kill line and choke line are connected to both sides of the drilling spool. There are very strong valves at the connection points of the drilling spool and lines to control the flow. The choke line transmits the high-pressure and hazardous gas coming from the well to the flare line and ensures that it is delivered to a point away from the rig. Dangerous gas is destroyed by burning here. Kill line ensures that when there is a kick from the well, high density mud is pumped into the well to stop the kick in the well. The top part of the Wellhead

design is the 11" annular bop with a strength of 10000 psi. The top of the Wellhead design is an 11" annular BOP rated at 10000 psi. BOP was purchased from the WEATHERFORD brand (Weatherford, 2006). BOP and wellhead equipment are shown in Figure 13.1.

### **13.4.2. Christmas tree**

The Christmas tree is the structure where valves and accessories are mounted, used for fluid control in oil or gas wells and providing the entrance to the pipe sequence for production. Christmas tree refers to the entire structure, from the pipe cap to the flange at the top. After the production casing, cementing and perforation processes, the well head equipment, except the casing heads, was dismantled. Before producing oil from the well, the Christmas tree was designed and installed. In the selection of equipment to be used in Christmas tree design, the safety factor was accepted to be 2.5 as a company policy. Therefore, equipment with 10000 psi pressure resistance was selected. The christmas tree equipment was supplied from SENRTY WELLHEAD SYSTEMS company (Sentry Wellhead, 2017) According to the Christmas tree design, a 7" tubing head was placed on a 11" casing hanger and 7" casing hanger. Flanges, flat valves, pressure gage and break valve were connected to the tubing head. 7" Tubing hanger and 7" tubing head adapter were mounted on it respectively. Upper and lower master valves were mounted on the tubing head adapter. The reason why there are 2 valves is that if one of them malfunctions, the other one can be used. The Christmas tree to which wing valves and choke valves are connected was mounted to the master valves. The Christmas tree design was completed by mounting the swab valve, tree cap test adapter and pressure gauge on the Christmas tree cross, respectively.



**Figure 13.1:** BOP and wellhead equipments (Weatherford, 2006).

## **14. DRILING COST ANALYSIS**

In the last part of this technical analysis, the approximate expenses will be tried to be estimated. The cost analysis section holds a significant standpoint since all operations require a budget for the initialization. However, since there is no prior drilling data or human experience within the Mount Doom Oilfield, three cases will be constructed. Those are the worst, middle, and best-level scenarios. In these scenarios, different cases will be constructed to evaluate the sensitivity of the tripping operations.

Aside from the time-dependent drilling cost, there are other types of costs such as the rig cost, tangible cost, intangible cost, and service cost (Hossain, 2015). Rigs' costs vary significantly from onshore and offshore wells. However, since Bane-01 is an onshore oil well, its rig cost may lie between \$10000 per day, and \$20000 per day (Hossain, 2015). Tangible costs include casing, wellhead, tubing, and other similar expenses that have physical meaning while intangible cost stands for employee wages, site preparation, etc (Hossain, 2015). Lastly, the service costs dictate the expenses on the LWD, MWD, or any other related services (Hossain, 2015). Lastly, these costs will be held in the General Expenses subsection.

Lastly, a correlation will be used on these constructed three different scenarios to estimate the dry-hole day, dry-hole cost, and total well cost. In the literature, before 1980, Joint Association Survey (JAS) method had been used to estimate the drilling operation costs. However, after 1980, by utilizing the Mechanical Risk Index (MRI) along with multidimensional regression, different authors have published several correlations; hence, these correlations are based on statistical analysis (Kaiser & Pulsipher, 2007). In the results section of this subsection, the correlation proposed by Kaiser and Pulsipher will be used to estimate the drilling cost; consequently, with the comparison with the cost estimated from research (Kaiser & Pulsipher, 2007).

## 14.1.General Expenses

As discussed previously, there are different types of costs that could be encountered during any drilling operation. In this section, the general expenses will be tried to identified. For this work, the costs were divided into two main sections; time dependent costs, and material costs. Time dependent costs include cementing, fuel consumption, mob-demob, rig rental prices, and so on. Hence, all of these expenses will be given in US Dollars per day. These time dependent expenses were dictated by our company's years of experience; except the daily fuel consumption. Because, the daily fuel consumption depends on the selected drilling rig, and its specific properties.

Diesel is consumed for the operation of the rig and rig equipment used in the drilling operation. Since the chosen drilling rig, F-200, uses the diesel engines, it was found to be necessary to estimate its daily fuel consumption. To estimate the total cost of diesel consumed by the rig and rig equipment during drilling, the sum of the kWh power of the rig, mud pump, drawworks and top drive was multiplied by the USD/kWh cost. To achieve the daily diesel consumption cost, (Eq. 14-1) was used (Kaiser & Pulsipher, 2007). For this estimation, the best range power was used for the estimation; hence, the value was given in Table 14.1. As a result of the estimation, the daily diesel consumption cost was found to be 10900 USD per day.

**Table 14.1:** Cost of power provided for three distinct engines used in the drilling rigs (Marchiano, Meola, Lopez, & Ajayi, 2019).

Cost of Power	Diesel Engines	Natural Gas Engines	Utility Power
Worst Range, USD/kWh	0.15	0.05	0.05
Best Range, USD/kWh	0.19	0.06	0.15

$$\text{Daily Diesel Consumption} = 24(W_{\text{engines(total)}}) (\text{Cost of Power}) \quad (\text{Eq. 14-1})$$

Since the daily fuel consumption was estimated, a general Authorization for Expenditure (AFE) was tried to be outlined. The AFE outline that will be used for each scenario was demonstrated in Table 14.2. The only parameter that will be changed in this table is operation duration. Thus, it was found to important to denote those other parameters will be fixed. Lastly, the time depend costs were given in USD per day.

## 14.2. Rate of Penetration Estimation

In the Mechanical Earth Model section, various properties of the formation that will be encountered as a function of depth were already constructed. By examining the literature, it can be observed that several researchers have tried to correlate the rate of penetration (ROP) with the mechanical properties of the rock. The prediction of the ROP is an imperative phenomenon since the ROP directly affects the drilling time; which influences the drilling cost.

In this section, the ROP will be tried to be estimated using the dynamic Young's modulus of the formation (Kahraman, Bilgin, & Feridunoglu, 2003). Moreover, the ROP values will be estimated as a function of depth. Kahraman et al. have analyzed different rock core samples, and fitted a linear line to predict the corresponding ROP value; as a result of this experiment, they have proposed (Eq. 14-2) to be used in the prediction of the ROP (Kahraman, Bilgin, & Feridunoglu, 2003). However, (Eq. 14-2) should be used carefully since it is based on the SI Unit System. Thus, a conversion factor should be applied to have the ROP value in the form of a convenient field unit.

$$ROP = -7 \times 10^{-5} E_{dyn} + 16.1 \quad (\text{Eq. 14-2})$$

**Table 14.2:** Authorization for expenditure table.

Description	Cost, \$	Time, day	Operation Duration, day	Operation Cost, \$	Percent Operation Cost, %
<b>Time Dependent Costs</b>					
<b>Cementing</b>	4634	1			
<b>Fuel</b>	10900	1			
<b>Mob - Demob</b>	1448	1			
<b>Shale Shaker Sieve</b>	579	1			
<b>Personnel Expenses</b>	2317	1			
<b>Rig Rental</b>	15000	1			
<b>Spare Parts, Maintenance</b>	965	1			
<b>Engineering</b>	1159	1			
<b>Coring Service</b>	86890	1			
<b>Log Service</b>	2896	1			
<b>Contingency</b>	965	1			
<b>Housing</b>	772	1			
<b>Invisible costs</b>	965	1			
<b>Risks</b>	1274	1			
<b>Depreciation</b>	10620	1			
<b>Security</b>	193	1			
<b>Transportation</b>	290	1			
<b>Day Total</b>	<b>141867</b>	1		<b>Operation Total</b>	
<b>Material Costs</b>					
<b>Bits</b>	202744	-			
<b>BHA</b>	144817	-			
<b>Mud Chemicals</b>	347561	-			
<b>Casing</b>	724085	-			
<b>Cementing</b>	463415	-			
<b>Wellhead System</b>	250000	-			
<b>Contingency</b>	40000	-			
<b>Site Prep</b>	100000	-			
<b>Logging</b>	150000	-			
<b>Material Total</b>	<b>242262</b>	2			
<b>TOTAL</b>					

After applying (Eq. 14-2) for various depths along the formation of interest, ROP values were estimated and tabulated in Appendix H. In addition, ROP values were plotted as a function of depth on the semi-log graph as can be seen in Figure 14.1. A linear line was fitted to the predicted ROP values to utilize the  $a_2$  constant; which is used in the prediction of the trip time (Bourgoyne Jr, Millheim, Chenevert , & Young Jr, 1991). This constant is found using the depth differences in the first and second log cycles.

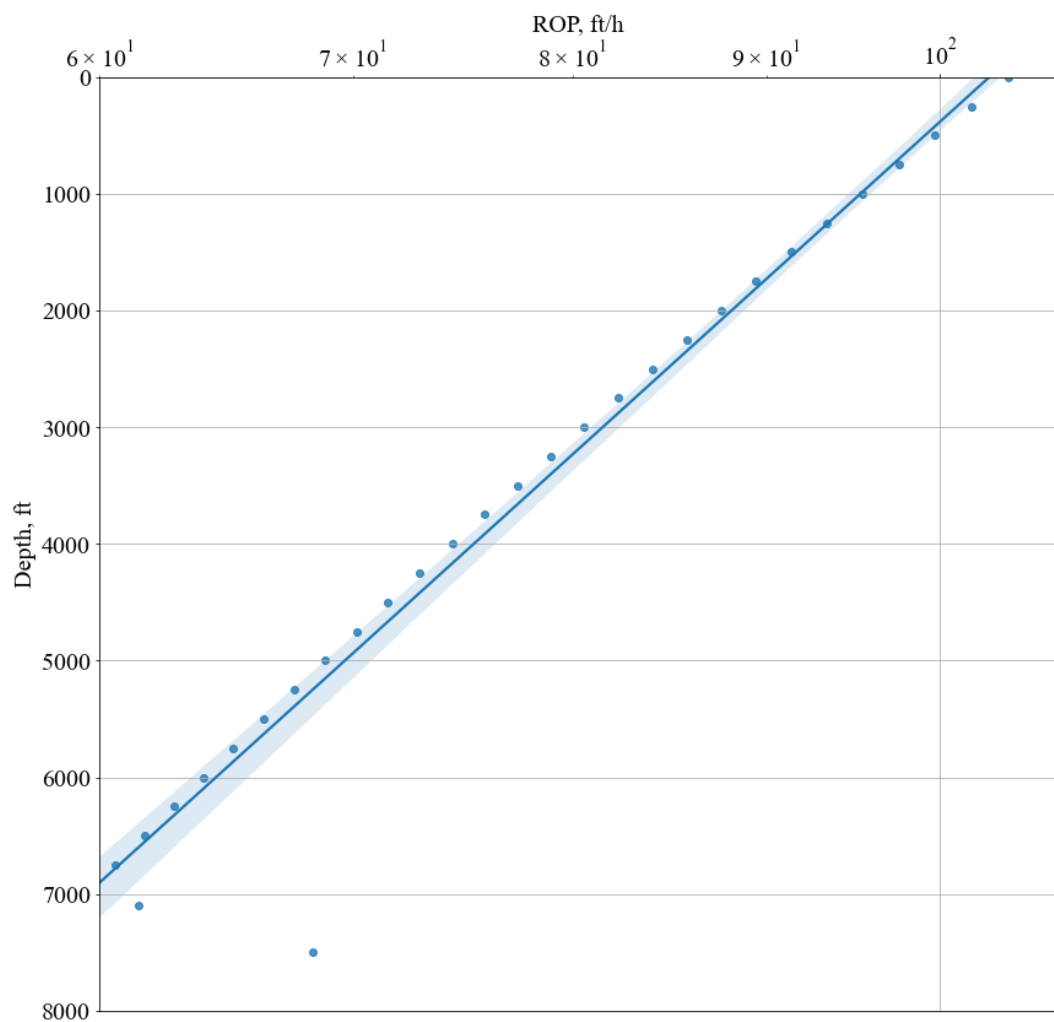


**Figure 14.1:** Predicted ROP values as function of depth with its linear regression.  
Blue shaded parts represent the 95% confidence interval.

However, one can observe from Figure 14.1 that the fitted linear line does not cross the first log cycle due to the lack of data. To overcome this issue, the fitted linear line equation was given in (Eq. 14-3), with the accuracy of 0.97, to estimate the depth of the second log cycle. Then, using Equation 2, the depth in the first log cycle was found to be 29762 ft. On the other hand, the depth at the first log cycle was found to be 385 ft. As a result, the constant  $a_2$  was estimated to be 0.0001. Moreover, the surface penetration rate, K, was chosen as 104 ft/h since the ROP value at 0 ft is 104 ft/h. Lastly, by leveraging those constants, the specific depth which the trip operation should be done can be estimated from (Eq. 14-4). On the other hand, (Eq. 14-5) can be used to estimate the trip time required for the depth obtained from (Eq. 14-4) (Bourgoyne Jr, Millheim, Chenevert , & Young Jr, 1991).

$$D_{cycle} = -12733 \ln ROP + 59027 \quad (\text{Eq. 14-3})$$

$$D_{out} = \frac{1}{2.303a_2} \ln(2.303a_2 K t_b + e^{2.303a_2 D_{in}}) \quad (\text{Eq. 14-4})$$

$$\bar{t}_t = 2 \left( \frac{\bar{t}_s}{\bar{l}_s} \right) \quad (\text{Eq. 14-5})$$

In addition to the above tripping estimations, one can also estimate the average drilling time that will be faced. However, this estimation assumes that there will be no troubles during the drilling, such as the lost circulation. To achieve the average drilling time required to drill, (Eq. 14-6) can be used (Bourgoyne Jr, Millheim, Chenevert , & Young Jr, 1991). It was found to be important to denote that, during the usage of (Eq. 14-6), the average depth should be used in the equation stated. This average depth can be achieved by averaging the depth out, and depth in values. Lastly, once the average drilling time required to drill the section is estimated, one can estimate the theoretical number of bits required to drill the specific section using (Eq. 14-7) (Bourgoyne Jr, Millheim, Chenevert , & Young Jr, 1991).

$$\overline{t}_d = \frac{1}{2.303a_2K} \left( e^{2.303a_2\overline{D}} - 1 \right) \quad (\text{Eq. 14-6})$$

$$N_b = \frac{\overline{t}_d}{\overline{t}_b} \quad (\text{Eq. 14-7})$$

### 14.3. Construction of Scenarios

In the following scenario construction parts, different assumptions were made on each scenario. These assumptions were performed on the time required to handle one stand of drill string, and the average bit life. It is unfortunate to apply assumptions on these parameters, yet it was essential since there is no prior data regarding to the past drilling operations.

#### 14.3.1. Worst-case scenario

For the worst-case scenario, the worst-case scenario was constructed. The chosen parameters for this worst-case scenario are demonstrated in Table 14.3. Consequently using the parameters in Table 14.3 with using (Eq. 14-4), (Eq. 14-5), (Eq. 14-6), and (Eq. 14-7), trip in, trip out, and required time for the tripping for each section, the drilling time, and number of bits required were estimated. Thus, the estimated trip scheme was displayed in Table 14.4.

For the sake of the better representation of the estimated trip times, the cumulative trip times estimated for the worst-case scenario were plotted on a semi-log graph as can be observed in Figure 14.2. Moreover, a second order regression line was fitted, and its 95% confidence interval was displayed on the same graph.

**Table 14.3:** Assumed parameters for the construction of the worst-case scenario.

$t_s$ , min	$\bar{t}_b$ , h	$\bar{l}_s$ , ft
7.5	10	90

**Table 14.4:** The estimated trip scheme for the worst-case scenario.

No <sub>t</sub>	D <sub>in</sub> , ft	D <sub>out</sub> , ft	$\bar{t}_t$ , h	$\sum \bar{t}_t$ , h	D <sub>seat</sub> , ft	d <sub>hole</sub> , in	$\bar{D}$ , ft	$\bar{t}_d$ , h	$\sum \bar{t}_d$ , h	N <sub>b</sub>
1	150	1139	3.2	3.2	3000	12.25	644.5	6.4	6.4	0.64
2	1139	2056	5.7	8.9	3000	12.25	1597.5	16.4	22.7	1.64
3	2056	2912	8.1	17	3000	12.25	2484	26.4	49.1	2.64
4	3000	3797	10.6	27.5	3000	12.25	3398.5	37.4	86.5	3.74
5	3797	4547	12.6	40.1	7600	8.5	4172	47.5	134	4.75
6	4547	5255	14.6	54.7	7600	8.5	4901	57.5	191.4	5.75
7	5255	5926	16.5	71.2	7600	8.5	5590.5	67.5	258.9	6.75
8	5926	6563	18.2	89.4	7600	8.5	6244.5	77.5	336.4	7.75
9	6563	7170	19.9	109.4	7600	8.5	6866.5	87.5	423.8	8.75
10	7170	7749	21.5	130.9	7600	8.5	7459.5	97.5	521.3	9.75
11	7600									

Furthermore, a signature plot for the worst-case scenario was plotted by using the estimated cumulative drilling time, and ROP values (Bourgoyne Jr, Millheim, Chenevert , & Young Jr, 1991). This graph was demonstrated in Figure 14.3. By examining this graph, the time required the drill up to formation of the interest, and its prospective ROP values can be compared.

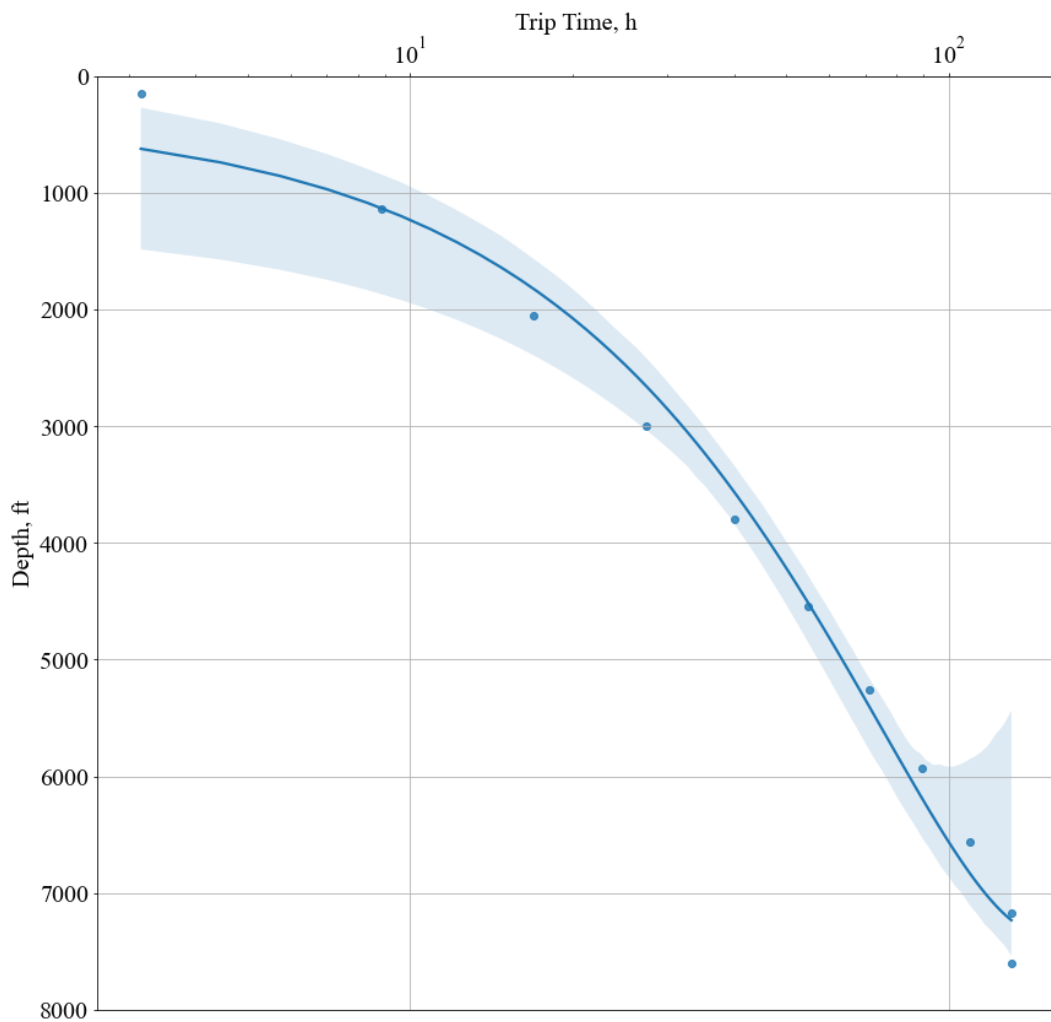


**Figure 14.2:** Estimated cumulative trip times as a function of depth for the worst-case scenario.

### 14.3.2. Middle-case scenario

For the middle-case scenario, the middle-case scenario was constructed. The chosen parameters for this middle-case scenario are demonstrated in Table 14.5. Consequently using the parameters in Table 14.5 with using (Eq. 14-4), (Eq. 14-5), (Eq. 14-6), and (Eq. 14-7), trip in, trip out, and required time for the tripping for each section, the drilling time, and number of bits required were estimated. Thus, the estimated trip scheme was displayed in Table 14.6.

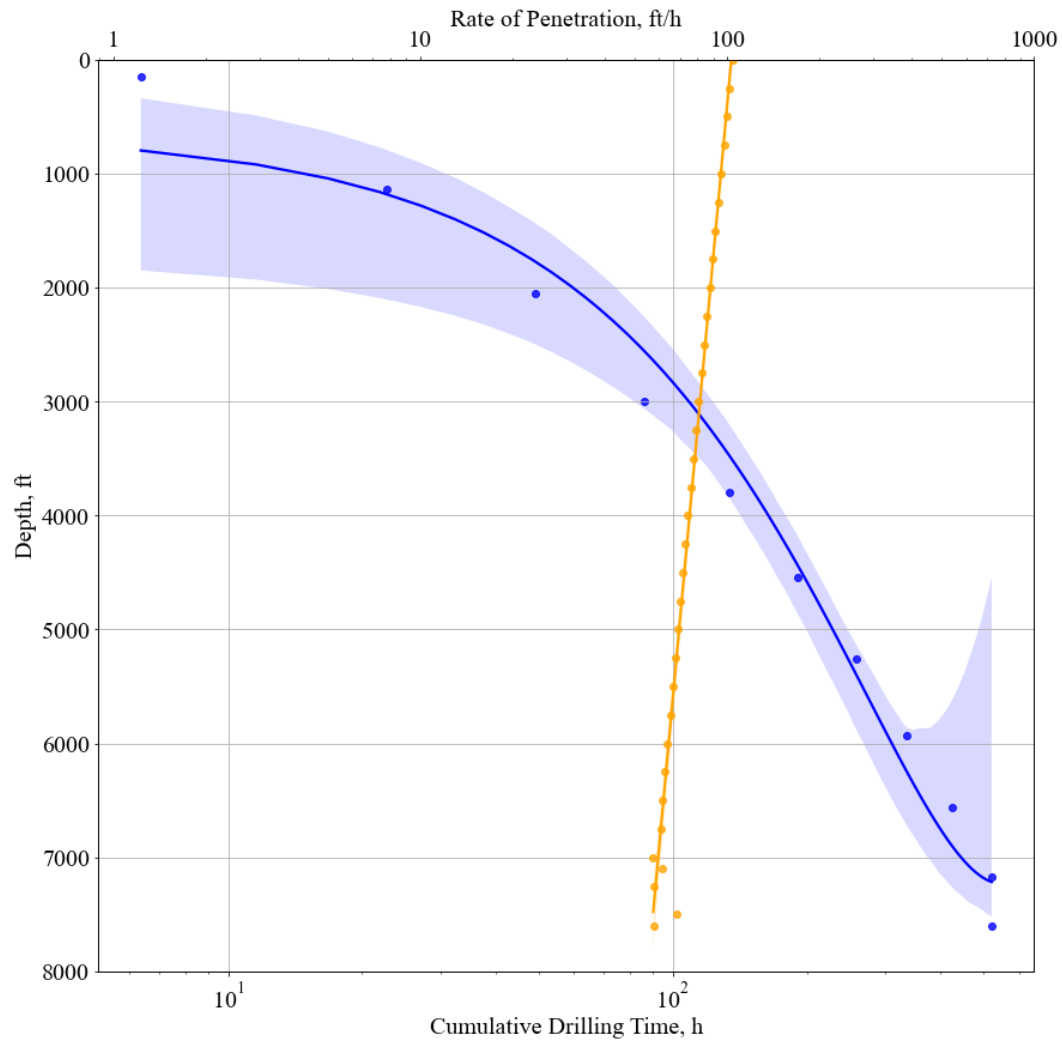


**Figure 14.3:** The predicted ROP values versus predicted cumulative drilling time for the worst-case scenario.

For the sake of the better representation of the estimated trip times, the cumulative trip times estimated for the middle-case scenario were plotted on a semi-log graph as can be observed in Figure 14.5. Moreover, a second order regression line was fitted, and its 95% confidence interval was displayed on the same graph.

**Table 14.5:** Assumed parameters for the construction of the middle-case scenario.

$t_s$ , min	$\bar{t}_b$ , h	$\bar{l}_s$ , ft
5	15	90

Furthermore, a signature plot for the middle-case scenario was plotted by using the estimated cumulative drilling time, and ROP values (Bourgoyne Jr, Millheim, Chenevert , & Young Jr, 1991). This graph was demonstrated in Figure 14.4. By examining this graph, the time required the drill up to formation of the interest, and its prospective ROP values can be compared.

**Table 14.6:** The estimated trip scheme for the middle-case scenario.

No <sub>t</sub>	D <sub>in</sub> , ft	D <sub>out</sub> , ft	̄t <sub>t</sub> , h	Σ̄t <sub>t</sub> , h	D <sub>seat</sub> , ft	d <sub>hole</sub> , in	̄D, ft	̄t <sub>d</sub> , h	Σ̄t <sub>d</sub> , h	N <sub>b</sub>
1	150	1605	3	3	3000	12.25	877.5	8.7	8.7	0.58
2	1605	2911	5.4	8.4	3000	12.25	2258	23.8	32.5	1.58
3	3000	4177	7.7	16.1	3000	8.5	3588.5	39.9	72.3	2.66
4	4177	5255	9.7	25.8	7600	8.5	4716	54.9	127.2	3.66
5	5255	6249	11.6	37.4	7600	8.5	5752	69.9	197.1	4.66
6	6249	7171	13.3	50.7	7600	8.5	6710	84.9	282	5.66
7	7171	8031	14.9	65.6	7600	8.5	7601	99.9	381.9	6.66
8	7600			65.6	7600	8.5			381.9	

### 14.3.3. Best-case scenario

For the best-case scenario, the best-case scenario was constructed. The chosen parameters for this best-case scenario are demonstrated in Table 14.8. Consequently using the parameters in Table 14.8 with using (Eq. 14-4), (Eq. 14-5), (Eq. 14-6), and (Eq. 14-7), trip in, trip out, and required time for the tripping for each section, the drilling time, and number of bits required were estimated. Thus, the estimated trip scheme was displayed in Table 14.7.

For the sake of the better representation of the estimated trip times, the cumulative trip times estimated for the best-case scenario were plotted on a semi-log graph as can be observed in Figure 14.6. Moreover, a second order regression line was fitted, and its 95% confidence interval was displayed on the same graph.

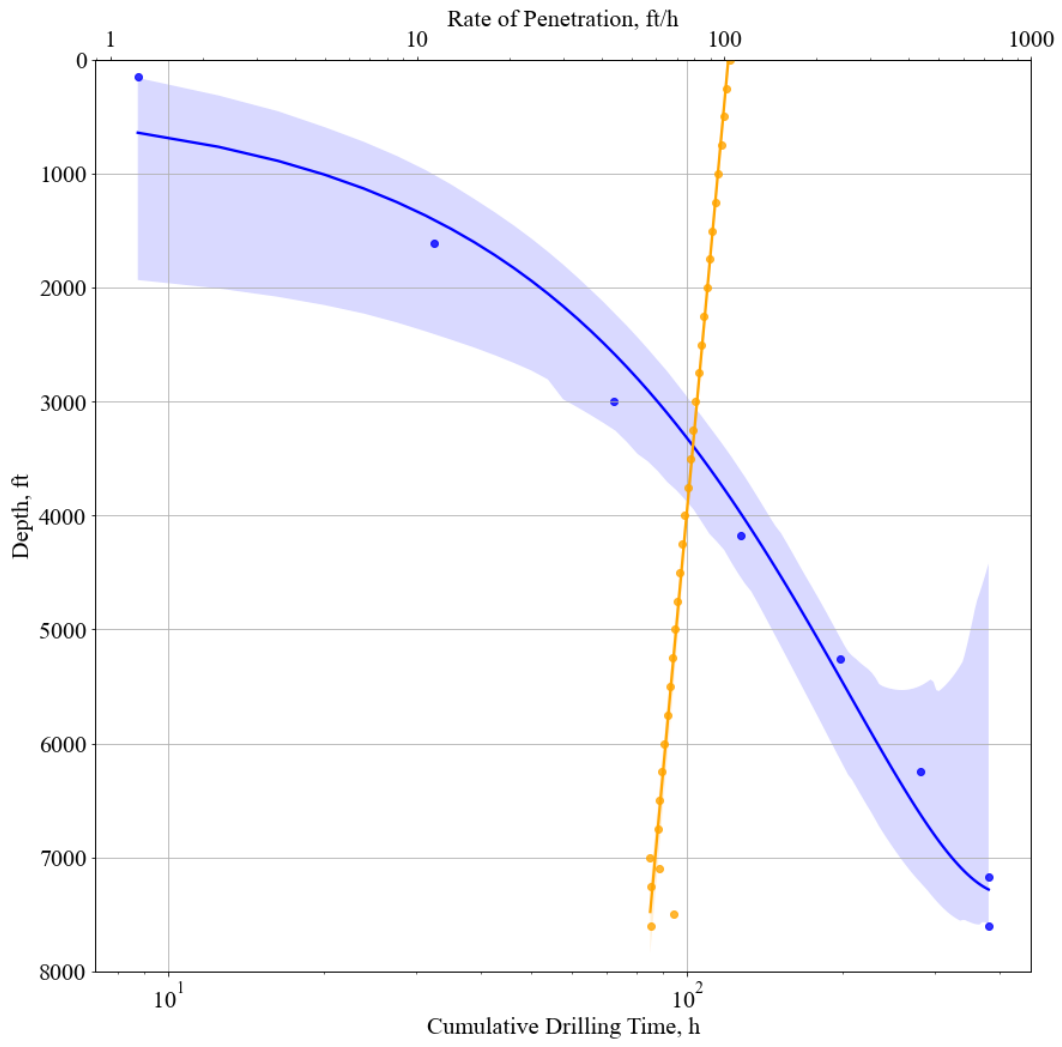


**Figure 14.4:** The predicted ROP values versus predicted cumulative drilling time for the middle-case scenario.

**Table 14.7:** The estimated trip scheme for the best-case scenario.

No <sub>t</sub>	D <sub>in</sub> , ft	D <sub>out</sub> , ft	$\bar{t}_t$ , h	$\sum \bar{t}_t$ , h	D <sub>seat</sub> , ft	d <sub>hole</sub> , in	$\bar{D}$ , ft	$\bar{t}_d$ , h	$\sum \bar{t}_d$ , h	N <sub>b</sub>
1	150	2056	1.9	1.9	3000	12.25	1103	11.1	11.1	0.55
2	2056	3714	3.4	5.3	3000	12.25	2885	31.1	42.2	1.56
3	3000	4546	4.2	9.55	3000	8.5	3773	42.2	84.4	2.11
4	4546	5925	5.5	15	7600	8.5	5235.5	62.2	146.7	3.11
5	5925	7169	6.6	21.7	7600	8.5	6547	82.3	229	4.11
6	7169	8303	7.7	29.4	7600	8.5	7736	102.3	331.2	5.11
7	7600			29.4					331.2	

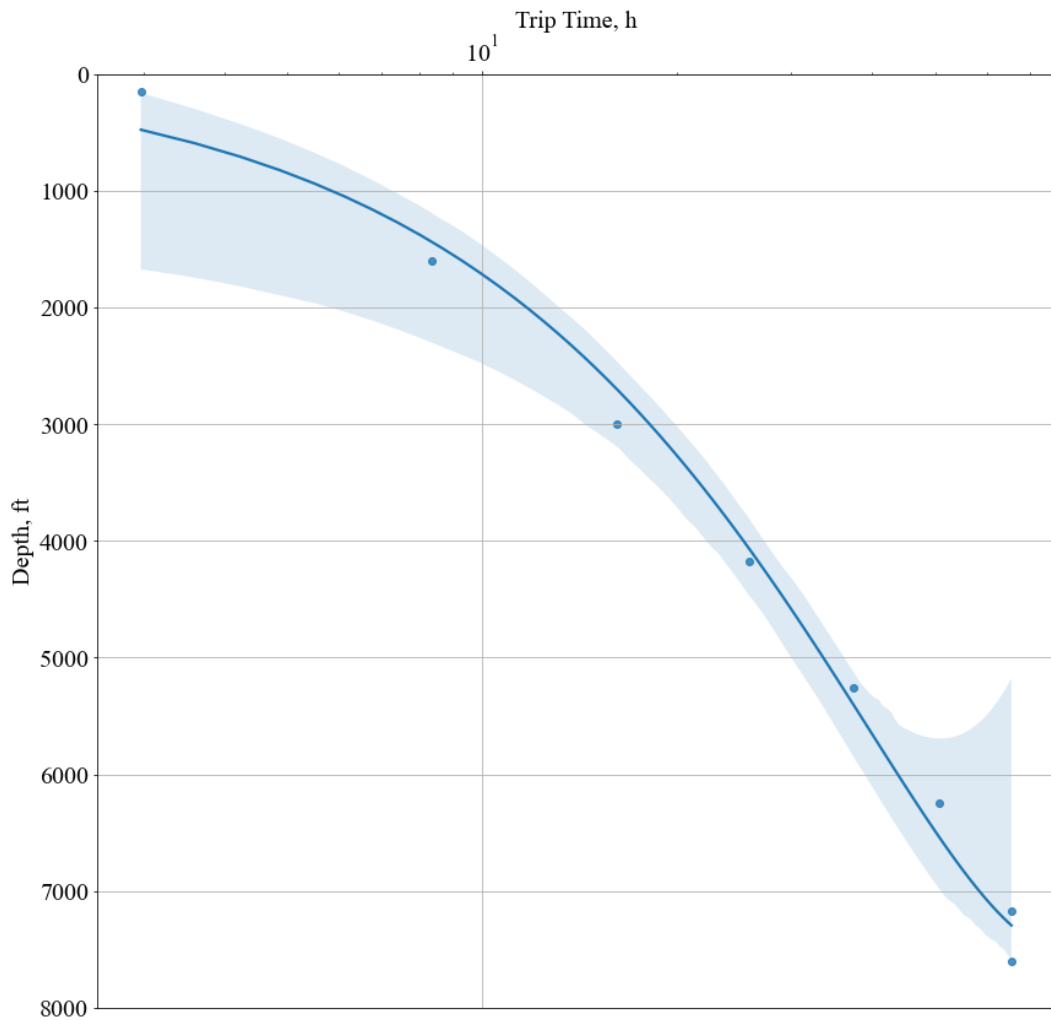


**Figure 14.5:** Estimated cumulative trip times as a function of depth for the middle-case scenario.

**Table 14.8:** Assumed parameters for the construction of the best-case scenario.

$t_s, \text{min}$	$\bar{t}_b, \text{h}$	$\bar{l}_s, \text{ft}$
2.5	20	90

Furthermore, a signature plot for the best-case scenario was plotted by using the estimated cumulative drilling time, and ROP values (Bourgoyne Jr, Millheim, Chenevert , & Young Jr, 1991). This graph was demonstrated in Figure 14.7. By examining this graph, the time required the drill up to formation of the interest, and its prospective ROP values can be compared.

#### **14.4.Statistical Model**

Over the years of experience, engineers, and researchers have been trying to estimate the drilling cost by utilizing various ways. In general, those methods are developed based on the historical drilling datas. Those drilling datas include the well type, water depth, drilling depth, inclination, and so on. The recent study of Kaiser and Pulsipher showed that the dry-hole day, and the dry-hole cost depends on the followings (Kaiser & Pulsipher, 2007):

- Well type (WT): There are two types of wells indicated in the study as exploration, and development.
- Water depth (WD): Depth of the water column if the well is located in an offshore area.
- Drilling interval (DI): The depth where the well will be drilled.
- Horizontal displacement (HD): The displacement on the horizontal side.
- Aspect ratio (AR): Curvature of the well trajectory.
- Number of strings (NS): Number of string sections.

Based on the above parameters, Kaiser and Pulsipher have proposed two equations on the prediction of the dry-hole days, and dry-hole cost (Kaiser & Pulsipher, 2007). The equation proposed for the prediction of the dry-hole day was given in (Eq. 14-8); whereas the cost estimation for the dry-hole was supplied in (Eq. 14-9) (Kaiser & Pulsipher, 2007). Thus, they observed a strong correlation between dry-hole cost, and total well cost. Also, they have stated that the correlation coefficient between DHC, and TWC is 0.94 (Kaiser & Pulsipher, 2007).

$$DHD = -23.5 + 1.83WT + 0.21WD + 1.1DI - 0.66HD + 13.7AR \quad (\text{Eq. 14-8})$$

$$+ 6.36 \text{ NS}$$

$$DHC = -13.9 + 1.79WT + 0.56WD + 0.3DI - 0.48HD + 6.5AR \quad (\text{Eq. 14-9})$$

$$+ 3.25 \text{ NS}$$

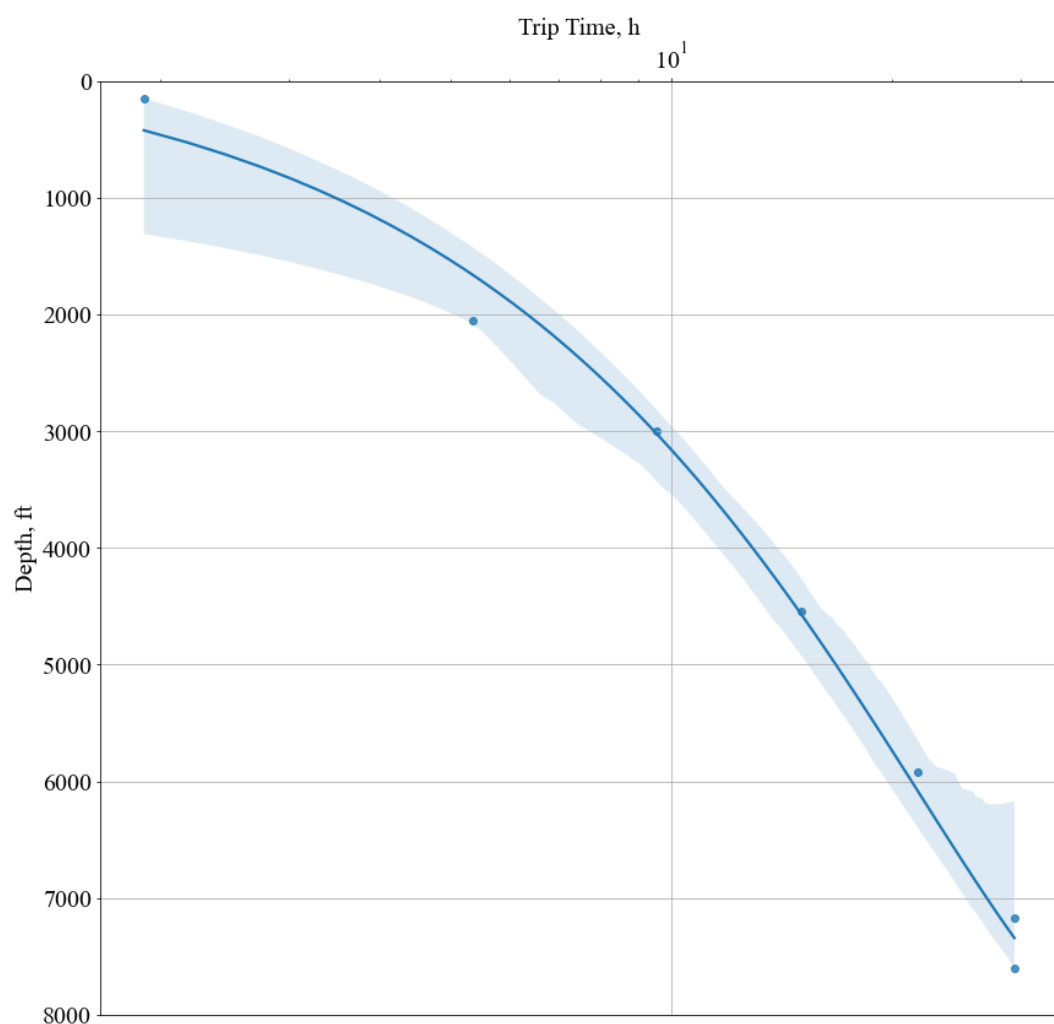


**Figure 14.6:** Estimated cumulative trip times as a function of depth for the best-case scenario.

In light of the provided resources, similar scenarios were constructed for the statistical cost analysis prediction. The worst-case scenario represents the worst-case scenario in which the planned vertical well will deviate with the amount of 0.3 aspect ratio. On the other hand, the middle case covers another deviated well scenario with an aspect ratio of 0.15. The last scenario, the best-case scenario, models a perfect vertical well. Lastly, all of the parameters, and their results for each scenario were summarized in Table 14.9.

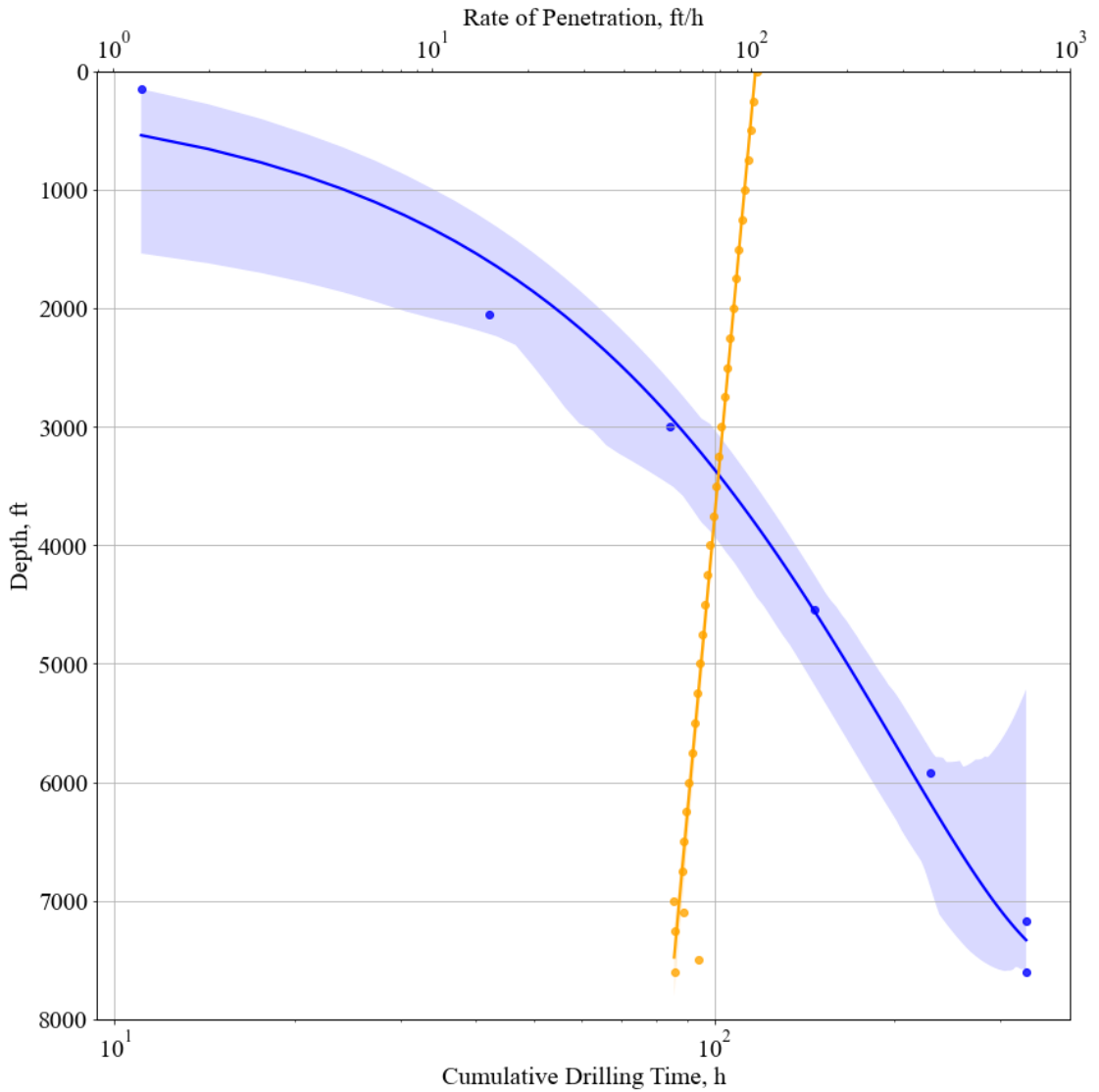


**Figure 14.7:** The predicted ROP values versus predicted cumulative drilling time for the best-case scenario.

## 14.5.Results

Together with using the estimated total time required to drill Bane-01, the AFE tables were constructed for each scenario; hence, they were sustained in Appendix H. Based on the constructed scenarios, the required times were found to be 27 hours, 19 hours, and 15 hours for the worst-case, middle-case, and best-case scenario respectively. In addition, these estimated times were used in the construction of AFE tables. Moreover, to create variation, the coring, and logging services were taken to be 3 days long for the worst-case scenario, 2 days for the middle-case scenario, and 1 day for the worst-case scenario.

As a result, the overall costs -all-inclusive- were demonstrated in Table 14.10. As can be seen from the table given, the cost of the operation decreases from the worst-case through the best-case scenario. It is not surprising since it was expected. On the other hand, when the statistical, and generalized AFE results were compared, one can observe that there is a 250000 USD difference between each scenario; hence, AFE results reflect the higher cost. However, since each method has huge uncertainties, the results were found to be promising.

**Table 14.9:** Assumed parameters, and their corresponding results for each scenario based on the statistical drilling cost prediction.

	Scenarios		
	Worst	Middle	Best
<b>WT, in 100 m</b>	0	0	0
<b>WD, in 100 m</b>	0	0	0
<b>DI, in 100 m</b>	23.16	23.16	23.16
<b>HD, in 100 m</b>	3	1.5	0
<b>AR</b>	0.3	0.15	0
<b>NS</b>	3	3	3
<b>DHD, days</b>	24	22	21
<b>DHC, million \$</b>	3.31	3.05	2.80
<b>TWC, million \$</b>	3.52	3.25	2.98

**Table 14.10:** Estimated overall cost for the drilling operation for each scenario.

Scenarios		
Worst, \$	Middle, \$	Best, \$
3977683	3508321	3228747

For better understanding purposes, the costs estimated from the AFE model are illustrated in Figure 14.8. This figure showcases the cost-per-depth relation on a semi-log graph for each scenario. As can be seen from the figure, the best-case scenario has the lowest cost per foot, while the worst-case one has the highest cost per foot. Moreover, it was observed that the blazing cost difference starts at about 750 ft; besides, the middle-case scenario seems close to the best-case scenario.

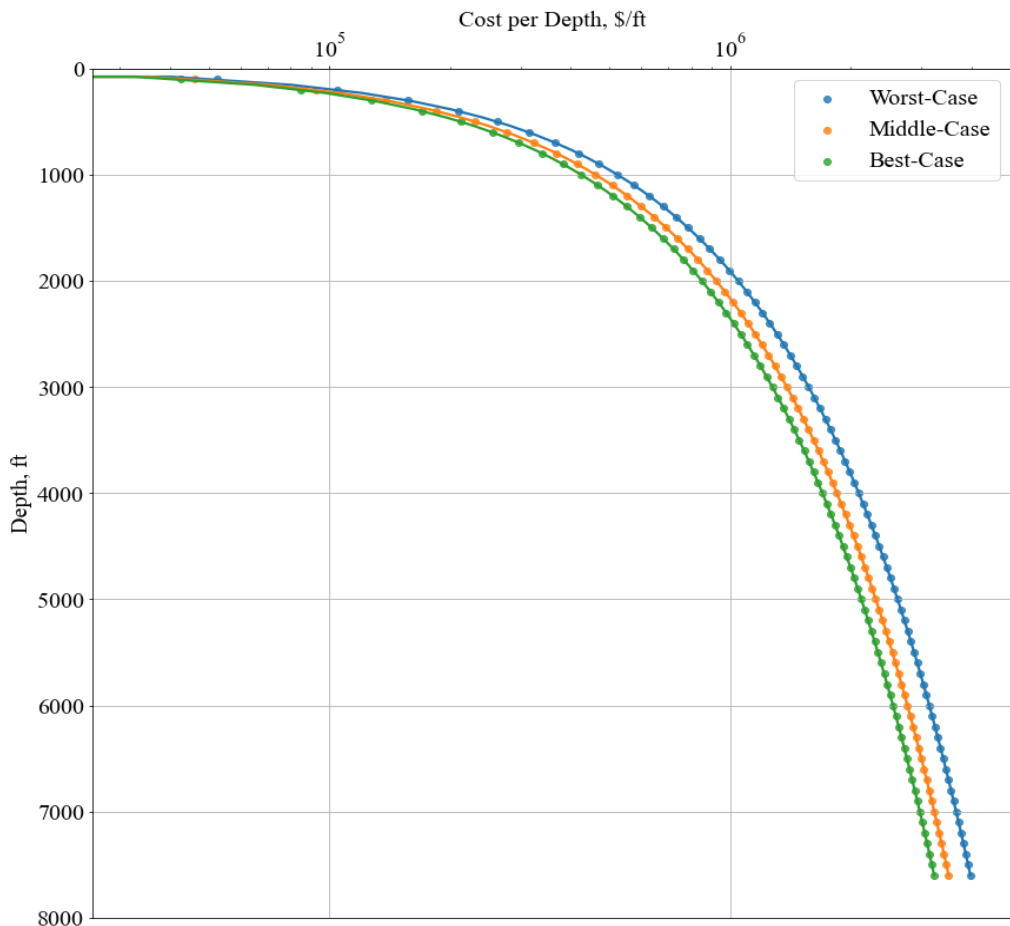


**Figure 14.8:** Cost per depth relation for each scenario.

## **15. RESERVOIR ENGINEERING**

In petroleum engineering, reservoir engineering is an essential discipline that focuses on comprehending the flow of gas, water, and oil underground, especially in relation to hydrocarbon recovery. It involves several different sub topics such as reserves estimation, fluid flow, data integration, modelling, simulation, etc. Mass conservation is central to the concept of material balance. The difference between what is produced (leaving the reservoir) and what is injected determines the change in mass in a reservoir. Material balance is carefully examined by reservoir engineers in order to evaluate production data, estimate the reserves, and forecast flow performance. It provides the framework for examining sectors with primary production.

In this study, the volumetric reserves estimation has been already applied. In this chapter, the material balance approach, specifically, the Havlena and Odeh straight-line method will be performed. In order to perform the straight-line approach proposed by Havlena and Odeh, there are a few parameters that needs to be described, and calculated. In the following subsections, these parameters will be described, and calculated.

### **15.1.Required Parameters for the Havlena and Odeh Straight Line Approach**

In the oil and gas industry, the reserves estimation plays a crucial role since it signifies the importance of the discovery. In the literature, distinct approaches have been developed, and published by scientists. Those can be inferred as the deterministic volumetric approach, stochastic volumetric approach, rate of decline analysis, and material balance approach. In this project, the stochastic volumetric approach has been already applied for the estimation of the Mount Doom Oil Field's reserves. Starting from this chapter, the material balance approach will be tried to be performed. Before getting started with the material balance approach, it was found to be important to denote some fundamental properties, such as the formation volume factor of oil. The formation volume factor of oil ( $B_o$ ) can be defined as the correspondence of the volume of oil in stock tank conditions to reservoir conditions (Craft, Hawkins, & Terry, 1991).

On the other hand,  $B_o$  has a tendency to increase up to bubble point pressure ( $P_b$ ). Thus, it starts to decrease below the bubble point pressure due to the release of liberated gas. So, it can be inferred from these descriptions, that  $B_o$  has an impact on the estimation of the reserves since it implies the volumetric relevance between the reservoir and the stock tank conditions. Fortunately, the PVT data has been already given for the Mount Doom Oil Field. If the corresponding data is to be drawn on a proper scale, Figure 15.1 can be obtained.

After an inspection of Figure 15.1, the bubble point of the reservoir was estimated to be 1614.7 psia thanks to the knowledge of the formation volume factor behavior. Since the initial reservoir pressure ( $P_{i,res}$ ) is 3777.1 psia, and the last average reservoir pressure recording is 3169.2 psia, the reservoir is said to be undersaturated. An undersaturated reservoir implies that there is no free gas within the reservoir; hence, all of the gas is dissolved in the crude oil (Towler, 2002).

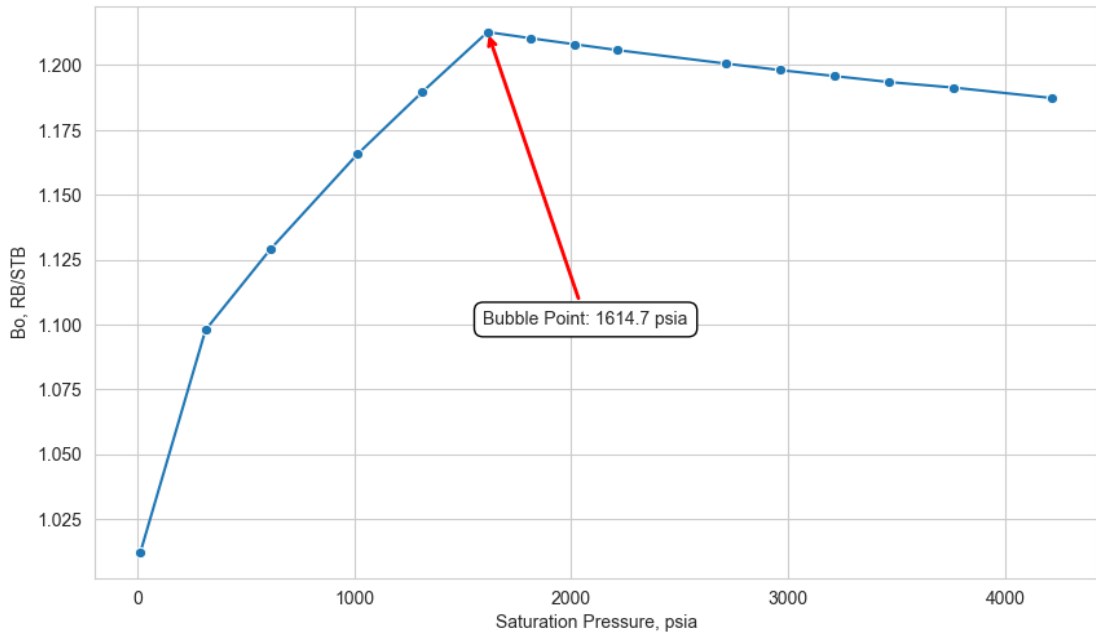


**Figure 15.1:** The formation volume factor of oil behavior with respect to pressure.

In addition to the  $B_o$ , the solution gas-oil ratio ( $R_{so}$ ) is the other fundamental property.  $R_{so}$  is defined as the amount of gas dissolved in the crude oil; hence, the solubility increases with increasing pressure up to a certain point (Craft, Hawkins, & Terry, 1991). This threshold pressure which the solution gas-oil ratio increases is called the bubble point pressure. Above the bubble point pressure, the solution gas-oil ratio remains constant. Moreover, this theoretical behaviour can be observed by looking at Figure 15.2. Lastly, during the estimation of the reserves by using the Havlena and Odeh straight-line approach, the initial solution gas-oil ratio ( $R_{soi}$ ) will be taken as 342.3 SCF/STB; which is obtained from Figure 15.2.

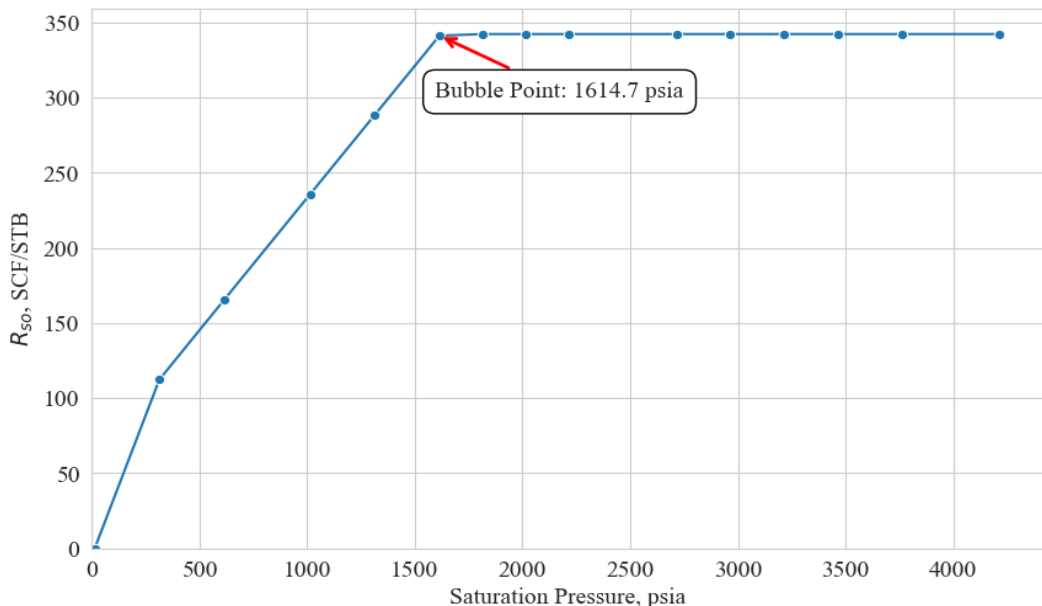


**Figure 15.2:** The solution gas-oil ratio behavior with respect to pressure

Since the reservoir drive mechanism is a depletion drive, and continuous gas production has been observed during the oil production, another crucial parameter that needs to be taken into account is the formation volume factor of gas ( $B_g$ ). It measures the change in gas volume in the reservoir between standard conditions (typically 60 °F and 14.696 psia) and reservoir conditions (temperature and pressure).  $B_g$  enables the correlation between the produced volumes under normal conditions and the gas quantities measured in the reservoir. Estimating recoverable reserves and optimizing

production techniques require this. Likewise, the  $B_o$ , related data about  $B_g$  was already given in PVT laboratory analysis. Thus, its behavior concerning pressure is displayed in Figure 15.3. As can be seen in Figure 15.3, pressure has an inverse relationship with  $B_g$ . The gas expands to take up more space in the reservoir as the pressure inside it drops.

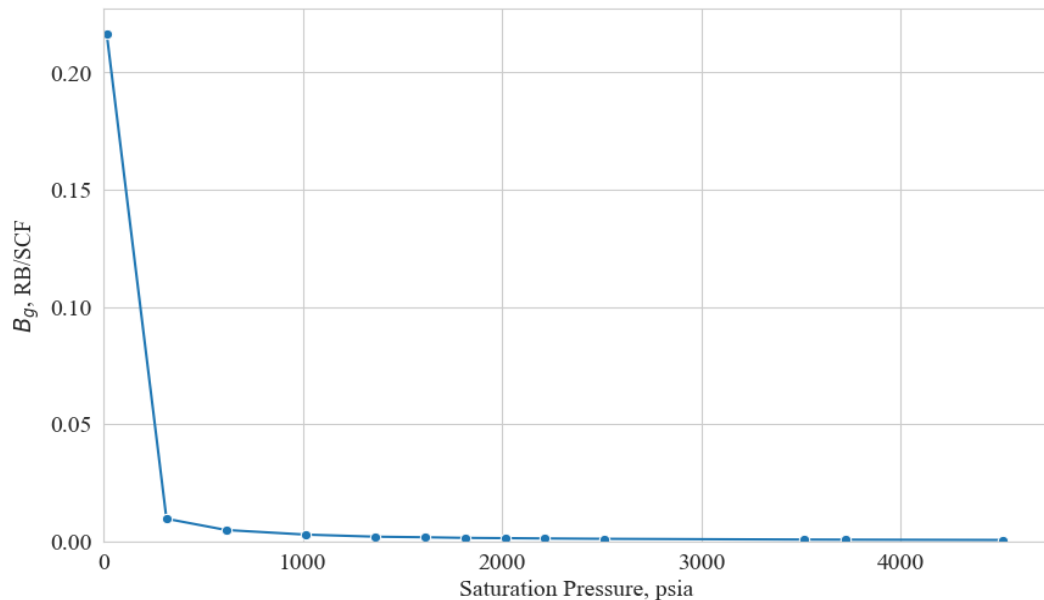


**Figure 15.3:** The formation volume factor of gas behavior with respect to pressure.

Another important parameter for the sake of the material balance approach is the cumulative oil production ( $N_p$ ). As the name implies, it stands for the summation of the production volumes up to the last production record. From the mathematical perspective, it should be increasing with respect to elapsed time. Based on the Mount Doom Oil Field's production data, Figure 15.4 was obtained; thus, this theoretical behavior was observed. However, there are some ranges in which the cumulative production has stayed fairly constant. To understand this behavior, an inspection of the average reservoir pressure ( $\bar{P}_r$ ) could be helpful.

As can be seen from Figure 15.1, the formation volume factor of oil is a function of pressure. That's why since the average reservoir pressure decreases with continuous production, the formation volume factor of oil changes. To compensate for this effect of the reduction in the pressure levels, it was found to be important to trace the average reservoir pressure along with the production. As a result of this objective, Figure 15.5 was obtained. The benefit of this graph is that it enables the comparison of the average reservoir pressure reduction concerning continuous production. Based on Figure 15.5, one can observe a sharp decrease in the average reservoir pressure in the 150<sup>th</sup> month along with a sharp increase in the cumulative oil production. This was found to be logical since the more the production, the more reduction in the pressure. On the other hand, several fairly constant pressure levels at times where the production has remained almost the same were observed. Lastly, the average reservoir pressure was found to be always greater than the bubble point pressure at all times.

Since the average reservoir pressure is above the bubble point pressure at all times, Figure 15.1's right hand-side, which is the part that above the bubble point pressure, was taken to perform a regression line. With the help of this regression line, the continuous change in the bubble point pressure was aimed to be compensated. Based on this aim, Figure 15.6 was obtained, and its regression equation along with the r-squared value was presented. Since the r-squared value is 1, it can be said that the estimated linear equation for the prediction of the formation volume factor of oil is representative. The same approach can be applied to predict the formation volume factor of gas change concerning decreasing pressure above the bubble point. To achieve this, the data was separated into two parts as above the bubble point pressure, and below the bubble point pressure. Moreover, since the reservoir is in the undersaturated region, the polynomial regression line was fitted on above the bubble point part. As a result of this, Figure 15.7 was maintained; and it will be used to predict the  $B_g$  values with the decreasing pressure as the r-squared value is 0.98.

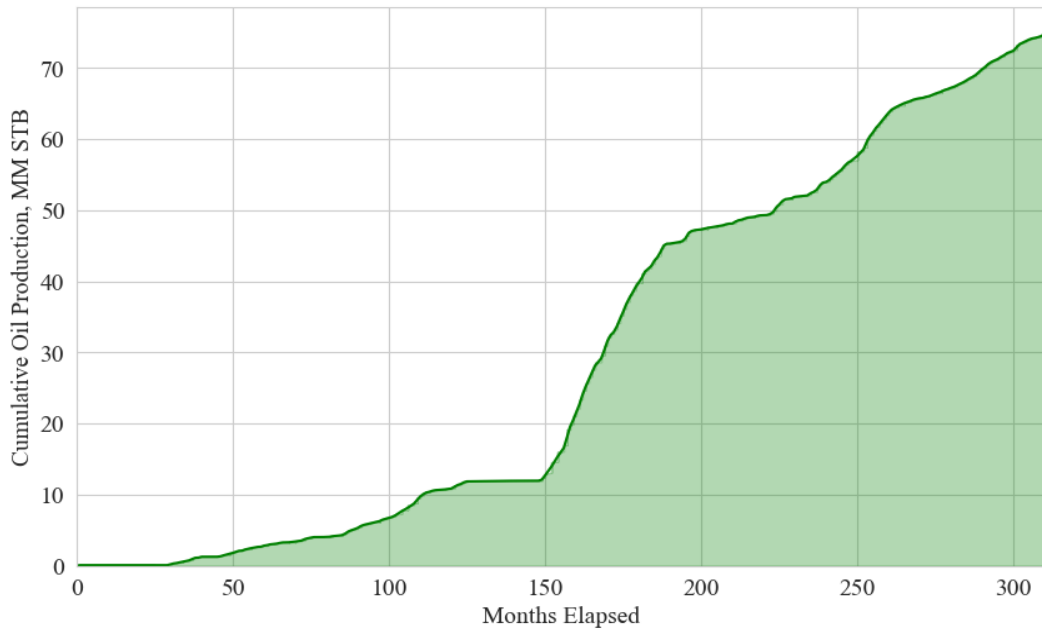


**Figure 15.4:** Cumulative oil production volume with respect to elapsed month.

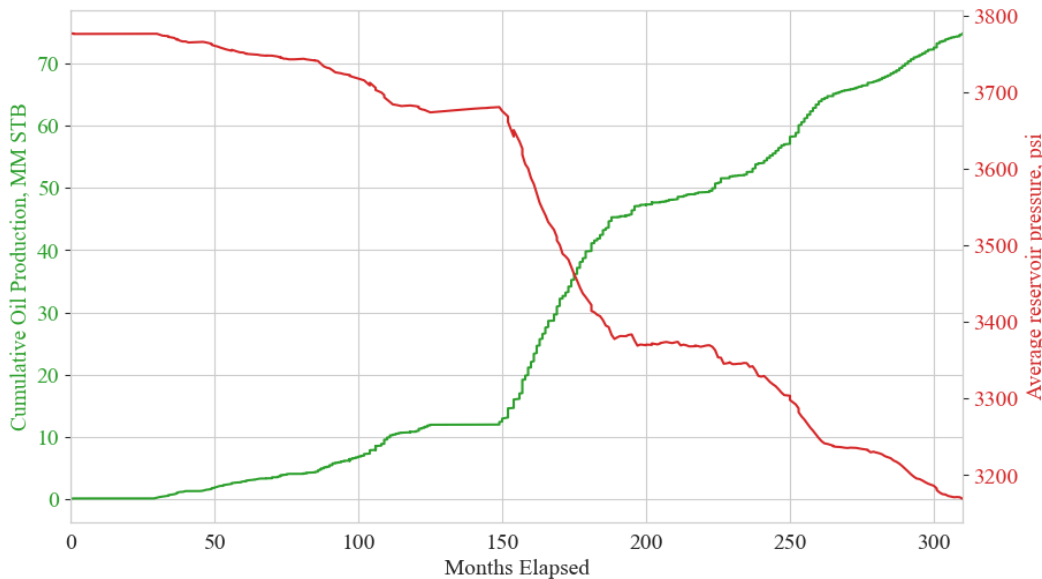


**Figure 15.5:** Average reservoir pressure reduction along the cumulative oil production.

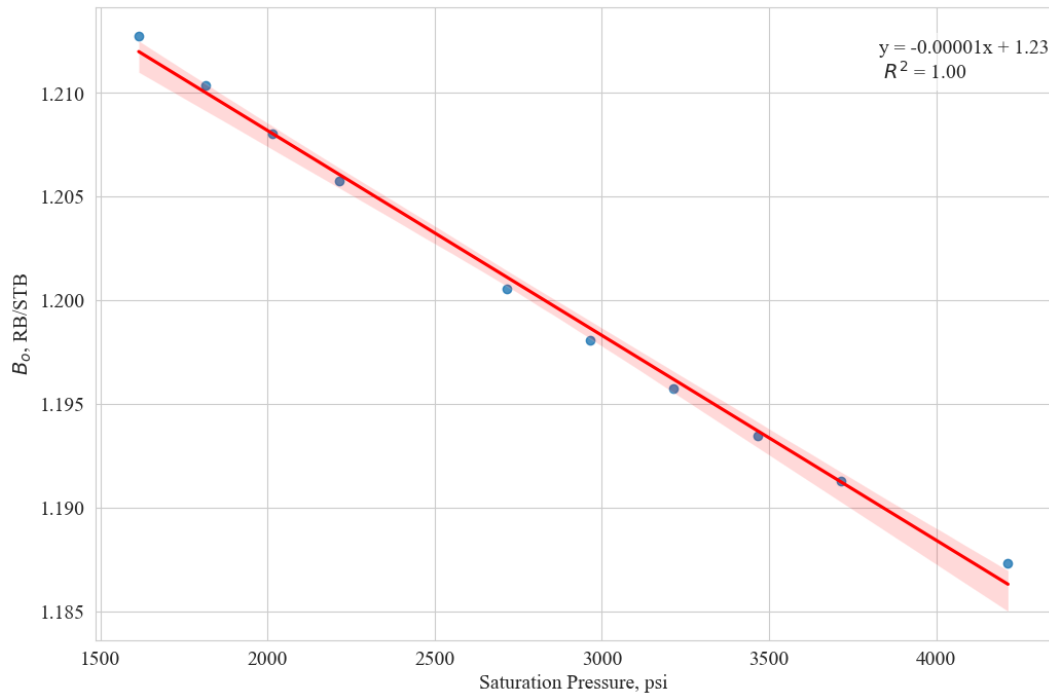


**Figure 15.6:** Regression line for the values above the bubble point pressure on the formation volume factor of oil with the 95% confidence interval.

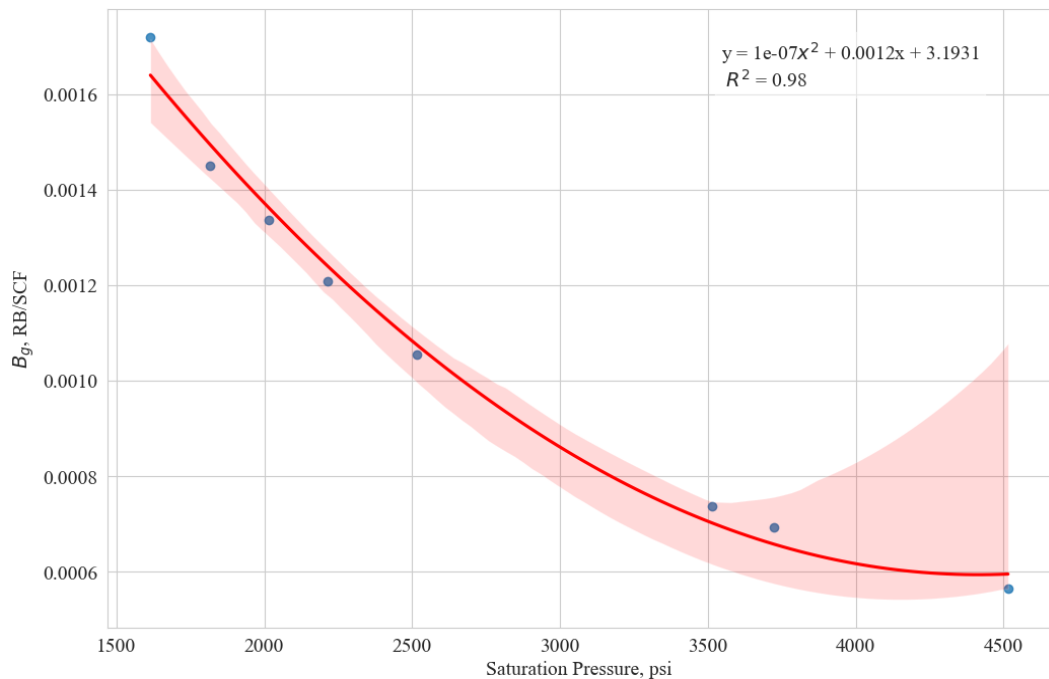


**Figure 15.7:** Regression line for the values above the bubble point pressure on the formation volume factor of gas with the 95% confidence interval

The last parameter that has to be reviewed, and calculated is cumulative produced gas-oil ratio. As the name implies, the total volume of gas produced in relation to the volume of oil produced from a reservoir over time is represented by the cumulative produced gas-oil ratio ( $R_p$ ).  $R_p$  sheds light on the behavior of the reservoir during production. It aids engineers in comprehending the evolution of gas and oil production. Precise  $R_p$  values are essential for optimizing field development plans and calculating recoverable reserves. For that reason, by using the available production data, the cumulative produced gas-oil ratio values were calculated as a function of elapsed time, and the result was demonstrated in Figure 15.8.

## **15.2.Havlena and Odeh Straight Line Approach**

The general material balance equation was firstly introduced by Schilthuis in the history (Craft, Hawkins, & Terry, 1991). Basically, it states that the algebraic sum of the volume changes on oil, free gas, water, and rock volumes must be zero since volume of the reservoir is constant. This physical understanding can be represented as in (Eq. 15-1). If those physical meanings were written in the mathematical form, the general material balance equation becomes as given in (Eq. 15-2) (Craft, Hawkins, & Terry, 1991).

$$\begin{aligned}
 & [\text{Oil Expansion}] + [\text{Gas Expansion}] && (\text{Eq. 15-1}) \\
 & + [\text{Change in the Void Space Volume}] \\
 & + [\text{Water Influx}] \\
 & = [\text{Oil and Gas Production}] + [\text{Water Production}]
 \end{aligned}$$

$$N(B_t - B_{ti}) + \frac{NmB_{ti}}{B_{gi}}(B_g - B_{gi}) + (1 + m)NB_{ti} \left[ \frac{c_w S_{wi} + c_f}{1 - S_{wi}} \right] \Delta \bar{P}_r \quad (\text{Eq. 15-2})$$

$$+ W_e = N_p [B_t + (R_p - R_{soi})B_g] + B_w W_p$$

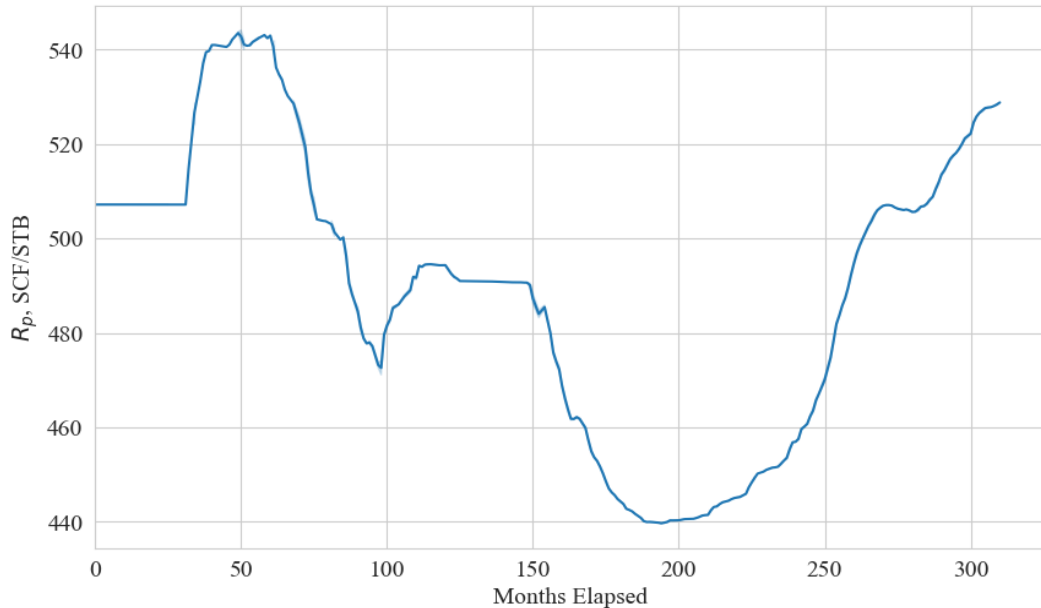


**Figure 15.8:** The cumulative produced gas-oil ratio with respect to the elapsed time.

Considering the character of the Mount Doom Oil Field's reservoir, a few changes can be applied on (Eq. 15-2). First of all, the reservoir fluid is a black oil, hence the drive mechanism is solution-gas drive. Furthermore, the average reservoir pressure always greater than the estimated bubble point pressure; which means that the reservoir is undersaturated. Lastly, no water production has been observed until the last production recording. Combining all of these considerations, following terms can be ignored from (Eq. 15-1): Gas Expansion, Water Influx, and Water Production. In conclusion, the general material balance equation can be simplified as given in (Eq. 15-3).

$$N(B_t - B_{ti}) + NB_{ti} \left[ \frac{C_w S_{wi} + C_f}{1 - S_{wi}} \right] \Delta \bar{P}_r = N_p [B_t + (R_p - R_{soi}) B_g] \quad (\text{Eq. 15-3})$$

The total formation volume factor states the combined effect of the two-phase fluid, meaning the oil and gas (Dake, 1978). This effect can be related to (Eq. 15-4) (Craft, Hawkins, & Terry, 1991). Furthermore, one can notice that the total formation volume factor becomes the oil formation volume factor since the average reservoir pressure is greater than the bubble point pressure. This phenomenon leads the initial solution-gas oil ratio to be equal to the solution-gas oil ratio. Hence, the  $B_g(R_{soi} - R_{so})$  term becomes zero. In addition, the initial total volume factor ( $B_{ti}$ ) equals the initial oil volume factor ( $B_{oi}$ ).

$$B_t = B_o + B_g(R_{soi} - R_{so}) \quad (\text{Eq. 15-4})$$

Furthermore, Havlena and Odeh proposed an approach to linearize the general material balance equation for interpretation purposes (Craft, Hawkins, & Terry, 1991). The main idea behind the linearization method was the reduction in the terms in the general material balance equation such that it becomes a linear equation. Thus, once it is plotted, the slope of the linear line, which passes through the origin, becomes the OOIP. Considering the conditions, and character of the Mount Doom Oil Field, the Havlena and Odeh linear equation can be written as in (Eq. 15-5). Moreover, F and  $E_0$  terms were given in (Eq. 15-6) and (Eq. 15-7) (Craft, Hawkins, & Terry, 1991). Lastly, the  $E_{fw}$  term in (Eq. 15-6) was given in (Eq. 18-16).

$$F = NE_0 \quad (\text{Eq. 15-5})$$

$$F = N_p [B_t + (R_p - R_{soi})B_g] = NE_0 + NB_t E_{fw} \quad (\text{Eq. 15-6})$$

$$E_0 = B_t - B_{ti} \quad (\text{Eq. 15-7})$$

$$E_{fw} = \left[ \frac{c_w S_{wi} + c_f}{1 - S_{wi}} \right] \Delta \bar{P}_r \quad (\text{Eq. 15-8})$$

Moreover, the following terms in (Eq. 18-16) was already given from laboratory analysis: the water compressibility factor ( $c_w$ ), initial water saturation ( $S_{wi}$ ), and formation compressibility ( $c_f$ ). Hence, these properties were summarized in Table 15.1, and assumed to be constant during the depletion of the reservoir fluid.

**Table 15.1:** The given properties of the reservoir fluid, and the formation.

<b><math>S_{wi}</math>, fraction</b>	<b><math>c_w</math>, <math>\text{psi}^{-1}</math></b>	<b><math>c_f</math>, <math>\text{psi}^{-1}</math></b>
0.16	$2.87 \times 10^{-6}$	$3.93 \times 10^{-6}$

Calculating the given parameters through (Eq. 15-5) to (Eq. 18-16), and plotting the graph of  $F$  versus  $E_0 + B_{ti}E_{fw}$  along with fitted linear line was represented in Figure 15.9. Once the resulting figure is inspected, one can conclude that the slope is 9142.8; which means that the OOIP is 9.14 MMM STB. Comparing the results obtained from the stochastic volumetric reserves estimation, and the OOIP estimated from Havlena and Odeh's straight-line approach, the reserve obtained from the straight-line approach was found to be around the P50 value, which is 8.88 MMM STB. Note that this reserves estimation was performed on the Precious-1 reservoir layer since the given production data only includes the production volumes from the Precious-1 reservoir layer.

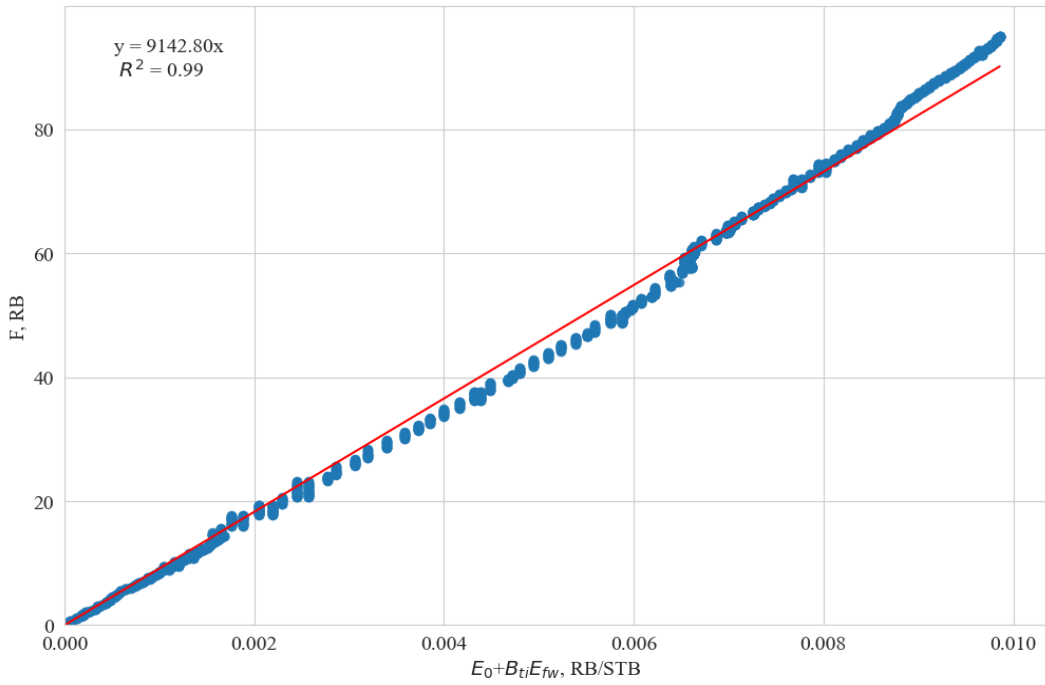


**Figure 15.9:** The Havlena and Odeh straight-line approach reserves estimation for the Precious-1 reservoir layer.

However, since the straight-line does not fit all of the acquired data, care should be taken. Referring back to (Eq. 15-5), the  $F$  value should be equal to the product of  $NE_0$ . In addition, by looking into the pressure decline behaviour during the period of 25 years of production, there should be water influx encroaching from an aquifer to sustain such pressure decline.

### 15.3.Reservoir Simulation Input Parameters

In simulation studies, reservoir input parameters such as porosity, permeability, and fluid characteristics, are important since they form the basis of realistic reservoir models. Simulation models that accurately depict reservoir features help predict fluid flow, estimate reserves, and optimize production strategies. Understanding parameter uncertainty facilitates sensitivity analysis, which leads to trustworthy simulation results.

In the Reservoir Engineering section  $B_o$  and  $R_s$  graphs were given, thus the bubble point pressure was already estimated as 1614.7 psi.

The graph that was displayed in Figure 15.10 illustrates the change in oil viscosity with pressure reveals details about the reservoir oil's properties. According to this, the viscosity of oil without solution gas, commonly known as dead oil viscosity, was found to be 14.585 cp, while the bubble point pressure is 1614.7 psi as it was previously determined (Craft, Hawkins, & Terry, 1991).

The  $B_g$  versus pressure graph given in Figure 15.11 indicates that with increasing reservoir pressure, the saturated gas in the oil will start to expand in order to take up space in the reservoir. Thus, this statement agrees with the high compressibility value for gases.

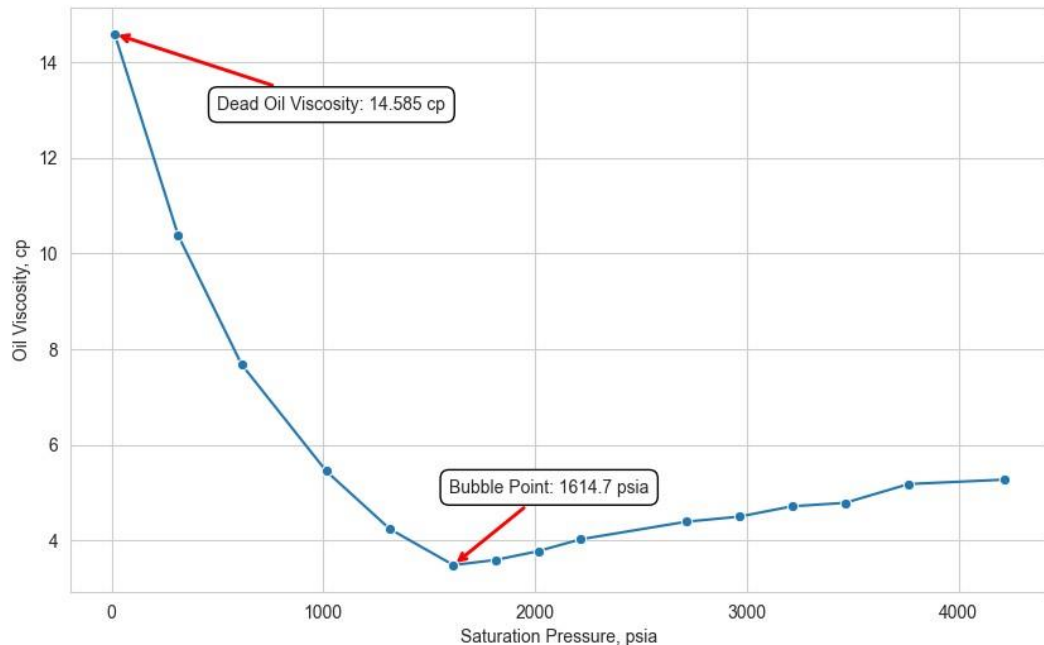


**Figure 15.10:** The viscosity of oil behaviour with respect to the pressure.

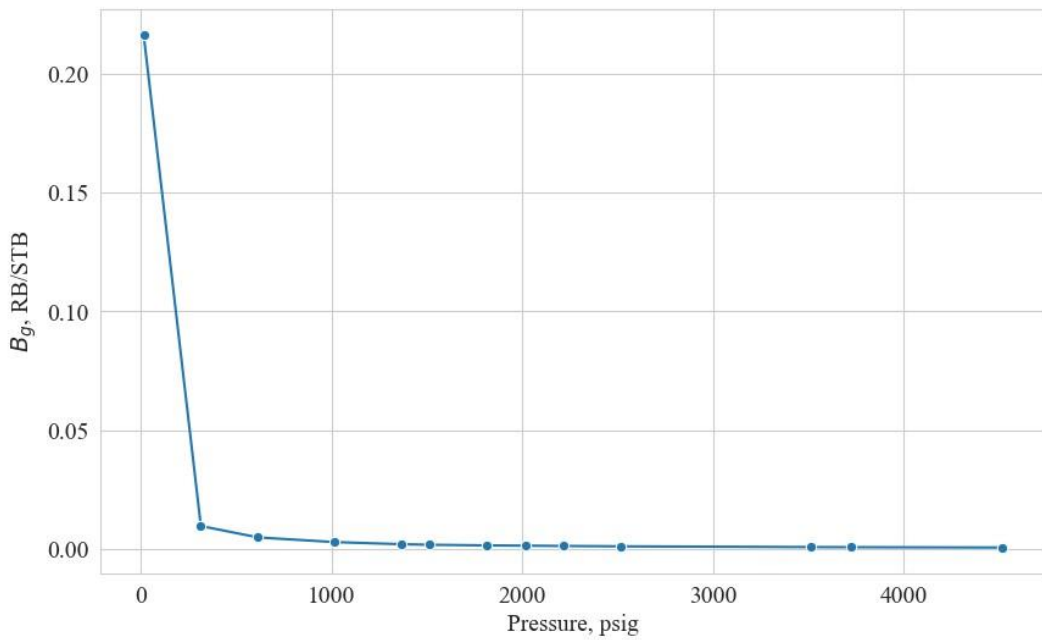


**Figure 15.11:** The formation volume factor of gas behavior with respect to the pressure.

The behavior of gas viscosity with respect to pressure is shown in Figure 15.12, satisfies the fact that increased pressure values will create a stronger intermolecular force, causing the flow of gas molecules to become more difficult. Moreover, in such conditions, gas molecules approach to the fluid behaviour in terms of the flow.

The wettability of the reservoir rock can be determined using relative permeability curves. By inspecting the relative permeability curves, irreducible water saturation ( $S_{wirr}$ ), residual oil saturation ( $S_{or}$ ) values are found to be 0.16, 0.3 respectively as shown in Figure 15.13.

According to the crossover point in Figure 15.13, where oil and water relative permeabilities are equal to each other, defines the wettability of the system. As the crossover point is around 0.46, the system can be indicated as water-wet as the water saturation at the crossover is  $S_w = 0.46 < 0.5$ . While this is true for imbibition curves, the opposite is true in migration cases. However, in field applications, the wettability is preferred to be used as mix-wet since the intersection point is significantly close to 0.5.

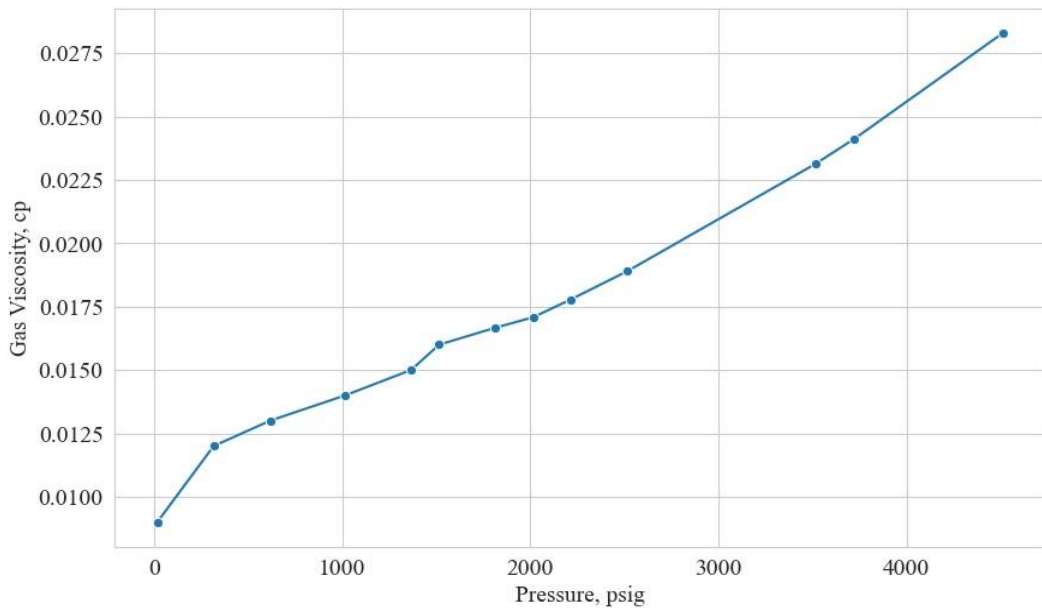


**Figure 15.12:** The viscosity of gas behaviors with respect to the pressure.

Based on the article called “Studying the effect of wettability heterogeneity on the capillary pressure curves using the centrifuge technique”, the research on various carbonate reservoirs in the Middle East, it was discovered that when oil saturation rises above the free water level (FWL), so does the proportion of oil-wet pores. Furthermore, the wettability of oil-filled pores can shift towards oil-wet or mixed-wet conditions, even at oil saturations as low as 20-30% (Masalmeh S. K., 2002).

On the other hand, based on Figure 15.14, critical gas saturation ( $S_{gc}$ ) can be observed as 0.278. Thus, critical gas saturation is defined as the level where the saturation level below which gas begins to mobilize during a gas flood within initially oil and/or water-saturated porous media (Iglauer, 2013). The term wettability brings another important component in oil recovery: capillary pressure. Capillary pressure can be represented as a capillary tube transporting both oil and brine, with the oil having a lower density than the brine. In this situation, the pressure in the oil phase above the oil-brine contact in the capillary tube will be somewhat higher than the pressure in the water phase just below the interface. The pressure difference between phases is used to define the system's capillary pressure, thus the highest pressure is always observed on nonwetting phase (Craft, Hawkins, & Terry, 1991).

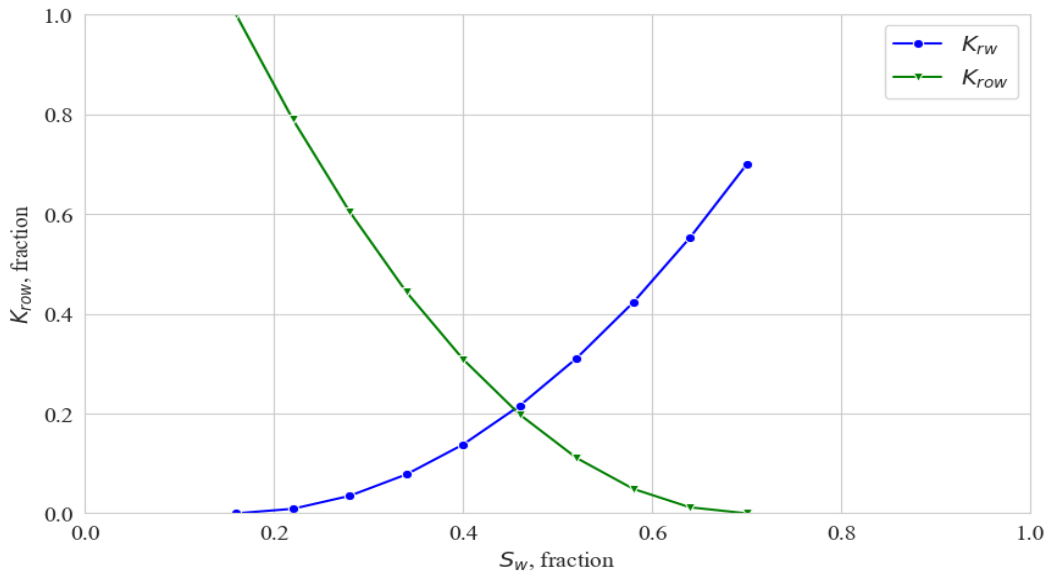


**Figure 15.13:** The relative permeability curves for oil, and water phases.

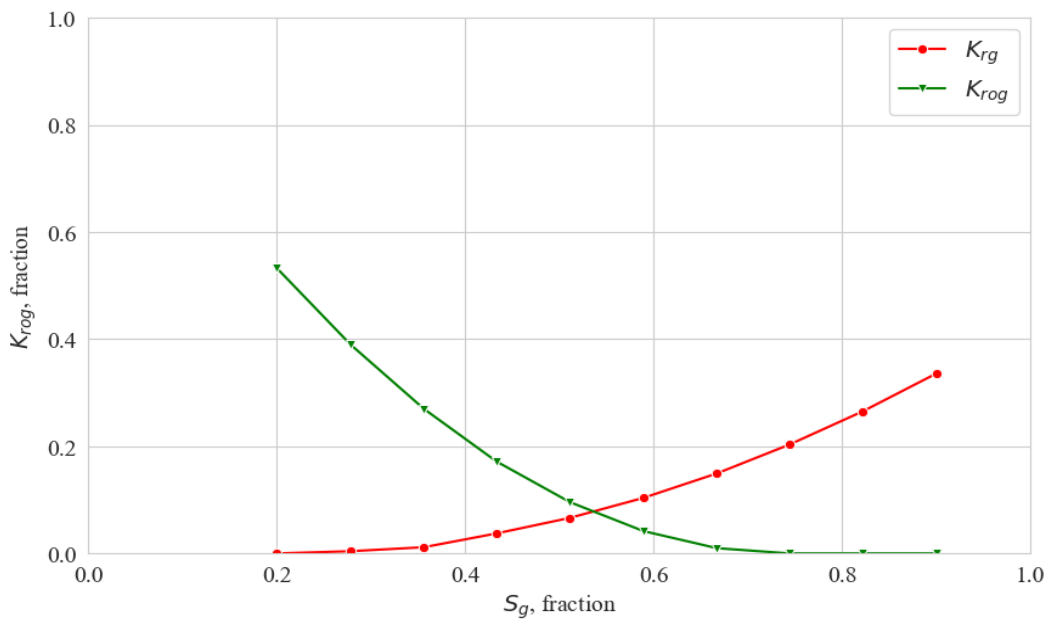


**Figure 15.14:** The relative permeability curves for oil, and gas phases.

In Figure 15.15, the capillary pressure curve for oil-water system is illustrated. The free water level (FWL) can be observed where the capillary pressure ( $P_{cp}$ ) value is approximately zero. In addition to that, the curve showing the capillary rise behaviour changes sharply from the FWL line indicates a high permeability reservoir rock. Thus, the transition zone's height and saturation distribution are influenced by the variation and arrangement of pore sizes in the rock, as well as the interfacial forces and density contrast between the two non-mixing fluids. (Masalmeh, Shiekah, & Jing, 2007). Figure 15.16 shows the capillary pressure behaviour where the two immiscible fluids are oil and gas.

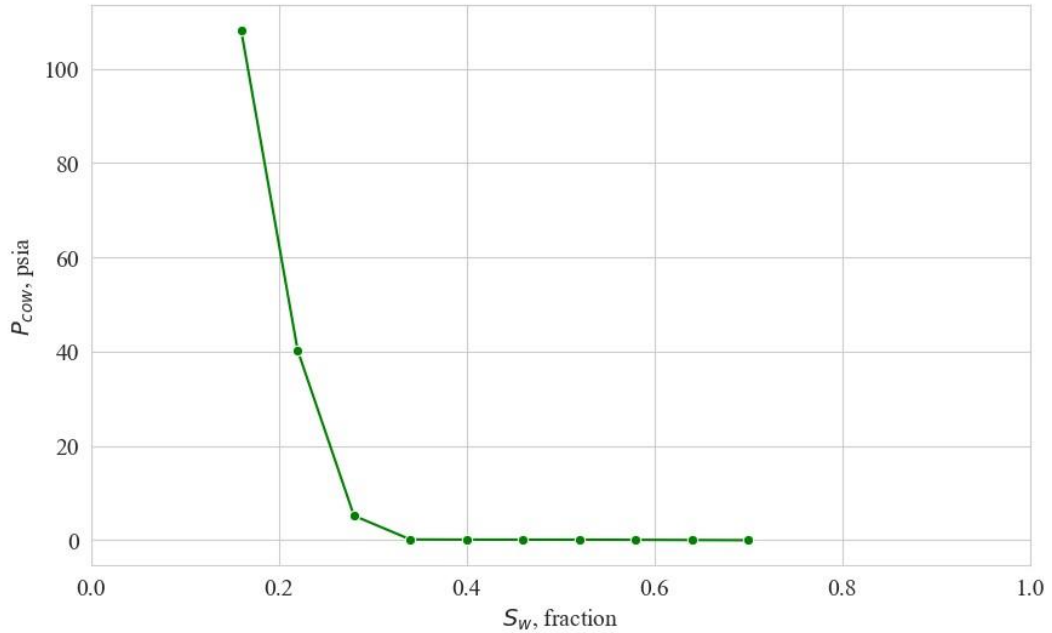


**Figure 15.15:** The capillary pressure curve for the oil-water system.

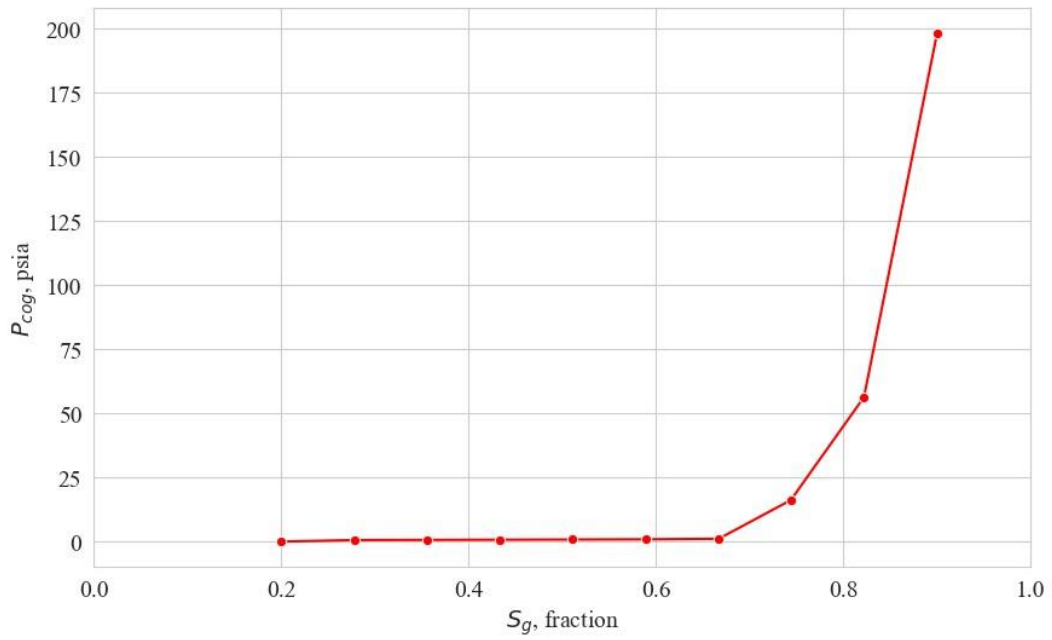


**Figure 15.16:** The capillary pressure curve for the oil-gas system.

#### 15.4.Reservoir Model and History Matching

History matching is a model validation technique based on the idea that if a model can reproduce the past, it may be useful in forecasting the future under a range of implementation circumstances (Abdulrazzaq & Hasan, 2023). For evaluating the reservoir performance and improving the future development strategies of the Mount Doom Oil Field, RUBIS was used as a software program.

As a first step for designing the reservoir simulation, the petrophysical properties that were obtained from the meticulous well log analysis such as effective porosity ( $\phi_e$ ), permeability ( $k$ ), thickness ( $h$ ), net to gross ratio (NTG), and top of reservoir were inputted in RUBIS, then distribution maps of those parameters were sketched. The provided topographic map of the 25 wells located in the Mount Doom Oil Field were rescaled and information of each well was loaded. Based on trial and error, a boundary for the whole reservoir was drawn. Afterwards, the petrophysical properties were uploaded as input data into the promising simulation. In order to distribute those elements throughout the whole reservoir, Gaussian-Kriging method was used as an

interpolation technique. The distribution maps of those parameters are shown in Appendix A.

Reservoir input parameters were precisely explained in the previous section. Formation volume factor of oil ( $B_o$ ), solution gas oil ratio ( $R_s$ ), viscosity of oil ( $\mu_o$ ), formation volume factor of gas ( $B_g$ ), viscosity of gas ( $\mu_g$ ), relative permeability of oil and gas ( $k_o, k_g$ ), capillary pressure behaviour of oil-water and oil-gas ( $P_{cow}, P_{cog}$ ) were inserted into the focused-on simulation draft. It is also important to mention that the used  $B_w$  and  $\mu_w$  values, 1.0231 and 0.683 respectively, were taken as the values at reference point where the reservoir pressure is 3700 psi. Besides that, the free water level (FWL) was taken as 7700 ft as a reference.

By applying an extrapolation, an average daily production data of 25 wells was assigned through each day of the month from the beginning date of the production. After inserting those data, a simulation was first run without an aquifer to see the outcomes whether they are compatible with the average pressure, oil, gas and water flow rate values. At this stage, different combinations of boundaries such as constant pressure boundary, no flow boundary, faulting, or aquifer were tried until finding the optimum design for the reservoir. Based on the imputations, the reservoir model has a rhomboid shape with two no flow boundaries, two not hydraulically interconnected aquifers and consist of 6405 grids as shown in Figure 15.17. The properties of the aquifer that is located on the north and north-east edges of the model shown in blue have a volume of 35000 MM STB, porosity of 0.12, permeability of 200 md, and compressibility of  $3.9 \times 10^{-5} \text{ psi}^{-1}$ , while the properties of the aquifer that supports the reservoir from the bottom have a volume of 18000 MM STB, porosity of 0.12, permeability of 200 md, and compressibility of  $3.9 \times 10^{-5} \text{ psi}^{-1}$ . It is critical to note that those aquifer parameters were obtained by numerical methods rather than using Havlena and Odeh estimations. Lastly, a numerical model type of aquifer modelling was chosen instead of a conventional model like Fetkovich.

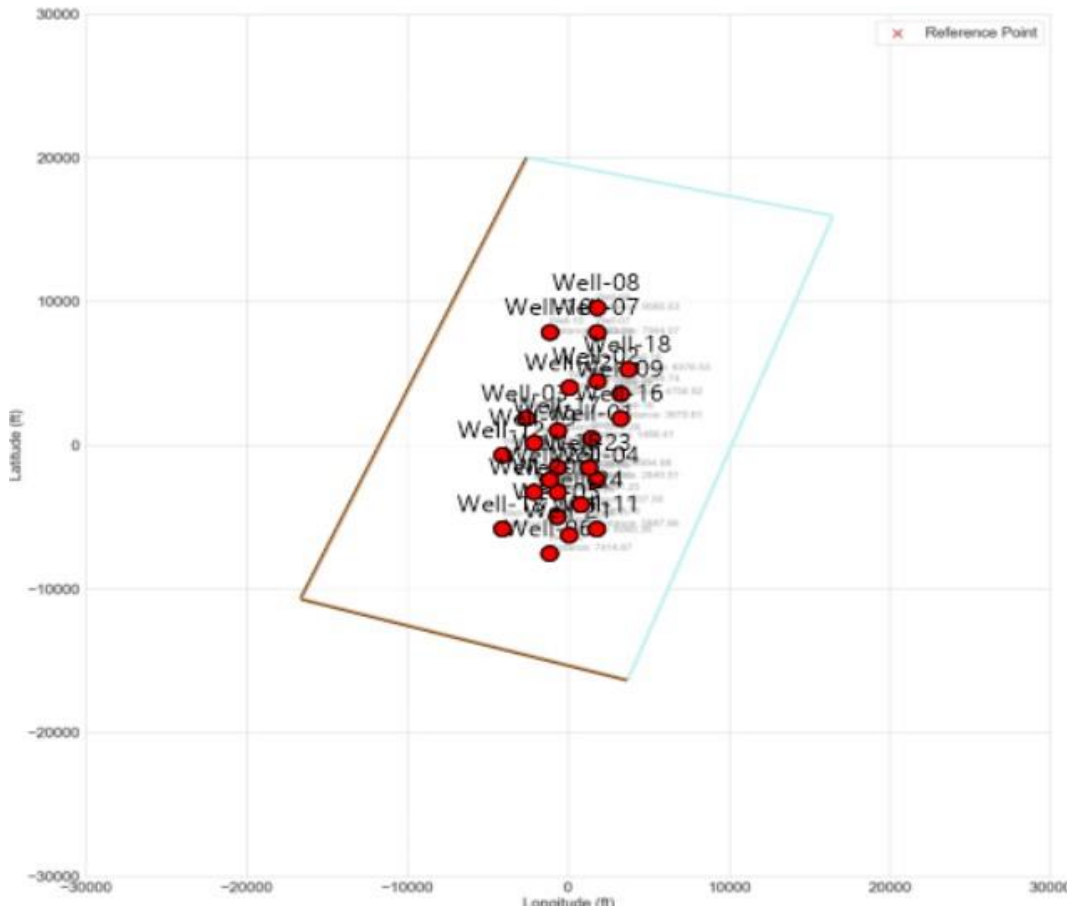


**Figure 15.17:** The model of the reservoir.

The OOIP value calculated by Havlena and Odeh method was 9.14 MMM STB while it is obtained as 1.04 MMM STB by the simulation. The reason for the inconsistency of those two values is explained by the presence of the provided aquifer support. Additionally, in the original data records there is no water production. However, in this improved simulation, the water production was estimated as 16 MM STB. Considering the fact that the provided data was started to be recorded in 1988, it is likely to have inconveniences in terms of reporting the water production values. Compatibility between the original and simulation outputs of reservoir pressure and cumulative oil production graphs as shown in Figure 15.18 and Figure 15.19 respectively, are strong indications of a probable missing data about water productions. Having the same starting and end data points for the both curves show an excellent simulation design. Based on meticulous observations, it can be expected to have water

production when the reservoir is strongly under the influence of aquifer influx. Figure 15.20 illustrates the cumulative oil and water production as a result of the simulation. Lastly, considering all of these matches in distinct but highly crucial parameters, the water production that was estimated from the simulation was found to be meaningful.

In conclusion, the overall goal of using RUBIS as a simulation program is to match the reservoir pressure and cumulative oil production data to the values obtained by using simulation. Designing the optimum model would help to forecast the production behaviour of Bane-01 in the future.

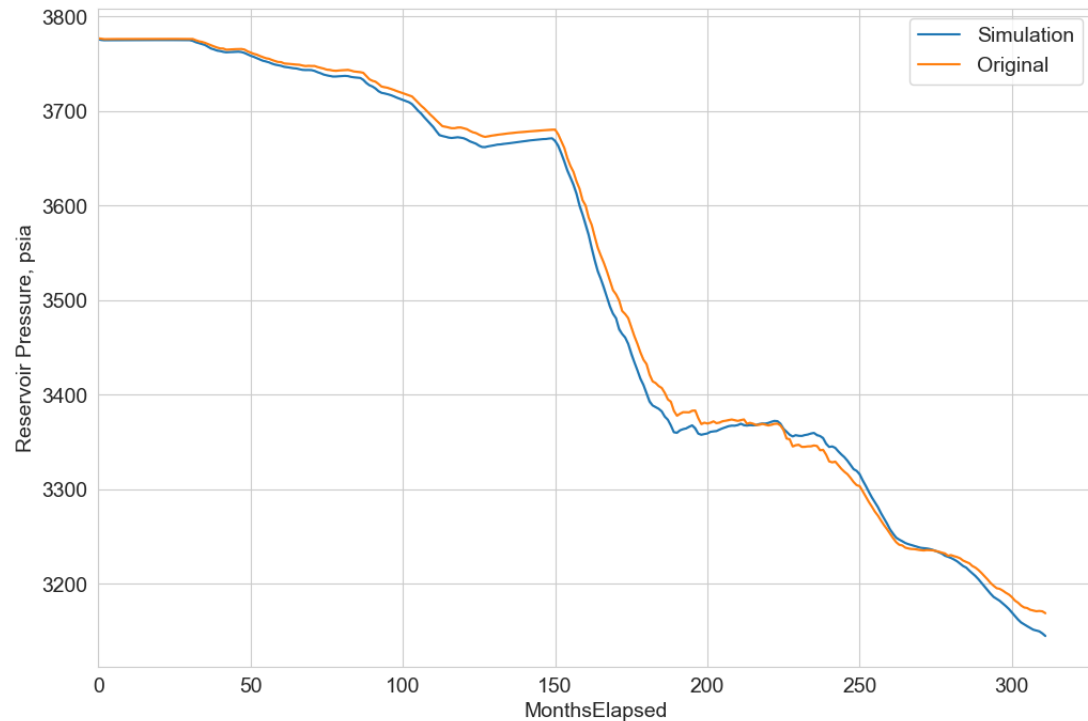


**Figure 15.18:** Average reservoir pressure comparison of original and simulation data.

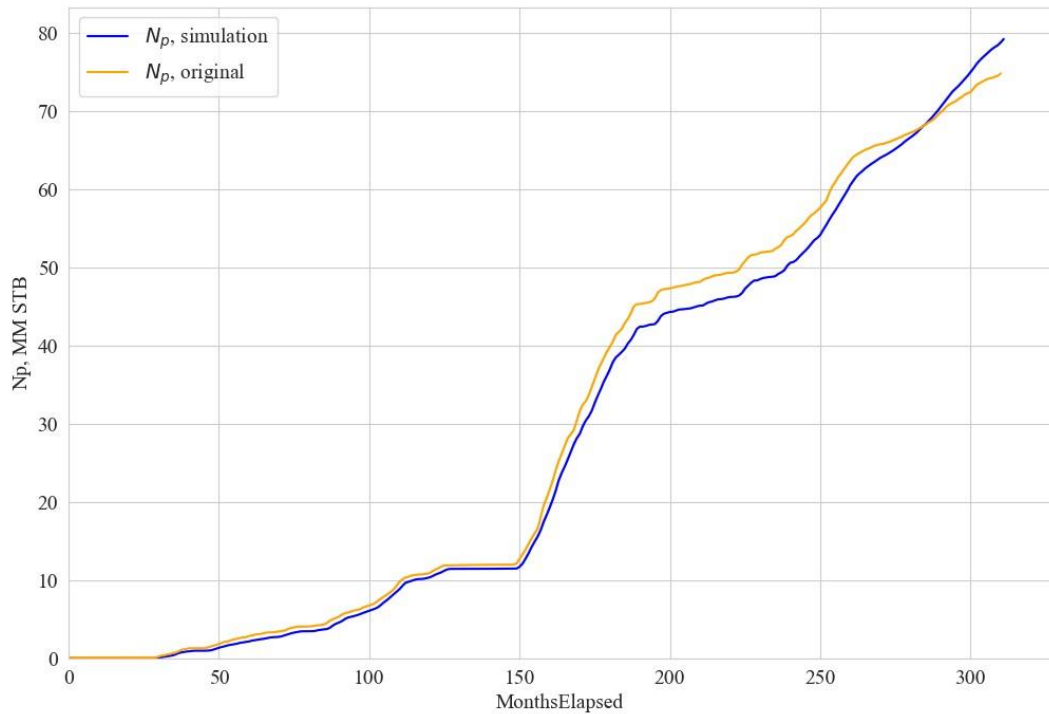


**Figure 15.19:** Cumulative oil production comparison of original and simulation data.

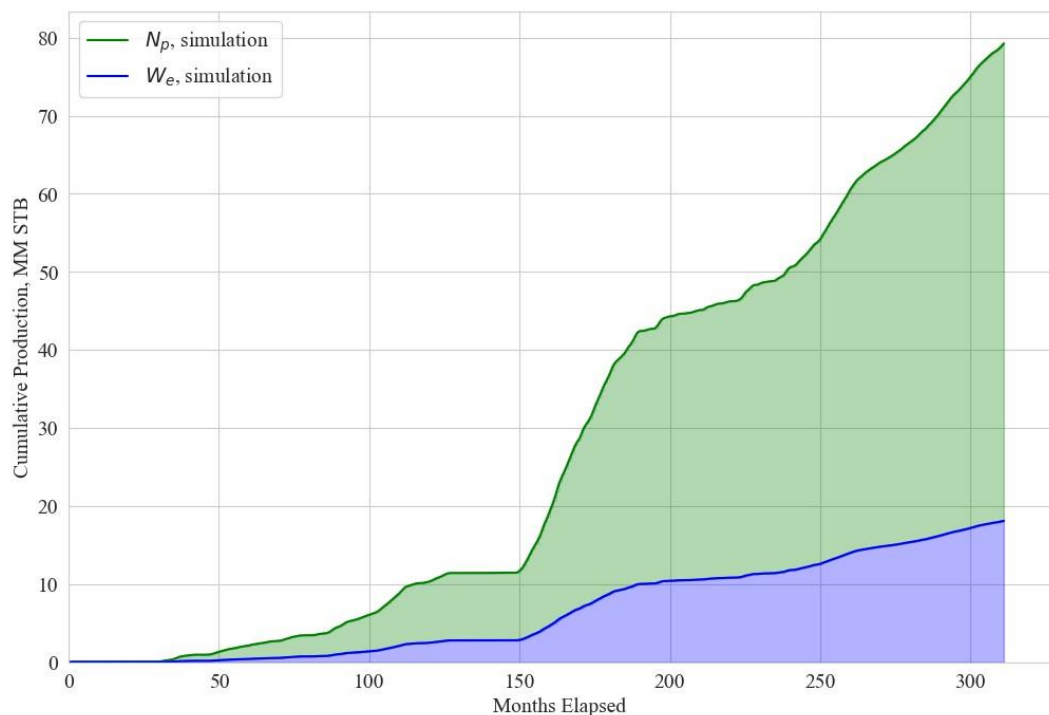


**Figure 15.20:** Cumulative oil and water production.

## **15.5.Results and Discussion**

Since one of the important parameters in the reservoir engineering is the average reservoir pressure, and its behaviors, the overall simulation can be said to be successful as the simulation outcome matches with the original data. On the other hand, as it was previously mentioned, the behaviour of the cumulative oil production, and the decline in average reservoir pressure had been correlating to each other by examining the original data. Moreover, one can also conclude the same fact by looking on Figure 15.18, and Figure 15.19.

To be informed more about the Precious-1 reservoir layer, it is highly important to examine the pressure distribution along the field. To achieve this objective, an animation from the simulation outcome was gathered, and it will be presented in the presentation. However, before the presentation, it can be said that thanks to the aquifer support from the edges, and bottom, the pressure decline has happened to be quite uniform through the reservoir. More importantly, the aquifer support from the bottom has enabled near-wellbore areas to have higher pressure values.

Despite the investigation of the history match on the reservoir parameters, the Lord of the Rigs Oil Company also examined the goodness of fits in each individual well. Hence, it was found that oil rates from each well also matched fairly well. To illustrate this, Figure 15.21 was displayed for the comparison purposes of Well-01's oil rates. As can be seen, even though there are some points that seem to be not matching, the simulation catches the general behaviour. Moreover, this could be caused due to the lack of production data. Because, once the production data were investigated, one can observe that there are times gaps between some measurement points, which could lead the simulation to take those gaps as shut-ins. Last but not least, since the last observation point in the average reservoir pressure is still larger than the bubble point pressure, the Mount Doom Oil Field persists its preciousness. To investigate this possible opportunity, one can try to understand the recovery factor of oil. To survey on this desire, the fractional recovery factor that was estimated from the simulation was displayed in Figure 15.21. As can be seen, the recovery factor is around 8% at the end of the simulation, which indicates a high potential of reaming oil reserves. In addition, it was found that the recovery factor behaves as same as the cumulative oil

production. Again, this is meaningful since the recovery factor is a function of the cumulative oil production.

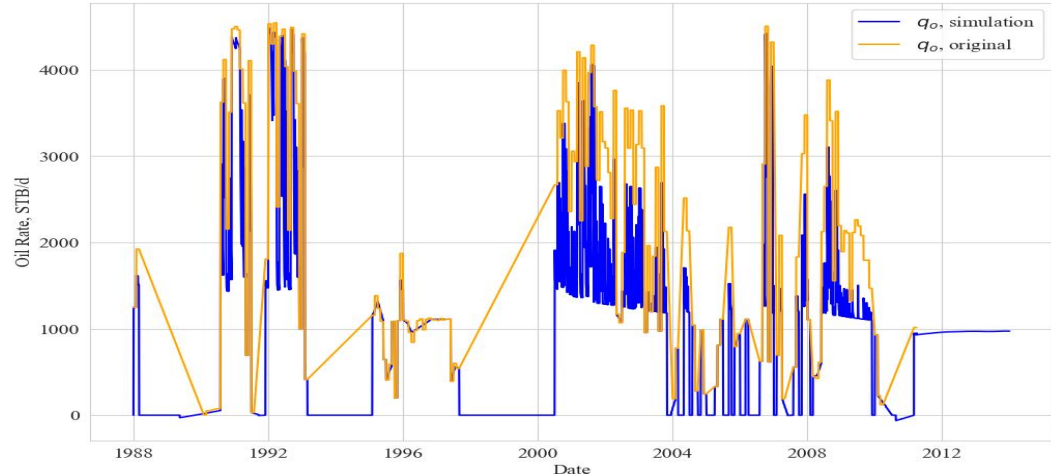


**Figure 15.21:** The comparison of oil rates for Well-01.

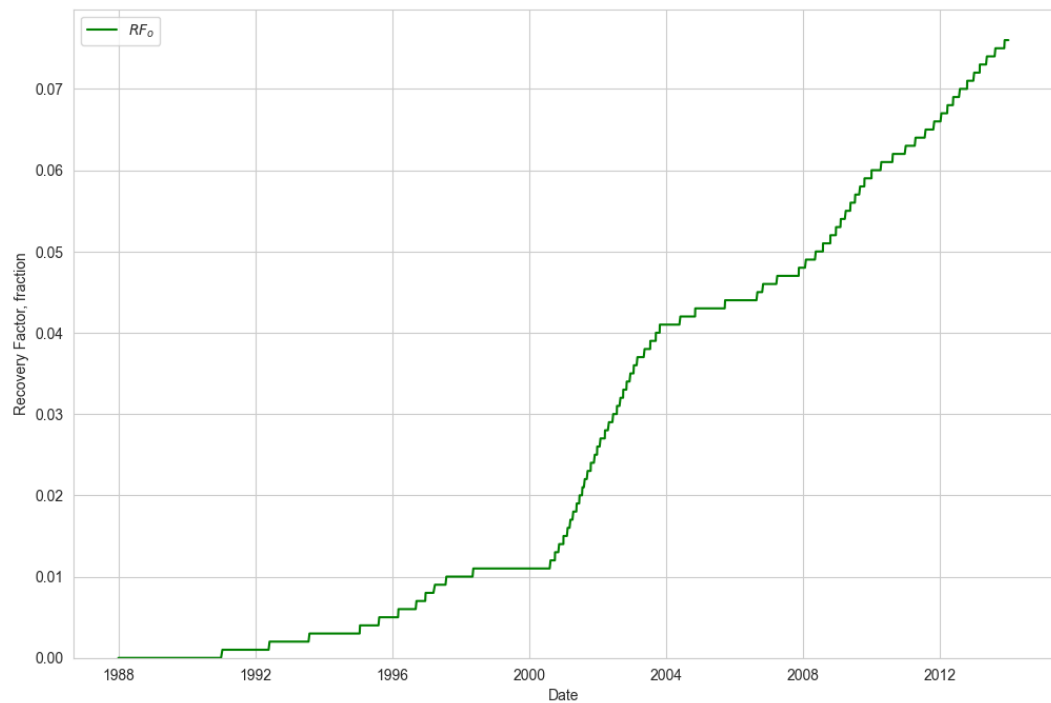


**Figure 15.22:** The oil recovery factor along the production.

## **15.6.Conclusion**

In this project, estimation of OOIP calculations based on both Havlena and Odeh and, reservoir simulation was aimed to be compared in order to design an optimum reservoir simulation model. It is important to develop a reservoir simulation model in order to overcome the uncertainties within the reservoir, and by applying history matching it was pursued to visualize the overall field and, also to forecast the future behaviors of Bane-01 and other development wells. The petrophysical parameters obtained from well log analysis of 25 previously drilled wells in the Mount Doom Oil Field were plugged into the simulation program RUBIS, with interpolation techniques. Thus, PVT properties were gathered from the laboratory experiments. The applied reservoir model was found to be explanatory and successful because the average reservoir pressure, cumulative oil production and behavior showed similarities over the years and matched at the starting and ending points.

## **16. ESTIMATION OF GAS PROPERTIES**

As demonstrated in the previous section, knowledge of gas properties is essential for designing an effective separator for specific operating conditions. Various methods proposed by scientists aim to determine gas mixture properties, with many relying on Kay's mixing rule (McCain, 1989). However, in the absence of specific information about the components of the produced natural gas, an assumption or approximation is necessary. Instead of making an assumption, we opted for an approximation method focused on estimating the gas's specific gravity. This property is crucial because it allows for the estimation of pseudoreduced properties of the gas, even when the gas mixture composition is unknown.

The approach involved an iterative technique that considers two key gas properties: the z-factor and gas viscosity. The z-factor, which represents the gas deviation factor, was estimated using the Abou-Kassem and Dranchuk correlation. Subsequently, once the z-factor was estimated using the correlation, a convergence algorithm was employed to match the real gas viscosity measurement obtained from PVT lab tests with the values predicted by the Lee Eakin and Gonzalez gas viscosity correlation. The iteration process continued until the desired level of accuracy was achieved, at which point the final estimated specific gravity of the gas was determined.

### **16.1.Dranchuk and Abou-Kassem (DAK) Z-Factor Correlation**

The Abou Kassem-Dranchuk correlation is primarily used in the oil and gas industry to estimate the gas deviation factor (z-factor) of natural gases. It is named after its creators, M. A. Abou-Kassem and P. M. Dranchuk. The Abou Kassem-Dranchuk correlation provides reasonably accurate results over a wide range of pressures and temperatures encountered in the oil and gas industry; this makes it a valuable tool for reservoir engineering, pipeline design and other applications where precise knowledge of gas behaviour is crucial. It is often implemented in software packages used for reservoir engineering or pipeline design. The correlation itself is quite complex and involves various parameters such as pressure, temperature and critical properties of the

gas. Correlation is an empirical equation derived from extensive experimental data and theoretical considerations. By fitting data, they have found the given correlation, (Eq. 16-1), along with (Eq. 16-2) (Dranchuk & Abou-Kassem, 1975).

$$z = 1 + \left( A_1 + \frac{A_2}{T_{pr}} + \frac{A_3}{T_{pr}^3} + \frac{A_4}{T_{pr}^4} + \frac{A_5}{T_{pr}^5} \right) \rho_r + \left( A_6 + \frac{A_7}{T_{pr}} + \frac{A_8}{T_{pr}^2} \right) \rho_r^2 - A_9 \left( \frac{A_7}{T_{pr}} + \frac{A_8}{T_{pr}^2} \right) \rho_r^5 + A_{10} (1 + A_{11} \rho_r^2) \frac{\rho_r^2}{T_{pr}^3} e^{(-A_{12} \rho_r^2)} \quad (\text{Eq. 16-1})$$

$$\rho_r = \frac{0.27 P_{pr}}{z T_{pr}} \quad (\text{Eq. 16-2})$$

Where;

$$P_{pr} = \frac{P_{\text{reservoir}}}{P_{pc}} \quad (\text{Eq. 16-3})$$

$$T_{pr} = \frac{T_{\text{reservoir}}}{T_{pc}} \quad (\text{Eq. 16-4})$$

The terms that are represent by A with subscripts are the regression coefficient for the estimated correlation. Hence, they are given in Table 16.1 (Dranchuk & Abou-Kassem, 1975). Lastly, the Dranchuk and Abou-Kassem z-factor correlation is applicable to following limits, and gives acceptable engineering error (Dranchuk & Abou-Kassem, 1975):

- $0.2 \leq P_{pr} < 30.0$  and  $1.0 \leq T_{pr} < 3.0$
- $P_{pr} < 1.0$ ;  $0.7 < T_{pr} \leq 1.0$

On the other hand,  $\rho_r$  term in (Eq. 16-1) stands for the reduced density, and can be calculated from (Eq. 16-2) (Dranchuk & Abou-Kassem, 1975). Moreover, as can be seen from (Eq. 16-1), there are pseudoreduced properties in the correlation. To overcome the ignorance on the gas mixture components, Sutton was developed a correlation to relate specific gravity of gas with the reduced properties. This correlation gives a proper error for the following limits:  $-0.57 < \gamma_g < 1.68$ ; hence, the expressions are given in (Eq. 16-5), and (Eq. 16-6) (Sutton, 1985).

$$P_{pc} = 756.8 - 131 \gamma_g - 3.6 \gamma_g^2 \quad (\text{Eq. 16-5})$$

$$T_{pc} = 169.2 + 349.5 \gamma_g - 74 \gamma_g^2 \quad (\text{Eq. 16-6})$$

**Table 16.1:** Regression coefficient for (Eq. 16-1) (Dranchuk & Abou-Kassem, 1975).

<b>A<sub>1</sub></b>	0.3265
<b>A<sub>2</sub></b>	-1.07
<b>A<sub>3</sub></b>	-0.5339
<b>A<sub>4</sub></b>	0.01569
<b>A<sub>5</sub></b>	-0.05165
<b>A<sub>6</sub></b>	0.5475
<b>A<sub>7</sub></b>	-0.7361
<b>A<sub>8</sub></b>	0.1844
<b>A<sub>9</sub></b>	0.1056
<b>A<sub>10</sub></b>	0.6134
<b>A<sub>11</sub></b>	0.721

## 16.2.Lee, Gonzalez, and Eakin (LGS) Gas Viscosity Correlation

To estimate the viscosity of gas under reservoir conditions, Lee et al. modified Starling and Ellington's (1964) method to derive correlations (Lee, Gonzalez, & Eakin, 1966). Eight natural gas mixes with specific gravities of less than 0.77 and measured data of pure component gases form the basis of the LGE correlation. Thus, based on a field experience, since the Mount Doom Oil Field's API gravity is around 27, the specific gravity of the associated gas cannot be greater than 0.77; which allows for the use of LGS correlation. The corresponding correlation is given in (Eq. 16-7), and its related parameters as in (Eq. 16-8) to (Eq. 18-16) (Lee, Gonzalez, & Eakin, 1966).

$$\mu_g = 10^{-4} K e^{X \rho_g Y} \quad (\text{Eq. 16-7})$$

$$K = \frac{(9.379 + 0.01607 M_w) T_{\text{reservoir}}^{1.5}}{209.2 + 19.26 M_w + T_{\text{reservoir}}} \quad (\text{Eq. 16-8})$$

$$X = 3.448 + \frac{986.4}{T_{\text{reservoir}}} + 0.01009 M_w \quad (\text{Eq. 16-9})$$

$$Y = 2.447 - 0.2224 X \quad (\text{Eq. 16-10})$$

## 16.3.Matching the Specific Gravity of the Associated Gas

As can be seen from the previous subsections, all of the correlations depend on the knowledge of the specific gravity of gas. Unfortunately, there is no information given regarding to the specific gravity of the associated gas that is being produced along with oil. Rather than making an assumption, an approximation method was established to

converge the real value of the specific gravity. To do that, the following methodology was performed step by step by using an iterative algorithm:

1. Estimate the z-factor using DAK correlation for a given specific gravity,  $\gamma_g$ .
2. Estimate the gas viscosity using LGS correlation for the same specific gravity,  $\gamma_g$ .
3. Compare the difference between the actual gas viscosity measurement with the predicted ones.
4. Repeat until the validation for different specific gravity values.

Using the described approach, the specific gravity of the associated gas was estimated to be 0.635 after 374 iterations. It's important to note that an error rate of 0.01 was used during the algorithm's execution, and the result is illustrated in Figure 16.1. The error rate of 0.01 is chosen to account for the variability in gas viscosity values, which typically vary from the second digit after the decimal point.

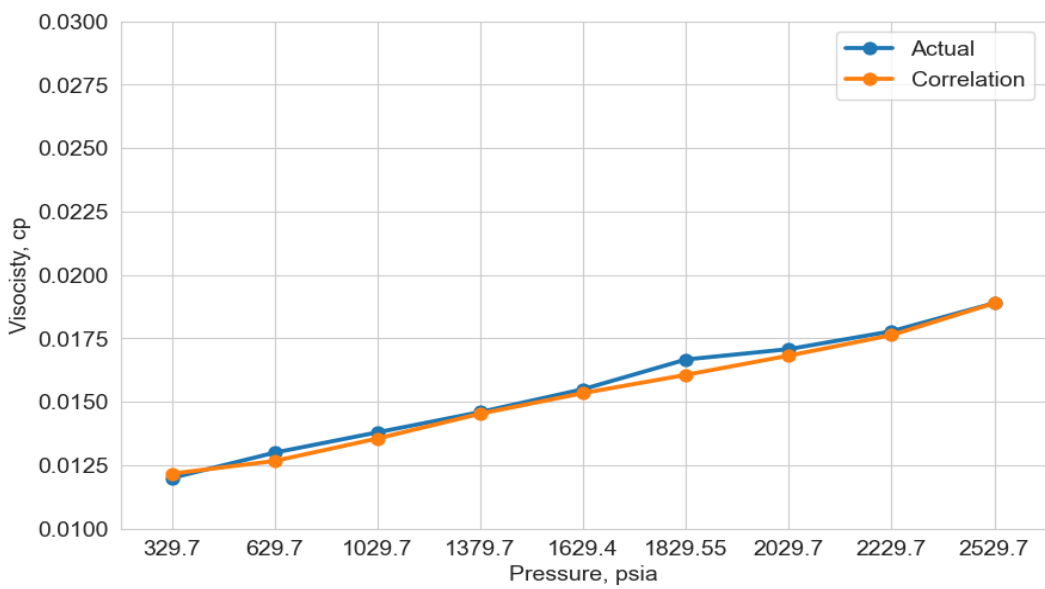


**Figure 16.1:** The gas viscosity matching based on the LGS correlation to estimate the specific gravity of the associated gas.

## 17. SIMULATION FORECASTS AND FIELD DEVELOPMENT PLANS

To effectively carry out field development scenarios, a robust methodology must be selected. Recently, simulations have become a widely adopted approach for forecasting production rates (Wang, et al., 2024). In this study, the simulation software Rubis, developed by Kappa Engineering, was employed. Various distinct scenarios were constructed to encompass different development possibilities. The ultimate objective was to devise the most advantageous field development plan, considering economic, environmental, and sustainability factors.

Moreover, including the base scenario, a total of four different field development plans were constructed. During the decision-making stage, the objectives were to maximize the net present value (NPV) of the project and to maximize the ultimate oil recovery rate (Litvak, Gane, McMurray, & Skinner, 2007). According to regulatory authorities, the base scenario was constructed with a wellhead pressure of 100 psia for each well after 31/12/2013, including the prospective well Bane-01. Additionally, all development plans were designed to be in production for 10 years. The conditions under which the economic evaluations will be performed are dictated by the authorities and are presented in Table 17.1.

**Table 17.1:** Economical properties used for the various field development scenarios.

<b>Interest Rate, %</b>	10
<b>Royalty Rate, %</b>	12.5
<b>Federal Tax Rate, %</b>	40
<b>Working Interest, %</b>	100
<b>Depletion Allowance, %</b>	20
<b>Oil Price, \$/bbl</b>	80
<b>Gas Price, \$/MSCF</b>	0
<b>Depreciation Method</b>	Method: Straight-line Salvage value to initial cost ratio: 10% Life of equipment used: 10 years
<b>Depletion Allowance Method</b>	Percentage depletion

The net present value (NPV) is defined as the present value of a project's cash inflows minus its cash outflows (Andersson, 2000). Given the value difference between present and future dollars, the net cash flow is discounted to calculate the present value of each yearly net cash flow at the project's reference date, which is the beginning of Year 1. A simple method is used to determine the present value ( $C_0$ ) of each future net cash flow ( $C_t$ ), using a discount rate ( $r$ ), where time ( $t$ ) denotes the year the net cash flow occurs, as measured from the reference date. The discount rate represents the company's cost of capital. (Eq. 17-1) shows the formula for calculating present value of a project. The cash flows' present values will be negative in the early years, but positive later on. The project's NPV is found by adding all of these present values together (Cook, 2021). Therefore, net present value can be calculated by using the formula stated in (Eq. 18-16).

A positive NPV indicates that the project is economically viable. When choosing between projects, the one with the highest NPV should be preferred, since calculating net present values allows converting future payments into present values to make a comparison (Andersson, 2000).

$$\text{Present Value } (C_0) = \frac{\text{Future Sum } (C_t)}{(1 + i^*)^{t_i^*}} \$ \quad (\text{Eq. 17-1})$$

$$\sum \text{Net Present Value} = \frac{\text{Future Sum } (C_t)}{(1 + i^*)^{t_i^*}} \$ \quad (\text{Eq. 17-2})$$

Rate of return (ROR) or internal rate of return (IRR) is defined as the point where the NPV becomes zero. IRR can be found by plotting discount rate versus NPV graph, or using an excel function. The first interpretation of the IRR surpasses the cost of capital, the project should be able to generate a positive NPV (Cook, 2021).

The division of the net present value (NPV) to the initial present value of capital investment gives the discounted profitability index which is a useful parameter in assessing the cost versus benefit of a project (Cook, 2021).

### 17.1. Base Scenario

The three-dimensional reservoir model was created using RUBIS, incorporating the processed data and resulting reservoir parameters. The base scenario simulation excluded any additional well drilling or enhanced oil recovery (EOR) techniques, providing a clear depiction of the field's natural performance. Figure 17.1 shows the cumulative discounted net cash flow over 10 years of production. After 0.04 months, the company reaches full profit, with significant economic indicators: an NPV of approximately \$2.728 billion, an ROR of 5,048%, and a DPI of 157. Net revenue after costs and depreciation is \$5.524 billion, while tangible capital investment is \$150 million.

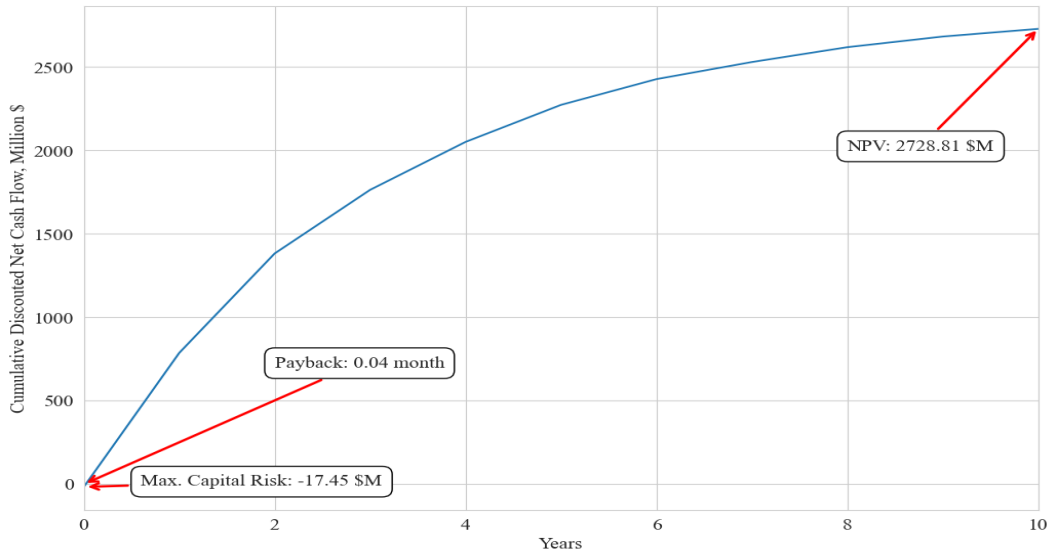


**Figure 17.1:** The cumulative discounted net cash flow in million dollars showing the project's breakthrough time

These figures demonstrate the project's strong economic viability and underscore the importance of maintaining a wellhead pressure of 100 psi to optimize output and

profitability over a 10-year period. Based on this base scenario, it can be concluded that the Mount Doom Oil Field continues to offer beneficial outcomes for further developments.

On the other hand, this massive project is driven by significant oil production over 10-years of production. Figure 17.2 illustrates the oil production versus water production for the base scenario. As shown, ultimate oil production reached 163.26 MM STB, while water production remained at 29.07 MM STB by the end of the 10-years of production forecast. This figure also suggests that water coning has not yet been observed, as the produced water at the end of the period is still lower than the oil production and does not hinder oil production.

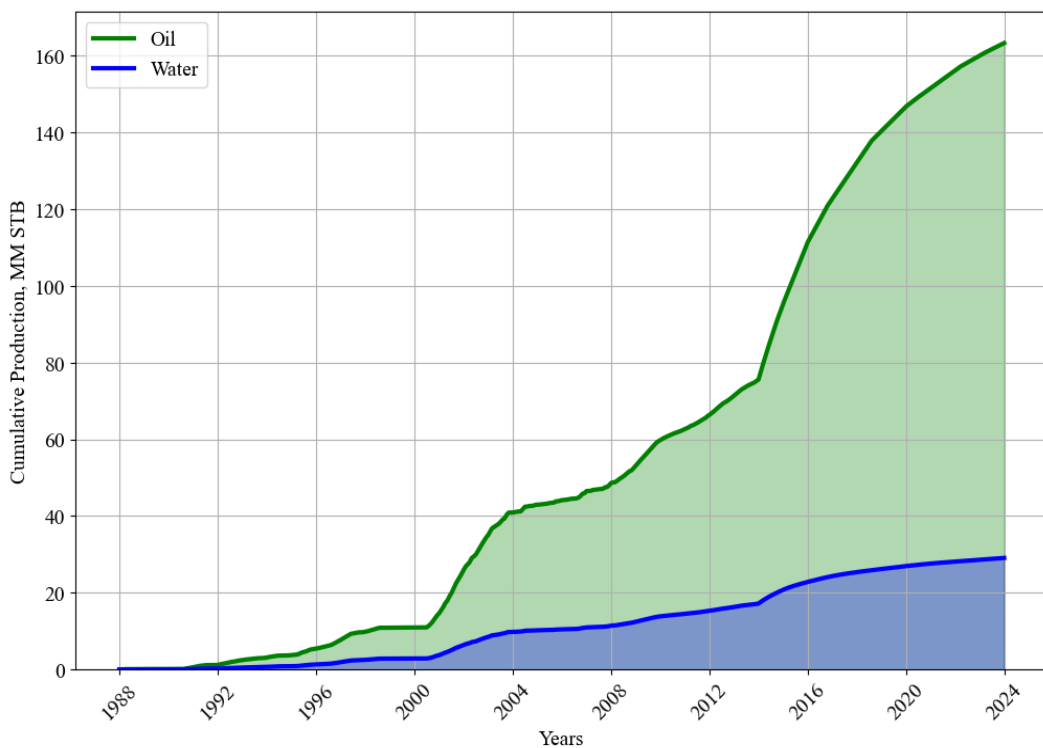


**Figure 17.2:** Oil production versus water production for the base scenario.

Furthermore, a crucial aspect of this investigation is evaluating the average reservoir pressure throughout the forecast period. To achieve this, the simulation outputs of cumulative oil production and average reservoir pressure values were cross-plotted and shown in Figure 17.3. This figure reveals that the average reservoir pressure remains above the bubble point pressure of 1614.7 psia. According to the simulation results, the average reservoir pressure at the end of the forecast is 2684 psia. Hence, it seems that the fluid flow enters pseudosteady state flow around year 2021; meaning that the rate change in the pressure decline is constant. Consequently, the Mount Doom Oil Field demonstrates its magnificent potential even in the base scenario.

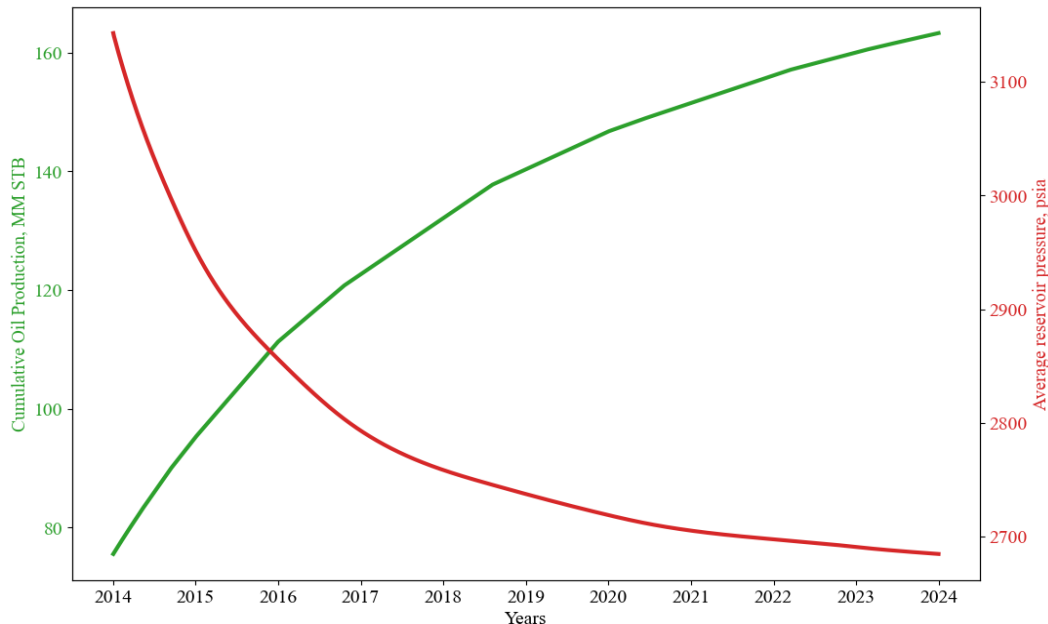


**Figure 17.3:** Average reservoir pressure profile along with the cumulative oil production throughout the forecast.

Lastly, the performance of the Bane-01 well was evaluated to inform decision-making processes. This involved examining the cumulative production of oil and water over the 10-years forecast period, as depicted in Figure 17.4. According to the simulation results and Figure 17.4, the total oil produced by the end of the period was estimated to be 5.5 MM STB, while the water production was 0.67 MM STB. These results

demonstrate that the Bane-01 well is strategically located, well-designed, and performs effectively. The substantial oil output coupled with minimal water production underscores the efficiency and productivity of the well, validating the strategic decisions made in its placement and engineering. This evaluation not only confirms the well's current performance but also provides a solid foundation for future planning and optimization efforts in the field.

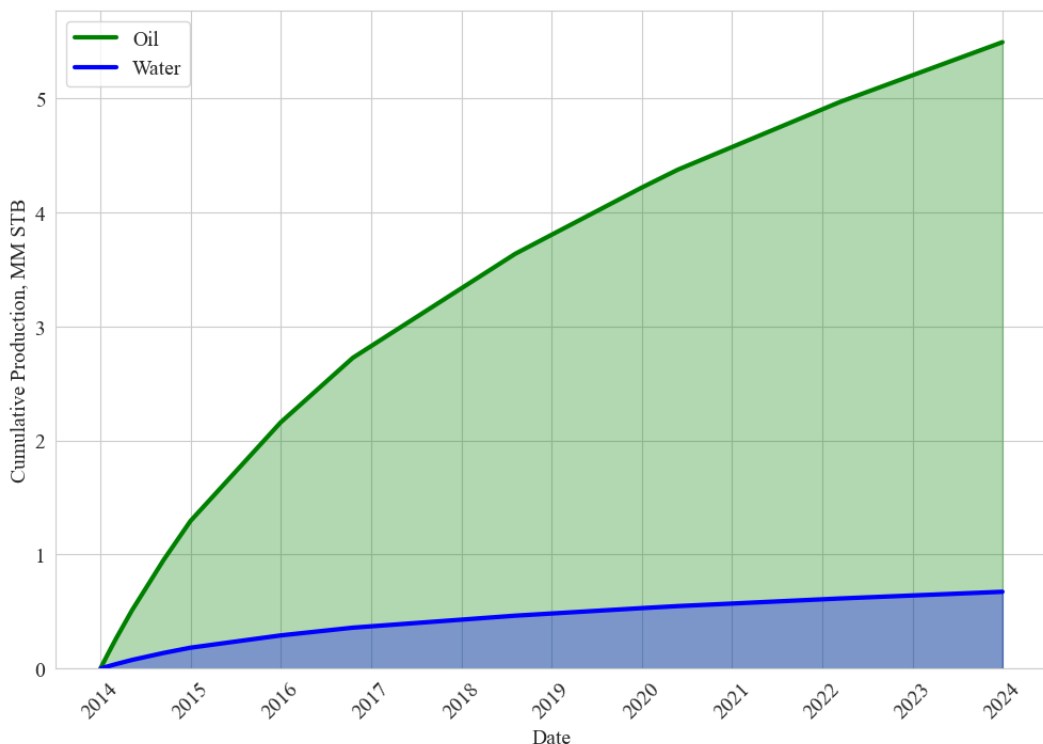


**Figure 17.4:** The cumulative oil produced along with water for Bane-01 during 10 years of production forecast.

To evaluate the relationship between the number of wells, cumulative oil production, and resulting net present value (NPV), various simulations were conducted. Six different simulation scenarios were analysed to calculate cumulative oil production and NPV. In each scenario, the number of wells was incrementally increased. The results, illustrated in Figure 17.5, show a positive correlation between the number of wells and NPV up to a certain point. For this particular oil field, the optimal number

of wells was determined to be 27, as this configuration yielded the highest NPV. Therefore, in subsequent scenarios, the number of wells will be maintained at 27.

Lastly, it is important to note that in each scenario, only vertical production wells were drilled, without any stimulation. Consequently, the economic analysis included the costs of drilling each well, their operating costs, and pipeline expenses.

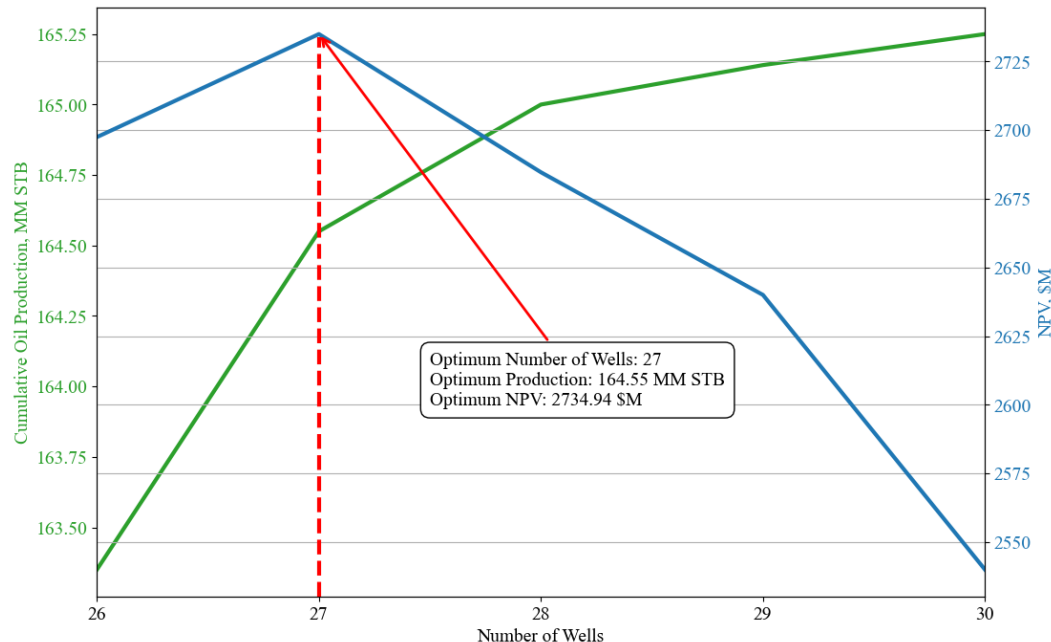


**Figure 17.5:** The relationship between number of wells, and the net present value.

## 17.2.Project: Watcher In the Water

In this simulation forecast scenario, it was tried to increase the cumulative oil production regimes, as well as the net present value of the overall project. To achieve this, one of the fundamental approaches was implemented in the Project Watcher in the Water. This approach is injecting the produced water to the reservoir so that the average reservoir pressure can be maintained in high levels while increasing the production rates.

According to the literature studies, the most widely applied water flooding pattern is the five spot type pattern. Thus, the average anticipated injection rates is minimum of 0.5 bbl/acre.ft based on the field experience (Langnes, Robertson, & Chilingar, 1972). However, since it was depicted previously, drilling more than one well decreases the net present value. That's why, the least productive wells were converted into injection wells; hence, these wells are displayed in Figure 17.6. Also, a new horizontal production well called Bane-02 was drilled since the net present value reaches its highest value based on Figure 17.5. This horizontal well has a drain angle of -35 degrees, and lateral perforation of 1,000 ft. On the other hand, to estimate the possible extra recovery amount that could be expected can be estimated using one of the predictive methods published in the literature.

For this project, the approach proposed by Buckley-Leverett was adopted due to its straightforward manner. This approach assumes the followings:

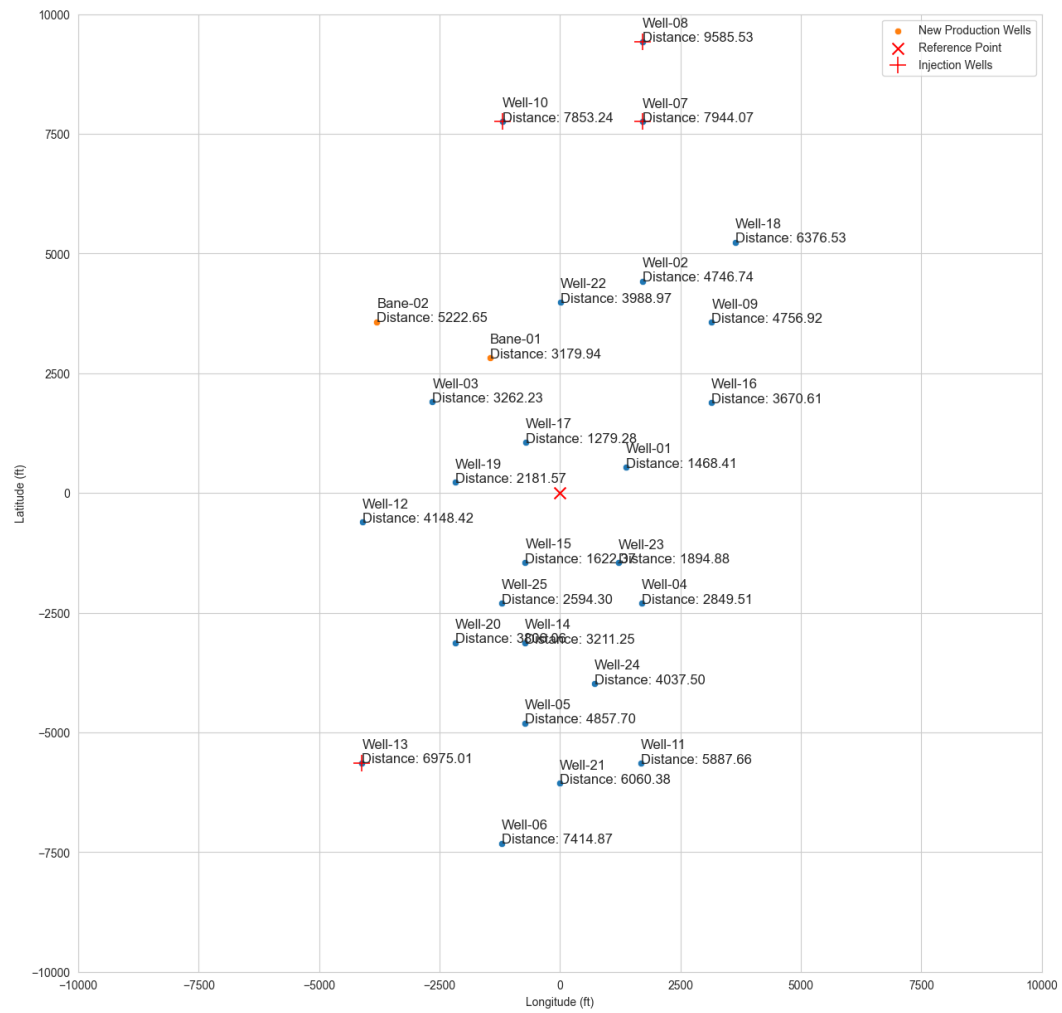
- Only oil moves ahead of the front; oil and water move together behind the front.
- Cross-sectional area perpendicular to flow is constant.
- Darcy's Law dominates the flow through the reservoir; hence, steady-state condition exists. This means, injected water is directly produced.
- Mobility ratio of the displacing and displaced fluids after breakthrough is used to calculate the fractional flow. If it was assumed that the capillary and gravitational forces are negligible, the fractional flow can be calculated by using (Eq. 17-3) (Langnes, Robertson, & Chilingar, 1972).

Figure 17.7 displays the fractional flow values for each saturation level that were computed using (Eq. 17-3) and the above-mentioned assumptions. To ascertain the average water saturation at and after the breakthrough, two tangent lines were also drawn on the fractional flow curve. The graphic illustrates how the average water saturation at the breakthrough may be determined thanks to the red tangent line that begins at  $S_w = S_{wirr} = 0.16$ . Conversely, the average water saturation following the breakthrough is determined by the green tangent line.

$$f_w = \frac{1}{1 + \left( \frac{K_{row} \mu_w}{K_{rw} \mu_o} \right)} \quad (\text{Eq. 17-3})$$

Once the average water saturation is determined at the breakthrough, several distinct tangent lines were drawn on the points where the water saturation is higher than the average water saturation at the breakthrough; which is  $S_{wo1} = 0.48$ . To make these tangent points, these points are displayed in Figure 17.8. Once the tangent lines are drawn on the corresponding points in Figure 17.8, the average water saturation values after the breakthrough and their corresponding fractional flow values were determined, and demonstrated in Figure 17.9.

Since the average water saturation values after the breakthrough are estimated, the cumulative recovery amount must be calculated in order to account for the efficiency of the water flooding operation. To achieve this, (Eq. 17-4) can be used to account for this incremental recovery amounts for each average water saturation after the breakthrough values (Langnes, Robertson, & Chilingar, 1972). As can be seen from (Eq. 17-4), the equation requires the knowledge of the pore vole, PV. Since the aim is injection the produced water into the reservoir, pore volume was taken as 29.086 MM STB. Thus, since the recovery amount is predicted, the injection volume can be determined from (Eq. 18-16) (Langnes, Robertson, & Chilingar, 1972). As a result, calculated incremental recovery amounts with their corresponding injection rates are illustrated in Figure 17.10.



**Figure 17.6:** The map of the Project Watcher in the Water.

$$N_{\text{recovery}} = PV \left( \frac{S_{\text{wa}} - S_{\text{wirr}}}{B_o} \right) \quad (\text{Eq. 17-4})$$

$$W_i = \frac{PV}{f'_w} \quad (\text{Eq. 17-5})$$

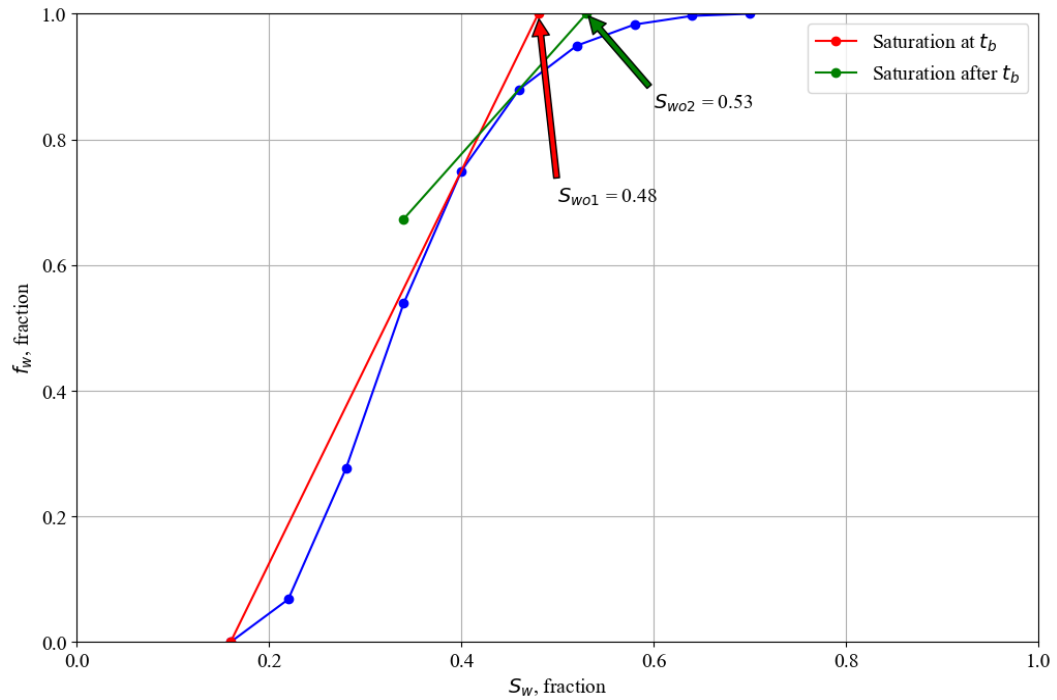


**Figure 17.7:** Fractional flow curve for each water saturation values.

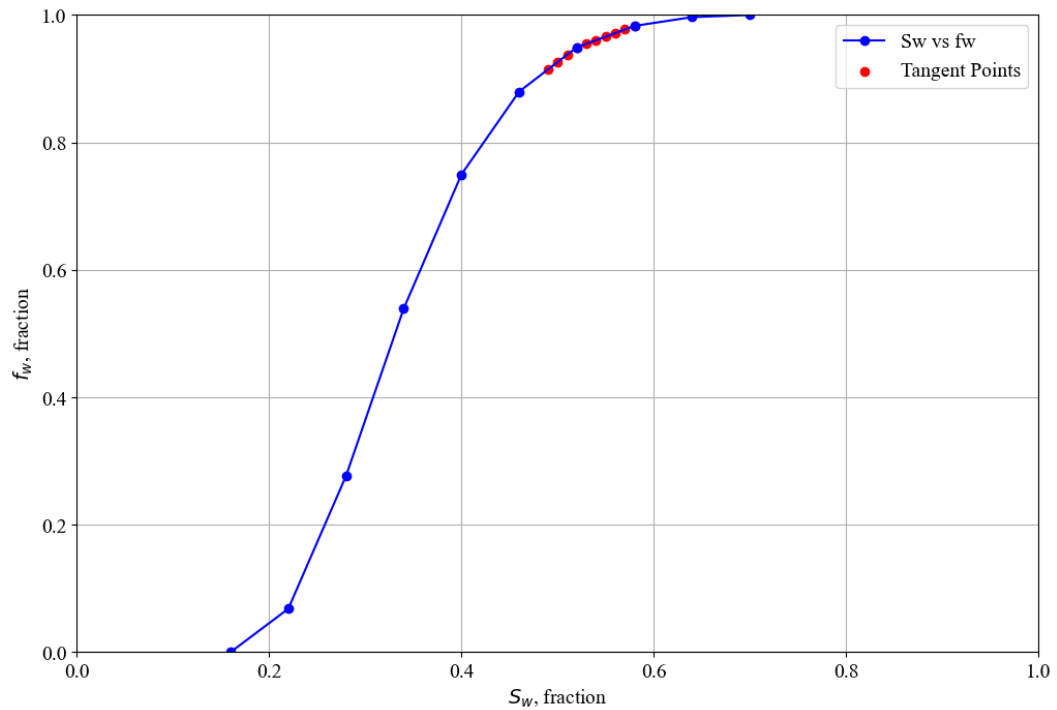


**Figure 17.8:** Tangent points above the average water saturation at the breakthrough.

The ultimate oil recovery after water flooding is 10.21 MM STB, according to Figure 17.10. The entire estimated amount of oil produced, according to the Buckley-Leverett predictive technique, is 173.21 MM STB. Next, using the Buckley-Leverett approach, the simulation was rebuilt with an injection rate of 2,025 STB/D per well. According to the simulation's results, at the conclusion of the forecast period with water flooding, the ultimate oil production is expected to be 181.66 MM STB, while the ultimate water production is 32.54 MM STB considering Figure 17.11. By comparing the analytical method and the simulation result, one can conclude that the analytical model underestimates the expected ultimate oil production at the end of the forecast period. This could be due to several reasons such as the absence of capillary forces, gravitational forces, areal sweep, and neglection of horizontal production well in the analytical method; yet, Buckley-Leverett method has provided quite good insight about process's efficiency.

Moreover, the average reservoir pressure after the water flooding is still found to be above the bubble point pressure since the final average reservoir pressure is 2,720 psia. Therefore, the Project Watcher in the Water was found to be efficient in terms of the maintenance of the average reservoir pressure. In addition, comparing the decline in the average reservoir pressure with the one anticipated in the base scenario, the decline was found to be smoother in the Project Watcher in the Water based on Figure 17.12. Hence, it seems that the flow enters the pseudo-steady state flow after year 2020, meaning that the rate change in pressure is constant. Comparing with the base scenario, the year that the flow starts to behave as pseudo steady state has shortened one year thanks to the water flooding.

To evaluate the profitability of Project Watcher in the Water, net present values (NPV) and other economic metrics were calculated under the base scenario. This economic assessment included the costs of new injection wells, their operational expenses, abandonment costs, and pipeline costs. A comprehensive economic analysis revealed that Project Watcher in the Water has an NPV of \$3.161 billion, a rate of return of 3,738%, and a discounted profitability index of 111. Figure 17.13 presents the project's NPV profile, along with capital risks and payback duration.

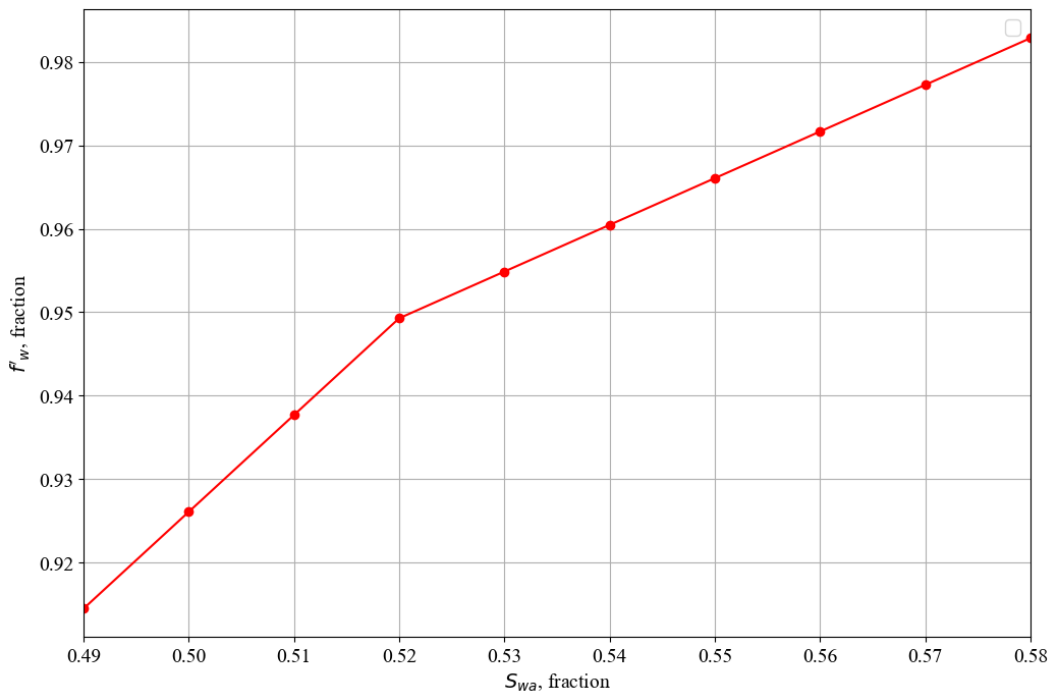


**Figure 17.9:** Average water saturation values after breakthrough with their corresponding fractional flow values.

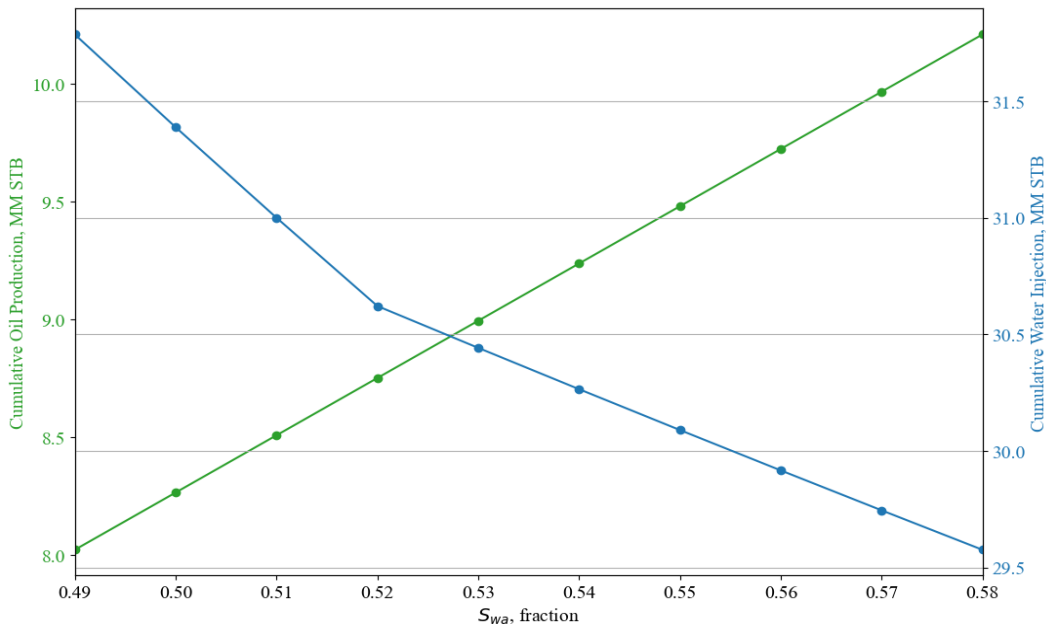


**Figure 17.10:** Calculated cumulative water injection rates and oil production amounts versus average water saturation after the breakthrough.

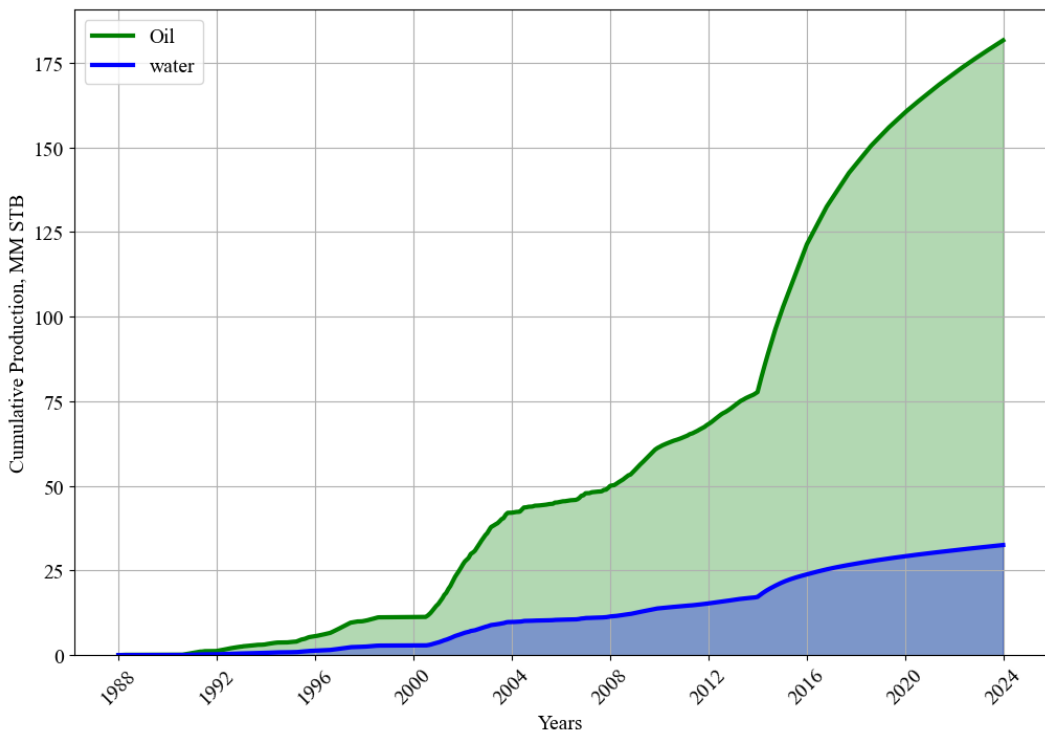


**Figure 17.11:** Oil production versus water production for the Project Watcher in the Water.

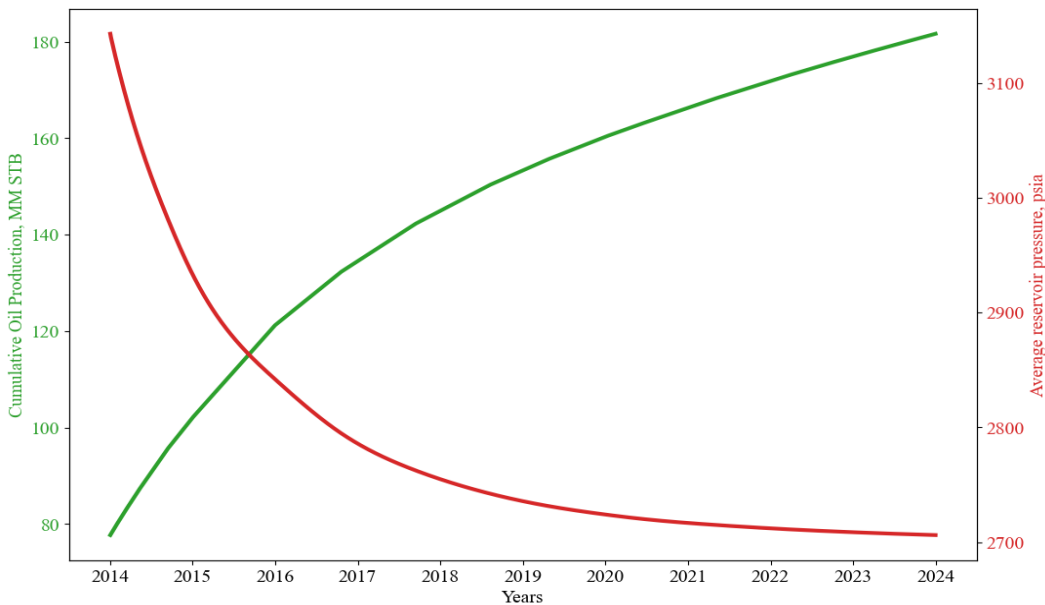


**Figure 17.12:** Average reservoir pressure profile along with the cumulative oil production throughout the Project Watcher in the Water.

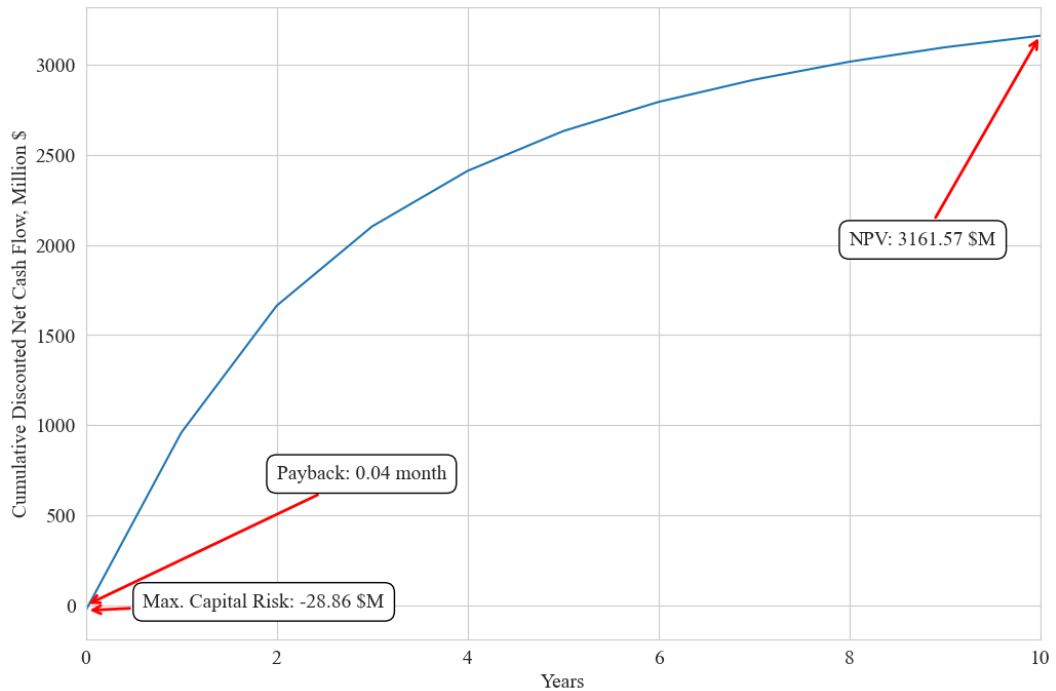


**Figure 17.13:** The cumulative discounted net cash flow in million dollars showing the project's breakthrough time for the Project Watcher in the Water.

As shown in Figure 17.13, the maximum capital investment risk is \$28.86 million, with a payback period of approximately 0.04 month. When comparing Project Watcher in the Water to the base scenario, this development plan has significantly increased overall profit. An additional 18.6 million barrels of oil were produced while maintaining the average reservoir pressure 40 psi higher than the base scenario. These factors highlight the strong profitability of Project Watcher in the Water.

### 17.3.Project: Deflate The Smaug

For Project Deflate the Smaug, a stimulation approach was employed. However, a crucial question arose prior to the well stimulation operation: which well or wells should be stimulated to achieve maximum profit? Initially, a trial-and-error method was used to determine the best approach for stimulation. This process revealed that the most effective strategy was to stimulate the 15 most productive wells identified in the

base scenario forecast. Consequently, the ultimate production of each well at the end of the 10-year production forecast was analysed, and stimulations were performed on the wells shown in Figure 17.14.

Additionally, acidizing stimulation was performed on the wells displayed in Figure 17.14 at the start of the 10-year production forecast. By the end of the forecast period, it was assumed that the skin factor was reduced to -5, indicating that the stimulation was highly effective and allowing fluid to flow more easily around the vicinity of the well. Furthermore, the wellhead pressure for all wells was maintained at 100 psia throughout the 10-year forecast, with the simulation running until December 31, 2023.

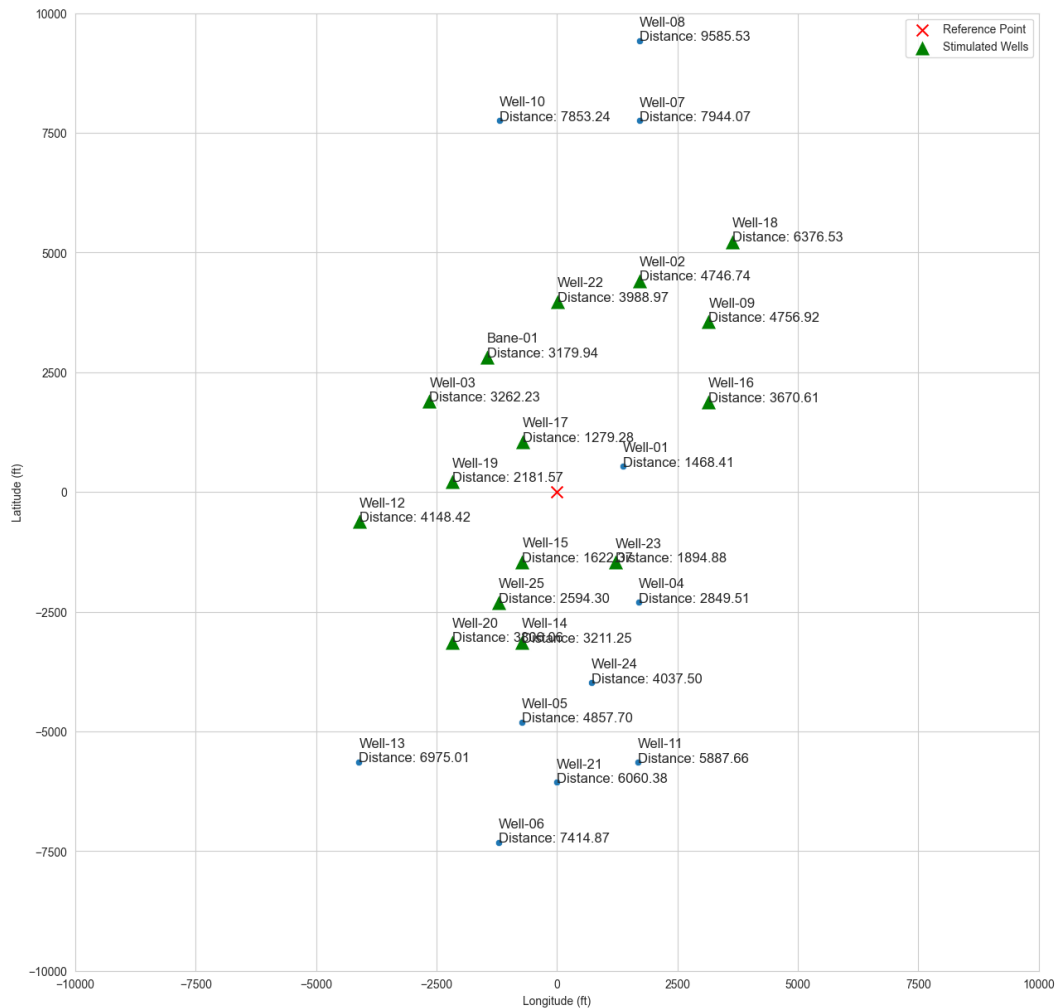


**Figure 17.14:** The map of Project Deflate the Smaug.

To evaluate the economic benefits of this future development project, the cumulative oil production throughout the forecast period, as well as water and gas production, were determined. Figure 17.15 shows that ultimate oil production reached 172.27 million STB, with water production at 29.61 million STB. Using the anticipated fluid production rates and the costs associated with acid stimulation on 15 wells, the project's net present value (NPV) was recalculated. The economic analysis indicated a significant increase in NPV, reaching \$3.288 billion, and a decrease in the payback period, as shown in Figure 17.16. Additionally, the maximum capital investment required decreased to \$20.45 million, further underscoring the project's profitability.

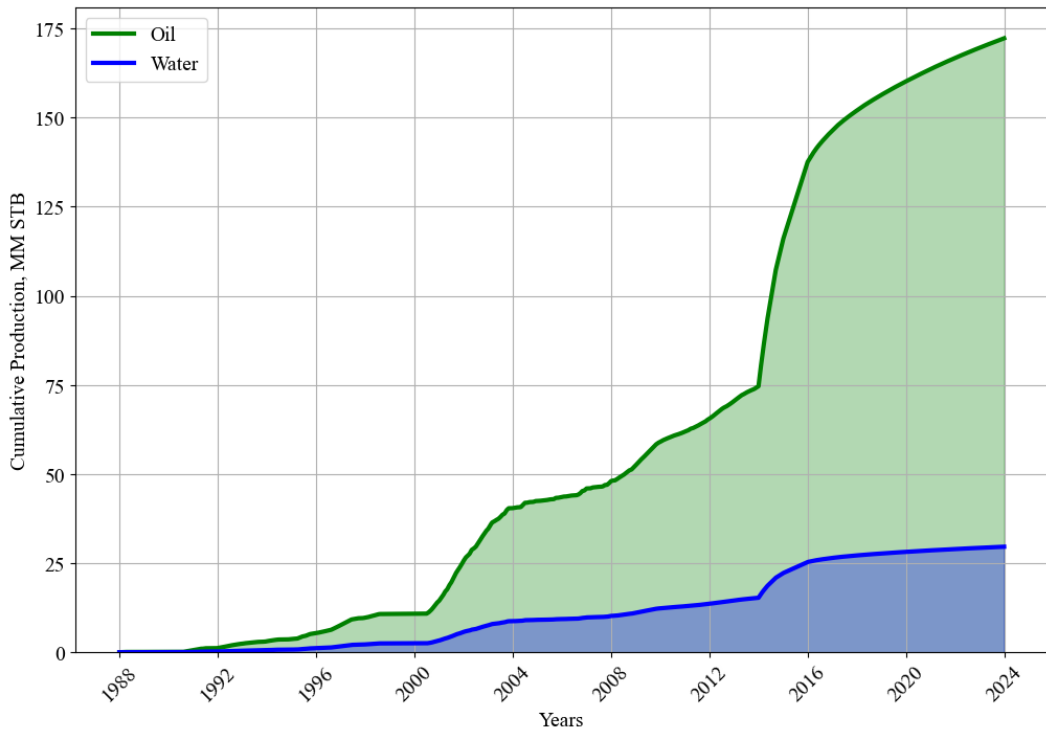


**Figure 17.15:** Oil production versus water production for the Project Deflate the Smaug.

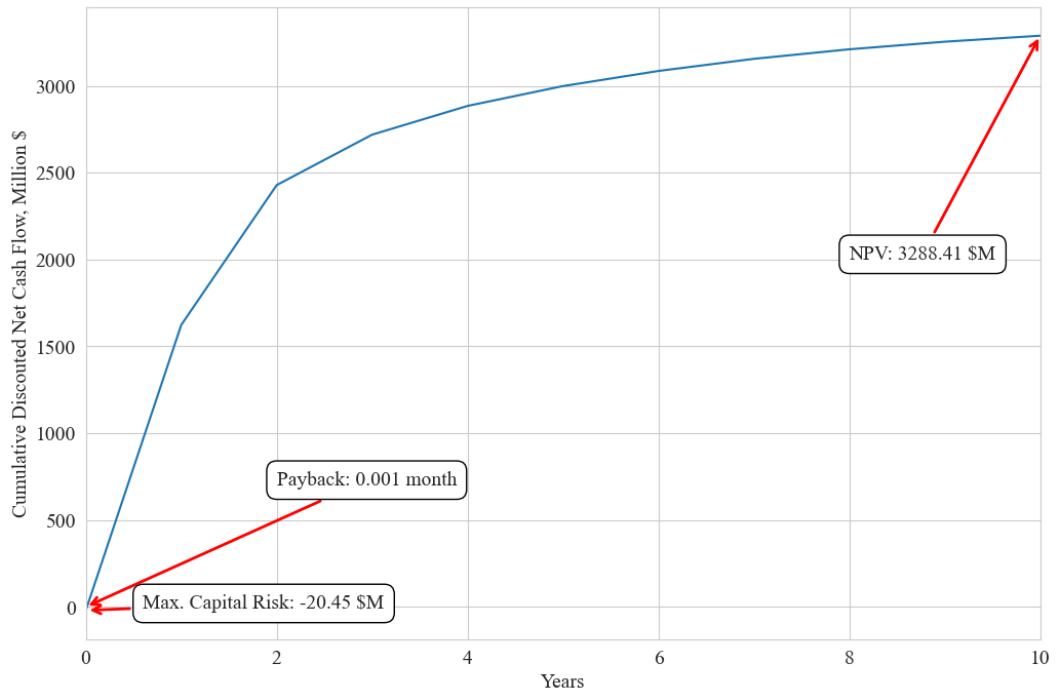


**Figure 17.16:** The cumulative discounted net cash flow in million dollars showing the project's breakthrough time for the Project Deflate the Smaug.

To investigate the efficiency of this development project in terms of pressure decline, the same approach used in previous future development scenarios was applied. Therefore, the pressure declines in the average reservoir pressure versus forecast years, along with cumulative oil production values, are plotted and shown in Figure 17.17. From this figure, it is evident that the stimulation operation was successful, as cumulative oil production increased significantly despite a sharp decline in average reservoir pressure until 2016. Additionally, the flow regime appears to enter a pseudo steady-state flow after 2018. Compared to Project Watcher in the Water, the onset of pseudo steady-state flow occurred earlier, which is advantageous. This earlier transition indicates a constant rate of pressure change and a stable flow behaviour over time, meaning the average reservoir pressure decreases slightly.

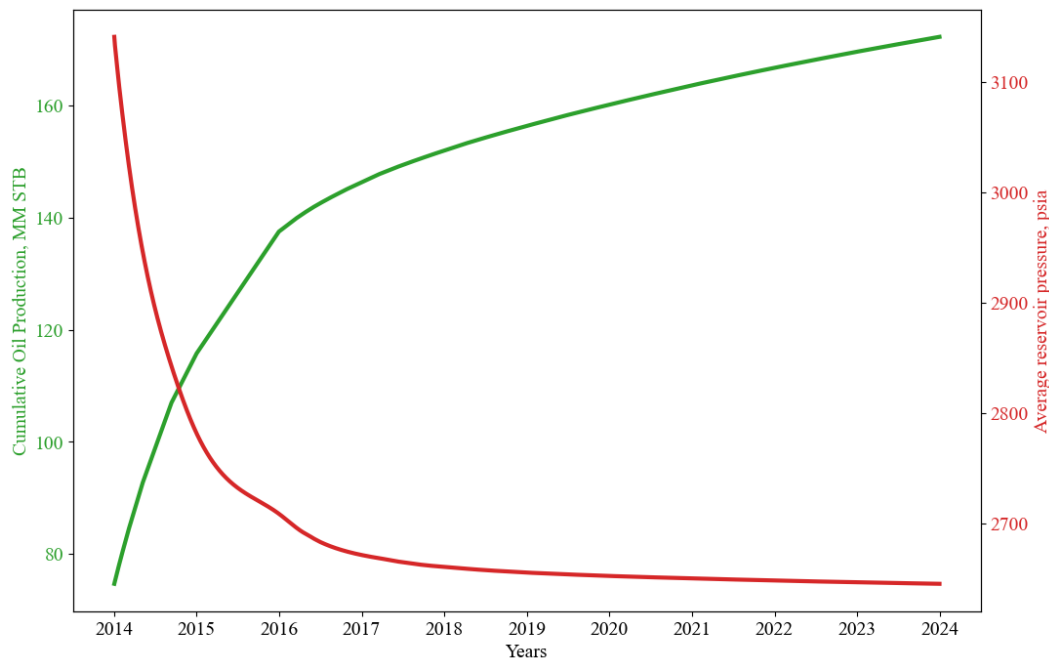


**Figure 17.17:** Average reservoir pressure profile along with the cumulative oil production throughout the Project Deflate the Smaug.

#### 17.4.Project: One Rig to Drill Them All

In the course of Project One Rig to Drill Them All, efforts were made to combine two previously performed scenarios. This approach was taken because water flooding helps maintain reservoir pressure while displacing oil to increase production, and stimulation enables high production rates. To achieve this, the same injection wells, each with a daily injection rate of 2,025 STB/D, were utilized alongside stimulation of the 15 most productive wells, as shown in Figure 17.18.

The same acidizing technique was used on the 15 most productive wells shown in Figure 17.18. This stimulation was performed at the beginning of the 10-year production forecast, specifically on January 1, 2014, assuming a reduction in the skin factor to -5. All production wells were then operated with a wellhead pressure of 100 psia until December 31, 2023. Unlike Project Watcher in the Water, no additional wells were drilled for production purposes, as the stimulation significantly increased production rates. This reduction in extra well drilling lowered costs and, consequently, increased overall profit.

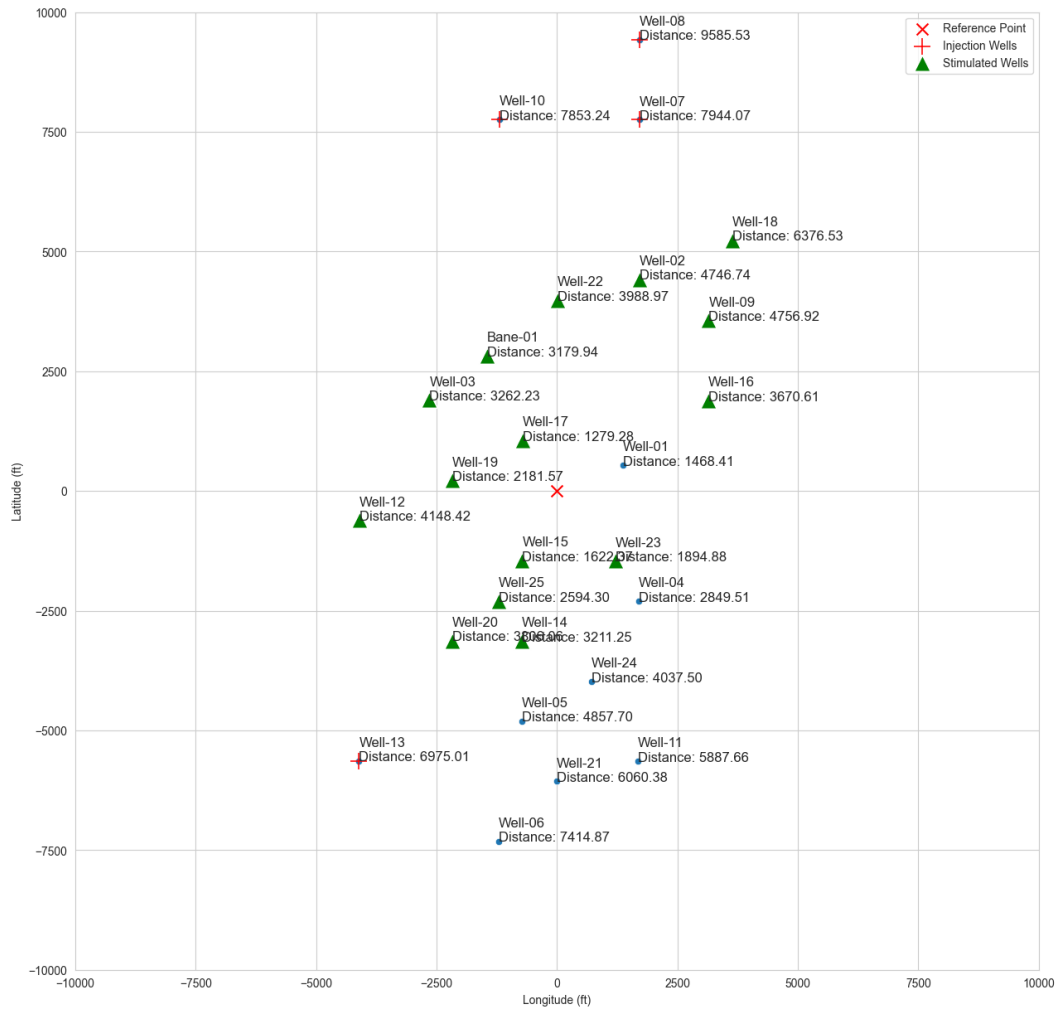


**Figure 17.18:** The map of Project One Rig to Drill Them All.

According to the simulation results obtained from the configuration shown in Figure 17.18, cumulative oil production is projected to reach 189.89 MM STB, with water production at 32.47 MM STB by the end of the production forecast, as depicted in Figure 17.19. This represents a significant increase when compared to the base scenario, where an additional 26.5 MM STB of oil production was achieved. Furthermore, the average reservoir pressure was maintained at 2,666 psi by the end of the forecast, as shown in Figure 17.20.

Evaluating the field performance, it becomes clear that the combination of stimulation and water flooding operations has led to a substantial boost in oil production. The

water flooding operation, in particular, played a crucial role in maintaining reservoir pressure at levels close to those of the base scenario, despite the significant increase in production. This maintenance of pressure is essential for ensuring the efficient displacement of oil and sustaining high production rates.

The results demonstrate that the strategic integration of water flooding and stimulation techniques not only enhances oil recovery but also preserves reservoir integrity. By comparing these results with the base scenario, the benefits of the combined approach are evident, highlighting the project's potential for increased profitability and extended field life. This comprehensive assessment underscores the importance of advanced reservoir management techniques in optimizing production and maximizing economic returns.

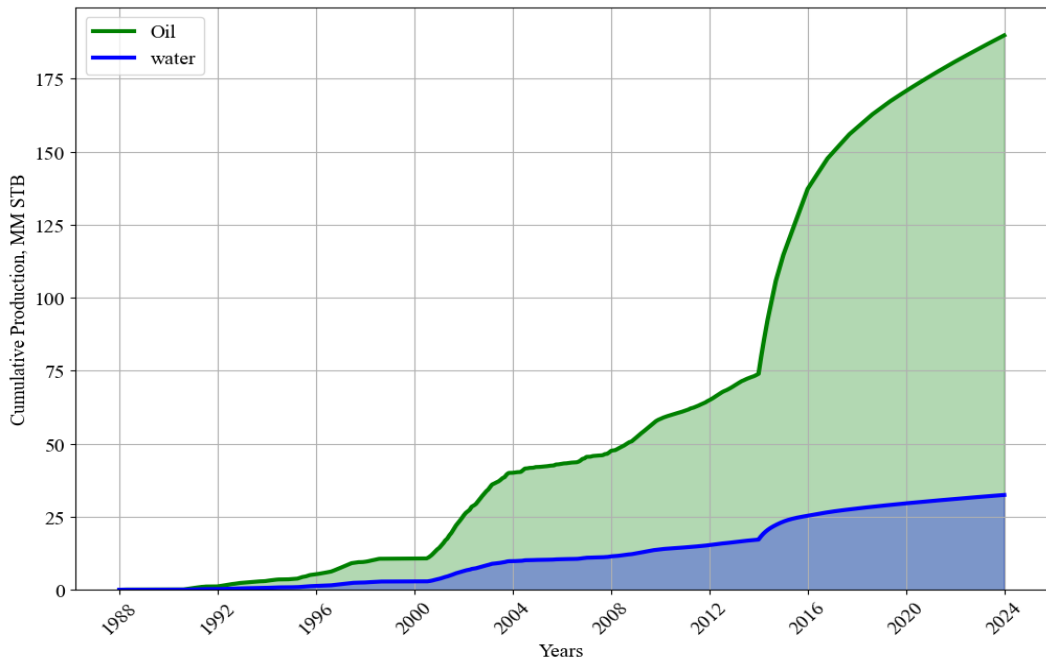


**Figure 17.19:** Oil production versus water production for the Project One Rig to Drill Them All.

In concluding the decision-making process, an economic evaluation of Project One Rig to Drill Them All was conducted. The analysis encompassed the costs of stimulating the 15 most productive wells, as well as the costs associated with water injection and producer-to-injector operations. The calculations revealed a predicted net present value of the development project reaching \$3.754 billion. This significant increase in the project's viability is illustrated in Figure 17.21.

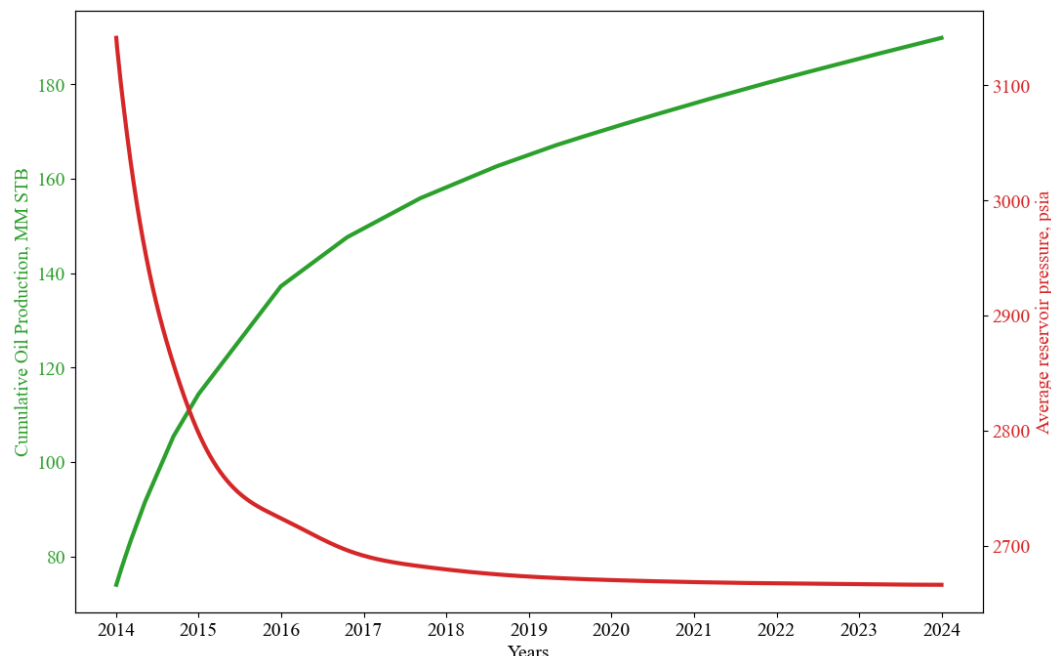


**Figure 17.20:** Average reservoir pressure profile along with the cumulative oil production throughout the One Rig to Drill Them All.

Moreover, it is notable that the maximum capital investment risk has shown a slight uptick compared to the previous development scenario, a trend illustrated in detail within Figure 17.21. Despite this marginal increase, there has been a noticeable decrement in the payback duration, indicating a favorable return on investment over a shorter period.

Furthermore, the comprehensive economic evaluation of the project has revealed some impressive figures. A striking rate of return of 7604% and a DPI of 162 were estimated,

showcasing the project's robust financial performance. These economic metrics, coupled with the consistent maintenance of average reservoir pressure, serve as compelling evidence of the project's overall success.

,

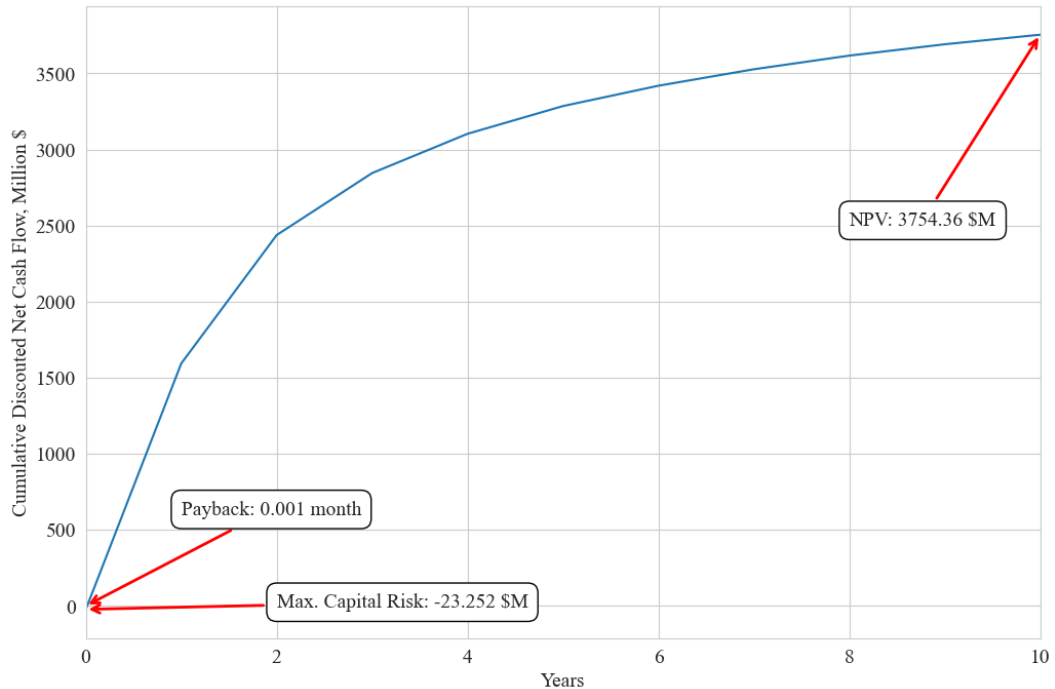


**Figure 17.21:** The cumulative discounted net cash flow in million dollars showing the project's breakthrough time for Project One Rig to Drill Them All.

Indeed, the project's favorable economic properties, coupled with its ability to sustain average reservoir pressure, position it as a highly beneficial endeavor. Moreover, it is noteworthy that these impressive outcomes have been achieved with a relatively modest initial investment at the outset of the 10-year production phase.

## 17.5.Final Decision on the Development

Project One Rig to Drill Them All stands out as the most compelling development scenario due to its comprehensive approach that integrates water flooding and well stimulation strategies. This innovative project maximizes oil recovery while effectively managing reservoir pressure, leading to substantial economic benefits. A key factor supporting this claim is the comparison of recovery factors from four scenarios, as illustrated in Figure 17.22. This comparison demonstrates that Project One Rig to Drill Them All achieves the highest recovery factor among the scenarios, indicating its superior performance in extracting oil from the reservoir.

Moreover, the sensitivity analysis conducted for Project One Rig to Drill Them All provides valuable insights into the project's robustness and viability. Figure 17.23 highlights the sensitivity of the project's net present value (NPV) to changes in key parameters. The analysis reveals that Oil Price is the most sensitive parameter, followed by OPEX and CAPEX. This finding underscores the importance of these factors in influencing the project's profitability and overall success.

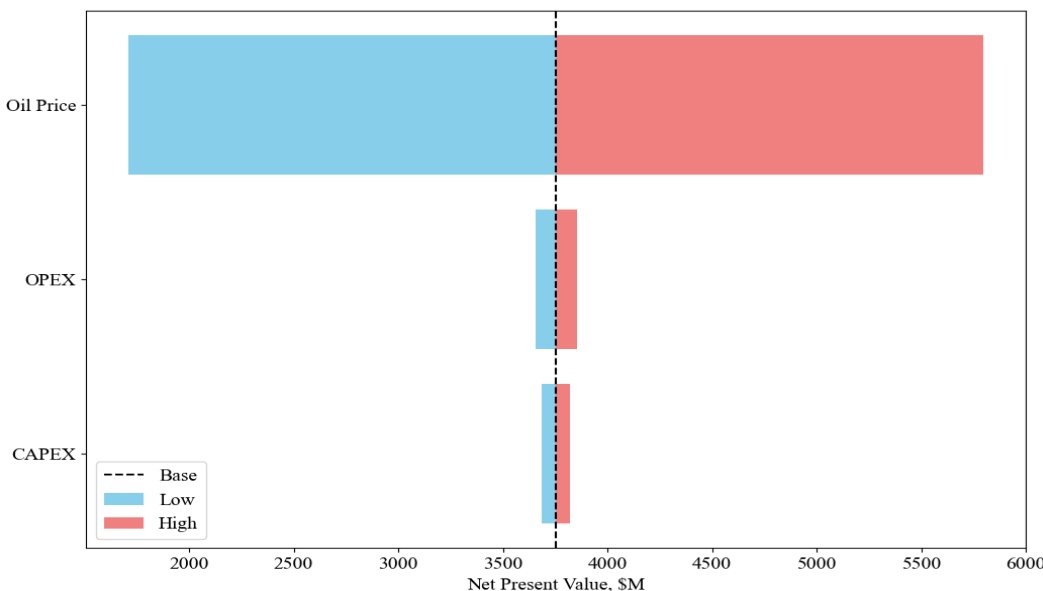


**Figure 17.22:** Sensitivity analysis on Project One Rig to Drill Them All.

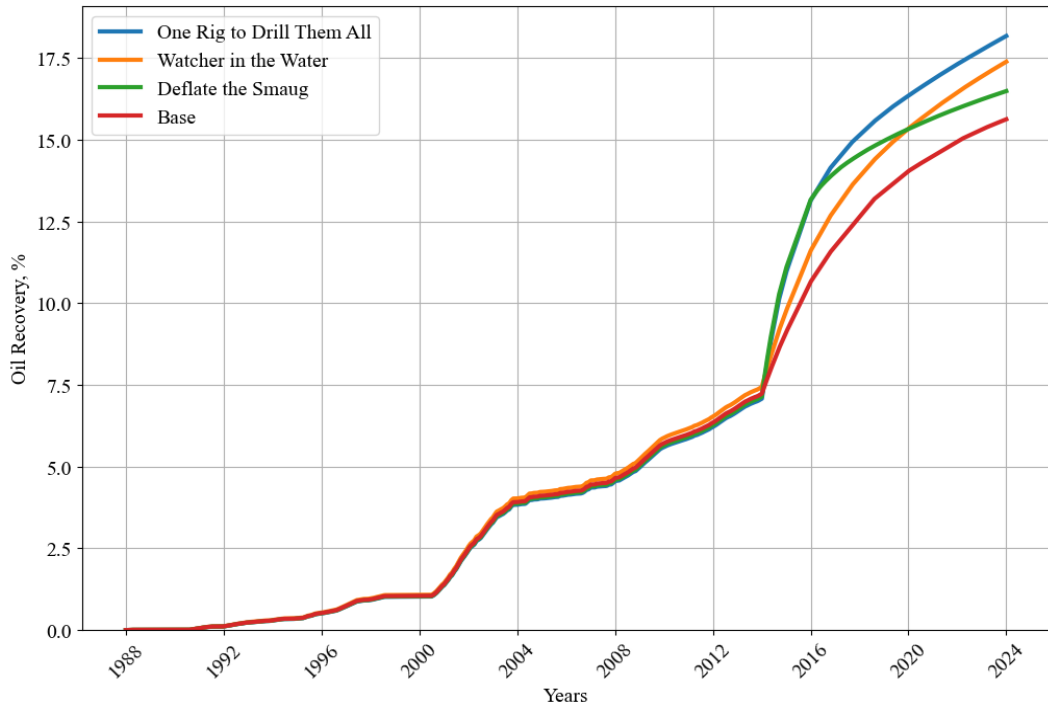


**Figure 17.23:** Recovery factor of oil comparison.

During the sensitivity analysis, low and high values were calculated using multipliers of 0.5 and 1.5, respectively. This approach allowed for a comprehensive assessment of the project's performance under different scenarios, considering both optimistic and pessimistic conditions. The results of the sensitivity analysis reaffirm the resilience of Project One Rig to Drill Them All, as it remains economically viable across a range of parameter variations.

Furthermore, the integration of water flooding and well stimulation techniques in Project One Rig to Drill Them All offers synergistic benefits that enhance the project's overall effectiveness. By stimulating the 15 most productive wells and implementing water flooding to maintain reservoir pressure, the project achieves a balance between maximizing oil recovery and minimizing operational costs. This balanced approach is reflected in the project's high NPV and rate of return.

Additionally, the maintenance of average reservoir pressure throughout the project's duration is crucial for sustaining high production rates and extending the field's economic life. Project One Rig to Drill Them All effectively manages reservoir

pressure, as evidenced by the smooth decline in average reservoir pressure over time. This indicates that the project is able to maintain reservoir pressure close to the base scenario, despite the increased production rates.

In conclusion, Project One Rig to Drill Them All emerges as the best development scenario due to its ability to maximize oil recovery, effectively manage reservoir pressure, and demonstrate resilience in the face of varying economic conditions. The integration of water flooding and well stimulation techniques, coupled with a comprehensive sensitivity analysis, highlight the project's potential for long-term success and profitability in the oil and gas industry.

## **18. PRODUCTION ENGINEERING: SEPARATORS**

Petroleum, as found in subsurface reservoirs, is not pure and contains a complicated mixture of hydrocarbons, non-hydrocarbon gasses such as hydrogen sulphate, nitrogen, carbon dioxide, water, and other contaminants. The hydrocarbons that have low amount of carbon start to decompose as it rises to the surface by drilling and production operation due to the pressure differences between the reservoir and atmosphere. At this stage, separators play an important role to properly separate and remove the various components, which enables the extraction of valuable products such as crude oil and natural gas while managing substances and optimizing the efficiency of production. Separators are categorized as "two-phase" when they segregate gas from the combined liquid stream, and as "three-phase" when they additionally divide the liquid stream into its constituent crude oil and water components (Arnold & Stewart, 2008). After extraction to the surface, it is usually critical to separate the gas, oil, and free water as quickly as possible. These steps must be controlled and transported independently. To separate liquids from gas phase, the well stream is sent via an oil-gas or oil-gas-water separator (Ikoku, 1992). In this project, the design of two-phase separators will be introduced to establish a solid foundation. Subsequently, the criteria for designing three-phase separators will be explained. Many of the steps involved in the design of two-phase separators are also applicable to three-phase separators. Additionally, since all reservoir simulation scenarios generate oil, water, and gas simultaneously, the theory behind three-phase separator design will be presented at the end of the section.

### **18.1. Separator Types**

The shape or the volume of separators used in oil fields may vary depending on the characteristics of the fluid and the reservoir. Accordingly, the separators that are encountered may be cylindrical in vertical and horizontal form, or spherical. They all have certain advantages and disadvantages.

### **18.1.1. Vertical separators**

Vertical separators are often utilized for well streams with low to intermediate gas-oil ratios and large liquid volumes. They effectively manage liquid without causing carryover to the gas outlet, and they require less important liquid level control. Because of their small size, they are ideal for limited space deployments such as offshore platforms. However, they require bigger diameters for a comparable gas capacity than horizontal vessels and are generally more expensive to manufacture and ship. Figure 18.1 shows an illustration of a vertical separator (Ikoku, 1992).

### **18.1.2. Horizontal separators**

In Figure 18.2, there is a cross-sectional image of a two-phase horizontal separator. As fluid enters, it encounters an inlet diverter, initiating the initial separation of liquid and vapor. Gravity then causes liquid droplets to descend and collect at the bottom, where a liquid section provides retention time before exit via a dump valve controlled by a level controller. Gas and oil mist pass over the inlet diverter and through a gravity settling section, where small droplets are separated out. Any remaining very small droplets are removed by a coalescing section or mist extractor before gas exits. Pressure within the separator is regulated by a controller on the gas outlet, adjusting a control valve as needed. Horizontal separators are favored for streams with high gas-liquid ratios and foaming crude due to their smaller size, offering cost-effectiveness (Arnold & Stewart, 2008).

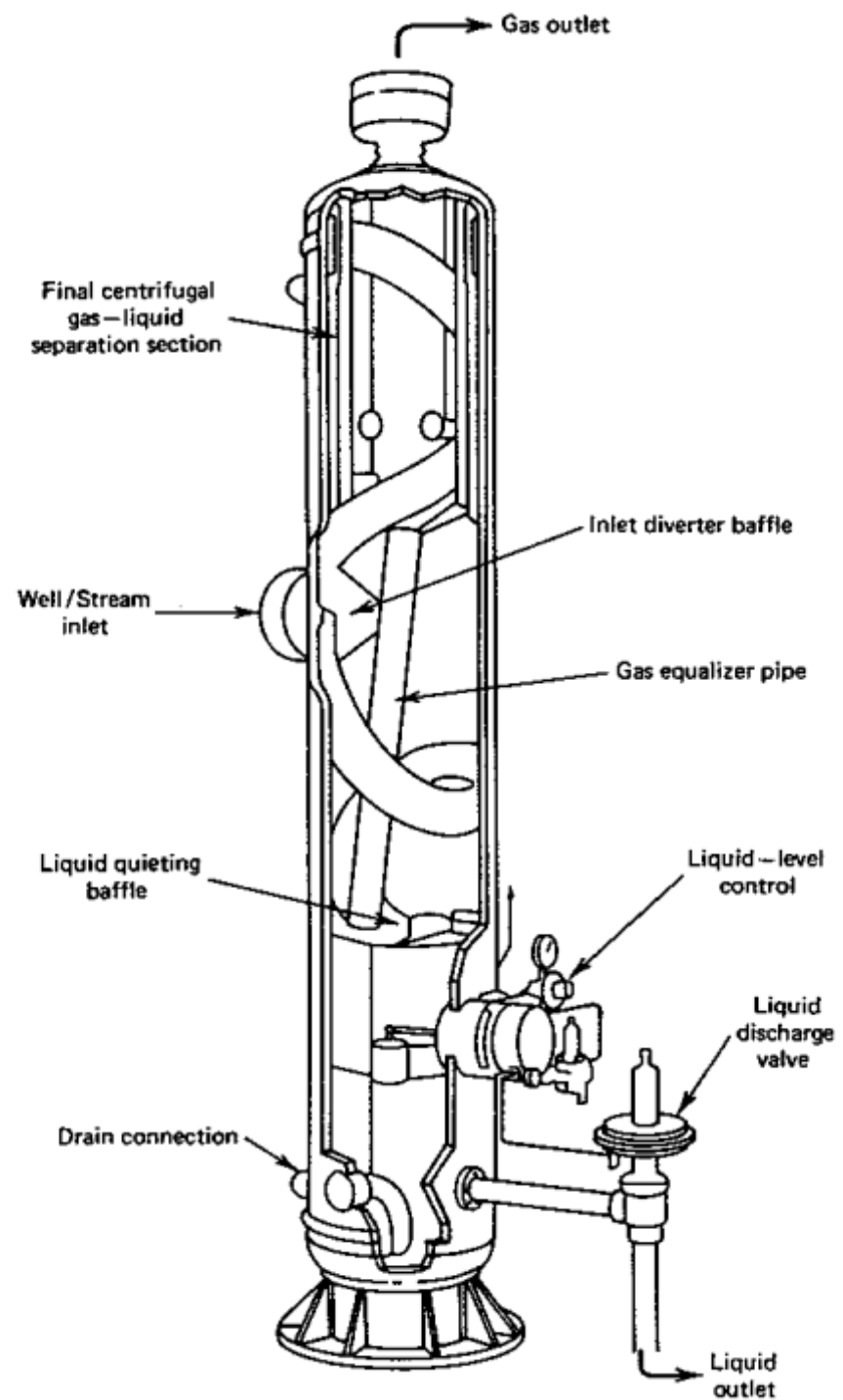


**Figure 18.1:** Vertical separator (Ikoku, 1992).

### 18.1.3. Spherical separators

Spherical separators offer an economical and space-efficient design, though they suffer from limited surge space and liquid settling areas, making precise placement and operation of liquid level controls crucial. Implementing three-phase separation in spherical separators is challenging due to space limitations, despite being achievable in any separator through specialized internal configurations (Ikoku, 1992).

Horizontal three-phase separators necessitate dual liquid level controls and dump valves for effective functioning, commonly utilized in well testing and situations where water readily separates from oil or condensate. In summary, horizontal single-tube separators are considered most effective for high-pressure gas-distillate wells with high gas-oil ratios, while vertical separators are preferable for high liquid loads (Ikoku, 1992). Figure 18.3 illustrates a spherical separator mechanism (Arnold & Stewart, 2008).

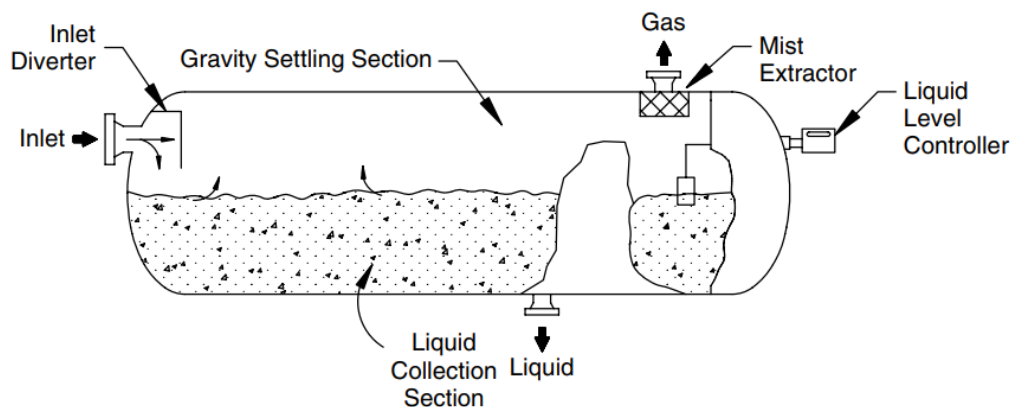


**Figure 18.2:** Horizontal separator (Arnold & Stewart, 2008).

## 18.2.Two-Phase Separator Design Theory

Understanding fluid properties such as density, viscosity, and composition is important. It is critical to determine the needed separation efficiency while also taking into account operational conditions. They include comprehending fluid properties, assessing phase behavior, assuring required separation efficiency, taking into account operating conditions, developing internal components, establishing control systems, and including safety measures.

In order to design a proper separator for the estimated conditions, following questions should be answered (Arnold & Stewart, 2008):

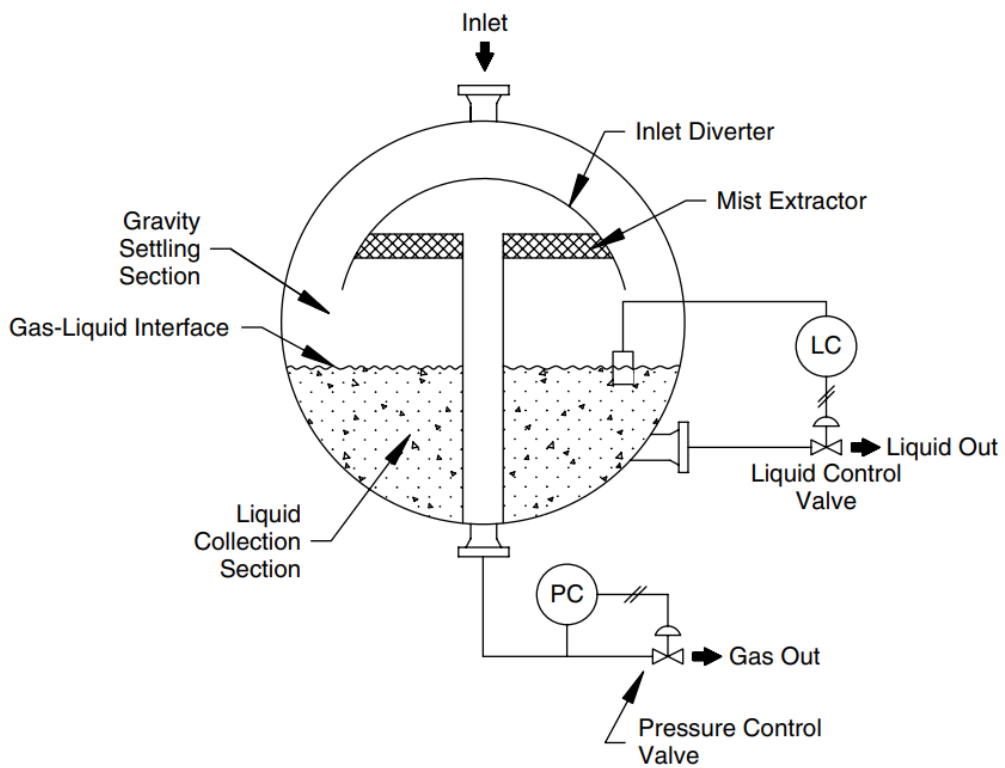


**Figure 18.3:** Spherical separator (Arnold & Stewart, 2008).

- How many fluid phases will be taken in place during the production?
- What will be the total liquid production, and gas production daily, if there is any?
- What are the fluid properties?
- What are the components of the fluid mixture?
- What will be the operating conditions?

Once all questions are answered, the separator type can be selected, followed by the necessary calculations to design it appropriately. According to the literature, horizontal half-full separators are the most widely used for two-phase or three-phase separation due to their solid standards and efficiencies (Arnold & Stewart, 2008). Based on the given data, the reservoir produces two-phase fluids, namely oil and gas. However, simulation results indicate three-phase production, leading to confusion in the design process. To address this, the separator will be initially designed based on the given production data, followed by the design of a three-phase separator.

No matter which type of separator is used, all of the separators have the same fundamental parts. Those parts are can be listed as follows, and Figure 18.4 illustrates all of these parts (Arnold & Stewart, 2008):

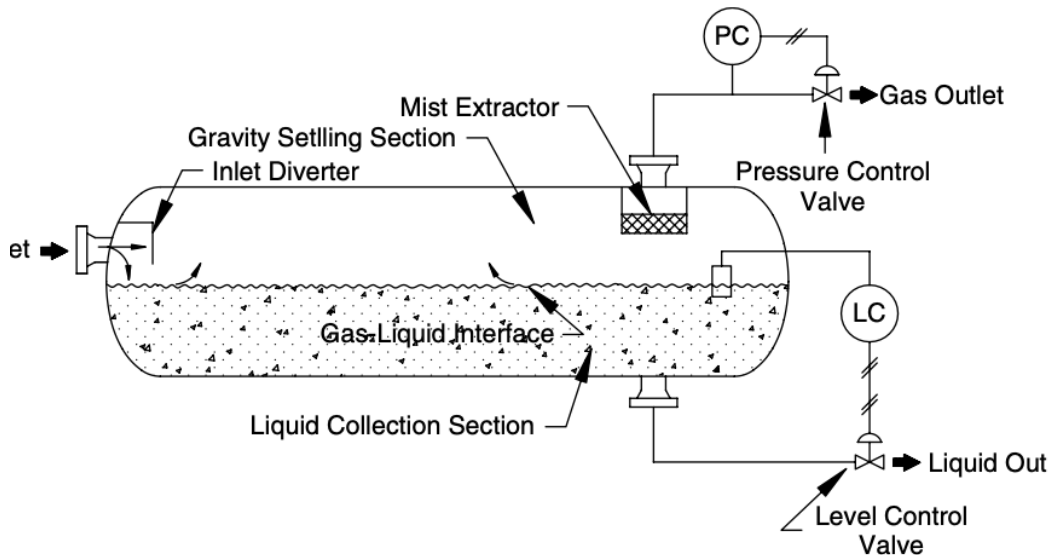


**Figure 18.4:** Horizontal separator, and its parts (Arnold & Stewart, 2008).

- Inlet divertor section
- Liquid collection section
- Gravity settling section
- Mist extractor section

### **18.2.1. The common separator parts**

In this particular part of the subsection, the common parts of a separator will be introduced. Those parts are essential for all types of separators, including three-phase separators. These parts encompass the inlet divertor section, liquid collection section, gravity settling section, mist extractor section. Moreover, in the following subsections, the selection criteria of the mist extractor will be described.

#### **18.2.1.1. inlet divertor section**

The separator's inlet typically receives a fast, turbulent mixture of gas and liquid with high momentum. The intake diverter, also known as the main separation section, abruptly reverses the flow, absorbing the liquid's momentum and helping to separate the gas and liquid, thus beginning the initial separation process (Arnold & Stewart, 2008).

#### **18.2.1.2. liquid collection section**

The liquid collection part at the bottom of the vessel allows any gas that has combined with the liquid to separate through gravity settling. It also functions as a buffer against abrupt surges. The effectiveness of separation is determined by the length of time the liquid remains in the separator, which is regulated by capacity, inlet flow rate, and fluid density differences. Separating liquids takes longer than separating gas and liquid (Arnold & Stewart, 2008).

### **18.2.1.3. Gravity settling section**

In the gravity settling portion, the gas's speed slows, causing tiny liquid droplets carried by the gas to separate due to gravity and descend to the gas-liquid interface. This part is intended to ensure that droplets larger than 100 to 140 microns settle out, while smaller ones remain in the gas phase. Larger droplets are hazardous because they can overpower the mist extractor at the separator exit (Arnold & Stewart, 2008).

### **18.2.1.4. Mist extractor section**

In the gravity settling portion, the gas's speed slows, causing tiny liquid droplets carried by the gas to separate due to gravity and descend to the gas-liquid interface. This part is intended to ensure that droplets larger than 100 to 140 microns settle out, while smaller ones remain in the gas phase. Larger droplets pose a risk due to the possibility of overpowering the mist extractor at the separator exit (Arnold & Stewart, 2008).

Mist extractors are necessary for removing liquid droplets and solid particles from gas streams. To choose the right one, factors like droplet size, pressure drop tolerance, plugging susceptibility, and installation feasibility must be considered (Arnold & Stewart, 2008). There are several impingement types of mist extractors such as baffles, vanes, mesh wires and micro-fibers. When choosing the appropriate mist extractor, the characteristics of the reservoir fluids

and thus, the most economical option should be taken into consideration. Based on the properties listed in Table 18.1, the mesh wire was determined as the ideal choice for the mist extractor.

**Table 18.1:** Features of impingement type of mist extractors (Arnold & Stewart, 2008).

Impingement Type of Mist Extractors			
Consideration	Wire-Mesh	Vane	Micro-Fiber
<b>Cost</b>	Lowest	2–3 times wire-mesh unit	Highest
<b>Efficiency</b>	100% (for droplets larger than 3–10 $\mu$ )	100% (for mists $>20\text{--}40 \mu$ )	Up to 99.9% (for mists $< 3 \mu$ )
<b>Pressure Drop</b>	$<25 \text{ mm H}_2\text{O}$	$< 15 \text{ mm H}_2\text{O}$	100-300 mm
<b>Gas Capacity</b>	Very good	Up to twice that of a wire-mesh unit	Lowest
<b>Liquid Capacity</b>	Good	Best	Lowest
<b>Solids</b>	Good	Best	Soluble particles with sprays only

### 18.2.2. Settling velocity

The force of gravity is used to remove liquid droplets from a separator's gravity settling section. The gas's containing liquid droplets sink at a terminal or settling velocity. This velocity is such that the drag forces the droplet experiences from moving through the continuous gas phase is equal to the force of gravity, or "negative buoyant force," acting on it. This relation can be estimated using the empirical equation given in (Eq. 18-1) (Arnold & Stewart, 2008). This equation aims to relate the drag coefficient with the drag force.

$$F_D = C_D A_d \rho_{continus} \left[ \frac{V_t^2}{2g} \right] \quad (\text{Eq. 18-1})$$

The term  $C_D$  denotes for the drag coefficient, which is highly correlated parameter with the fluid flow regime. Considering the high pressure, and velocity conditions during operations, one can expect a turbulent flow, rather than laminar flow. During the turbulent flow, the drag coefficient deviates from the straight-line; hence, this relation can be found in (Eq. 18-2) (Arnold & Stewart, 2008). Moreover, equating the buoyant, and drag forces, the given relation, (Eq. 18-3), can be written for the terminal settling velocity (Arnold & Stewart, 2008).

$$C_D = \frac{24}{Re} + \frac{3}{Re^{1/2}} + 0.34 \quad (\text{Eq. 18-2})$$

$$V_t = 0.0119 \left[ \left( \frac{\rho_l - \rho_o}{\rho_g} \right) \frac{d_m}{C_D} \right]^{1/2} \quad (\text{Eq. 18-3})$$

### 18.2.3. Droplet size

The vessel's gravity settling portion serves to prepare the gas for the mist extractor's final polishing. Based on field experience, it seems that the mist extractor will not flood and will be able to remove droplets with sizes between 10 and 140 microns if 140-micron droplets are eliminated in this area (Arnold & Stewart, 2008). That's why, in this project, since there is no prior information regarding to the droplet size, it will be assumed that the droplet size is 140 microns.

Apart from the droplet size, the retention time must be specified to separate phases from each other in the gravity settling section. Based on the field experience, a table was provided for different oil gravities (Arnold & Stewart, 2008). This table can be found in Table 18.2; and since the oil produced from Mount Doom Oil Field is around 27 API, the design criteria will be based on the 2.5 minutes, if the two-phase separator design is applied.

It's critical to choose a vessel length and diameter for a horizontal separator that fulfil gas capacity requirements so that liquid droplets can separate from the gas. The design

should also provide for adequate retention time so that the liquid may reach equilibrium (Arnold & Stewart, 2008). To quantify this occasion, the gas capacity, and liquid capacity should be introduced.

**Table 18.2:** Retention time for two-phase separators (Arnold & Stewart, 2008).

Oil Gravity, API	Retention Time, min
35+	0.5 to 1
30	2
25	3
20+	4+

#### 18.2.4. Gas capacity

Setting the gas retention time to the amount of time it takes for a droplet to settle at the liquid interface is the foundation of the gas capacity constraint equations. Moreover, this relation can be written as given in (Eq. 18-4). For the half full horizontal separators (Arnold & Stewart, 2008).

$$d_{sep} L_{eff} = 420 \left[ \frac{T_{op} z Q_g}{P_{op}} \right] \left[ \left( \frac{\rho_g}{\rho_l - \rho_g} \right) \frac{C_D}{d_m} \right]^{1/2} \quad (\text{Eq. 18-4})$$

#### 18.2.5. Liquid capacity

Similar to the gas capacity constraint, the liquid phases may also be compared using this analogy to account for the equilibrium between the vessel length and the necessary retention period. For this purpose, again, for the half full horizontal separators, (Eq. 18-5) can be used (Arnold & Stewart, 2008).

$$d_{sep} L_{eff} = \frac{t_r Q_l}{0.7} \quad (\text{Eq. 18-5})$$

### 18.2.6. Seam-to-seam length

It is important to consider the length needed to accommodate the mist extractor and distribute flow uniformly at the input diverter when sizing vessels based on gas capacity. Using particular formulas, this length also referred to as the effective length is determined. The mist extractor and flow distribution take up a portion of the length, regardless of the vessel diameter. Larger vessel diameters require greater length for uniform gas flow distribution (Arnold & Stewart, 2008). The representation for the effective length, and seam-to-seam length is illustrated in Figure 18.5.

A vessel's seam-to-seam length can be approximated using the bigger results of (Eq. 18-16) based on these notions combined with field experience. Moreover, the seam-to-seam length should be lower than the result of (Eq. 18-16) (Arnold & Stewart, 2008).

$$L_{ss} = L_{eff} + \frac{d_{sep}}{12} \quad (\text{Eq. 18-6})$$

$$L_{ss} = \frac{4}{3} L_{eff} \quad (\text{Eq. 18-7})$$

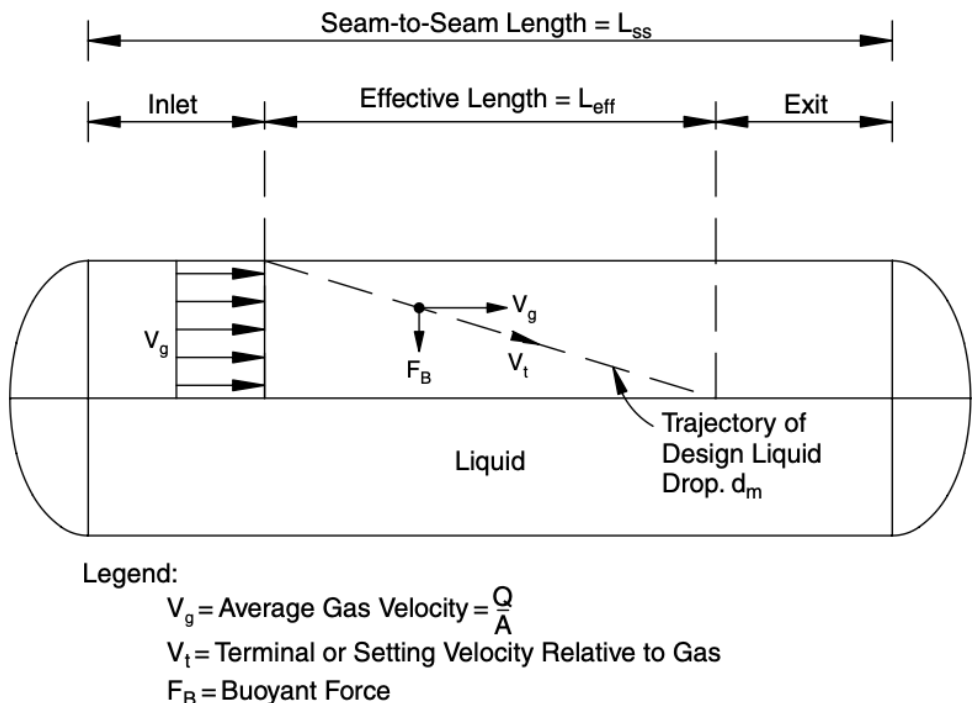


**Figure 18.5:** The representation of the seam-to-seam length, effective length for a horizontal separator (Arnold & Stewart, 2008).

### 18.3.Two-Phase Separator Design Result

In this section, the design theory for the two-phase separator procedure outlined previously was used to design a proper two-phase separator for the 25-years of production data given. According to the production data given, it was found that the production regimes are quite high; thus, it was observed that there is no water production et all. To illustrate this huge production regimes, and their consecutive years, Figure 18.6 is used to achieve this objective. Moreover, in order to account for all production regimes that were encountered during 25-years of production, the idea of percentiles was incorporated. To be more specific, 95<sup>th</sup> percentile of oil, and gas phase productions were calculated to account for hole production duration.

A percentile is a metric in statistics that is used to show the value below which a specific percentage of observations in a dataset fall. The figure below which 50% of the observations may be found, for instance, is the 50th percentile, commonly referred

to as the median. Understanding the relative position of a single observation inside a dataset is made easier with the help of percentiles (Bornmann, 2012).

The 95<sup>th</sup> percentile of oil production is 23,719 STB/D, whereas the 95<sup>th</sup> percentile of gas output is 15,272 MSCF/D, based on percentile estimates. On the other hand, the required calculations were attempted to be executed since the controlled working conditions are 200 psia pressure and 77 degrees Fahrenheit. Since the ultimate goal of the two-phase design theory was to approximate a slenderness ratio between three and four, a trial-and-error method was employed. This trial-and-error method led to the discovery that a vessel with a diameter of 96 inches could maintain the slenderness ratio within the acceptable range. This diameter is appropriate while taking into account the API criteria; nevertheless, because of its high diameter, this kind of vessel has to be properly built. It was attempted to decrease the vessel size's diameter to 60 inches since the specifically developed separator is expected to boost costs. In order to accomplish this goal, it was believed that the whole production would be gathered by directing flow regime into three identical horizontal half-full separators utilising a manifold located in the field's middle. Using this method, the expected flow regimes for each phase were divided by the total number of separators to determine each phase's contribution. At the end of the calculations, necessary parameters were maintained and displayed in Table 18.3; thus, by using these parameters, the vessel diameters along with their slenderness ratios were demonstrated in Table 18.4.

**Table 18.3:** Calculated parameters for the two-phase separator for the 25-years of production.

<b>Q<sub>o</sub>, STB/D</b>	7,906
<b>Q<sub>g</sub>, MSCF/D</b>	5,090
<b>ρ<sub>o</sub>, lb/ft<sup>3</sup></b>	55.71
<b>ρ<sub>g</sub>, lb/ft<sup>3</sup></b>	0.66
<b>μ<sub>o</sub>, cp</b>	11.75
<b>μ<sub>g</sub>, cp</b>	0.01
<b>z</b>	0.97
<b>V<sub>t</sub>, ft/s</b>	1.12
<b>C<sub>d</sub>, dimensionless</b>	1.31

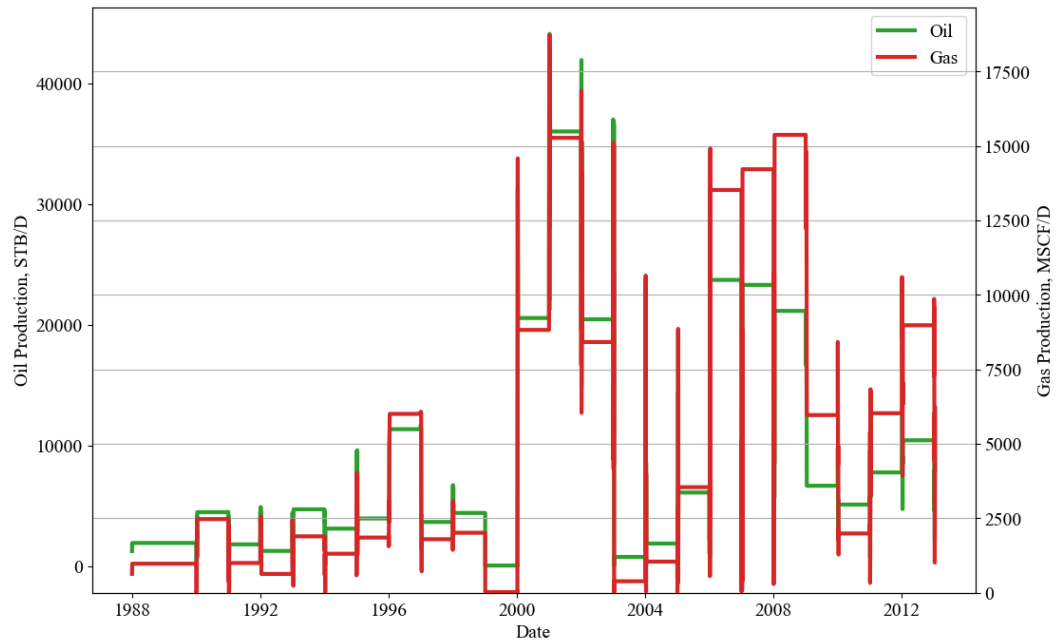


**Figure 18.6:** Anticipated daily production regimes for each phase during 25-years of production.

**Table 18.4:** Calculated different design dimensions of two-phase separators for the 25-years of production.

$d_{sep}$ , in	Gas L <sub>eff</sub> , ft	Liquid L <sub>eff</sub> , ft	L <sub>ss</sub> , ft	SR
16	3.7	176.5	235.3	176.5
20	2.9	113.0	150.6	90.4
24	2.5	78.4	104.6	52.3
30	2	50.2	66.9	26.8
36	1.6	34.9	46.5	15.5
42	1.4	25.6	34.2	9.8
48	1.2	19.6	26.1	6.5
54	1.1	15.5	20.7	4.56
60	1.0	12.6	15.0	3.1
72	0.8	8.7	11.2	1.9
84	0.7	6.4	8.9	1.3
96	0.6	5.0	7.4	0.9
108	0.6	3.9	6.4	0.7

Table 18.4 makes it clear that only the 60-inch-diameter two-phase horizontal separator design meets the design requirement on the slenderness ratio. Furthermore, it is evident from a comparison of the effective lengths needed for each phase that the liquid phase dominates the design criterion due to its larger effective length requirements. Consequently, it was discovered that three identical horizontal half-full two-phase separators with 60x15 in sizes were incorporated into the system in order to achieve the expected flow rates during the course of the system's 25-years of production.

#### **18.4.Three-Phase Separator Design Theory**

Same as the two-phase separators, three-phase separators also have quite similar design theory. However, three-phase separator design theory differs a bit since it tries to separate oil, gas, and water phases. The oil-gas separation design criteria are exactly the same with the two-phase separator design criteria (Arnold & Stewart, 2008). The difference is present due to the oil-water separation. Hence, in the following subsections, this design criteria will be clarified.

On the other hand, the interface level should be carefully taken into account during the three-phase separator design. Also, just like the two-phase horizontal separators, three-phase horizontal separators execute more efficient gravity separation compared to vertical ones as the settling velocity is perpendicular to the flow velocity (Arnold & Stewart, 2008). Since the vessel with horizontal configuration is the most widely used in the industry due to its economic benefits, the design criteria will be based on the half-full horizontal three-phase separators (Arnold & Stewart, 2008).

##### **18.4.1. Oil-water settling**

According to the laboratory tests, it was shown that the oil-water system within the separator obeys the laminar flow conditions (Arnold & Stewart, 2008). To account for this phenomenon mathematically, (Eq. 18-8) can be used utilized. As can be seen from this equation, the droplet size,  $d_m$ , should be introduced. However, due to the difficulty

in the prediction of the water droplet size in oil, it can be assumed that the water droplets are 500 microns in size (Arnold & Stewart, 2008).

According to (Eq. 18-8), separation of oil from the water-phase is much easier compared to the separation of water from the oil-phase (Arnold & Stewart, 2008). According to field data, the amount of oil in produced water from a three-phase separator used to remove water from oil can vary from a few hundred to two thousand milligrams per litre. The settling equation must be applied in order to eliminate oil droplets that are 200 microns or smaller in size when the water phase's viscosity is equal to or greater than that of the liquid hydrocarbon phase (Arnold & Stewart, 2008).

$$V_t = \frac{1.78 \times 10^{-6} (\Delta SG) d_m^2}{\mu_o} \quad (\text{Eq. 18-8})$$

#### **18.4.2. Retention time**

To guarantee that oil finds equilibrium and releases flared gas, oil storage is necessary; data-driven retention periods generally range from 3 to 30 minutes. Large oil droplets need to agglomerate in water storage, which calls for retention periods of 3 to 30 minutes. If particular data is not available, a retention time of 10 minutes is advised. Unless laboratory results indicate differently, compute retention durations for both maximal oil and water rates while designing. Moreover, in the existence of lack of available data, Table 18.5 can be used to select a proper retention time (Arnold & Stewart, 2008). Lastly, in this study, the retention time will be taken as 8.5 minutes since the produced oil lies in the category of intermediate crude oil as shown in Table 18.5. Lastly, to account for the both oil and water retention times in total, (Eq. 18-9) can be used.

$$d_{sep} L_{eff} = 1.42 [Q_w(t_r)_w + Q_o(t_r)_o] \quad (\text{Eq. 18-9})$$

**Table 18.5:** The suggest oil retention times based on the field experience (Arnold & Stewart, 2008).

<b>Oil Retention Time</b>	
<b>API Gravity</b>	<b>Retention Time, min</b>
Condensate	2 – 5
Light Crude Oil (30 - 40)	5 – 7.5
Intermediate Crude Oil (20 - 30)	7.5 – 10
Heavy Crude Oil (< 20)	10 +

#### 18.4.3. Gas capacity

The gas capacity constraint condition is the same with the two-phase separator design. Hence, the same equation, (Eq. 18-4), is valid for the three-phase separator design.

#### 18.4.4. Settling water droplets from oil-phase

The maximum oil pad thickness is determined by calculating the velocity of water droplets settling through oil using Stokes' equation in conjunction with the oil phase retention time. Hence, the following formula, (Eq. 18-10), may be applied to determine the maximum oil-pad thickness. Note that in the existence of no laboratory data, 500 microns are suggested for water droplets to settle down in the continuous oil-phase (Arnold & Stewart, 2008).

$$h_o = \frac{0.00128(t_r)_o(\Delta SG)d_m^2}{\mu_o} \quad (\text{Eq. 18-10})$$

Moreover, to account for the maximum oil-pad thickness that allows the maximum diameter that a vessel may have, the ratio of the vessel cross-sectional area to area of the water-phase must be calculated. To achieve this, the following equation, (Eq. 18-11), is given to account for this objective (Arnold & Stewart, 2008).

$$\frac{A_w}{A_{sep}} = 0.5 \frac{Q_w(t_r)_w}{(t_r)_o Q_o + (t_r)_w Q_w} \quad (\text{Eq. 18-11})$$

Once the  $A_w/A_{sep}$  is determined from (Eq. 18-11), the coefficient beta,  $\beta$ , should be found by the help of Figure 18.7. Then, the maximum diameter that a half-full horizontal vessel may have can be calculated from (Eq. 18-12). While iterating over different vessel diameters provided by API 12J standards, the vessel diameter must not exceed the calculated maximum diameter. Any combination that satisfies this criterion can be used in further computations (Arnold & Stewart, 2008; Specification for Oil and Gas Separators, 1989).

$$(d_{sep})_{\max} = \frac{h_o}{\beta} \quad (\text{Eq. 18-12})$$

#### **18.4.5. Separating oil droplets from water-phase**

Stokes' law determines the final velocity of oil droplets in water, which is usually less than the droplet size of 500 microns water droplet that falls through oil. Therefore, the greatest diameter of a 500-micron water droplet settling through oil usually determines the construction of the vessel. To account for the maximum water-pad thickness, (Eq. 18-13) is given to determine it (Arnold & Stewart, 2008).

$$(h_w)_{\max} = \frac{1520(t_r)_w(\Delta SG)}{\mu_w} \quad (\text{Eq. 18-13})$$

#### 18.4.6. Seam-to-seam length

When sizing a vessel based on its gas capacity, one segment of the vessel's length is required for the mist extractor and another for uniform flow distribution at the inlet diverter. To guarantee uniform gas flow distribution, the length ( $L_{\text{eff}}$ ) between these components rises with vessel diameter. When gas capacity is the limiting factor, use (Eq. 18-14), and when liquid capacity is the governing factor, use (Eq. 18-15) (Arnold & Stewart, 2008).

$$L_{\text{ss}} = L_{\text{eff}} + d/12 \quad (\text{Eq. 18-14})$$

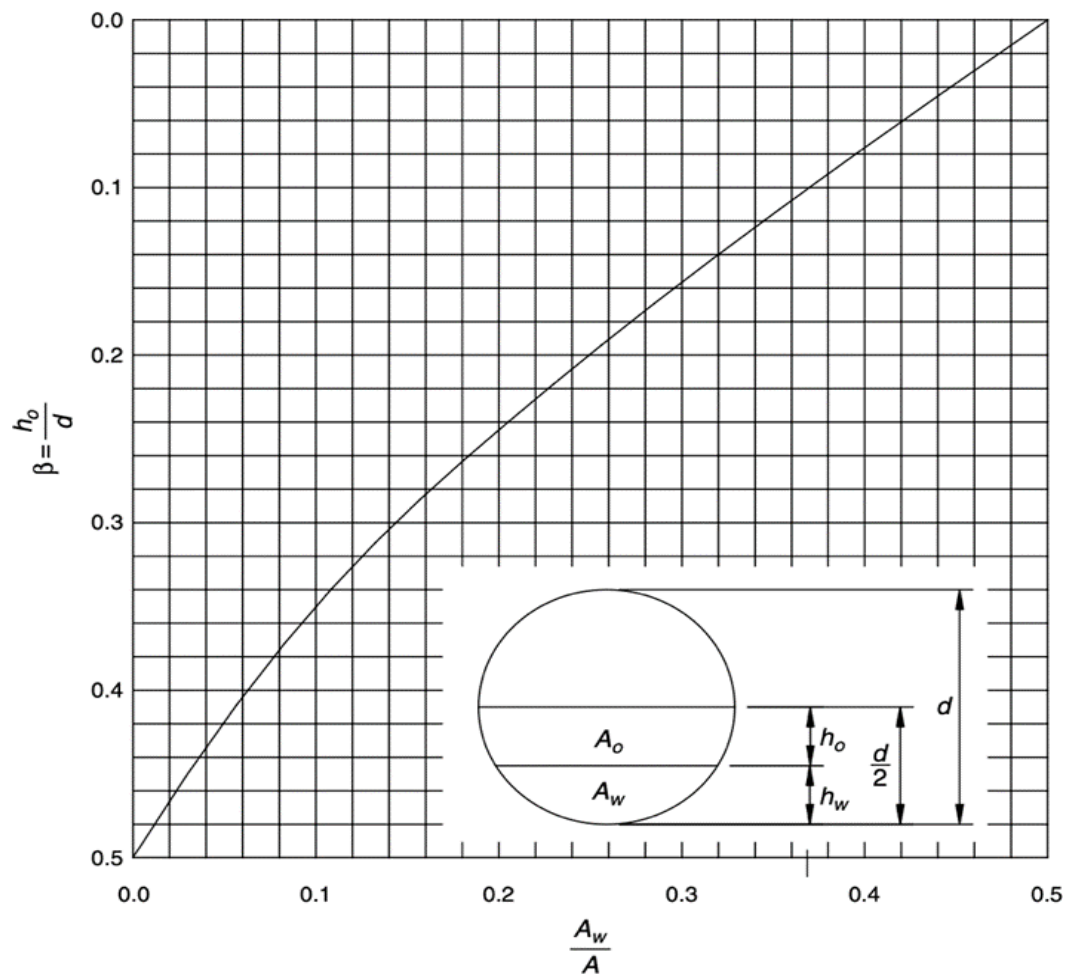


**Figure 18.7:** Coefficient  $\beta$  for a horizontal half-full liquid (Arnold & Stewart, 2008).

$$L_{ss} = \frac{4}{3} L_{eff} \quad (\text{Eq. 18-15})$$

#### 18.4.7. Slenderness ratio

A balance between  $L_{eff}$  and diameter is essential for cost-effective vessel construction, with smaller diameters often resulting in lower costs. Reduced diameter, however, may result in higher fluid velocities and turbulence, which may cause problems with the oil/water contact or gas re-entrainment. The slenderness ratio, SR, which is the seam-to-seam length divided by the outer diameter, is generally advised to be between 3 and 5, however alternative ratios may be utilised with proper design consideration. To calculate the slenderness ratio, (Eq. 18-16) can be used (Arnold & Stewart, 2008).

$$SR = \frac{12L_{ss}}{d_{sep}} \quad (\text{Eq. 18-16})$$

#### 18.5.Three-Phase Separator Design Results

In order to calculate, and design a proper three-phase separator, it is crucial to estimate the future production rates for each phase. Since four different field development plans were proposed, including the base scenario, the design criteria will be based on the base scenario, and the best profitable scenario. However, since each scenario is based on 10 years of production forecast, rates of each phase vary throughout the subsequent years. To overcome this uncertainty, 95<sup>th</sup> percentile of each phase was calculated to design a proper three-phase separator.

However, calculations have revealed that a single separator cannot accommodate the simulated conditions for each field development scenario. Therefore, the following subsections will provide detailed explanations for each design criterion. This limitation arises from the expected high flow rates over the next 10 years of production, which have resulted in unfavourable slenderness ratio values.

### 18.5.1. Separator for the base scenario

As discussed in Simulation Forecasts and Field Development Plans chapter, the estimated total production is 163.26 million STB of oil and 29.07 million STB of water. To translate these totals into daily production rates, we estimated the daily production rates for each phase, which are illustrated in Figure 18.8. Additionally, to address the variability in flow rates, the 95<sup>th</sup> percentiles were calculated for each phase. The 95<sup>th</sup> percentiles for the oil, water, and gas phases were found to be 54,298 STB/D, 11,060 STB/D, and 27,518 MSCF/D, respectively.

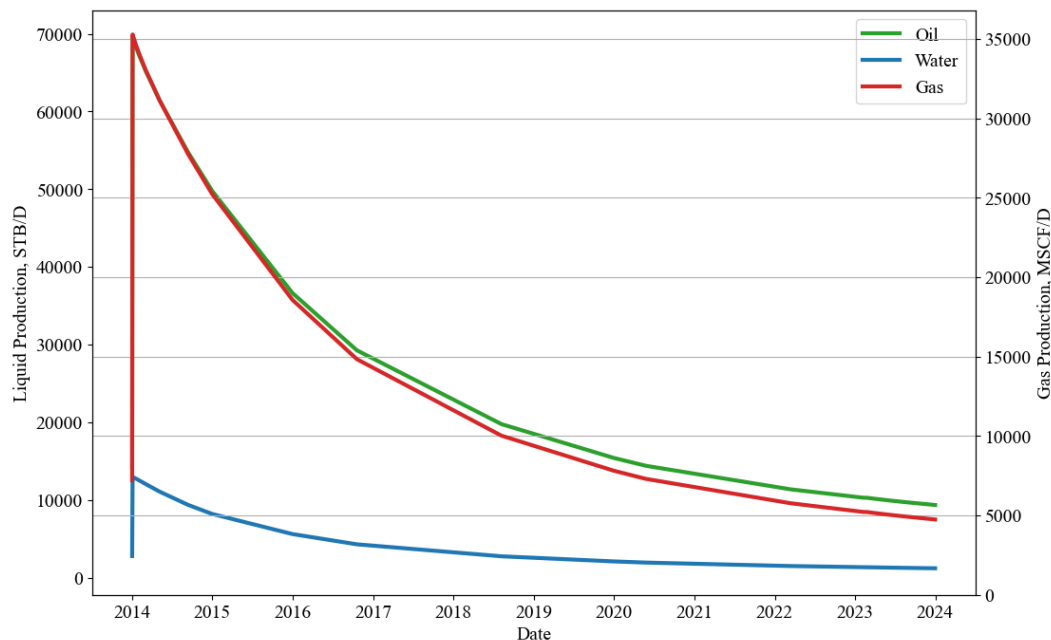


**Figure 18.8:** Daily production rates for each phase during 10 years of production in the base scenario.

In addition, the design procedures described in the section on three-phase separator design were closely adhered to. `GasProperties` and `SeparatorDesign` are two Python routines that were created to automate this procedure. Operating conditions for these tasks were 200 psia and 77 degrees Fahrenheit. However, it was concluded that a single separator would not be adequate for this development scenario because of the projected high output rates shown in Figure 18.9. After a process of trial and error, it was determined that, in the base case scenario, 13 identical three-phase separators would be sufficient. That's why the calculated 95<sup>th</sup> percentile values for each phase were divided by the number of separators to calculate the contribution for each separator. As a result, this design criterion was used to determine the parameters shown in the Table 18.7; thus, by using Table 18.7, the three-phase separator dimensions were calculated and displayed in Table 18.6.

The slenderness ratio (SR) for successful phase separation should be between 3 and 5, according to field experience and prior recommendations (Arnold & Stewart, 2008). Table 18.6 illustrates that just one separator satisfies this requirement. For this development scenario, a three-phase separator with a 60-inch diameter with 25 ft in length was adopted. Additionally, this option satisfies API requirements (Specification for Oil and Gas Separators, 1989).

**Table 18.6:** Calculated different design dimensions of three-phase separators for the base scenario.

d, in	Liquid L <sub>eff</sub> , ft	L <sub>ss</sub> , ft	SR
36	46.8	62.4	20.8
42	34.4	45.9	13.1
48	26.3	35.1	8.8
54	20.81	27.8	6.2
60	16.8	22.5	4.5
72	11.7	15.6	2.6
84	8.6	11.5	1.6

**Table 18.7:** Calculated parameters for the three-phase separator for the base scenario.

<b>Q<sub>o</sub>, STB/D</b>	4,177
<b>Q<sub>w</sub>, STB/D</b>	851
<b>Q<sub>g</sub>, MSCF/D</b>	2,117
<b>ρ<sub>o</sub>, lb/ft<sup>3</sup></b>	55.71
<b>ρ<sub>g</sub>, lb/ft<sup>3</sup></b>	0.66
<b>μ<sub>o</sub>, cp</b>	11.75
<b>μ<sub>g</sub>, cp</b>	0.01
<b>z</b>	0.97
<b>V<sub>t</sub>, ft/s</b>	0.75
<b>C<sub>d</sub>, dimensionless</b>	2.08
<b>Maximum Separator Diameter, in</b>	85.4
<b>Maximum Oil Pad Thickness, in</b>	31.8
<b>A<sub>w</sub>/A<sub>sep</sub></b>	0.08
<b>β</b>	0.37

### 18.5.2. Separator for the best-case scenario

According to the comparison section in Simulation Forecasts and Field Development Plans, the Project: One Rig to Drill Them All was found to be the best model due its high production volumes, low capital risk, low payback duration, and high net present value. And since this is the best choice among the others, a three-phase half full horizontal separator will be designed based on this development plan's schedule.

Upon analysing the expected flow patterns over the 10-year production period in this specific forecast, it was determined that there is a high probability of encountering exceptionally high production rates, as depicted in Figure 18.9. As illustrated in the figure, negative water production volumes are observed. This anomaly arises from the daily injection rates surpassing the daily water production rates. Conversely, oil production peaks at the beginning of the forecast period, followed by a sharp decline. To summarize all production patterns over the forecast period, the 95<sup>th</sup> percentile of

each phase was once again calculated. According to this calculation, the 95<sup>th</sup> percentile values for oil, water, and gas production are 110,723 STB/D, 13,067 STB/D, and 56,129 MSCF/D, respectively.

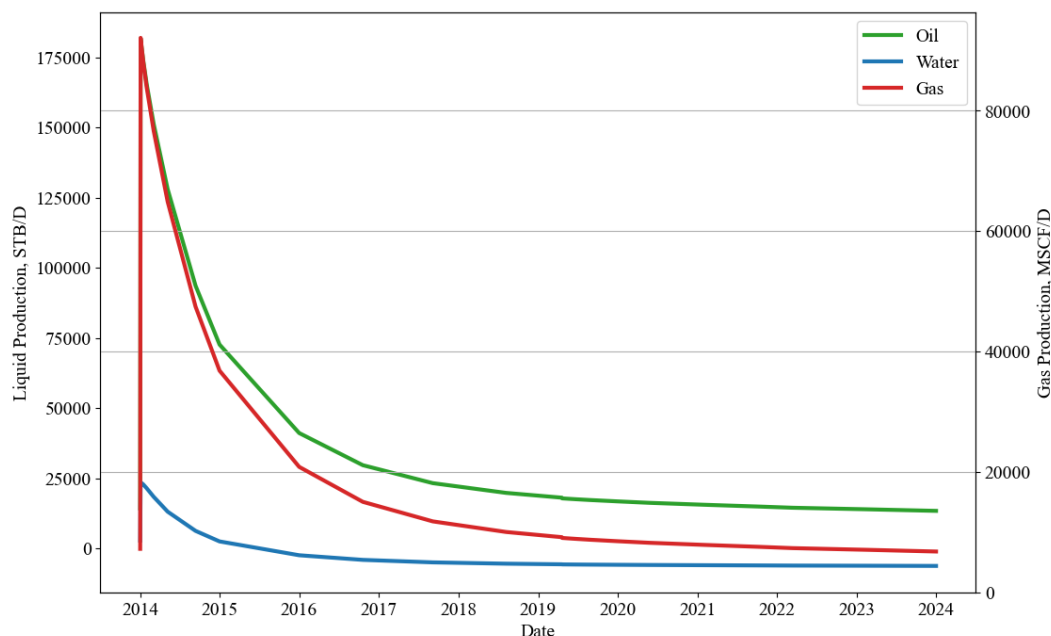


**Figure 18.9:** Daily production rates for each phase during 10 years of production in One Rig to Drill Them All.

In addition, the design procedures described in the section on three-phase separator design were closely adhered to. `GasProperties` and `SeparatorDesign` are two Python routines that were created to automate this procedure. Operating conditions for these tasks were 200 psia and 77 degrees Fahrenheit; thus, the retention time of oil, and water was taken as 8.5 minutes. However, it was concluded that a single separator would not be adequate for this development scenario because of the projected high output rates shown in Figure 18.9. After a process of trial and error, it was determined that, in the base case scenario, 13 identical three-phase separators would be sufficient. That's why the calculated 95<sup>th</sup> percentile values for each phase were divided by the number of separators to calculate the contribution for each separator. As a result, this design criterion was used to determine the parameters shown in the Table 18.8; thus,

by using Table 18.8, the three-phase separator dimensions were calculated and displayed in Table 18.9.

The slenderness ratio (SR) for successful phase separation should be between 3 and 5, according to field experience and prior recommendations (Arnold & Stewart, 2008). Table 18.9 illustrates that just one separator satisfies this requirement. For this development scenario, a three-phase separator with a 72-inch diameter with 30 ft in length was adopted. Additionally, this option satisfies API requirements (Specification for Oil and Gas Separators, 1989).

**Table 18.8:** Calculated parameters for the three-phase separator for Project One Rig to Drill Them All.

<b><math>Q_o</math>, STB/D</b>	<b>8,517</b>
<b><math>Q_w</math>, STB/D</b>	<b>1,005</b>
<b><math>Q_g</math>, MSCF/D</b>	<b>4,320</b>
<b><math>\rho_o</math>, lb/ft<sup>3</sup></b>	<b>55.71</b>
<b><math>\rho_g</math>, lb/ft<sup>3</sup></b>	<b>0.66</b>
<b><math>\mu_o</math>, cp</b>	<b>11.75</b>
<b><math>\mu_g</math>, cp</b>	<b>0.01</b>
<b><math>z</math></b>	<b>0.97</b>
<b><math>V_t</math>, ft/s</b>	<b>1.12</b>
<b><math>C_d</math>, dimensionless</b>	<b>1.31</b>
<b>Maximum Separator Diameter, in</b>	<b>77.8</b>
<b>Maximum Oil Pad Thickness, in</b>	<b>30.0</b>
<b><math>A_w/A_{sep}</math></b>	<b>0.08</b>
<b><math>\beta</math></b>	<b>0.38</b>

**Table 18.9:** Calculated different design dimensions of three-phase separators for Project One Rig to Drill Them All.

<b>d<sub>sep</sub>, in</b>	<b>Liquid L<sub>eff</sub>, ft</b>	<b>L<sub>ss</sub>, ft</b>	<b>SR</b>
16	444.8	593.1	444.8
20	284.7	379.6	227.8
24	197.7	263.6	131.8
30	126.5	168.7	67.5
36	87.9	117.2	39.1
42	64.6	86.1	24.6
48	49.4	65.9	16.5
54	39.1	52.1	11.6
60	31.6	42.2	8.4
72	22.0	29.3	4.9

## **19. ENVIRONMENTAL AND SOCIAL SUSTAINABILITY**

In line with the increasing demand for energy over the years, studies on the drilling process have started to increase. For this reason, studies in the drilling process have started to become more comprehensive and sustainability. Thus, experiments in the field and laboratory environment have also increased more in that process whereas it affects environment negatively like degradation of natural places results from the building of access roads and drilling facilities which divides ecosystems and reduces biodiversity. At the same time, there may be many social issues like concern is the displacement of local people which live in the drilling areas. It is seen that to ensure sustainability of drilling process have many effects in terms of social and environmental so in this study, the sustainability of the drilling process is discussed under these two main headings.

### **19.1.Evaluation of Environmental Impact of Development Scenarios**

The field developments in the oil and natural gas sector have led to an increase in field and laboratory experiments. This situation brings many risks for public health. A lot of chemical gases are released as seen in the oil industry. These harmful chemical gases mix into the air and cause great harm to public health by human respiration or other means. In particular, more exploration of oil and natural gas leads to the establishment of more fields. These sites are increasingly damaging public health as they are getting established near cities and places where there is a large population of people. The Wall Street Journal estimates that nearly five million residents in the US live within one-mile proximity of an oil or gas well (Gold & McGinty, 2013). As a result of the researches, it is seen that the shale gas released in the oil and natural gas fields has a lot of damage on public health. For example, the population near shale gas wells may be affected via physical hazards, including noise, light, vibration, and ionizing radiation that can damage the health of individuals directly, as well as indirectly via pathway stresses (Gorski & Schwartz, 2019). As a result, the development of the drilling causes many issues for environment. One of the most important events in this regard is the effects of greenhouse gas emissions.

Currently, 5.1 billion tons of greenhouse gas emissions, or 15% of all energy-related emissions worldwide, come from oil and gas operations (IEA, 2023). Therefore, as part of the environmental sustainability, the greenhouse gas emissions and energy consumption associated with the field development scenarios were assessed. OPGEE tool which is developed by Stanford University, was utilized to assess greenhouse gas emissions and energy consumption. The Oil Production Greenhouse Gas Emissions Estimator (OPGEE) is an engineering-based life cycle assessment tool designed to estimate greenhouse gas (GHG) emissions associated with the production, processing, and transportation of crude oil and natural gas (Brandt & Masnadi, 2022). According to our company policy, we have taken necessary care in this regard and worked to minimize GHG and the energy consumption. According to the below results, separate calculations were made for each scenario to estimate GHG emissions and energy consumption with the specified tool, and while making these calculations, many parameter data; reservoir pressure and temperature, injection wells number, field age and depth, gas-oil and water-oil ratios, cumulative productive oil and gas volume were entered into the tool as input and as a result, approximate values were forecasted. In a comprehensive comparison of all scenarios, the data reveals both the highest and lowest outcomes. Specifically, the greenhouse gas (GHG) emissions and energy consumption graphs for the base scenario are illustrated in Figure 19.1 and Figure 19.2, respectively. In contrast, the corresponding graphs for Project One Rig to Drill Them All are depicted in Figures Figure 19.7 and Figure 19.8. These comparisons indicate that the scenario characterized by the highest production levels and maximum income also exhibits significantly elevated GHG emissions and energy consumption. Consequently, the company is projected to achieve greater savings in these areas under the subsequent scenario, rather than focusing solely on production and income maximization. The GHG emissions and energy consumption metrics for Project Watcher in the Water and Project Deflate the Smaug fall within an intermediate range and are detailed in Figure 19.3, Figure 19.4, Figure 19.5 and Figure 19.6, respectively. This nuanced analysis underscores the environmental and economic trade-offs inherent in the company's operational strategies across different scenarios.

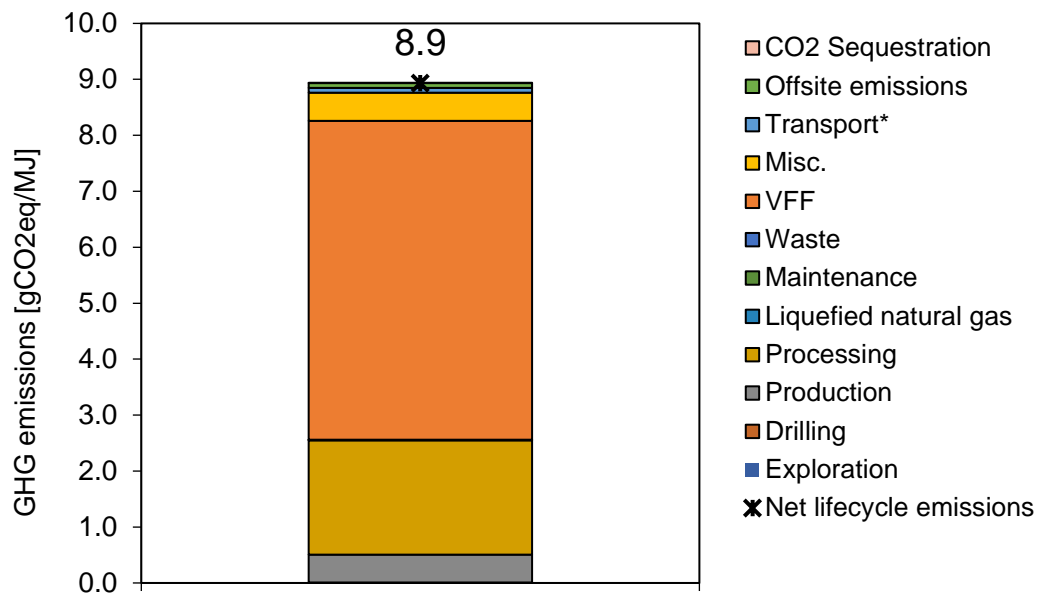


**Figure 19.1:** GHG emission distributions for Base Scenario (Brandt & Masnadi, 2022)

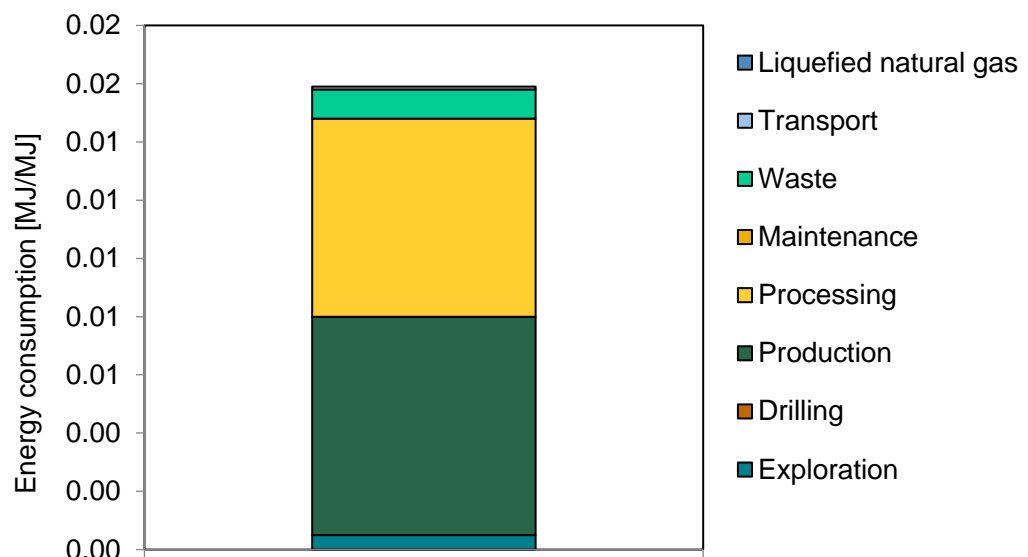


**Figure 19.2:** Energy consumption distribution for Base Scenario (Brandt & Masnadi, 2022)

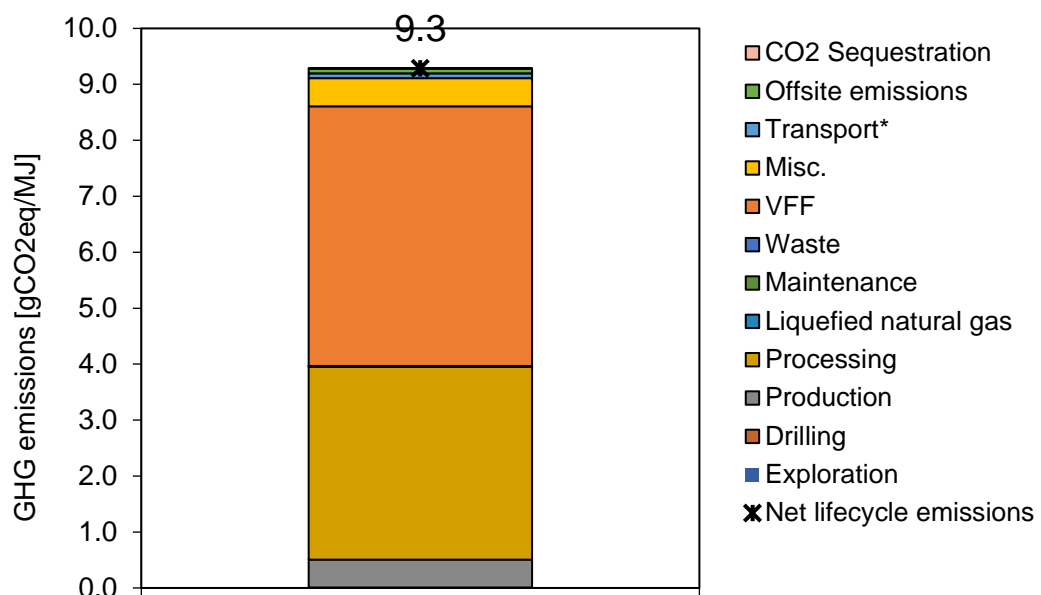


**Figure 19.3:** GHG emission distributions for Project Watcher in the Water (Brandt & Masnadi, 2022).

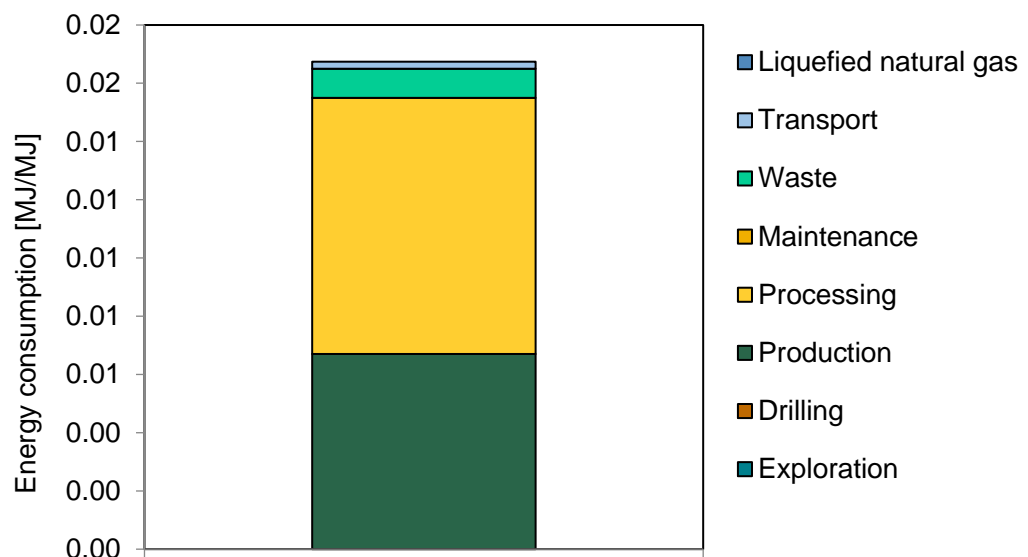


**Figure 19.4:** Energy consumption distribution for Watcher in the Water (Brandt & Masnadi, 2022).

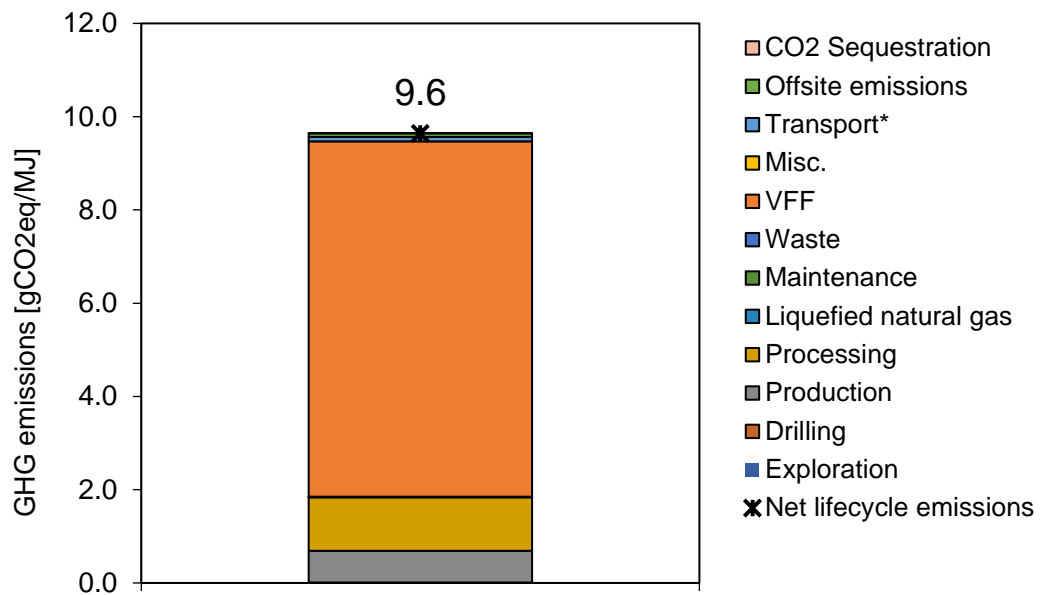


**Figure 19.5:** GHG emission distribution for Project Deflate the Smaug (Brandt & Masnadi, 2022)

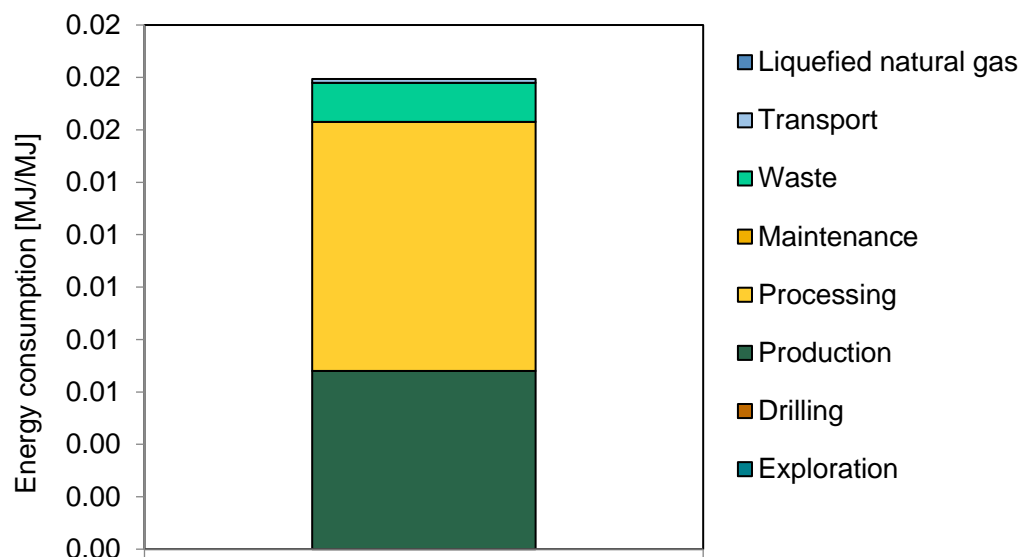


**Figure 19.6:** Energy consumption distribution for Project Deflate the Smaug (Brandt & Masnadi, 2022)

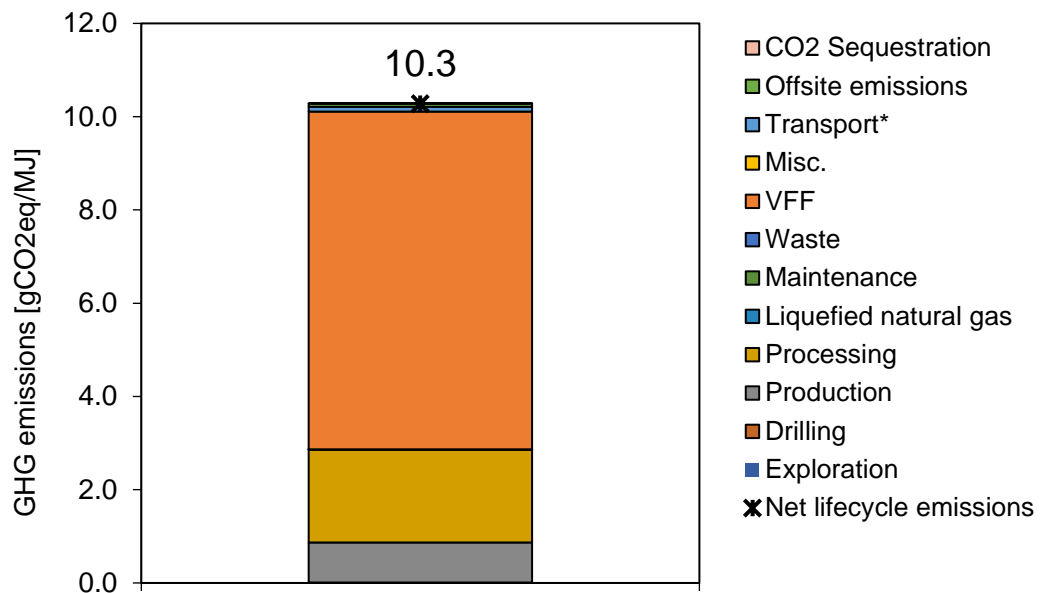


**Figure 19.7:** GHG emission distribution for One Rig to Drill Them All (Brandt & Masnadi, 2022)

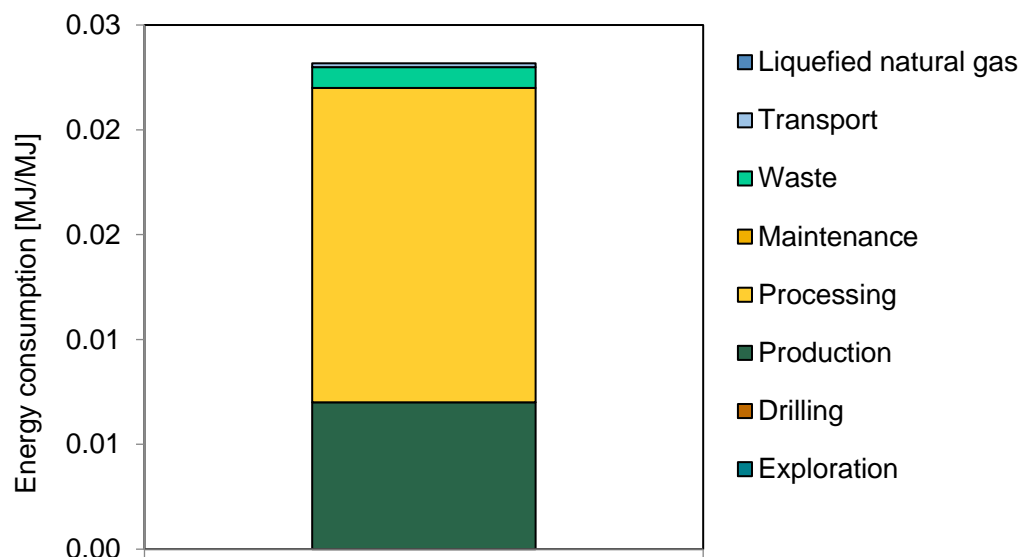


**Figure 19.8:** Energy consumption distribution for One Rig to Drill Them All (Brandt & Masnadi, 2022).

## **19.2.Evaluation of Social Impact of Development Scenarios**

The communities and surrounding areas that are affected by field development have major consequences socially. To make sure that the benefits of field development exceed the disadvantages, both the positive and negative social impacts must be carefully evaluated and managed. The significant social effect in drilling projects is the disagreements between stakeholders within the drilling company. According to Davis and Frankis research, it was observed that non-technical risks in drilling projects are almost at the same rate as technical risks and the majority of non-technical risks are associated with stakeholders (Davis & Frankis, 2014). Table 19.1 illustrates the non-technical and other risks that our company prioritizes and aims to minimize.

The development of oil fields has a significant social impact on the communities and cities where they are located. Both the positive and negative societal impacts of oil field development must be carefully evaluated and managed to ensure that the benefits exceed the negatives. Hence, the list of possible stakeholders seeks to ensure the continued advancement of society and unity within the context of this topic.

The most important stakeholders for field development are oil and gas companies. These companies are indispensable participants among stakeholders by making financial investments and using the highest technologies in the field of drilling sustainability. Environmental non-governmental organizations are also common among these participants because they are important in preventing potential harm to the environment and protecting it. Financial institutions are also among these participants because they provide investment purposes and financing to companies. They contribute to the developments made during development economically and with their future-oriented work. Another participant may be labor unions. They work with companies on workers' wages and safety to achieve maximum momentum and resolve issues on both sides. The mapping diagram indicating the influence and importance of stakeholders for Lord of the Rigs company is shown in Figure 19.9.

**Table 19.1:** Non-technical and other Causes in field development (Laking & McNicoll, 2013).

<b>Non-Technical Causes</b>	
<b>Environmental concerns</b>	Stakeholder concerns over potential environmental impacts
<b>Permitting issues</b>	Difficulty in securing required permits (mainly environmental)
<b>Land Access</b>	Difficulties securing rights to land and physical access to site
<b>Stakeholder opposition</b>	Protests by communities, NGOs or other organizations
<b>Health and Safety</b>	Health and safety concerns or incidents
<b>Extreme weather</b>	Extreme weather conditions preventing activities
<b>Other Causes</b>	
<b>Revenue sharing</b>	Commercial negotiations with governments
<b>Technical challenges</b>	Engineering challenges or unavailability of equipment
<b>Commercial issues</b>	Changes in the commercial viability (commodity / input prices)

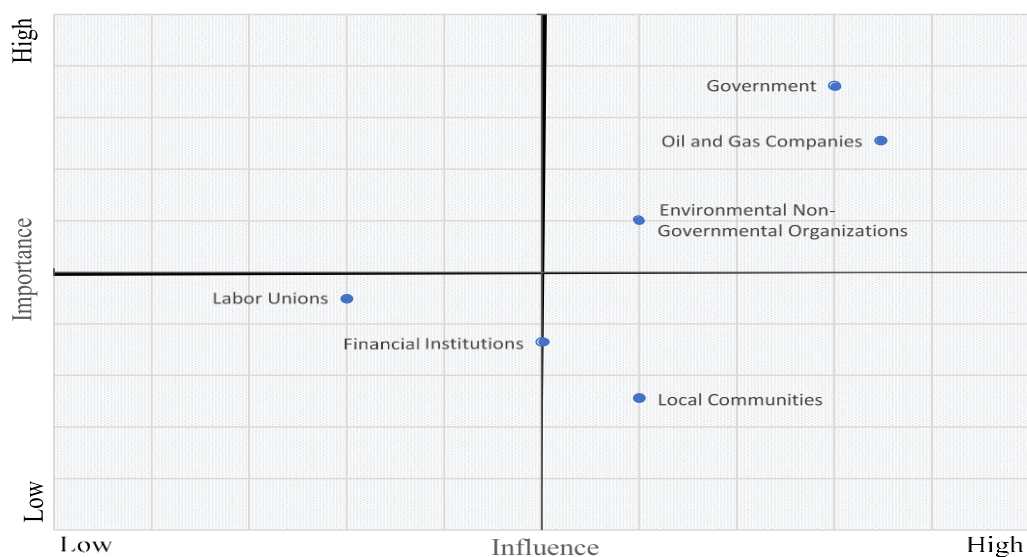


**Figure 19.9:** Stakeholders mapping diagram.

### **19.3.Sustainable Solutions for Future Development**

In examining Figure 19.7 and Figure 19.8 from the provided document, it is evident that the best economic scenario also yields significant CO<sub>2</sub> emissions. This scenario reflects a balance between financial viability and environmental impact. However, the associated CO<sub>2</sub> emissions highlight the necessity for sustainable solutions to mitigate environmental harm while maintaining economic benefits.

Our company, Lord of the Rigs Oil Company, is eager to implement the aforementioned sustainable solutions in our future development projects, particularly in the "One Rig to Drill Them All" scenario. We recognize the importance of balancing economic success with environmental stewardship and social responsibility. Here's how we plan to integrate these solutions into our operations:

- **Adoption of Carbon Capture and Storage (CCS):** We will invest in CCS technology to capture CO<sub>2</sub> emissions from our extraction and production processes. This captured CO<sub>2</sub> will be transported and stored in geological formations, significantly reducing our carbon footprint. By collaborating with leading research institutions, we aim to implement state-of-the-art CCS techniques that can capture up to 90% of CO<sub>2</sub> emissions (Mavar, Gaurina-Medimurec, & Hrnčević, 2021; Zhang, et al., 2023).
- **Enhanced Oil Recovery using CO<sub>2</sub> Injection:** In our oil recovery processes, we will use CO<sub>2</sub>-EOR to enhance extraction efficiency and simultaneously sequester CO<sub>2</sub>. This dual-benefit approach not only boosts our oil production but also contributes to our emission reduction goals. The success of CO<sub>2</sub>-EOR in enhancing oil recovery by 4.83% and increasing CO<sub>2</sub> sequestration rates by 2.29% highlights its potential for sustainable development (Perera, et al., 2016; Zhang, et al., 2023).
- **Integration of Renewable Energy Sources:** We are committed to transitioning our energy supply for extraction and processing operations to renewable sources such as solar and wind power. This shift will help us reduce our reliance on fossil fuels and lower our overall greenhouse gas emissions. By adopting renewable

energy technologies, we align with the IEA's recommendations for a more sustainable oil and gas industry.

- **Utilization of Advanced Monitoring Technologies:** To ensure efficient and effective emission management, we will deploy advanced monitoring technologies, including satellite imagery, drones, and IoT sensors. These tools will enable us to detect and address methane leaks and other emissions in real-time, enhancing our environmental performance and compliance with regulatory standards.
- **Commitment to Sustainable Practices and Policies:** We will adopt industry best practices and comply with stringent environmental regulations to minimize our impact on the environment. Our sustainability strategy will include regular environmental audits, transparent reporting of our emissions, and continuous improvement of our operational practices.
- **Engagement with Communities and Stakeholders:** We believe in fostering strong relationships with the communities where we operate. By engaging with local stakeholders and involving them in our sustainability initiatives, we can ensure that our operations benefit both the environment and the society. Our educational programs and community engagement efforts will promote environmental awareness and support sustainable development goals.

Through these comprehensive measures, Lord of the Rigs Oil Company is committed to leading the industry towards a sustainable future. Our dedication to implementing CCS, CO<sub>2</sub>-EOR, renewable energy, advanced monitoring, sustainable practices, and community engagement reflects our commitment to reducing CO<sub>2</sub> emissions and promoting environmental and social well-being. By integrating these solutions into our operations, we aim to achieve a balance between economic prosperity and environmental responsibility, ensuring a sustainable future for generations to come.

## **20. HSE REGULATIONS**

HSE stands as the acronym for Health, Safety, and Environmental concerns. Within the drilling and drilling fluids community, as well as the broader petroleum industry, these three aspects hold paramount significance (Schlumberger , 2024). Global operators are obligated to adhere to HSE guidelines, a mandatory requirement imposed by internal policies of the majority of corporations within the industry. HSE regulations are examined in the following two sections and applied within the company.

### **20.1. Health and Safety**

The paramount concern of the oil and gas industry is, and will continue to be, safety, with frontline workers playing a pivotal role in upholding secure work practices and averting workplace incidents. Every worker present at a worksite bears the responsibility to execute tasks in a manner that prioritizes safety, incorporating safety considerations into each and every assigned duty. The company policy has been shaped according to API standards on safety and the following items have been implemented. (API R. , 2019)

- The orientation and oversight of newly recruited personnel.
- Providing comprehensive guidance to personnel on work procedures, job responsibilities, and the management of procedural changes.
- Conducting regularly scheduled safety meetings to highlight and discuss job tasks, potential hazards, and associated safe practices.
- Developing a structured plan to coordinate and organize actions by employers and employees during workplace emergencies.
- Disseminating safety education through various channels such as safety meetings, company publications, training programs, and other media.

- Implementing a systematic process for shift changes or personnel turnovers to effectively communicate ongoing operations and potential hazards.
- Adhering to and promoting good housekeeping practices within the workplace.

## **20.2.Environment**

The company acts and takes precautions in accordance with the basic rules of API standards regarding the environment. (Environment Principles, 2021) The progress in this regard is given below.

- Acknowledging and addressing community concerns regarding our raw materials, products, and operational practices.
- Operating our plants, facilities, and managing raw materials and products with a commitment to safeguarding the environment, as well as ensuring the safety and health of our employees and the public.
- Prioritizing safety, health, and environmental considerations in the planning and development of new products and processes.
- Promptly informing relevant officials, employees, customers, and the public about significant safety, health, and environmental hazards related to our industry, and recommending appropriate protective measures.
- Providing guidance to customers, transporters, and other stakeholders on the safe use, transportation, and disposal of our raw materials, products, and waste materials.
- Economically developing and producing natural resources while efficiently utilizing energy to conserve these resources.
- Advancing knowledge through the conduct or support of research on the safety, health, and environmental impact of our raw materials, products, processes, and waste materials.
- Committing to reducing overall emissions and waste generation.
- Collaborating with others to address challenges arising from the handling and disposal of hazardous substances resulting from our operations.

- Participating with governmental and non-governmental entities in the development of responsible laws, regulations, and standards aimed at protecting the community, workplace, and environment.
- Promoting these principles and practices by sharing experiences and offering assistance to others involved in the production, handling, use, transportation, or disposal of similar raw materials, petroleum products, and wastes.

## **21. CONCLUSION**

The goal of this project is to design and plan the location and operation of a new well to be drilled using well log and reservoir data from the 25 wells located in the Mount Doom Oil Field. The project began with the creation of a two-dimensional map of the field that calculated the distances between the wells to the chosen reference point. It subsequently moved on to data analysis, which resulted in the discovery of petrophysical characteristics. The research led to the discovery of three unique hydrocarbon layers: Precious-1, Gollum-1, and Thorin-1. These layers were eventually presented in three dimensions with Surfer, making it easier to understand the subsurface structures. As a result, a latitude of 791288.6 and a longitude of 407557.6 was found to be the ideal location for the new well, Bane-01.

The design steps involve choosing casing, cement, tubing, mud, and a wellhead. The Mechanical earth model was developed to better understand the properties of rocks under stress. The calculated Poisson ratio of 0.33 indicates that the rock is isotropic and uniformly elastic. The closeness of the maximum Poisson ratio value to 0.5 implies that the rock has a low bulk modulus but a high compressibility. The decrease in frictional angle between 1750 and 3500 ft suggests the presence of troublesome shaly zones in the formation. Mechanical properties were used to determine pressure gradients, yielding a safety factor of  $\pm 0.5$  ppg for the mud window. This led to the decision to use 9.5 ppg of KCl polymer mud up to 3000 ft from the surface, and 11 ppg KCl polymer mud for the production section up to 7600 ft from the surface.

The bit and casing sizes were selected based on the bit size of Well-03 near Bane-01 and certain API standards. As a result, outside diameters of 133/8, 95/8, and 65/8 inches, as well as bit sizes of 171/2, 121/4, and 81/2 inches, were chosen successively for the conductor, surface, and production respectively. Following burst and collapse calculations, H-40,48 lbm/ft was selected for conductor up to 150 feet from the surface, H-40, 32.3 lbm/ft for the surface, and C-75, 32 lbm/ft for production. According to API standards, Class A cement with 8% bentonite was used for surface applications up to a depth of 3000 ft, while Class G cement containing 8% bentonite was used for production between 5600 and 7600 ft. Cementing activities used MKP750 pump from

the PT Mudking Asia Pacific Raya brand. The single-acting triplex pump has been shown to be more efficient than duplex pumps since it can transport more liquid per stroke, generates a smoother flow, and has less vibration.

Drill string designs now follow the Huber-Von Mises Law. The drill string consists of drill pipe, heavy-weight drill pipe, drill collars, and drill bits. Soft drill bit variations were utilized for conductor and surface applications, whereas medium drill bits were employed in manufacturing. The weight on bit (WOB) values for each segment were calculated by multiplying the unit weight on bit values by bit size. The drill collar outer diameter was computed using the selected drill bit size. The inner diameter (ID) and weight of the drill collar were determined based on the information provided. The drill collar length was then calculated, and because the Range 2 type was selected, it was corrected to the nearest whole number divisible by 30 ft, yielding the number of drill collars needed. The optimal drill pipe solutions for surface and production were determined using production data and drill collar diameters. Heavy weight drill pipe (HWDP) was selected to ensure a bending stress ratio of 2.5-3 when connecting drill collars directly to drill pipes. Calculations were performed to determine the total length and weight of the bottom hole assembly. Stress calculations for the drill string were then performed using the Huber Von Mises Law, which took into account scenarios such as the dog-leg scenario. Following that, torque calculations for connection types, which play a major role in drilling string resistance, were performed and their strengths were confirmed. Furthermore, the neutral point, where there is no stress in the drilling string, was found to be either above the drill collar or above the drill pipe. In the event that the drilling string becomes stuck during the drilling process, shock loading, or the situation in which the force on top of the drilling string must be released by pushing it upward with a given force, was calculated. The amount of elongation induced by the weight of a freely suspended drilling string in the well was then calculated. The use of jars and stabilizers was then discussed, and the number and placement of stabilizers were calculated to finish the drilling string design.

The parasitic pressure loss values of the selected 9.5 ppg KCl polymer mud for the conductor and surface, as well as 11 ppg for the production section, were estimated using the Bingham plastic and Herschel-Bulkley rheological models based on the mud window. Because of its capacity to balance hydrostatic pressure, convey cuttings

satisfactorily, and cool the drill bit, the mud's rheological properties were investigated using the Herschel-Bulkley model for additional pressure loss study.

Estimations were carried out at appropriate 1000-ft intervals to accomplish hydraulic optimization. As a result, pressure loss estimations were carried out operating the mud pump at 450 gal/min for the surface stage, and 350 gal/min for the production stage. Moreover, for each interval, the hydraulic optimization was performed. Since it was found to be not possible to reach the maximum jet impact force on the bit during the surface stage, hydraulic optimization for the surface stage was performed to achieve the maximum possible pressure loss on the bit. On the other hand, the idea of sustaining the maximum jet impact force on the bit was applied during the optimization of the production stage since the parasitic pressure losses are high enough.

Cost analysis is a critical step in the decision-making process since it involves examining all well-related expenses, including exploration, design, and staff. The Young's modulus mentioned in the Mechanical Earth Model was utilized to estimate the rate of penetration by referring to the analysis of scientists. Trip time and drilling time calculations were utilized to determine the duration of drilling and other operations, as well as the associated costs. F-200 was the chosen rig that consumes diesel for its engines, therefore daily cost for the fuel consumption was calculated. By adding the kWh power of the rig, mud pump, draw works, and top drive and multiplying with USD/kWh cost, cumulative cost analysis for needed diesel was observed in USD dollars. Trip and drilling time estimates have been estimated for worst-, middle-, and best-case scenarios, taking coring and logging completion times of 1, 2, and 3 days into account. As a consequence, the worst-case scenario was found to be 27 hours, followed by 19 hours in the medium and 15 hours in the best situation. In addition, the AFE approach, and a statistical approach were used to estimate the total cost of the drilling operation for each scenario. Besides, the results estimated from each approach were compared within each scenario. As a result, it was found that there is a 250000 USD difference between the two approaches within each scenario. This might be acceptable since each approach has lots of uncertainties.

Estimation of OOIP calculations based on both Havlena and Odeh and, reservoir simulations were aimed to be compared in order to design an optimum reservoir

simulation model. It is important to develop a reservoir simulation model in order to overcome the uncertainties within the reservoir, and by applying history matching it was pursued to visualize the overall field and, also to forecast the future behaviour of Bane-01 and other development wells. The petrophysical parameters obtained from well log analysis of 25 previously drilled wells in the Mount Doom Oil Field were plugged into the simulation program RUBIS, with interpolation techniques. Thus, PVT properties were gathered from the laboratory experiments. The applied reservoir model was found to be explanatory and successful because the average reservoir pressure, cumulative oil production and behavior showed similarities over the years and matched at the starting and ending points.

In order to design separators, z-factor and gas viscosity properties were estimated with using Dranchuk and Abu-Kassem, and Lee, Gonzalez and Eakin correlations. As a result, the specific gravity of the associated gas was evaluated to be 0.635. After estimating the gas properties two-phase and three-phase separator designs were applied.

## REFERENCES

- (2024). Retrieved from Schlumberger :  
<https://glossary.slb.com/en/terms/h/hse#:~:text=Abbreviation%20for%20health%2C%20safety%20and,to%20the%20entire%20petroleum%20industry>.
- 250 EMI 400 Top Drive - TESCO Corporation.* (2011). Retrieved from Yumpu website: <https://www.yumpu.com/en/document/read/50666658/250-emi-400-top-drive-tesco-corporation>
- Abdulrazzaq, F. N., & Hasan, O. F. (2023). A review of automatic history matching. *Materials Today Proceedings*, 3817-3822.
- AlBajalan. (2021, July 28). Evaluation of the Performance of Conventional Water-Based Mud Characteristics by Applying Zinc Oxide and Silica Dioxide Nanoparticle Materials for a Selected Well in the Kurdistan/Iraq Oil Field. p. 4.
- Alford, J., Blyth, M., Tollesen, E., Crowe, J., Loreto, J., Mohammed, S., & Pistre, V. (2012). Sonic Loggin While Drilling-Shear Answers. *Oilfield Review*(24), pp. 4-15.
- Al-Rubaii, M. M., Al-Shehri, D., Mahmoud, M. N., Al-Harbi, S. M., & Al-Qahtani, K. A. (2021). Real Time Automation of Cutting Carrying Capacity Index to Predict Hole. *SPE Annual Technical Conference and Exhibition*. Dubai, UAE: OnePetro. doi:<https://doi.org/10.2118/206235-MS>
- Andersson, E. R. (2000). Economic evaluation of ergonomic solutions: Part I – Guidelines for the practitioner. In *Ergonomics Guidelines and Problem Solving* (pp. 463-471). Elsevier.
- API, R. (2019). *Occupational Safety and Health for Oil and Gas Well Drilling and Servicing Operations*. American Petroleum Institute.
- API, R. 7.-1. (1998). *Recommended Practice for Drill Stem Design and Operating Limits*. American Petroleum Institute.

- Arnold, K., & Stewart, M. (2008). *Surface Production Operations Design of Oil Handling Systems and Facilities* (1 ed., Vol. 1). Gulf Professional Publishing.
- Asquith, G. (1982). *Basic Well Log Analysis*. Tulsa, Oklahoma: The American Association of Petroleum Geologists.
- Baker, R. O., Jensen, J. L., & Yarranton, H. W. (2015). *Practical Reservoir Engineering and Characterization*. Gulf Professional Publishing.  
doi:<https://doi.org/10.1016/C2011-0-05566-7>
- Bassiouni, Z. (1994). *Theory, Measurement and Interpretation of Well Logs* (Vol. 4). (P. Schenewerk, & D. Pert, Eds.) Richardson, Texas, United States of America: Society of Petroleum Engineers.
- Bateman, R. M. (2020). *Formation Evaluation with Pre-Digital Well Logs*. Elsevier.  
doi:<https://doi.org/10.1016/C2018-0-03023-6>
- Bornmann, L. (2012, 06 08). How to analyse percentile impact data meaningfully in bibliometrics: The statistical analysis of distributions, percentile rank classes and top-cited papers.
- Bourgoyne Jr, A. T., Millheim, K. K., Chenevert , M. E., & Young Jr, F. S. (1991). *Applied Drilling Engineering* (Vol. II). Society of Petroleum Engineers.  
doi:<https://doi.org/10.2118/9781555630010>
- Brandt, A. R., & Masnadi, M. S. (2022). *Oil Production Greenhouse Gas Emissions Estimator*. California Environmental Protection Agency, Air Resources Board.
- BRANDT™ Ideal Mud Tank System*. (n.d.). Retrieved from nov.com/wellsite website: <https://edge.sitecorecloud.io/nationaloil37c5-novinc-prod-e309/media/nov/files/products/wbt/wellsite-services/ideal-mud-tank-system/brandt-ideal-mud-tank-system-spec-sheet-english.pdf>
- Carmichael, R. (1982). *Handbook of Physical Properties of Rocks Volume II*. Iowa City : CRC Press.

- Cook, M. (2021). *Petroleum Economics and Risk Analysis A Practical Guide to E&P Investment Decision-Making*. Society of Petroleum Engineers.
- Craft, B. C., Hawkins, M. F., & Terry, R. E. (1991). *Applied Petroleum Reservoir Engineering*. Prentice Hall.
- Crain, E. (2011). *Crain's Petrophysical Handbook*.
- Dake, L. P. (1978). *Fundamentals of Reservoir Engineering* (Vol. 8). Elsevier.
- Darley, H., & Gray, G. R. (1983). *Composition and Properties of Drilling and Completion Fluids* (5th ed.). Gulf Professional Publishing.
- Davis, & Frankis. (2014).
- Devereux, S. (1998). *Practical Well Planning and Drilling Manual*. PennWell Corporation.
- Dranchuk, P. M., & Abou-Kassem, H. (1975). Calculation of Z Factors For Natural Gases Using Equations of State. *J Can Pet Technol*, 14(3).
- Eaton, B. A. (1975). The Equation for Geopressure Prediction from Well Logs. *Society of Petroleum Engineers*.
- Environment Principles*. (2021). Retrieved from American Petroleum Institute:  
<https://www.api.org/oil-and-natural-gas/environment/environmental-principles>
- Glover, P. (2001). Formation Evaluation MSc Course Notes. University of Leeds.  
Retrieved from  
[https://www.academia.edu/25574527/Formation\\_Evaluation\\_MSc\\_Course\\_Notes](https://www.academia.edu/25574527/Formation_Evaluation_MSc_Course_Notes)
- Gold, R., & McGinty, T. (2013). *Energy boom puts wells in America's backyards*. Wall Street Journal.
- Gorski, I., & Schwartz, B. S. (2019). *Environmental Health Concerns From Unconventional Natural Gas Development*. Oxford Research Encyclopedia of Global Public Health.

- Gucuyener, Y. G. (2023). New Approaches to Improve Rheological Characterization of KCl/Polymer. *SPE/IADC International Drilling Conference and Exhibition*, (p. 1).
- Halliburton. (2010). Retrieved from Halliburton eRed Book:  
[www.halliburton.com/eRedbook](http://www.halliburton.com/eRedbook)
- Hossain, M. E. (2015). Drilling Costs Estimation for Hydrocarbon Wells. *Journal of Sustainable Energy Engineering*, 3, 3–32. doi:doi:10.7569/jsee.2014.629520
- IEA. (2023, May). *International Energy Agency*. Retrieved from International Energy Agency: [www.iea.org](http://www.iea.org)
- Iglauer, S. (2013, March 9). *Relative permeability*. Retrieved from PetroWiki:  
[https://petrowiki.spe.org/Relative\\_permeability#:~:text=The%20critical%20gas%20saturation%20is,range%20from%20zero%20to%2020%25.](https://petrowiki.spe.org/Relative_permeability#:~:text=The%20critical%20gas%20saturation%20is,range%20from%20zero%20to%2020%25.)
- Ikoku, C. U. (1992). *Natural Gas Production Engineering*. Florida: Krieger Publishing Company.
- Islam, A., Habib, M., Islam, M., & Mita, M. (2013). Interpretation of wireline log data for reservoir characterization of the Rashidpur Gas Field, Bengal Basin, Bangladesh. *Journal of Applied Geology and Geophysics*, 1(4), 47-54.
- Jiimaa, G. (2014). Cutting Transport Models and Parametric Studies in Vertical and Deviated Wells. *Master's Thesis in Petroleum Engineering*. Retrieved from <http://hdl.handle.net/11250/183530>
- Kahraman, S., Bilgin, N., & Feridunoglu, C. (2003, July). Dominant rock properties affecting the penetration rate of percussive drills. *International Journal of Rock Mechanics and Mining Sciences*, 40, 711-723. doi:10.1016/S1365-1609(03)00063-7
- Kaiser, M. J., & Pulsipher, A. G. (2007). Generalized Functional Models for Drilling Cost Estimation. *SPE Drill & Completion*, 22(2), 67-73.  
doi:<https://doi.org/10.2118/98401-PA>

- Kolesnikov, F. A., Kolesnikov, N. S., Bocharnikov, V. S., Kozinskaya, O. V., & Denisova, M. A. (2023). Comparative characteristics of duplex and triplex pumps with cylinder-piston modification. *AIP Conf. Proc.*, 2911. doi:<https://doi.org/10.1063/5.0168785>
- Laking, S., & McNicoll, I. (2013). *Social Licence to Operate - Non-technical Risk In New Field Development*. SPE.
- Langnes, G. L., Robertson, J. O., & Chilingar, G. V. (1972). *Secondary Recovery and Carbonate Reservoirs*. New York: Elsevier.
- Lee, A. L., Gonzalez, M. H., & Eakin, B. E. (1966). The Viscosity of Natural Gases. *J Pet Technol*, 18(8).
- Litvak, M., Gane, B., McMurray, L., & Skinner, R. (2007). Field Development Optimization in a Giant Oil Field in Azerbaijan and a Mature Oil Field in the North Sea. *Offshore Technology Conference*. Houston, Texas.
- Lukić, D. (2018). FRICTION ANGLE OF SOIL AND ROCK. *Contemporary achievements in civil engineering*, (pp. 349-357). Subotica. doi:10.14415/konferencijaGFS2018.034
- Marchiano, M., Meola, A. A., Lopez, M., & Ajayi, O. (2019). Utility Power for Onshore Drilling Rigs: An Application Guide. *2019 IEEE Petroleum and Chemical Industry Committee Conference (PCIC)*, (pp. 121-130). doi:10.1109/PCIC30934.2019.9074528
- Masalmeh, S. K. (2002). Studying the effect of wettability heterogeneity on the capillary pressure curves using the centrifuge technique. *Journal of Petroleum Science and Engineering*, 29-38.
- Masalmeh, S. K., Shiekah, I. A., & Jing, X. D. (2007). Improved Characterization and Modeling of Capillary Transition Zones in Carbonate Reservoirs . *SPE Reservoir Evaluation & Engineering*, 191-204.
- Mavar, K. N., Gaurina-Medimurec, N., & Hrnčević, L. (2021). Significance of Enhanced Oil Recovery in Carbon Dioxide Emission Reduction. *Sustainability*, 13(4), 1800.

- McCain, W. D. (1989). *The Properties of Petroleum Fluids, 2nd Edition*. Tulsa, Oklahoma: PennWell Books, LLC, 2017.
- Merlo, A. (1995). An Innovative Model For Drilling Fluid Hydraulics. *Society of Petroleum Engineers*, 79.
- Mitchel, R. F. (1988). New Concepts for Helical Buckling. *SPE Drill Eng* 3, 303–310. doi:<https://doi.org/10.2118/15470-PA>
- Najibi, A. R., Ghafoori, M., Lashkaripour, G. R., & Asef, M. R. (2017). Reservoir geomechanical modeling: In-situ stress, pore pressure, and mud design. *Journal of Petroleum Science and Engineering*, 151, 31-39. doi:<https://doi.org/10.1016/j.petrol.2017.01.045>
- Özbayoğlu, M. E., & Altun, G. (2010). *Sondaj Mühendisleri İçin Kurs Serisi* (Vol. 1). Lüleburgaz: Türkiye Petrolleri Anonim Ortaklığı Sondaj Dairesi Başkanlığı.
- Peng. (2009, November 24). An Environmentally Friendly WBM System Can Prevent Hard Brittle Shale Instability. *LEMIGAS SCIENTIFIC CONTRIBUTIONS*, 133-134.
- Perera, M. S., Gamage, R. P., Rathnaweera, T. D., Ranathunga, A. S., Koay, A., & Choi, X. (2016). A Review of CO<sub>2</sub>-Enhanced Oil Recovery with a Simulated Sensitivity Analysis. *Energies*, 9(7), 481.
- Qin, X., Zhao, L., Cai, Z., Wang, Y., Xu, M., Zhang, F., . . . Geng, J. (2022). Compressional and shear wave velocities relationship in anisotropic organic shales. *Journal of Petroleum Science and Engineering*, 219, 111070. doi:<https://doi.org/10.1016/j.petrol.2022.111070>
- (2006). *Rheology and Hydraulics of Oil-well Drilling Fluids*. Washington D.C: API Publishing Services.
- Ruiz, J., & C., L. (2014). Measurement of the Basic Friction Angle of Rock by Three Different Tilt Test Methods. *ISRM Regional Symposium - EUROCK 2014, Vigo*. Spain.

- Schlumberger. (1997). *Log Interpolation Charts*. Houston, Texas.
- Schlumberger. (2017). *Techlog Geomechanics Workflow/Solutions Training Version 2016*.
- Sentry Wellhead*. (2017, January). Retrieved from Sentry Wellhead website:  
<http://sentrywellhead.com>
- Serra, O. (1984). *Fundamentals of Well-Log Interpretation*. Amsterdam: Elsevier.
- Specification for Oil and Gas Separators. (1989, October 1). *API SPECIFICATION 12J*, 7. Washington, DC, United States of America: American Petroleum Institute.
- Starling, K. E., & Ellington, R. T. (1964). Viscosity correlations for nonpolar dense fluids. *AICHE J.*, 10, 11-15.
- Stawisz, T. (2002). Successfully Replacing Oil-Based Drilling Fluids with Water-Based Drilling Fluids: Case Study Demonstrates Value of Extensive Planning and Execution in Extended-Reach Well. *IADC/SPE Drilling Conference*, (p. 11).
- Sutton, R. P. (1985). Compressibility Factors for High-Molecular-Weight Reservoir Gases. *Paper presented at the SPE Annual Technical Conference and Exhibition*. Las Vegas, Nevada.
- Swaco, M. (1998). *MI Swaco Mud Engineering Handbook*.
- Timur, A. (1968). An Investigation Of Permeability, Porosity, And Residual Water Saturation Relationships. *SPWLA 9th Annual Logging Symposium*. New Orleans.
- Towler, B. F. (2002). *Fundamental Principles of Reservoir Engineering*. Society of Petroleum Engineers. doi:<https://doi.org/10.2118/9781555630928>
- upet.com*. (1991). Retrieved from upet.com website:  
<https://upet.com/equipment/drawworks/>
- Wang, Z.-w., Lin, B., Wang, Y.-j., Wang, M., Yang, B., Zhang, Z.-z., . . . Yang, Z.-w. (2024). Application of Reservoir Simulation in Production and

Development Management. *Proceedings of the International Field Exploration and Development Conference 2023* (pp. 248–256). Singapore: Springer, Singapore.

*Weatherford*. (2006). Retrieved from Weatherford website:

<https://www.weatherford.com/documents/brochure/products-and-services/drilling/blowout-preventers/>

Wu, J. (2021). Chapter Two - Casing string and design. In G. Liu (Ed.), *Applied Well Cementing Engineering* (pp. 17-67). Gulf Professional Publishing.  
doi:<https://doi.org/10.1016/B978-0-12-821956-0.00007-9>

Ya-nan, S., Weiting, L., Jinbao, J., Kai, L., Hua, K., & Yupeng, Y. (2021). Quantitative characterization of collapse and fracture pressure uncertainty based on Monte Carlo simulation. *Journal of Petroleum Exploration and Production Technology*, 2199–2206. doi:<https://doi.org/10.1007/s13202-021-01159-5>

Zhang, J. (2013). Effective stress, porosity, velocity and abnormal pore pressure prediction accounting for compaction disequilibrium and unloading. *Marine and Petroleum Geology*, 45, 2-11.  
doi:<https://doi.org/10.1016/j.marpetgeo.2013.04.007>

Zhang, J., & Yin, S.-X. (2017, September). Fracture gradient prediction: an overview and an improved method. *Petroleum Science*, 14. doi:[10.1007/s12182-017-0182-1](https://doi.org/10.1007/s12182-017-0182-1)

Zhang, L., Sun, T., Han, X., Shi, J., Zhang, J., Huiting , T., & Yu, H. (2023). Feasibility of Advanced CO<sub>2</sub> Injection and Well Pattern Adjustment to Improve Oil Recovery and CO<sub>2</sub> Storage in Tight-Oil Reservoirs. *Process*, 11(11), 3104.

## **APPENDICES**

### **A. APPENDIX: Well Log Charts**

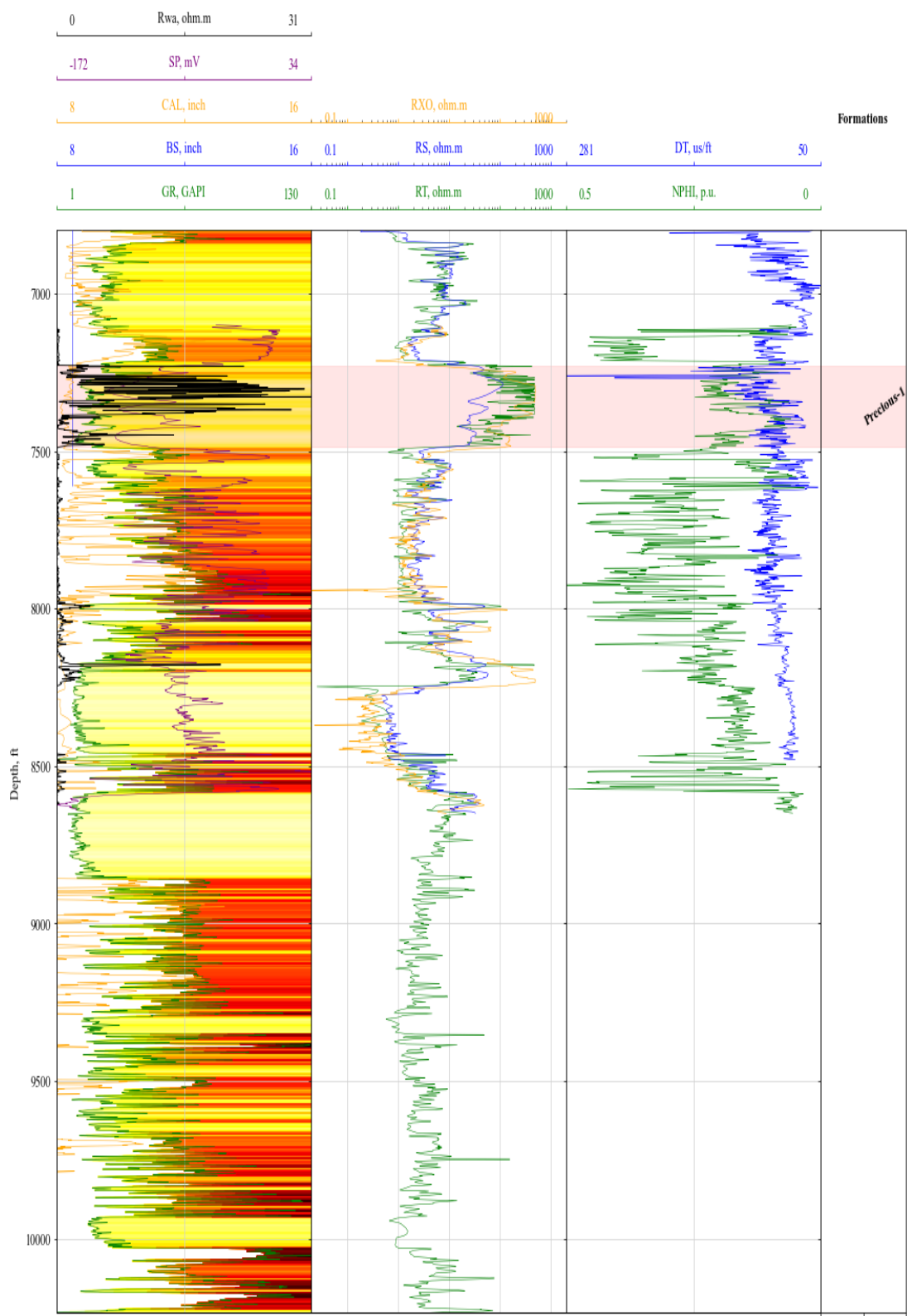


**Figure A.1:** Well log display of Well-02 along with designated formations.

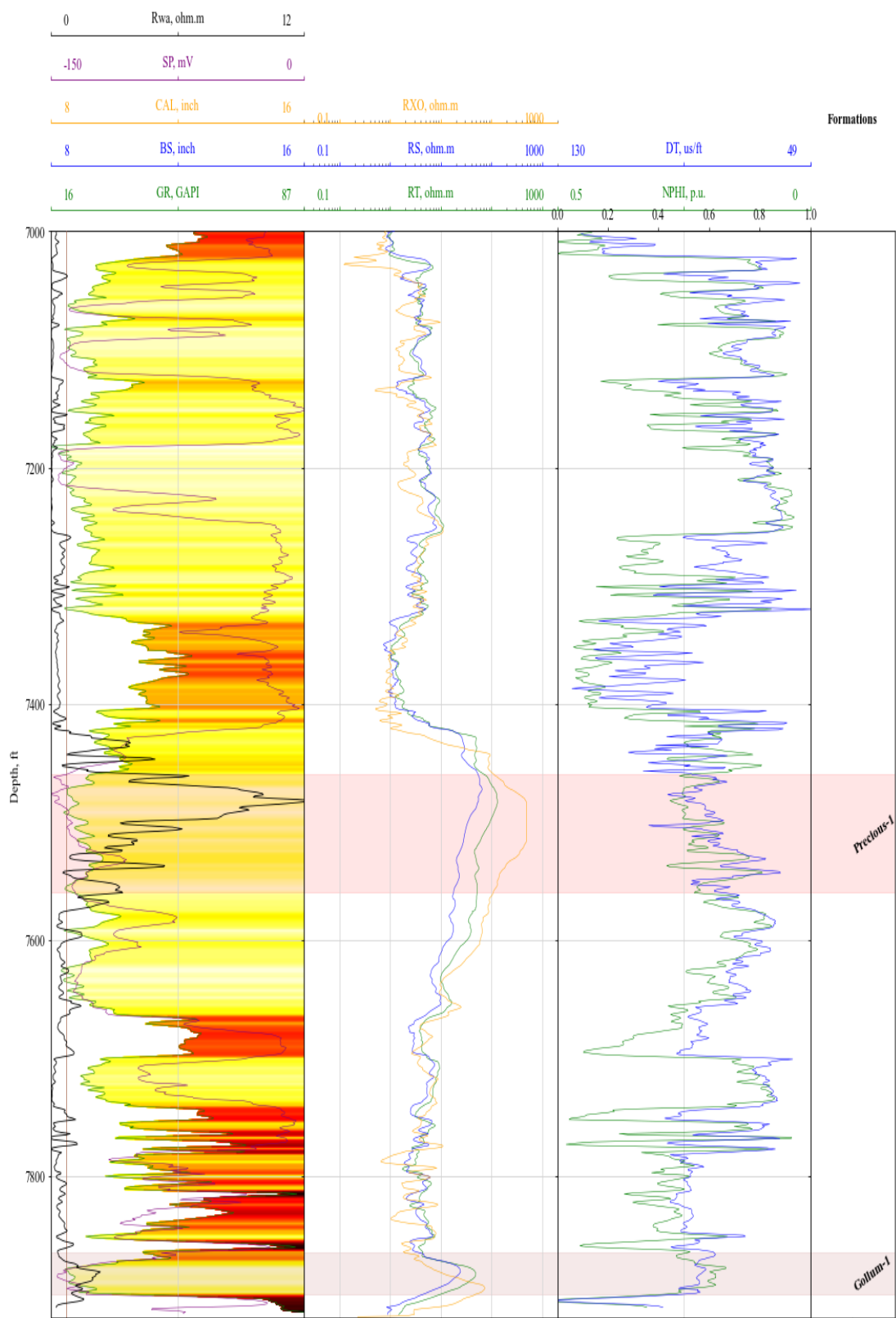


**Figure A.2:** Well log display of Well-03 along with designated formations.

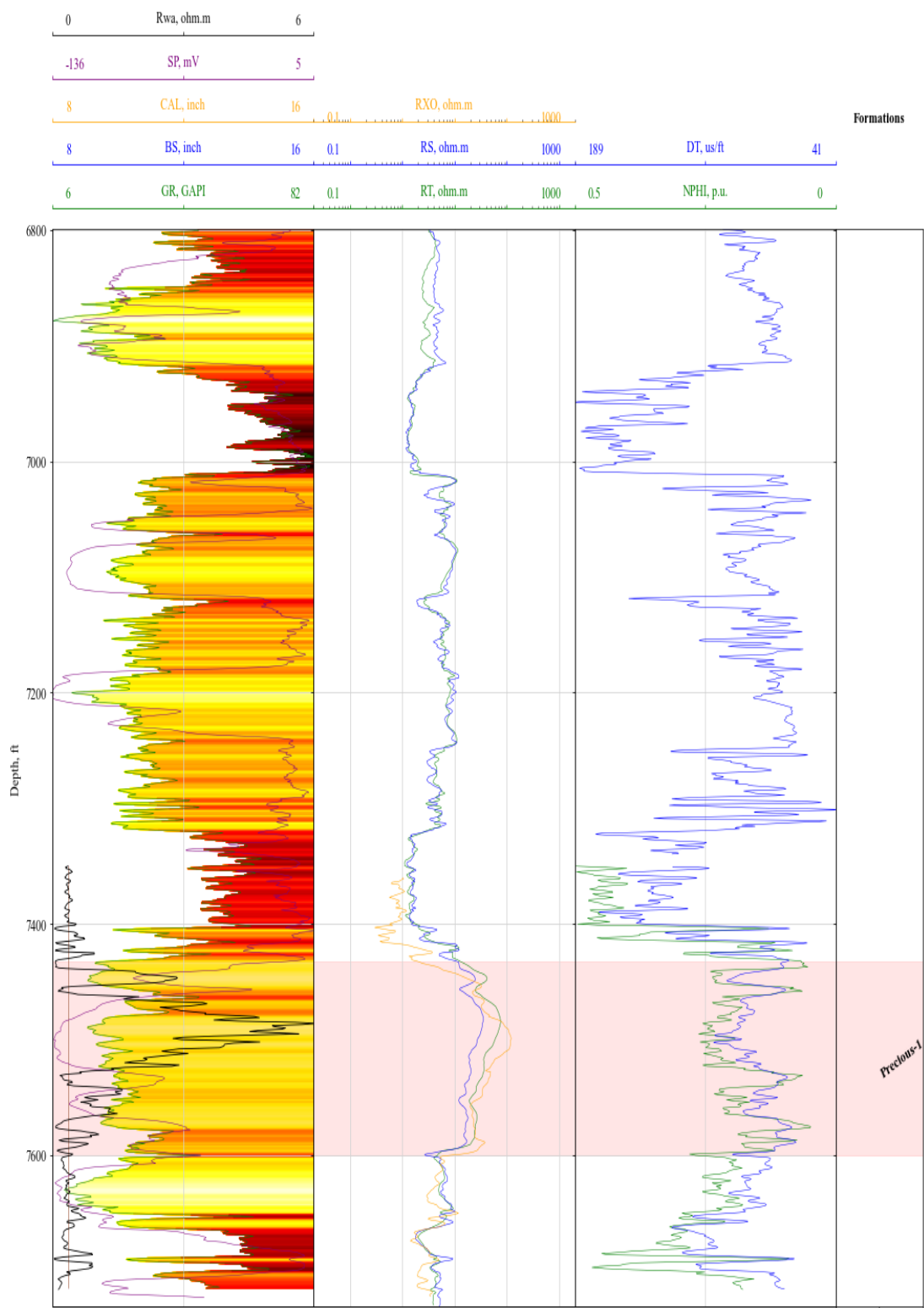


**Figure A.3:** Well log display of Well-04 along with designated formations.

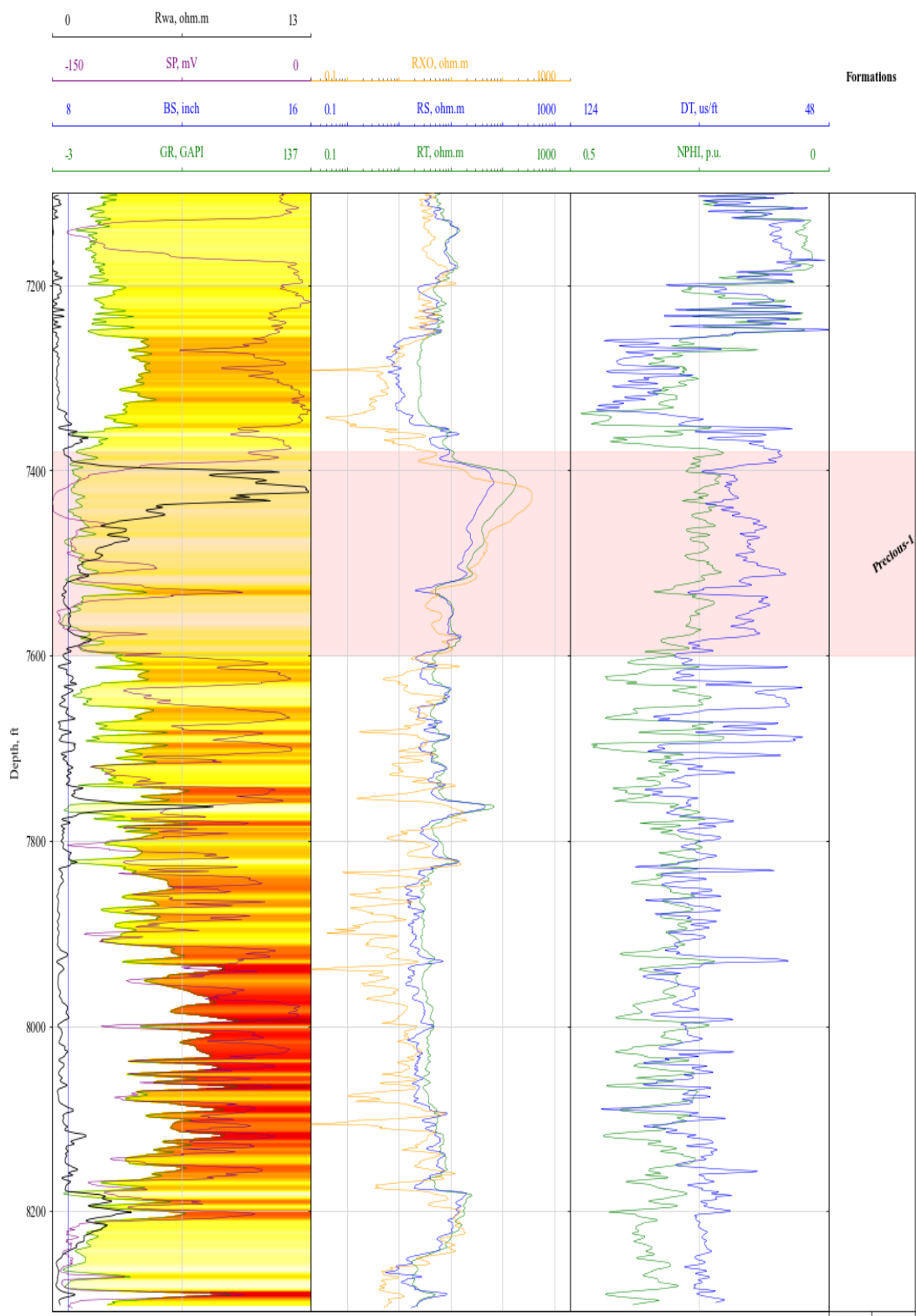


**Figure A.4:** Well log display of Well-05 along with designated formations.

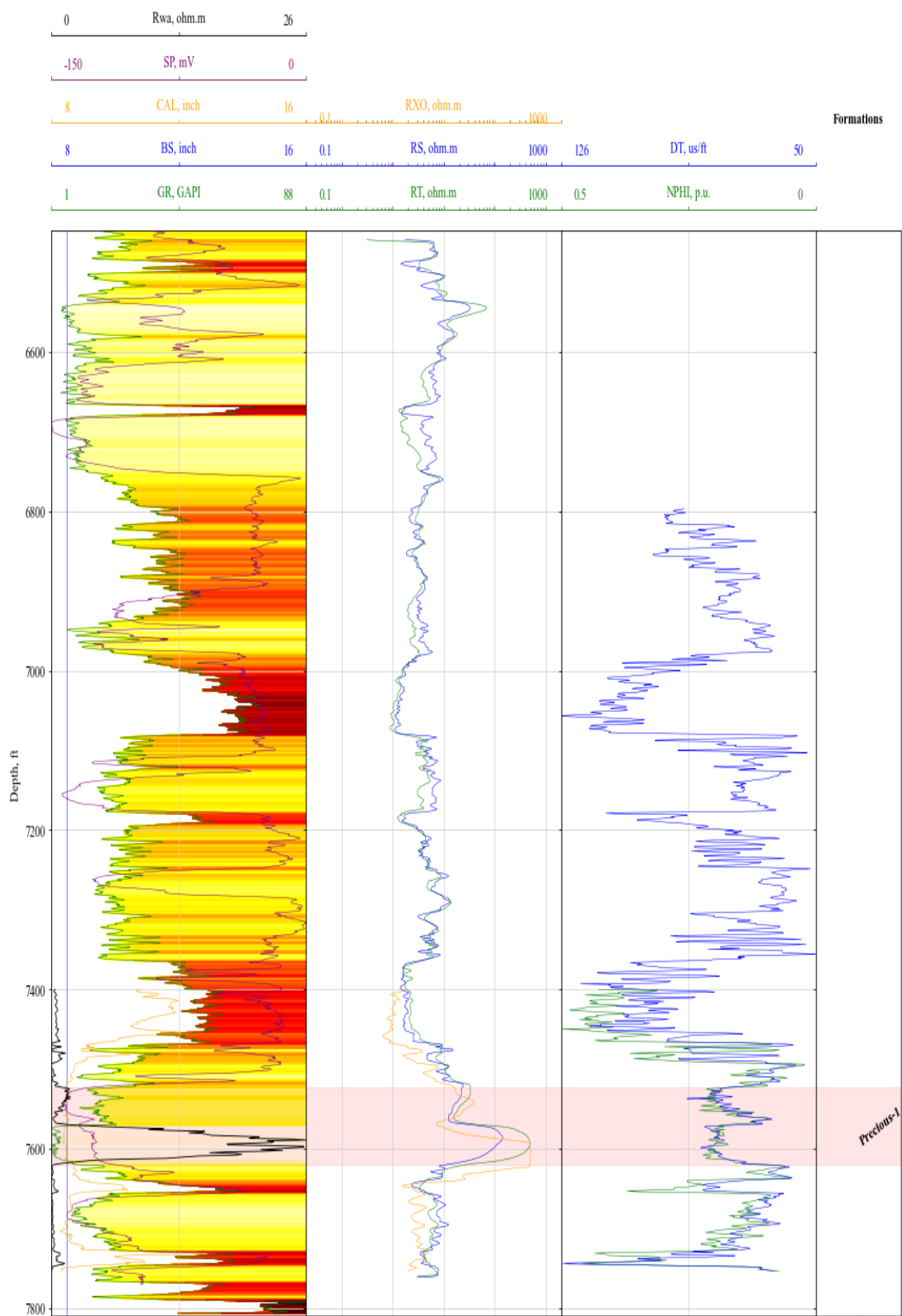


**Figure A.5:** Well log display of Well-06 along with designated formations.

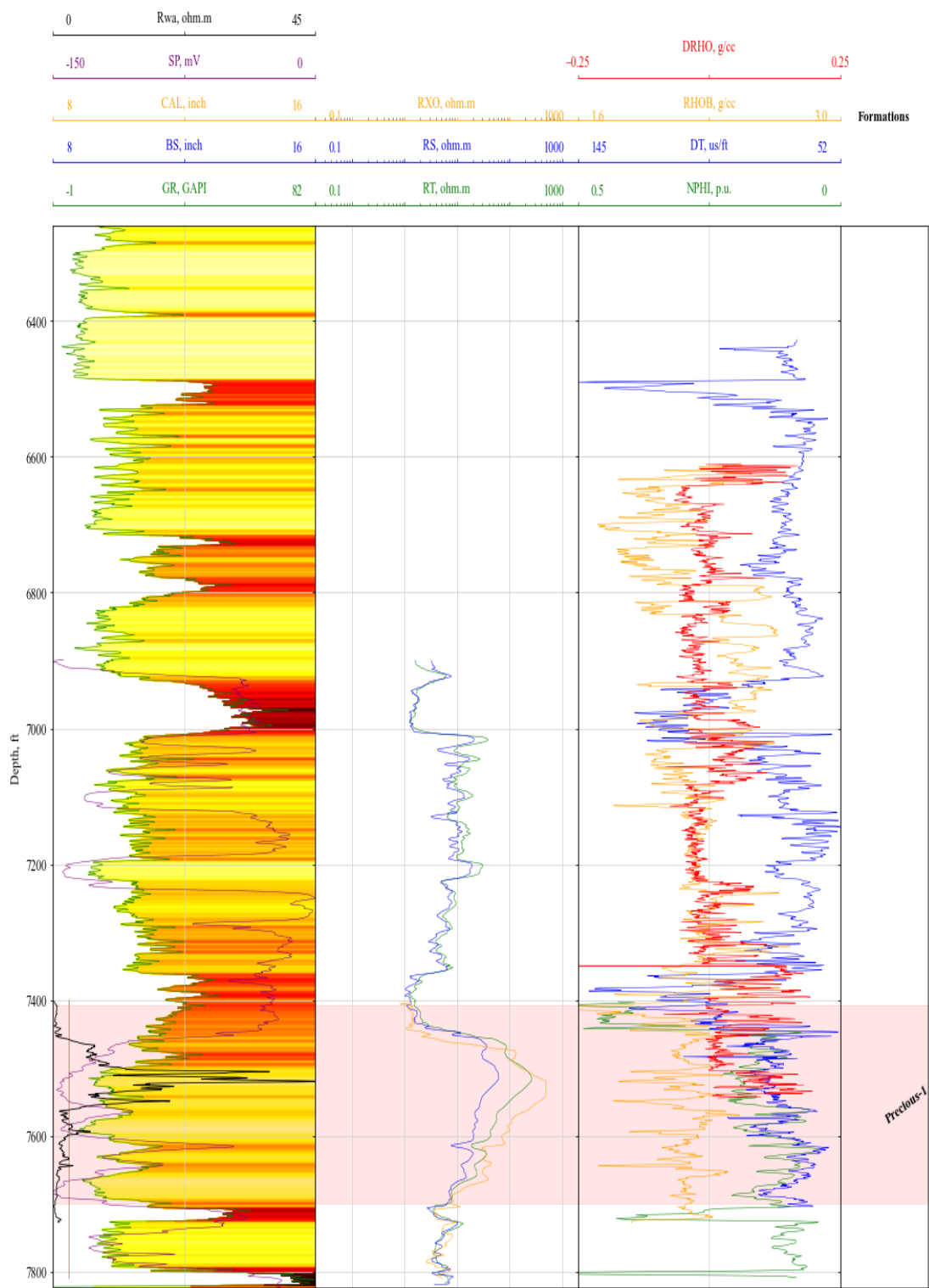


**Figure A.6:** Well log display of Well-07 along with designated formations.

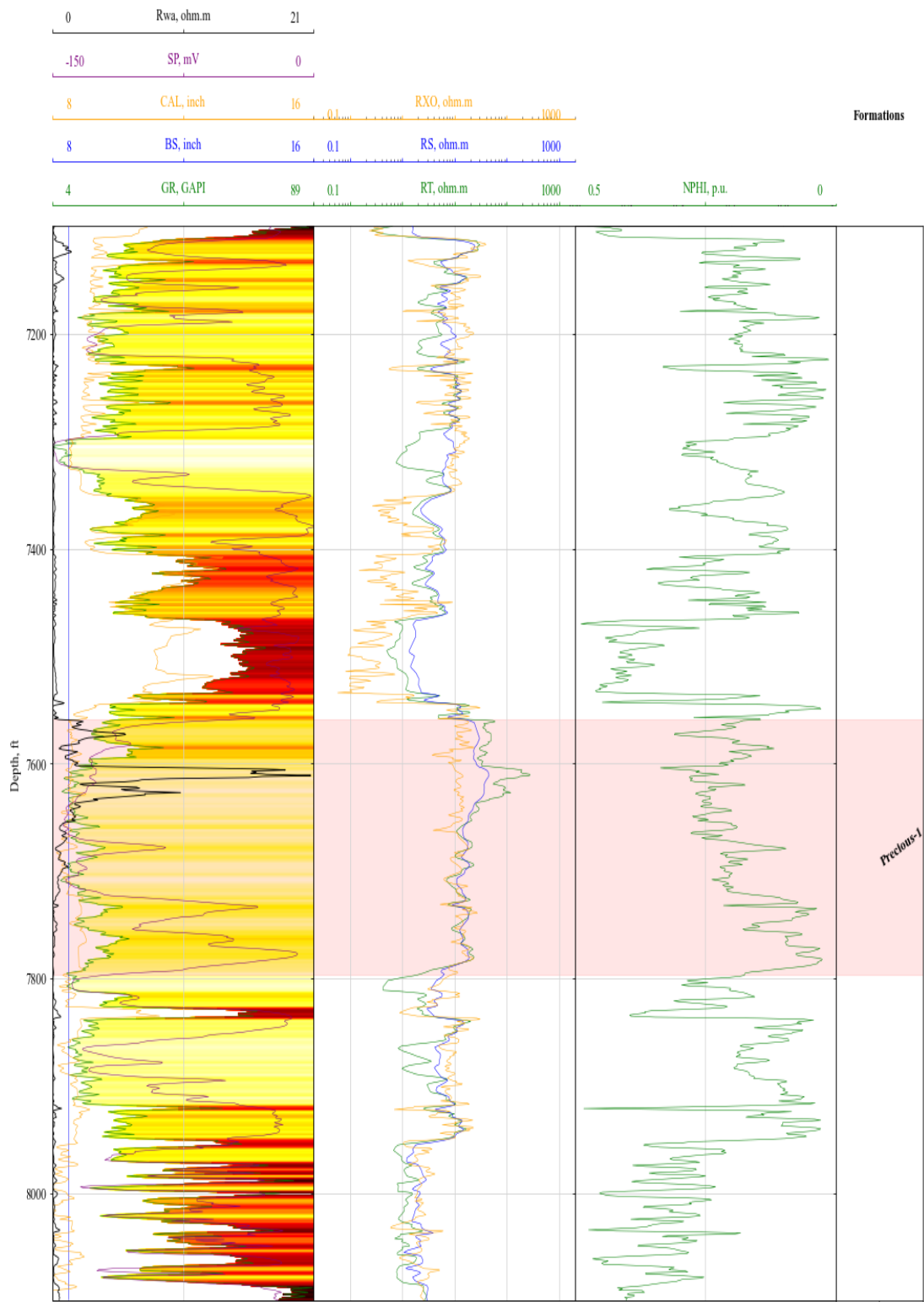


**Figure A.7:** Well log display of Well-08 along with designated formations.

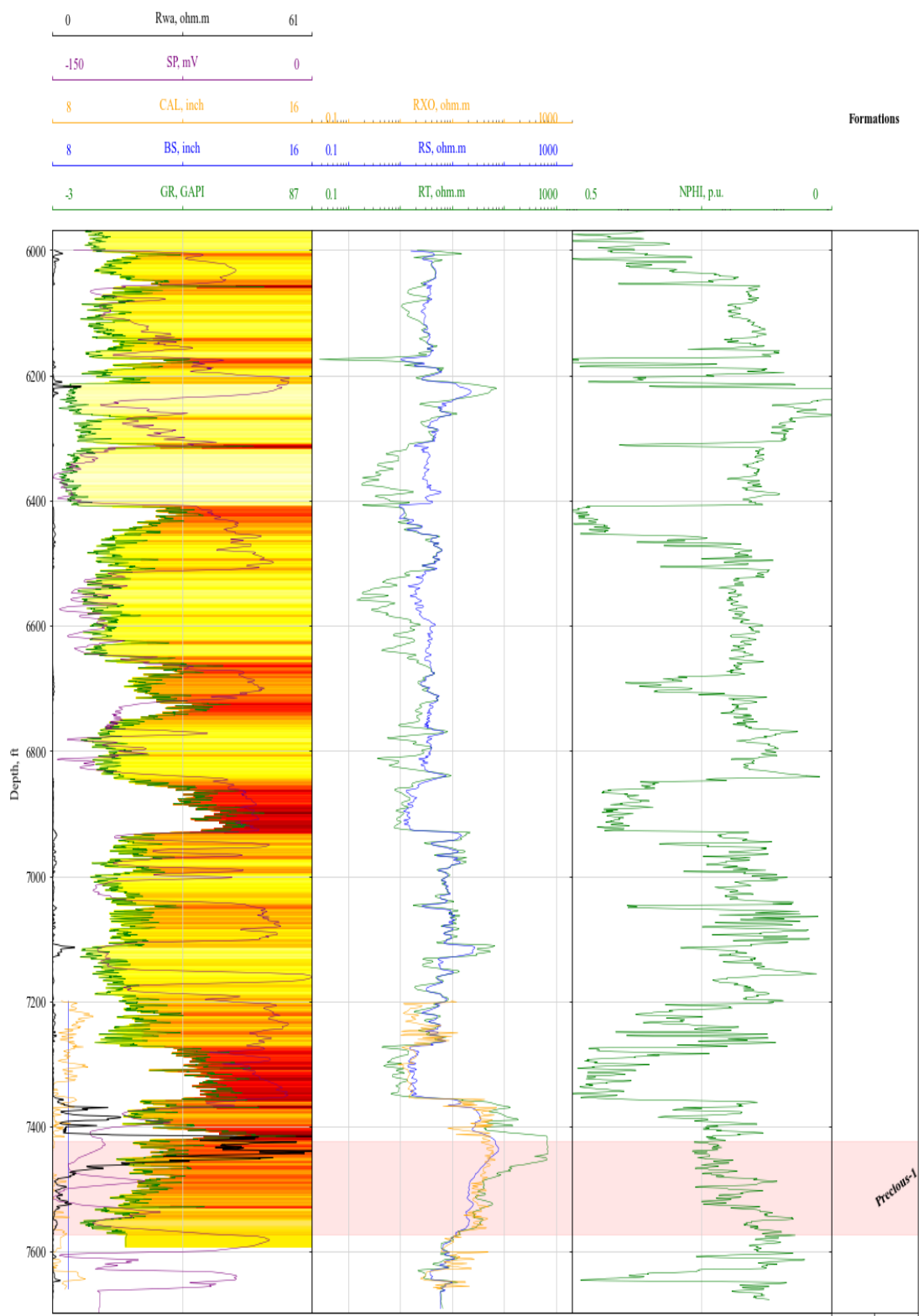


**Figure A.8:** Well log display of Well-09 along with designated formations.

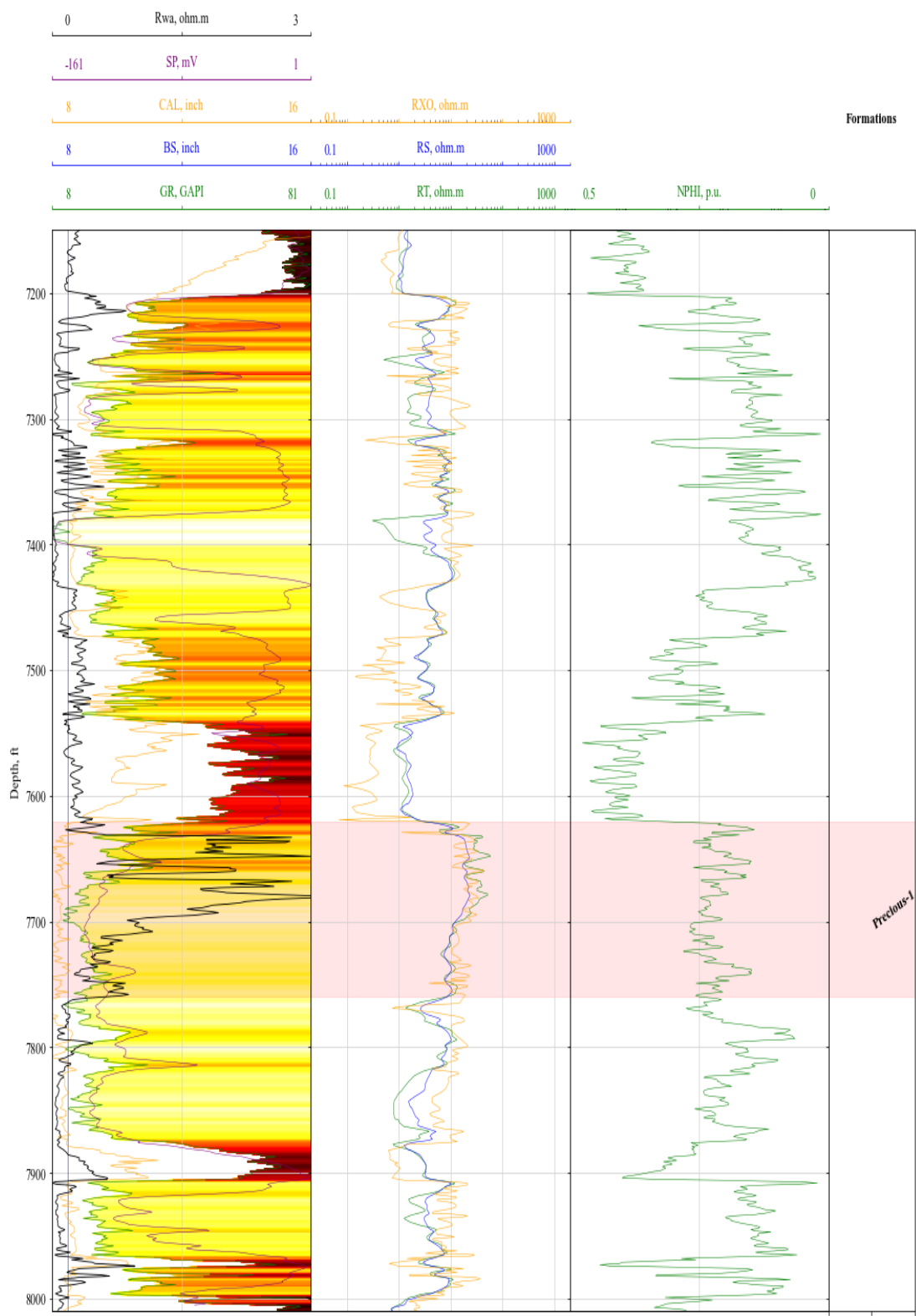


**Figure A.9:** Well log display of Well-10 along with designated formations.

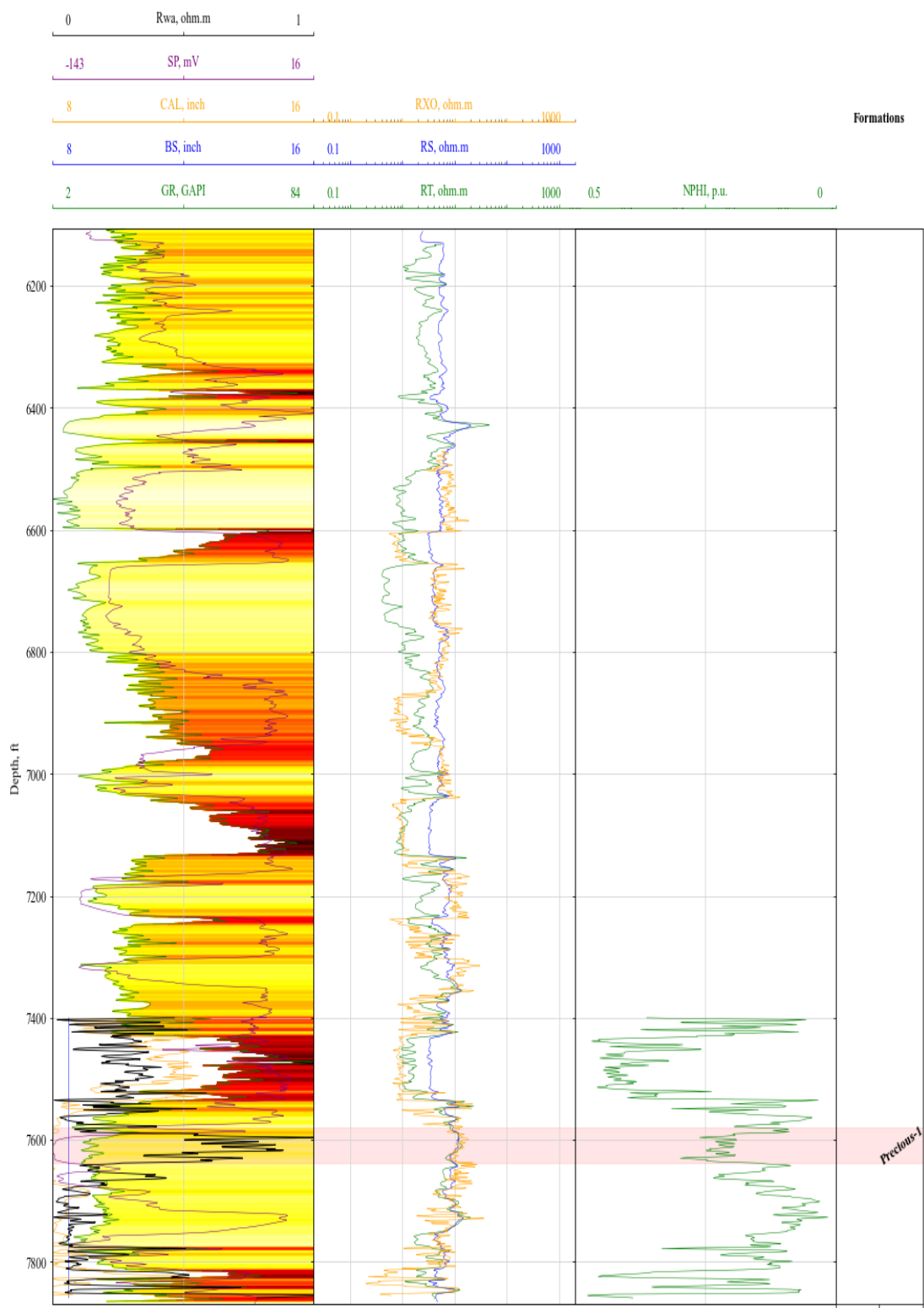


**Figure A.10:** Well log display of Well-11 along with designated formations.

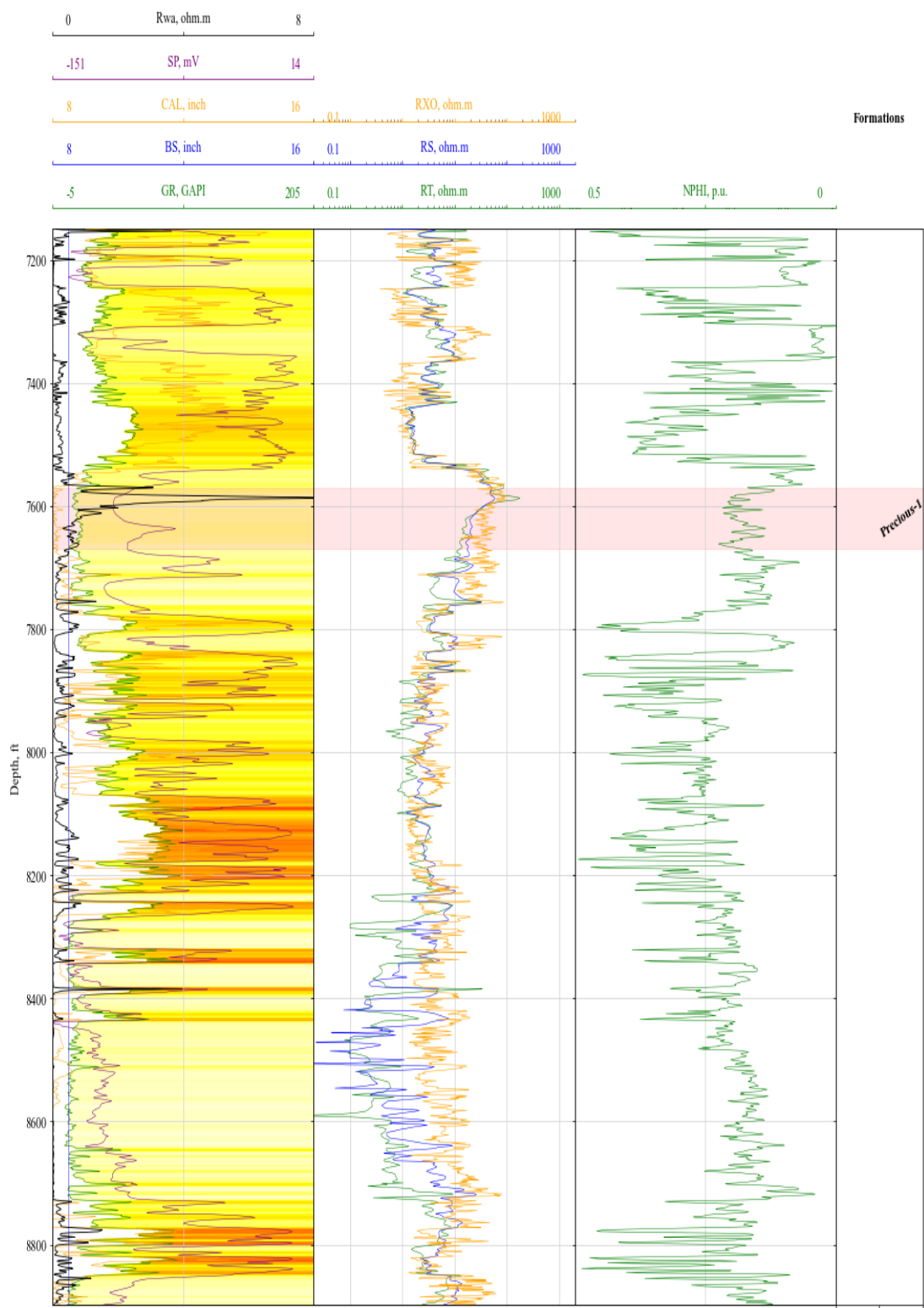


**Figure A.11:** Well log display of Well-12 along with designated formations.

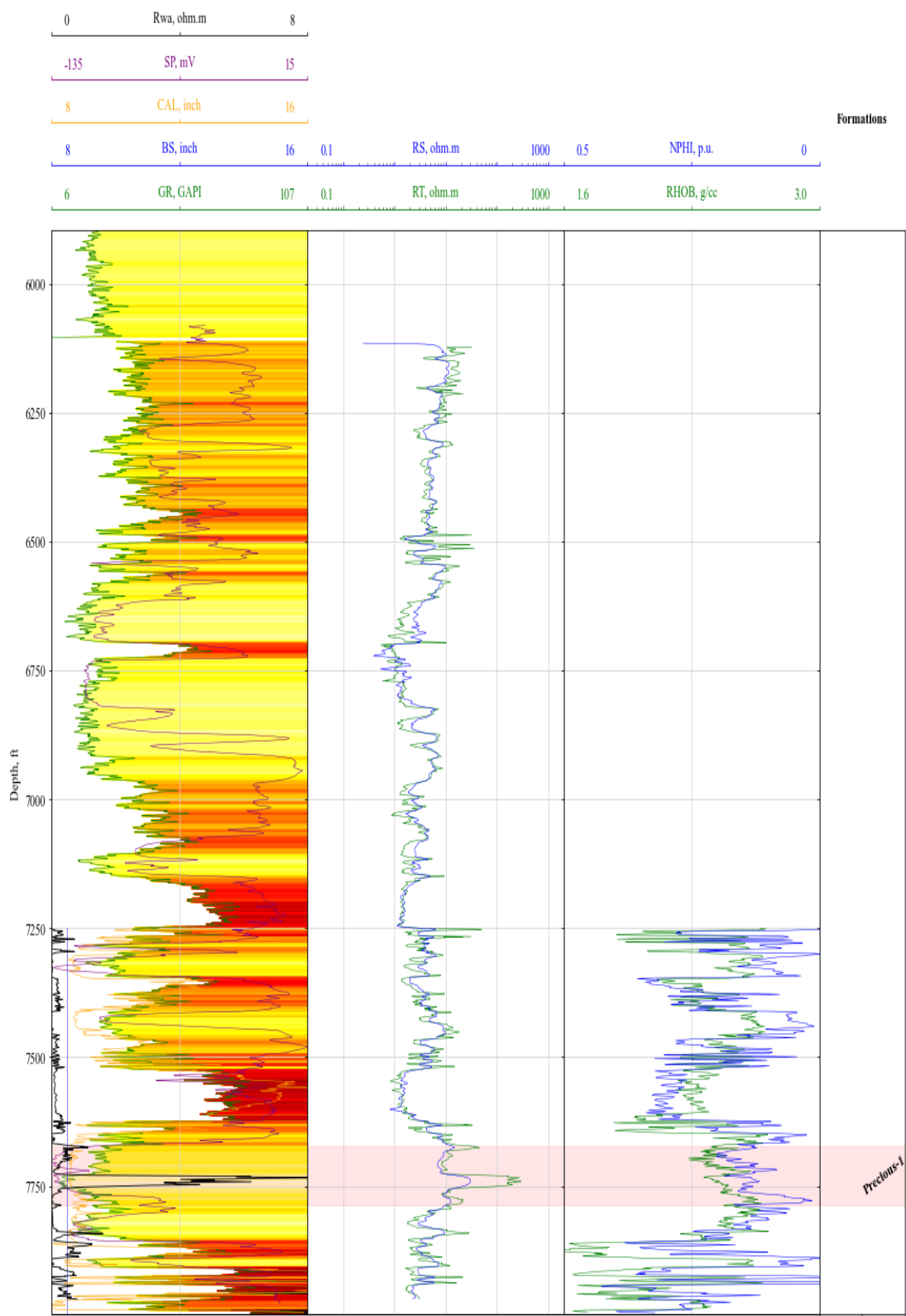


**Figure A.12:** Well log display of Well-13 along with designated formations.

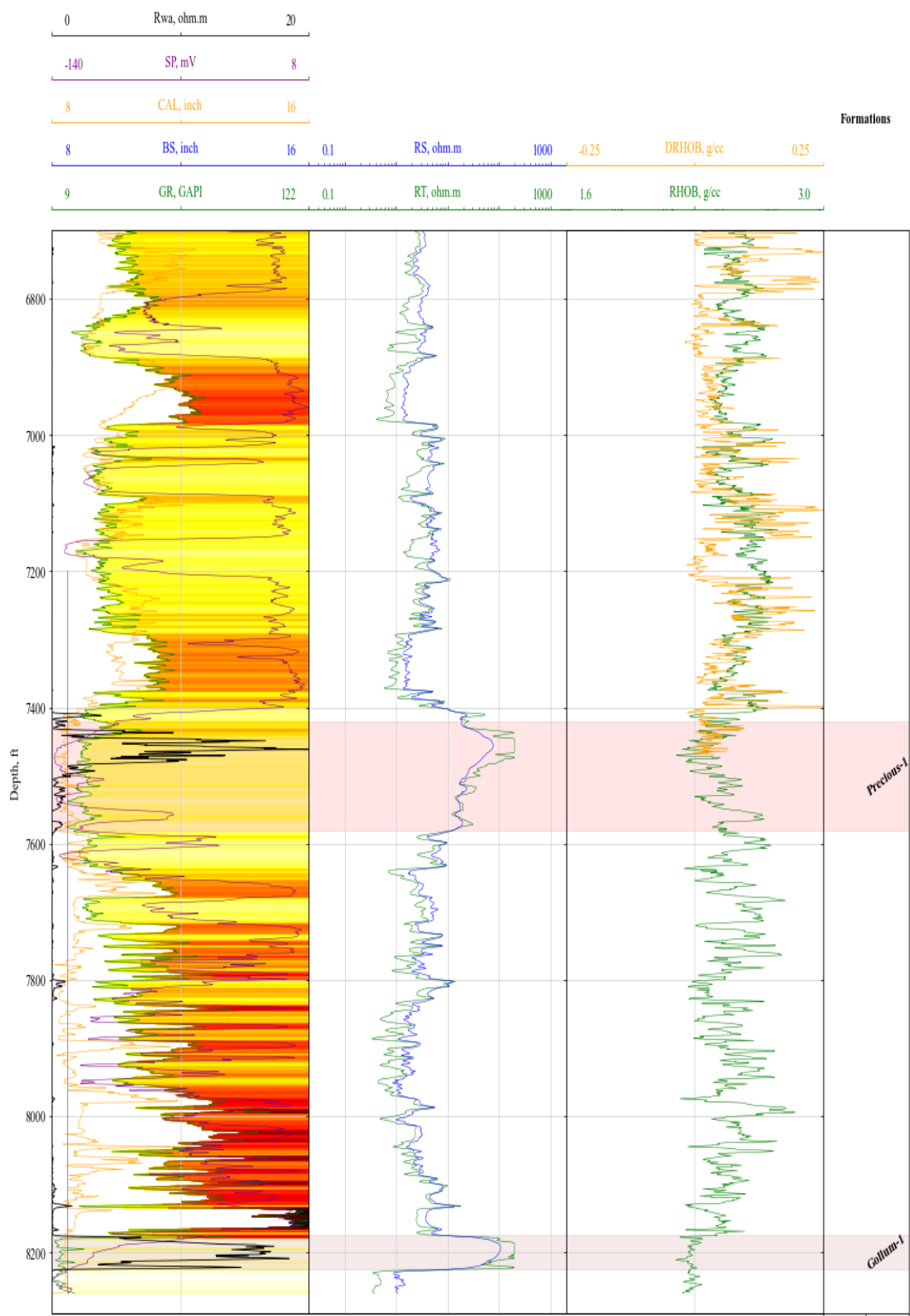


**Figure A.13:** Well log display of Well-15 along with designated formations.

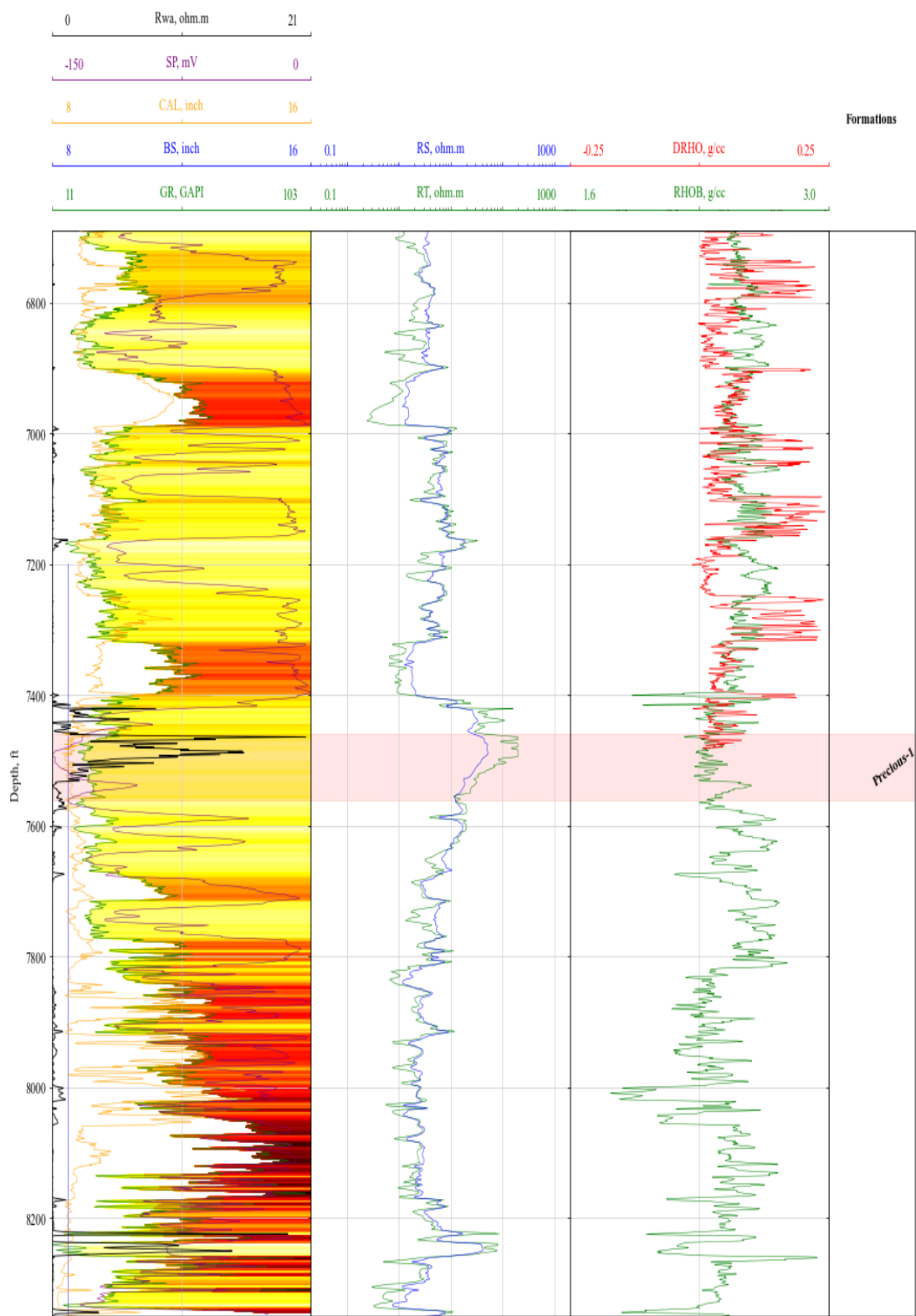


**Figure A.14:** Well log display of Well-16 along with designated formations.

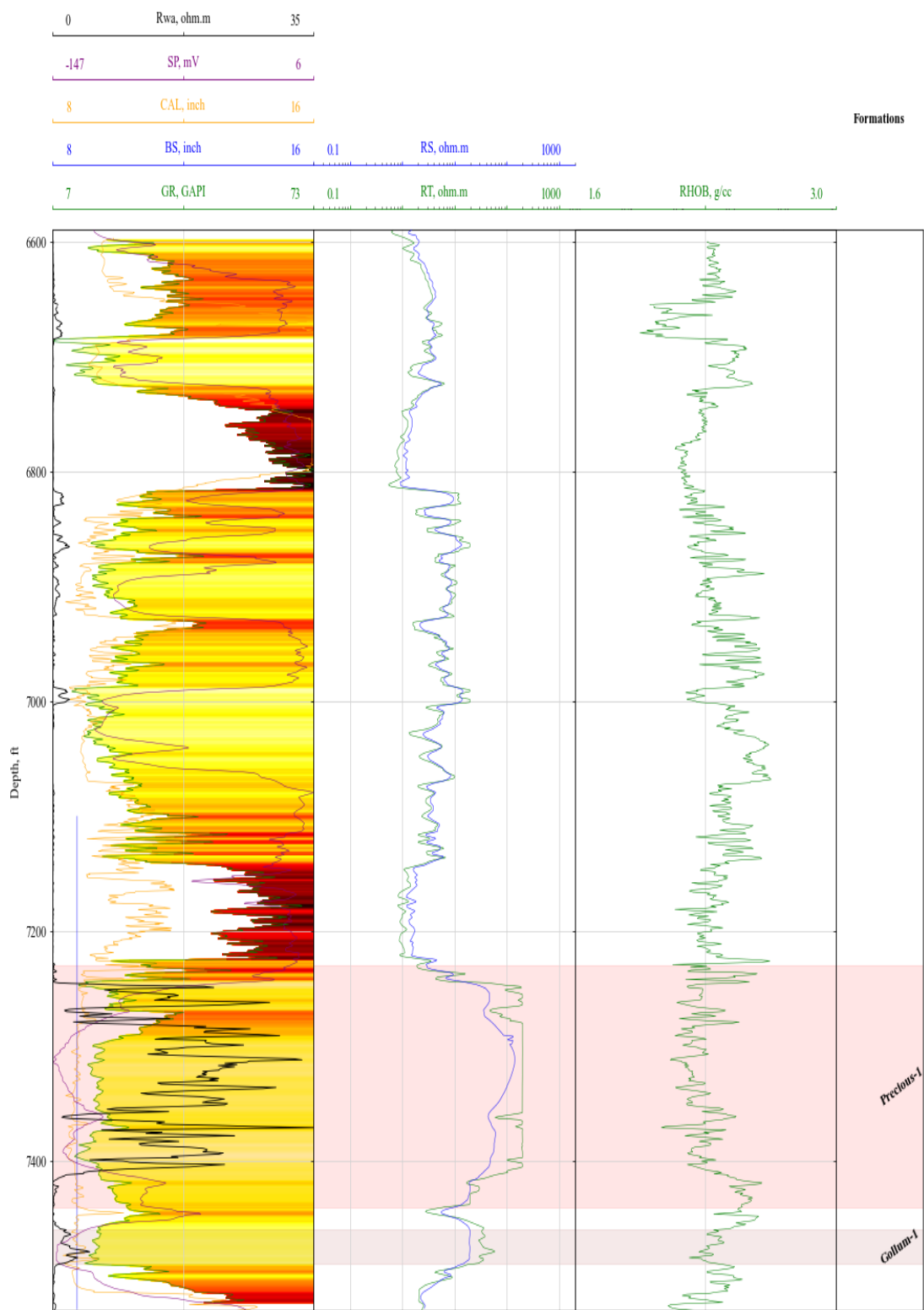


**Figure A.15:** Well log display of Well-17 along with designated formations.

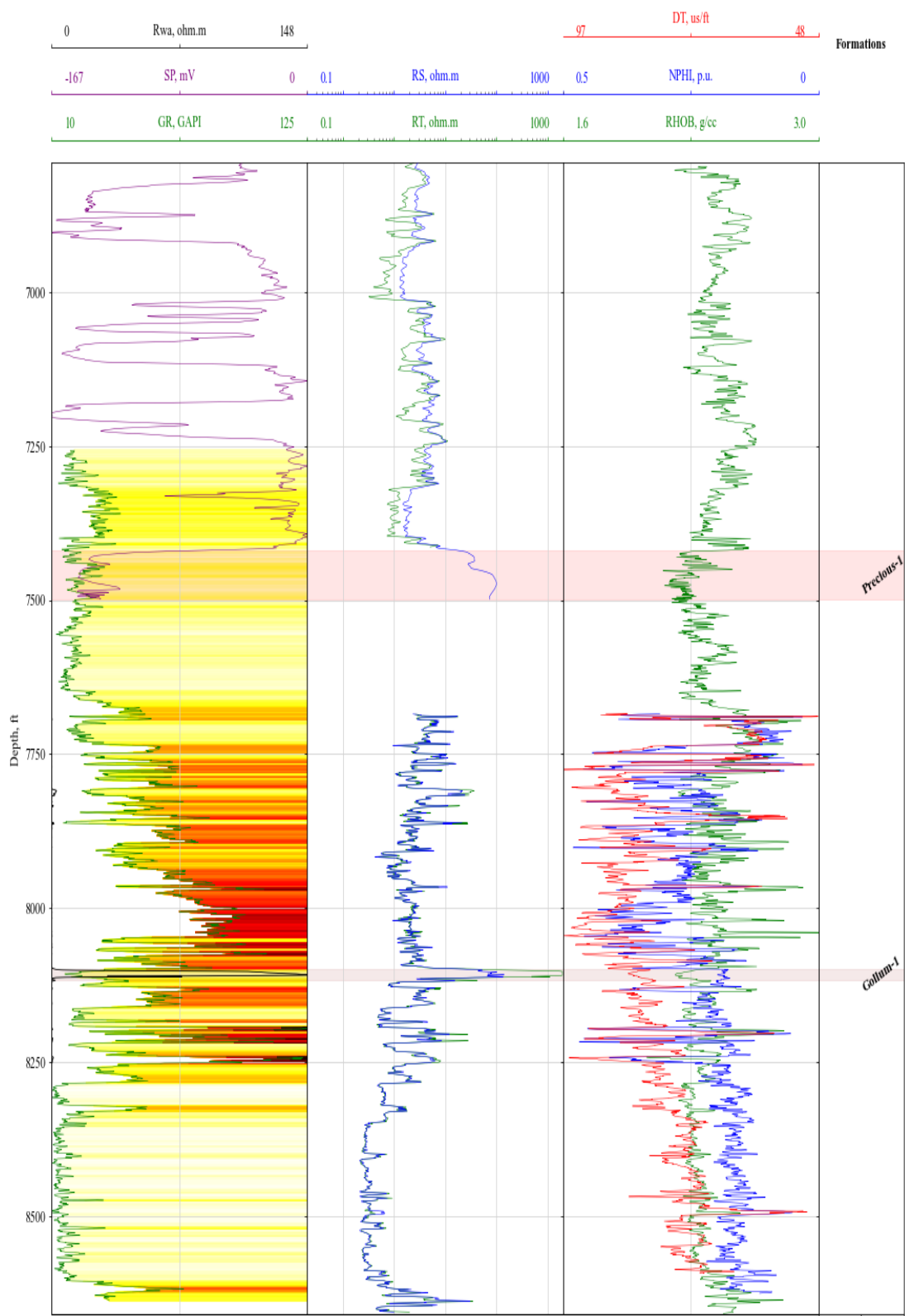


**Figure A.16:** Well log display of Well-19 along with designated formations.

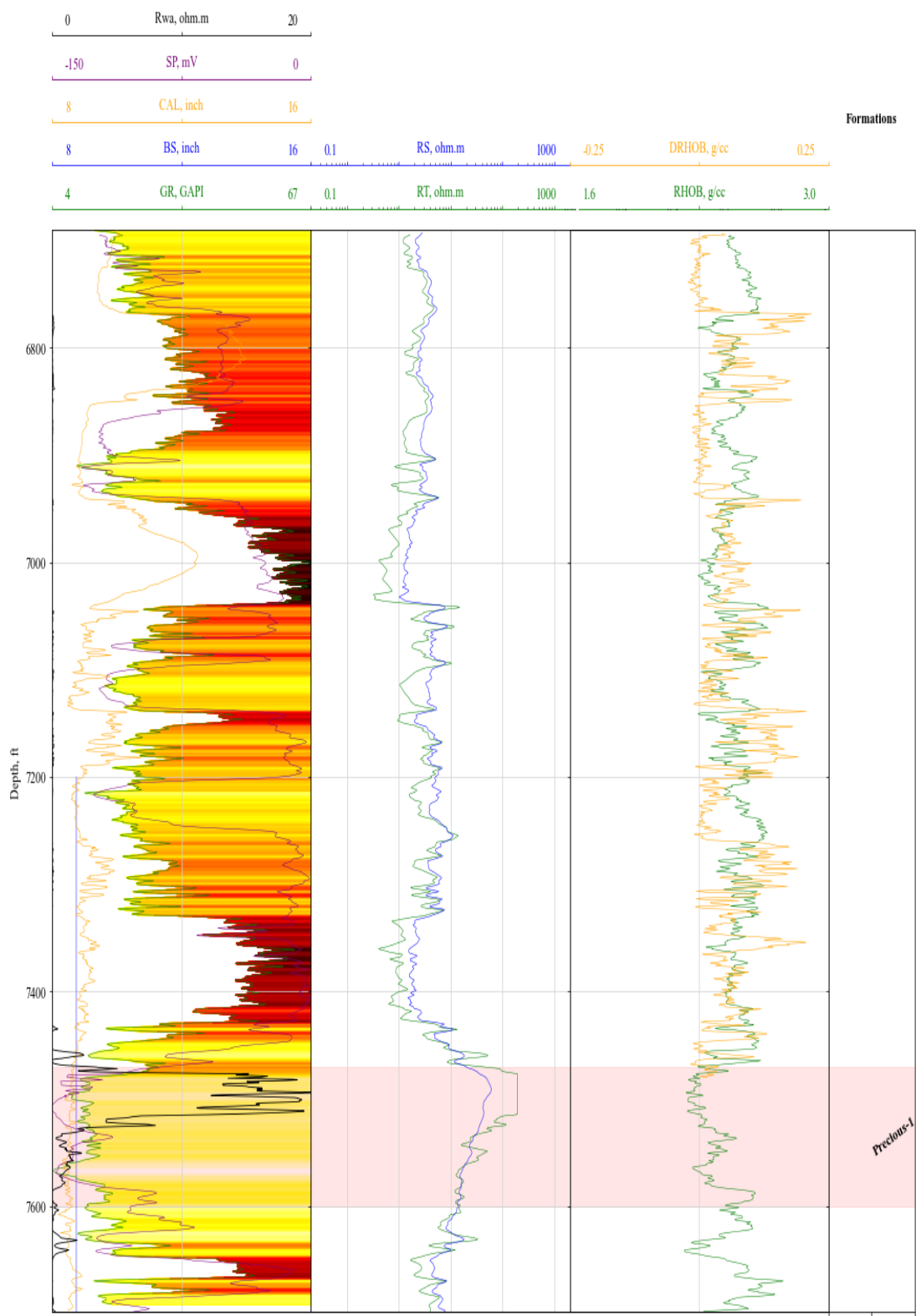


**Figure A.17:** Well log display of Well-20 along with designated formations.

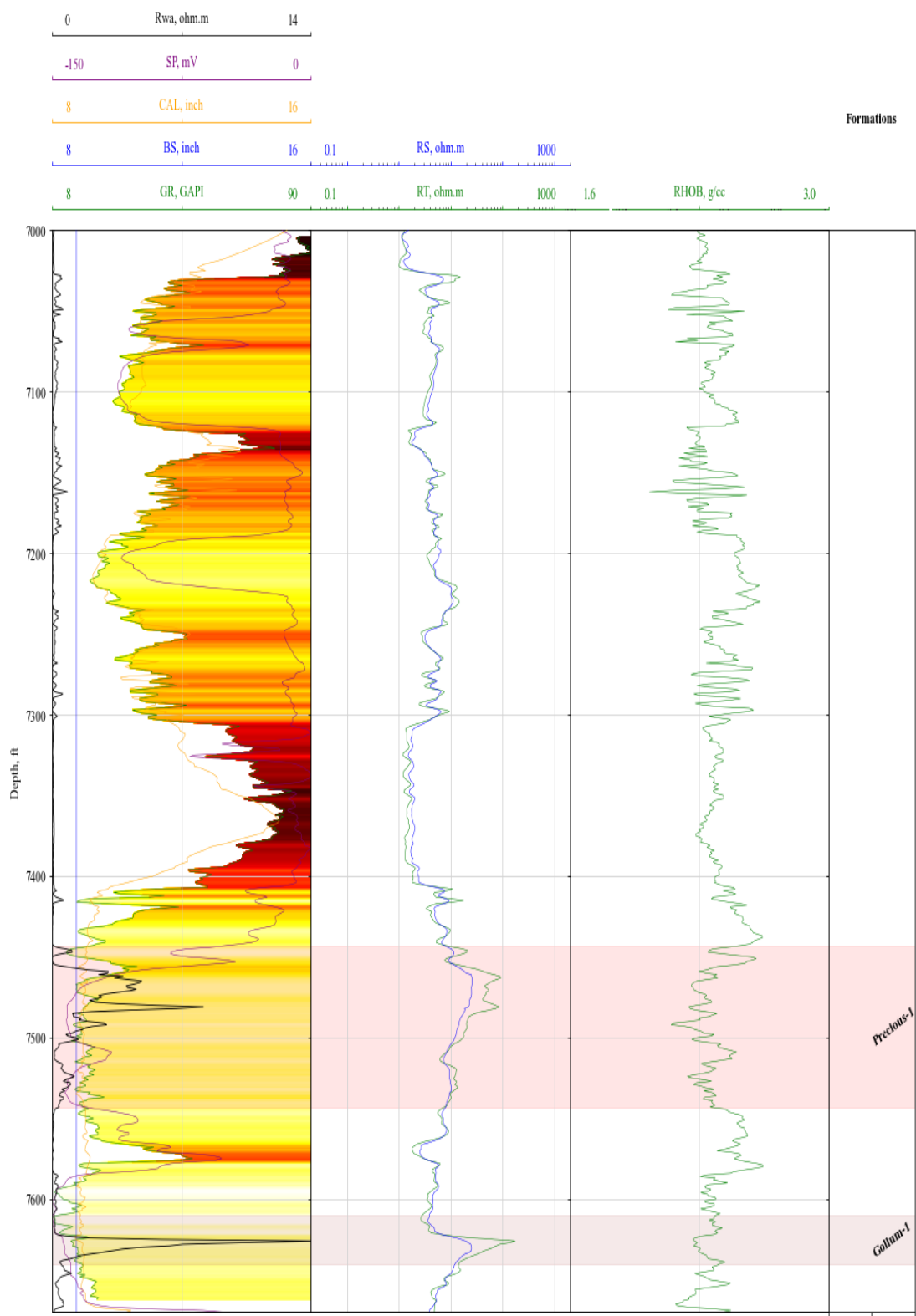


**Figure A.18:** Well log display of Well-21 along with designated formations.

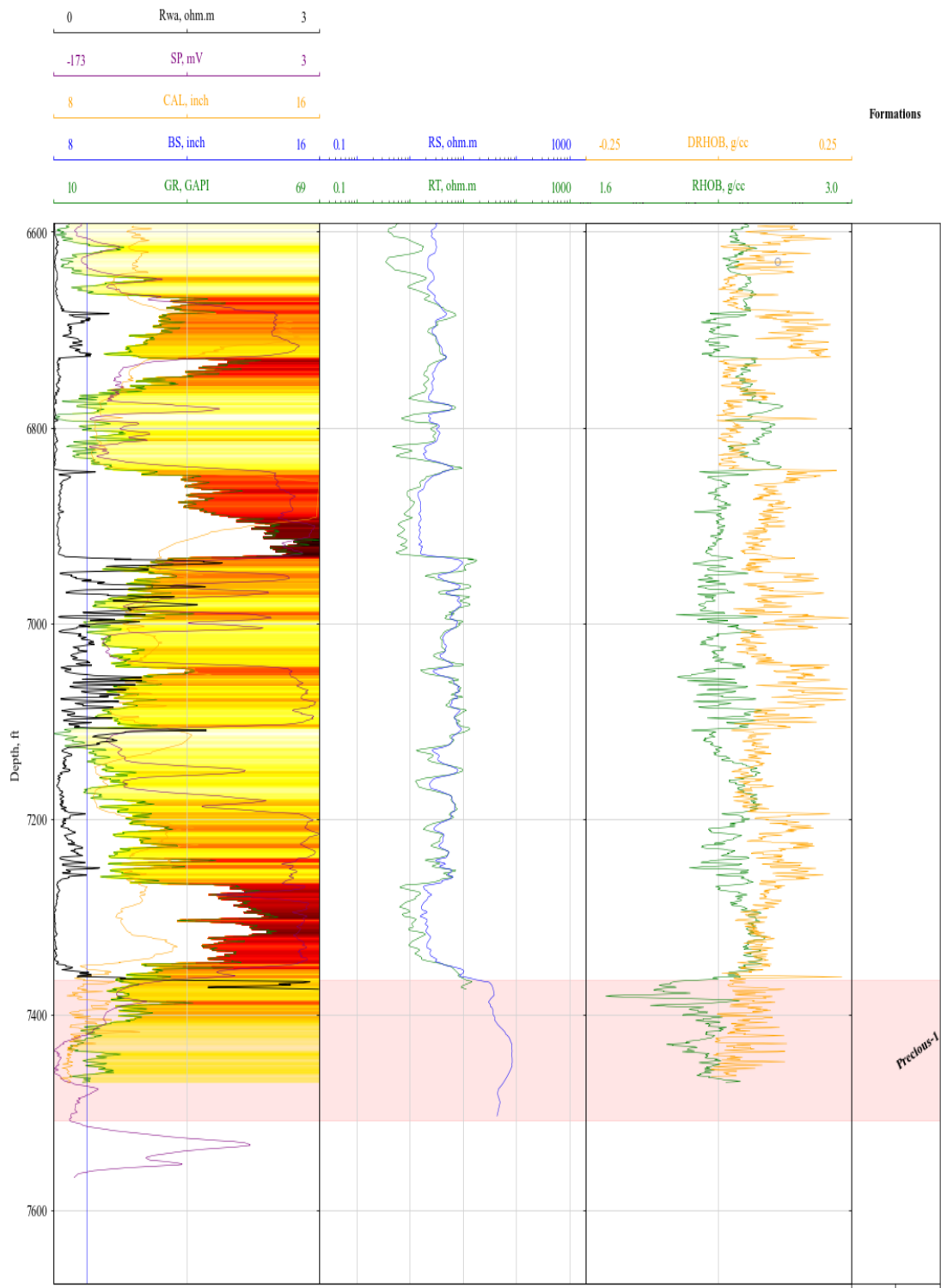


**Figure A.19:** Well log display of Well-22 along with designated formations.

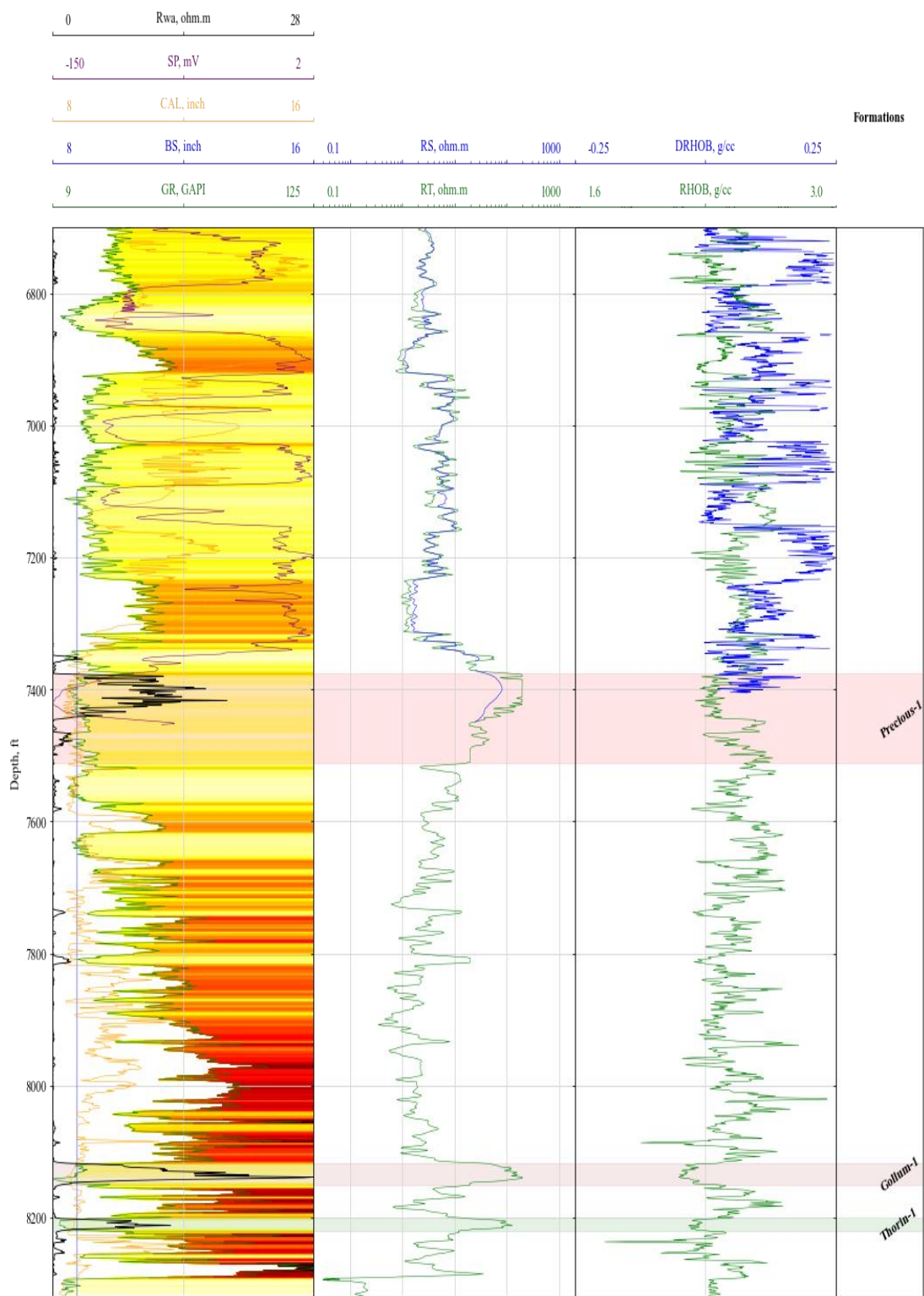


**Figure A.20:** Well log display of Well-23 along with designated formations.

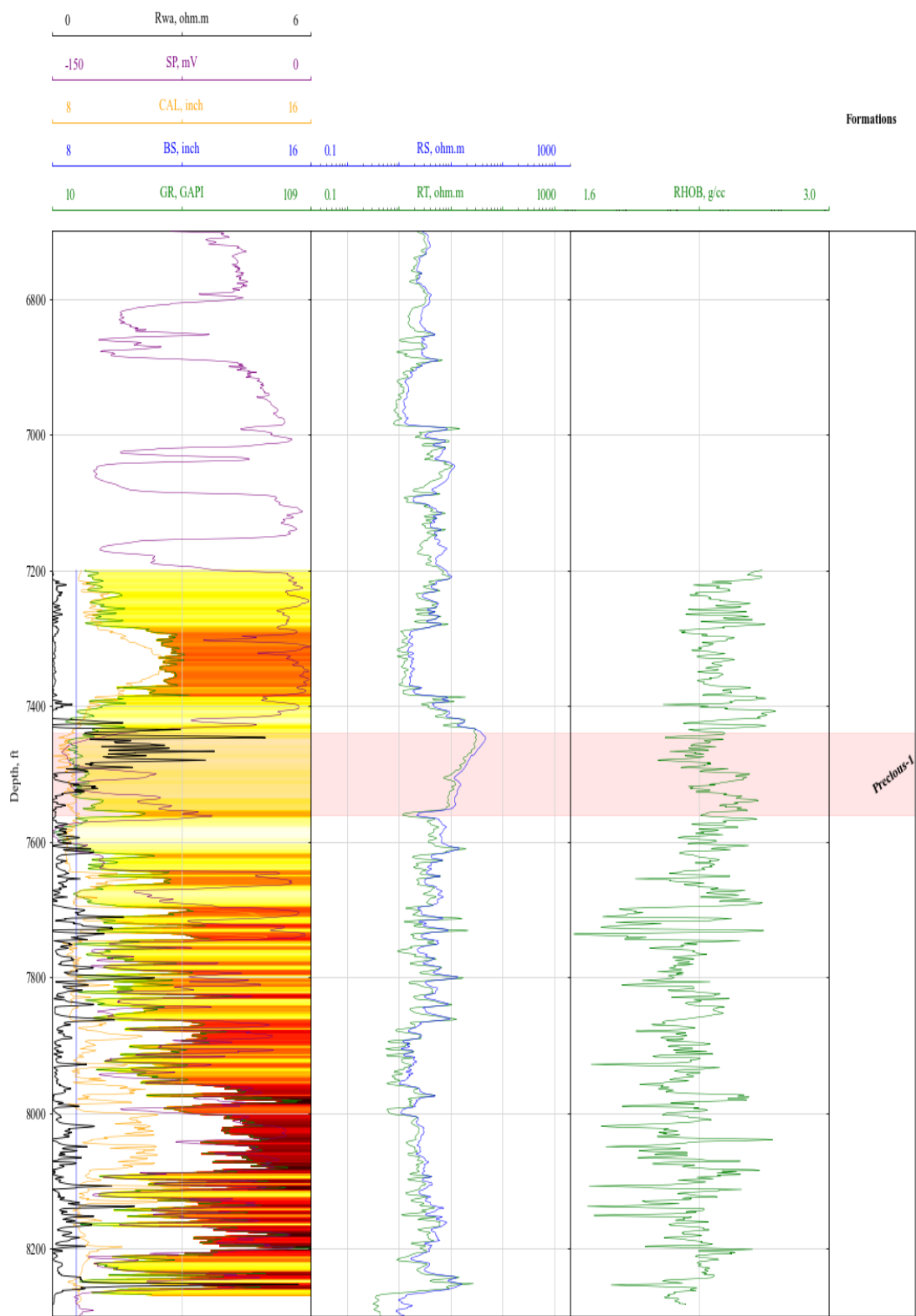


**Figure A.21:** Well log display of Well-24 along with designated formations.

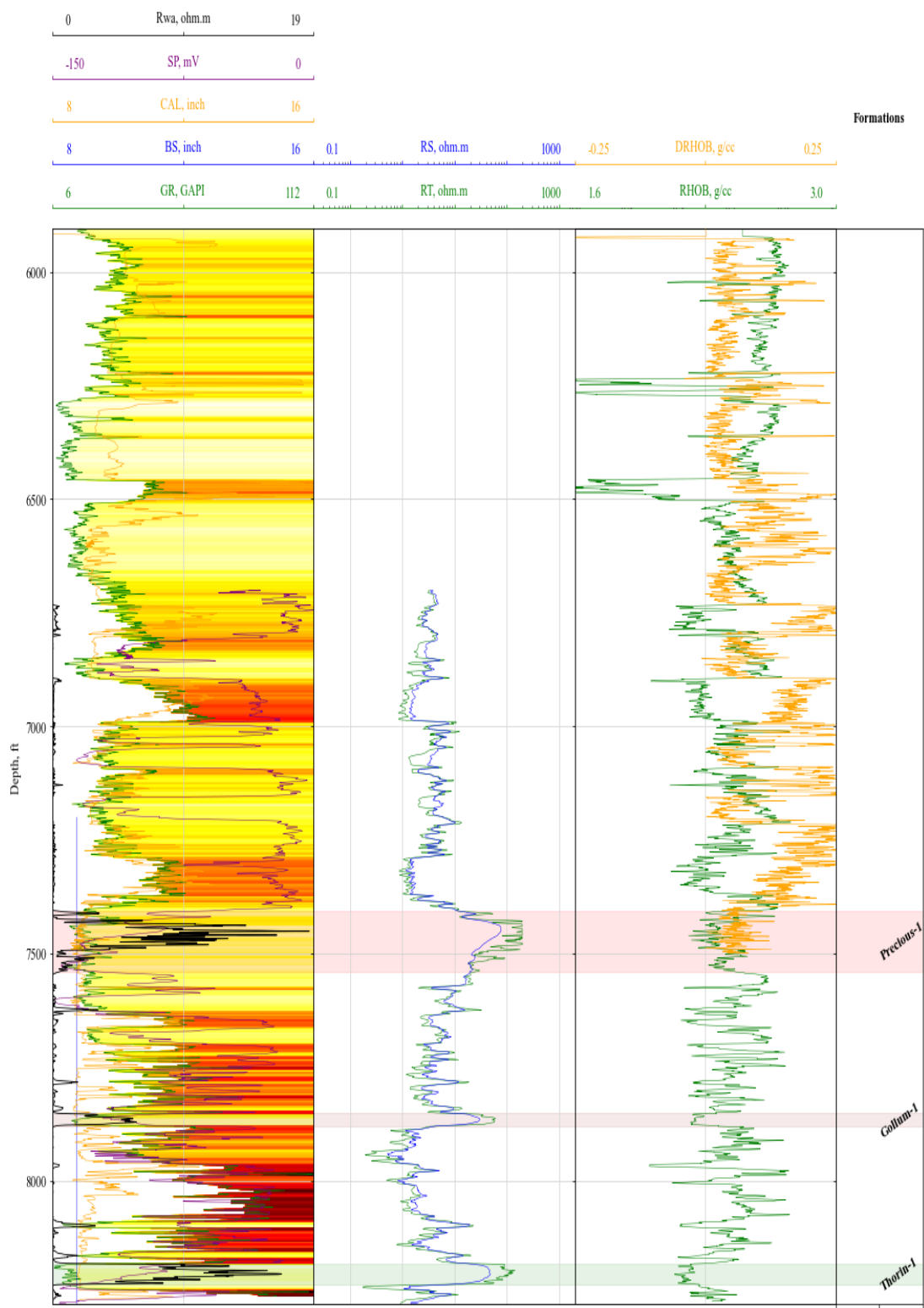


**Figure A.22:** Well log display of Well-25 along with designated formations.

**B. APPENDIX:** Estimated Petrophysical Properties Summary

**Table B.1:** Summary table about lithology.

Well Name	Reservoir Layer	Interval, ft	Net Pay Thickness, ft	NTG	Lithology
Well-01	Precious-1	7275 - 7400	122.5	0.98	Sandstone (76%) - Limestone (21%) - Dolomite (3%)
	Gollum-1	8195 - 8246.5	51.5	1	Sandstone
	Thorin-1	8568 - 8620	26.5	0.51	Sandstone
Well-02	Precious-1	7228.5 - 7485	240	0.93	Sandstone
Well-03	Precious-1	7460 - 7560	100	1	Sandstone
	Gollum-1	7864 - 7900	36	1	Sandstone
Well-04	Precious-1	7432 - 7600	126	0.75	Sandstone (96%) - Limestone (4%)
Well-05	Precious-1	7380 - 7600	220	1	Sandstone (10%) - Limestone (60%) - Dolomite (30%)
Well-06	Precious-1	7523 - 7620	97	1	Sandstone (50%) - Limestone (50%)
Well-07	Precious-1	7408 - 7700	265.5	0.91	Sandstone (44%) - Limestone (53%) - Dolomite (3%)
Well-08	Precious-1	7559 - 7796.5	168	0.71	Sandstone (57%) - Limestone (43%)
Well-09	Precious-1	7424 - 7572	125	0.84	Sandstone (68%) - Limestone (32%)
Well-10	Precious-1	7620 - 7760	139	0.99	Sandstone (46%) - Limestone (54%)
Well-11	Precious-1	7580 - 7638.5	54	0.92	Sandstone (10%) - Limestone (60%) - Dolomite (30%)
Well-12	Precious-1	7570 - 7670	100	1	Sandstone (76%) - Limestone (24%)
Well-13	Precious-1	7672 - 7787	98.5	0.86	Sandstone (55%) - Limestone (45%)
Well-14	Precious-1	7419 - 7600	162	0.9	Sandstone (71%) - Limestone (27%) - Dolomite (2%)
	Gollum-1	8127 - 8150.5	23.5	1	Sandstone (99%) - Limestone (1%)
	Thorin-1	8198.5 - 8217.5	19	1	Sandstone (99%) - Limestone (1%)
Well-15	Precious-1	7420 - 7580	145.5	0.9	Sandstone (70%) - Limestone (28%) - Dolomite (2%)
	Gollum-1	8174.5 - 8225	50	0.99	Sandstone
Well-16	Precious-1	7460 - 7560	99.5	0.99	Sandstone (63%) - Limestone (37%)
Well-17	Precious-1	7230 - 7440	204.5	0.97	Sandstone (61%) - Limestone (39%)

	Gollum-1	7459 - 7489.5	30.5	1	Sandstone
<b>Well-18</b>	Precious-1	7460 - 7660	188.5	0.94	Sandstone (44%) - Limestone (56%)
<b>Well-19</b>	Precious-1	7420 - 7498.5	78.5	1	Sandstone (96%) - Limestone (4%)
	Gollum-1	8098.5 - 8117	18.5	1	Sandstone (97%) - Limestone (3%)
<b>Well-20</b>	Precious-1	7470 - 7600	119.5	0.92	Sandstone (89%) - Limestone (11%)
<b>Well-21</b>	Precious-1	7443 - 7543	100	1	Sandstone (10%) - Limestone (60%) - Dolomite (30%)
	Gollum-1	7610 - 7640	30	1	Sandstone (10%) - Limestone (60%) - Dolomite (30%)
<b>Well-22</b>	Precious-1	7365 - 7508	143	1	Sandstone
<b>Well-23</b>	Precious-1	7376.5 - 7512	121	0.89	Sandstone (66%) - Limestone (32%) - Dolomite (2%)
	Gollum-1	8118 - 8150	32	1	Sandstone
	Thorin-1	8201 - 8220	19	1	Sandstone
<b>Well-24</b>	Precious-1	7440 - 7560	117	0.97	Sandstone (10%) - Limestone (60%) - Dolomite (30%)
<b>Well-25</b>	Precious-1	7405.5 - 7540	131	0.97	Sandstone (96%) - Limestone (4%)
	Gollum-1	7851 - 7880	28.5	0.99	Sandstone
	Thorin-1	8181 - 8228	47	1	Sandstone

**Table B.2:** Average values of the estimated petrophysical properties.

Well Name	Reservoir Layer	Interval, ft	$\phi_t$	$\phi_e$	$S_{wi}$	$S_{wirr}$	$S_{xo}$	$S_{oi}$	$S_{or}$	$S_{mo}$	RF	HCMI	k, md
<b>Well-01</b>	Precious-1	7275 - 7400	0.13	0.13	0.22	0.23	0.73	0.78	0.27	0.51	0.66	0.3	49
	Gollum-1	8195 - 8246.5	0.17	0.17	0.15	0.15	0.68	0.85	0.32	0.53	0.63	0.22	217
	Thorin-1	8568 - 8620	0.1	0.1	0.34	0.35	0.8	0.66	0.2	0.46	0.7	0.42	10.75
<b>Well-02</b>	Precious-1	7228.5 - 7485	0.14	0.13	0.07	0.07	0.56	0.93	0.44	0.49	0.53	0.11	554
<b>Well-03</b>	Precious-1	7460 - 7560	0.19	0.18	0.07	0.08	0.59	0.93	0.41	0.51	0.56	0.12	540
	Gollum-1	7864 - 7900	0.18	0.16	0.17	0.2	0.69	0.83	0.31	0.52	0.63	0.24	203
<b>Well-04</b>	Precious-1	7432 - 7600	0.15	0.13	0.22	0.25	0.72	0.78	0.28	0.51	0.65	0.29	57
<b>Well-05</b>	Precious-1	7380 - 7600	0.24	0.22	0.13	0.14	0.65	0.7	0.35	0.52	0.6	0.19	58
<b>Well-06</b>	Precious-1	7523 - 7620	0.18	0.17	0.09	0.1	0.6	0.91	0.4	0.5	0.56	0.14	268
<b>Well-07</b>	Precious-1	7408 - 7700	0.19	0.16	0.2	0.24	0.69	0.8	0.31	0.49	0.62	0.27	147
<b>Well-08</b>	Precious-1	7559 - 7796.5	0.19	0.18	0.14	0.29	0.75	0.73	0.25	0.48	0.67	0.34	174
<b>Well-09</b>	Precious-1	7424 - 7572	0.11	0.09	0.1	0.12	0.59	0.9	0.41	0.49	0.55	0.15	165
<b>Well-10</b>	Precious-1	7620 - 7760	0.18	0.16	0.18	0.21	0.7	0.82	0.3	0.52	0.64	0.25	191
<b>Well-11</b>	Precious-1	7580 - 7638.5	0.18	0.17	0.27	0.3	0.77	0.73	0.23	0.49	0.68	0.35	71
<b>Well-12</b>	Precious-1	7570 - 7670	0.18	0.17	0.12	0.13	0.65	0.88	0.35	0.53	0.6	0.19	316
<b>Well-13</b>	Precious-1	7672 - 7787	0.14	0.13	0.15	0.16	0.66	0.85	0.34	0.51	0.61	0.21	197
<b>Well-14</b>	Precious-1	7419 - 7600	0.15	0.14	0.2	0.22	0.7	0.8	0.3	0.49	0.63	0.27	209
	Gollum-1	8127 - 8150.5	0.24	0.23	0.09	0.1	0.61	0.91	0.39	0.52	0.57	0.15	323
	Thorin-1	8198.5 8217.5	0.22	0.21	0.08	0.09	0.6	0.92	0.4	0.52	0.57	0.14	847
<b>Well-15</b>	Precious-1	7420 -7580	0.16	0.15	0.15	0.16	0.66	0.85	0.34	0.51	0.6	0.21	190
	Gollum-1	8174.5 - 8225	0.24	0.23	0.06	0.07	0.56	0.94	0.44	0.5	0.54	0.11	554
<b>Well-16</b>	Precious-1	7460 - 7560	0.17	0.16	0.08	0.08	0.57	0.92	0.43	0.49	0.54	0.12	376
<b>Well-17</b>	Precious-1	7230 - 7440	0.2	0.18	0.07	0.08	0.53	0.93	0.47	0.46	0.5	0.1	187

	Gollum-1	7459 - 7489.5	0.19	0.18	0.3	0.32	0.79	0.7	0.21	0.49	0.69	0.38	50
<b>Well-18</b>	Precious-1	7460 - 7660	0.18	0.16	0.16	0.17	0.67	0.84	0.33	0.51	0.61	0.23	204
<b>Well-19</b>	Precious-1	7420 -7498.5	0.23	0.22	0.06	0.07	0.57	0.94	0.43	0.51	0.54	0.07	536
	Gollum-1	8098.5 - 8117	0.2	0.18	0.06	0.07	0.48	0.94	0.52	0.42	0.46	0.09	281
<b>Well-20</b>	Precious-1	7470 - 7600	0.19	0.18	0.08	0.08	0.57	0.92	0.43	0.49	0.54	0.12	295
<b>Well-21</b>	Precious-1	7443 - 7543	0.23	0.21	0.16	0.17	0.67	0.84	0.33	0.51	0.62	0.22	445
	Gollum-1	7610 - 7640	0.25	0.24	0.18	0.18	0.68	0.82	0.32	0.5	0.62	0.24	314
<b>Well-22</b>	Precious-1	7365 - 7508	0.27	0.24	0.4	0.48	0.83	0.6	0.17	0.43	0.72	0.48	236
<b>Well-23</b>	Precious-1	7376.5 - 7512	0.17	0.16	0.09	0.09	0.58	0.91	0.42	0.49	0.54	0.13	263
	Gollum-1	8118 - 8150	0.28	0.27	0.03	0.04	0.5	0.97	0.5	0.47	0.48	0.07	532
	Thorin-1	8201 - 8220	0.25	0.25	0.05	0.05	0.53	0.95	0.47	0.48	0.51	0.09	438
<b>Well-24</b>	Precious-1	7440 - 7560	0.24	0.23	0.24	0.26	0.73	0.76	0.27	0.49	0.66	0.31	379
<b>Well-25</b>	Precious-1	7405.5 - 7540	0.17	0.16	0.08	0.09	0.58	0.92	0.42	0.5	0.55	0.13	309
	Gollum-1	7851 - 7880	0.24	0.23	0.08	0.09	0.59	0.92	0.41	0.5	0.55	0.13	481
	Thorin-1	8181 - 8228	0.3	0.29	0.04	0.04	0.52	0.96	0.48	0.48	0.5	0.08	-

**Table B.3:** Standard deviation values of the estimated petrophysical properties.

<b>Well Name</b>	<b>Reservoir Layer</b>	<b>Interval, ft</b>	$\phi_t$	$\phi_e$	$S_{wi}$	$S_{wirr}$	$S_{xo}$	$S_{oi}$	$S_{or}$	$S_{mo}$	RF	HCMI	k, md
<b>Well-01</b>	Precious-1	7275 - 7400	0.03	0.03	0.08	0.08	0.05	0.08	0.05	0.03	0.03	0.08	55
	Gollum-1	8195 - 8246.5	0.02	0.01	0.01	0.01	0.01	0.01	0.01	0	0.01	0.02	202
	Thorin-1	8568 - 8620	0.03	0.03	0.08	0.08	0.04	0.08	0.04	0.04	0.02	0.08	28
<b>Well-02</b>	Precious-1	7228.5 - 7485	0.05	0.05	0.06	0.06	0.08	0.06	0.08	0.04	0.07	0.07	409
<b>Well-03</b>	Precious-1	7460 - 7560	0.05	0.05	0.03	0.03	0.04	0.03	0.04	0.01	0.03	0.04	464
	Gollum-1	7864 - 7900	0.02	0.03	0.09	0.13	0.06	0.09	0.06	0.03	0.04	0.1	155
<b>Well-04</b>	Precious-1	7432 - 7600	0.05	0.05	0.1	0.12	0.07	0.1	0.07	0.04	0.04	0.1	79
<b>Well-05</b>	Precious-1	7380 - 7600	0.03	0.03	0.06	0.07	0.07	0.06	0.07	0.01	0.05	0.07	395
<b>Well-06</b>	Precious-1	7523 - 7620	0.03	0.03	0.06	0.07	0.09	0.06	0.09	0.03	0.07	0.06	268
<b>Well-07</b>	Precious-1	7408 - 7700	0.07	0.06	0.16	0.19	0.12	0.16	0.12	0.06	0.08	0.17	257
<b>Well-08</b>	Precious-1	7559 - 7796.5	0.05	0.05	0.09	0.15	0.08	0.13	0.08	0.06	0.05	0.14	301
<b>Well-09</b>	Precious-1	7424 - 7572	0.03	0.03	0.08	0.09	0.13	0.08	0.13	0.06	0.1	0.1	319
<b>Well-10</b>	Precious-1	7620 - 7760	0.04	0.05	0.08	0.1	0.06	0.08	0.06	0.02	0.04	0.09	198
<b>Well-11</b>	Precious-1	7580 - 7638.5	0.04	0.04	0.07	0.08	0.04	0.07	0.04	0.04	0.02	0.07	66
<b>Well-12</b>	Precious-1	7570 - 7670	0.02	0.02	0.04	0.05	0.05	0.04	0.05	0.01	0.04	0.05	316
<b>Well-13</b>	Precious-1	7672 - 7787	0.03	0.03	0.08	0.09	0.09	0.08	0.09	0.02	0.06	0.1	399
<b>Well-14</b>	Precious-1	7419 - 7600	0.04	0.04	0.14	0.15	0.1	0.14	0.1	0.05	0.07	0.15	351
	Gollum-1	8127 - 8150.5	0.03	0.04	0.05	0.06	0.06	0.05	0.06	0.01	0.05	0.06	367
	Thorin-1	8198.5 8217.5	0.01	0.01	0.03	0.03	0.04	0.03	0.04	0.01	0.03	0.04	423
<b>Well-15</b>	Precious-1	7420 - 7580	0.06	0.05	0.09	0.11	0.1	0.09	0.1	0.02	0.07	0.11	322
	Gollum-1	8174.5 - 8225	0.04	0.04	0.05	0.06	0.05	0.05	0.05	0.02	0.04	0.06	535
<b>Well-16</b>	Precious-1	7460 - 7560	0.05	0.05	0.06	0.06	0.09	0.06	0.09	0.04	0.07	0.06	419
<b>Well-17</b>	Precious-1	7230 - 7440	0.07	0.07	0.1	0.13	0.11	0.1	0.11	0.04	0.08	0.12	340

	Gollum-1	7459 - 7489.5	0.03	0.03	0.03	0.03	0.01	0.03	0.01	0.01	0.01	0.03	40
<b>Well-18</b>	Precious-1	7460 - 7660	0.06	0.06	0.1	0.1	0.1	0.1	0.1	0.02	0.07	0.11	346
<b>Well-19</b>	Precious-1	7420 -7498.5	0.05	0.05	0.03	0.03	0.05	0.03	0.05	0.02	0.04	0.03	452
	Gollum-1	8098.5 - 8117	0.05	0.05	0.03	0.03	0.05	0.03	0.05	0.02	0.04	0.03	452
<b>Well-20</b>	Precious-1	7470 - 7600	0.05	0.06	0.06	0.06	0.1	0.06	0.1	0.05	0.08	0.08	344
<b>Well-21</b>	Precious-1	7443 - 7543	0.06	0.06	0.1	0.11	0.08	0.1	0.08	0.04	0.05	0.11	427
	Gollum-1	7610 - 7640	0.03	0.03	0.11	0.11	0.1	0.11	0.1	0.02	0.07	0.13	350
<b>Well-22</b>	Precious-1	7365 - 7508	0.08	0.08	0.04	0.05	0.02	0.04	0.02	0.02	0.01	0.04	175
<b>Well-23</b>	Precious-1	7376.5 - 7512	0.06	0.06	0.08	0.09	0.1	0.08	0.1	0.03	0.08	0.1	429
	Gollum-1	8118 - 8150	0.03	0.03	0.02	0.02	0.04	0.02	0.04	0.03	0.04	0.03	390
	Thorin-1	8201 - 8220	0.04	0.04	0.03	0.04	0.06	0.03	0.06	0.02	0.04	0.05	391
<b>Well-24</b>	Precious-1	7440 - 7560	0.08	0.08	0.13	0.15	0.08	0.13	0.08	0.06	0.05	0.14	460
<b>Well-25</b>	Precious-1	7405.5 - 7540	0.05	0.05	0.05	0.06	0.08	0.05	0.08	0.03	0.06	0.07	393
	Gollum-1	7851 - 7880	0.04	0.05	0.07	0.1	0.07	0.07	0.07	0.02	0.05	0.1	465
	Thorin-1	8181 - 8228	0.02	0.03	0.02	0.03	0.04	0.02	0.04	0.02	0.03	0.03	-

**C. APPENDIX:** Estimated Petrophysical Properties and Visualizations

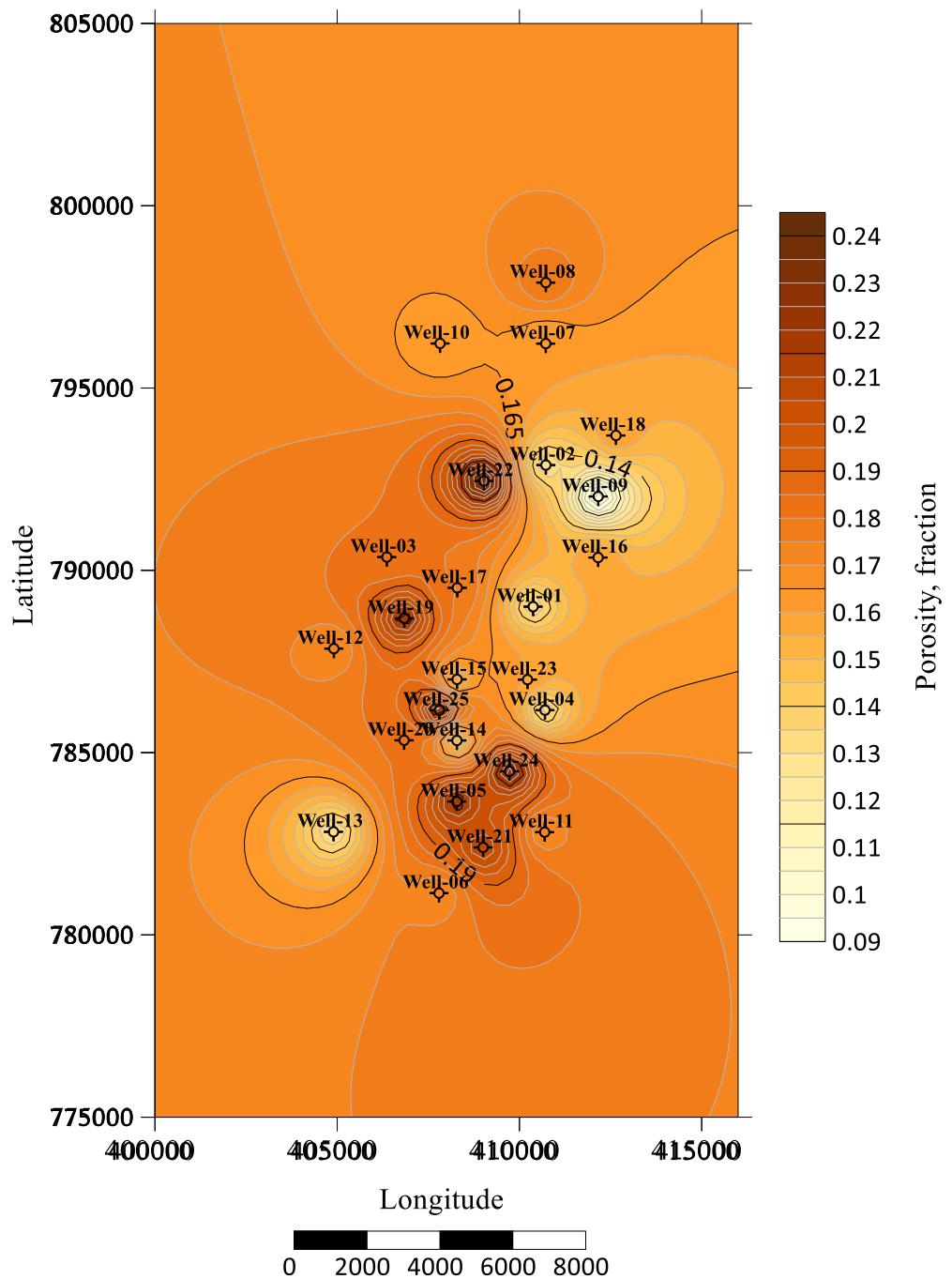


**Figure C.1:** Porosity map of Precious-1

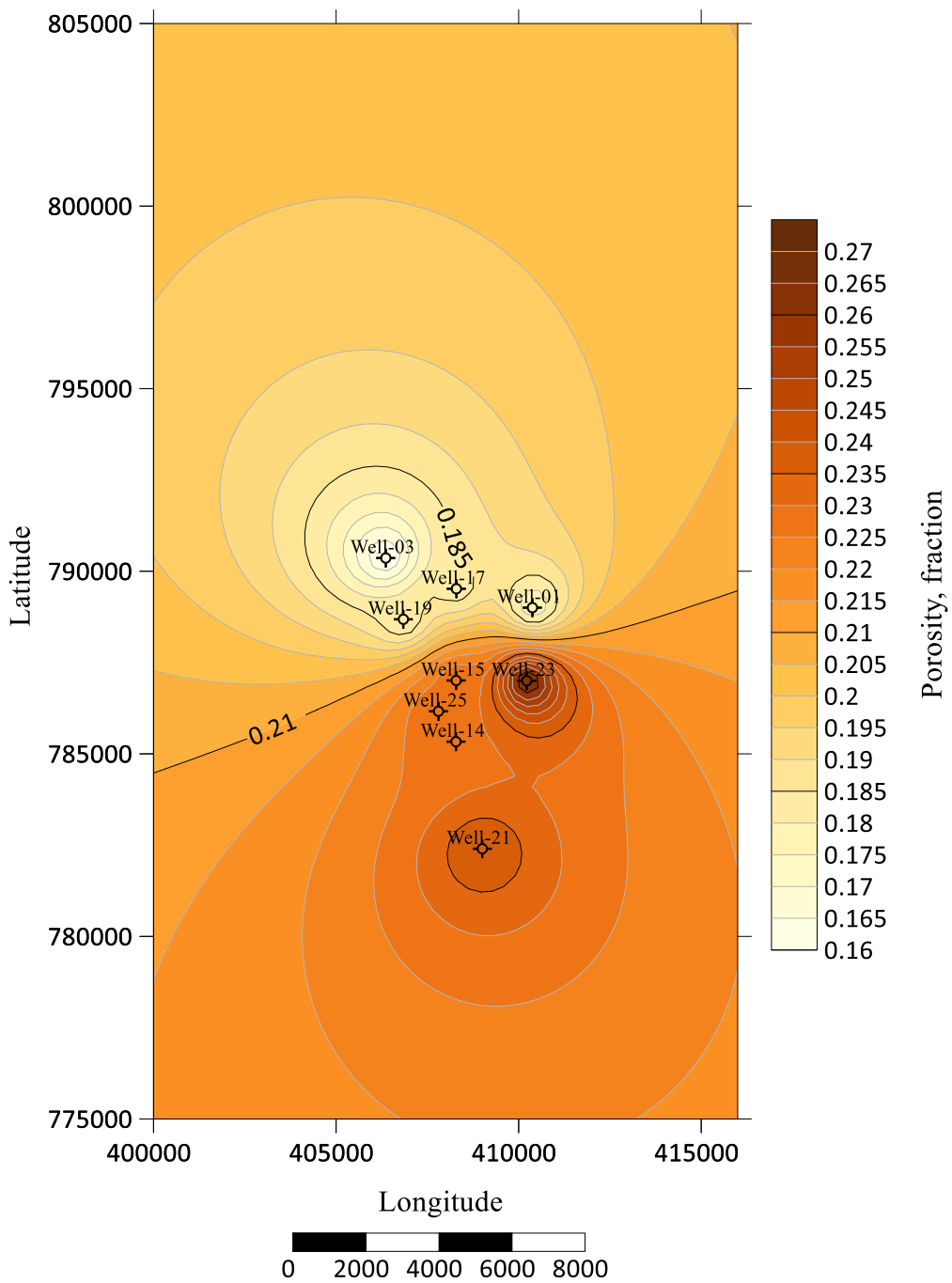


**Figure C.2:** Porosity map of Gollum-1.

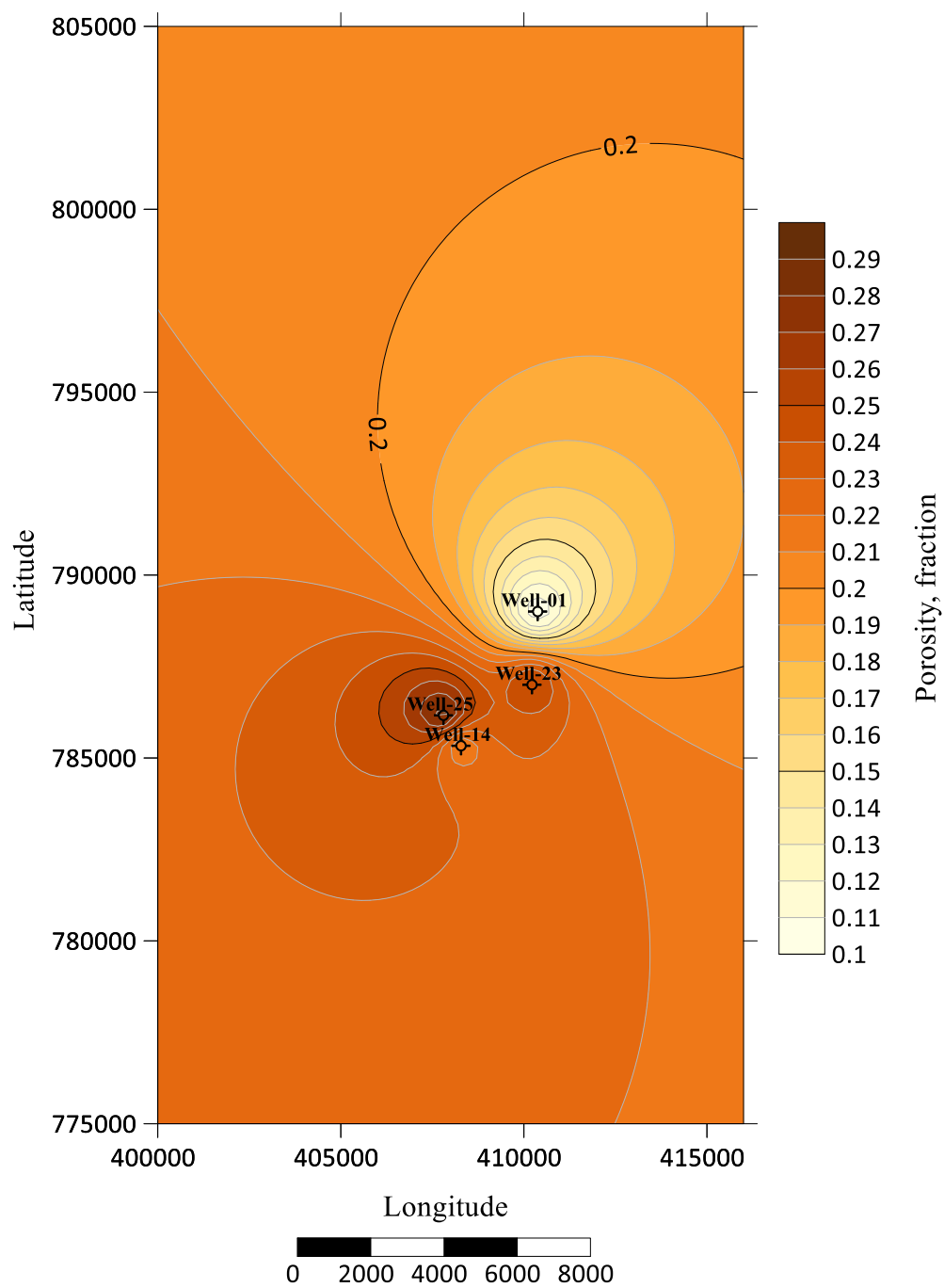


**Figure C.3:** Porosity map of Thorin-1.

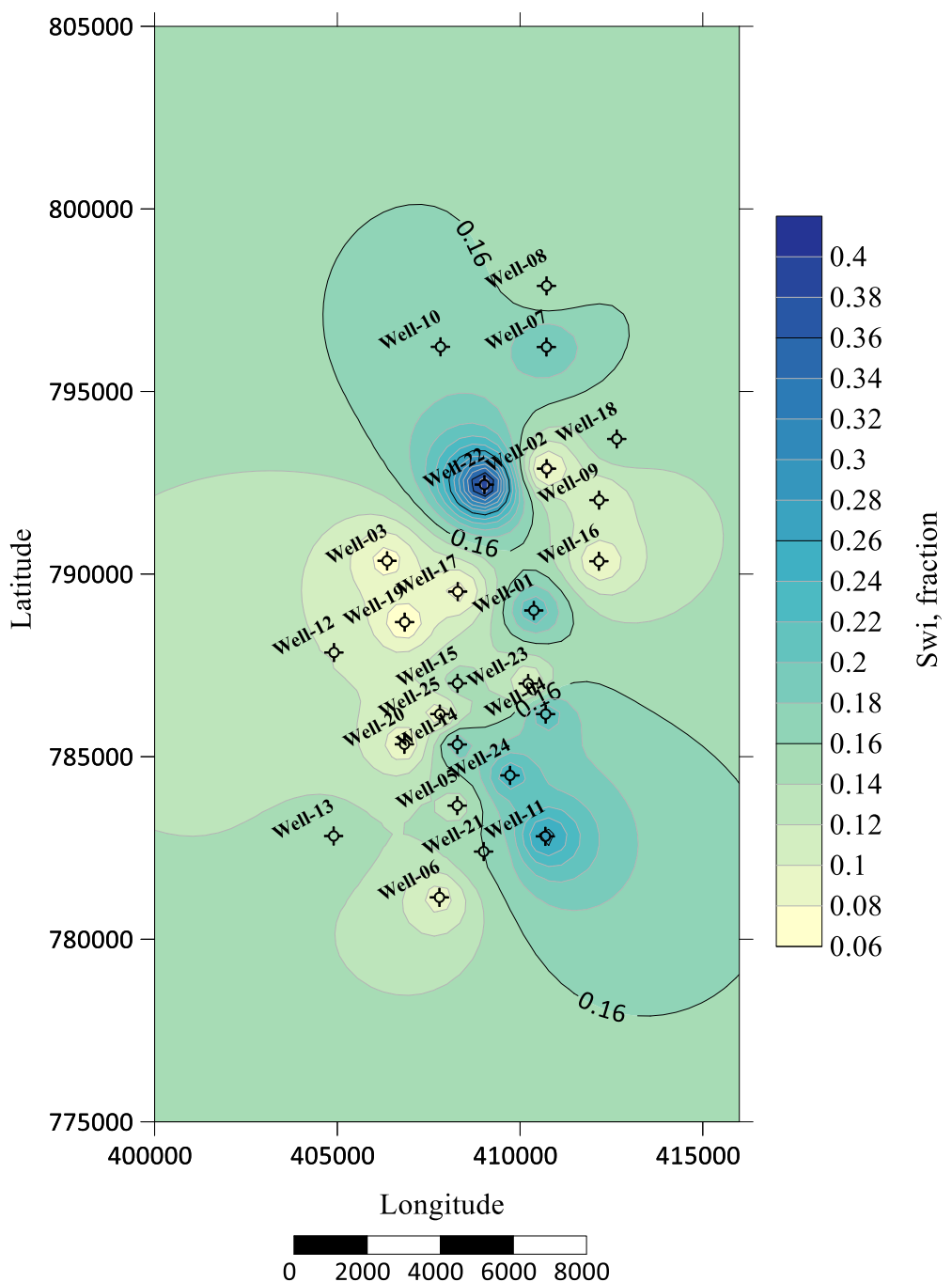


**Figure C.4:** Initial water saturation map of Precious-1.

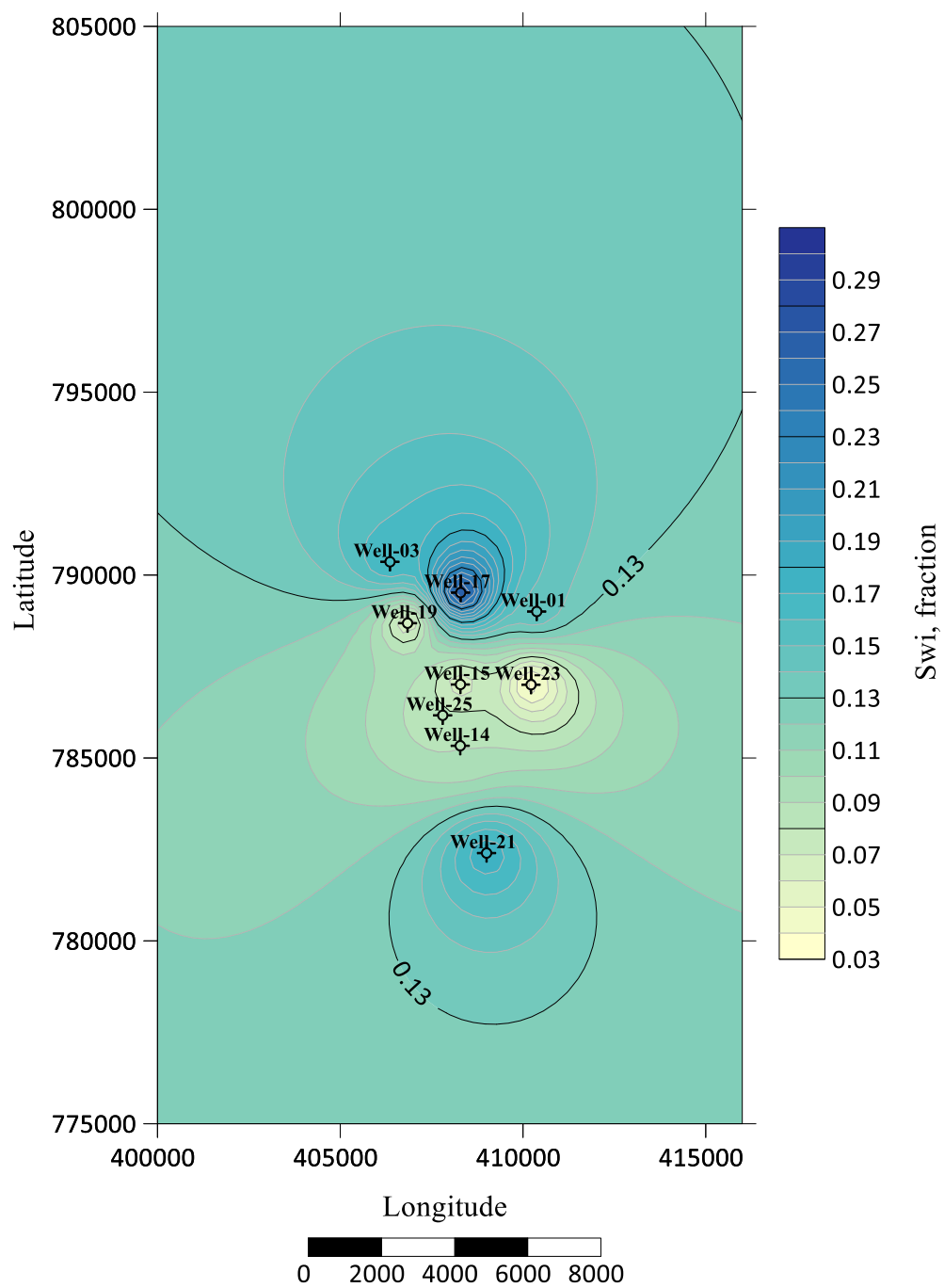


**Figure C.5:** Initial water saturation map of Gollum-1.

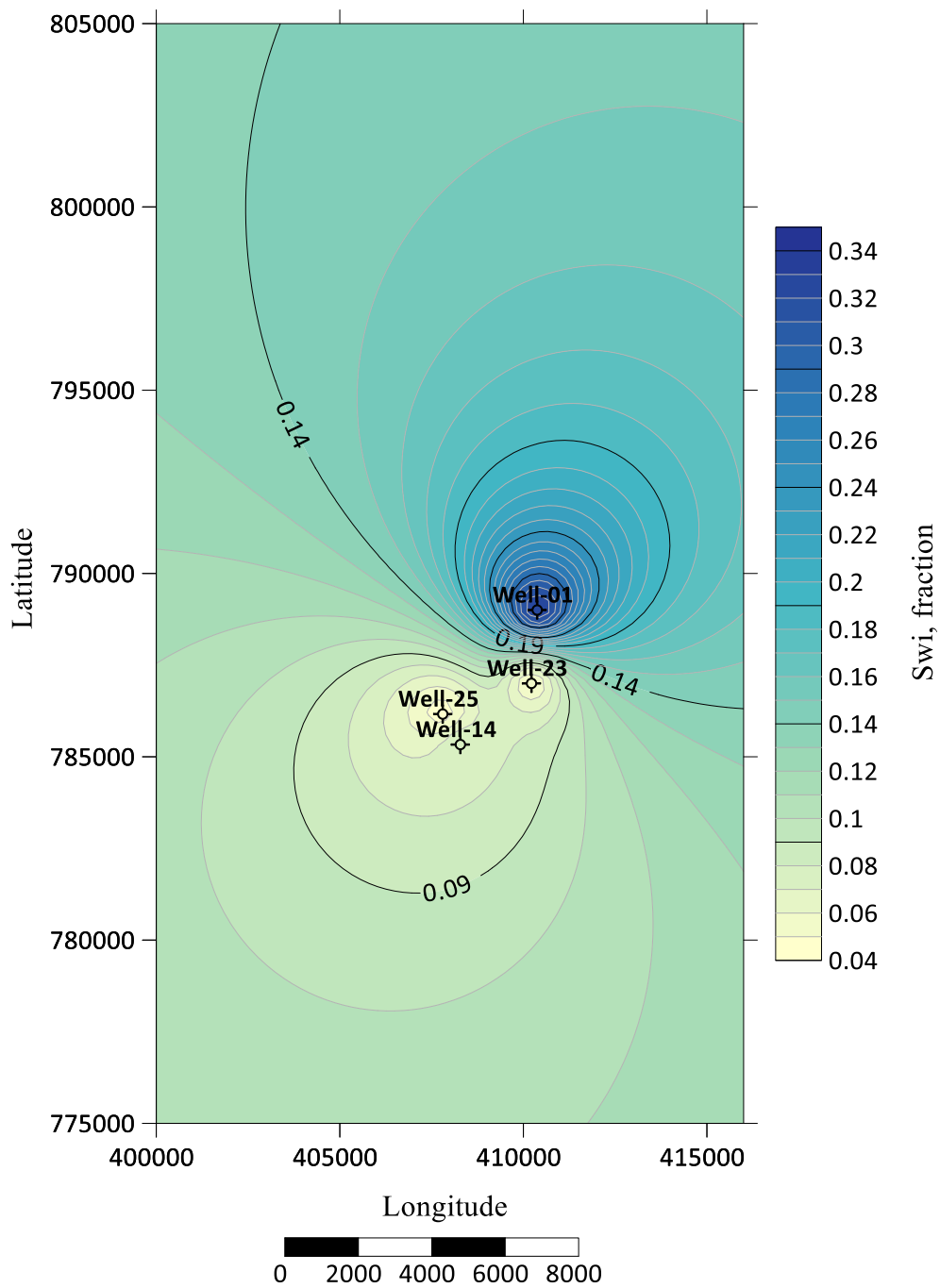


**Figure C.6:** Initial water saturation map of Thorin-1.

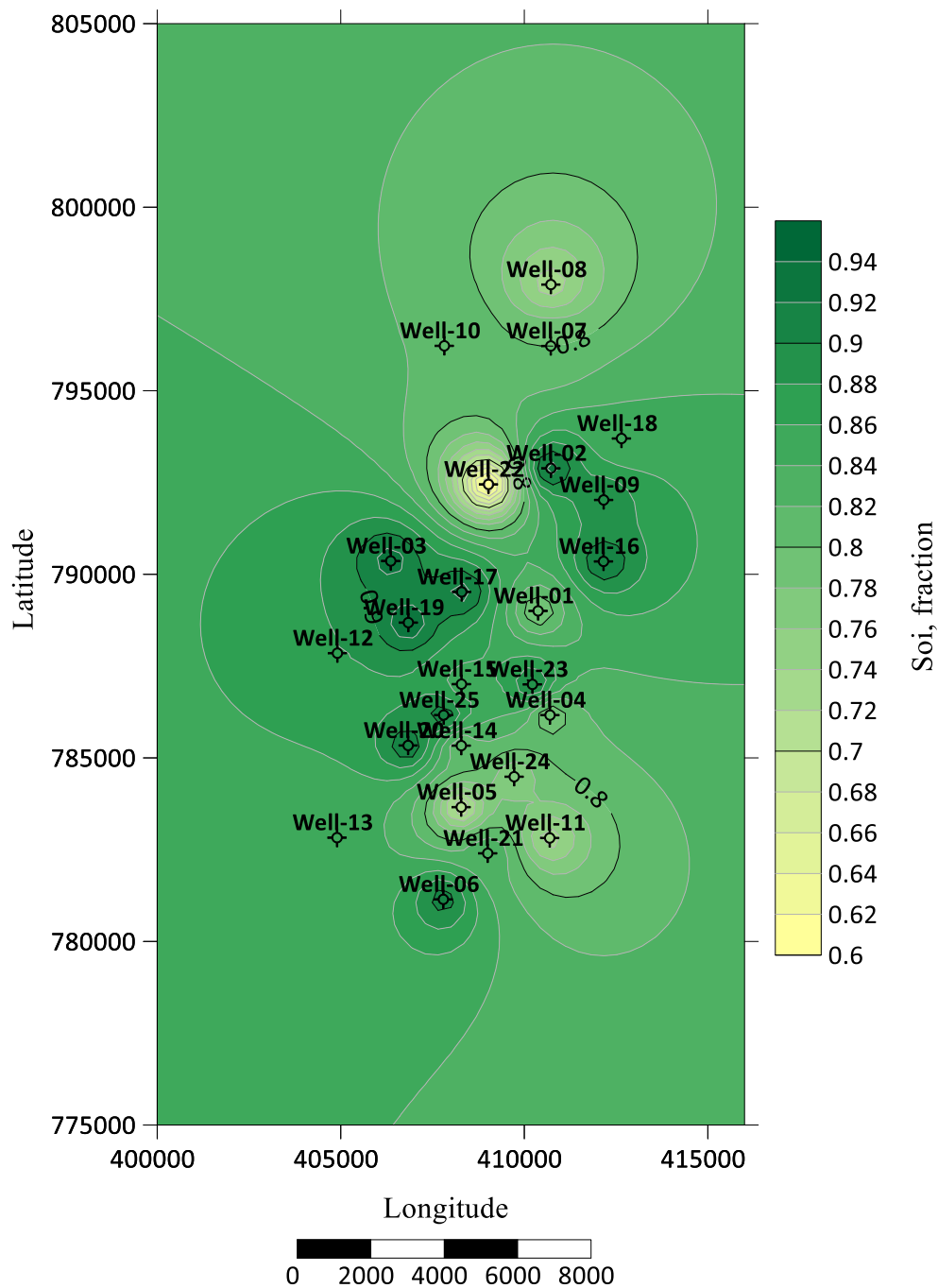


**Figure C.7:** Initial oil saturation map of Precious-1.

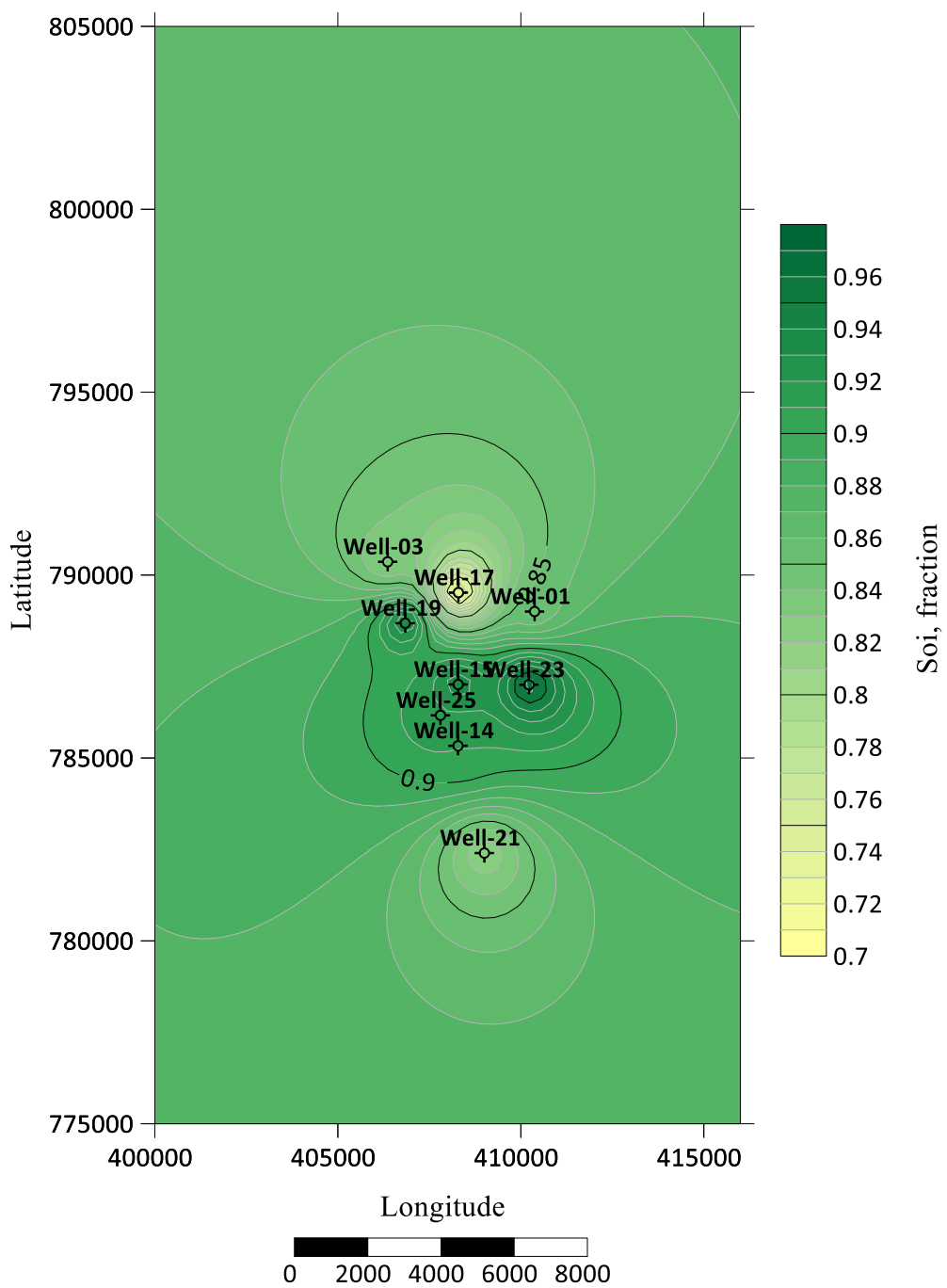


**Figure C.8:** Initial oil saturation map of Gollum-1.

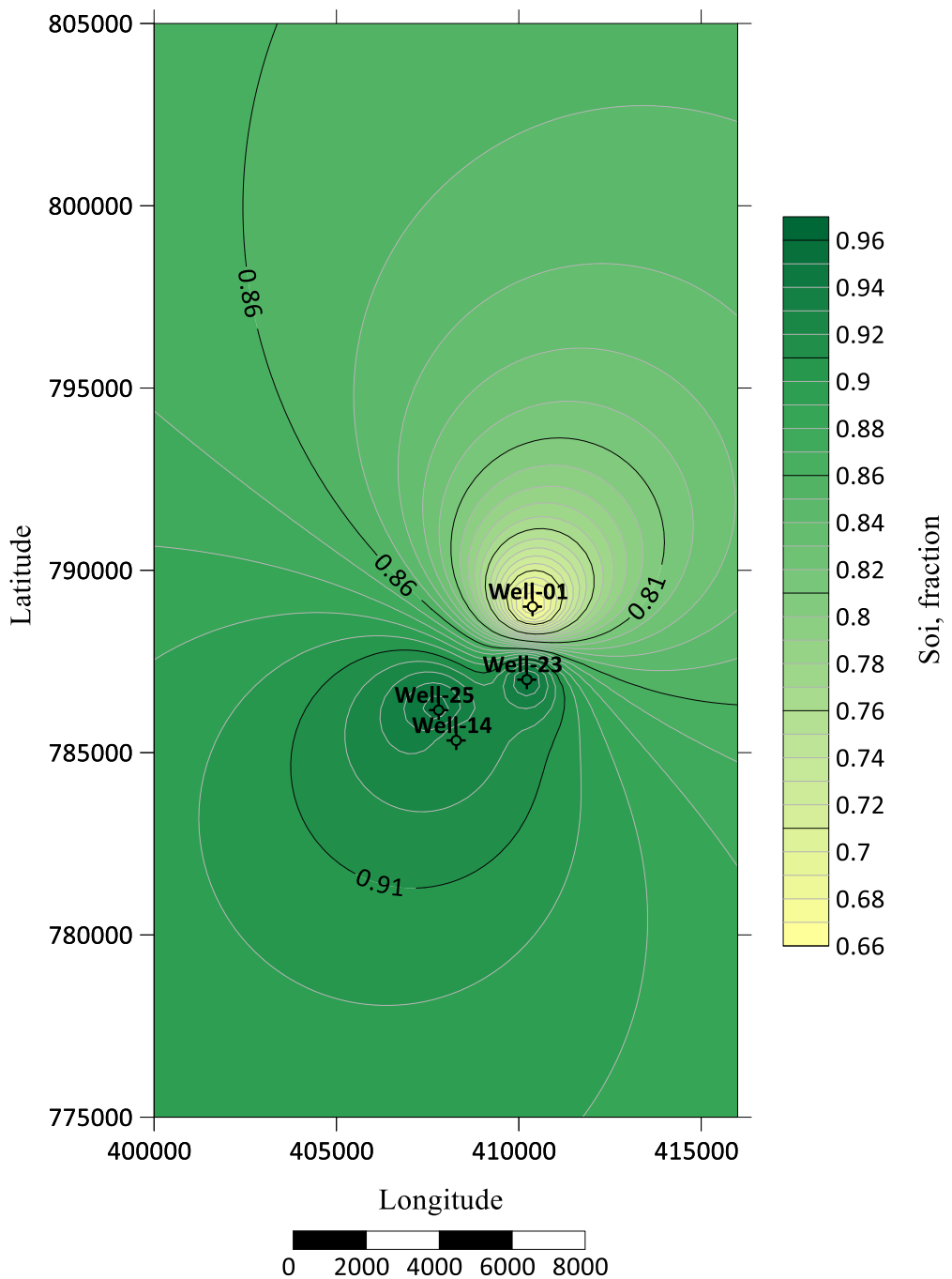


**Figure C.9:** Initial oil saturation map of Thorin-1

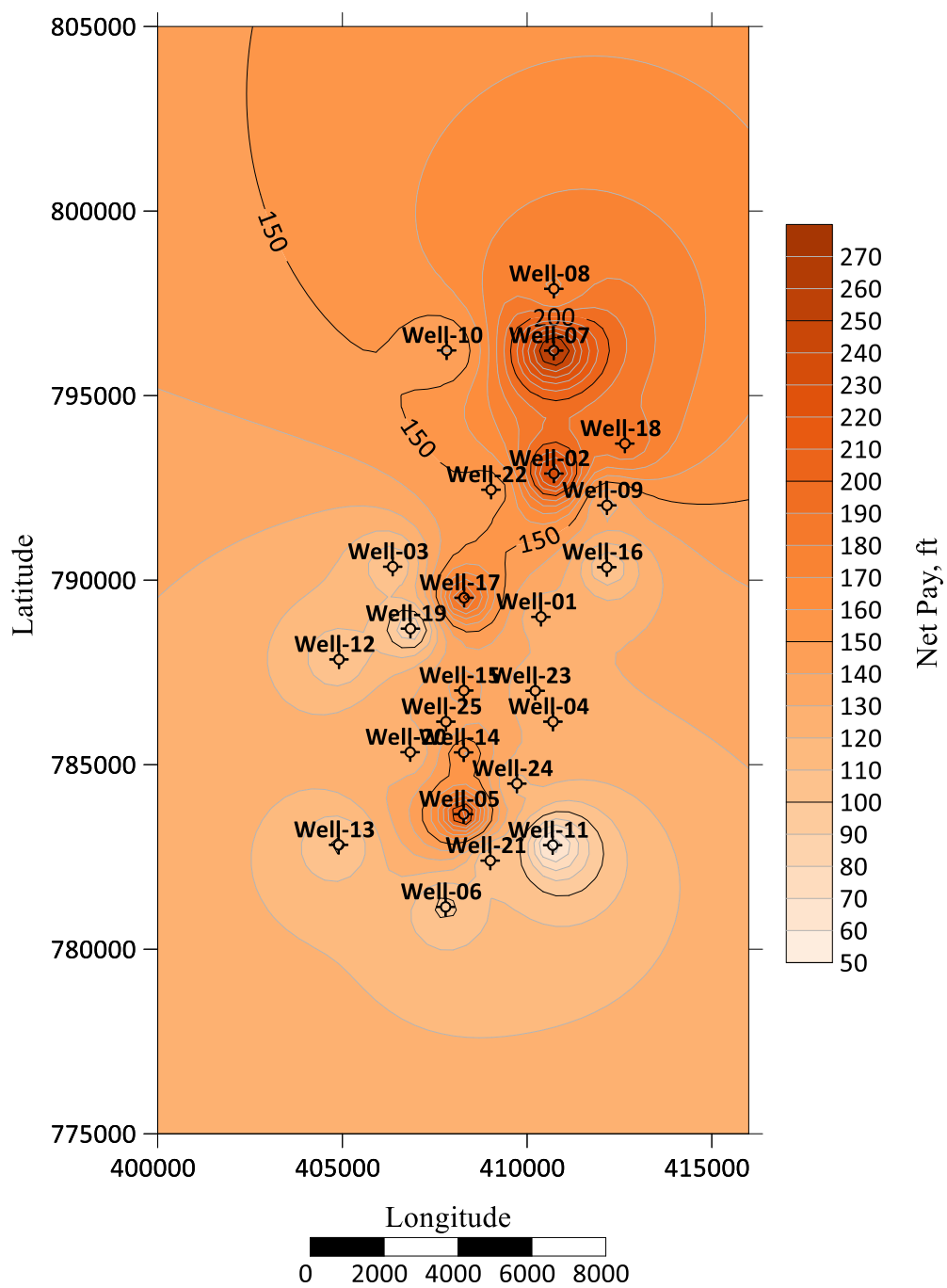


**Figure C.10:** Net pay thickness map of Precious-1.

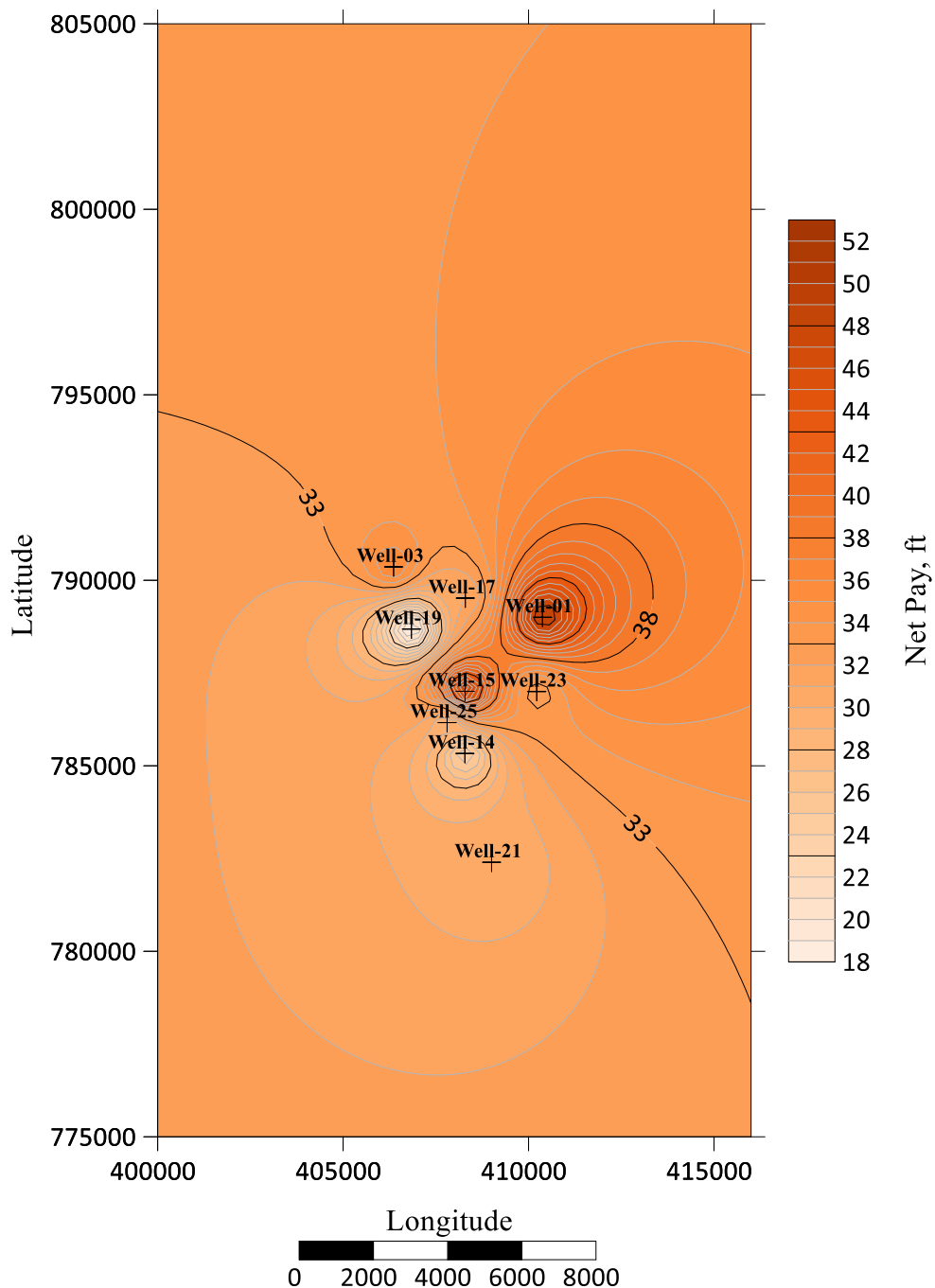


**Figure C.11:** Net pay thickness map of Gollum-1.

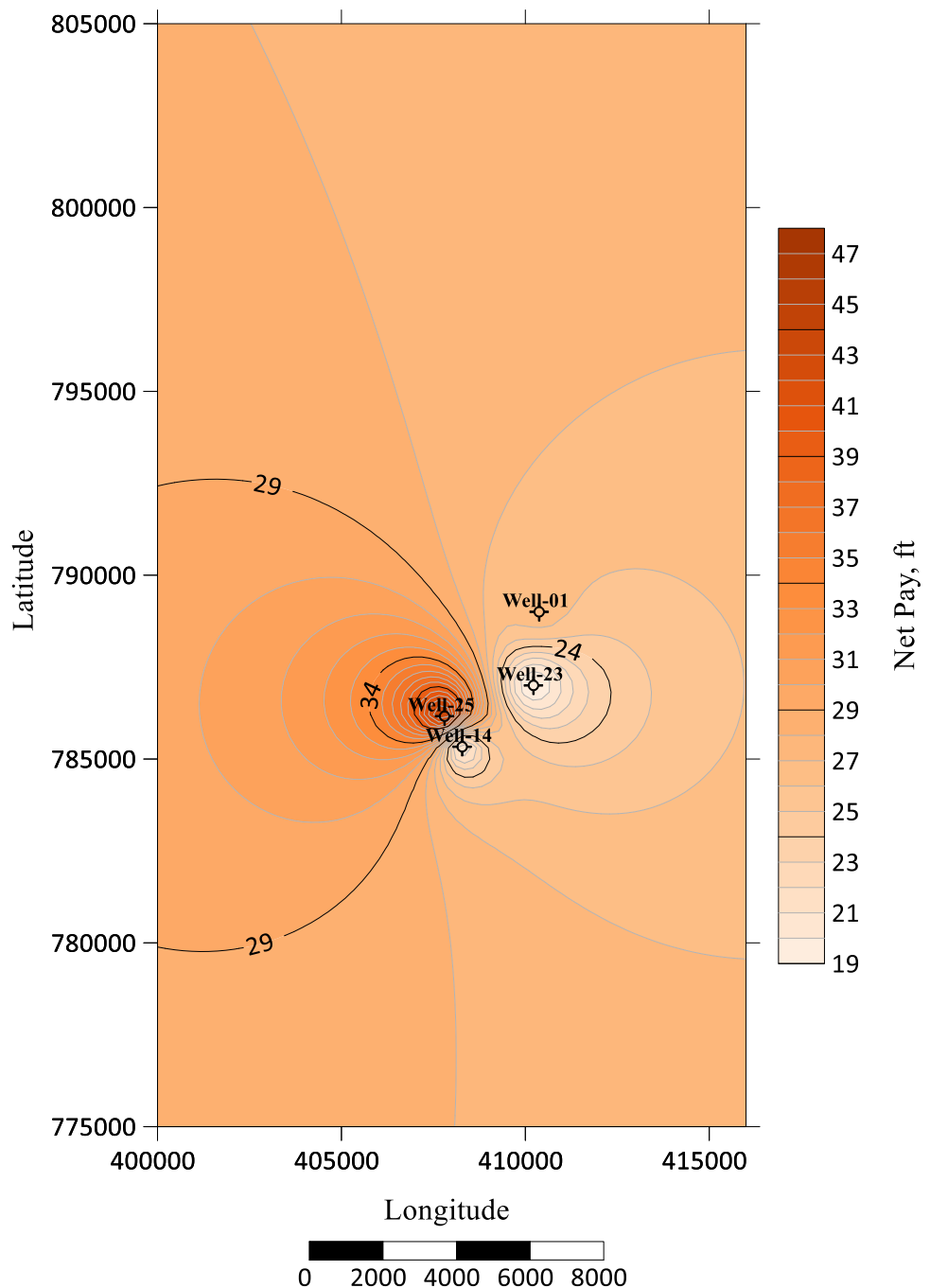


**Figure C.12:** Net pay thickness map of Thorin-1

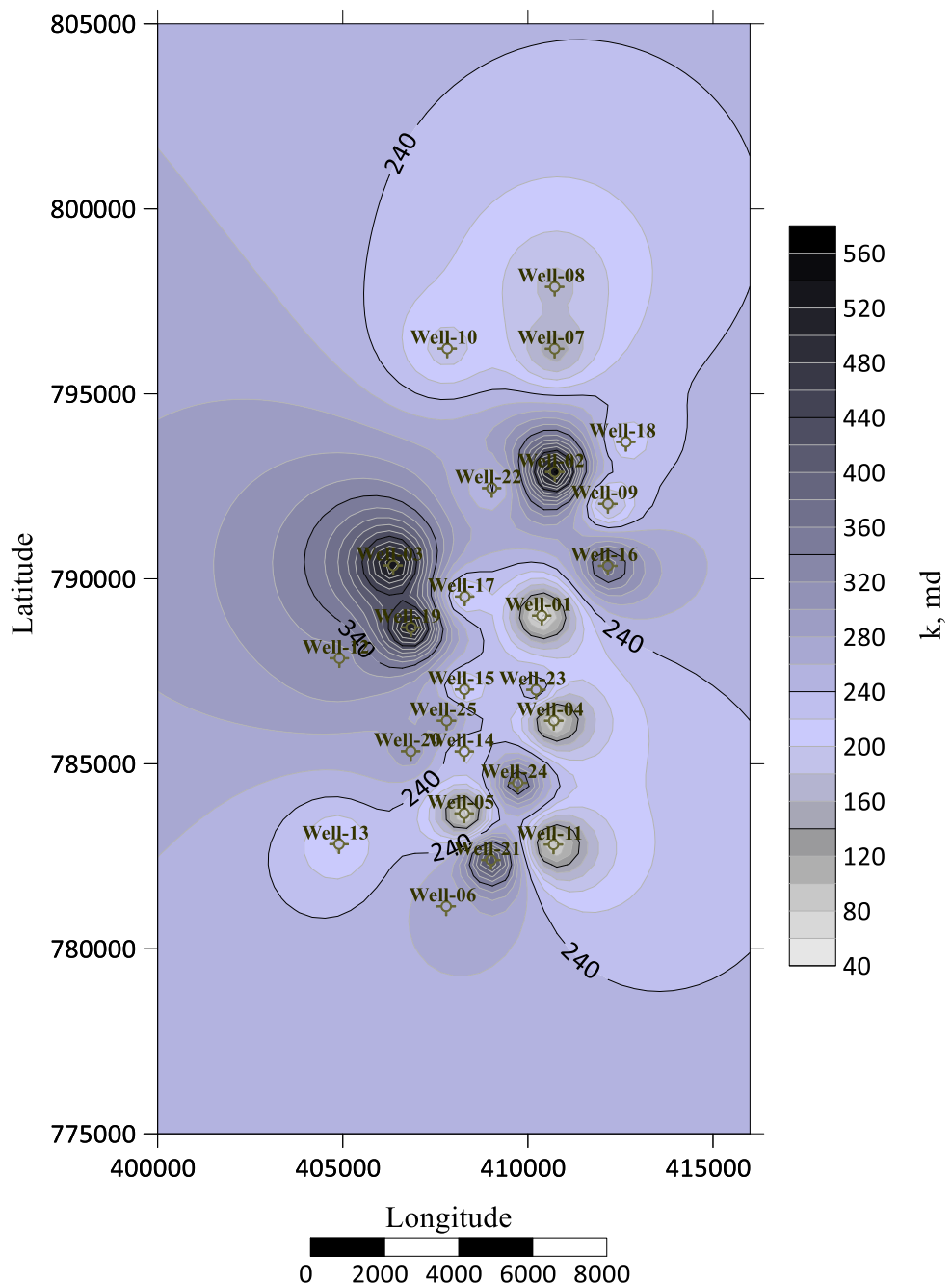


**Figure C.13:** The permeability map of Precious-1 reservoir layer.

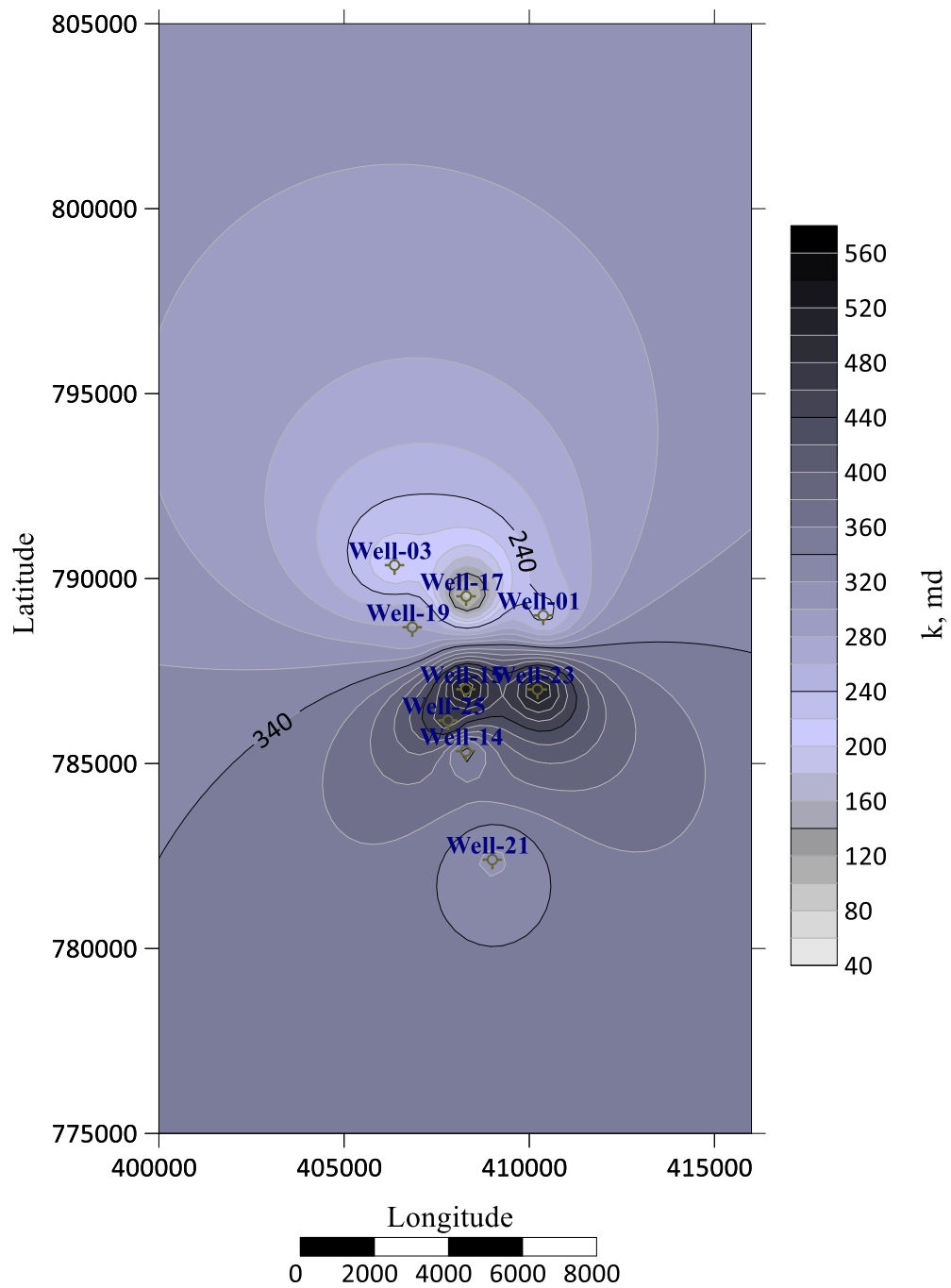


**Figure C.14:** The permeability map of Gollum-1 reservoir layer.

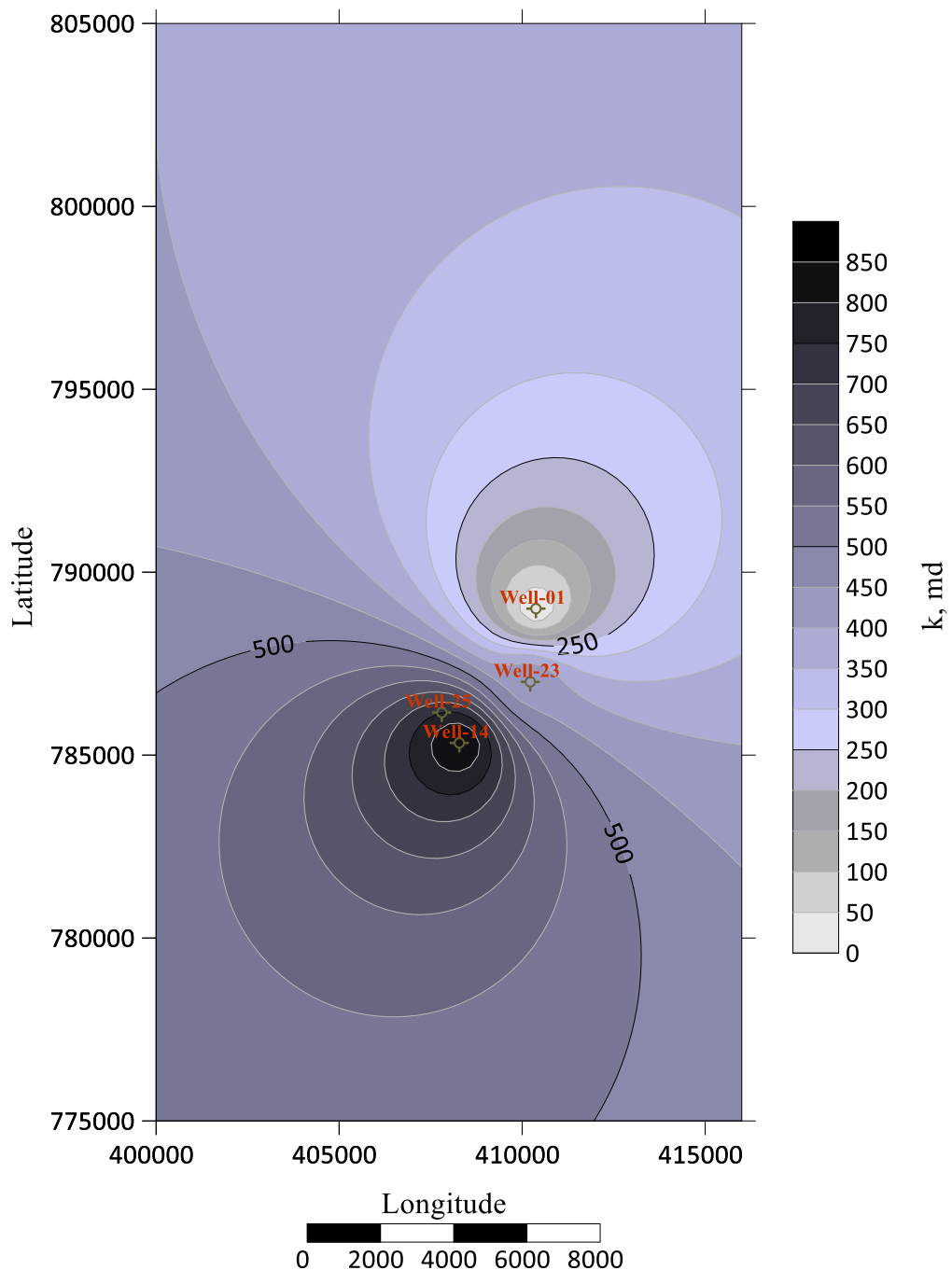


**Figure C.15:** The permeability map of Thorin-1 reservoir layer.

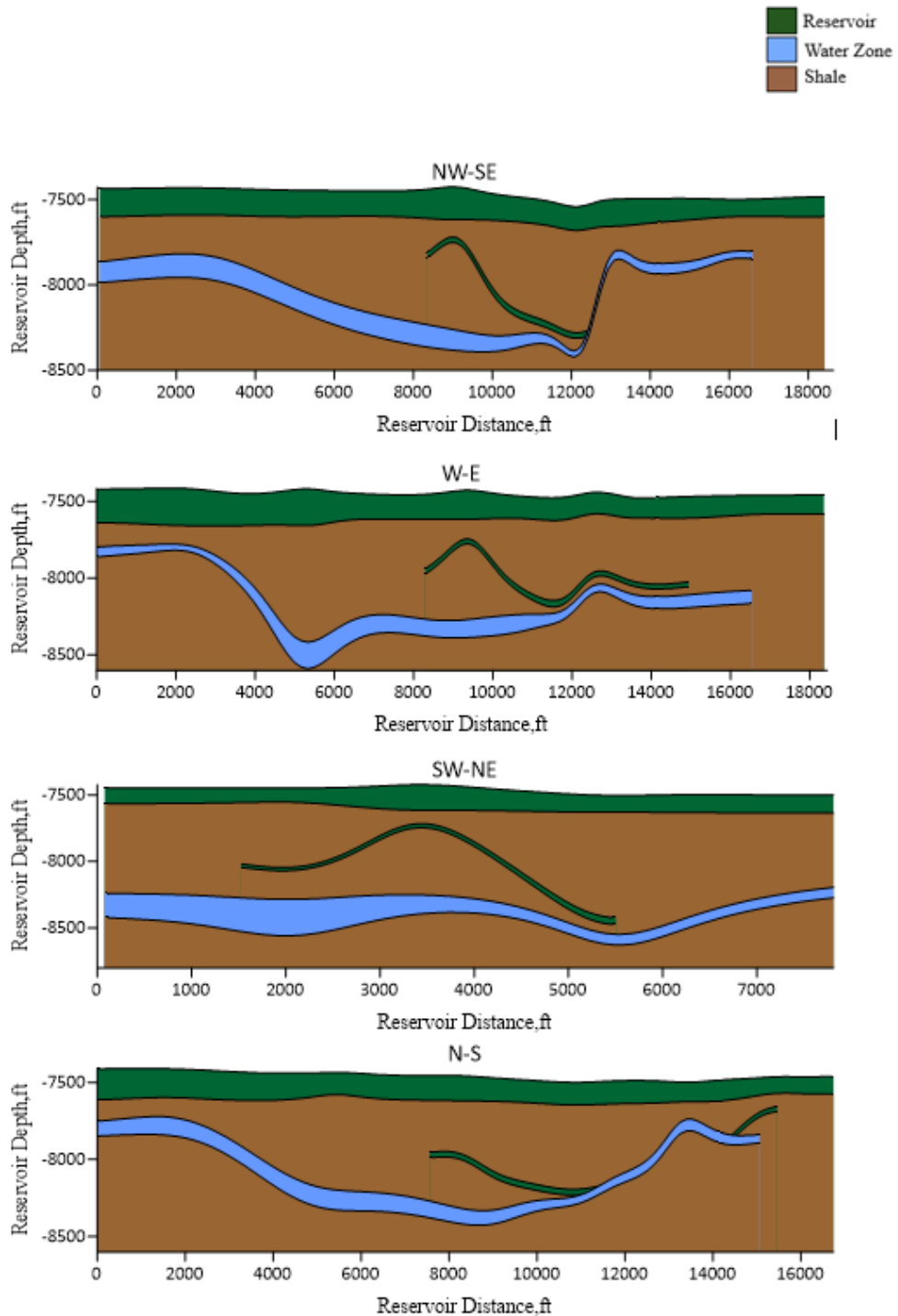


**Figure C.16:** Various cross sections of the Mount Doom Oil Field.

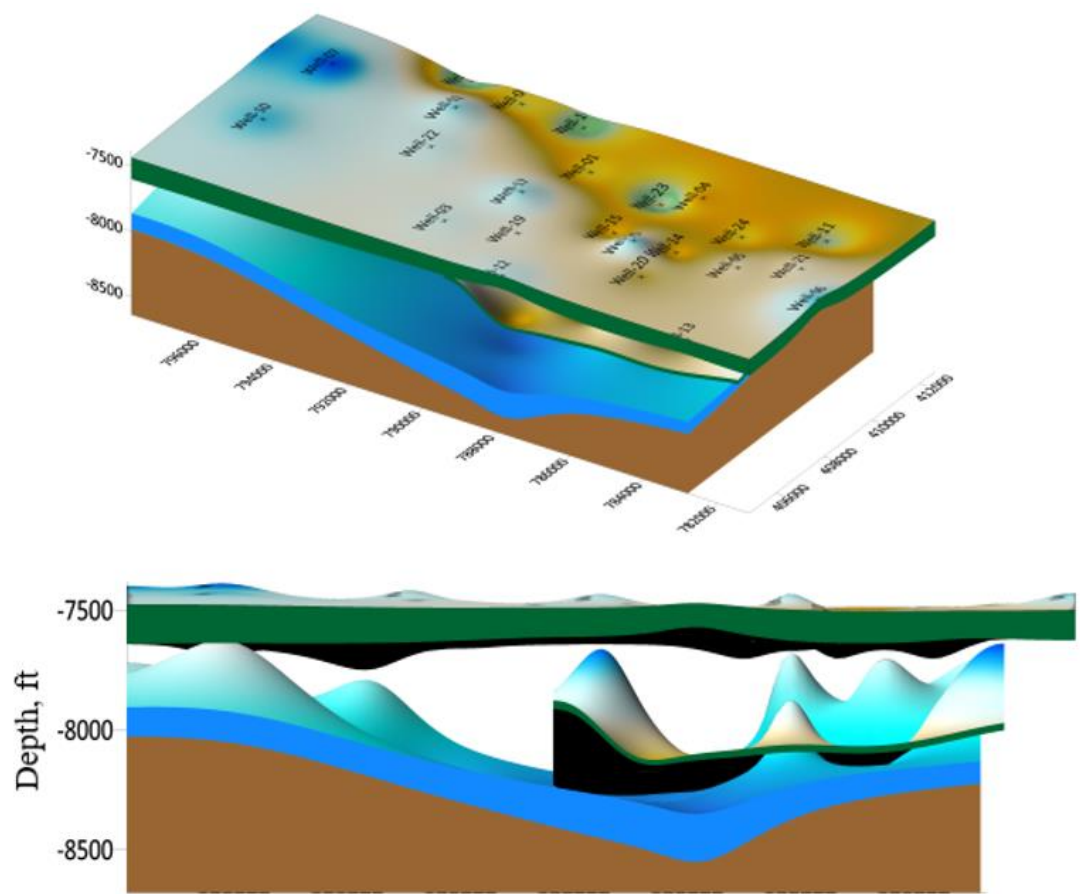


**Figure C.17:** 3D representation of the Mount Doom Oil Field.

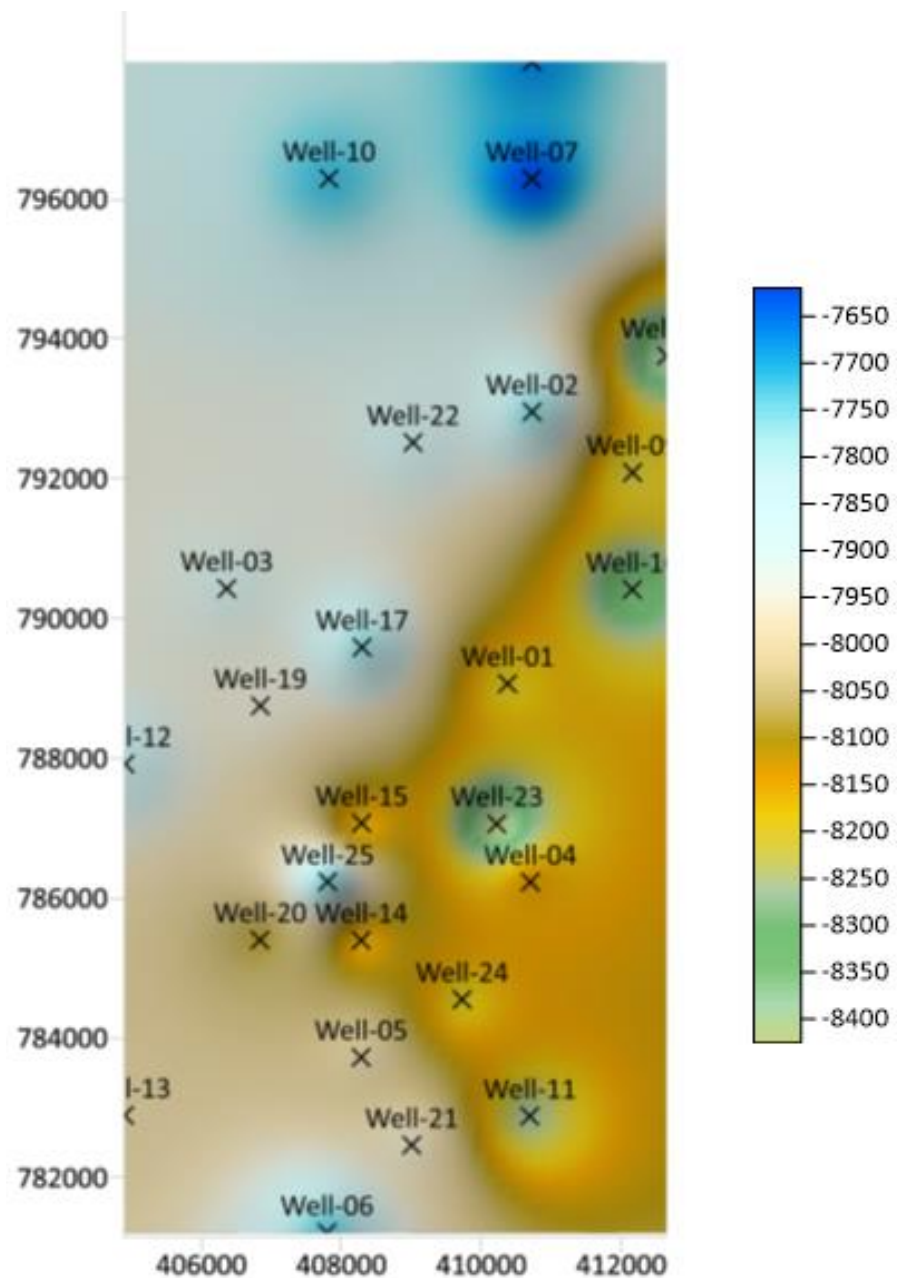


**Figure C.18:** Bird-eye view of the Mount Doom Oil Field.



**Figure C.19:** Initial oil saturation and movable oil saturation as a function of depth for Well-01 Precious-1 layer.



**Figure C.20:** Initial oil saturation and movable oil saturation as a function of depth for Well-01 Gollum-1 layer.



**Figure C.21:** Initial oil saturation and movable oil saturation as a function of depth for Well-01 Thorin-1 layer.

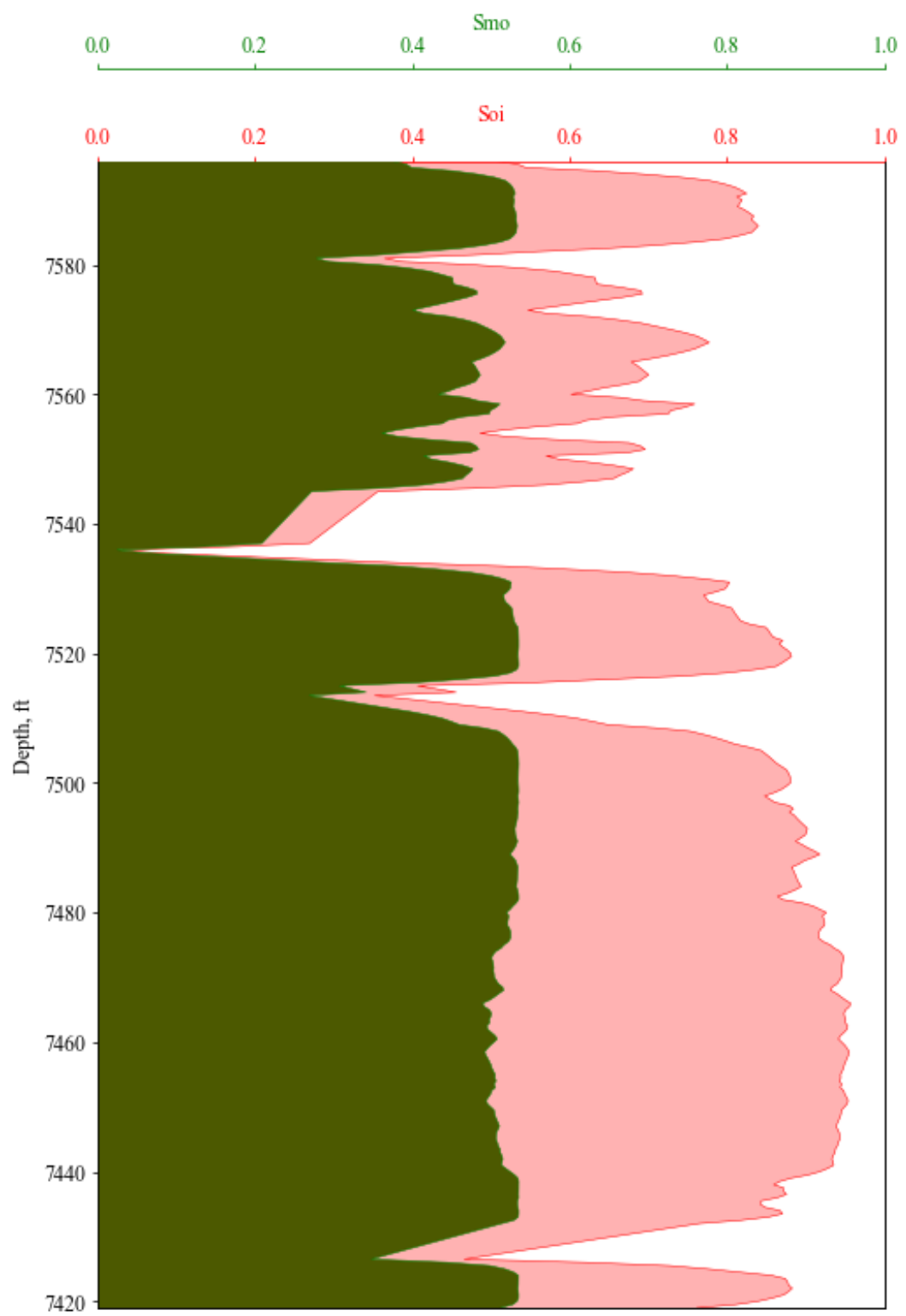


**Figure C.22:** Initial oil saturation and movable oil saturation as a function of depth for Well-14 Precious-1 layer.

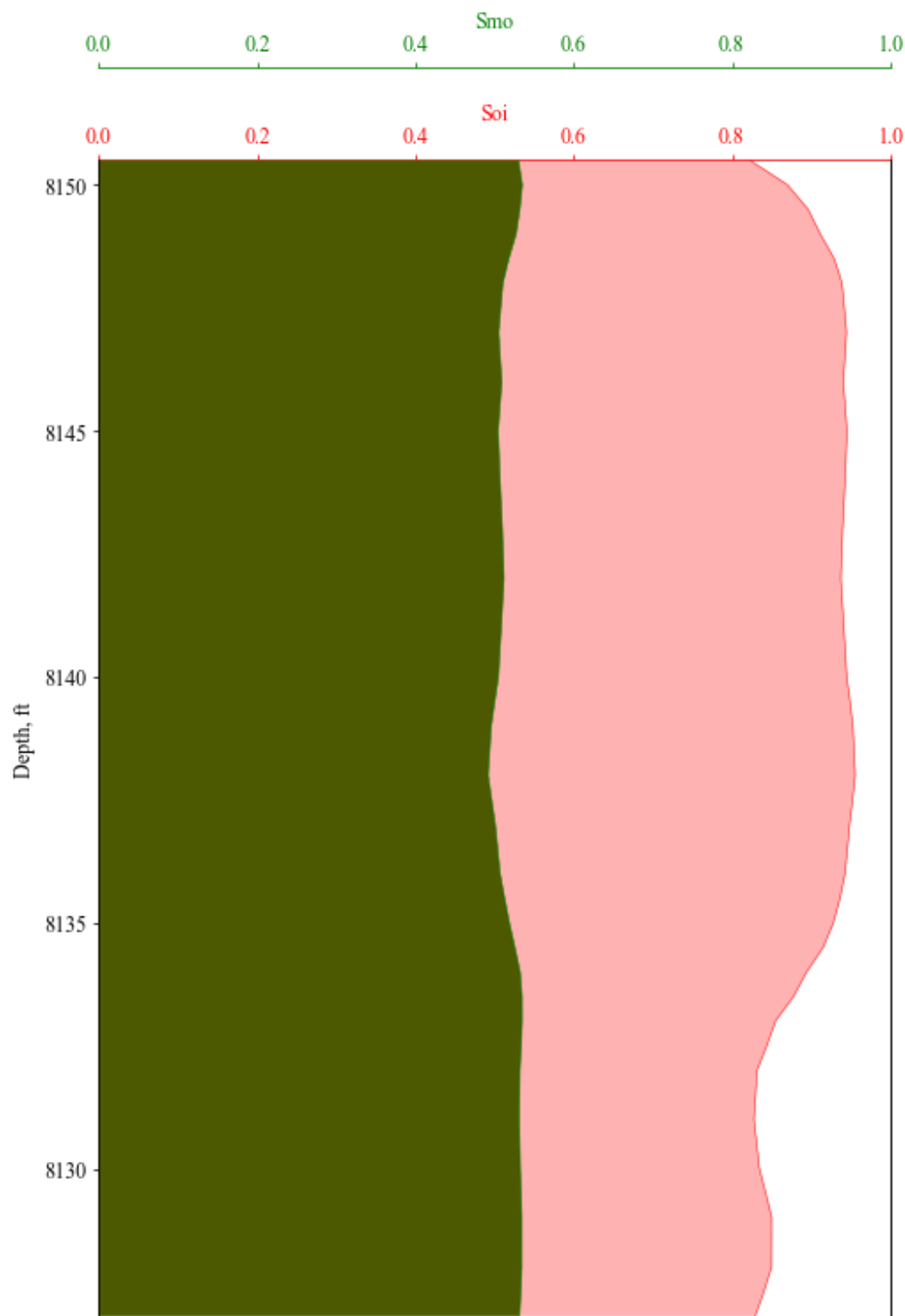


**Figure C.23:** Initial oil saturation and movable oil saturation as a function of depth for Well-14 Gollum-1 layer.

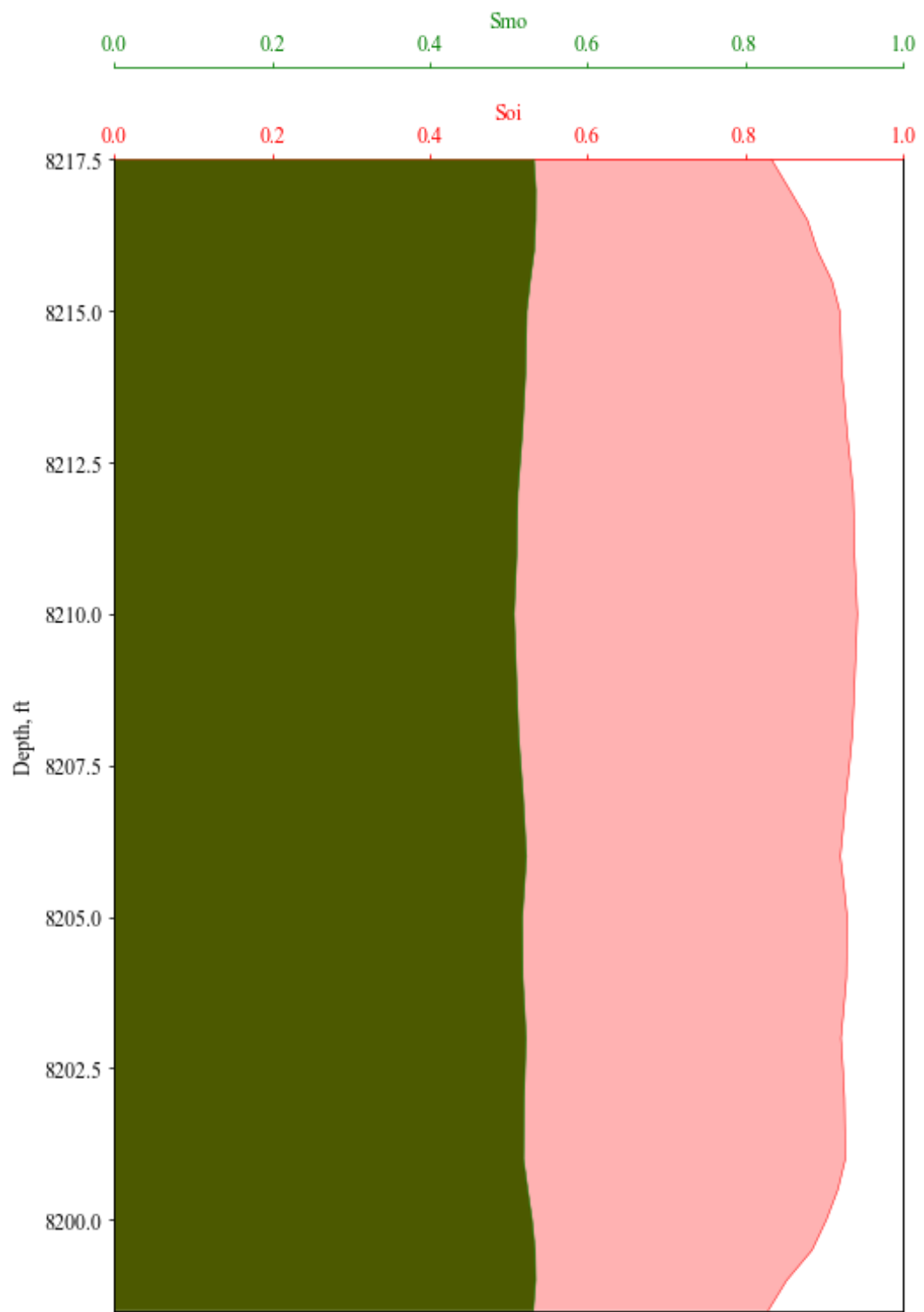


**Figure C.24:** Initial oil saturation and movable oil saturation as a function of depth for Well-14 Thorin-1 layer.

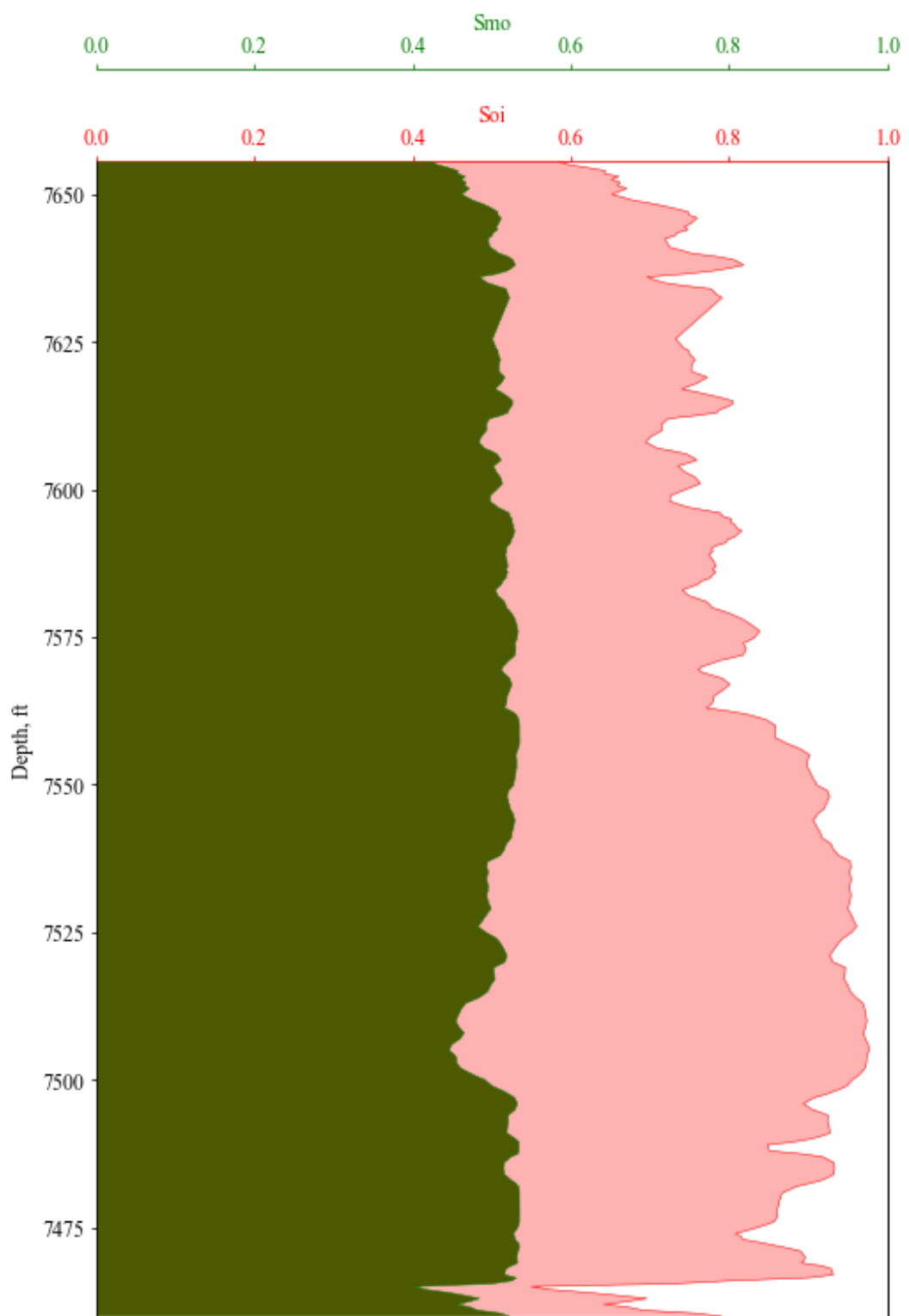


**Figure C.25:** Initial oil saturation and movable oil saturation as a function of depth for Well-18 Precious-1 layer.

**D. APPENDIX:** Reserves Estimation

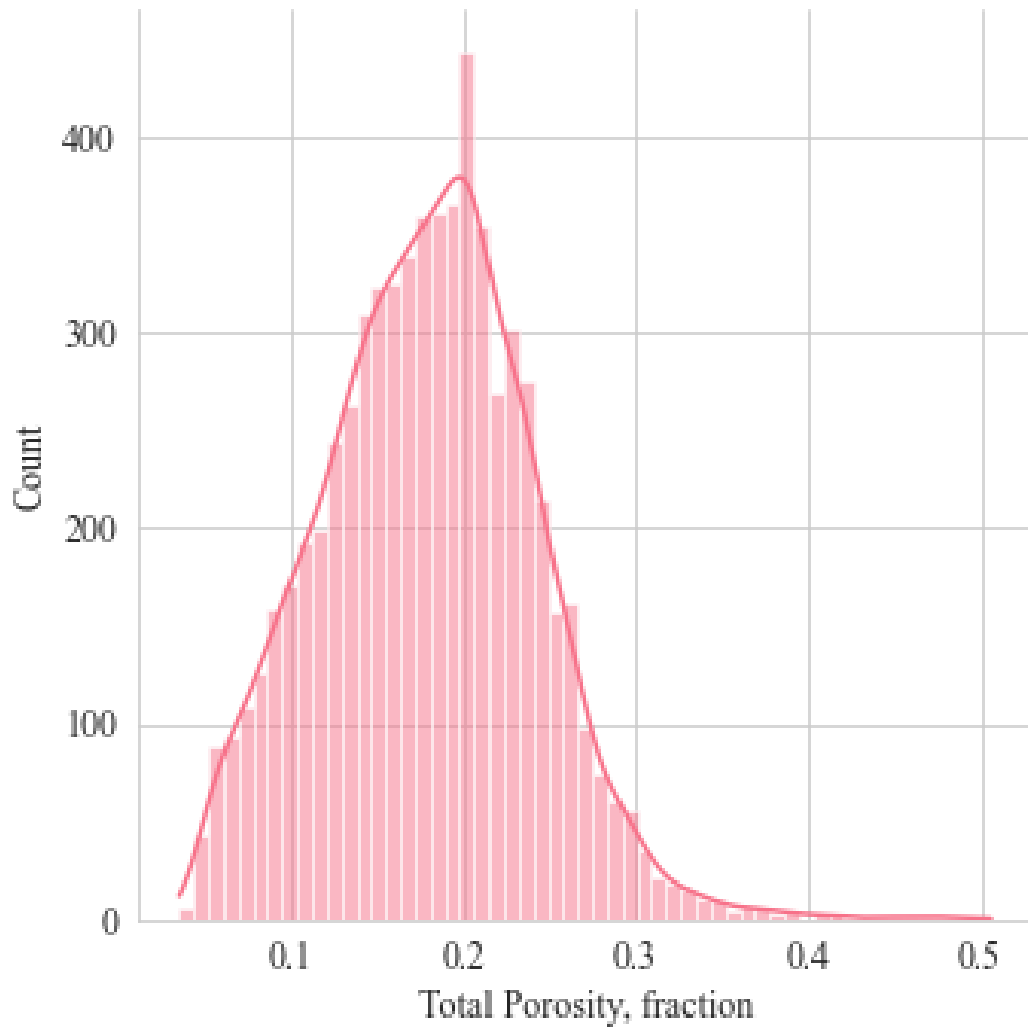


**Figure D.1:** Total porosity distribution obtained from all wells for Precious-1 reservoir layer.

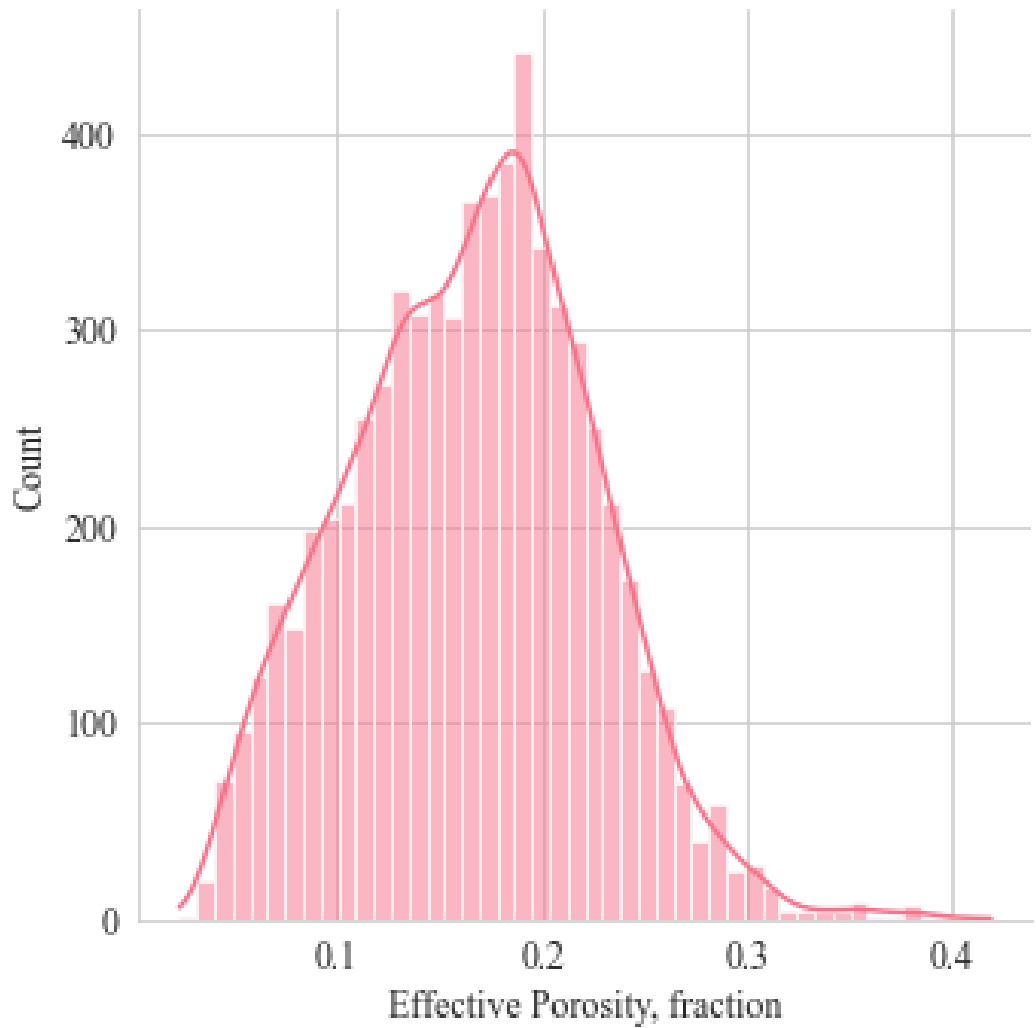


**Figure D.2:** Effective porosity distribution obtained from all wells for Precious-1 reservoir layer.

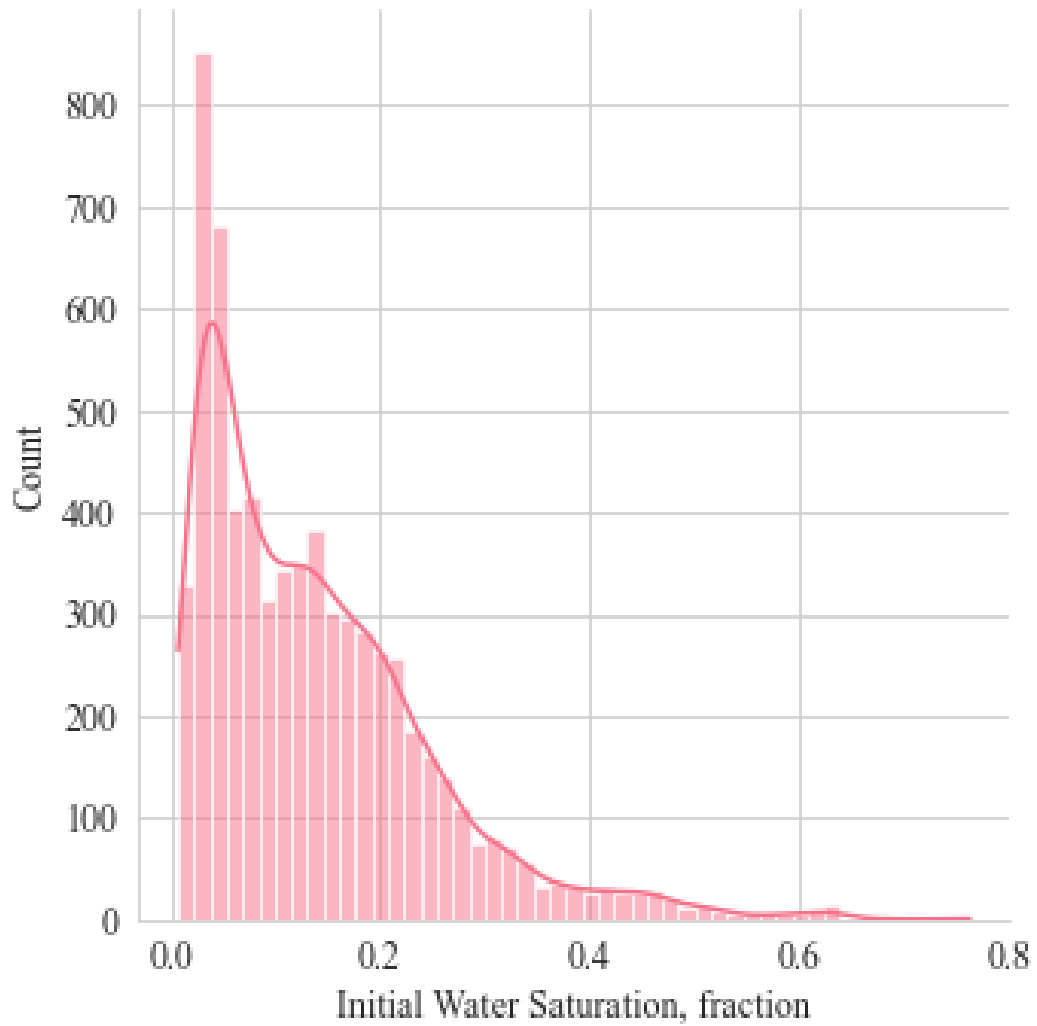


**Figure D.3:** Initial water saturation distribution obtained from all wells for Precious-1 reservoir layer.

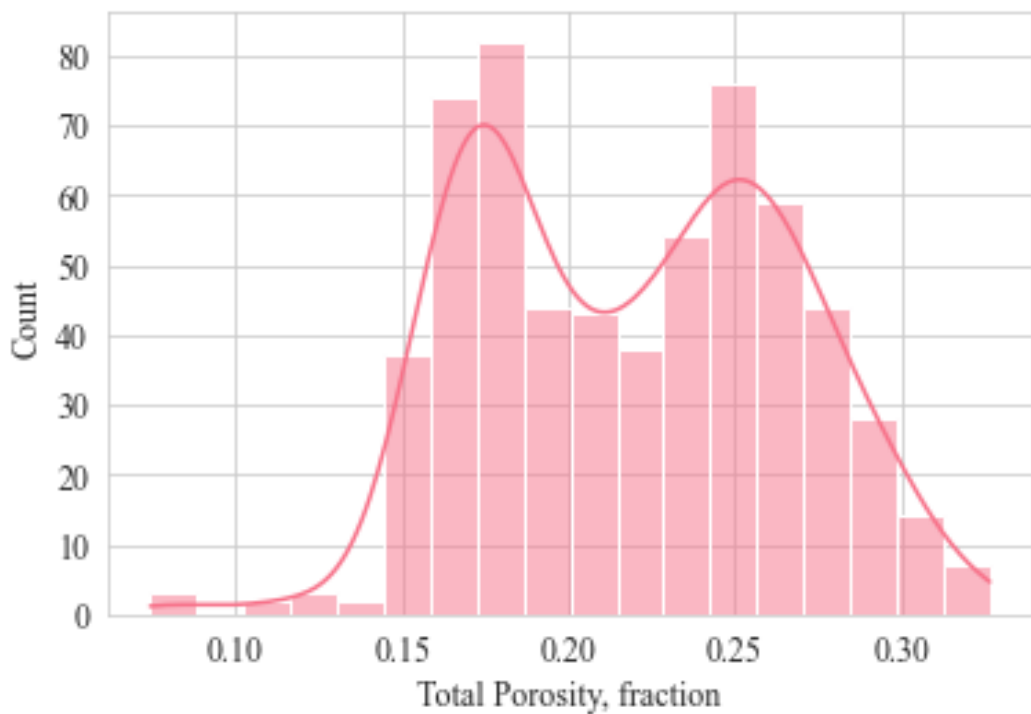


**Figure D.4:** Total porosity distribution obtained from all wells for Gollum-1 reservoir layer.

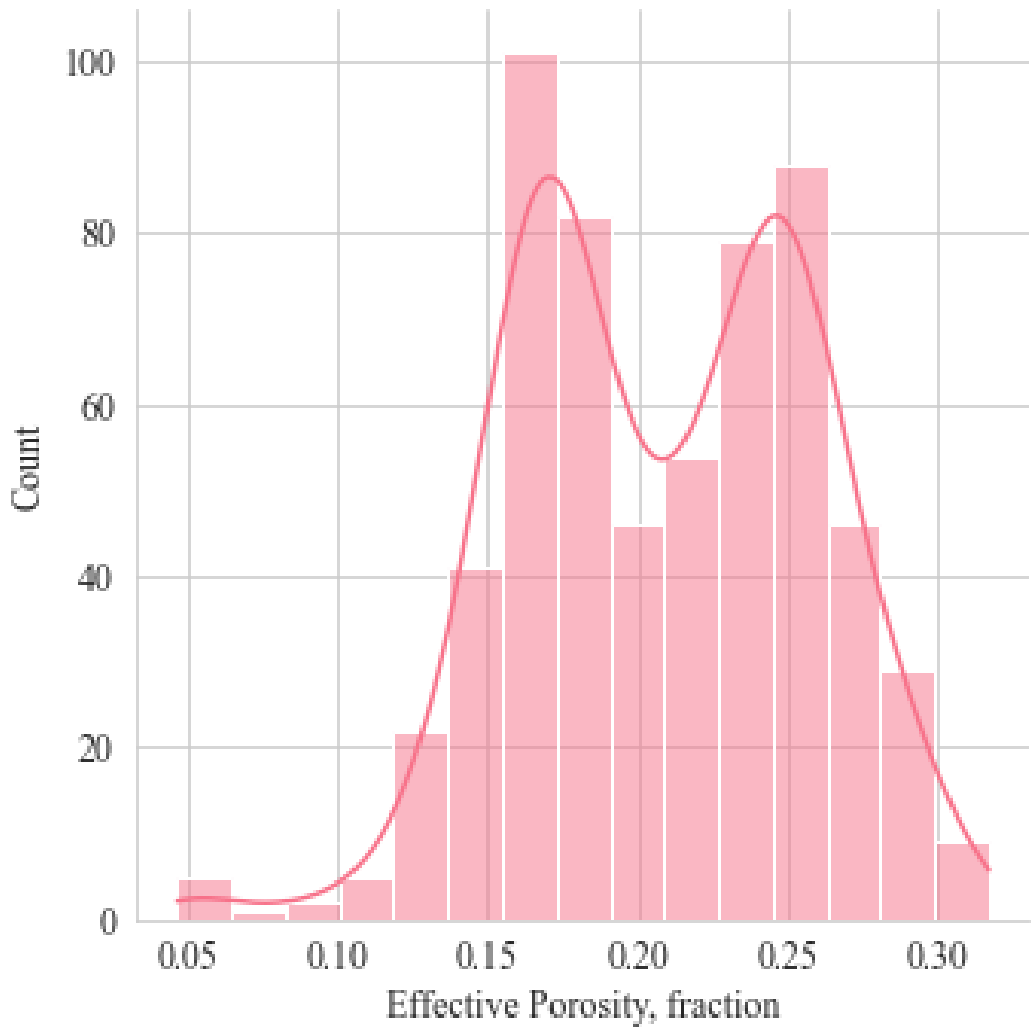


**Figure D.5:** Effective porosity distribution obtained from all wells for Gollum-1 reservoir layer.

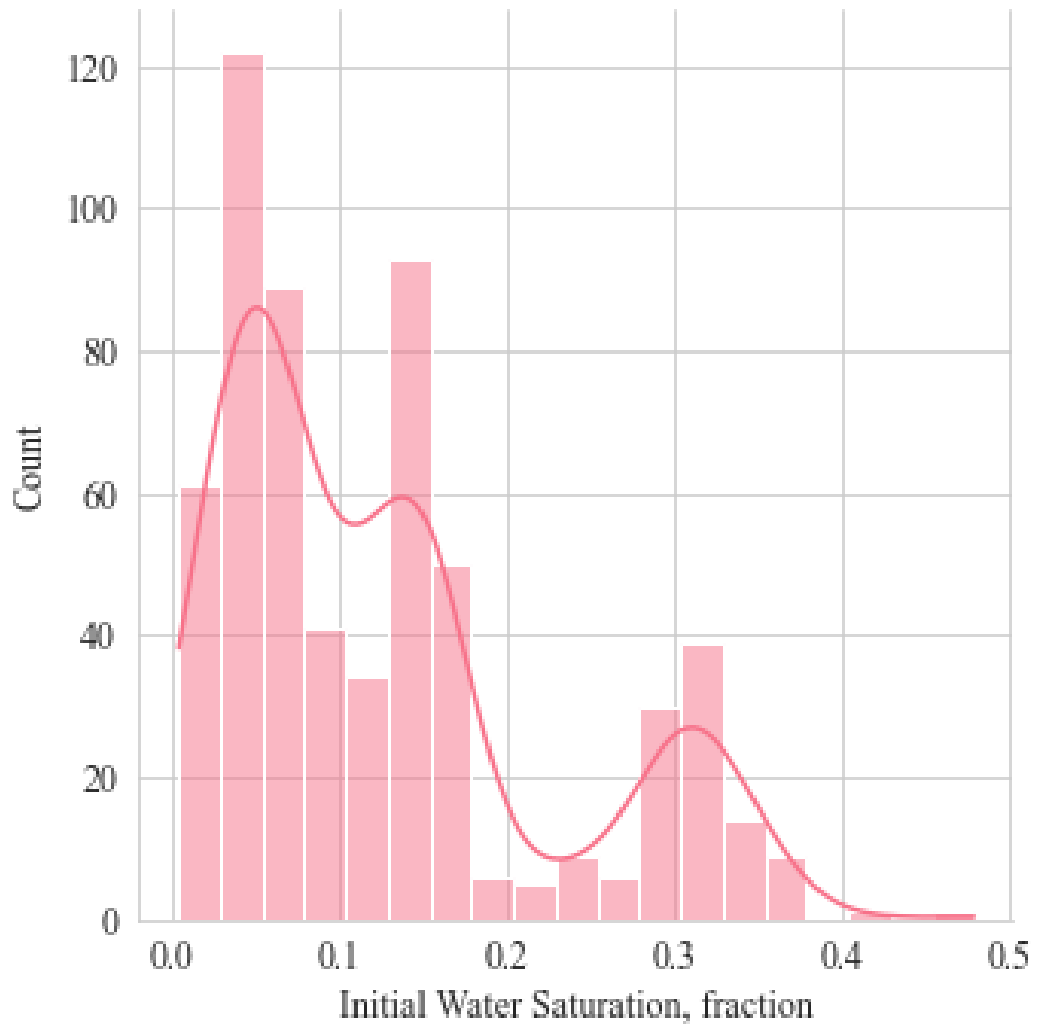


**Figure D.6:** Initial water saturation distribution obtained from all wells for Gollum-1 reservoir layer.

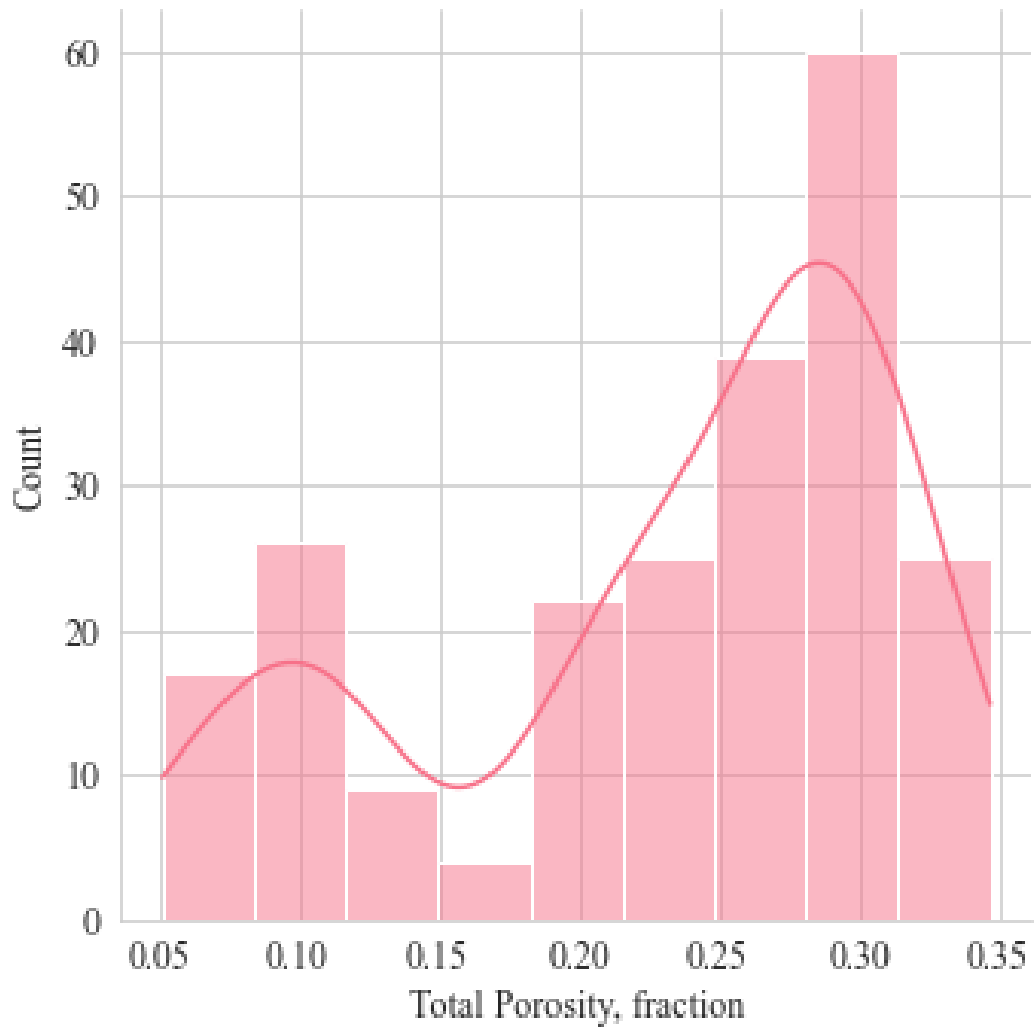


**Figure D.7:** Total porosity distribution obtained from all wells for Thorin-1 reservoir layer.

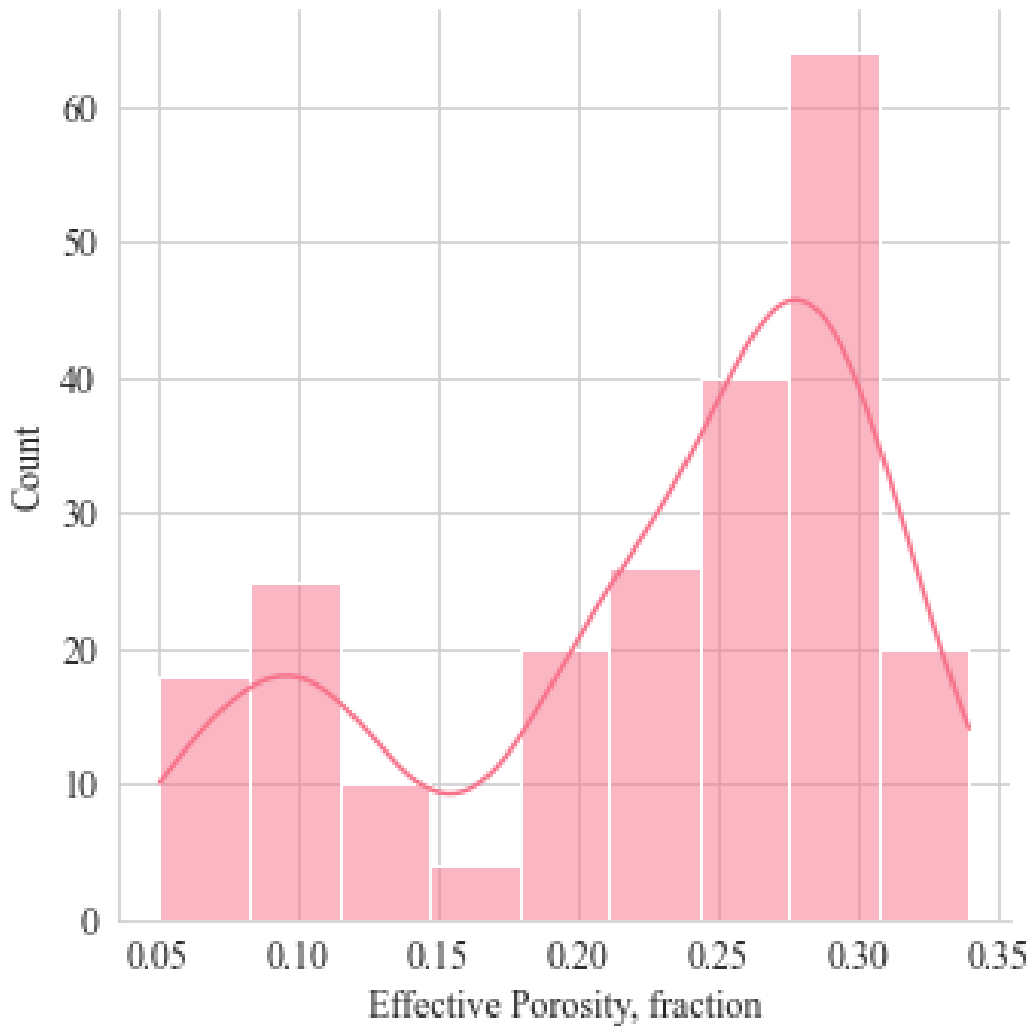


**Figure D.8:** Effective porosity distribution obtained from all wells for Thorin-1 reservoir layer.

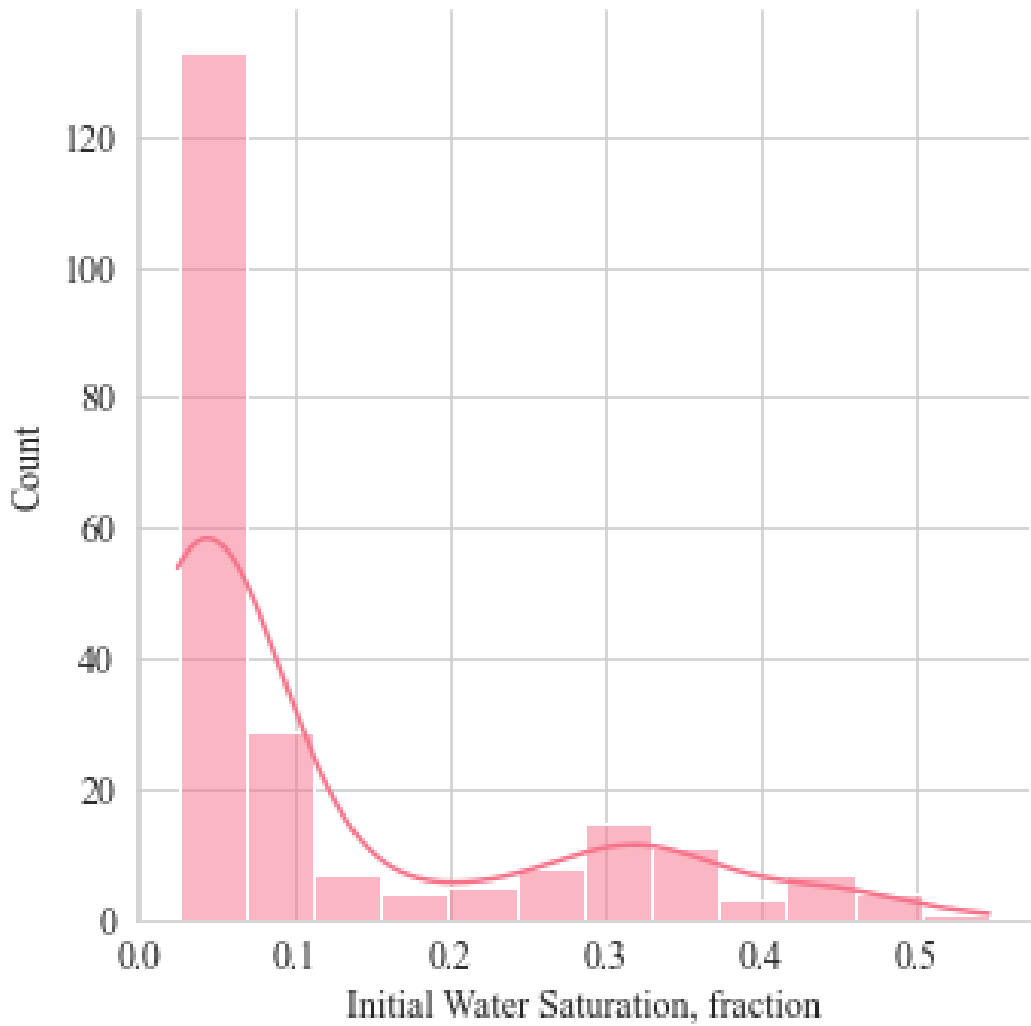


**Figure D.9:** Initial water saturation distribution obtained from all wells for Thorin-1 reservoir layer.

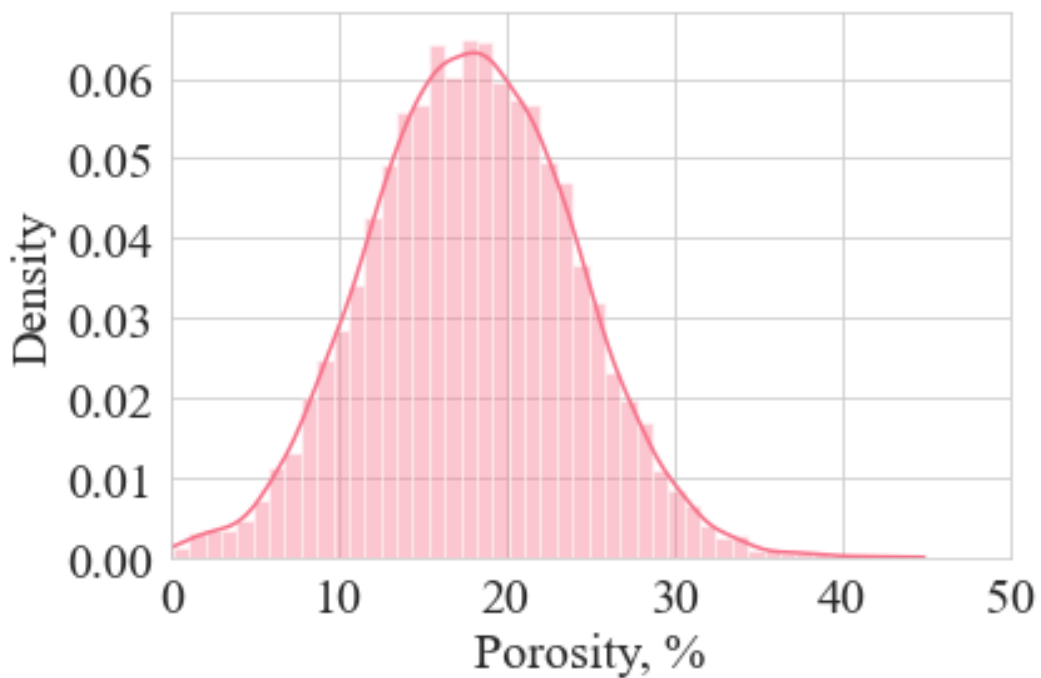


**Figure D.10:** Random 10000 samples of total porosity for Precious-1 reservoir layer.

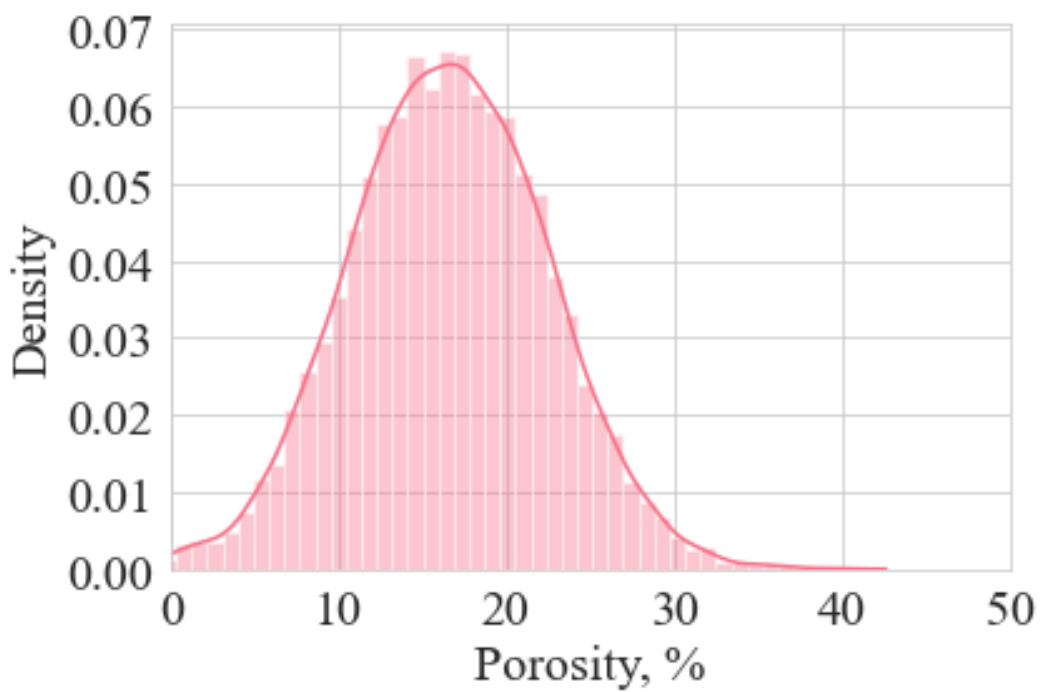


**Figure D.11:** Random 10000 samples of effective porosity for Precious-1 reservoir layer.

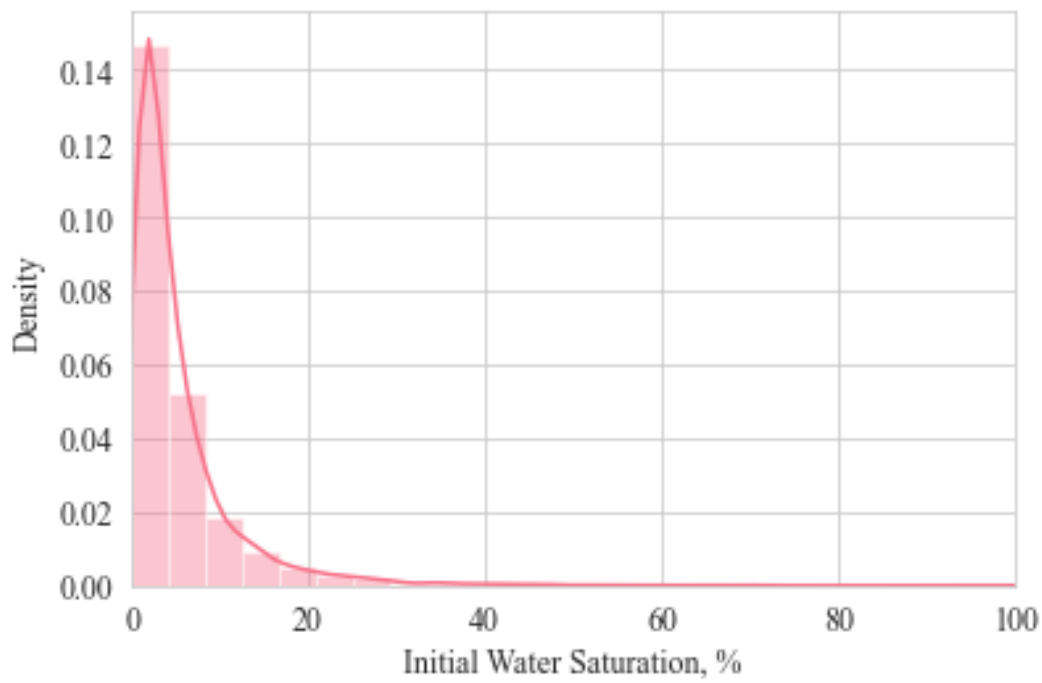


**Figure D.12:** Random 10000 samples of initial water saturation for Precious-1 reservoir layer.

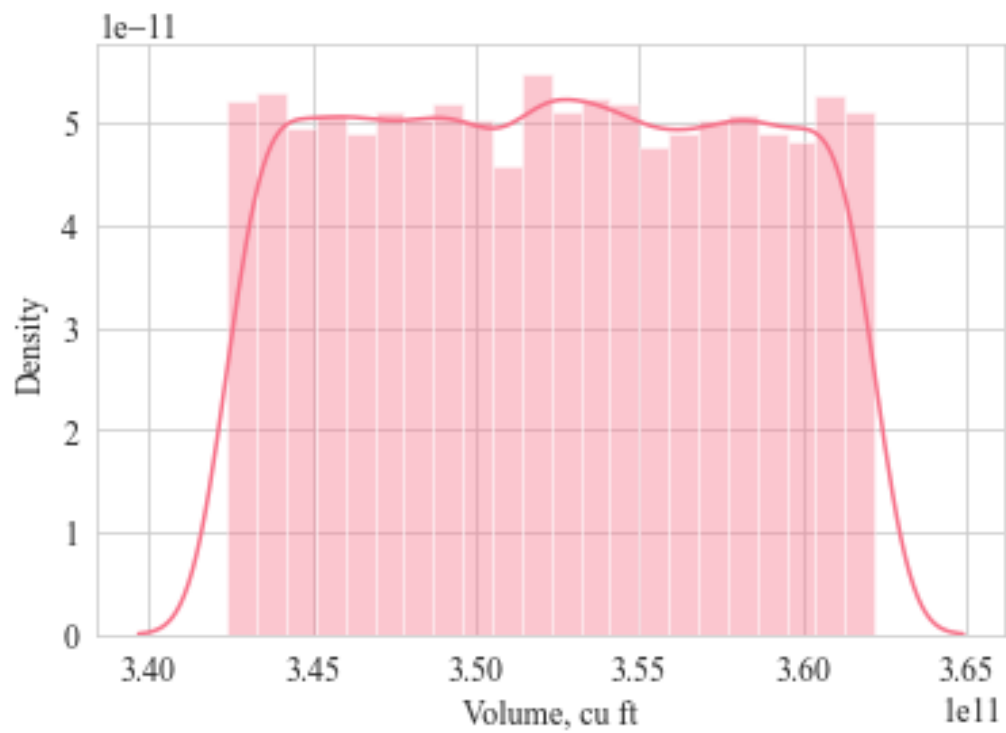


**Figure D.13:** Random 10000 samples of volume for Precious-1 reservoir layer.

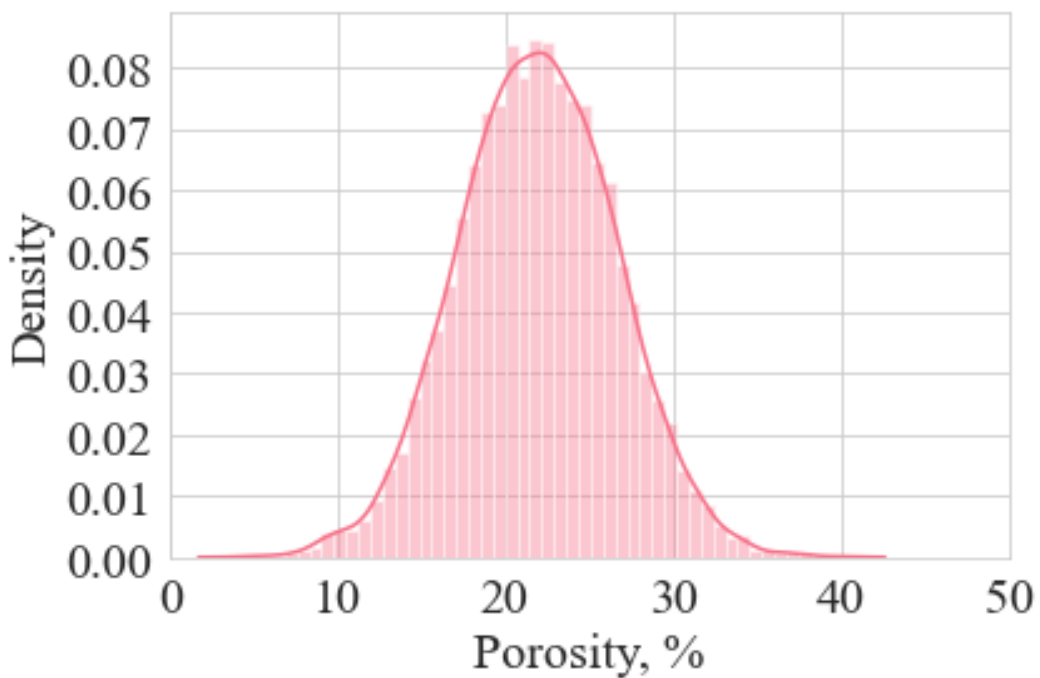


**Figure D.14:** Random 10000 samples of total porosity for Gollum-1 reservoir layer.

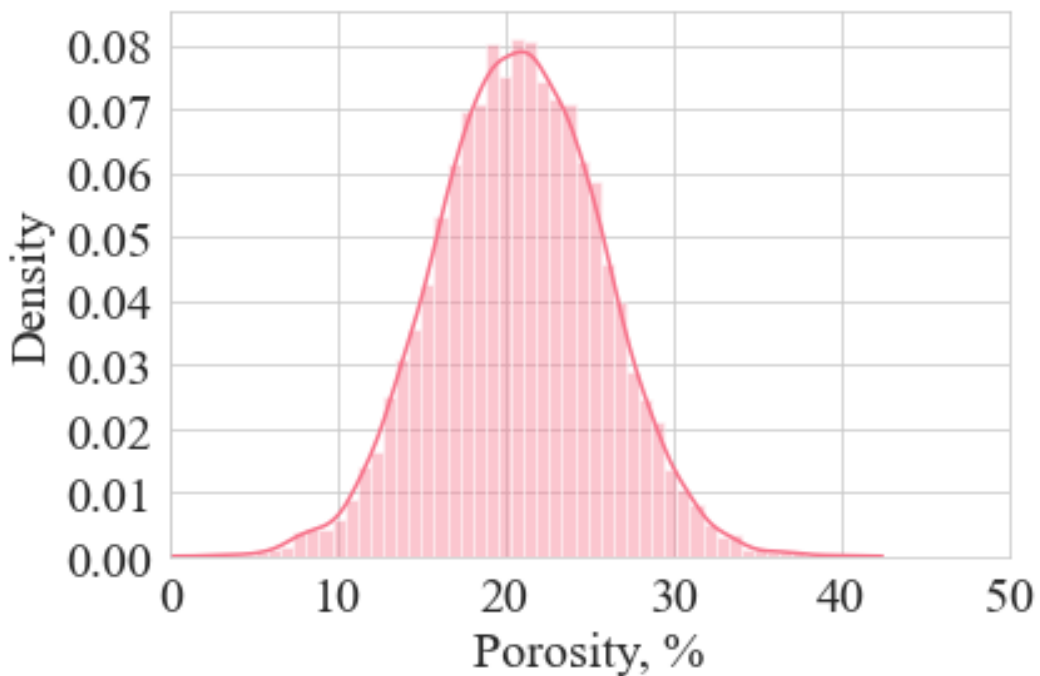


**Figure D.15:** Random 10000 samples of effective porosity for Gollum-1 reservoir layer.

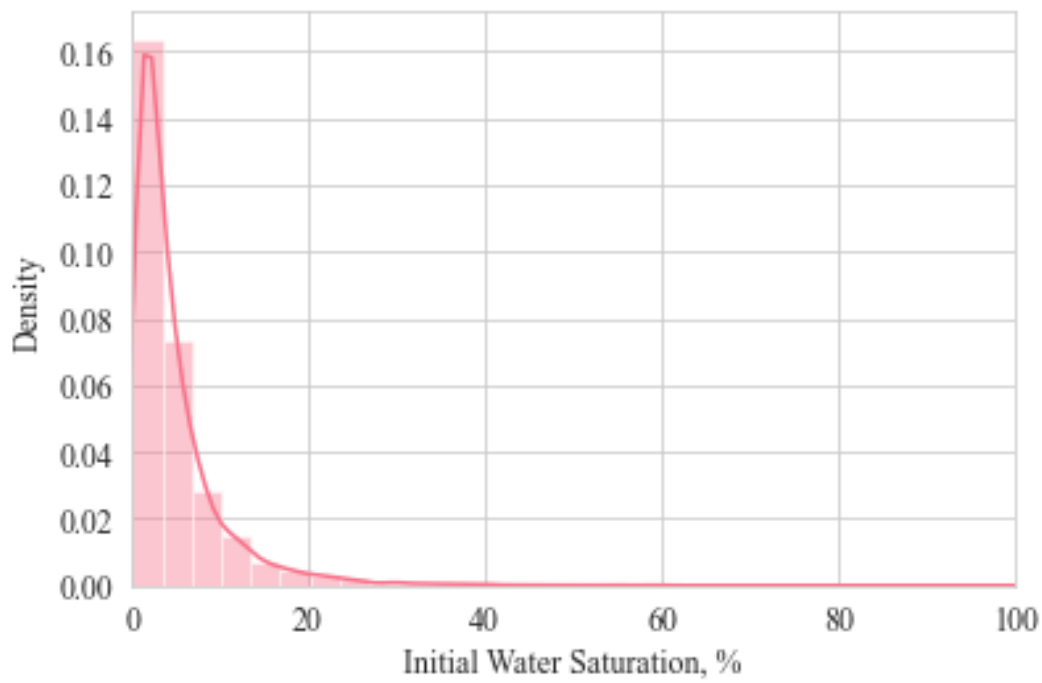


**Figure D.16:** Random 10000 samples of initial water saturation for Gollum-1 reservoir layer.

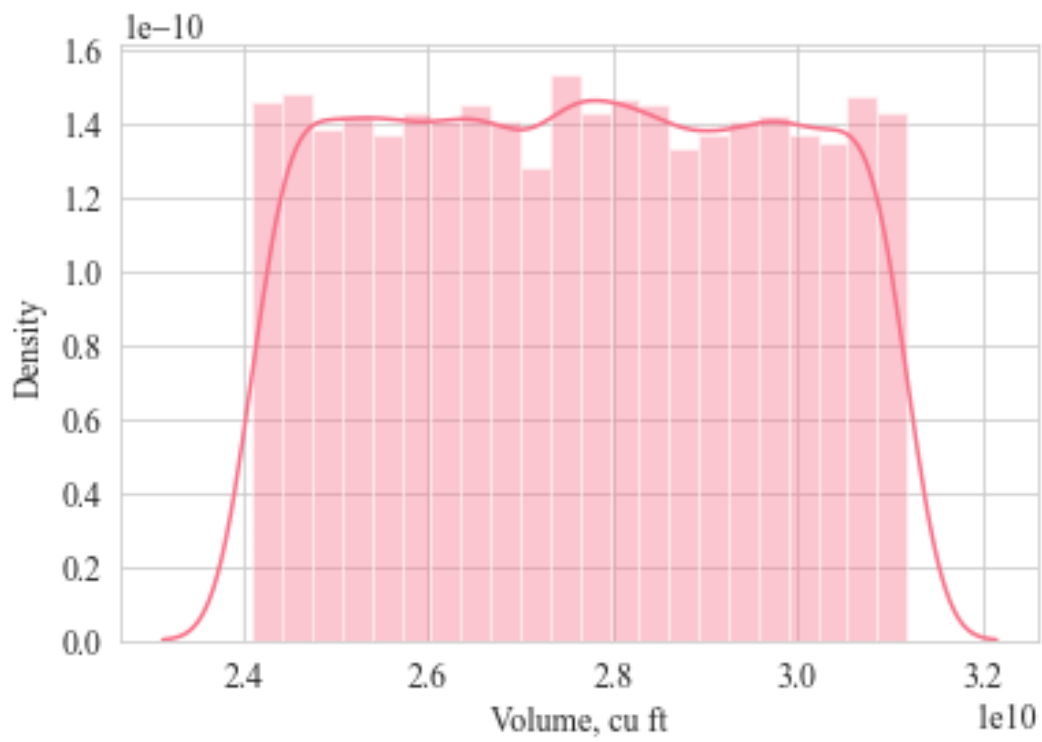


**Figure D.17:** Random 10000 samples of volume for Gollum-1 reservoir layer.

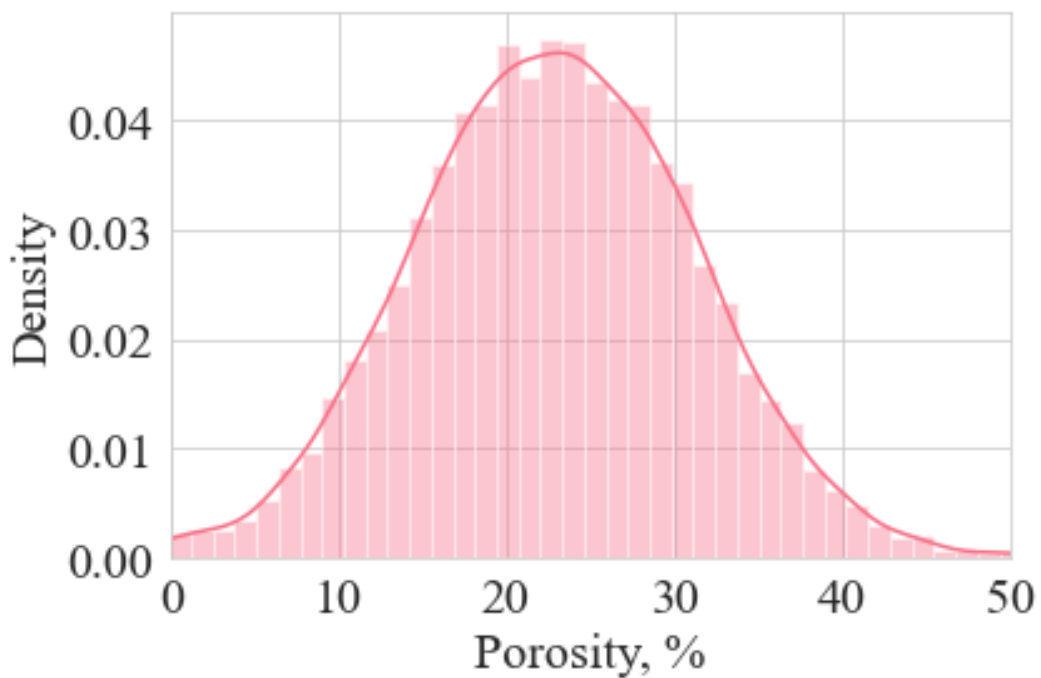


**Figure D.18:** Random 10000 samples of total porosity for Thorin-1 reservoir layer.

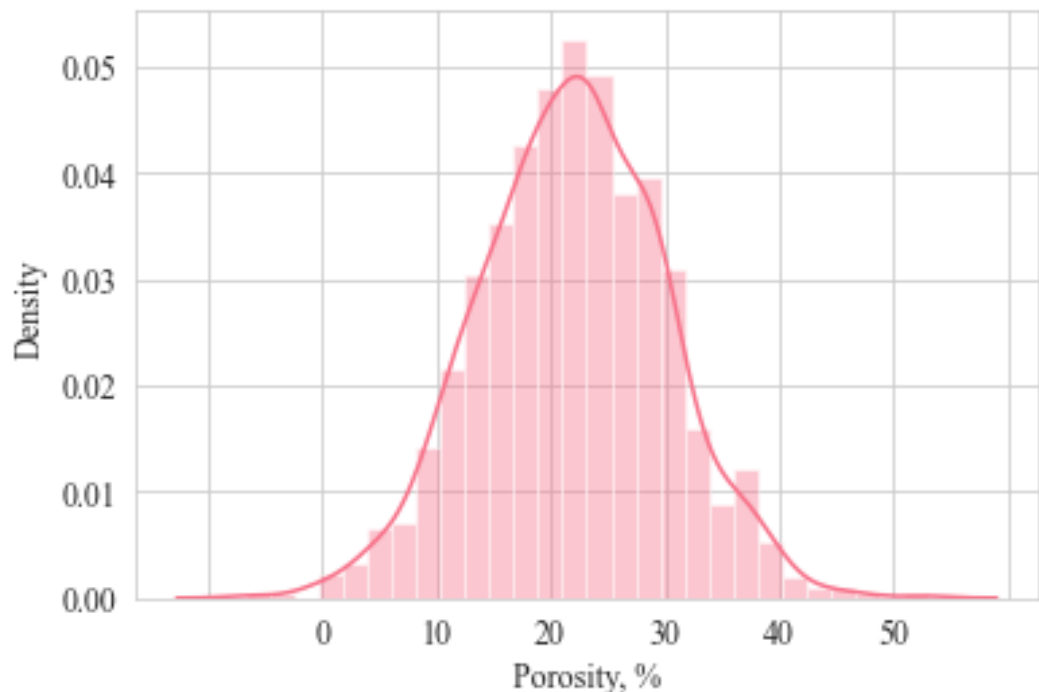


**Figure D.19:** Random 10000 samples of effective porosity for Thorin-1 reservoir layer.

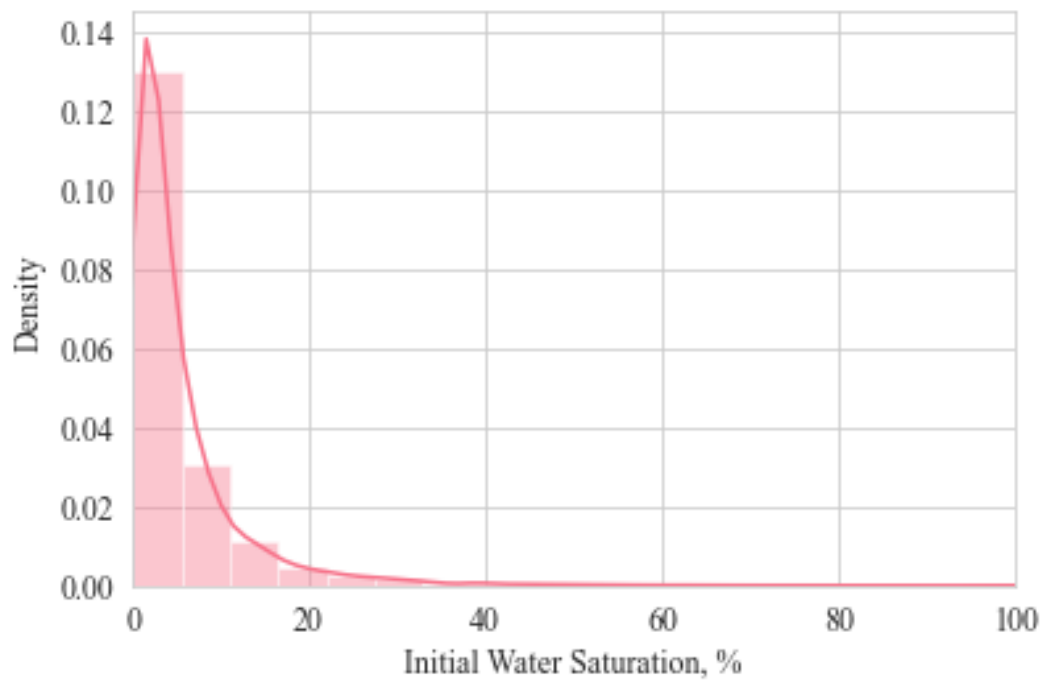


**Figure D.20:** Random 10000 samples of initial water saturation for Thorin-1 reservoir layer.

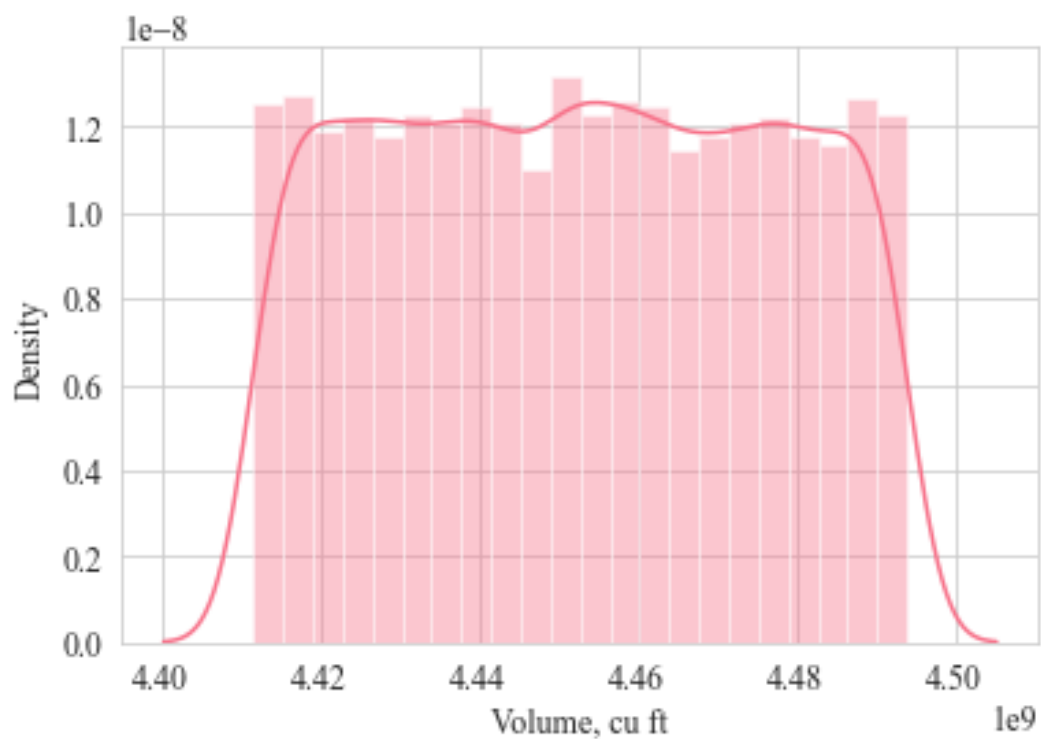


**Figure D.21:** Random 10000 samples of volume for Thorin-1 reservoir layer.

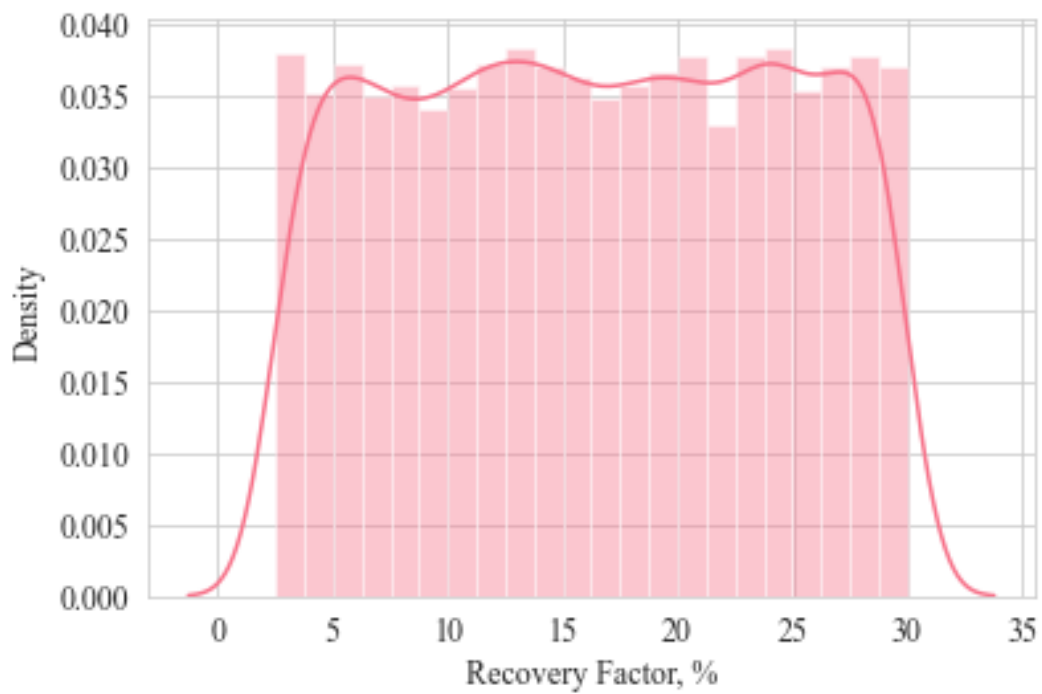


**Figure D.22:** Recovery factor uniform distribution based on the literature.

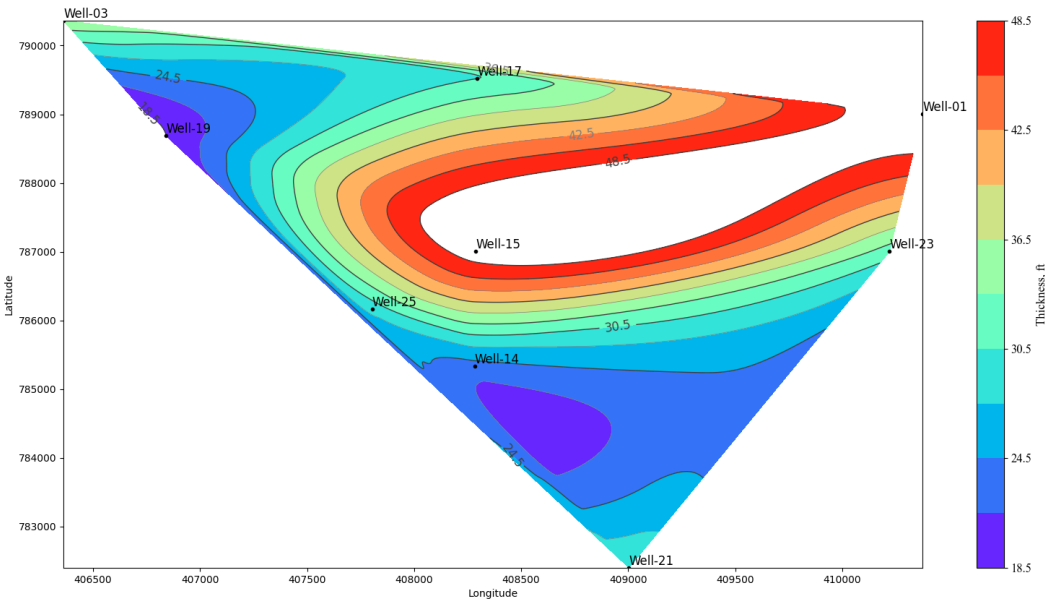


**Figure D.23:** Thickness isopach map of the Gollum-1 reservoir layer.

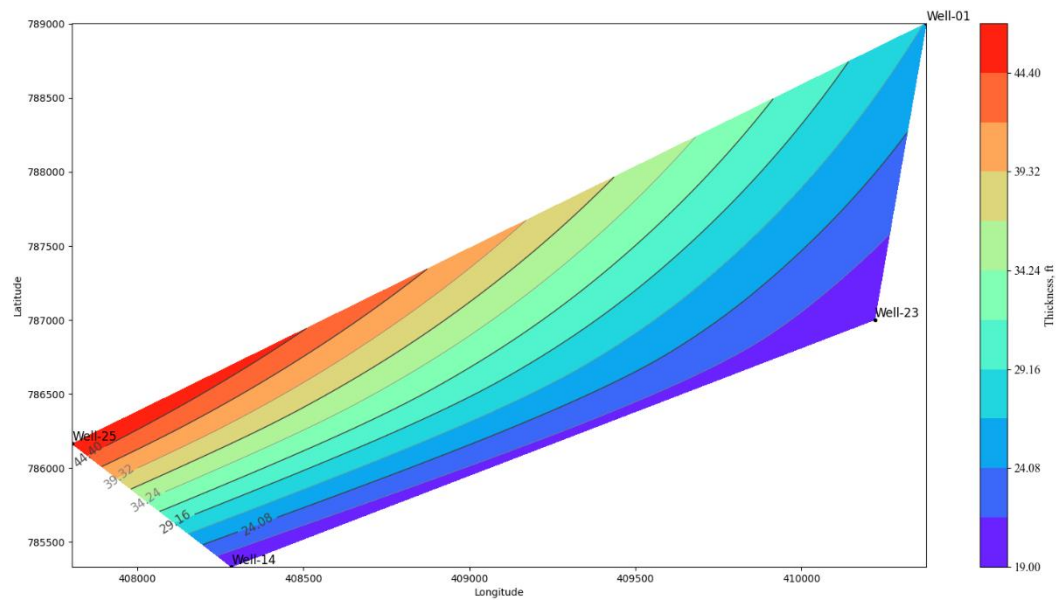


**Figure D.24:** Thickness isopach map of the Thorin-1 reservoir layer.

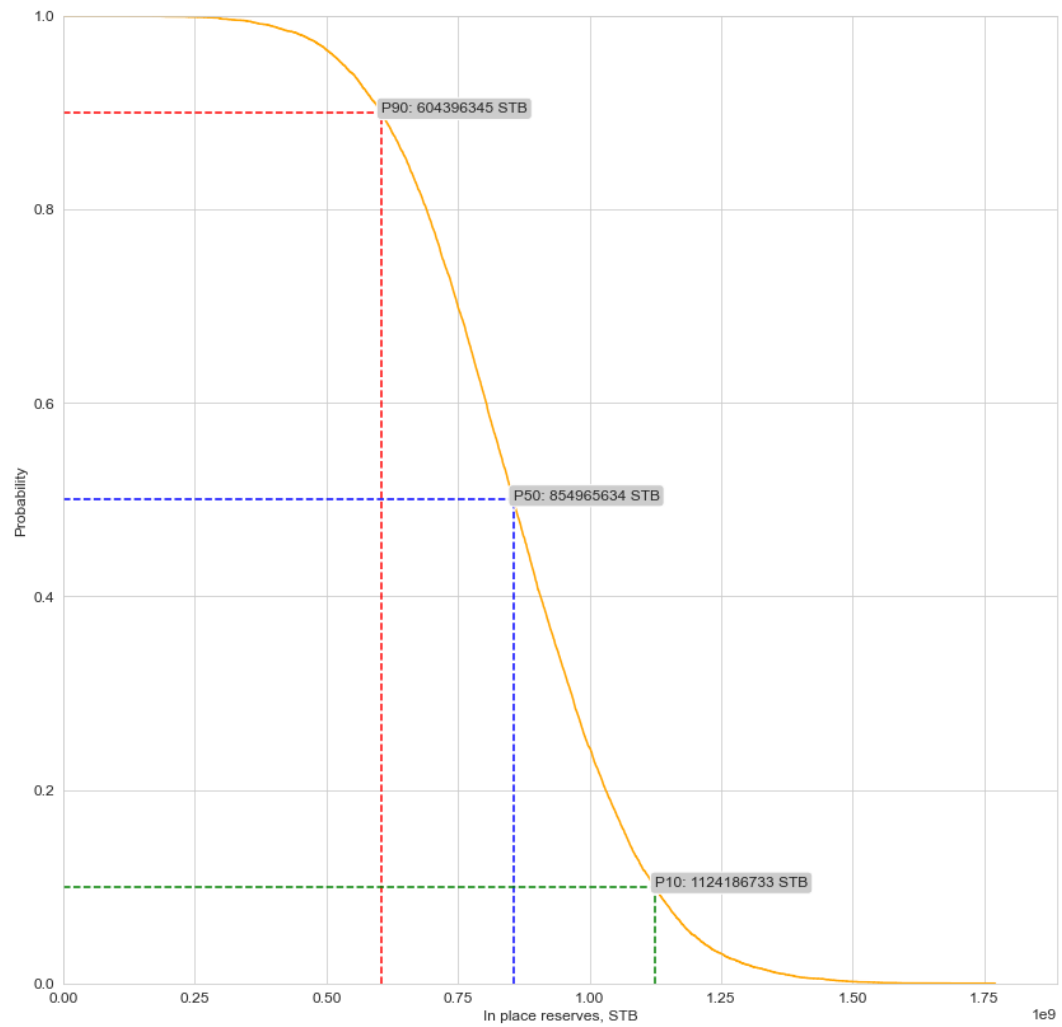


**Figure D.25:** OOIP estimation result for the Gollum-1 reservoir layer.

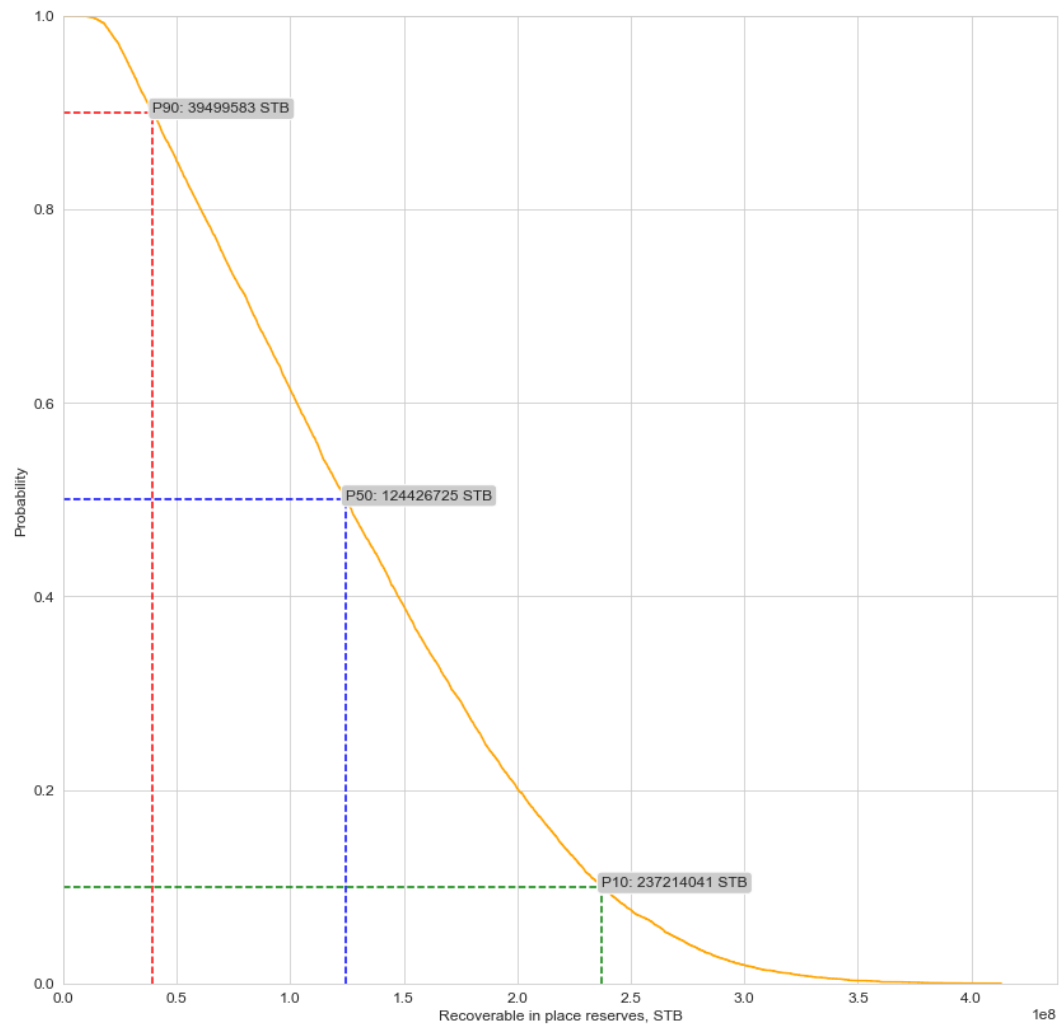


**Figure D.26:** ROIP estimation result for the Gollum-1 reservoir layer.

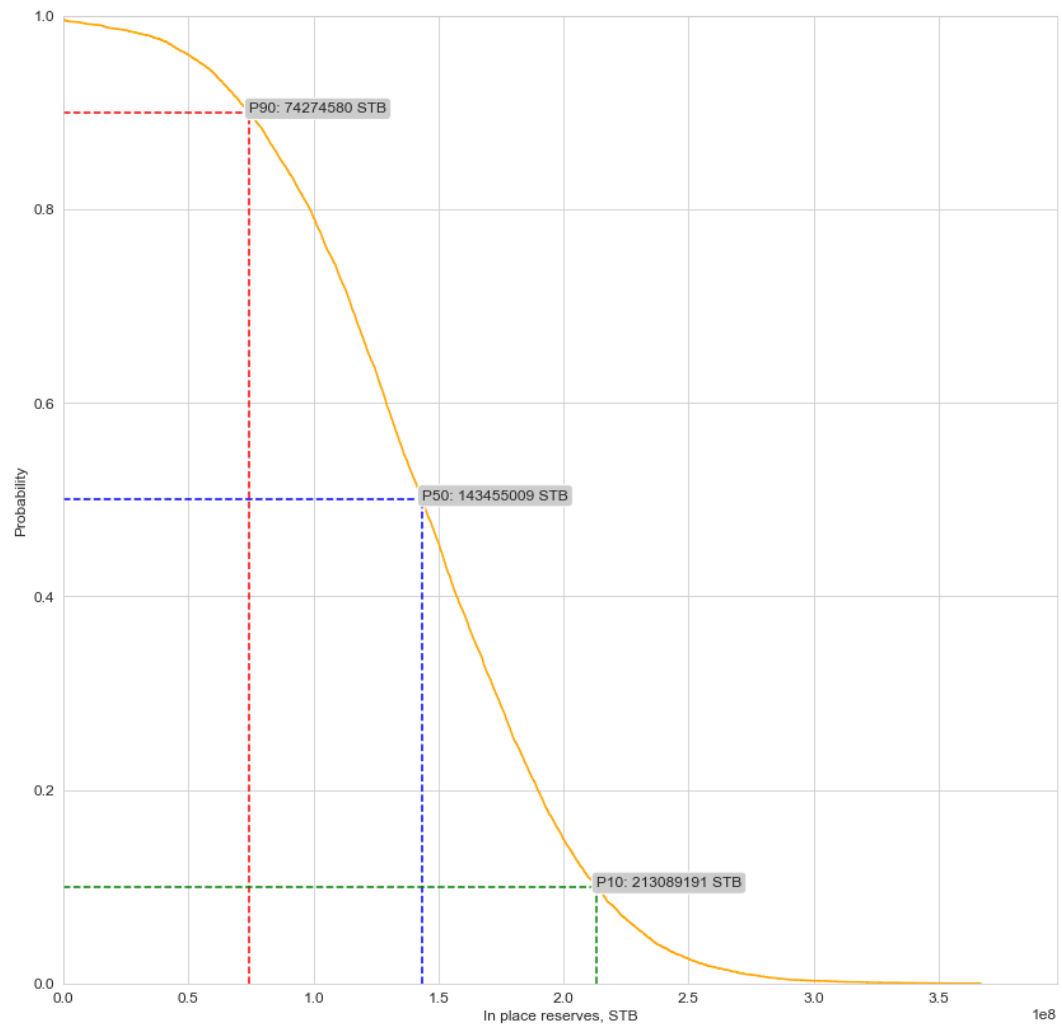


**Figure D.27:** OOIP estimation result for the Thorin-1 reservoir layer.

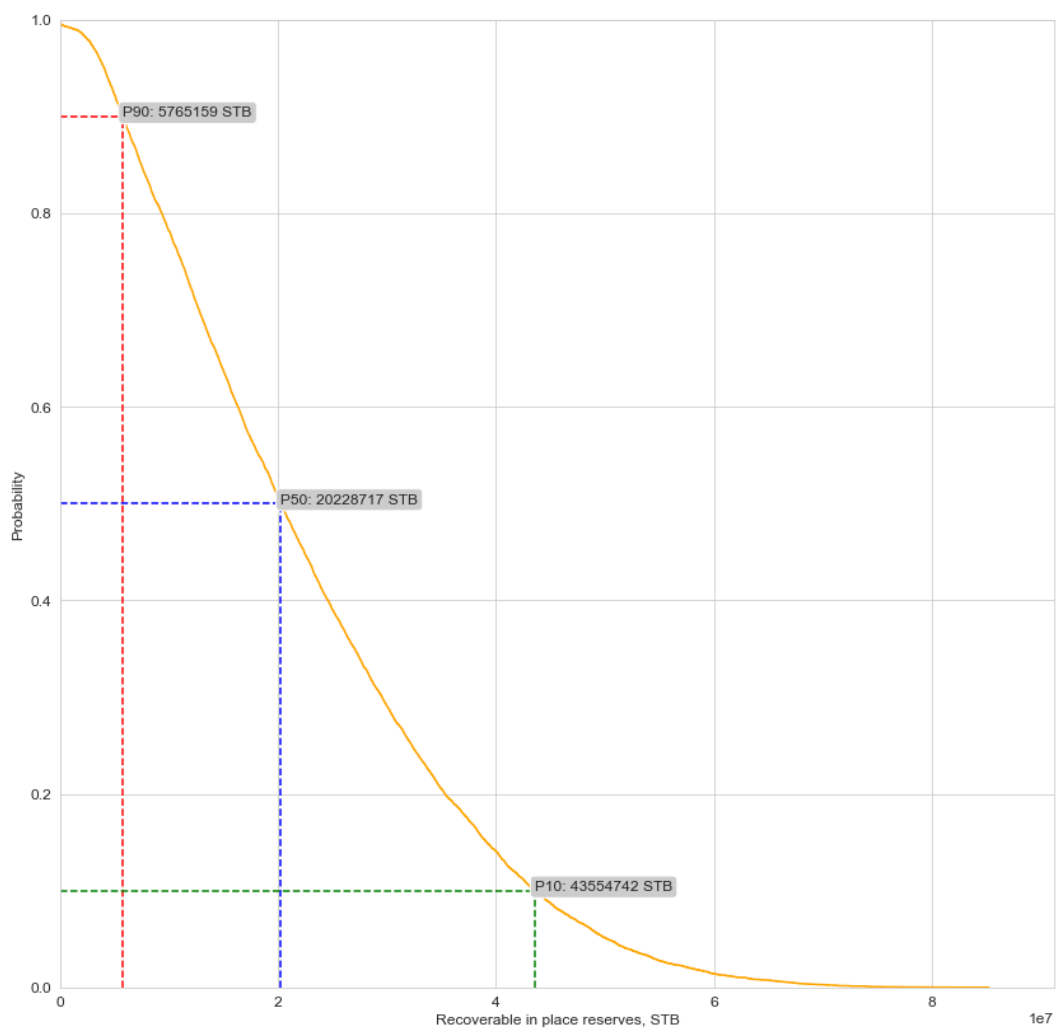


**Figure D.28:** ROIP estimation result for the Thorin-1 reservoir layer.

**E. APPENDIX : Mechanical Earth Model**

**Table E.1:** Mechanical earth model results.

<b>Depth, ft</b>	<b><math>\phi_{ext}</math></b>	<b><math>\rho_s</math></b>	<b><math>G_{dyn}, Mpsi</math></b>	<b><math>K_{dyn}, Mpsi</math></b>	<b><math>E_{dyn}, Mpsi</math></b>	<b><math>V_{dyn}</math></b>	<b>Friction Angle, °</b>
<b>0</b>	0.44	1.95	0.84	2.16	2.24	0.33	24.52
<b>250</b>	0.43	1.97	0.85	2.18	2.26	0.33	24.92
<b>500</b>	0.41	1.99	0.86	2.20	2.29	0.33	25.32
<b>750</b>	0.40	2.01	0.87	2.22	2.31	0.33	25.74
<b>1000</b>	0.39	2.03	0.88	2.25	2.33	0.33	26.26
<b>1250</b>	0.38	2.05	0.89	2.27	2.35	0.33	26.68
<b>1500</b>	0.37	2.07	0.89	2.29	2.37	0.33	33.28
<b>1750</b>	0.36	2.09	0.90	2.31	2.39	0.33	21.87
<b>2000</b>	0.34	2.10	0.91	2.33	2.41	0.33	27.88
<b>2250</b>	0.33	2.12	0.92	2.34	2.43	0.33	28.51
<b>2500</b>	0.32	2.14	0.92	2.36	2.45	0.33	28.61
<b>2750</b>	0.32	2.15	0.93	2.38	2.47	0.33	29.03
<b>3000</b>	0.31	2.17	0.94	2.40	2.49	0.33	28.77
<b>3250</b>	0.30	2.18	0.94	2.41	2.50	0.33	27.09
<b>3500</b>	0.29	2.20	0.95	2.43	2.52	0.33	23.28
<b>3750</b>	0.28	2.21	0.96	2.44	2.54	0.33	30.75
<b>4000</b>	0.27	2.22	0.96	2.46	2.55	0.33	30.53
<b>4250</b>	0.26	2.24	0.97	2.47	2.57	0.33	31.80
<b>4500</b>	0.26	2.25	0.97	2.49	2.58	0.33	31.04
<b>4750</b>	0.25	2.26	0.98	2.50	2.60	0.33	32.29
<b>5000</b>	0.24	2.28	0.98	2.52	2.61	0.33	32.96
<b>5250</b>	0.23	2.29	0.99	2.53	2.62	0.33	33.24
<b>5500</b>	0.23	2.30	0.99	2.54	2.64	0.33	33.83
<b>5750</b>	0.22	2.31	1.00	2.55	2.65	0.33	34.16
<b>6000</b>	0.21	2.32	1.00	2.57	2.66	0.33	34.53
<b>6250</b>	0.21	2.33	1.01	2.58	2.68	0.33	34.97
<b>6500</b>	0.20	2.34	1.01	2.59	2.69	0.33	35.35
<b>6750</b>	0.19	2.35	1.02	2.60	2.70	0.33	35.59
<b>7000</b>	0.19	2.36	1.03	2.66	2.73	0.33	35.88
<b>7101</b>	0.19	2.36	1.01	2.59	2.69	0.33	35.83
<b>7250</b>	0.18	2.37	1.03	2.63	2.73	0.33	36.23
<b>7500</b>	0.18	2.38	0.99	2.52	2.62	0.33	34.65
<b>7600</b>	0.18	2.38	1.03	2.63	2.73	0.33	33.46

**Table E.2:** Pressure gradient results from Eaton's and modified Matthew and Kelly's methods.

Depth , ft	$\sigma_{ob}$ , psi/ft	$\sigma_{ho}$ , psi/ft	$P_{pg}$ , psi/ft	P <sub>fg</sub> , psi/ft	
				Eaton	Modified Matthew and Kelly
<b>0</b>	0.00	0.000	0.000	0.00	0.00
<b>250</b>	0.85	0.446	0.446	0.64	0.81
<b>500</b>	0.85	0.446	0.446	0.64	0.81
<b>750</b>	0.86	0.446	0.446	0.65	0.81
<b>1000</b>	0.86	0.446	0.446	0.65	0.81
<b>1250</b>	0.87	0.446	0.446	0.65	0.81
<b>1500</b>	0.87	0.446	0.446	0.65	0.82
<b>1750</b>	0.88	0.446	0.446	0.65	0.82
<b>2000</b>	0.88	0.446	0.446	0.66	0.82
<b>2250</b>	0.88	0.446	0.446	0.66	0.82
<b>2500</b>	0.89	0.446	0.446	0.66	0.82
<b>2750</b>	0.89	0.446	0.446	0.66	0.83
<b>3000</b>	0.89	0.446	0.446	0.66	0.83
<b>3250</b>	0.90	0.446	0.451	0.67	0.83
<b>3500</b>	0.90	0.446	0.456	0.67	0.83
<b>3750</b>	0.91	0.446	0.461	0.68	0.83
<b>4000</b>	0.91	0.446	0.466	0.68	0.84
<b>4250</b>	0.91	0.446	0.471	0.69	0.84
<b>4500</b>	0.92	0.446	0.476	0.69	0.84
<b>4750</b>	0.92	0.446	0.481	0.69	0.84
<b>5000</b>	0.92	0.446	0.486	0.70	0.85
<b>5250</b>	0.93	0.446	0.491	0.70	0.85
<b>5500</b>	0.93	0.446	0.496	0.71	0.85
<b>5750</b>	0.93	0.446	0.501	0.71	0.85
<b>6000</b>	0.93	0.446	0.506	0.71	0.86
<b>6250</b>	0.94	0.446	0.511	0.72	0.86
<b>6500</b>	0.94	0.446	0.516	0.72	0.86
<b>6750</b>	0.94	0.446	0.521	0.73	0.86
<b>7000</b>	0.95	0.446	0.526	0.73	0.86
<b>7101</b>	0.95	0.446	0.531	0.73	0.87
<b>7250</b>	0.95	0.446	0.531	0.73	0.87
<b>7500</b>	0.95	0.446	0.531	0.74	0.87
<b>7600</b>	0.95	0.446	0.531	0.74	0.87

**F. APPENDIX: Drill String Design**

**Table F.1:** Tensile and buckling capacities for a new drill pipe (Özbayoğlu & Altun, 2010).

(1)	(2)	(3)	(4)	(5)	(6)	(7)	(8)	(9)	(10)
Size OD in.	Nominal Weight Threads and Couplings lb/ft		Torsional Data Torsional Yield Strength, ft-lb				Tensile Data Based on Minimum Values Load at the Minimum Yield Strength, lb		
	E75	X95	G105	S135	E75	X95	G105	S135	
	$2\frac{1}{8}$	4.85	4763.	6033.	6668.	8574.	97817.	123902.	136944.
$2\frac{1}{8}$	6.65	6250.	7917.	8751.	11251.	138214.	175072.	193500.	248786.
$2\frac{1}{4}$	6.85	8083.	10238.	11316.	14549.	135902.	172143.	190263.	244624.
	10.40	11554.	14635.	16176.	20798.	214344.	271503.	300082.	385820.
$3\frac{1}{2}$	9.50	14146.	17918.	19805.	25463.	194264.	246068.	271970.	349676.
	13.30	18551.	23498.	25972.	33392.	271569.	343988.	380197.	488825.
	15.50	21086.	26708.	29520.	37954.	322775.	408848.	451885.	580995.
4	11.85	19474.	24668.	27264.	35054.	230755.	292290.	323057.	415360.
	14.00	23288.	29498.	32603.	41918.	285359.	361454.	399502.	513646.
	15.70	25810.	32692.	36134.	46458.	324118.	410550.	453765.	583413.
$4\frac{1}{2}$	13.75	25907.	32816.	36270.	46633.	270034.	342043.	378047.	486061.
	16.60	30807.	39022.	43130.	55453.	330558.	418707.	462781.	595004.
	20.00	36901.	46741.	51661.	66421.	412358.	522320.	577301.	742244.
	22.82	40912.	51821.	57276.	73641.	471239.	596903.	659734.	848230.
5	16.25	35044.	44389.	49062.	63079.	328073.	415559.	459302.	590531.
	19.50	41167.	52144.	57633.	74100.	395595.	501087.	553833.	712070.
	25.60	52257.	66192.	73159.	94062.	530144.	671515.	742201.	954259.
$5\frac{1}{2}$	19.20	44074.	55826.	61703.	79332.	372181.	471429.	521053.	669925.
	21.90	50710.	64233.	70994.	91278.	437116.	553681.	611963.	786809.
	24.70	56574.	71660.	79204.	101833.	497222.	629814.	696111.	894999.
$6\frac{1}{8}$	25.20	70580.	89402.	98812.	127044.	489464.	619988.	685250.	881035.
	27.70	76295.	96640.	106813.	137330.	534199.	676651.	747877.	961556.

<sup>1</sup>Based on the shear strength equal to 57.7 percent of minimum yield strength and nominal wall thickness.

Minimum torsional yield strength calculated from Equation A.15.

<sup>2</sup>Minimum tensile strength calculated from Equation A.13.

**Table F.2:** Collapse and burst pressure capacities for a new drill pipe (Özbayoğlu & Altun, 2010).

(1)	(2)	(3)	(4)	(5)	(6)	(7)	(8)	(9)	(10)
Size OD in.	Nominal Weight Threads and Couplings lb/ft	Collapse Pressure Based on Minimum Values, psi				Internal Pressure at Minimum Yield Strength, psi			
		E75	X95	G105	S135	E75	X95	G105	S135
$2\frac{3}{8}$	4.85	11040.	13984.	15456.	19035.	10500.	13300.	14700.	18900.
	6.65	15599.	19759.	21839.	28079.	15474.	19600.	21663.	27853.
$2\frac{7}{8}$	6.85	10467.	12940.	14020.	17034.	9907.	12548.	13869.	17832.
	10.40	16509.	20911.	23112.	29716.	16526.	20933.	23137.	29747.
$3\frac{1}{2}$	9.50	10001.	12077.	13055.	15748.	9525.	12065.	13335.	17145.
	13.30	14113.	17877.	19758.	25404.	13800.	17480.	19320.	24840.
	15.50	16774.	21247.	23484.	30194.	16838.	21328.	23573.	30308.
4	11.85	8381.	9978.	10708.	12618.	8597.	10889.	12036.	15474.
	14.00	11354.	14382.	15896.	20141.	10828.	13716.	15159.	19491.
	15.70	12896.	16335.	18055.	23213.	12469.	15794.	17456.	22444.
$4\frac{1}{2}$	13.75	7173.	8412.	8956.	10283.	7904.	10012.	11066.	14228.
	16.60	10392.	12765.	13825.	16773.	9829.	12450.	13761.	17693.
	20.00	12964.	16421.	18149.	23335.	12542.	15886.	17558.	22575.
	22.82	14815.	18765.	20741.	26667.	14583.	18472.	20417.	26250.
5	16.25	6938.	8108.	8616.	9831.	7770.	9842.	10878.	13986.
	19.50	9962.	12026.	12999.	15672.	9503.	12037.	13304.	17105.
	25.60	13500.	17100.	18900.	24300.	13125.	16625.	18375.	23625.
$5\frac{1}{2}$	19.20	6039.	6942.	7313.	8093.	7255.	9189.	10156.	13058.
	21.90	8413.	10019.	10753.	12679.	8615.	10912.	12061.	15507.
	24.70	10464.	12933.	14013.	17023.	9903.	12544.	13865.	17826.
$6\frac{3}{8}$	25.20	4788.	5321.	5500.	6036.	6538.	8281.	9153.	11768.
	27.70	5894.	6755.	7103.	7813.	7172.	9084.	10040.	12909.

Note: Calculations are based on formulas in API Bulletin 5C3.

**Table F.3:** Related BHA design parameters and their results for both section.

<b>BHA Design</b>			
<b>Parameters</b>	<b>Surface</b>	<b>Production</b>	<b>Unit</b>
<b>D<sub>b</sub></b>	12.25	8.5	in
<b>WOB</b>	49000	51000	lb
<b>ρ<sub>m</sub></b>	9.5	11	ppg
<b>OD<sub>dc</sub></b>	9	6.5	in
<b>ID<sub>dc</sub></b>	3	2	in
<b>W<sub>dc</sub></b>	192.40	102.21	lbf/ft
<b>L<sub>dc</sub></b>	342.7	689.6	ft
<b>Net L<sub>dc</sub></b>	360	690	ft
<b>Total DC</b>	12	23	-
<b>BSR<sub>dc-dp</sub></b>	7.22	5.22	-
<b>BSR<sub>dc-hwdp</sub></b>	2.86	2.50	-
<b>BSR<sub>hwdp-dp</sub></b>	2.53	2.09	-
<b>L<sub>hwdp</sub></b>	90	90	ft
<b>W<sub>BHA</sub></b>	64603.8	62426.2	lbf
<b>L<sub>BHA</sub></b>	450	780	ft
<b>BF</b>	0.855	0.832	-

**Table F.4:** Related parameters for design the drill string and calculations made for both section.

	Parameters	Surface	Production	Units
<b>Drill String Design Where Only Axial Stress Is Taken Into Account</b>	L <sub>dp</sub>	13907	13586	ft
	Net L <sub>dp</sub>	2550	6820	ft
	P <sub>a</sub>	124122	187779	lbf
	σ <sub>s</sub> /σ <sub>a</sub>	1.59	1.37	
	P <sub>s</sub>	196799	257395	lbf
<b>Drill String Design That Takes Pressure-Related Stress Into Account</b>	P <sub>h</sub>	1259	3901	psi
	L <sub>dp</sub>	13555	12420	ft
	P <sub>a</sub>	124122	187779	lbf
	σ <sub>s</sub> /σ <sub>a</sub>	1.59	1.37	
	P <sub>s</sub>	196799	257395	lbf
	σ <sub>a</sub>	9904	11359	psi
	Y <sub>pa</sub>	69555	68672	psi
	OD <sub>p/t</sub>	20.08	10.47	
	F <sub>1</sub>	3.05	3.05	
	F <sub>2</sub>	0.06	0.06	
<b>Drill String Design That Takes Buckling Into Account</b>	F <sub>3</sub>	1642	1616	
	F <sub>4</sub>	1.96	1.96	
	F <sub>5</sub>	0.04	0.04	
	RPM	150	75	
	J	64.80	23.01	in <sup>4</sup>
	T <sub>q</sub>	4200	3850	lbf-ft
	τ <sub>b</sub>	2576	4517	psi
	P <sub>h</sub>	1259	3901	psi
	L <sub>dp</sub>	13518	12297	ft
	P <sub>a</sub>	124122	187779	lbf
<b>Make-up Torque</b>	σ <sub>s</sub> /σ <sub>a</sub>	1.59	1.37	
	P <sub>s</sub>	196799	257395	lb
	A <sub>pin</sub>	4.74	8.38	in <sup>2</sup>
	A <sub>box</sub>	21.98	12.82	in <sup>2</sup>
	T <sub>q</sub>	16208	24951	lb-ft

**Continue Table F.4:** Related parameters for design the drill string and calculations made for both section.

<b>String Design That Takes Bending Into Account Applying Dog-leg Scenarios</b>	<b>I</b>	<b>32.40</b>	<b>11.51</b>	<b>in<sup>4</sup></b>
P	83276	123448	lb	
K	0.00926	0.0189	in <sup>-1</sup>	
KL <sub>h</sub>	1.666	3.404		
A <sub>w</sub>	6.523	5.495	in <sup>2</sup>	
σ <sub>t</sub>	12766	22464	psi	
σ <sub>b-max</sub>	17020	15984	psi	
DLS <sub>max</sub>	6.58	4.77	degree/100ft	
E	30x10 <sup>6</sup>	30x10 <sup>6</sup>		
c	0.000096	0.000069		
r	1.5	1.5		
c <sub>p</sub>	0.00017	0.00024		
σ <sub>b</sub>	15332	12936		
L <sub>dp</sub>	9233	8430	ft	
<b>Neutral Point</b>	L <sub>np</sub>	298.5	600.92	ft
	L <sub>np</sub>	-170.73	-184.65	ft
<b>Shock Loading</b>	Y <sub>m</sub>	75000	75000	
	A <sub>w</sub>	6.523	5.495	
	F <sub>H</sub>	123354	194960	
	MOP	316939	175973	
<b>Amount of Elongation</b>	e	4.85	29.8	in
	L <sub>h</sub>	180	180	in
<b>Stabilizer Design</b>	I	0.015	0.004	in <sup>4</sup>
	F <sub>cr</sub>	23564	9847	psi
	E	4320x10 <sup>6</sup>	4320x10 <sup>6</sup>	psi
	WOB	49000	51000	lb
	L <sub>1</sub>	130.7	60.7	ft
	WOB-(L <sub>1</sub> W <sub>dc</sub> )	23861	44797	lb

**Table F.5:** Drill pipe and related connection type physical properties

Size in.	Nominal Weight lb/ft	Grade and Upset Type	Torsional Yield Strength ft-lb	Tensile Yield Strength lb	Wall Thickness in.	Nominal ID in.	Pipe Body Section Area sq.in.	Pipe Body Section Modulus cu.in.	Pipe Body			Connection Type	Outside Diameter in.	Inside Diameter in.	Torsional Yield Strength ft-lb	Tensile Yield Strength lb	Make-up Torque ft-lb	Torsional Ratio Tool Joint to Pipe	* Pin Tong Space in.	* Box Tong Space in.	Minimum Tool Joint OD for Prem. Class in.	Drift Diameter in.	
									Polar Section Modulus cu.in.	Internal Pressure psi	Collapse Pressure psi												
4 1/2	20.00	E-75 IEU	36,900	412,400	0.430	3.640	5.498	5.116	10,232	12,542	12,964	NC46	6 1/4	3	39,700	1,048,400	20,500	1.08	9	12	22.69	5 1/2	2 7/8
	20.00	E-75 IEU	36,900	412,400	0.430	3.640	5.498	5.116	10,232	12,542	12,964	OH6	3 1/2	34,100	884,800	19,200	0.92	9	12	21.64	5 17/32	3 3/8	0.538
	20.00	E-75 IEU	36,900	412,400	0.430	3.640	5.498	5.116	10,232	12,542	12,964	H80	6	3 1/4	39,000	938,400	16,800	1.06	9	12	21.94	5 7/16	3 1/8
	20.00	E-75 IEU	36,900	412,400	0.430	3.640	5.498	5.116	10,232	12,542	12,964	HT46	6 1/4	3 1/4	47,600	901,200	29,600	1.29	9	15	22.69	5 13/32	3 1/8
	20.00	E-75 EU	36,900	412,400	0.430	3.640	5.498	5.116	10,232	12,542	12,964	NC50	6 5/8	3 5/8	41,700	1,026,000	21,600	1.13	9	12	22.77	5 13/16	3 1/2
	20.00	E-75 EU	36,900	412,400	0.430	3.640	5.498	5.116	10,232	12,542	12,964	HT50	6 1/4	3 5/8	59,200	1,028,000	35,500	1.60	9	15	22.31	5 13/16	3 1/2
	20.00	E-75 EU	36,900	412,400	0.430	3.640	5.498	5.116	10,232	12,542	12,964	XT46	6	3 1/2	58,100	910,300	34,900	1.57	10	15	21.93	5 5/8	3 3/8
	20.00	E-75 EU	36,900	412,400	0.430	3.640	5.498	5.116	10,232	12,542	12,964	XT50	6 3/8	3 1/2	81,200	1,256,300	48,700	2.20	10	15	22.99	5 31/32	3 3/8
	20.00	X-95 IBU	46,700	522,900	0.430	3.640	5.498	5.116	10,232	15,696	16,421	NC46	6 1/4	3	39,700	1,048,400	20,500	0.85	9	12	22.69	5 21/32	2 7/8
	20.00	X-95 EU	46,700	522,900	0.430	3.640	5.498	5.116	10,232	15,696	16,421	OH	6 1/4	3 1/4	40,700	1,043,800	21,500	0.87	9	12	22.59	5 11/16	3 1/8
4 1/2	20.00	X-95 IBU	46,700	522,900	0.430	3.640	5.498	5.116	10,232	15,696	16,421	H90	6	3 1/4	39,000	938,400	16,800	0.84	9	12	21.94	5 9/16	3 1/8
	20.00	X-95 IBU	46,700	522,900	0.430	3.640	5.498	5.116	10,232	15,696	16,421	HT46	6 1/4	3 1/4	47,600	901,200	29,600	1.02	9	15	22.69	5 13/32	3 1/8
	20.00	X-95 EU	46,700	522,900	0.430	3.640	5.498	5.116	10,232	15,696	16,421	NC50	6 5/8	3 1/2	41,500	1,109,900	23,400	0.97	9	12	23.00	5 15/16	3 3/8
	20.00	X-95 EU	46,700	522,900	0.430	3.640	5.498	5.116	10,232	15,696	16,421	HT50	6 1/4	3 1/2	62,700	1,109,900	37,600	1.34	9	15	22.55	5 13/16	3 3/8
	20.00	X-95 EU	46,700	522,900	0.430	3.640	5.498	5.116	10,232	15,696	16,421	XT46	6	3 1/2	58,100	910,300	34,900	1.24	10	15	21.93	5 5/8	3 3/8
	20.00	X-95 EU	46,700	522,900	0.430	3.640	5.498	5.116	10,232	15,696	16,421	XT50	6 3/8	3 1/2	81,200	1,256,300	48,700	1.74	10	15	22.99	5 31/32	3 3/8
	20.00	G-105 IEU	51,700	577,300	0.430	3.640	5.498	5.116	10,232	17,558	18,149	NC46	6 1/4	2 3/4	44,900	1,193,900	23,200	0.87	9	12	23.28	5 23/32	2 5/8
	20.00	G-105 EU	51,700	577,300	0.430	3.640	5.498	5.116	10,232	17,558	18,149	OH	6 1/4	3	46,600	1,191,100	24,600	0.90	9	12	22.97	5 3/4	2 7/8
	20.00	G-105 IEU	51,700	577,300	0.430	3.640	5.498	5.116	10,232	17,558	18,149	H90	6 1/4	3	45,700	1,065,700	21,800	0.88	9	12	22.69	5 5/8	2 7/8
	20.00	G-105 EU	51,700	577,300	0.430	3.640	5.498	5.116	10,232	17,558	18,149	HT46	6 1/4	3 1/4	47,600	901,200	28,600	0.92	9	15	22.69	5 7/16	3 1/8
4 1/2	20.00	G-105 EU	51,700	577,300	0.430	3.640	5.498	5.116	10,232	17,558	18,149	NC50	6 5/8	3 1/2	45,100	1,109,900	23,400	0.87	9	12	23.00	6 1/32	3 3/8
	20.00	G-105 EU	51,700	577,300	0.430	3.640	5.498	5.116	10,232	17,558	18,149	HT50	6 1/4	3 1/2	62,700	1,109,900	37,600	1.21	9	15	22.55	5 13/16	3 3/8
	20.00	G-105 EU	51,700	577,300	0.430	3.640	5.498	5.116	10,232	17,558	18,149	XT46	6	3 1/2	58,100	910,300	34,900	1.12	10	15	21.93	5 5/8	3 3/8
	20.00	S-135 IBU	66,400	742,200	0.430	3.640	5.498	5.116	10,232	22,575	23,935	NC46	6 1/4	2 3/4	44,900	1,193,900	23,200	0.88	9	12	23.28	5 15/16	2 5/8
	20.00	S-135 IBU	66,400	742,200	0.430	3.640	5.498	5.116	10,232	22,575	23,935	OH	6 3/8	2 3/4	52,200	1,326,600	27,400	0.79	9	12	23.61	5 31/32	2 5/8
	20.00	S-135 IBU	66,400	742,200	0.430	3.640	5.498	5.116	10,232	22,575	23,935	H90	6 3/8	2 3/4	51,700	1,221,100	24,600	0.78	9	12	23.57	5 27/32	2 5/8
	20.00	S-135 IBU	66,400	742,200	0.430	3.640	5.498	5.116	10,232	22,575	23,935	HT46	6 1/4	3	57,700	1,048,400	34,600	0.87	9	15	23.34	5 9/16	2 7/8
	20.00	S-135 EU	66,400	742,200	0.430	3.640	5.498	5.116	10,232	22,575	23,935	NC50	6 5/8	3 1/4	51,700	1,269,000	28,600	0.78	9	12	23.43	6 7/32	3 1/8
	20.00	S-135 EU	66,400	742,200	0.430	3.640	5.498	5.116	10,232	22,575	23,935	HT50	6 3/8	3 1/2	65,700	1,109,900	39,400	0.99	9	15	23.85	5 13/16	3 3/8
4 1/2	20.00	S-135 EU	66,400	742,200	0.430	3.640	5.498	5.116	10,232	22,575	23,935	XT46	6	3 1/4	64,800	1,069,300	38,900	0.98	10	15	22.42	5 5/8	3 1/8
	20.00	S-135 EU	66,400	742,200	0.430	3.640	5.498	5.116	10,232	22,575	23,935	XT50	6 3/8	3 1/2	81,200	1,256,300	48,700	1.22	10	15	23.99	5 31/32	3 3/8
	20.00	S-135 EU	66,400	742,200	0.430	3.640	5.498	5.116	10,232	22,575	23,935	GPD546	6 1/4	3	53,400	1,048,400	32,000	0.80	9	12	22.69	5 21/32	2 7/8
	20.00	Z-140 IEU	66,900	769,700	0.430	3.640	5.498	5.116	10,232	23,411	24,199	HT46	6 1/4	3	57,700	1,048,400	34,600	0.84	9	15	23.34	5 19/32	2 7/8
	20.00	Z-140 IEU	66,900	769,700	0.430	3.640	5.498	5.116	10,232	23,411	24,199	HT50	6 3/8	3 1/2	65,700	1,109,900	39,400	0.95	9	15	22.65	5 27/32	3 3/8
	20.00	Z-140 IEU	66,900	769,700	0.430	3.640	5.498	5.116	10,232	23,411	24,199	XT46	6 1/4	3 1/8	75,700	1,144,400	45,400	1.03	10	15	23.26	5 5/8	3
	20.00	Z-140 IEU	66,900	769,700	0.430	3.640	5.498	5.116	10,232	23,411	24,199	XT50	6 3/8	3 1/2	81,200	1,256,300	48,700	1.16	10	15	22.99	5 31/32	3 3/8
	20.00	V-150 IEU	73,900	824,700	0.430	3.640	5.498	5.116	10,232	25,093	25,927	GPD546	6 1/4	3	53,400	1,048,400	32,000	0.78	9	12	22.69	5 11/16	2 7/8
4 1/2	20.00	V-150 IEU	73,900	824,700	0.430	3.640	5.498	5.116	10,232	25,093	25,927	HT46	6 1/4	3	57,700	1,048,400	34,600	0.79	9	15	23.34	5 21/32	2 7/8
	20.00	V-150 IEU	73,900	824,700	0.430	3.640	5.498	5.116	10,232	25,093	25,927	HT50	6 3/8	3 1/2	65,700	1,109,900	39,400	0.89	9	15	22.85	5 29/32	3 3/8
	20.00	V-150 IEU	73,900	824,700	0.430	3.640	5.498	5.116	10,232	25,093	25,927	XT46	6 1/4	3 1/8	75,700	1,144,400	45,400	1.03	10	15	23.26	5 5/8	3
	20.00	V-150 IEU	73,900	824,700	0.430	3.640	5.498	5.116	10,232	25,093	25,927	XT50	6 3/8	3 1/2	81,200	1,256,300	48,700	1.10	10	15	22.99	5 31/32	3 3/8
	20.00	V-150 IEU	73,900	824,700	0.430	3.640	5.498	5.116	10,232	25,093	25,927	GPD546	6 1/2	4	56,700	902,900	32,000	0.72	9	12	22.69	5 3/4	2 7/8
5	19.50	E-75 IEU	41,200	395,600	0.362	4.276	5.275	5.708	11,415	9,503	9,962	NC50	6 5/8	3 3/4	36,100	999,100	19,800	0.92	9	12	22.12	5 7/8	3 5/8
5	19.50	E-75 IEU	41,200	395,600	0.362	4.276	5.275	5.708	11,415	9,503	9,962	HT50	6 5/8	3 3/4	53,300	939,100	32,000	1.29	9	15	22.57	5 13/16	3 5/8
5	19.50	E-75 IEU	41,200	395,600	0.362	4.276	5.275	5.708	11,415	9,503	9,962	FH	7	3 3/4	62,800	1,448,400	33,400	1.53	10	12	23.20	6 2/8	3 5/8

**Continue Table F.5: Drill pipe and related connection type physical properties.**

Size OD in.	Nominal Weight lb/ft	Grade and Upset Type	Torsional Yield Strength ft-lb	Tensile Yield Strength lb	Wall Thickness in.	Nominal ID in.	Pipe Body Section Area sq in.	Pipe Body Modulus cu in.	Polar Section Modulus cu in.	Internal Pressure psi	Collapse Pressure psi	Connection Type	Outside Diameter in.	Inside Diameter in.	Torsional Yield Strength ft-lb	Tensile Yield Strength lb	Make-up Torque ft-lb	Torsional Ratio Tool Joint to Pipe	Pin Tong Space in.	Box Tong Space in.	Minimum Tool Joint OD for Prem. Class in.		Drift Diameter in.	
																					* Box Tong Space in.	* Adjusted Weight lb/ft		
5 1/2	24.70	Z-140 IEU	105,600	926,100	0.415	4.670	6.630	7.944	15.698	17,489	18,486	FH7 1/2	3	90,200	1,925,500	47,700	0.95	10	12	30.69	7 1/32	2 7/8	0.848	
	24.70	Z-140 IEU	105,600	926,100	0.415	4.670	6.630	7.944	15.698	17,489	18,486	HT55	7	3 3/4	87,700	1,448,400	52,600	0.83	10	15	28.42	6 21/32	3 5/8	
	24.70	Z-140 IEU	105,600	926,100	0.415	4.670	6.630	7.944	15.698	17,489	18,486	XT54	6 3/4	4	86,600	1,155,100	52,000	0.82	10	15	27.17	6 11/32	3 7/8	
	24.70	Z-140 IEU	105,600	926,100	0.415	4.670	6.630	7.944	15.698	17,489	18,486	XT57	7	4 1/4	94,300	1,206,700	56,800	0.89	10	15	27.25	6 15/32	4 1/8	
	24.70	Z-140 IEU	105,600	926,100	0.415	4.670	6.630	7.944	15.698	17,489	18,486	GPDS65	7 1/8	3 3/4	89,300	1,475,100	53,600	0.85	10	12	28.12	6 23/32	3 5/8	
5 1/2	24.70	V-150 IEU	113,100	994,400	0.415	4.670	6.630	7.944	15.698	18,386	19,807	FH	7 1/2	3	90,200	1,925,500	47,700	0.80	10	12	30.69	7 3/32	2 7/8	
	24.70	V-150 IEU	113,100	994,400	0.415	4.670	6.630	7.944	15.698	18,386	19,807	HT55	7	3 3/4	87,700	1,448,400	52,600	0.78	10	15	28.42	6 23/32	3 5/8	
	24.70	V-150 IEU	113,100	994,400	0.415	4.670	6.630	7.944	15.698	18,386	19,807	XT54	6 3/4	4	86,600	1,155,100	52,000	0.77	10	15	27.17	6 7/16	3 7/8	
	24.70	V-150 IEU	113,100	994,400	0.415	4.670	6.630	7.944	15.698	18,386	19,807	XT57	7	4	106,200	1,403,100	63,700	0.94	10	15	27.85	6 15/32	3 7/8	
	24.70	V-150 IEU	113,100	994,400	0.415	4.670	6.630	7.944	15.698	18,386	19,807	GPDS65	7 1/8	4 1/8	86,600	1,196,700	40,000	0.59	10	12	27.31	6 31/32	4	
5 7/8	23.40	E-75 IEU	58,600	469,000	0.361	5.153	6.254	8.125	16,251	7,453	8,065	XT57	7	4 1/4	94,300	1,206,700	56,800	1.61	10	15	26.48	6 15/32	4 1/8	
	23.40	X-95 IEU	74,200	594,100	0.361	5.153	6.254	8.125	16,251	8,775	10,216	XT57	7	4 1/4	94,300	1,206,700	56,800	1.27	10	15	26.48	6 15/32	4 1/8	
5 7/8	23.40	G-105 IEU	82,000	656,600	0.361	5.153	6.254	8.125	16,251	9,362	11,291	XT57	7	4 1/4	94,300	1,206,700	56,800	1.15	10	15	26.48	6 15/32	4 1/8	
	23.40	S-135 IEU	106,500	644,200	0.361	5.153	6.254	8.125	16,251	10,825	14,517	XT57	7	4 1/4	94,300	1,206,700	56,800	0.89	10	15	26.48	6 15/32	4 1/8	
5 7/8	23.40	Z-140 IEU	109,400	975,500	0.361	5.153	6.254	8.125	16,251	11,023	15,054	XT57	7	4 1/4	94,300	1,206,700	56,800	0.86	10	15	26.48	6 17/32	4 1/8	
	23.40	V-150 IEU	117,200	939,000	0.361	5.153	6.254	8.125	16,251	11,378	16,130	XT57	7	4 1/4	94,300	1,206,700	56,800	0.80	10	15	26.48	6 5/8	4 1/8	
5 7/8	26.30	E-75 IEU	65,500	533,900	0.415	5.045	7.119	9,093	18,165	9,558	9,271	XT57	7	4 1/4	94,300	1,206,700	56,800	1.44	10	15	29.12	6 15/32	4 1/8	
	26.30	X-95 IEU	93,000	676,900	0.415	5.045	7.119	9,093	18,165	11,503	11,744	XT57	7	4 1/4	94,300	1,206,700	56,800	1.14	10	15	29.12	6 15/32	4 1/8	
5 7/8	26.30	G-105 IEU	91,700	747,400	0.415	5.045	7.119	9,093	18,165	12,414	12,990	XT57	7	4 1/4	94,300	1,206,700	56,800	1.03	10	15	29.12	6 15/32	4 1/8	
	26.30	S-135 IEU	117,900	961,000	0.415	5.045	7.119	9,093	18,165	14,892	16,698	XT57	7	4 1/4	94,300	1,206,700	56,800	0.80	10	15	29.12	6 5/8	4 1/8	
5 7/8	26.30	Z-140 IEU	122,300	996,600	0.415	5.045	7.119	9,093	18,165	15,266	17,306	XT57	7	4 1/4	94,300	1,206,700	56,800	0.77	10	15	29.12	6 21/32	4 1/8	
	26.30	V-150 IEU	131,000	1,067,800	0.415	5.045	7.119	9,093	18,165	15,976	18,543	XT57	7	4 1/4	94,300	1,206,700	56,800	0.72	10	15	29.12	6 3/4	4 1/8	
6 5/8	25.20	E-75 IEU	70,800	489,500	0.330	5.965	6.526	9.788	19,572	4,788	6,538	FH	8	5	73,700	1,448,400	38,400	1.04	10	13	29.79	7 7/16	4 7/8	
	25.20	E-75 IEU	70,800	489,500	0.330	5.965	6.526	9.788	19,572	4,788	6,538	HT65	8	5	99,700	1,448,400	59,800	1.41	10	16	29.38	7 11/32	4 7/8	
	25.20	E-75 IEU	70,800	489,500	0.330	5.965	6.526	9.788	19,572	4,788	6,538	XT85	8	5	125,300	1,543,700	81,200	1.92	10	15	29.18	7 11/32	4 7/8	
6 5/8	25.20	X-95 IEU	89,400	620,000	0.330	5.965	6.526	9.788	19,572	5,321	8,281	FH	8	5	73,700	1,448,400	38,400	0.82	10	13	29.79	7 5/8	4 7/8	
	25.20	X-95 IEU	89,400	620,000	0.330	5.965	6.526	9.788	19,572	5,321	8,281	HT65	8	5	99,700	1,448,400	59,800	1.12	10	16	29.38	7 11/32	4 7/8	
	25.20	X-95 IEU	89,400	620,000	0.330	5.965	6.526	9.788	19,572	5,321	8,281	XT85	8	5	125,300	1,543,700	81,200	1.51	10	15	29.18	7 11/32	4 7/8	
6 5/8	25.20	G-105 IEU	98,800	685,200	0.330	5.965	6.526	9.788	19,572	5,500	9,153	FH	8 1/4	4 3/4	98,200	1,676,100	44,600	0.87	10	13	30.25	7 11/16	4 5/8	
	25.20	G-105 IEU	98,800	685,200	0.330	5.965	6.526	9.788	19,572	5,500	9,153	HT65	8	5	99,700	1,448,400	59,800	1.01	10	16	29.38	7 11/32	4 7/8	
	25.20	G-105 IEU	98,800	685,200	0.330	5.965	6.526	9.788	19,572	5,500	9,153	XT85	8	5	125,300	1,543,700	81,200	1.37	10	15	29.18	7 11/32	4 7/8	
6 5/8	25.20	S-135 IEU	127,000	881,000	0.330	5.965	6.526	9.788	19,572	6,036	11,769	FH	8 1/2	4 1/4	109,200	2,102,900	56,100	0.86	10	13	32.36	7 29/32	4 1/8	
	25.20	S-135 IEU	127,000	881,000	0.330	5.965	6.526	9.788	19,572	6,036	11,769	HT65	8	5	99,700	1,448,400	59,800	0.79	10	16	29.38	7 5/8	4 7/8	
	25.20	S-135 IEU	127,000	881,000	0.330	5.965	6.526	9.788	19,572	6,036	11,769	XT85	8	5	125,300	1,543,700	81,200	1.07	10	15	29.18	7 11/32	4 7/8	
	25.20	S-135 IEU	127,000	881,000	0.330	5.965	6.526	9.788	19,572	6,036	11,769	GPDS65	8	4 7/8	107,500	1,598,400	64,500	0.85	10	13	29.13	7 5/8	4 3/4	
6 5/8	25.20	Z-140 IEU	131,700	913,700	0.330	5.965	6.526	9.788	19,572	6,121	12,204	FH	8 1/2	4 1/4	109,200	2,102,900	56,100	0.83	10	13	32.36	7 31/32	4 1/8	
	25.20	Z-140 IEU	131,700	913,700	0.330	5.965	6.526	9.788	19,572	6,121	12,204	HT65	8	5	99,700	1,448,400	59,800	0.78	10	16	29.38	7 11/16	4 7/8	
	25.20	Z-140 IEU	131,700	913,700	0.330	5.965	6.526	9.788	19,572	6,121	12,204	XT85	8	5	125,300	1,543,700	81,200	1.03	10	15	29.18	7 11/32	4 7/8	
	25.20	Z-140 IEU	131,700	913,700	0.330	5.965	6.526	9.788	19,572	6,121	12,204	GPDS65	8 1/4	4 7/8	108,200	1,598,400	64,900	0.82	10	13	29.91	7 21/32	4 3/4	

STRING SCHEMATIC				Page 1 of 2				
Company:	Lord of the Rigs Oil Company			Casing:	Size	Weight	Grade	Thread
Field:	Mount Doom			Conductor:	13 3/8	48	H-40	RTS
Well:	Bane-01			Surface:	9 5/8	32.300	H-40	RTS
Rig Type:	F-200			Production:	6 5/8	32.000	C-75	RTL
Location:	Middle Earth	Date:	January, 2024					
		Depth (feet)	Length (Feet)	WOB: 49000 lbf	Mud Type: KCL/Polymer			
				RPM: 150	Mud Weight: 9.5 ppg			
				BF: 0.85	Max OD & Min' ID of String: 9.000 3.000			
						OD (Inches)	ID (Inches)	
					E-75, 25.2 lbm/ft (NEW)	6.625	5.965	
		2550.00			HWDP-65 HWMS, 70 lbm/ft	6.625	4.000	
		2550.00	90.00		DRILL COLLAR, 192 lbm/ft	9.000	3.000	
		2640.00			STABILIZER	9.000	3.000	
		2880.00	240.00		DRILL COLLAR, 192 lbm/ft	9.000	3.000	
		2885.00	5.00		STABILIZER	9.000	3.000	
		JAR	120.00		DRILL COLLAR, 192 lbm/ft	9.000	3.000	
		3005.00	5.00		STABILIZER	9.000	3.000	
		3010.00			DRILL BIT	12.250	-	
<b>Engineers</b>								
Berat Tuğberk Günel, Enis Kırca, Defne Acar, Yusuf Sinan Şahin, Abdulkadir Sarıoğlu								

**Figure F.1:** Drill string tally for the surface stage.

STRING SCHEMATIC						Page 1 of 2										
Company: Lord of the Rigs Oil Company				Casing:		Size	Weight	Grade	Thread							
Field: Mount Doom	Well: Bane-01			Conductor:	13 3/8	48	H-40	RTS								
Rig Type: F-200	Location: Middle Earth			Surface:	9 5/8	32.300	H-40	RTS								
				Production:	6 5/8	32.000	C-75	RTL								
				Date:	January, 2024											
				Length	WOB: 51000 lbf		Mud Type: KCL/Polymer									
				(Feet)	RPM: 70		Mud Weight: 11 ppg									
					BF: 0.83		Max OD & Min' ID of String: 6.500 2.000									
							OD (Inches)	ID (Inches)								
				6820.00	E-75, 20 lbm/ft (NEW)											
				6820.00												
				90.00	HWDP-65 HWMS, 50 lbm/ft											
				6910.00												
				630.00	DRILL COLLAR, 102 lbm/ft											
				7540.00												
				5.00	STABILIZER											
				7545.00												
				60.00	DRILL COLLAR, 102 lbm/ft											
				7605.00												
				5.00	STABILIZER											
				7610.00	DRILL BIT											
Engineers																
Berat Tuğberk Günel, Enis Kırca, Defne Acar, Yusuf Sinan Şahin, Abdulkadir Sarıoğlu																

**Figure F.2:** Drill string tally for the production stage.

**G. APPENDIX:** Drilling Fluid Design

**Table G.1:** The cutting transport ratio modelling parameters for the conductor stage.

$Q_{\text{fluid}}$ , gal/min	$v_a$ , ft/min	$v_{\text{slip}}$ , gal/min	$v_t$ , gal/min	$F_t$
25	2	35	-33	-16.50
50	5	35	-30	-6.00
100	9	35	-26	-2.89
150	14	35	-21	-1.50
200	19	35	-16	-0.84
250	23	35	-12	-0.52
300	28	35	-7	-0.25
350	33	35	-2	-0.06
375	35	35	0	0.00
400	37	35	2	0.05
450	42	35	7	0.17
500	47	35	12	0.26

**Table G.2:** The cutting transport ratio modelling parameters for the surface stage.

$Q_{\text{fluid}}$ , gal/min	$v_a$ , ft/min	$v_{\text{slip}}$ , gal/min	$v_t$ , gal/min	$F_t$
25	5	35	-30	-6
50	12	35	-23	-1.92
100	22	35	-13	--0.59
150	35	35	-0.5	-0.01
200	35	35	0	0
250	47	35	12	0.26
300	57	35	22	0.39
350	69	35	34	0.49
375	81	35	46	0.57
400	92	35	57	0.62
450	104	35	69	0.66
500	116	35	81	0.70

**Table G.3:** The cutting transport ratio modelling parameters for the production stage.

<b><math>Q_{\text{fluid}}</math>, gal/min</b>	<b><math>v_a</math>, ft/min</b>	<b><math>v_{\text{slip}}</math>, gal/min</b>	<b><math>v_t</math>, gal/min</b>	<b><math>F_t</math></b>
25	11	45	-34	-3.09
50	25	45	-20	-0.8
95	45	45	0	0
100	53	45	8	0.15
150	71	45	26	0.37
200	95	45	50	0.53
250	116	45	71	0.61
300	141	45	96	0.68
350	166	45	121	0.73
400	187	45	142	0.76
450	212	45	167	0.79
500	236	45	191	0.81

**H. APPENDIX: Drilling Cost Analysis**

**Table H.1:** Authorization of Expenditure of the worst-case scenario.

Description	Cost, \$	Time, day	Operation Duration, day	Operation Cost, \$	Percent Operation Cost, %
<b>Time Dependent Costs</b>					
<b>Cementing</b>	4634	1	1	4634	0.3
<b>Fuel</b>	10900	1	27	294300	18.93
<b>Mob - Demob</b>	1448	1	27	39096	2.51
<b>Shale Shaker Sieve</b>	579	1	27	15633	1.01
<b>Personnel Expenses</b>	2317	1	27	62559	4.02
<b>Rig Rental</b>	15000	1	27	405000	26.04
<b>Spare Parts, Maintenance</b>	965	1	27	26055	1.68
<b>Engineering</b>	1159	1	27	31293	2.01
<b>Coring Service</b>	86890	1	3	260670	16.76
<b>Log Service</b>	2896	1	3	8688	0.56
<b>Contingency</b>	965	1	27	26055	1.68
<b>Housing</b>	772	1	27	20844	1.34
<b>Invisible costs</b>	965	1	27	26055	1.68
<b>Risks</b>	1274	1	27	34398	2.21
<b>Depreciation</b>	10620	1	27	286740	18.44
<b>Security</b>	193	1	27	5211	0.34
<b>Transportation</b>	290	1	27	7830	0.5
<b>Day Total</b>	<b>141867</b>	1	<b>Operation Total</b>	<b>1555061</b>	<b>100</b>
<b>Material Costs</b>					
<b>Bits</b>	202744	-			
<b>BHA</b>	144817	-			
<b>Mud Chemicals</b>	347561	-			
<b>Casing</b>	724085	-			
<b>Cementing</b>	463415	-			
<b>Wellhead System</b>	250000	-			
<b>Contingency</b>	40000	-			
<b>Site Prep</b>	100000	-			
<b>Logging</b>	150000	-			
<b>Material Total</b>	<b>2422622</b>				
<b>TOTAL</b>	<b>3977683</b>				

**Table H.2:** Authorization for Expenditure of the middle-case scenario.

Description	Cost, \$	Time , day	Operation Duration, day	Operation Cost, \$	Percent Operation Cost, %
<b>Time Dependent Costs</b>					
<b>Cementing</b>	4634	1	1	4634	0.43
<b>Fuel</b>	10900	1	19.00	207100	19.08
<b>Mob - Demob</b>	1448	1	19.00	27512	2.53
<b>Shale Shaker Sieve</b>	579	1	19.00	11001	1.01
<b>Personnel Expenses</b>	2317	1	19.00	44023	4.05
<b>Rig Rental</b>	15000	1	19.00	285000	26.25
<b>Spare Parts, Maintenance</b>	965	1	19.00	18335	1.69
<b>Engineering</b>	1159	1	19.00	22021	2.03
<b>Coring Service</b>	86890	1	2	173780	16.01
<b>Log Service</b>	2896	1	2	5792	0.53
<b>Contingency</b>	965	1	19.00	18335	1.69
<b>Housing</b>	772	1	19.00	14668	1.35
<b>Invisible costs</b>	965	1	19.00	18335	1.69
<b>Risks</b>	1274	1	19.00	24206	2.23
<b>Depreciation</b>	10620	1	19.00	201780	18.59
<b>Security</b>	193	1	19.00	3667	0.34
<b>Transportation</b>	290	1	19.00	5510	0.51
<b>Day Total</b>	<b>141867</b>	1	<b>Operation Total</b>	<b>1085699</b>	<b>100</b>
<b>Material Costs</b>					
<b>Bits</b>	202744	-			
<b>BHA</b>	144817	-			
<b>Mud Chemicals</b>	347561	-			
<b>Casing</b>	724085	-			
<b>Cementing</b>	463415	-			
<b>Wellhead System</b>	250000	-			
<b>Contingency</b>	40000	-			
<b>Site Prep</b>	100000	-			
<b>Logging</b>	150000	-			
<b>Material Total</b>	<b>242262</b>	<b>2</b>			
<b>TOTAL</b>	<b>350832</b>	<b>1</b>			

**Table H.3:** Authorization for Expenditure of best-case scenario.

Description	Cost, \$	Time, day	Operation Duration, day	Operation Cost, \$	Percent Operation Cost, %
<b>Time Dependent Costs</b>					
<b>Cementing</b>	4634	1	1	4634	0.57
<b>Fuel</b>	10900	1	15.00	163500	20.28
<b>Mob - Demob</b>	1448	1	15.00	21720	2.69
<b>Shale Shaker Sieve</b>	579	1	15.00	8685	1.08
<b>Personnel Expenses</b>	2317	1	15.00	34755	4.31
<b>Rig Rental</b>	15000	1	15.00	225000	27.91
<b>Spare Parts, Maintenance</b>	965	1	15.00	14475	1.8
<b>Engineering</b>	1159	1	15.00	17385	2.16
<b>Coring Service</b>	86890	1	1	86890	10.78
<b>Log Service</b>	2896	1	1	2896	0.36
<b>Contingency</b>	965	1	15.00	14475	1.8
<b>Housing</b>	772	1	15.00	11580	1.44
<b>Invisible costs</b>	965	1	15.00	14475	1.8
<b>Risks</b>	1274	1	15.00	19110	2.37
<b>Depreciation</b>	10620	1	15.00	159300	19.76
<b>Security</b>	193	1	15.00	2895	0.36
<b>Transportation</b>	290	1	15.00	4350	0.54
<b>Day Total</b>	<b>141867</b>	1	<b>Operation Total</b>	<b>806125</b>	<b>100</b>
<b>Material Costs</b>					
<b>Bits</b>	202744	-			
<b>BHA</b>	144817	-			
<b>Mud Chemicals</b>	347561	-			
<b>Casing</b>	724085	-			
<b>Cementing</b>	463415	-			
<b>Wellhead System</b>	250000	-			
<b>Contingency</b>	40000	-			
<b>Site Prep</b>	100000	-			
<b>Logging</b>	150000	-			
<b>Material Total</b>	<b>2422622</b>				
<b>TOTAL</b>	<b>3228747</b>				

**i. APPENDIX: Reservoir Engineering**

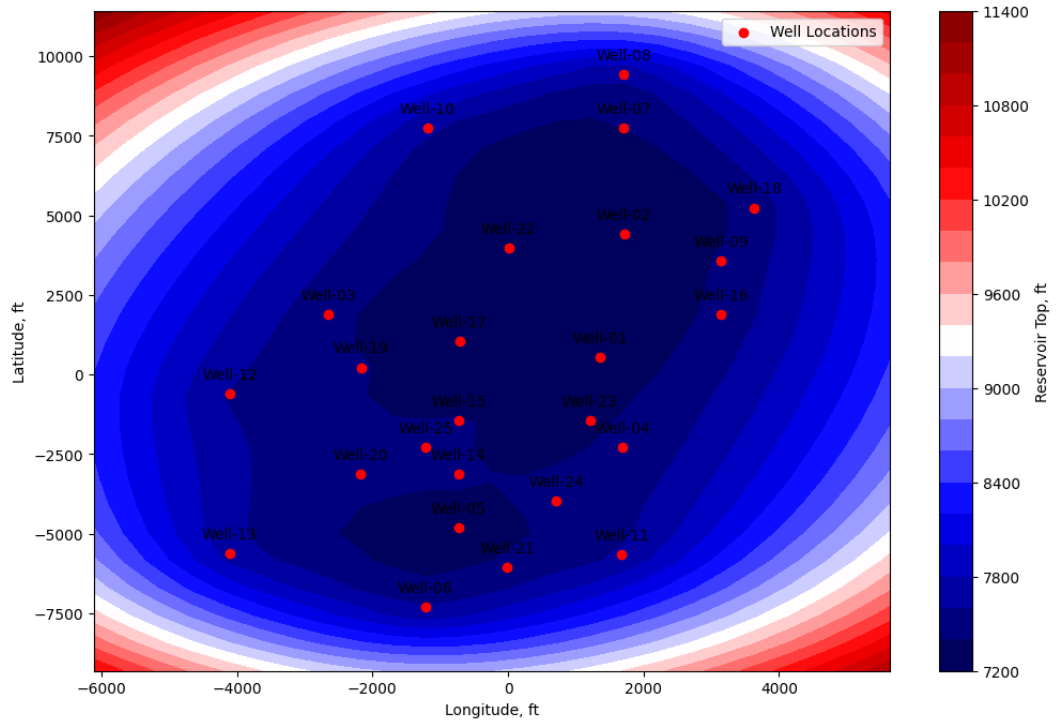


**Figure I.1:** The Distribution map of reservoir tops.

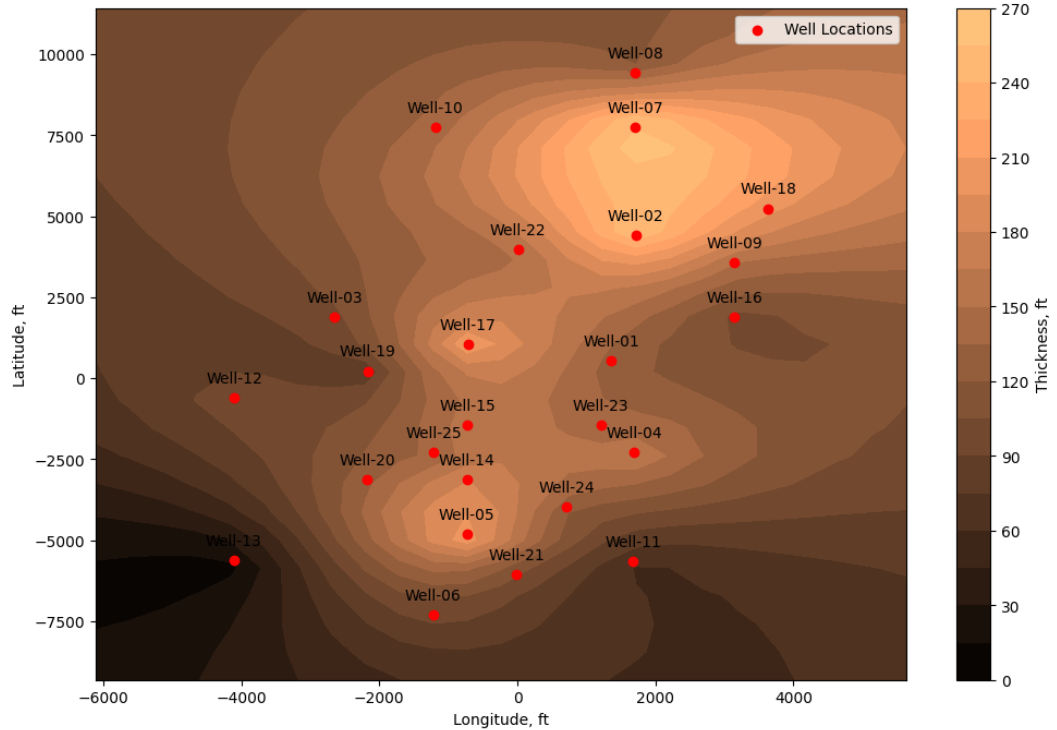


**Figure I.2:** The distribution map of the pay thicknesses.

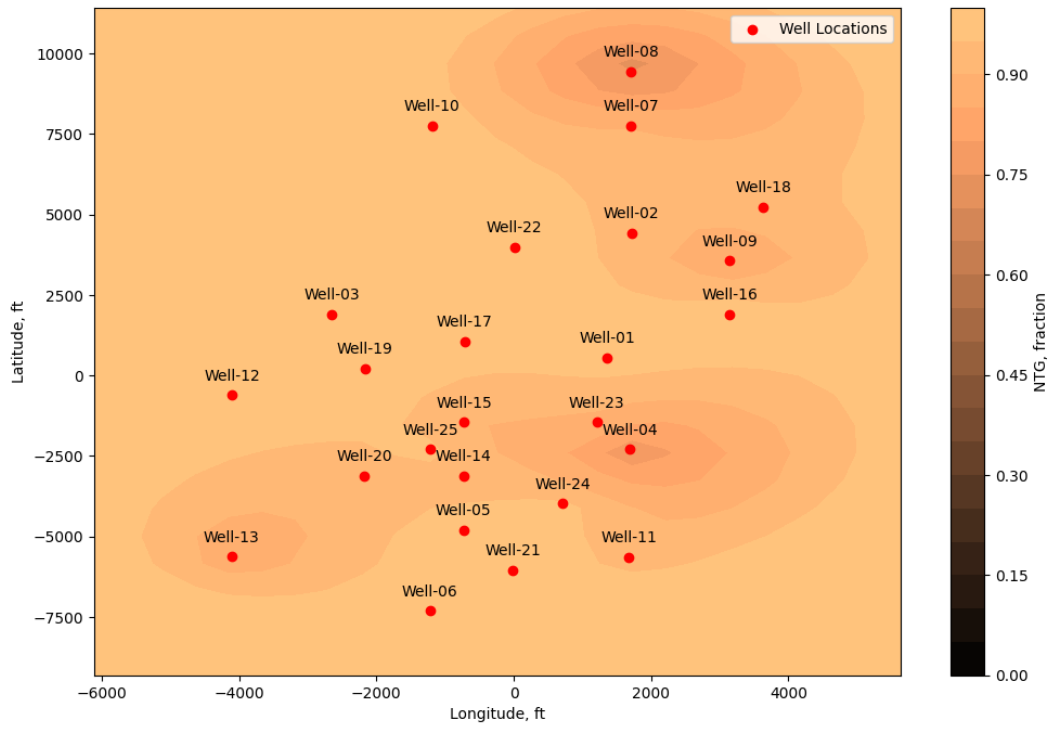


**Figure I.3:** The distribution map of the net to gross ratios.

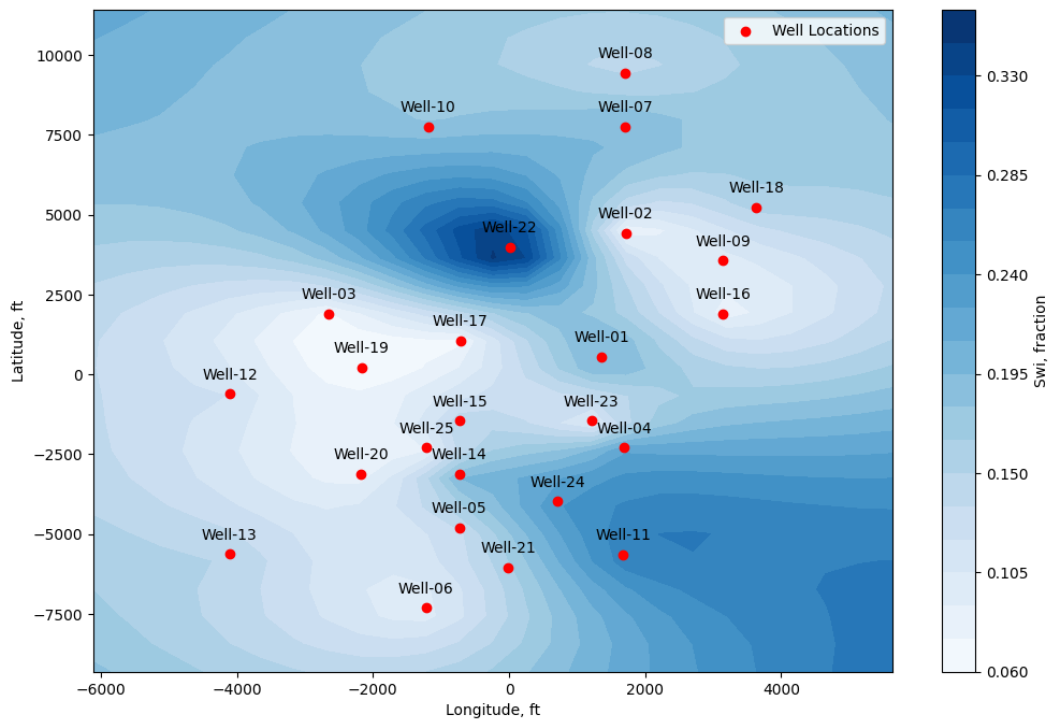


**Figure I.4:** The distribution map of the initial water saturation.

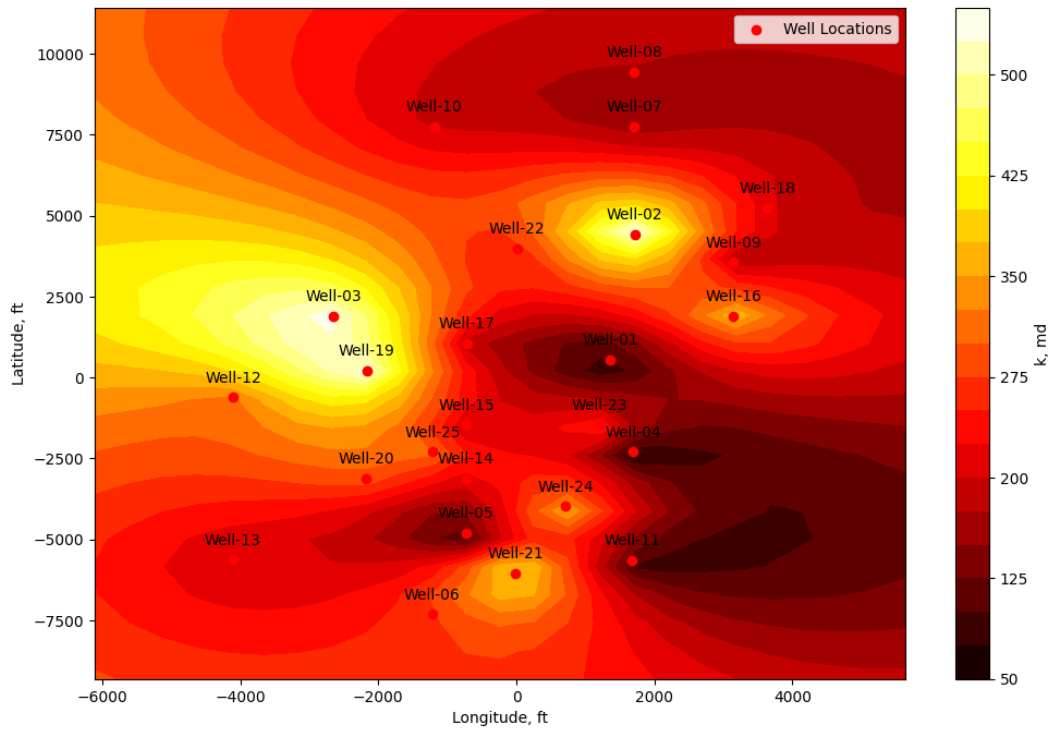


**Figure I.5:** The distribution map of permeabilities in absolute.

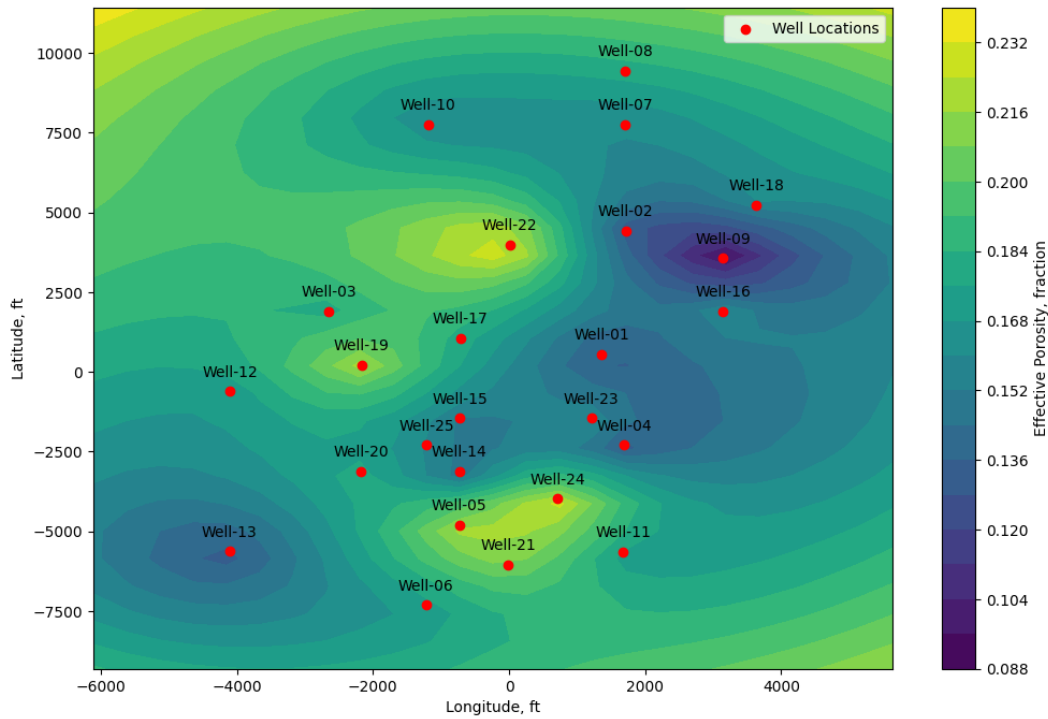


**Figure I.6:** The distribution map of effective porosities.

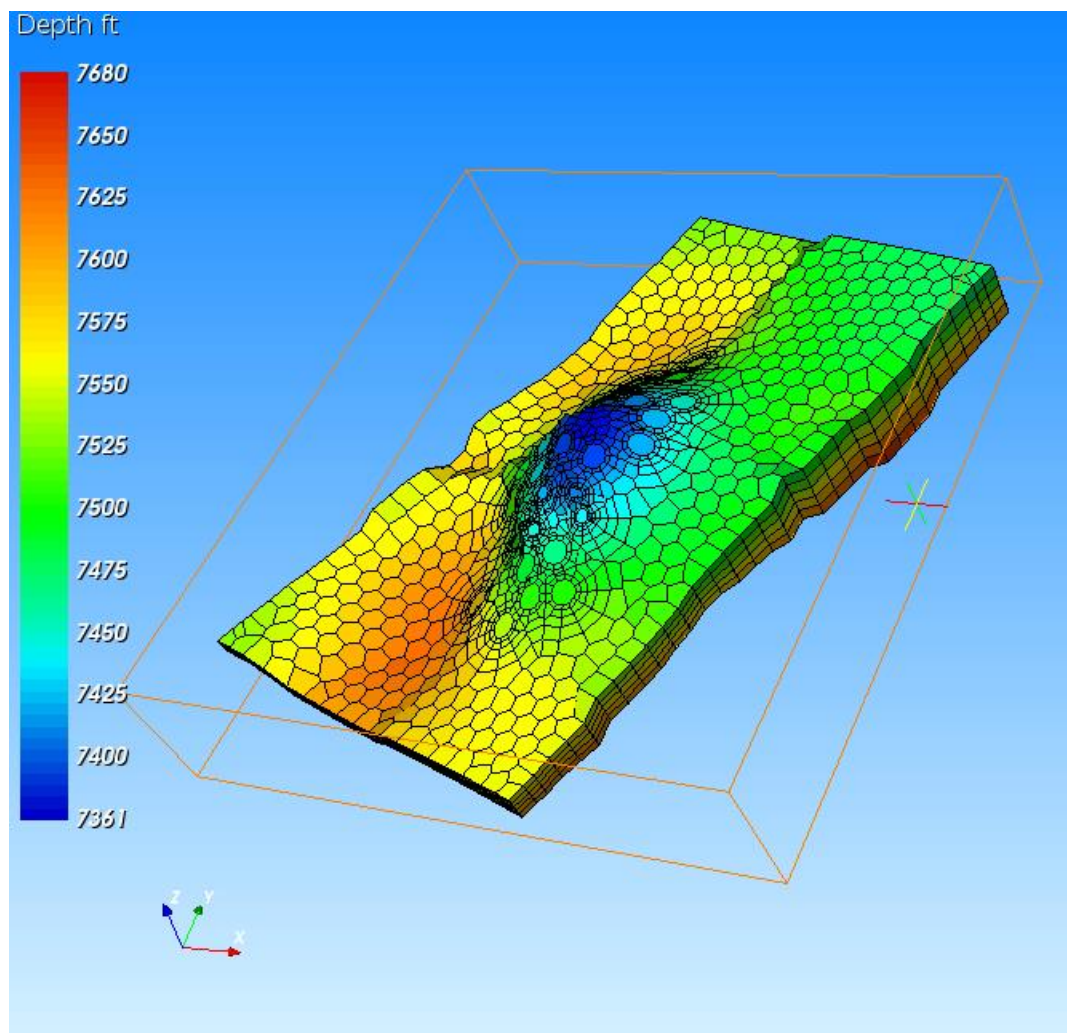


**Figure I.7:** The depth of the reservoir in 3-D given with its grid blocks.

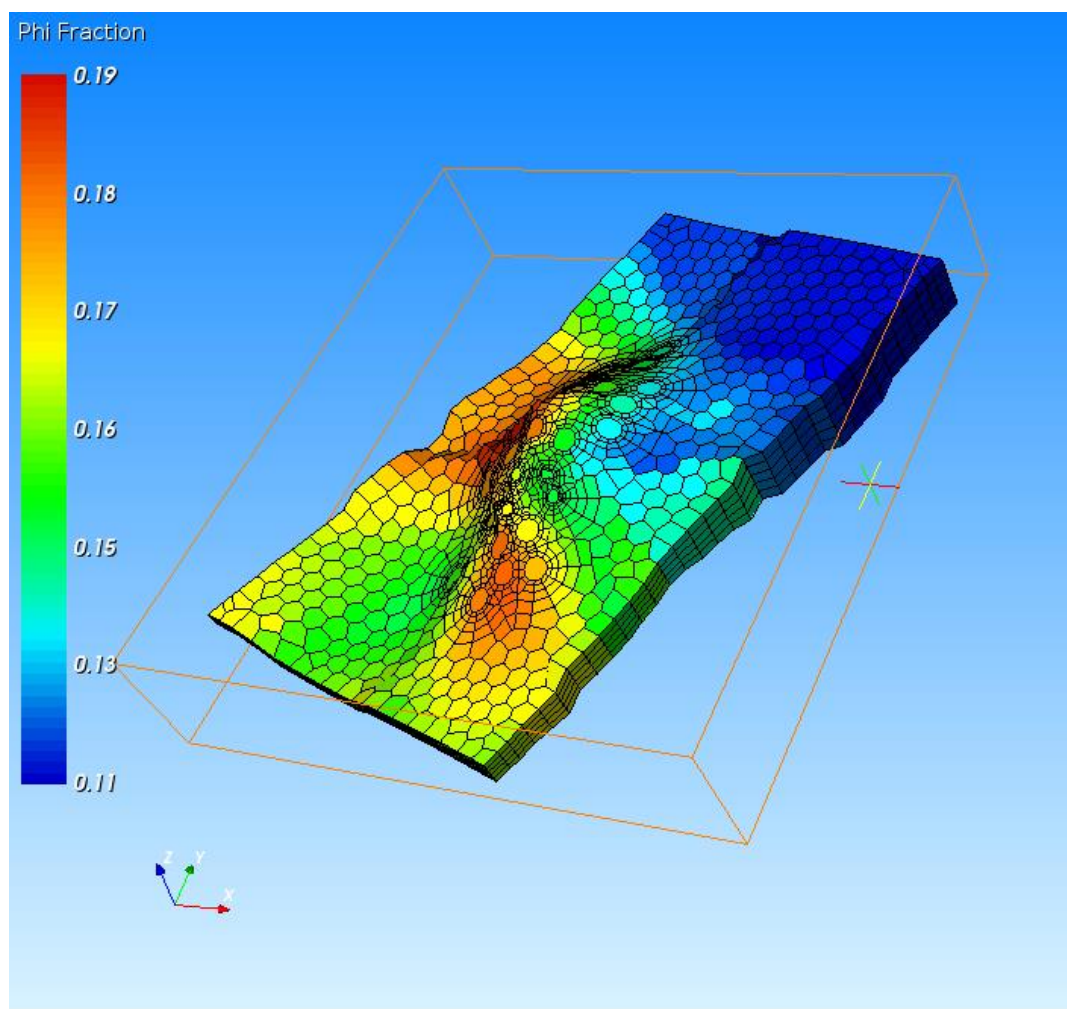


**Figure I.8:** The porosity values of the reservoir in 3-D given with its grid blocks.

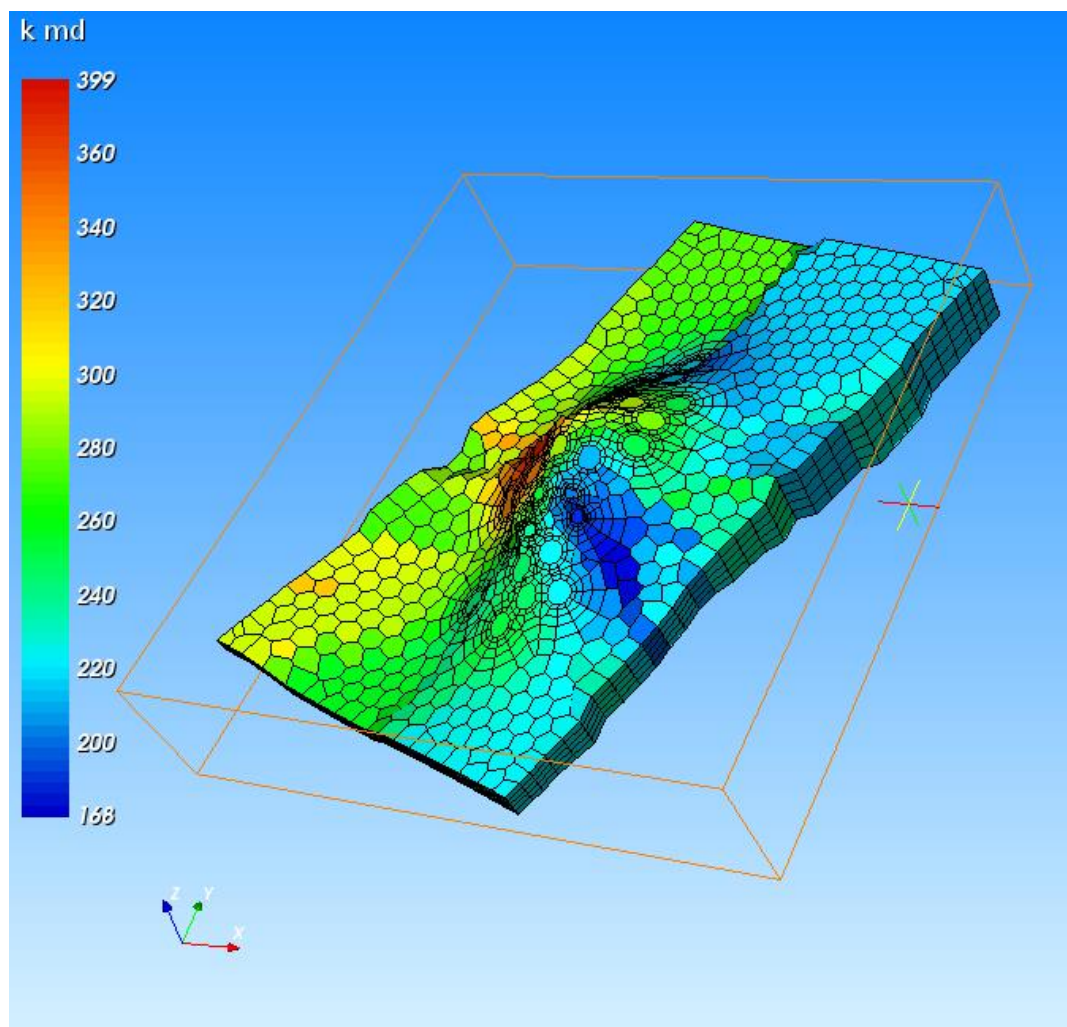


**Figure I.9:** The permeability values of the reservoir in 3-D given with its grid blocks.

**J. APPENDIX: Simulation Forecasts and Field Development Plans**

**Table J.1:** Cash flow table for the base scenario.

	1	2	3	4	5	6	7	8	9	10	11	12	13	14	15	16
BASE	Gross Production		WI Production			R	Capital Investment		Oper. & Main.	Net Revenue	NCF	Income	NCF	Depreciation	Net Revenue	
Year	Oil (STB)	Gas (MSCF)	Oil	Gas	Oil	Gas	Total	Tangible	Intangible	Expenses	After Expenses	Before Tax	Tax	After Tax		After Expenses & Depr.
0	0	0	0	0	0	0	0	7,815,900	3,136,000	6,500,000	-6,500,000	-17,451,900	0	-17,451,900	14,920,306	-24,556,306
1	19,562,569	9,914,132	17,117,248	8,674,866	1,369,379,862	0	1,369,379,862	13,294,865	3,449,600	62,653,591	1,306,726,271	1,289,981,807	405,792,157	884,189,650	14,920,306	1,288,356,365
2	15,937,269	8,077,603	13,945,110	7,067,902	1,115,608,807	0	1,115,608,807	9,906,770	3,794,560	52,025,327	1,063,583,480	1,049,882,150	328,698,741	721,183,409	14,920,306	1,044,868,613
3	11,303,163	5,729,297	9,890,268	5,013,134	791,221,408	0	791,221,408	10,402,963	4,174,016	39,335,650	751,885,758	737,308,779	229,818,862	507,489,917	14,920,306	732,791,435
4	9,454,498	4,792,399	8,272,686	4,193,349	661,814,843	0	661,814,843	11,443,259	4,591,418	34,962,009	626,852,834	610,818,157	189,991,257	420,826,901	14,920,306	607,341,110
5	8,117,732	4,114,871	7,103,016	3,600,512	568,241,270	0	568,241,270	12,587,585	5,050,559	32,222,831	536,018,439	518,380,295	160,959,728	357,420,567	14,920,306	516,047,573
6	6,339,544	3,213,611	5,547,101	2,811,910	443,768,059	0	443,768,059	13,846,344	5,555,615	28,362,353	415,405,706	396,003,747	122,470,469	273,533,278	14,920,306	394,929,785
7	4,784,155	2,425,230	4,186,135	2,122,076	334,890,822	0	334,890,822	15,230,978	6,111,177	25,299,174	309,591,648	288,249,493	88,632,800	199,616,693	14,920,306	288,560,165
8	4,651,472	2,357,975	4,070,038	2,063,228	325,603,006	0	325,603,006	16,754,076	6,722,295	26,208,732	299,394,274	275,917,904	85,052,429	190,865,475	14,920,306	277,751,673
9	3,834,686	1,943,956	3,355,350	1,700,961	268,428,006	0	268,428,006	18,429,483	7,394,524	25,403,384	243,024,622	217,200,614	66,809,676	150,390,938	14,920,306	220,709,791
10	3,236,232	1,640,603	2,831,703	1,435,528	226,536,242	0	226,536,242	20,272,432	8,133,976	25,332,764	201,203,478	172,797,070	53,136,779	119,660,291	14,920,306	178,149,195
	17	18	19	20	21			\$149,984,654								\$5,524,949,399
	Depletion		Net Revenue After			Tax	Discounted NCF	Cum. Discount. NCF	NPV for Profile		NPV for Profile					
Year	Gross	Net	Allowable	Exp. Depr., Depl.		Year			i*		i*					
0				-\$24,556,306		\$0	0	-\$17,451,900	-\$17,451,900	0%	\$3,807,725,220	55%	\$1,141,460,476			FRACTIONS
1	\$273,875,972	\$644,178,182	\$273,875,972	\$1,014,480,392	\$405,792,157	1	\$803,808,772	\$786,356,872	5%	\$3,188,988,908	60%	\$1,070,538,045	Salvage Cost	\$781,590.00		
2	\$223,121,761	\$522,434,307	\$223,121,761	\$821,746,852	\$328,698,741	2	\$596,019,346	\$1,382,376,219	10%	\$2,728,813,537	65%	\$1,007,776,898	Salvage / Initial Cost	10.00%	0.1	
3	\$158,244,282	\$366,395,718	\$158,244,282	\$574,547,154	\$229,818,862	3	\$381,284,686	\$1,763,660,905	15%	\$2,376,742,368	70%	\$951,852,976	Gas Price, per MSCF	\$0.00		
4	\$132,362,969	\$303,670,555	\$132,362,969	\$474,978,141	\$189,991,257	4	\$287,430,436	\$2,051,091,340	20%	\$2,100,642,179	75%	\$901,711,283	Life of Equipment, years	10		
5	\$113,648,254	\$258,023,787	\$113,648,254	\$402,399,319	\$160,959,728	5	\$221,930,051	\$2,273,021,392	25%	\$1,879,405,540	80%	\$856,501,640	Oil Price, per barrel	\$80.00		
6	\$88,753,612	\$197,464,892	\$88,753,612	\$306,176,173	\$122,470,469	6	\$154,402,405	\$2,427,423,796	30%	\$1,698,770,504	85%	\$815,531,770	Working Interest	100.00%	1	
7	\$66,978,164	\$144,280,082	\$66,978,164	\$221,582,000	\$88,632,800	7	\$102,434,927	\$2,529,858,723	35%	\$1,548,849,129	90%	\$778,232,572	Royalty Interest	12.50%	0.125	
8	\$65,120,601	\$138,875,837	\$65,120,601	\$212,631,072	\$85,052,429	8	\$89,040,153	\$2,618,898,876	40%	\$1,422,623,146	95%	\$744,132,080	Federal Tax Rate	40.00%	0.4	
9	\$53,685,601	\$110,354,896	\$53,685,601	\$167,024,190	\$66,809,676	9	\$63,780,439	\$2,682,679,314	45%	\$1,315,003,341	100%	\$712,835,710	Depreciation Method	Straight Line		
10	\$45,307,248	\$89,074,598	\$45,307,248	\$132,841,947	\$53,136,779	10	\$46,134,222	\$2,728,813,537	50%	\$1,222,226,613			Depletion Method	20.00%	0.2	
							NPV \$2,728,813,537		RoR	5048%	DPI	157	Interest Rate *	10.00%	0.1	

**Table J.2:** Cash flow table for Project Watcher in the Water.

	1	2	3	4	5	6	7	8	9	10	11	12	13	14	15	16
PLAN 1	Gross Production		WI Production			Re	Capital Investment			Oper. & Main.	Net Revenue	NCF	Income	NCF	Depreciation	Net Revenue
Year	Oil (STB)	Gas (MSCF)	Oil	Gas	Oil	Gas	Total	Tangible	Intangible	Expenses	After Expenses	Before Tax	Tax	After Tax		After Expenses & Depr.
0	0	0	0	0	\$0	\$0	\$10,142,015	\$11,970,400	\$6,750,000	-\$6,750,000	-\$28,862,415	\$0	-\$28,862,415	\$19,467,403	-\$38,187,803	
1	24,172,578	12,252,715	21,151,006	10,721,125	\$1,692,080,443	\$0	\$1,692,080,443	\$18,085,347	\$13,167,440	\$78,615,376	\$1,613,465,067	\$1,582,212,280	\$496,965,654	\$1,085,246,626	\$19,467,403	\$1,580,830,224
2	19,014,125	9,638,609	16,637,359	8,433,783	\$1,330,988,720	\$0	\$1,330,988,720	\$13,087,563	\$14,484,184	\$63,552,193	\$1,267,436,528	\$1,239,864,781	\$386,914,879	\$852,949,902	\$19,467,403	\$1,233,484,941
3	13,230,417	6,707,065	11,576,615	5,868,682	\$926,129,171	\$0	\$926,129,171	\$13,499,022	\$15,932,602	\$47,782,591	\$878,346,580	\$848,914,956	\$263,088,296	\$585,826,659	\$19,467,403	\$842,946,575
4	10,362,727	5,253,438	9,067,387	4,596,758	\$725,390,924	\$0	\$725,390,924	\$14,848,924	\$17,525,863	\$40,727,471	\$684,663,453	\$652,288,666	\$201,036,801	\$451,251,865	\$19,467,403	\$647,670,188
5	8,340,861	4,228,519	7,298,253	3,699,954	\$583,860,272	\$0	\$583,860,272	\$16,333,817	\$19,278,449	\$36,187,530	\$547,672,741	\$512,060,476	\$156,861,934	\$355,198,542	\$19,467,403	\$508,926,890
6	6,941,336	3,519,060	6,073,669	3,079,177	\$485,893,549	\$0	\$485,893,549	\$17,967,198	\$21,206,294	\$33,502,470	\$452,391,079	\$413,217,586	\$125,815,469	\$287,402,118	\$19,467,403	\$411,717,382
7	5,988,259	3,035,912	5,239,727	2,656,423	\$419,178,136	\$0	\$419,178,136	\$19,763,918	\$23,326,923	\$32,118,044	\$387,060,092	\$343,969,251	\$104,172,056	\$239,797,195	\$19,467,403	\$344,265,766
8	5,540,614	2,808,984	4,848,037	2,457,861	\$387,842,994	\$0	\$387,842,994	\$21,740,310	\$25,659,615	\$32,277,635	\$355,565,358	\$308,165,433	\$93,147,896	\$215,017,536	\$19,467,403	\$310,438,340
9	5,064,144	2,567,444	4,431,126	2,246,513	\$354,490,070	\$0	\$354,490,070	\$23,914,341	\$28,225,577	\$32,468,271	\$322,021,800	\$269,881,882	\$81,372,322	\$188,509,559	\$19,467,403	\$274,328,820
10	4,712,123	2,388,990	4,123,107	2,090,366	\$329,848,582	\$0	\$329,848,582	\$26,305,775	\$31,048,135	\$33,136,197	\$296,712,385	\$239,358,476	\$72,090,853	\$167,267,623	\$19,467,403	\$246,196,848
17	18	19	20	21			\$195,688,229									\$6,362,618,171
Depletion		Net Revenue After			Tax		Discounted NCF		Cum. Discount. NCF		NPV for Profile		NPV for Profile			
Year	Gross	Net	Allowable	Exp., Depr., Depl.	Year			i*		i*						
0	\$0	-\$19,093,901	-\$19,093,901	-\$19,093,901	\$0	0	-\$28,862,415	-\$28,862,415	0%	\$4,399,605,211	55%	\$1,345,596,183				FRACTIONS
1	\$338,416,089	\$790,415,112	\$338,416,089	\$1,242,414,136	\$496,965,654	1	\$986,587,842	\$957,725,427	5%	\$3,688,587,338	60%	\$1,263,688,687	Salvage Cost	\$1,014,201.50		
2	\$266,197,744	\$616,742,471	\$266,197,744	\$967,287,197	\$386,914,879	2	\$704,917,275	\$1,662,642,702	10%	\$3,161,571,898	65%	\$1,191,052,492	Salvage / Initial Cost	10.00%	0.1	
3	\$185,225,834	\$421,473,287	\$185,225,834	\$657,720,741	\$263,088,296	3	\$440,140,240	\$2,102,782,941	15%	\$2,759,196,987	70%	\$1,126,193,889	Gas Price, per MSCF	\$0.00		
4	\$145,078,185	\$323,835,094	\$145,078,185	\$502,592,003	\$201,036,801	4	\$308,211,096	\$2,410,994,037	20%	\$2,443,948,746	75%	\$1,067,922,765	Life of Equipment, years	10		
5	\$116,772,054	\$254,463,445	\$116,772,054	\$392,154,835	\$156,861,934	5	\$220,550,348	\$2,631,544,386	25%	\$2,191,355,658	80%	\$1,015,279,767	Oil Price, per barrel	\$80.00		
6	\$97,178,710	\$205,858,691	\$97,178,710	\$314,538,672	\$125,815,469	6	\$162,231,003	\$2,793,775,388	30%	\$1,984,983,362	85%	\$967,483,252	Working Interest	100.00%	1	
7	\$83,835,627	\$172,132,883	\$83,835,627	\$260,430,139	\$104,172,056	7	\$123,053,877	\$2,916,829,266	35%	\$1,813,497,507	90%	\$923,890,116	Royalty Interest	12.50%	0.125	
8	\$77,568,599	\$155,219,170	\$77,568,599	\$232,869,741	\$93,147,896	8	\$100,307,268	\$3,017,136,534	40%	\$1,668,888,646	95%	\$883,966,468	Federal Tax Rate	40.00%	0.4	
9	\$70,898,014	\$137,164,410	\$70,898,014	\$203,430,806	\$81,372,322	9	\$79,946,455	\$3,097,082,989	45%	\$1,545,369,740	100%	\$847,265,418	Depreciation Method	Straight Line		
10	\$65,969,716	\$123,098,424	\$65,969,716	\$180,227,131	\$72,090,853	10	\$64,488,910	\$3,161,571,898	50%	\$1,438,673,861			Depletion Method	20.00%	0.2	
					NPV	\$3,161,571,898			RoR	3738%	DPI	111	Interest Rate *	10.00%	0.1	

**Table J.3:** Cash flow table for Project Deflate the Smaug.

	1	2	3	4	5	6	7	8	9	10	11	12	13	14	15	16
PLAN 1	Gross Production		WI Production			Re	Capital Investment		Oper. & Main.	Net Revenue	NCF	Income	NCF	Depreciation	Net Revenue	
Year	Oil (STB)	Gas (MSCF)	Oil	Gas	Oil	Gas	Total	Tangible	Intangible	Expenses	After Expenses	Before Tax	Tax	After Tax	After Expenses & Depr.	
0	0	0	0	0	\$0	\$0	\$7,815,900	\$6,136,000	\$6,500,000	-\$6,500,000	-\$20,451,900	\$0	-\$20,451,900	\$18,061,947	-\$30,697,947	
1	40,242,189	20,398,477	35,211,915	17,848,667	\$2,816,953,235	\$0	\$2,816,953,235	\$41,480,746	\$6,749,600	\$115,654,261	\$2,701,298,973	\$2,653,068,628	\$845,238,712	\$1,807,829,916	\$18,061,947	\$2,676,487,427
2	21,490,092	10,894,019	18,803,830	9,532,267	\$1,504,306,410	\$0	\$1,504,306,410	\$13,137,292	\$7,424,560	\$63,750,281	\$1,440,556,129	\$1,419,994,277	\$445,683,336	\$974,310,941	\$18,061,947	\$1,415,069,623
3	8,677,261	4,398,987	7,592,604	3,849,114	\$607,408,286	\$0	\$607,408,286	\$10,402,963	\$8,167,016	\$30,760,478	\$576,647,808	\$558,077,829	\$171,574,875	\$386,502,954	\$18,061,947	\$550,418,845
4	5,591,747	2,834,836	4,892,779	2,480,482	\$391,422,301	\$0	\$391,422,301	\$11,443,259	\$8,983,718	\$23,653,857	\$367,768,444	\$347,341,467	\$104,975,328	\$242,366,139	\$18,061,947	\$340,722,780
5	4,373,095	2,217,056	3,826,458	1,939,924	\$306,116,676	\$0	\$306,116,676	\$12,587,585	\$9,882,089	\$21,478,319	\$284,638,357	\$262,168,682	\$78,188,394	\$183,980,288	\$18,061,947	\$256,694,320
6	3,778,169	1,915,459	3,305,898	1,676,027	\$264,471,832	\$0	\$264,471,832	\$13,846,344	\$10,870,298	\$21,007,137	\$243,464,695	\$218,748,053	\$64,655,233	\$154,092,820	\$18,061,947	\$214,532,450
7	3,446,678	1,747,410	3,015,843	1,528,983	\$241,267,448	\$0	\$241,267,448	\$15,230,978	\$11,957,328	\$21,315,045	\$219,952,402	\$192,764,096	\$56,671,855	\$136,092,241	\$18,061,947	\$189,933,127
8	3,116,309	1,579,928	2,726,771	1,382,437	\$218,141,649	\$0	\$218,141,649	\$16,754,076	\$13,153,061	\$21,744,470	\$196,397,179	\$166,490,042	\$48,621,537	\$117,868,506	\$18,061,947	\$165,182,171
9	2,865,140	1,452,596	2,506,998	1,271,022	\$200,559,801	\$0	\$200,559,801	\$18,429,483	\$14,468,367	\$22,501,959	\$178,057,843	\$145,159,992	\$42,166,227	\$102,993,765	\$18,061,947	\$145,527,529
10	2,651,542	1,344,310	2,320,099	1,176,271	\$185,607,914	\$0	\$185,607,914	\$20,272,432	\$15,915,204	\$23,493,551	\$162,114,363	\$125,926,728	\$36,406,252	\$89,520,476	\$18,061,947	\$128,137,213
	17	18	19	20	21			\$181,401,057								\$6,052,007,538
	Depletion		Net Revenue After			Tax	Discounted NCF	Cum. Discount. NCF		NPV for Profile		NPV for Profile				
Year	Gross	Net	Allowable	Exp., Depr., Depl.		Year			i*		i*					
0	\$0	-\$15,348,973	-\$15,348,973	-\$15,348,973	\$0	0	-\$20,451,900	-\$20,451,900	0%	\$4,175,106,145	55%	\$1,741,869,483				FRACTIONS
1	\$563,390,647	\$1,338,243,713	\$563,390,647	\$2,113,096,780	\$845,238,712	1	\$1,643,481,742	\$1,623,029,842	5%	\$3,675,275,197	60%	\$1,658,232,706	Salvage Cost	\$781,590.00		
2	\$300,861,282	\$707,534,811	\$300,861,282	\$1,114,208,341	\$445,683,336	2	\$805,215,654	\$2,428,245,496	10%	\$3,288,405,678	65%	\$1,582,462,883	Salvage / Initial Cost	10.00%	0.1	
3	\$121,481,657	\$275,209,423	\$121,481,657	\$428,937,188	\$171,574,875	3	\$290,385,390	\$2,718,630,885	15%	\$2,980,186,938	70%	\$1,513,457,730	Gas Price, per MSCF	\$0.00		
4	\$78,284,460	\$170,361,390	\$78,284,460	\$262,438,319	\$104,975,328	4	\$165,539,334	\$2,884,170,220	20%	\$2,728,585,517	75%	\$1,450,317,907	Life of Equipment, years	10		
5	\$61,223,335	\$128,347,160	\$61,223,335	\$195,470,985	\$78,188,394	5	\$114,237,284	\$2,998,407,503	25%	\$2,518,966,329	80%	\$1,392,301,490	Oil Price, per barrel	\$80.00		
6	\$52,894,366	\$107,266,225	\$52,894,366	\$161,638,083	\$64,655,233	6	\$86,981,379	\$3,085,388,883	30%	\$2,341,303,509	85%	\$1,338,790,272	Working Interest	100.00%	1	
7	\$48,253,490	\$94,966,564	\$48,253,490	\$141,679,638	\$56,671,855	7	\$69,836,838	\$3,155,225,721	35%	\$2,188,532,568	90%	\$1,289,264,462	Royalty Interest	12.50%	0.125	
8	\$43,628,330	\$82,591,086	\$43,628,330	\$121,553,841	\$48,621,537	8	\$54,986,528	\$3,210,212,249	40%	\$2,055,546,656	95%	\$1,243,283,430	Federal Tax Rate	40.00%	0.4	
9	\$40,111,960	\$72,763,764	\$40,111,960	\$105,415,569	\$42,166,227	9	\$43,679,410	\$3,253,891,659	45%	\$1,938,567,555	100%	\$1,200,470,857	Depreciation Method	Straight Line		
10	\$37,121,583	\$64,068,606	\$37,121,583	\$91,015,630	\$36,406,252	10	\$34,514,019	\$3,288,405,678	50%	\$1,834,740,944			Depletion Method	20.00%	0.2	
							NPV \$3,288,405,677.97			RoR	8793%	DPI	162	Interest Rate *	10.00%	0.1

**Table J.4:** Cash flow table for Project One Rig to Drill Them All.

	1	2	3	4	5	6	7	8	9	10	11	12	13	14	15	16
PLAN 1	Gross Production		WI Production			Re	Capital Investment		Oper. & Main.	Net Revenue	NCF	Income	NCF	Depreciation	Net Revenue	
Year	Oil (STB)	Gas (MSCF)	Oil	Gas	Oil	Gas	Total	Tangible	Intangible	Expenses	After Expenses	Before Tax	Tax	After Tax	After Expenses & Depr.	
0	0	0	0	0	\$0	\$0	\$9,815,900	\$6,936,000	\$6,500,000	-\$6,500,000	-\$23,251,900	\$0	-\$23,251,900	\$21,387,302	-\$34,823,302	
1	39,652,065	20,100,703	34,695,557	17,588,116	\$2,775,644,545	\$0	\$2,775,644,545	\$40,693,798	\$7,629,600	\$121,054,916	\$2,654,589,630	\$2,606,266,232	\$828,177,528	\$1,778,088,704	\$21,387,302	\$2,625,572,728
2	22,604,609	11,459,750	19,779,033	10,027,281	\$1,582,322,613	\$0	\$1,582,322,613	\$14,935,455	\$8,392,560	\$71,847,350	\$1,510,475,263	\$1,487,147,248	\$465,692,351	\$1,021,454,897	\$21,387,302	\$1,480,695,401
3	12,158,849	6,164,298	10,638,992	5,393,761	\$851,119,398	\$0	\$851,119,398	\$13,064,963	\$9,231,816	\$43,919,492	\$807,199,906	\$784,903,127	\$242,542,763	\$542,360,364	\$21,387,302	\$776,580,788
4	8,636,484	4,378,594	7,556,924	3,831,270	\$604,553,885	\$0	\$604,553,885	\$14,371,459	\$10,154,998	\$35,349,859	\$569,204,026	\$544,677,569	\$166,700,380	\$377,977,189	\$21,387,302	\$537,661,726
5	6,857,854	3,476,888	6,000,622	3,042,277	\$480,049,795	\$0	\$480,049,795	\$15,808,605	\$11,170,497	\$31,560,019	\$448,489,776	\$421,510,674	\$127,968,807	\$293,541,866	\$21,387,302	\$415,931,977
6	5,688,606	2,884,118	4,977,530	2,523,603	\$398,202,413	\$0	\$398,202,413	\$17,389,466	\$12,287,547	\$29,515,299	\$368,687,114	\$339,010,102	\$102,148,713	\$236,861,388	\$21,387,302	\$335,012,266
7	5,194,747	2,633,750	4,545,404	2,304,531	\$363,632,313	\$0	\$363,632,313	\$19,128,412	\$13,516,302	\$29,341,313	\$334,291,000	\$301,646,286	\$90,664,374	\$210,981,913	\$21,387,302	\$299,387,397
8	4,865,359	2,466,763	4,257,189	2,158,417	\$340,575,109	\$0	\$340,575,109	\$21,041,253	\$14,867,932	\$29,787,261	\$310,787,848	\$274,878,662	\$82,567,037	\$192,311,625	\$21,387,302	\$274,532,614
9	4,588,740	2,326,526	4,015,148	2,035,710	\$321,211,805	\$0	\$321,211,805	\$23,145,379	\$16,354,725	\$30,465,589	\$290,746,216	\$251,246,112	\$75,504,731	\$175,741,381	\$21,387,302	\$253,004,190
10	4,404,953	2,233,354	3,854,334	1,954,184	\$308,346,722	\$0	\$308,346,722	\$25,459,917	\$17,990,198	\$31,530,329	\$276,816,393	\$233,366,279	\$70,307,820	\$163,058,459	\$21,387,302	\$237,438,894
	17	18	19	20	21			\$214,854,607								\$7,200,994,679
	Depletion			Net Revenue After	Tax		Discounted NCF	Cum. Discount. NCF		NPV for Profile		NPV for Profile				
Year	Gross	Net	Allowable	Exp., Depr., Depl.		Year		i*		i*						
0	\$0	-\$17,411,651	-\$17,411,651	-\$17,411,651	\$0	0	-\$23,251,900	-\$23,251,900	0%	\$4,969,125,886	55%	\$1,831,113,561				FRACTIONS
1	\$555,128,909	\$1,312,786,364	\$555,128,909	\$2,070,443,819	\$828,177,528	1	\$1,616,444,276	\$1,593,192,376	5%	\$4,276,370,201	60%	\$1,735,636,346	Salvage Cost	\$981,590.00		
2	\$316,464,523	\$740,347,701	\$316,464,523	\$1,164,230,879	\$465,692,351	2	\$844,177,600	\$2,437,369,977	10%	\$3,754,364,804	65%	\$1,649,904,882	Salvage / Initial Cost	10.00%	0.1	
3	\$170,223,880	\$388,290,394	\$170,223,880	\$606,356,909	\$242,542,763	3	\$407,483,369	\$2,844,853,345	15%	\$3,348,788,324	70%	\$1,572,451,795	Gas Price, per MSCF	\$0.00		
4	\$120,910,777	\$268,830,863	\$120,910,777	\$416,750,950	\$166,700,380	4	\$258,163,506	\$3,103,016,851	20%	\$3,025,272,700	75%	\$1,502,095,922	Life of Equipment, years	10		
5	\$96,009,959	\$207,965,989	\$96,009,959	\$319,922,018	\$127,968,807	5	\$182,266,404	\$3,285,283,255	25%	\$2,761,344,279	80%	\$1,437,875,226	Oil Price, per barrel	\$80.00		
6	\$79,640,483	\$167,506,133	\$79,640,483	\$255,371,783	\$102,148,713	6	\$133,702,079	\$3,418,985,334	30%	\$2,541,854,710	85%	\$1,378,997,718	Working Interest	100.00%	1	
7	\$72,726,463	\$149,693,698	\$72,726,463	\$226,660,934	\$90,664,374	7	\$108,267,081	\$3,527,252,415	35%	\$2,356,305,196	90%	\$1,324,805,040	Royalty Interest	12.50%	0.125	
8	\$68,115,022	\$137,266,307	\$68,115,022	\$206,417,592	\$82,567,037	8	\$89,714,793	\$3,616,967,208	40%	\$2,197,231,771	95%	\$1,274,745,052	Federal Tax Rate	40.00%	0.4	
9	\$64,242,361	\$126,502,095	\$64,242,361	\$188,761,829	\$75,504,731	9	\$74,531,501	\$3,691,498,709	45%	\$2,059,203,292	100%	\$1,228,350,934	Depreciation Method	Straight Line		
10	\$61,669,344	\$118,719,447	\$61,669,344	\$175,769,550	\$70,307,820	10	\$62,866,095	\$3,754,364,804	50%	\$1,938,183,284			Depletion Method	20.00%	0.2	
					NPV	\$3,754,364,804		RoR	7604%	DPI	162		Interest Rate *	10.00%	0.1	